Dissertation zur Erlangung des Doktorgrades
der Fakultät für Chemie und Pharmazie
der Ludwig-Maximilians-Universität München

Advanced Fluorescence Methodologies
for the Exploration of the Nanoworld

Nader Danaf

aus
Baalichmay, Libanon

2021

Erklärung

Diese Dissertation wurde im Sinne von § 7 der Promotionsordnung vom 28. November 2011 von Herrn Prof. Don C. Lamb, Ph.D., betreut.

Eidesstattliche Versicherung

Diese Dissertation wurde eigenständig und ohne unerlaubte Hilfe erarbeitet.

München, 21. 09. 2021

Nader Danaf

Dissertation eingereicht am: 16. 08. 2021

1. Gutachter Prof. Don C. Lamb
2. Gutachter Prof. Dr. Stefan Wuttke

Mündliche Prüfung am: 07. 09. 2021

Abstract

Advanced Fluorescence Methodologies for the Exploration of the Nanoworld

by Nader Danaf

Fluorescence spectroscopy and microscopy have emerged in the last few decades as robust methods to unravel the secrets of materials, their interactions and photophysical properties, on the nanoscale level. Confocal laser scanning microscopy (CLSM) is an important technique that utilizes the versatility of fluorescence as a tool to explore phenomena in the life- and material- sciences. In the scope of this thesis, a home built CLSM was upgraded and its advanced fluorescence method capabilities were used to investigate metal-organic frameworks (MOFs) and organic light emitting diodes (OLEDs). The interaction of differently functionalized MOF nanoparticles and serum proteins was studied by monitoring the fluorescence intensity fluctuations arising from the diffusion of fluorescently labeled nanoparticles through the small (~fL) confocal volume. This approach, known as the fluorescence correlation spectroscopy (FCS) analyzes the fluctuations of the recorded signal and extracts information regarding the rate of diffusion and the interaction between the MOFs and the proteins. In a second study, contrary to what was anticipated, rigid MOFs showed that a bulky linker was able to post-synthetically replace the organic likers of the original framework. Investigating the linker exchange via fluorescence imaging, combining the intensity and lifetime information, a new post synthetic linker exchange (PSE) mechanism in rigid MOFs was established. These studies show the versatility of utilizing CLSM measurements for FCS and fluorescence lifetime imaging microscopy (FLIM). The FLIM approach is a useful technique that relates the spatial variations in lifetime with the morphology of the examined structures. Investigating crystals and crystal-like luminescent structures via FLIM combined with the Hirshfeld surface (HS) analysis, provides information regarding the intermolecular interactions, structural-photophysical relationships could be established. Employing this tool on luminescent materials such as potential OLEDs structures provided new insights regarding their emissive properties, which is important for display and lighting technologies. Another application of fluorescence lifetime, via fluorescence spectroscopy, was employed to investigate the active center of a europium-dependent methanol dehydrogenase enzyme (Eu-MDH). Simultaneous measurements of the fluorescent cofactor and Eu metal ion, present in the MDH active center, showed their proximity to one another and provided a tool to characterize their photophysical behavior. Overall, utilizing the strengths of the upgraded CLSM, capable of the fluorescence methods presented within the scope of this thesis, elucidates a vast of relevant nanostructure properties especially in the field of material science.

Contents

1. Introduction

Observations, sophisticated reasoning and an incentive for knowledge have always been the foundation of science. The pursuit of understanding and exploring the unknown using these foundations coexisted with the life of human beings since their beginning. This pursuit is still ongoing; however, it has become less straightforward and more demanding. Nowadays, a complicated experimental approach is almost a necessity in different areas, especially for conducting research in advanced scientific fields such as biophysics and material sciences. Several approaches have been developed throughout the years that enabled the examination of systems beyond what can be resolved by the naked eye. Seeing beyond what is visible to the naked eye was rendered possible and pioneered by the invention of the light microscope in the 17th century and opened a whole new world. This invention enabled, for the first time, the exploration of the micro-world such as the sub-cellular realm. This first observation of small structures inflamed the desire to discover even smaller domains. Eventually, attempts to achieve these goals, encouraged further development of light microscopy and imaging techniques to resolve structures beyond the micro-world. The frontiers of these techniques were reached when the diffraction limit in images became obtainable, beyond which additional resolution enhancement could not be achieved until recently. Hence, extending the resolution for exploring molecular structures on the nanometer level and beyond would be hindered for over a hundred years. Overcoming the resolution obstacle was achieved in the last few decades through the development of techniques like X-ray diffraction (XRD), atomic force microscopy (AFM), scanning and transmission electron microscopes (SEM and TEM) and recently with super-resolution microscopy.

X-ray and electron microscopy have constrains that deter their implementation to examine samples that require gentle measurement conditions. Therefore, the aim of studying unperturbed samples remained the drive for developing similar high-resolution techniques that could be used for studying samples without destroying their structure or altering their morphology. Concurrent to the other techniques, fluorescence has emerged in the last few decades as an essential tool for conducting research in the areas of the life and material sciences. Ensemble fluorescence spectroscopy measurements are powerful tools for characterizing the average properties of samples in bulk. In the 90's, the ability of using fluorescence to detect single molecules evolved with the advancement of optics and electronics in the field of microscopy.[1, 2] The developed single-molecule techniques improved the resolution power to distinguish structures on the nanometer scale. For instance, in the last 15 years, approaches such as photo-activated localization microscopy (PALM)[3, 4] and stochastic optical reconstruction microscopy (STORM)[5] that rely on the detection of single molecules are now recognized as prominent types of super-resolution techniques. These techniques have pushed microscopy beyond the diffraction limit and

overcame the constrains within the field - an achievement honored with the Nobel prize in Chemistry in the year 2014.

Despite the advances in super-resolution microscopy over the last years, it is noteworthy to highlight the importance of other current fluorescence tools that have preceded super-resolution techniques and made it not only feasible to resolve single molecules, but also to study their behavior on fast timescales. For example, methods that monitor and analyze fluorescence intensity fluctuations, such as fluorescence (cross-) correlation spectroscopy (FCS or FCCS), or lifetime differences, such as fluorescence lifetime imaging microscopy (FLIM), have been employed in the last decades to disclose several secrets of the nanoworld. In order to successfully develop and implement such techniques, several factors other than the resolution are important in distinguishing different objects and studying them on the single molecule level. In this respect, fluorescence provides a versatile tool that increases the sensitivity and specificity of the detected signal to overcome the signal-to-noise ratio (SNR) barriers and selectively monitor the sample of interest. This holds especially true in confocal fluorescence microscopy, that relies on minimizing the size of the observation volume in solution. In this case, the contribution of the Rayleigh and Raman scattering to the signal is decreased and thereby the SNR increases. Fluorescence provides a distinctive capability for filtering out the scattering originating from the excitation source. This capability was observed by Stokes[6] in 1852 when he reported on the bathochromic shift observed for the fluorescence emission with respect to the source's excitation wavelength. This property of fluorescence has been utilized to improve the contrast by specifically labeling the sample of interest.

The high specificity of fluorescence is demonstrated by applying the desired labels to monitor the sample of interest and is the fundament in state-of-the-art techniques that involve fluorescence microscopy. By labeling the sample of interest, it is possible to detect and separate the emission of the sample (at a shifted wavelength) from the scattered light, which originates from Rayleigh scattering by the excitation source, and hence suppresses its contribution to the background. This, however, is not always possible due to limitations in positioning the specific labels on the sample of interest. Moreover, the attached fluorophores can induce additional steric hindrance - in particular, when labeling small molecular structures and samples. When introducing fluorescent probes, it is necessary to carefully consider and account for the size of introduced probes, as well as to perform the necessary controls in order to verify and characterize the presence or absence of interactions between the reporter molecule and the sample of interest. Along with specificity, the high number of photons emitted by fluorescent labels is an important factor that explains the sensitivity of fluorescence in distinguishing the probe of interest from its surrounding. Therefore, fluorescence provides the means of obtaining a good SNR, which have been utilized to establish different single molecule techniques.

In the scope of this thesis, different fluorescence microscopy tools were employed in material science on the nanoscale. FCS and FCCS are solid spectroscopy approaches to study the interaction between molecules, where information about the diffusion coefficients and number or interacting particles can be determined. Nowadays, fluctuation spectroscopy techniques such as FCS employ a small confocal volume that reduces the number of observed particles, which, in turn, increases the fluctuations in the fluorescence intensity. FCS and FCCS were utilized to investigate the interactions between differently functionalized metal-organic frameworks (MOFs) and the most abundant serum proteins immunoglobulin G (IgG) and albumin. MOFs are formed by bridging inorganic metal ions with organic linkers that are very modular and are highly desired for different applications. For example, fabrication of highly porous materials, like MOF nanoparticles, can be utilized for different medicinal purposes such as drug delivery vehicles or therapeutic agents. One of the important requirements, which was investigated in our studies, is the inertness of these nanoparticles to the *in serum* protein interactions.

Similarly, the fluorescence lifetime can be utilized as a powerful tool in the field of material sciences. In this regard, FLIM is an excellent technique for investigating the spatial lifetime variations within the sample of interest and provides additional information about its nanoscopic environment and properties. The capabilities of FLIM to investigate luminescent materials is demonstrated in the scope of this work. Here, FLIM was used to study the post-synthetic exchange (PSE) mechanism of a bulky fluorescently labeled linker that was found to be gradually incorporating into MOF crystals by replacing the smaller framework organic linkers. The capability of introducing bulky linkers (larger than the pore's window) into a rigid Zr-prototype MOF was a surprising outcome that intrigued us to study the mechanism of the observed linker exchange. The discovered PSE mechanism - described as a through-backbone diffusion mechanism - can be used as an approach to exploit UiO-67 MOFs by functionalizing their pores with complex linkers. The insights of the discovered mechanism can be exploited to introduce bulky linkers into rigid MOFs - a possibility that was, hitherto, deemed unfeasible.

Another illustration of the potential of FLIM in material science is demonstrated by combining it with the Hirshfeld surface (HS) analysis to provide a standard tool for characterizing various types of luminescent materials. The HS analysis provides information about the crystal packing properties and the intermolecular interactions within the crystal-like structures such as the newly synthesized picolyl-derived phosphine materials that we showed. The auto-luminescence of these materials have a great potential for their successful usage as organic light emitting diodes (OLEDs) and was investigated using FLIM. Combining the HS analysis with FLIM provided new insights between the photophysical properties of the synthesized phosphines, in particular their autofluorescence emission and lifetime properties, and the diverse intermolecular interactions they possess. These findings show the potential of employing the FLIM-HS

analysis tool as a standard characterization approach that is applicable to examine different luminescent materials. The lifetime expertise that are demonstrated within this thesis were implemented to characterize a lanthanide-dependent methanol dehydrogenase enzyme (Ln-MDH) in bulk. For this purpose, fluorescence spectroscopy was utilized to monitor the fluorescence emission and lifetime of a luminescent europium (Eu) metal ion present in the active center of the MDH.

Taken together, the use of fluorescence in general and fluorescence microscopy, in particular, is an excellent and versatile approach to study interactions, mechanisms and photophysical properties of different materials on the nanometer level. The developed single molecule techniques have enabled the simultaneous measuring of a set of important parameters contained in the fluorescence signal. Such parameters like emission intensity, fluorescence polarization, and fluorescence lifetime encode valuable information that renders fluorescence an excellent method for conducting research in the life and material sciences.

Outline

After a brief introduction to the basics of fluorescence, the general features of the different methods and concepts associated with confocal laser scanning fluorescence microscopy are discussed in chapter 2. The first part of this chapter encloses a short introduction into fluorescence with a brief description of the main fluorescence microscopy approaches used nowadays. The second part describes the advanced fluorescence methodologies such as the fluorescence lifetime and fluorescence fluctuation spectroscopy (FFS). The former is discussed with a summary of the different lifetime approaches and the currently used instrumentation. Subsequently, a short description of the FFS methods is presented. In short, these fluctuation spectroscopy techniques allow the extraction of temporal information that are important to investigate the sample of interest. The spatial fluctuations observed from a fluorescence intensity image are then described, with a brief overview of some currently used image correlation spectroscopy approaches. In section 2.5, a detailed discussion of the confocal laser scanning microscope (CLSM), which was developed and upgraded within the scope of this work are presented. The CLSM upgrade involved the incorporation of an improved telescope system to reduce the aberrations, alongside extending the setup's capabilities by the addition of a widefield and total internal reflection (TIRF) microscopy modality to it. The following part shows the potentials of the developed microscope by using the advanced fluorescence techniques to characterize and demonstrate the capabilities of the upgraded CLSM. The last fluorescence method, described in the end of this chapter, is the fluorescence spectroscopy. This is accomplished via a T-geometry fluorimeter that comprises both the bulk fluorescence intensity and lifetime characterizations measured on ensembles.

Chapter 3 includes an overview of the work published in the scope of this thesis, which relies on the different techniques presented in chapter 2. The utilization of fluorescence lifetime in material science is less common than in the life sciences and has great potential for elucidating the photophysical properties of these materials. Fluorescence fluctuation spectroscopy was used in paper 1 to investigate the interaction between differently coated MOF particles and the abundant serum proteins IgG and albumin. In papers 2 and 3, fluorescence lifetime was used to investigate MOFs and OLEDs. In paper 4, the fluorimeter capabilities alongside the acquired fluorescence lifetime expertise were applied to study the photophysical properties of the Eu metal ion and the quinine co-factor present at the active center of a methanol dehydrogenase enzyme (MDH). Utilizing an LED laser, operating in burst mode, a thorough and simultaneous characterization of the proximity of the Eu (µs lifetime decay) to the quinine co-factor (ns lifetime decay) present at the MDH active site was performed. Chapter 4 encloses a brief summary of the work presented in the scope of this thesis and a general conclusion that sheds the light on the distinct advantages and outcomes of the applied fluorescence techniques.

2. Introduction to Advanced Fluorescence Methodologies

2.1. Fundamentals of Fluorescence

2.1.1. The History and Basics of Fluorescence

The first description of fluorescence was recorded in the 16th century by Nicolás Monardes,[7] a Spanish physician, who reported on the blue opalescence tinge of the liquid solution obtained from the wood of *Lignum nephriticum*, a Mexican medicinal tree described by the Aztecs as coatli. These observations intrigued several scientists to investigate this phenomenon for years, nevertheless the detailed molecular structure of the fluorescing molecule remained unknown for many centuries. Only recently has the identification of the Lignum nephriticum fluorophore, matlaline, been accomplished. A detailed report of the compound's formation as a product of some of the tree's flavonoids alongside its photophysical properties were published in 2009.[8]

An observation similar to the blue tinge from the coatli wood was reported from a solution of quinine sulphate in 1845 by Sir John Herschel who described it as an extremely vivid and beautiful celestial blue color, which he named epiploic dispersion.[9] The quinine sulphate phenomenon was further investigated by Sir George Stokes in his detailed report on the change of refrangibility (*i.e.* wavelength change) of light in 1852. In his detailed treatise, Stokes laid the foundation for several characteristics of this phenomenon, which he firstly named dispersive reflection. Eventually, Stokes suggested coining a new word for the phenomenon's appearance that conceived the term fluorescence, coming from the fluorite mineral known as fluor-spar, which emits a blue light upon absorption in the UV range.[6]

After this brief introduction into the first observations of fluorescence, it's important to mention that the details of its general attributes have been developing in the last 150 years. Fluorescence a type of interaction between light and matter, which was described by Einstein in his 1916 postulate under one of three different categories. These categories were classified for a two-level system. The first form of interaction initiates immediately after a molecule or an atom absorbs a photon, which promotes its electron from the lower energy level to a higher energy state (Figure 2.1, Einstein coefficient B_{01}, left).[10] The second form of interaction was described as spontaneous emission, where the excited electron, without external stimuli, de-excites from the higher energy level to the ground state resulting in the emission of a photon (Figure 2.1, Einstein coefficient A_{10}, middle). The third category of interaction is referred to as stimulated emission, where the de-excitation of the electron from the excited state to the ground state is induced. However,

the photon's emission, in this case, is initiated by the presence of a photon, which has a similar frequency to that of the transition of the de-excited electron (Figure 2.1, Einstein coefficient B_{10}, right). Noteworthy, stimulated emission is the basis for developing lasers and is of significance in the field of super-resolution spectroscopy, being applied in stimulated emission depletion (STED) microscopy.[11, 12]

For the three different interactions addressed by Einstein, a relation between the number of molecules, N_0, in the lower energy ground state, S_0, and the number of molecules, N_1, in the higher energy excited state, S_1, is represented according to the following equation 2.1:

$$\frac{dN_0}{dt} = -\frac{dN_1}{dt} = -N_0 B_{01} U_\nu + N_1 A_{10} + N_1 B_{10} U_\nu \qquad (2.1)$$

where U_ν describes the spectral energy density of the isotropic radiation field at its transition frequency (ν). The probabilities of the absorption, spontaneous emission and stimulated emission are denoted by $-N_0 B_{01} U_\nu$, $N_1 A_{10}$ and $N_1 B_{10} U_\nu$, respectively.

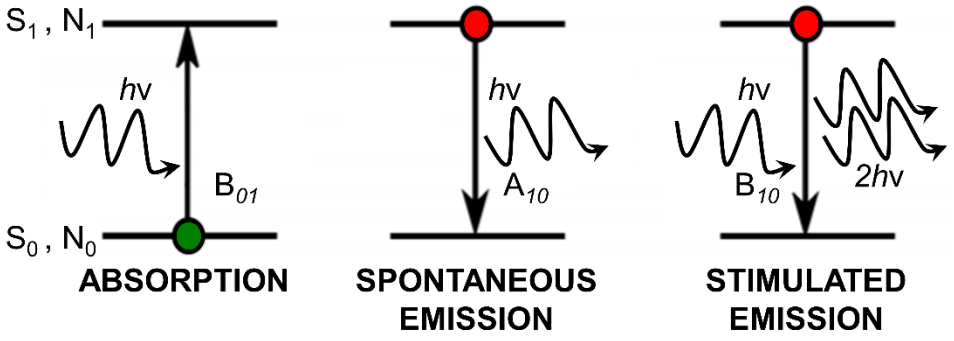

Figure 2.1: The three categories of light interaction with matter for a two-level system as postulated by Einstein in 1916, where B_{01}, A_{10}, and B_{10} are the respective Einstein coefficients for the different interactions. The transitions are depicted between the lower energy ground state S_0 containing N_0 molecules and the higher energy excited state S_1 containing N_1 molecules.

Visualization of the various possible processes involved in the molecule's excitation and de-excitation can be depicted through a *Jablonski diagram*.[13] This diagram is named after the Polish physicist Prof. Alexander Jablonski and has been used in various forms to address the different pathways that occur in the excited states (Figure 2.2). In the following diagram, S_0 depicts the singlet electronic ground state while the first two singlet excited energy levels are described by S_1, and S_2, respectively. As shown in the diagram, the ground level has several possible vibrational states. For example, the thermal energy available for a fluorophore at room temperature (RT) is insufficient for populating the excited electronic states or the higher level vibrational states. In this case, the fluorophore resides mostly in the lowest energy vibrational state. Upon the absorption of light, the ground level electron in S_0 acquires sufficient energy to be excited into a higher energy

vibrational state of the excited electronic levels S_1 or S_2. The excitation process is an example of an electronic transition between two different states, which is depicted in the Jablonski diagram with the vertical lines. The excitation of a fluorophore induces a change in the molecule's electronic configuration, which leads to a shift in the electronic density. This electronic density shift alters the columbic force field, which in turn causes the rearrangement of the fluorophore's nuclear configuration. The rearrangement or movement of the nucleus, however, is a noticeably slower process (~10^{-12} s) in comparison to an electronic transition which occurs on the femtosecond scale (~10^{-15} s). The is due to the fact that the nucleus typically contains more than 99.99% of the fluorophore's mass, which makes the electronic mass negligible in comparison. Based on that, the Born Oppenheimer approximation approaches the electrons and nucleus wavefunctions separately. Taking the Born Oppenheimer approximation into account, it is stated that an electronic transition or motion is most likely to occur without a major nuclear movement accompanying this process. This approximation is also the basis of a very important rule in spectroscopy that has been observed and described by James Frank, which is nowadays known as the Frank-Codon principle.[14]

Following the excitation of the fluorophore to the higher vibrational state of the excited level, a relaxation to the lowest energy level of the electronic excited state via internal conversion (IC) is observed. This process is a few orders of magnitude slower than the excitation and usually occurs on the picosecond timescale (~10^{-12} s). IC occurs on a significantly faster time scale compared to the decay time from the excited electronic levels. Hence, IC precedes the decay from the excited electronic state. Subsequent to this relaxation, the fluorophore's electron decays to an excited vibrational state of the lowest energy ground level S_0. This process is often referred to as de-excitation and there are several possibilities of bringing the excited fluorophore back to the S_0 ground state. The competing de-excitation processes can be usually grouped into two categories: emissive and non-emissive decays. The emissive decays include fluorescence and phosphorescence routes, and the non-emissive decays include quenching and non-radiative routes (Figure 2.2).

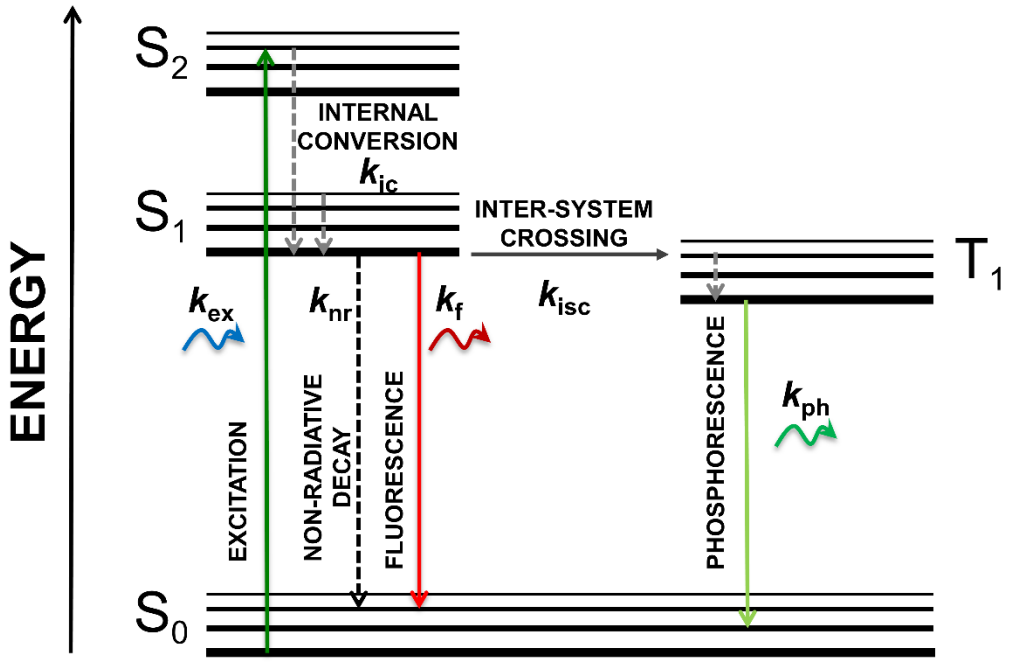

Figure 2.2: A general Jablonski diagram visualizing the possible excitation and de-excitation processes. The S_0, S_1 and S_2 singlet states and the T_1 triplet state are represented by the thick black lines and their corresponding various vibrational levels are represented by the thinner lines. The arrows represent the different transitions and k represents the respective rates, where k_{ic} is the internal conversion rate, k_{ex} is the excitation rate, k_{nr} is the non–radiative relaxation rate, k_f is the intrinsic fluorescence emission rate, k_{isc} *is the* intersystem crossing rate and k_{ph} is the phosphorescence emission rate.

The fact that radiative decays such as fluorescence and phosphorescence involve the emission of a photon, makes these two processes valuable methods to probe different interactions. The emissive properties of a molecule are unique traits of its electronic levels, which designates the molecule's fluorescence or phosphorescence. Fluorescence, the significantly faster process, typically occurs on the 1-10 ns time scale, where the excited state electron returns to the higher vibrational state of the lower energy ground state S_0. Subsequently, the energy of the electron in the excited vibrational state of S_0 is dissipated on the order of the 10^{-12} s leading to its relaxation (IC) to the lowest vibrational state of the S_0. Phosphorescence, on the other hand, is significantly slower than fluorescence and occurs on longer timescales that are typically longer than 1 µs. Phosphorescence occurs when an electron in the excited state experiences a spin conversion, so that it can undergo a process of inter-system crossing (ISC) from the singlet excited state to the triplet state followed by a decay to the ground state S_0. The main reason behind this prolonged phosphorescence decay, as shown in the example of the Jablonski diagram of Figure 2.2, is that the electron in the T_1 triplet state has to overcome the symmetry forbidden T_1 to S_0 transition via spin conversion, resulting in a significantly slower phosphorescence decay compared to fluorescence. This process is known to occur in heavy atoms like lanthanides, which are famous for their slow emissive properties. Similarly, molecules encompassing

heavy atoms such as Iodine or Bromine have pronounced spin-orbit coupling, which enhances ISC and increases the likelihood of phosphorescence to occur.

After defining the transitions leading to fluorescence, it is insightful to address some of its important features such as the Stoke's shift, Kasha's rule and the mirror-image rule. As indicated in the Jablonski diagram (Figure 2.2), excitation occurs when an electron in the ground level absorbs a photon. This yields an increase in energy that populates the higher energy level vibrational states of the excited electronic states with electrons. The fluorescence decay occurs from the lowest energy vibrational level of the excited state S_1 to a higher vibrational level of the ground state S_0. Comparing these two processes make it obvious that the fluorescence emission results in a loss of energy between the excitation and the de-excitation processes. This loss of energy results in a longer emission wavelength compared to the excitation wavelength, which is clear in the Jablonski diagram from the gap between the excitation transition (dark green line) and the emission transition (red line). An example of this shift, named after Sir George Stokes, who was the first to describe this phenomenon in 1852, is depicted in Figure 2.3 as a shift in the wavelengths between the maxima of the absorption and emission spectra of the Atto565 fluorophore. This feature of fluorescence is extremely useful for separating the excitation and emission light, which is utilized in fluorescence microscopy.[6, 14]

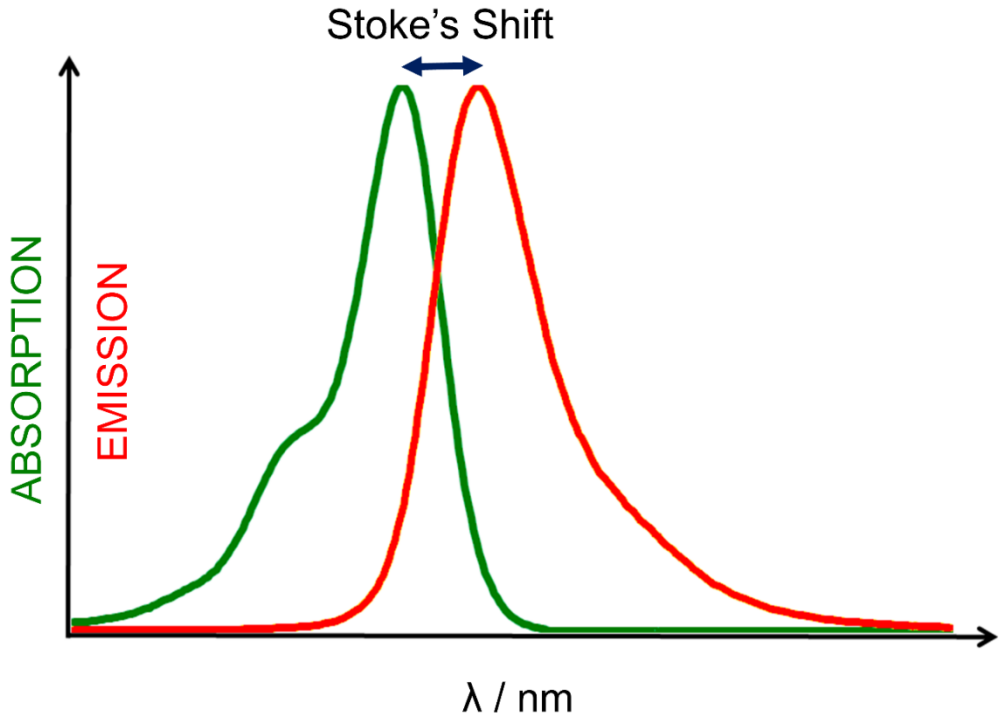

Figure 2.3: Stoke's shift depicted in the wavelength differences between the peaks of the absorption (dark green line) and emission spectra (red line) of the fluorophore Atto565 in water.

Another important aspect of fluorescence is Kasha's rule, which states that the emission spectrum of a fluorophore is independent of the used excitation wavelength. The reason behind this observation is that fluorescence is preceded by a very fast relaxation of the electron from the higher energy level vibrational states of the S_1 to the lowest energy level vibrational state via IC, despite the used excitation wavelength. This as well explains the high likelihood of fluorescence emission to only occur from the lowest vibrational state of the S_1 state.[15]

The third important feature of fluorescence is the mirror-image rule, which describes the similarities between the spectral peaks of the different electronic transitions as previously explained by the Frank-Codon principle.[16] The similarities between the nuclear configuration in the excited and ground states, result in a similar spacing between the vibrational states of the excited electronic levels and the vibrational states of the ground level. Hence, the emission spectrum is generally known to be a mirror-image for the transition between the ground state and the first excited state (*i.e.* the $S_0 \rightarrow S_1$ absorption spectrum). An example of the mirror-image rule is depicted in Figure 2.4, which illustrates the electronic transitions between S_0 and S_1 resulting in the absorption-emission spectra mirror-image (Figure 2.4, inset).

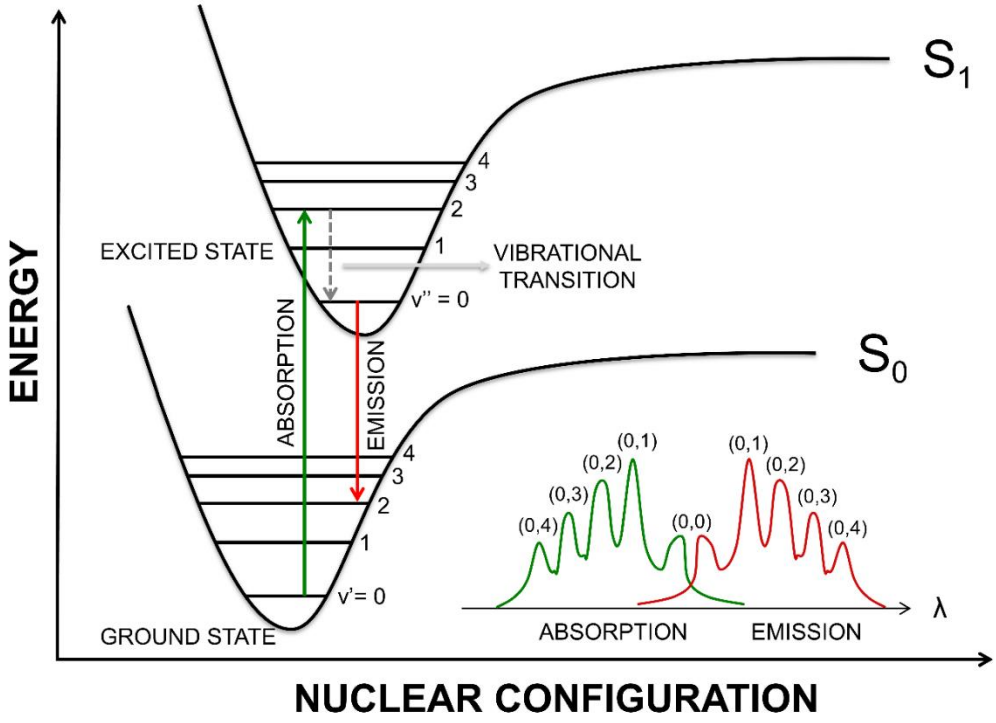

Figure 2.4: A simplified Jablonski diagram of the ground state S_0 and the 1st excited state S_1 with their respective vibrational states as a function of the nuclear configurations of these states. The Frank-Codon principle is depicted in the diagram via the vertical absorption and emission transition represented by the vertical lines. The figure inset shows the absorption and emission spectra exhibiting the presented transitions in the diagram. These spectra display an example of the mirror-image rule between the different marked transitions.

2.1.2 Wide-field Microscopy

The versatility of fluorescence facilitates its implementations in a variety of techniques. Next to its extensive usage in spectroscopy, in the last 30 years fluorescence turned out to be a cornerstone for several microscopy techniques. Wide-field microscopy, for example, is a basic microscopy technique, which has been well established and widely used to investigate and characterize different samples of interest. A common feature of wide-field microscopy is the illumination of the whole field of view (FOV) and its simplest form utilizes a white illumination light. The two common approaches applied for wide-field are either the illumination from below via an upright microscope or from above via an inverted microscope. In all cases, the resolution of a wide-field microscope is limited by its ability to differentiate between two points within a specimen, which is determined by the wavelength of light and the numerical aperture of the objective. The optical resolution of a conventional wide-field microscope is typically restricted to half of the wavelength λ, which is well known as the Abbe diffraction limit as depicted in eq. 2.2, named after the German physicist Ernst Abbe who characterized this resolution in 1873.[17]

$$d_{min} \backsimeq \frac{\lambda}{2\,NA} = \frac{\lambda}{2\,n\,sin\theta} \qquad (2.2)$$

where d_{min} denotes the Abbe-Limit, which is the minimum distance at which two distinct points can be resolved and λ denotes the excitation wavelength. The NA represents the numerical aperture, which is defined by the angular aperture θ of the incident beam after passing through the objective lens and n is the index of refraction of the medium, between the lens and the specimen.

An extension of Abbe's-Limit was investigated in the end of the 19th century by the British physicist Lord Rayleigh, who addressed the image formation of microscopes and telescopes examined how an ideal point-shaped object would be imaged in two-dimensional (2D) space. The diffracted signal from the point-shaped object, referred to as a point emitter, gives an intensity pattern known as the Airy pattern which is referred to as the point spread function (PSF). Taking this into consideration, the Rayleigh criterion defines the resolution based on the distance from the center of the Airy disk to its first minimum. In this case, the shortest distance d_{min} at which two point emitters can still be resolved (eq. 2.3)[18] is given by:

$$d_{min} = \frac{0.61\,\times\,\lambda}{NA} = \frac{0.61\,\times\,\lambda}{n\,sin\theta} \qquad (2.3)$$

The resolution limit could be improved by having a higher NA, which could be achieved by choosing a higher index of refraction medium, such as immersion oil used for oil objectives.

2.1.3 Total Internal Reflection Fluorescence Microscopy (TIRF Microscopy)

A limitation of wide-field microscopy arises from the diffraction limited axial resolution, which could be improved by utilizing the TIRF microscopy approach to excite only an extremely thin axial layer of the specimen. This key feature of TIRF microscopy offers a better axial resolution and fluorescence signal-to-background ratio.[19, 20]. Here, the laser beam used to excite the sample is totally reflected upon hitting, at an oblique angle, the interface between the immersion medium or prism and the sample medium that has a lower refractive index. In this case, the laser impinging on the lower refractive index plane with an oblique angle is incapable of fulfilling the Snell's law, as depicted in Figure 2.5, and thus can only be totally internally reflected. This law (eq. 2.4) is attributed to the observations of the Dutch astronomer Willebrod Snellius in the beginning of the 17th century.

$$n_{inc} sin\theta_{inc} = n_{ref} sin\theta_{ref} \qquad (2.4)$$

where n_{inc} and n_{ref} represent the refractive indices of the incidence medium and the refraction medium, respectively, and θ_{inc} and θ_{ref} denote the incidence and the refraction angles, respectively. the refraction of the laser upon impinging on the specimen's plane is governed by the relation between the incidence (θ_{inc}) and refractive (θ_{ref}) angles and the corresponding refractive indices of the incidence medium n_{inc} and refraction medium n_{ref}

The special case of total internal reflection observation described above only happens under high or oblique incidence angles. This high angle of incidence is known as the critical angle (θ_c), which is given by ($\theta_c = sin^{-1} \frac{n_{ref}}{n_{inc}}$) where the refractive angle is then substituted in the Snell's law (eq. 2.4) with a value of 90°. At the interface, an evanescent electromagnetic field that decays exponentially into the lower refractive index medium is created. This narrow, 100 to 200 nm, evanescent field excitation is nicely utilized in TIRF microscopy to study single molecules on or near to the surface of the sample holder.[21] Similarly, TIRF microscopy can be exploited for in-cell measurements to focus on the cellular membrane minimizing the influence of the cytoplasmic signal.

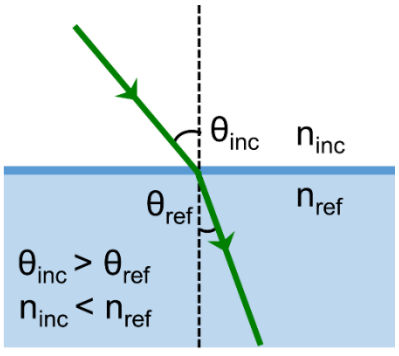

Figure 2.5: The refraction of the light between two media, with different indices of refraction n_{inc} and n_{ref}. The laser beam is refracted at a smaller angle θ_{ref} to the normal of the interface following eq. 2.4.

2.2. Confocal Fluorescence Microscopy

2.2.1. Basics and Principles of a Confocal Fluorescence Microscope

Another basic fluorescence microscopy technique that improved the axial resolution is the confocal microscope. The concept of confocal microscopy was first described by the American scientist Marvin Minsky.[22] The principles that Minsky introduced in 1957 are still true nowadays. However, further developments have been applied to this original concept in the last 50 to 60 years that improved confocal microscopy and established it as a solid method for many applications. The basic idea behind the confocal microscope is the small observation volume that reduces the scattered and the out of focus signal upon exciting the molecules of interest, thereby improving the signal-to-background ratio. Here, a collimated laser beam, typically with a Gaussian irradiance profile, is focused by an objective on the sample generating a light cone. The narrowest width of this cone defines the lateral size of the confocal volume. Noteworthy, the light cone excites molecules from the planes below and above the image plane. Therefore, it is critical to place a pinhole in the detection pathway, which removes the out of focus signal and defines the axial size of the small confocal volume (Figure 2.6).

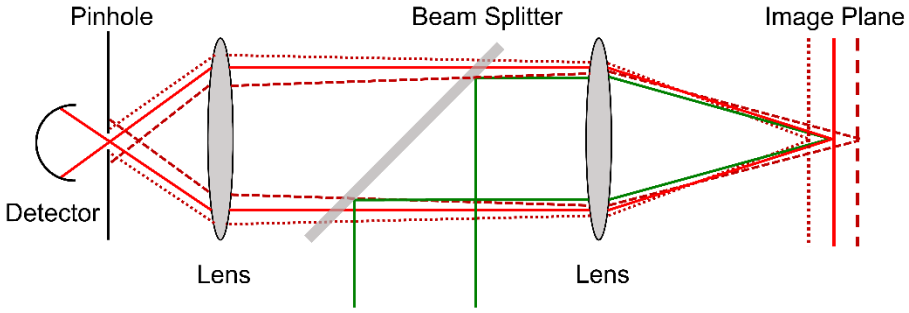

Figure 2.6: A schematic beam showing the principle of a confocal microscope. The dark green lines indicate the excitation beam. The presence of a pinhole still allows the detection of the light coming from the focal plane (solid-red line), whereas the out of focus light (dotted and dashed dark-red lines) is blocked.

The emitted light from the point source in the image plane is typically collected by a high NA objective, where the 3D pattern of this spot is described as the PSF. In the case of single photon excitation, the PSF has an approximately ellipsoidal shape that defines the intensity distribution of the emitting point source (typically ~250 nm in the lateral direction and 4× to 6× larger (~ 1 to 1.5 µm) in the axial direction) and can be nicely modeled using a 3D Gaussian function (eq. 2.5):

$$PSF(x,y,z) = \exp\left(-\frac{2(x^2+y^2)}{{\omega_r}^2} - \frac{2z^2}{{\omega_z}^2}\right) \qquad (2.5)$$

where, ω_r and ω_z represent the distances from the center to the point where the intensity decreases to $\frac{1}{e^2}$ ~ 13.5% of its maximum, along the lateral and the axial axes, respectively.

2.2.2 Confocal Laser-Scanning Microscopy (CLSM)

The simple confocal principle, described in the previous section, which focuses the laser into a single spot is limited to single point detection. Therefore, a desirable upgrade of a confocal microscope can be accomplished by enabling scanning the sample of interest, which allows the reconstruction of a full image from the different data points. Imaging via confocal microscopy can be attained by either moving the laser (*i.e.* focus) in the sample or by moving the sample itself. The latter, although easier to implement, has the disadvantage that moving the sample limits its accessibility that is a must for measurements such as microinjection or patch clamp techniques. Additionally, moving the sample is a considerably slower approach once compared to the laser movement. Therefore, it is quite common for advanced confocal microscopes to scan the laser among the sample. The type of microscopes featuring this concept are nowadays frequently referred to as confocal laser scanning microscope (CLSM) techniques.

The lateral movement in a CLSM is achieved by changing the laser's incident angle at the back focal length (BFL) plane of the objective. The simplest way to achieve this movement is by introducing a rotatable mirror in the excitation pathway, before the objective, where tilting the mirror along the vertical and horizontal axes would correspondingly change the observation volume along the specimen in the x and y directions. In reality, having a CLSM with only a tilting mirror before the focusing objective has certain drawbacks. These drawbacks arise because the mirror's rotation not only changes the angle of the laser, but also changes in the laser position at the BFL plane, which would lead to clipping of the beam. The common way to overcome these limitations is by introducing relay optics, such as a Keplerian telescope or parabolic mirrors, that are placed after the scanning mirror and before the objective. Alignment of the optical elements (*i.e.* the scanning mirror, expander and objective) in the right manner results in coinciding focal planes between the different components even upon tilting of the scanning mirror (Figure 2.7). The relay optics then eliminate the lateral movement of the laser at the BFL plane of the objective, enabling the scanning of large regions of interest (ROI) without artifacts. Noteworthy, in such a CLSM, the excitation and the fluorescence emission undergo the same pathway, where the latter is separated by placing a polychroic mirror before the scanner. In this way, the excitation and the fluorescence emission hit the polychroic mirror under an identical angle regardless of the scanner position, a term referred to as ''descanning'' which enables the use of pinholes and detectors with a small active area.

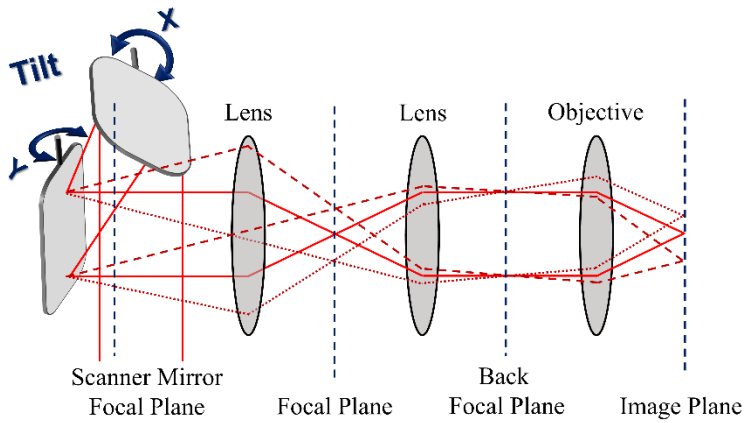

Figure 2.7: A schematic showing the principle of a CLSM. Aligning the scanning mirrors and the other optical elements to have coinciding focal planes relays the tilting of the scanning mirror relay into a lateral movement of the focal volume in the image plane while keeping the position of the laser beam constant in the BFL plane.

To obtain a full image of the specimen, several scanning approaches have been implemented, where the conclusive scanning capabilities of the CLSM are governed by the tilting properties of the mirrors. The simplest scanning approach is achieved by installing a 2-axes rotatable mirror, which provides a certain degree of compactness and flexibility but usually has a limited scanning range and speed. The desire to obtain images on faster timescales, makes such mirrors out of favor, especially since their speed is almost similar to piezo stages that enable scanning for significantly larger ROI by moving the sample holder itself. Hence, to obtain much faster scanning rates, most current CLSMs use galvanometric scanning mirrors that offer scanning speeds at frequencies around 1 kHz for a single line scan. A small drawback of galvanometric mirrors is that the fast rotation they provide is limited to a single axis. Thus, two galvanometric mirrors with perpendicular rotation axes are needed to achieve the desired fast 2D scanning (Figure 2.7). For this purpose, the focus point of the beam expanding telescope has to be precisely positioned in between the two mirrors to minimize the laser beam shift at the objective BFL plane. Conversely, more optics or an additional third mirror can be introduced to control the focus point positioning. In this case, the alignment becomes critical to minimize the small deviations that could affect the precision of the CLSM.

Using a galvanometric scanner enables 2D images to be collected on timescales up to ~10 frames per second, depending on the desired resolution. Galvanometric mirrors, however, are also limited in speed due to their inertia, which results in distorted images upon approaching the resonance frequency of the scanning mirrors. If faster scanning speeds are desired, resonant scanners can be used. Resonant scanners are galvanometric scanners where the fast axis mirror oscillates at the resonance frequency of the mirror, which can provide a good alternative to achieve almost video rate images. On the other hand, the scan frequency of such scanners is not adjustable, hence their implementation demands complex image reconstruction procedures to precisely retrieve the correct pixel position and adjust the varying pixel dwell times.

2.2.3 Time Correlated Single Photon Counting (TCSPC)

Nowadays, an important add-on for CLSM that allows for obtaining 2D images with nanosecond fluorescence lifetime information is based on recording the arrival time of the detected photons. Several advanced spectroscopy and lifetime measurements techniques employed by fluorescence microscopy benefits from a setup that is capable of measuring the arrival times of single photons, which is these days possible by implementing a valuable technique known as TCSPC.[23, 24] Here, the detection of individual photons by counting devices such as an avalanche photodiode (APD) generate an electronic signal that is transmitted to and processed via TCSPC devices. TCSPC devices record the arrival times of single photons on multiple timescales from tens of picoseconds over nanoseconds and sometimes up to few hours. Moreover, depending on the desired timing resolution, recent TCSPC devices can accurately measure the arrival times with a few picoseconds resolution.

In TCSPC, the start of an experiment triggers a TCSPC device to record the arrival times for the detected electronic signal transmitted from the APD upon registering a photon on two different timescales. The recorded photon arrival times with respect to the start of the experiment are referred to as the macro-time (t_{macro}) and the arrival time with respect to the next laser pulse or synchronization signal (sync) is the micro-time (t_{micro}). The t_{macro} provides the necessary information for the longer timescales detection (usually > 10 ns) relative to the start of experiment signal (Figure 2.8). This timing information is obtained by counting the number of synchronization signals from the start of experiment (t). It is common to have a sync that acts as a master clock between the different system components such as the TCSPC device, scanner and lasers. The master clock reduces the inaccuracies arising from the dephasing of the timing electronics.

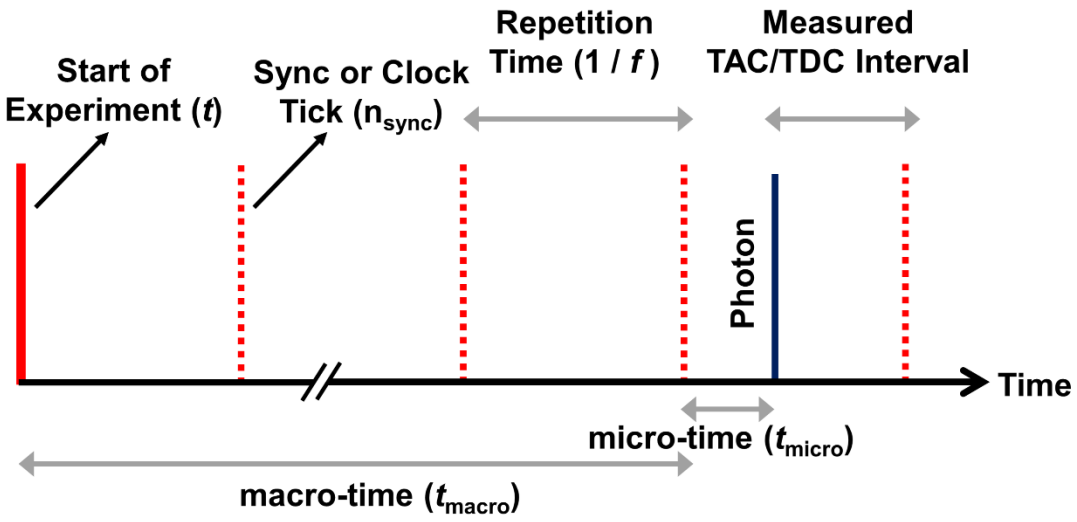

Figure 2.8: Schematic showing the TCSPC principle. The sync pulse operates at a fixed repetition frequency (f) and is used to measure the time delay between the detection of a photon and the following sync pulse,

which determines the micro-time (t_{micro}). The macro-time (t_{macro}) utilizes the start of experiment (t) signal to count the consequent number of sync pulses that elapsed since the beginning of the measurement.

The t_{micro} provides the necessary information for the short timescales (*i.e.* photon detection events within two consecutive pulses). Here, the time resolution is a critical factor that defines the capabilities of the TCSPC system. Therefore, an accurate measurement of the t_{micro}, defined as the delay between the detection of a sync signal and a photon, provides typically time resolutions on the order of a few picoseconds. Advanced electronics are thus needed to achieve such accurate resolutions, where resolving the t_{micro} is performed by a high precision timer, which is usually a time-to-amplitude converter (TAC). The TAC, in this case, is similar to a stopwatch, which starts upon the trigger from the sync signal and stops once a photon is detected. During the start-stop period, the TAC being a linear voltage ramp generator translates the voltage changes to a measurable time duration. This voltage-time duration relationship is afterwards digitized by using an analog-to-digital converter (ADC), which determines the maximum reachable timing resolution. In this case, the arrival time $T_{arrival}$ is precisely calculated using the following equation given by:

$$T_{arrival} = t_{macro} + t_{micro} = n_{sync} \frac{1}{f} + n_{ADC} \frac{T_{ADC}}{N_{ADC}} \qquad (2.6)$$

where f and n_{sync} represent the frequency and the number of sync signals detected since the beginning of the experiment, respectively, N_{ADC} and n_{ADC} represent the maximum and the measured numbers of ADC bins, respectively, and T_{TAC} represents the maximum time limits of the available TAC range, where typical values of the T_{TAC} are around $\frac{1}{f}$. Common repetition periods $\left(\frac{1}{f}\right)$ for a sync signal are typically around 10 to 100 MHz and thus the t_{macro} resolution ranges between 10 to 100 ns.

Nowadays, advanced TCSPC electronics tend to utilize a time-to-digital converter (TDC), which in principle carries out the functions of the TAC and ADC by performing a single task. Another important modification that has been applied to the TCSPC electronics is the well-known inverted or reversed start-stop configuration, whereby the detection process starts upon registering a single photon and ends by the next consequent sync signal. The main reason behind inverting the start-stop principle is due to the TCSPC electronics dead time, where mainly the TDC or TAC enters a dormant state rendering the TCSPC device incapable of registering any newly incoming photon for a certain period of time (usually ~ 50 ns). Since, in practice, detecting a photon is a scarce event in comparison to the regular and repetitive sync signals, it becomes very useful for the TCSPC electronics to adopt the inverse configuration, which allows to measure at higher repetition frequencies and reduces the dead time durations.

2.2.4 Pulsed Interleaved Excitation

After introducing the principles of TCSPC in the previous section, it becomes clear that it offers several advantages, one of which is that it enables an elegant implementation of pulsed interleaved excitation (PIE).[25, 26] Briefly, the implementation of PIE enables the alternation of the excitation lasers on the nanosecond timescale. In PIE, the time delay between consequent laser pulses (typically different excitation wavelengths) controlled depending on the desired fluorescence lifetimes. Delay of the laser pulse is usually achieved by either installing a delay box that shifts the lasers in time or via a laser driver that enables this feature electronically. Controlling the delay between the lasers allows one to tune the pulse position based on the lifetime of the sample on interest (Figure 2.9). For example, if the fluorophores of a dually-labeled sample have known lifetime values of 1 and 4 ns, respectively, one can assign the 4 ns lifetime fluorophore ~ 80% of the micro time channel, thus allowing to better fit a complete fluorescence lifetime decay histogram and explicitly assign the photons to the right excitation laser source. By applying PIE, we control the signal on two aspects, the first being the excitation where the lasers' microtime is controlled and the second being the emission that is split spectrally via emission filters and dichroic mirrors. Nowadays, advanced multichannel laser drivers provide remarkable delay options down to a few picoseconds alongside the option of combining the pulses of different lasers in an arbitrary fashion.

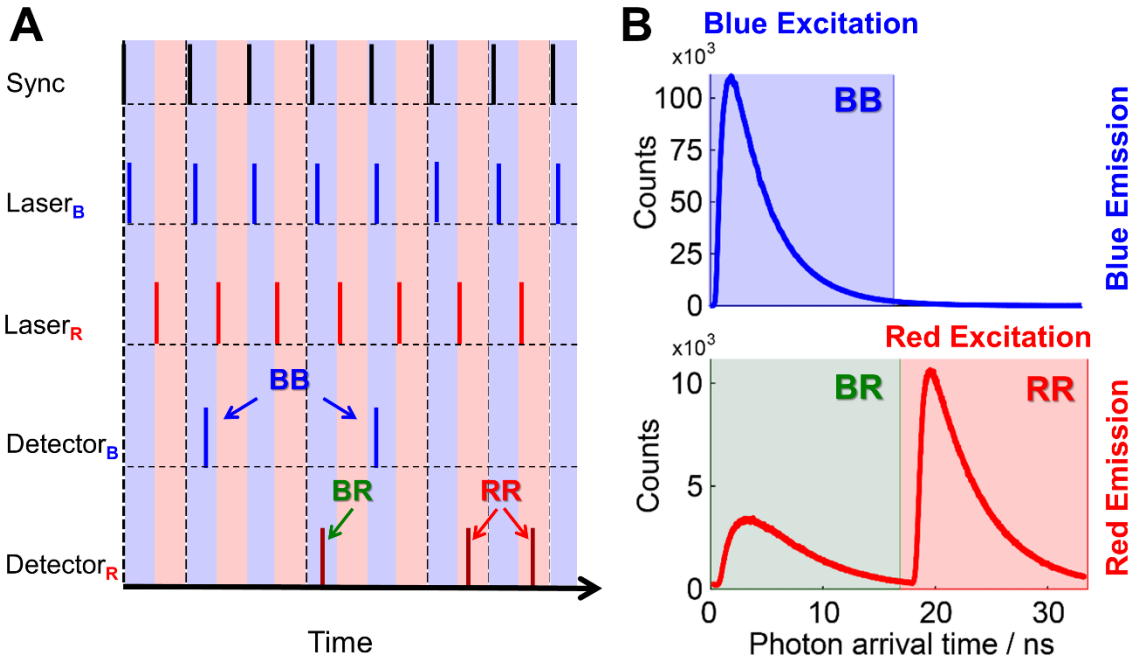

Figure 2.9: Schematic showing the principle of photon sorting in a two-color PIE system. A) A constant repetition clock controls the start of the excitation cycle via the consequent sync pulses, which sets the basis for triggering the blue and red lasers with a given time delay on the order of 20 ns. Therefore, the possibility of an emitted photon arises from, either the excitation after the blue or after the red laser. Thus, based on the delay between the two lasers, the arrival times of the photons are sorted under four different channels: (BB) which represents the blue photons after blue excitation and (BR) representing the red photons after blue

excitation. Here, the BR arises from either the direct excitation of a red emitter, spectral crosstalk or from direct energy transfer from the green emitter to the red emitter, such as Förster resonance energy transfer (FRET). Similarly, the (RR) represents the red photons after red excitation and (RB) represents the blue photons after red excitation. Usually, the RB photons are neglected for a common fluorescence measurement because it is unlikely to excite a higher energetic photon (*i.e.* blue emission) after excitation with a red laser. B) Shows the histograms of the t_{micro} from the detection channels for a dually-labeled Atto488-Atto647 DNA sample with the consequent four channels explained in (A) used to register and sort the photons emitted from the sample.

One of the methods that strongly utilize PIE and benefit from its implementation is fluorescence correlation spectroscopy (FCS). For FCS, sorting the photons based on their excitation source is an important criterion to improve the specificity. Here, we demonstrate an example of the capabilities of PIE in a two-color experiment, showing the fluorescence autocorrelation (ACF) and cross-correlation functions (CCF) of two independently diffusing fluorophores. The autocorrelation functions for Atto488 and Atto565 originate from the BB (*i.e.* blue emission after blue excitation) and RR (*i.e.* red emission after red excitation) channels, respectively (Figure 2.9 B). In the case of PIE, we can control the lasers to make sure that the BB and RR channels only contain the photons originating from the two corresponding dyes respectively. On the other hand, in the absence of PIE, there is a significant amount of spectral crosstalk from the blue fluorophore that is detected in the red channel. This crosstalk results in a cross-correlation amplitude even for a sample with two independently diffusing species (Atto488 and Atto565) that do not interact together (Figure 2.10, dotted-green *vs* green-crosses curve). Moreover, the ACFs show that the amplitude of the ACF for Atto565 decreases in the absence of PIE, indicating more molecules in the observation volume that, in this case, originate from photons emitted from the blue Atto488 dye and detected in the yellow channel, contributing to the yellow ACF (Figure 2.10, yellow curves).

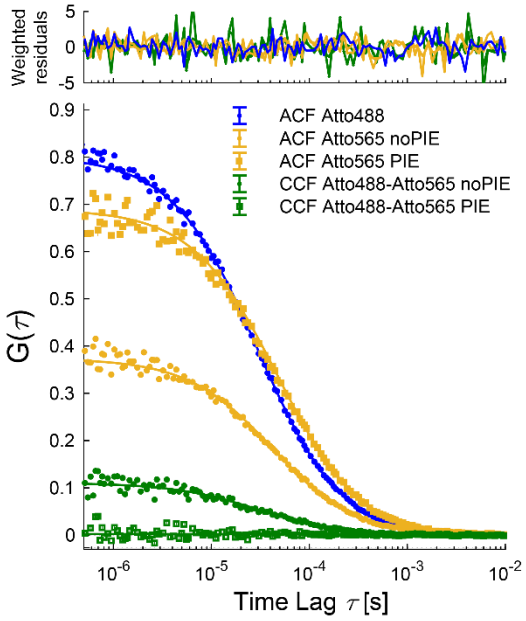

Figure 2.10: The fluorescence auto- and cross-correlation functions of two independently diffusion fluorophores, Atto488 and Atto565, are shown. The effectiveness of PIE to decrease the spectral crosstalk in a measurement can be seen. In the presence of PIE, no CCF is observed (dotted-green *vs* green-crosses curve).

2.3. Fluorescence Lifetime Spectroscopy

An advantage when using TCSPC electronics is that the fluorescence lifetime information is available and can be analyzed. In this section, the fundamentals of fluorescence lifetime will be discussed with a brief description of the implemented methods for studying and analyzing the fluorescence lifetime data. In particular, we discuss the importance of fluorescence lifetime once combined with CLSM. Shortly, a CLSM capable of measuring fluorescence lifetime utilizes the strengths of laser scanning to spatially resolve fluorescence lifetimes, which is an important added-on value. Several CLSM offer fluorescence lifetime imaging microscopy (FLIM) as a corresponding method to determine the lifetimes of 2D images on a pixel to pixel basis.[27-30] Accurate and practicable methods for investigating the fluorescence lifetime decays are highly desired for several applications.

2.3.1 Basics of Fluorescence Lifetime

With the aid of the Jablonski diagram (section 2.1), it becomes clear that IC (occurring on the ps timescale) and the lifetime of the excited state (occurring on the ns timescale) of a fluorophore are both noticeably slower processes than the excitation upon absorbing a photon (occurring on the fs timescale). Hence, the rate at which an electron returns from the excited state to the ground state becomes effectively a first order process. The fluorescence lifetime not only provides information on the fluorophores' photophysical properties but also the surrounding nano-environment. The main parameters used to characterize the fluorescence decay are the lifetime (τ) and the quantum yield (Q), which are calculated using the following two equations given by:

$$\tau = \frac{1}{k_{fl} + k_{nr}} \qquad (2.7)$$

$$\mathrm{Q} = \frac{k_{fl}}{k_{fl} + k_{nr}} \qquad (2.8)$$

where k_{fl} and k_{nr} represent the rate constants of the fluorescence decay and the non-radiative decays, respectively. The latter is the sum of all non-emissive pathways like IC, quenching mechanisms or energy transfer. It is worthy to note that the fluorescence lifetime has the characteristics of a first order exponential decay. Thus, observing multi-exponential decays is often an indication of several decaying species, which commonly arises from different quenching pathways or from excited states influenced by the surrounding environment. The latter feature is often observed in fluorescence proteins, such as eGFP, which exhibits a bi-exponential decay, mainly depending on its emission state, which interchanges among two states on a timescale faster than the fluorescence decay.[31]

The factors that influence the fluorescence quantum yield (Q) are the fluorescence rate and the excited state non-radiative decay rates. The former parameter is often steady and can be characterized from the steady state (*i.e.* excitation and emission spectra) properties. On the other hand, non-radiative decays are easily altered due to several effects, such as the solvatochromic effects or perturbances resulting from moieties in close proximity to the fluorophore. Therefore, the choice of fluorophore, taking its photophysical properties and the deployed readout methods into account, is crucial for developing an assay or to study the sample of interest.[32-36]

2.3.2 Frequency Domain Lifetime

Frequency modulation is one of the two main methods used to determine the fluorescence lifetimes. Here the excitation light is modulated, commonly between 1 to 100 MHz, and the fluorescence intensity and phase are measured as a function of frequency. Noteworthy, the frequency of the fluorescence emission is the same as the frequency of the excitation. The fluorescence lifetime leads to a slight delay in the fluorescence emission and a decrease in the amplitude of the demodulation, as depicted in Figure 2.11.

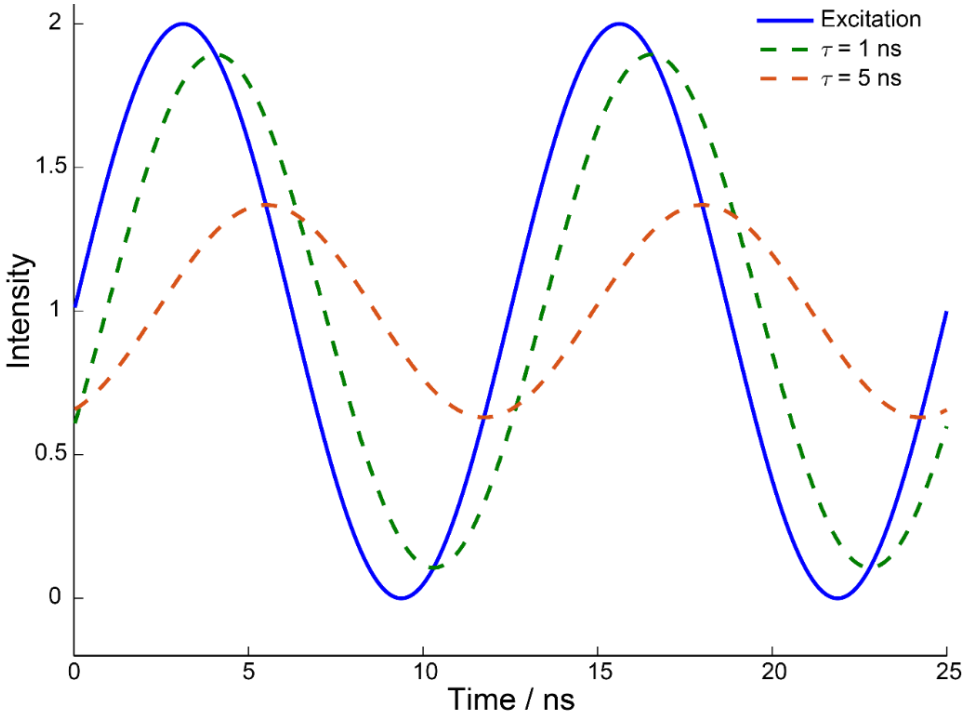

Figure 2.11: A graph showing the principle of a frequency modulated lifetime measurement where the excitation light is modulated at 80 Mhz. The emission signals show different demodulation amplitudes and phase shifts for a fluorescence lifetime of 1 ns (green) and 5 ns (orange).

A frequency domain measurement uses the demodulation (M_ω) and the phase shift of the signal (Φ_ω) to determine the lifetime of the fluorescence emission using the following two equations:

$$\Phi_\omega = \arctan(\omega\tau_\Phi) \qquad (2.9)$$

$$M_\omega = (1 + \omega^2{\tau_\mathrm{m}}^2)^{-\frac{1}{2}} \qquad (2.10)$$

According to equation 2.9 and 2.10, the frequency domain measurements result in two apparent lifetimes, the modulation lifetime (τ_m) and the phase lifetime (τ_Φ). In the case of a mono-exponential lifetime decay (*i.e.* a single component) the obtained value of both apparent lifetimes would be identical. However, when the fluorescence decay contains more than one component (*i.e.* a multi-exponential decay), then two different values are obtained for the τ_m and τ_Φ lifetimes. These values depend on the excitation modulation frequency and the fractional intensities (f_i) and lifetime of the different components. In this case, the fluorescence emission lifetime of the individual components can be determined by measuring the demodulation and phase shifts, calculated using the following two equations:

$$\Phi_\omega = \arctan\frac{\sum_i\left(\frac{f_i\omega\,\tau_\mathrm{i}}{1 + \omega^2{\tau_\mathrm{i}}^2}\right)}{\sum_i\left(\frac{f_i}{1 + \omega^2{\tau_\mathrm{i}}^2}\right)} \qquad (2.11)$$

$$M_\omega = \left(\left(\sum_i \frac{f_i\omega\,\tau_\mathrm{i}}{(1 + \omega^2{\tau_\mathrm{i}}^2)}\right)^2 + \left(\sum_i \frac{f_i}{(1 + \omega^2{\tau_\mathrm{i}}^2)}\right)^2\right)^{\frac{1}{2}} \qquad (2.12)$$

The frequency domain lifetime offers certain advantages in comparison to the traditional CLSM lifetime approach when performing FLIM, which mostly relies on point detectors imaging a single pixel at once. For example, in frequency domain lifetime measurements, a fast acquisition speed can be implemented by using a camera for detection, which makes it possible to image a larger ROI quickly by acquiring the fluorescence signal of all pixels simultaneously.[37, 38] For this to be possible, certain prerequisites are required to resolve fast fluorescence signal fluctuations during a measurement. The faster acquisition is typically achieved by adapting the sensitivity and gain of the camera to match the excitation modulation frequency, which makes it possible to quickly determine the phase and demodulation values from the modulated signal. The two obtained values are then used to determine the lifetime. It is also worth noting that a sample of interest exhibiting multi-component lifetime species would require imaging it with various modulation frequencies.

2.3.3 Time Domain Lifetime

The other common approach to determine the fluorescence lifetime is known as time domain measurements. Here, a pulsed laser (ordinarily with a short pulse width) is used to excite the sample of interest followed by measuring the fluorescence intensity decay for a certain time interval, which is usually at least 4× to 5× longer than the fluorescence decay lifetime. For a first order fluorescence decay, the highest intensity is observed directly after the excitation pulse after which an exponential intensity decay is obtained. This intensity decay can be nicely described using the following equation:

$$I(t) = \sum_{i=1}^{N} \alpha_i \, e^{-\frac{t}{\tau_i}} \qquad (2.13)$$

where N represents the number of different species of the fluorescence decay (*i.e.* i = 1 depicts a single exponential decay). The lifetime of the decaying species (i) and its relative amplitude directly after the excitation pulse (*i.e.* $t = 0$) are depicted by τ and α, respectively. For multiple species (*i.e.* multi-exponential decay), it becomes important to define the fractions of each species and how to address the average fluorescence decay.[39, 40] The fractional intensity of the different species, f_i, and the average lifetime, τ_{avg}, typically obtained via the intensity-weighted lifetime represent the average time spent in the excited state and are described by using the following two equations:

$$f_i = \frac{\alpha_i \, \tau_i}{\sum_i \alpha_i \, \tau_i} \qquad (2.14)$$

$$\tau_{avg} = \sum_{i=1}^{N} \frac{\alpha_i \tau_i^2}{\alpha_i \tau_i} \qquad (2.15)$$

The time domain measurements are nowadays the main approach used for a confocal microscope capable of measuring lifetimes. In principle, the microscope is equipped with pulsed lasers which are used to excite the fluorophores in the confocal volume. The relatively low fluorophore concentration, in addition to the fact that only one photon can be detected per excitation cycle, results in a relatively low number of emitted photons. To address this issue, most modern confocal microscopes capable of measuring lifetimes deploy the TCSPC detection system to precisely measure (on the picosecond timescale) the arrival times of the emitted photons upon excitation.[23, 24] As mentioned in the TCSPC section 2.3, the components of the confocal microscope, such as the lasers and detectors are synchronized enabling an accurate mapping of the recorded photons, which are then presented on a histogram showing the photon arrival times distribution after several excitation cycles. This histogram defines the fluorescence decay and is thus used to describe the fluorescence lifetime distributions (Figure 2.12).

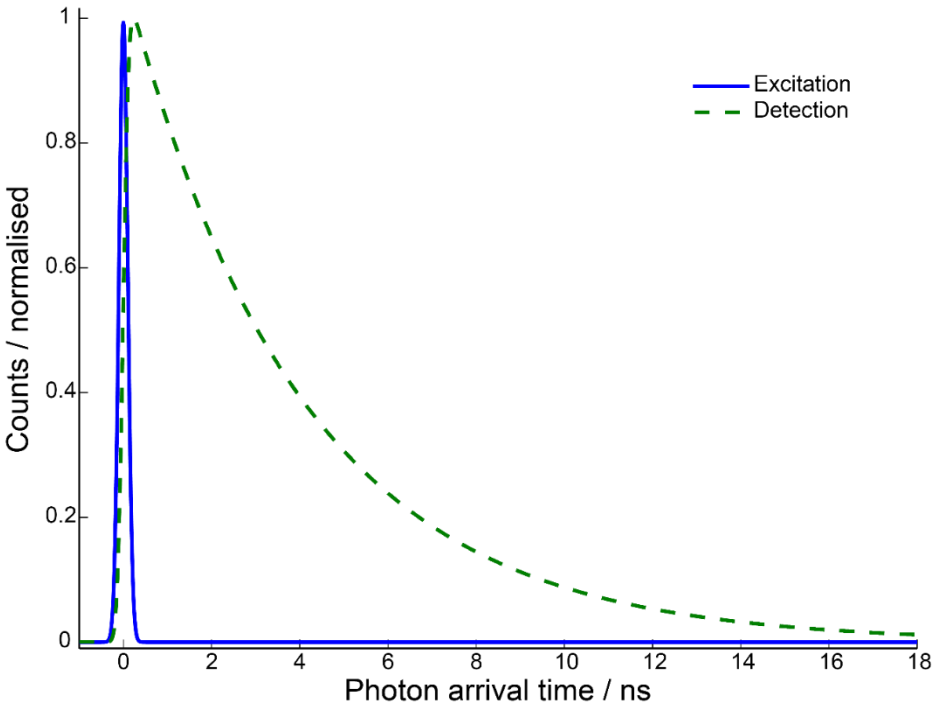

Figure 2.12 A typical histogram of the photon arrival time obtained from the TCSPC data of an Atto488 carboxylic acid fluorophore. The pulse width of the LDH-P-C-470 nm laser excitation source is shown (blue solid line) in comparison to the measured lifetime decay.

In the real world, certain considerations need to be taken in account for a time domain lifetime measurement. For example, the excitation source should ideally have a very short pulse width, which is often described by a Dirac delta function. For example, using the narrow pluses generated from femtosecond laser as an excitation source is a good approximation of a Dirac delta function. This, however, is not the case for other common excitation sources such as diode lasers that typically have pulse width of ~ 100 ps (Figure 2.12). It is worth noting that light emitting diodes and ns flash lamps, although uncommon, are still used nowadays especially for bulk measurements, which results in very broad nanosecond pulse widths that must be corrected for before a good fluorescence lifetime decay fit can be obtained. Furthermore, the other components of the system (*i.e.* TCSPC devices and detectors) exhibit similar uncertainties that affect the measured lifetimes due to their electronic jitters and timing inaccuracies. The currently used TCSPC devices in confocal microscopy have a minor internal timing jitter and a very well characterized timing resolution, both on the order of a few picoseconds. Therefore, such TCSPC devices have the least contributing component to the overall timing error. On the other hand, the single photon detectors offer a wider variety of options with very narrow timing responses, such as photomultiplier tubes (PMT) and hybrid-PMTs. The drawback of the former is its low quantum efficiency; therefore, it is quite common to either use hybrid-PMTs or avalanche photodiode detectors (APD, typically with an improved timing resolution for lifetime measurements) that offer up to ~ 65%-70% quantum efficiency approximately 3× higher than PMTs, which have a detection efficiency of ~ 20-25%. The summation of all the

uncertainties and timing inaccuracies of the system (*i.e.* excitation source, timing electronics and detectors) characterize its total time response. This temporal response is referred to as the instrument response function (IRF), which is often used in combination of the actual fluorescence decay to obtain the definite fluorescence lifetime value. This is mainly achieved via the convolution of the IRF and the fluorescence decay. There are two main approaches to measure the IRF: either by measuring a scattering sample (such as Ludox, a silica colloidal solution) or by measuring a highly quenched (usually by using potassium iodide) fluorescence sample.[41]

The convolution fit is one of several approaches for analyzing the time domain lifetime data. Although this approach is one of the most accurate ways for determining correct lifetimes after taking the IRF into account, it still has the disadvantage of being a fit. In this case, obtaining a proper fit requires high quality data and enough photons to prevent its misfitting, especially for more complex multi-exponential decays.[42, 43] The convolution approach is, thus, very accurate for a single point experiment where the obtained good signal-to-noise data for the fluorescence decay is fitted in a one-step fitting-process that is obtained in a few seconds. On the other hand, utilizing the convolution approach for a FLIM measurement differs with respect to a single point experiment. Here, the lifetime information is spread over the pixels constructing the image of interest, where the photon counts in this case are typically 100-1000 photons per pixel, significantly lower than for a single point measurement. Therefore, obtaining lifetimes values via a convolution fit for every pixel becomes a tedious and time-consuming approach, which is not desirable for FLIM measurements.

Several approaches have been developed to address the problems arising from the typical convolution procedure. For example, the photons resulting from the entire image are pooled together into one data set, which is then fitted to obtain the number of species and their different fluorescence lifetimes. Afterwards, the obtained lifetimes are related to the individual pixels by only fitting the fraction of the relevant lifetimes while keeping the lifetimes values constant. This approach speeds up the typical convolution process since only one initial fit is applied, after which a single parameter (*i.e.* the fraction of the different species in the pixel) needs to be adjusted. A more simplified approach, which is also commonly used, is the tail fit. As indicated by its name, this approach does not utilize the whole measured decay but rather its later part (*i.e.* the tail), thus neglecting the initial photon arrival times where the IRF influences the signal. Although, this approach is very simple, since an IRF (*i.e.* convolution) is no longer required, it can be misleading since the cutoff of the IRF effects the early part of the decay. For example, if the IRF is on the 200-300 ps timescale, the tail fit will not provide accurate results for lifetimes ≤ 1 ns. Moreover, deviations from the correct lifetime values arise when fitting multi-exponential decays, where the early or late cutoff of the tail fit data generates a further bias in determining the accurate lifetime values.

2.3.4 The Phasor Approach

In the last 15 to 20 years, a method to analyze the fluorescence lifetime results known as the phasor approach for FLIM,[44, 45] based on transforming the data into the Fourier space, has gained a lot in popularity and is broadly used nowadays. The phasor approach used for analyzing the FLIM measurements allows a graphical interpretation of the measured fluorescence lifetime data (*i.e.* no data fitting is required) in which each measured pixel has two values plotted on a Cartesian coordinate system. The pixel's coordinate values can be described by a vector where the demodulation (M_ω) and the phase shift (Φ_ω) determine the vector's length and angle, respectively. Accordingly, the pixels abscissa and ordinate values are represented with s (being the 1st sine Fourier coefficient of the phasor vector) and g (being the 2nd cosine Fourier coefficient of the phasor vector), respectively. The s and g coordinates are calculated using the following two equations:

$$\mathrm{s} = \mathrm{M}_\omega \sin(\Phi_\omega) = \frac{\int_0^\infty I_{i,j}(\mathrm{t}) \cdot sin(\omega t)\, dt}{\int_0^\infty I_{i,j}(\mathrm{t})\, dt} \qquad (2.16)$$

$$\mathrm{g} = \mathrm{M}_\omega \cos(\Phi_\omega) = \frac{\int_0^\infty I_{i,j}(t) \cdot cos(\omega t)\, dt}{\int_0^\infty I_{i,j}(t)\, dt} \qquad (2.17)$$

where $I(t)$ represents the photon counts of the time bin, t, in the fluorescence lifetime decay histogram; the indices i and j define the measured pixel in the image and ω represents the angular modulation frequency.

Although the phasor approach was originally applied to frequency lifetime domain data, minor modifications to the initial formulae enable its usage for time domain lifetime measurements as well. In principle, the phasor utilizes a modulated excitation source after which the demodulation and phase values are used to represent lifetime values onto a Cartesian coordinate phasor plot. The typically sinusoidally modulated excitation source is replaced by a pulsed laser excitation source for time domain experiments. The trick relies on the fact that the pulsed laser, with certain modifications that must be accounted for, is a sort of modulation source that can be used for the phasor approach. Here, the conversion from the time domain via a Fourier transformation changes the base of the Cartesian coordinate system, which are corrected for by rescaling and rotating it. A subsequent implication of changing the coordinate system is mainly depicted by the IRF, which is relatively easy to account for by measuring a calibration sample (a reference with a known lifetime). Thus, after the necessary corrections, the IRF phase shift Φ_{Inst} and the IRF demodulation M_{Inst} can be determined. Afterwards, Φ_{Inst} and M_{Inst} are applied to equations 2.16 and 2.17 resulting in the following modified equations:

$$s_{ref} = \frac{M_\omega}{M_{Inst}} \sin(\Phi_\omega - \Phi_{Inst}) = \frac{\int_0^\infty I_{i,j}(t) \cdot sin(\omega t - \Phi_{Inst})\, dt}{\left(M_{Inst} \cdot \int_0^\infty I_{i,j}(t) dt\right)} \qquad (2.18)$$

$$g_{ref} = \frac{M_\omega}{M_{Inst}} \cos(\Phi_\omega - \Phi_{Inst}) = \frac{\int_0^\infty I_{i,j}(t) \cdot cos(\omega t - \Phi_{Inst})\, dt}{\left(M_{Inst} \cdot \int_0^\infty I_{i,j}(t) dt\right)} \qquad (2.19)$$

The correction terms Φ_{Inst} and M_{Inst} are thus easy to implement by inducing a rotation and scaling of the phasor plot, such that the new coordinate system results in the corrected theoretically expected phasor plot (Figure 2.13 A).

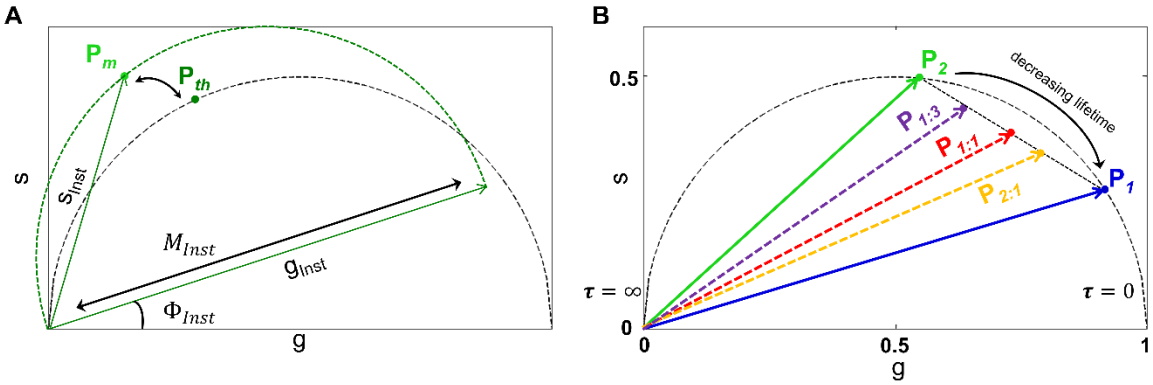

Figure 2.13: Schematic of two phasor plots where the dotted curve represents the universal phasor semicircle. A) Transformation of the phasor plot after measuring the IRF, which determines the phase shift Φ_{Inst} and demodulation M_{Inst} that needs to be accounted for. After the rotation and scaling of the phasor plot, P_m (measured phasor) falls on the theoretical position of the expected phasor plot P_{th} in the new coordinate system. B) Shows two measured phasors, P_1 and P_2, depicting a mono-exponential decay (lying on the arc). A mixture of different fractions of these two phasors results in a mixture of phasors on the line connecting P_1 and P_2. In this case, the exact positions of $P_{1:3}$ (purple phasor), $P_{1:1}$ (red phasor) and $P_{2:1}$ (yellow phasor) represent mixtures of 1:3, 1:1 and 2:1 of P_2 and P_1, respectively.

Another important aspect of the phasor plot is depicted in equations 2.9 and 2.10. To better visualize it, the lifetime is displayed with respect to the phase and demodulation values as such:

$$\omega\tau_\Phi = \tan(\Phi_\omega) \qquad (2.9, modified)$$

$$\omega\tau_m = \left(\frac{1}{M^2 - 1}\right)^{-\frac{1}{2}} \qquad (2.10, modified)$$

Here, the Fourier transform in the case of a mono-exponential lifetime decay results in equal phase and demodulation lifetimes. Inserting these values into the Cartesian coordinate phasor plot results in the following equation:

$$\frac{\mathrm{s}}{\mathrm{g}} = \left(\frac{1}{(s^2 + g^2) - 1}\right)^{-\frac{1}{2}} \qquad (2.20)$$

Equation 2.20 can be simplified into $s^2 + g^2 = g$, which defines a semicircle of radius 0.5 centered at the ordinates (0.5, 0). This semicircle is referred to as the universal circle, where all mono-exponential lifetime data points lie on the radius of this semicircle and lifetimes exhibiting multi-exponential decays fall within the arc of this universal semicircle. The pixels depicting shorter lifetime decays lie next to the (1, 0) coordinates whereas pixels depicting long lifetime decays lie next to the (0, 0) coordinates (Figure 2.13 B). Noteworthy, the position of the pixel, which defines short and long lifetimes, is relative to the semicircle's scale. This can be modified by the modulation frequency, where the pixel's position on the phasor semicircle shifts to the right for higher modulation frequencies. Utilizing the two phasor coordinates can be used to derive two different lifetime values, determined based on the phase shift (τ_Φ) and the demodulation (τ_M), described using the following two equations given by:

$$\tau_\Phi(\omega) = \frac{1}{\omega} \cdot \frac{s}{g} \qquad (2.21)$$

$$\tau_M(\omega) = \frac{1}{\omega}\sqrt{\frac{1}{g^2 + s^2} - 1} \qquad (2.22)$$

Another distinctive and important feature of the phasor approach is that the lifetimes of multiple species within a sample can be added vectorially (*i.e.* a fraction weighted vector addition) via a line connecting the individual components of the two species on the arc of the universal semicircle (Figure 2.13 B).

2.4. Fluorescence Fluctuation Spectroscopy (FFS)

Similar to the fluorescence lifetime approach, FFS techniques also utilizes the temporal variations of the detected photons on a longer time range beyond the typical ns fluorescence lifetime timescales. FFS is a tool employed to explore the dynamics of a system by recording the intensity fluctuations from fluorescent particles in a small observation volume. In FFS, monitoring the intrinsic fluctuations arising from the fluorophores provides a suitable method to probe the properties and interactions of the labeled system of interest. For example, observing and analyzing the fluctuations of fluorescently labeled molecules in the confocal volume comprises a set of different processes occurring at different timescales,[46-50] which can be utilized to address processes such as rotational or translational diffusion and photophysical properties like the fluorophore's intrinsic blinking. The earliest attempts to use fluctuation spectroscopy date back to the beginning of the 20th century.[51] The main usage of this tool, back then, attempted to provide a general explanation of the Einstein's intrinsic fluctuations and Brownian motion observations,[52] after which fluctuation spectroscopy remained infrequently exploited for several decades. Only in the last 50 years, fluorescence was realized as a tool for fluctuation spectroscopy,[53] however, the remarkable features of FFS were first realized upon combining it with confocal microscopy.[54] The combination of FFS with confocal microscopy evolved into a frequently utilized approach to study fluctuations in femtoliter sized observation volumes. This small volume reduced the number of particles observed, which made the fluctuations more pronounced and suitable to monitor and analyze.

Alongside the development of confocal microscopy, which allows a small observation volume, different FFS methods have been established and utilized to study the dynamics and interactions of various biological and physical systems. One FFS approach examines the amplitude of the fluctuations by analyzing the probability distribution, such as the fluorescence intensity distribution analysis,[55] photon counting histogram[56] or fluorescence cumulant analysis.[57] These methods are good for calculating the concentrations and the molecular brightness of the various fluorescent species in the sample. Another approach to analyze the fluctuations is by studying its temporal changes. To picture this approach, consider for example the intensity fluctuations that arise from the temporal movement of a fluorophore in the confocal volume and the cumulative information that can be obtained regarding its diffusion and emissive properties. Here, the visualized changes are correlated in time in what is commonly known as FCS. These two approaches of FFS have been used to study phenomena such as translational diffusion,[54, 58] flow[59] and

transport processes,[60] chemical reactions[61] and protein oligomerization[62, 63] both in vivo and in vitro.

In this section, the details of FCS will be described with a brief overview of the different processes that can be observed on the different timescales. For example, investigating the fast correlations can be used to study rotational diffusion, whereas the slower correlations are used for studying the photophysics and translational diffusion of the sample of interest. Furthermore, a brief description on the spatial correlation spectroscopy will be introduced, such as image correlation spectroscopy and one of its temporal extensions, raster image correlation spectroscopy (RICS). Characterization measurements using some of these different techniques are demonstrated (later on in section 2.5.7) within the scope of showing the capabilities of the developed CLSM.

2.4.1. Fluorescence Correlation Spectroscopy (FCS)

Fluorescence correlation spectroscopy is a powerful method that utilizes the fluorescence intensity fluctuations to acquire insights into dynamic processes.[64] In this method, the measured fluorescence intensity is correlated with itself to determine the time dependence (self-similarity) of the intensity fluctuations, *i.e.* the autocorrelation function (ACF). The theory behind FCS has been addressed thoroughly in the 1970s, where its first implementation was used to study the binding of ethidium bromide to DNA.[53, 65, 66] Such binding and diffusion studies are analyzed by calculating the temporal ACF, which can be described using the following equation:

$$G(\tau) = \frac{\langle I(t).\langle I(t+\tau)\rangle\rangle}{\langle I(t)\rangle^2} - 1 = \frac{\langle \delta I(t).\delta I(t+\tau)\rangle}{\langle I(t)\rangle^2} \quad (2.23)$$

where $G(\tau)$ describes the autocorrelation amplitude as a function of lag time τ, determined from the intensity $I(t)$ and the fluctuations in the intensity $\delta I(t) = I(t) - \langle I(t)\rangle$. The intensity or fluctuations within the $\langle ... \rangle$ angled brackets represent the average over all the possible time points combination.

FCS is mostly used to investigate the diffusion of the particles of interest through the observation volume. The random diffusion of the fluorescent particles in and out of the confocal volume results in changes of the measured fluorescence intensity, which causes fluctuations from the average fluorescence signal (Figure 2.14). Observing the ACF decay provides insights into the diffusion time of fluorescent particles in the observation volume. In this case, the diffusion time depends on the particles' diffusion coefficient and the confocal volume size. Noteworthy, correlating the fluctuations on long time scales leads,

in the end, to a zero-correlation, which indicates that, after a certain time, the fluctuations are totally randomized and the ACF decays to zero (Figure 2.14, right).

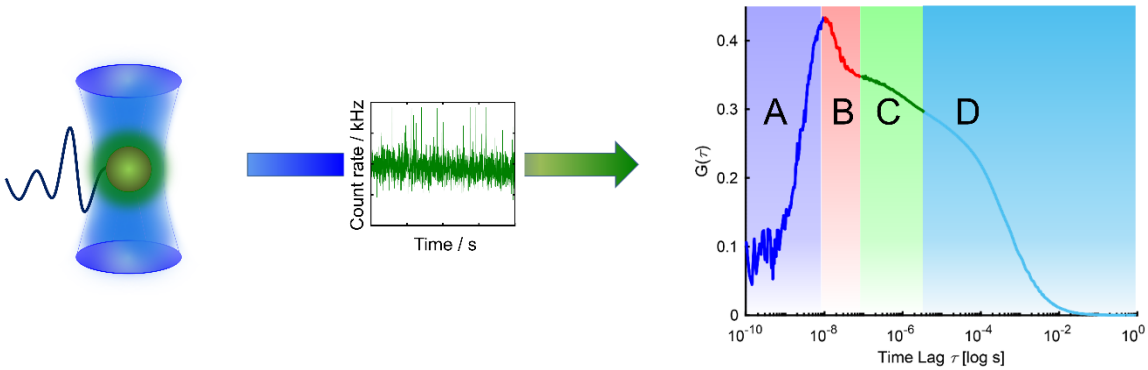

Figure 2.14: Schematic representation of a fluorescently labeled molecule diffusing through the confocal observation volume (left), which generates a fluctuating intensity throughout the measurement (middle). The analysis of the fluctuations is presented by an example of the correlation function that ranges from ~100 ps to ~100 ms. A range of different processes are observed throughout the correlation function (right) like antibunching (**A**), rotational dynamics (**B**), photophysics (**C**) and translational diffusion (**D**).

Another important feature of an FCS measurement is the amplitude of the ACF at lag time zero $G(0)$. In the case of a freely diffusing particle, the amplitude is inversely proportional to $\langle N \rangle$ (the average number of particles in the observation volume), consequently inversely proportional to the concentration (C). Here, the relationship between the measured fluorescence intensity $I(t)$ and the number of particles N can be described as $I(t) = \varepsilon\, N$, where ε represents the molecular brightness of the individual particles. In this case, the distribution of the fluorescent particles follows Poissonian statistics where $\langle N \rangle$ is the mean value, and the intensity deviations $\delta I(t)$ scale with the standard deviation $\sigma = \sqrt{N}$. Hence, the ACF at lag time zero can be described as shown in eq. 2.24:

$$G(0) = \frac{\langle \delta I(t)^2 \rangle}{\langle I(t) \rangle^2} = \frac{\varepsilon^2 \langle \delta N^2 \rangle}{\varepsilon^2 \langle N \rangle^2} = \frac{\langle N \rangle}{\langle N \rangle^2} = \frac{1}{\langle N \rangle} \qquad (2.24)$$

In eq. 2.24, the ACF at lag time zero is ideally described with an observation volume that exhibits a uniform illumination. This, however, is not the case for confocal illumination, which is well approximated by a 3D Gaussian model. Therefore, a geometric correction factor (γ) is used to account for the differences arising from the inhomogeneity of a single-photon excitation observation profile. The corrected $G(0)$ from eq. 2.24 is then modified for by $\gamma = \frac{1}{\sqrt{2^3}}$ to describe it as follows:

$$G(0) = \frac{\gamma}{\langle N \rangle} = \frac{1}{\sqrt{2^3}\,\langle N \rangle} \qquad (2.25)$$

Noteworthy, the correction factor γ is sometimes neglected as shown for eq. 2.24. In this case, relating the number of particles to a concentration should be corrected for by considering an effective observation volume that is given by $V_{eff} = \pi^{\frac{3}{2}}\omega_r^2\omega_z$. This effective volume deviates from the γ factor corrected confocal volume accounting for the non-uniform illumination profile and is represented by $V = \gamma . V_{eff}$. Hence, including or neglecting the γ factor determines the appropriate volume to be used, which is important to obtain the correct concentrations. Moreover, accounting for the γ factor is critical to clarify what value of the molecular brightness ε is reported. In the case where the γ factor is included, ε is defined as the peak molecular brightness for the emitting fluorescent particle at the center of the PSF. Otherwise, for the uncorrected V_{eff} volume, the brightness value will be an average value over the whole observation volume.

The time dependent decay of the temporal ACF can be utilized for describing the diffusion of the fluorescent particles in the confocal volume. Here, the previously described 3D Gaussian model can be used as an approximation to determine the particles' diffusion time (τ_D) using the following equation:

$$G(\tau) = \frac{\gamma}{\langle N \rangle} \cdot \left(1 + \frac{\tau}{\tau_D}\right)^{-1} \cdot \left(1 + \frac{\tau}{\left(\frac{\omega_z}{\omega_r}\right)^2 \tau_D}\right)^{-\frac{1}{2}} \qquad (2.26)$$

where, τ_D represents the diffusion time. After an accurate determination of the observation volume size, τ_D can be applied to determine the diffusion coefficient of the fluorescent particle by the following equation:

$$D = \frac{{\omega_r}^2}{4\tau_D} \qquad (2.27)$$

Generally, diffusion occurs on the ms timescale and is the last process observed in an ACF, given that once a particle leaves the volume, the correlation is lost. It usually takes fast, small particles ~10 µs to 500 µs (depending on the particles' volume and mass) to diffuse through the confocal volume (Figure 2.14, D), whereas large particles can be significantly slower and their diffusion times can go up to seconds in the case of nanoparticles. Therefore, it is quite common to utilize the diffusion behavior to study molecular interactions such as dissociation or binding that alter the mobility of the molecule of interest, which in turn changes its diffusion time.

The diffusion of fluorescent particles is, however, not the only process that can be observed in an ACF. Some of these processes are relevant for studying dynamics on timescales faster than the translational diffusion. For example, observing the rotational dynamics that the fluorescent particle of interest undergoes allows one to measure

conformational changes (Figure 2.14, B). Typical rotation conformations of small molecules occur on the ps timescale and can extend to longer ns timescales for fluorescent proteins.[67-70] It is also worth mentioning that molecular rotations can be utilized to study interactions.

The fastest process that is typically observed in an ACF arises from antibunching,[71, 72] which usually results in a decrease of the correlation amplitude on timescales similar to the lifetimes of a fluorophore that is typically ~1 to 10 ns (Figure 2.14, A). In short terms, the photon antibunching arises from the properties of single emitter fluorophores. The lifetime of a fluorophore defines the delay between the emission of two consecutive photons. This behavior is measured by splitting the emission on two separate detectors to avoid dead time effect after detecting a photon (typically 10 to 100 ns) and results in an anticorrelation. Antibunching can be used to study, for example oligomeric interactions, where the stoichiometry of the single emitter fluorophore changes upon oligomeric formation. This results in a densely labeled oligomer having multi emitters, where the emitter stoichiometry is inversely proportional to the decrease in the curve.[73, 74]

Another correlation that can be observed in the ACF comes from the photophysics of fluorophores in the observation volume. These fluctuations occur on timescales that are usually faster than the translational diffusion and result from the fluorophore transitioning into a dark (non-emissive) state such as ISC into a triplet state (Figure 2.14, C).[75-78] Since the triplet state usually appears on the ~ 10 µs timescale, it is common to measure this term in FCS, which can be obtained by the following equation:

$$G_{triplet}(\tau) = 1 + \frac{T}{1-T} . e^{-\frac{t}{\tau_T}} \quad (2.28)$$

where, T and τ_T represents the triplet molecular fraction and their transition rates, respectively. In experiments focusing on translational diffusions, the triplet state contribution is often artificially suppressed by reducing the laser power in order to lessen the undesired dark states. Nevertheless, this process can still be utilized in certain experiments to study, for example, photophysical transitions such as the cis-trans conformations of cyanine dyes.[79]

2.4.2 Fluorescence Cross-Correlation Spectroscopy (FCCS)

It is possible to take FCS a step further, if the sample of interest possess two or more labels with different emissive properties. In this case, the fluctuating signal on a certain detector is correlated for similarity from the fluorescence signal measured on another detector, which is different than FCS where the signal on one detector is correlated with itself. In FCCS, similarity in the fluctuations observed between two species, i and j, is

measured in two channels and extracted using the cross-correlation function (CCF). The CCF can be described using the following equation:

$$G(\tau) = \frac{\langle \delta I_i(t).\, \delta I_j(t + \tau) \rangle}{\langle I_i(t) \rangle.\, \langle I_j(t) \rangle} \quad (2.30)$$

One application of FCCS is the study of fast correlations and is implemented using a 50/50 beam splitter that equally splits the signal into two different channels. Similarly, rotational diffusion can be measured by using a polarizing beam splitter that splits the parallel and perpendicular components of the polarized light onto two different channels.[80, 81] However, the most common application of FCCS is by spectrally correlating signals on detectors that are sensitive to different wavelengths; dual-color FCCS (dc-FCCS). The strength of dc-FCCS is its unambiguity in investigating molecular interactions, where the presence of an interaction or cojoined movement between two differently labeled species is best visualized by the cross-correlation signal.[26, 61, 82-85] The precise quantification of interactions is achieved by monitoring the amplitude of the CCF. In this case, the amplitude is inversely proportional to the total number of labeled particles ($N_{i,t}$ and $N_{j,t}$) and proportional to the number of dually labeled particles dually ($N_{i,j}$). The CCF amplitude at lag time zero can be implemented to determine the dual labeled species fraction[86] as described in the following equation:

$$G_{CCF}(0) = \gamma \frac{N_{i,j}}{N_{i,t}.\, N_{j,t}} \quad (2.31)$$

Noteworthy, the presence of a cross-correlation signal might sometimes arise from the measurement conditions where spectral crosstalk of the shorter emission wavelength can bleed-through and be detected in the longer wavelength detector. Therefore, it is crucial to account for the crosstalk signal when accurately investigating interactions. An elegant way to achieve this is by applying pulsed interleaved excitation as previously described in section 2.2.4.

2.4.3 Image Correlation Spectroscopy (ICS)

In a CLSM, it is possible to extend FCS into spatial dimensions by correlating the measured fluorescence signal of the pixels in the x- and y- directions within an image to determine the 2D spatial self-similarity in the desired ROI. This equivalent of FCS in space is known as ICS[87, 88] and is resolved in two dimensions using the following equation:

$$G(\xi, \psi) = \frac{\langle I(x,y).\, I(x + \xi,\ y + \psi) \rangle}{\langle I(x,y) \rangle^2} - 1 = \frac{\langle \delta I(x,y).\, \delta I(x + \xi,\ y + \psi) \rangle}{\langle I(x,y) \rangle^2} \quad (2.32)$$

where, x and y represent the two axial dimensions of an image and ξ and ψ denote the pixel lag in space along the x and y dimensions, respectively. The intensity and the

fluctuations of the intensity are represented with $I(x,y)$ and $\delta I(x,y) = I(x,y) - \langle I(x,y)\rangle$, respectively, where the $\langle \ldots \rangle$ angled brackets represent the intensity fluctuations average over the 2D spatial positions. The random spatial fluctuations of particles that are smaller than the confocal observation volume provide an excellent measure of the PSF and can be approximated by a 2D Gaussian model given by:

$$G(\xi,\psi) = \frac{\gamma}{\langle N\rangle} \cdot e^{\left(-\frac{\delta r^2(\xi^2+\psi^2)}{{\omega_r}^2}\right)} \qquad (2.33)$$

where, δr represents the pixel size in the acquired image.

The main implementation of ICS is to analyze the spatial fluctuations in 2D images. The spatial autocorrelation of a ROI in an image can be utilized to determine the average number of the fluorescing particles in the observation volume and investigate their interactions such as the formation of aggregates. Here, the fluorescence intensity and the amplitude at lag time zero of the spatial correlation function (inversely proportional to the average number of particles) makes it possible to determine the concentration and molecular brightness of the fluorescing particles. Hence, ICS is a tool suitable to study the stoichiometry of particles, which can be utilized to investigate oligomer formation and explore the distribution and density of these formed oligomers.

Two approaches are commonly implemented to acquire the 2D images. Fast frame-to-frame acquisition is mostly recorded with a camera, where all the pixels are acquired at once. On the other hand, images acquired on a CLSM equipped with a single point detector such as APDs (PMTs have been utilized as well, mainly in the 1990's) are quite common but are drastically slower than the camera due to the pixel-to-pixel acquisition of a 2D image. When using a camera, the images are recorded over a larger FOV, which increases the sampling speed and improves the sampling accuracy by correlating fluctuations on a larger FOV (typically > 50 µm) compared to the size of the confocal observation volume.

As for FCS, ICS can be extended beyond a single detection channel, enabling the cross-correlation between two different images and is known as image cross-correlation spectroscopy (ICCS).[89] In this case, the fluctuating signal is often split spectrally between two different channels, where a cross-correlation between the two differently labeled species i and j is observed once the two species exhibit a certain degree of colocalization. The ICCS function can be described using the following equation:

$$G(\xi,\psi) = \frac{\langle \delta I_i(x,y).\, \delta I_j(x+\xi,\ y+\psi)\rangle}{\langle I_i(x,y)\rangle.\, \langle I_j(x,y)\rangle} \qquad (2.34)$$

2.4.4 Raster Image Correlation Spectroscopy (RICS)

The correlations as described by ICS can be modified and extended to combine both the spatial and temporal aspects of the 2D image acquisition when raster scanning is used. For camera-based acquisition, all pixels are simultaneously acquired over a large area illuminated by excitation. In this case, there is no temporal information with a single image. Alternatively, a large ROI can be scanned using a CLSM where the image acquisition is realized by the consecutive pixel to pixel acquisition, which adds a time component to the spatial 2D image measurement. Utilizing this spatio-temporal aspect of the image acquisition enables the extension of ICS into RICS. Nowadays, RICS is a widely applied image correlation method to study dynamic movements occurring on the image acquisition timescale.[90-92] In RICS, a predetermined rastering of the confocal volume is performed to obtain a 2D image. Here, a fast pixel wise movement along the x-axis is applied, which is governed by the pixel dwell time τ_p. Following the acquisition of the first line, the confocal volume is retracted to start the whole process again on a second line shifted one pixel on the y-axis (Figure 2.15). Due to this retraction to start a second line, the overall acquisition of the pixels in the y-direction, described by the line time τ_l, is slower than in the x-direction. Small particles that diffuse rapidly (*i.e.* quicker than the laser movement on the x-axis) exhibit a temporal decay that is observed by a fast pixel-to-pixel correlation decay in the x-direction. On the contrary, slowly diffusing particles are nearly static on the fast x-axis acquisition time, thus displaying a correlation resembling the squared confocal volume profile. Due to the slower movement on the line-to-line y-direction, the profile changes of slow diffusing particles can be easily seen on the y-axis timescale. As a result, RICS is a robust approach to study the mobility of diffusing fluorescent molecules. Fast dynamics are observed on the x-axis (µs diffusion times) while slow dynamics that are relatively immobile during the line scan are observed on the y-axis (ms diffusion times).

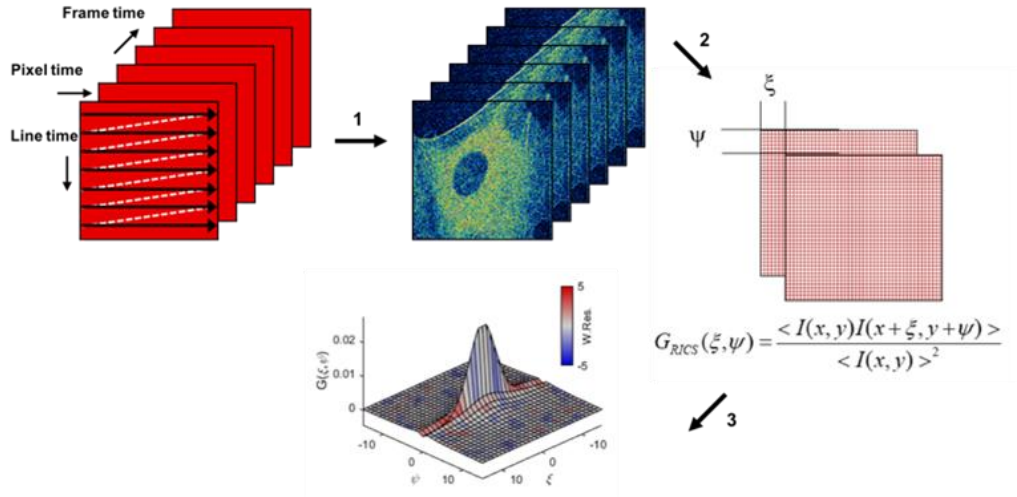

Figure 2.15: Schematic showing the RICS data acquisition. (1) The 2D raster scan pattern of pixels to obtain the different images. (2) The correlation of the 2D acquired images with horizontal and vertical spatial increments, which provides spatio-temporal diffusion information of the particles moving on the different pixel,

line and frame timescale. (3) Fit of the obtained correlation values from (2) that enables the extraction of the number of particles and their diffusion values. Figure is adapted from Gegenfurtner et. al.[93]

For RICS measurements the correlation algorithm is the same as in equation 2.32, which was applied for ICS as well. The adjustment here is to include the temporal factor by modifying the fit, yet assuming that the confocal volume is approximated with a 3D Gaussian focus. For a single mobile component N_{mob}, the spatial ACF can be described using the following equation given by:

$$G(\xi,\psi) = \frac{\gamma}{N_{mob}} \cdot \left(1 + \frac{4D \cdot (\xi\tau_p + \psi\tau_l)}{{\omega_r}^2}\right)^{-1} \cdot \left(1 + \frac{4D \cdot (\xi\tau_p + \psi\tau_l)}{{\omega_z}^2}\right)^{-\frac{1}{2}} \cdot e^{\left(-\frac{\delta r^2(\xi^2+\psi^2)}{{\omega_r}^2+4D\cdot(\xi\tau_p+\psi\tau_l)}\right)} \quad (2.35)$$

where ξ and ψ represent the spatial lag in pixels along the fast x-axis and the slow y-axis, respectively, while δr represents the pixel size. In some measurements, certain particles of interest might be static or move on timescales that are much slower than the line-to-line scanning speed (typically 10-50 ms/line). In this case, these particles are characterized as immobile particles N_{imm}, which can be described using the following equation:

$$G(\xi,\psi) = \frac{\gamma}{N_{imm}} \cdot \exp\left(-\frac{\delta r^2(\xi^2+\psi^2)}{{\omega_r}^2 + 4D \cdot (\xi\tau_p + \psi\tau_l)}\right) \quad (2.36)$$

The unique spatio-temporal combination aspect of RICS offers a set of features that are advantageous compared to FCS. For example, the pixel size can be used as an external ruler providing the opportunity to measure the focus size and diffusion coefficients at same time. Moreover, the diffusion information from a RICS measurement is acquired from a much larger ROI, which (in comparison to a single point detection) provides spatially averaged results. Another important advantage of RICS arises from the fast laser scanning of the sample of interest, where molecules are only exposed for a short time. This decreases the photobleaching and blinking effects compared to FCS.[25] This feature is especially advantageous for cellular measurements where the typically-used fluorescent proteins are less photostable.

In the past, RICS measurements were feasible only by selecting a squared ROI to image. A quite useful add-on for RICS is the arbitrary region RICS (ARICS),[94] which enables a preferential selection of the ROI that can differ from the standard squared ROI. Hence, ARICS removed the previous constraints and enabled various pixel selection tools, such as applying an intensity mask or drawing a random shape that chooses the desired pixels. An advantageous implementation of ARICS is regarded for heterogeneous samples where the spatial correlations are drastically affected by any tiny inhomogeneities that are brighter than the average fluorescence. For example, to remove the effect of aggregates while performing a cellular scan, ARICS can be applied to remove these regions that could bias the outcomes of a measurement.

2.5. Details of the Developed CLSM

In this section, a thorough explanation of the home-built CLSM used in the scope of this work is presented. The detailed setup schematization is shown in Figure 2.16, where the different setup components and capabilities are discussed in the following sub-sections. Following the discussion of setup components, a brief description of the perfect focus system (PFS) and the electronics is shown in Figures 2.17 and 2.18, respectively. The transmission spectra of the used polychroics, dichroics and filters are presented in the appendix A.1. The development of the setup was carried out with the help of Fabian Knechtel during my supervision of his master thesis, therefore, his assistance with the setup's upgrade and figures, alongside the preparation of the electronics drawing are highly acknowledged.

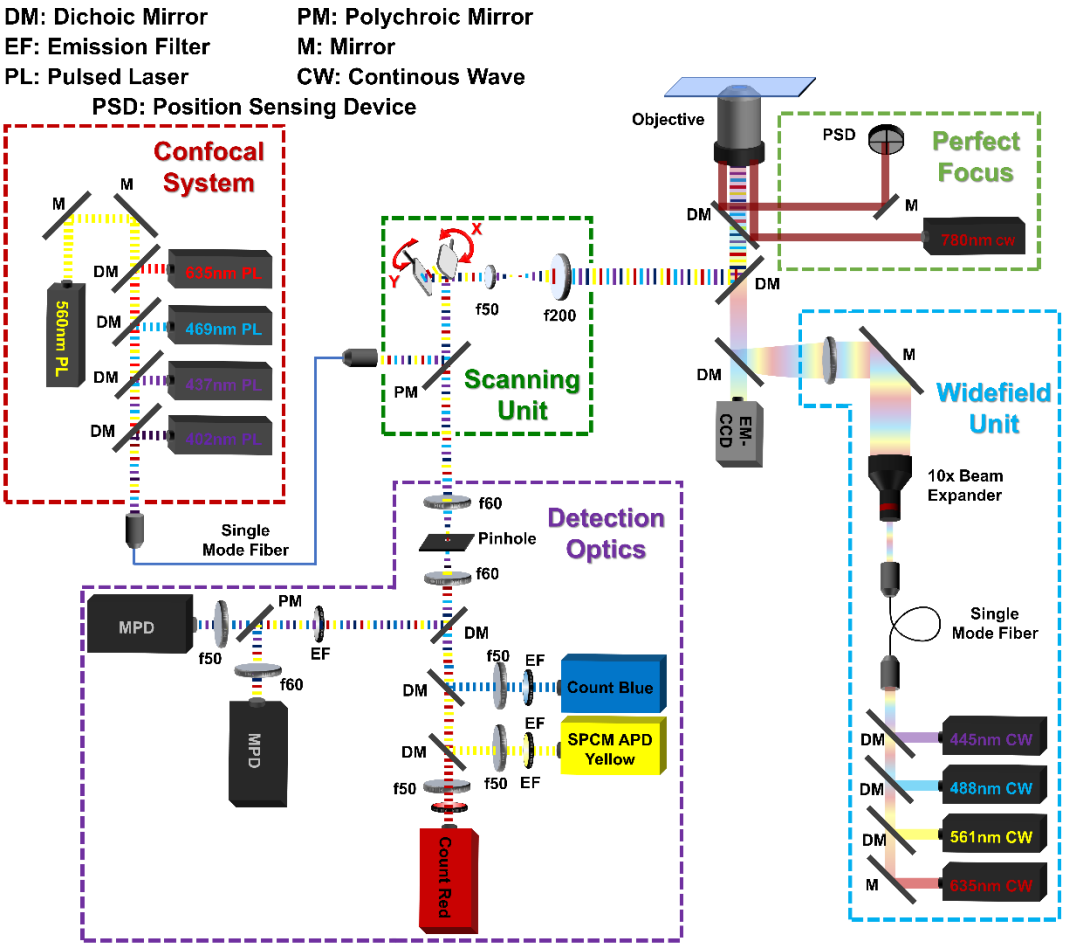

Figure 2.16: Scheme showing the details of the CLSM setup used during the scope of this thesis for performing the different fluorescence experiments. A thorough description of the individual components is presented in the following sections.

2.5.1. Laser and Excitation Optics

The excitation unit consists of a confocal and a wide-field modality. The excitation unit for the confocal pathway (Figure 2.16, red box) features five pulsed diode lasers for excitation at 402 nm (LDH-P-C-400B, PicoQuant), at 437 nm (LDH-P-C-440, PicoQuant), at 469 nm (LDH-P-C-470, PicoQuant), at 559 nm (LDH-P-FA-565, PicoQuant) and at 635 nm (LDH-P-C-635B, PicoQuant). The most frequently used lasers for the fluorescence measurements consists of the blue, yellow and red laser combination (469 nm, 559 nm, 635 nm), especially for live-cellular studies featuring the fluorescent proteins GFP, YFP or mCherry, and RFP, respectively. The 445 nm laser is mostly used in live cell measurements to excite the fluorescent protein CFP. The 402 nm laser is mainly used for investigating the auto-fluorescence of a sample or for photo activation of fluorophores. All lasers are driven by a picosecond pulsed driver (PDL 828 Sepia II, PicoQuant) with the possibility of three different main master repetition rates of 80, 64 and 50 MHz with dividers among each of these frequencies to achieve repetition rates as low as 610 Hz. Moreover, the laser driver can be used to optimize the PIE experiments where the lasers can be electronically delayed (with a resolution down to a few picoseconds). The laser driver also provides the synchronizing signal for the scanner and the TCSPC cards. All lasers are superimposed using a caged system with different dichroics (for further details, check Appendix A.2, Microscope parts list) after which they are coupled into a single mode fiber, to ensure an optimal overlay and beam shape of the coupled lasers (coupler: PAF2A, Thorlabs; fiber: QPMJ-A3A, 3AF-488-3.5/125-3-5-1, OZ Optics). The beam, at the fiber exit, is then collimated by a 20x apochromatic objective (Mitutoyo Plan Apochromat Objective 20x, Mitutoyo). To achieve the desired count rates for a certain measurement, the laser power is adjusted using a neutral density filter-wheel (NDC-100C-2M, Thorlabs) before the beam is coupled into the fiber. For lowering the laser power further (< 50 to 100 nW), a neutral density filter-wheel with OD 4 (NDC-100C-4M, Thorlabs) was added to the pathway.

2.5.2 Confocal Laser Scanning Path

To perform scanning measurements, the light beam is guided through a scanning unit (Figure 2.16, green box). A polychroic mirror (Semrock Di01–R405/488/561/635, AHF Analysentechnik, Figure A.2) is used to separate the laser excitation and the fluorescence emission, reflecting the former into the back port of the microscope. Two, closely-spaced galvanometer scanning mirrors (scanner: 6210H; controller: MicroMax 671 Series, Cambridge Technology) provide the possibility for fast beam scanning. A Field Programmable Gate Array (FPGA, cRIO-9076 model, National Instruments) controls the scanning shape, size and speed. An achromatic Keplerian telescope (achromatic lens doublets scanning lens SL50–CLS2 and tube lens TL200–CLS2, Thorlabs) expands and projects the midpoint between the scanning mirrors onto the back focal plane of the

objective, slightly overfilling the back aperture of the oil immersion objective. The microscope body is equipped with two different objectives. For measurements close to the glass surface demanding a high lateral resolution and axial stability, the 1.49 NA 100x oil immersion objective (CFI Apo TIRF 100×, Nikon) is used. For distances deeper than 3 µm above the surface, the 1.27 NA 60x water immersion objective (Plan Apo IR 60× WI, Nikon) is used. In this case, the sample should desirably have a similar index of refraction to water so that the aberrations do not increase for larger distances.

2.5.3 Detection Optics

The fluorescence of the sample is collected by the same objective that is used to focus the laser beam. Here, the fluorescence emission returns along the same excitation pathway until it reaches the polychroic mirror after which the emission is separated from the excitation beam. The fluorescence emission is then focused with a 60 mm achromatic lens (AC254-060-A-ML, Thorlabs) onto an 80 µm pinhole and enters the detection box (Figure 2.16, purple box). In the detection box, the beam is recollimated with an identical 60 mm achromatic lens. The collimated emission is then spectrally split by reflecting the blue-green emission wavelength (565DCXR, AHF Analysentechnik) and then the orange-red wavelengths (Chroma Q660LP, AHF Analysentechnik), Figure A.3. The three different emission wavelengths, blue-green, yellow-orange and red-IR are then focused on single photon avalanche photodiodes (SPAD or APD). Depending on the emission wavelength and the desired timing resolution of the APDs, the emission light in the detection unit is focused on either a CountBlue® (Laser Components), a SPCM-AQR-14 (Perkin Elmer), a Count® module (Laser Components) or two MPD's (PDM series, PicoQuant). To successfully block the scattered or reflected laser light, a Chroma ET520/40 bandpass filter, a Chroma ET595/50, and a Semrock 635 nm Edge-Basic long pass filter (all AHF Analysentechnik) are used for the blue-green, the yellow-orange, and the red-IR detection elements, respectively (Figure A.3). Noteworthy, the timing of the recorded photons by each APD are achieved via three separate but synchronized TCSPC cards (SPC-150, Becker&Hickl) utilized for each detector.

2.5.4 Wide-Field and TIRF Microscopy Paths

The wide-field microscopy path (Figure 2.16, blue box) consists of four continuous wave lasers (CW lasers), a 445 nm laser (MDL 0445-06-01.0050-100, Cobolt), a 488 nm laser (55mW 488nm Diodenlaser, Lasertack), a 561 nm laser (LC GCL-025-561-0.25%, CrystaLaser) and a 635 nm laser (200mW 635nm Diodenlaser, Lasertack). These wavelengths were chosen to have the same capabilities as for the confocal modality, with the advantage that the wide-field modality allows illumination of the sample with a larger FOV. The larger FOV facilitates the quick identification and location of the desired ROI, such as a successfully GFP transfected cell when live-cell imaging is performed. Although

the back port of the microscope is used for both the wide-field and confocal pathways, the former is separated from the confocal pathway by a double-staged microscope body (Eclipse Ti Series, Nikon). The CW lasers are focused on the back focal plane of the objective using a 300 mm achromatic doublet lens (AC254-300-A-ML, Thorlabs). The collected fluorescence is separated by a dichroic mirror (405/488/561/647 rcp, AHF Analysentechnik, Figure A.4) and imaged on an Electron-Multiplying-Charged-Coupled-Device (EMCCD) camera (iXon Ultra 897, Andor) at the left port exit of the microscope body. Alternatively, the collected fluorescence can be guided to the ocular lens for a quick investigation of the sample by eye. Furthermore, the wide-field modality can be used for performing TRIF microscopy measurements. Here, the 300 mm focusing lens is mounted on a motorized stage that allows traveling up to 12 mm controlled through an actuator (Z812B and KDC101 servo motor, Thorlabs). This makes it possible to move the focus of the lens on the BFL plane to achieve total internal reflection at the coverslip-specimen interface and enables investigation of the sample of interest on or near to the surface.

2.5.5 Perfect Focus Built-in Unit

One issue that arises while performing a set of experiments is the drift of the sample, especially in the axial dimension. This drift is often due to air flows, thermal expansions or difficulties with the focusing mechanisms, which results in the image moving out of focus. Therefore, the Nikon Eclipse-Ti microscope has an extra built in PFS modality, which is described in Figure 2.17. The PFS is introduced via a flip in mirror that directs a 780 nm laser towards the objective after which the laser gets reflected at the interface between the sample holder and the specimen. The reflected laser beam is then directed to a position-sensitive detector (PSD) that is used to monitor the specimen's position and correct for the possible drift that changes the laser positioning on the PSD.

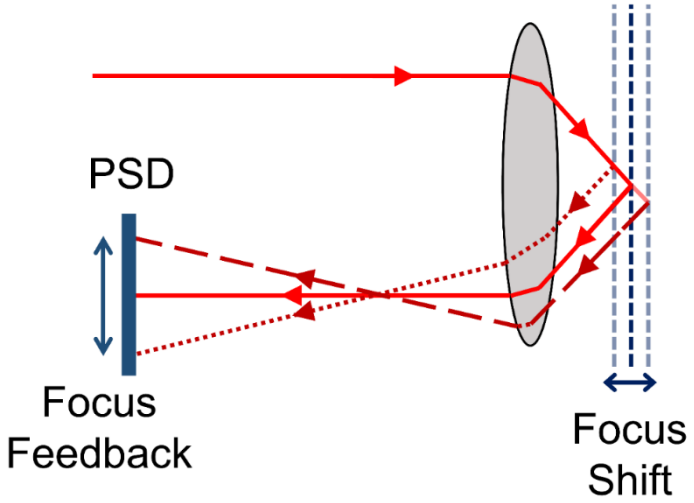

Figure 2.17 Scheme showing the principle of a PFS, where a laser is reflected at the coverslip-buffer interface. The angle of the reflected beam is directed to the PSD and changes with the position of the coverslip. The laser beam displacement on the PSD is used to correct for axial drifts.

2.5.6 Setup Electronics

The home-built CLSM setup is operated by an assembly of precise electronics that needs to be synchronized. The detailed overview of the electronics for the developed CLSM setup are presented in Figure 2.18. The main components are the multichannel laser driver (PDL 828 Sepia II, PicoQuant), the National Instruments NI 6008 Box (NI USB-6008, National Instruments), the FPGA (cRIO-9076 model, National Instruments), the two galvanometric mirror controller boards (Micro Max 671XX single axis analog servo driver, Cambridge Technology), the three Becker&Hickl TCSPC cards (SPC-150, Becker&Hickl) and the computer (American Megatrends). The diode lasers and the TCSPC electronics are synchronized via the multichannel laser driver Sepia II. Here, the sync out from the laser driver is split into three signals by an adapter, where each sync out connects to a separate TCSPC card. The measurement is initialized by the PC with a self-written C# program (Fabsurf), which is, as well, responsible for recording the measurement signal and controlling the electronics hardware. In detail, Fabsurf initializes the NI Box to start a measurement, which in turn send a trigger to the master TCSPC card (pin 13) and the FPGA. The triggered FPGA determines the shape, size and speed of the galvanometer scanner movement. This is achieved via the specified FPGA voltage controlling the two Micro Max 671XX boards, where each board is responsible for either the x-axis or the y-axis mirror movement. Note, the mirrors are positioned at the center of the ROI when zero volts is applied. Secondly, the FPGA sends a linesync (pin 9/ marker 1) to the master Becker&Hickl card. The line synchronization sets a marker that a new line (in the y-axis direction) in an image will start after the laser beam has been retracted along the fast x-axis. As mentioned previously, the NI box also triggers the master TCSPC card, which simultaneously triggers and communicates the linesync it receives with the other two cards.

After the synchronized measurement starts, the detected photons, depending on the emission wavelength, are recorded by the analogous APD. For optimization of the PIE experiments, the signal generated by the detector upon recording a photon is connected to a delay box constructed out of different cable lengths to delay the signal up to 32 ns in steps down to 1 ns. As indicated previously, the measurement is started upon the detection of a single photon and ends by the next consequent sync signal, which has been referred to as the reversed start-stop configuration (see the TCSPC section 2.2.3 for further details). The arrival time of the recorded photon is measured by a constant fraction discriminator (CFD). The CFD uses a constant fraction of the arriving signal from the detectors to precisely determine the timing of the output signal relative to the input signal, which in turn provides an amplitude-independent timing of the detector's signal. All in all, this procedure determines the TCSPC microtime of the recorded photons. The blue (Count Blue), yellow (SPCM-AQR-14) and the red detector (Count Red) transmit a positive voltage Transistor-Transistor-Logic (TTL) input signal to the TCSPC cards. As the

Becker&Hickl cards require the negative voltage Nuclear-Instrumentation-Module (NIM) signal, an inverter and attenuator module (SIA 400, PicoQuant) is implemented. The fact that most TCSPC cards only read the negative NIM pulses is for historical reasons, as PMTs were previously used, particularly in nuclear and high energy physics, and operate with negative voltages.

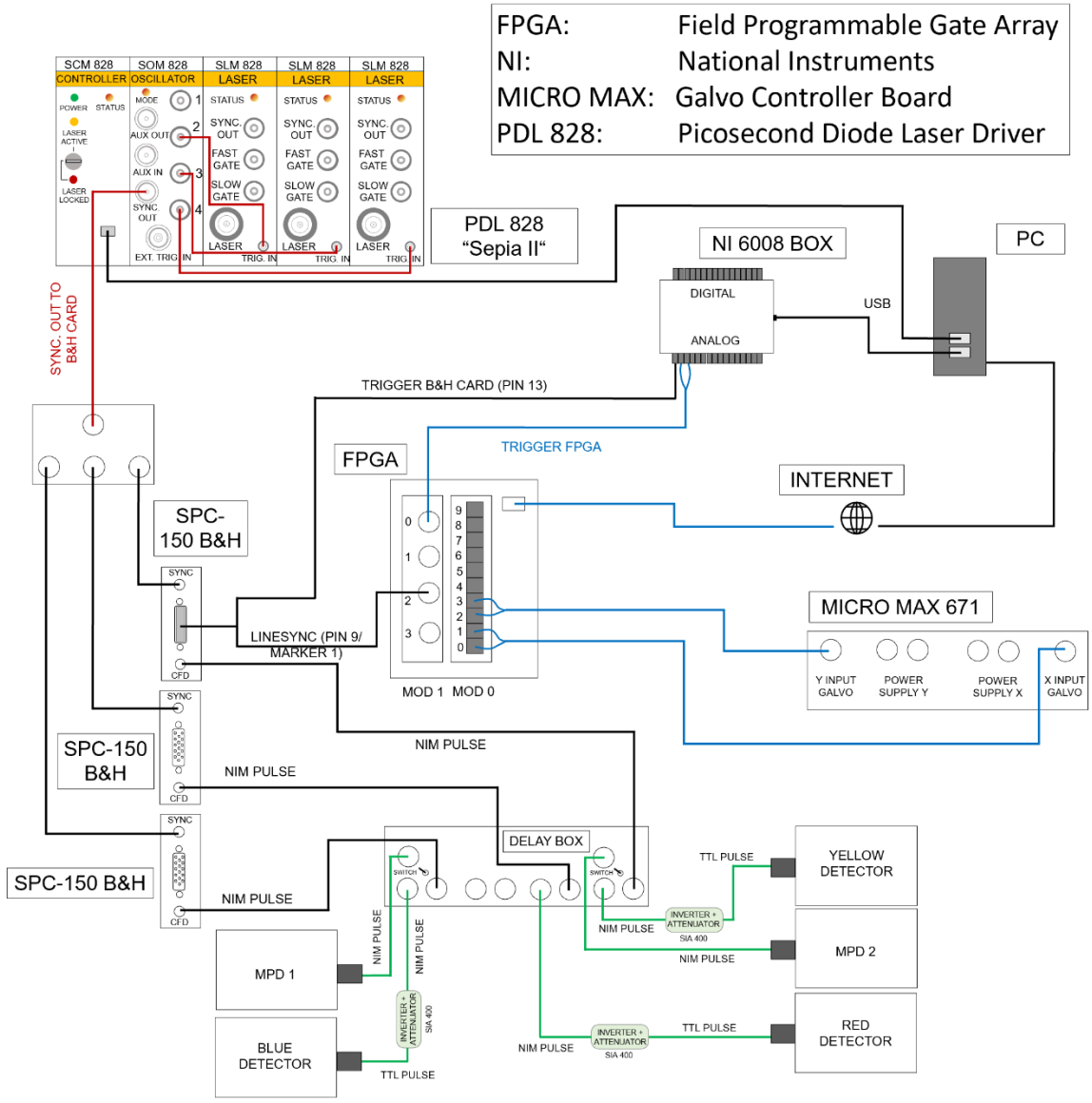

Figure 2.18: A scheme giving a detailed overview of the CLSM electronics that is used to synchronize the lasers, galvanometric scanner, timing electronics and detectors, and to show the start of the experiment.

2.5.7. CLSM Characterization Using FCS, ICS and RICS

Upon rebuilding the setup with improved optics and functionalities, it was necessary to characterize the setup. First, FCS was used as one of the tools to characterize the home-built CLSM and check its alignment with a well-defined calibration sample. A calibration sample consisting of a mixture of Atto488 (blue emission, Atto-tec Germany), Atto565 (yellow emission, Atto-tec Germany) and Atto655 (red emission, Atto-tec Germany) was prepared and measured to record three FCS curves simultaneously (Figure 2.19). The performed measurements were used to optimize the molecular brightness for the three corresponding detectors (Atto488, blue detection), (Atto565, yellow detection) and (Atto655, red detection). The laser powers were set to 10 µW before the objective to avoid populating the triplet state once higher powers are used. The predetermined diffusion coefficients (D = 373 µm^2/s for Atto488 and Atto565 and D = 393 µm^2/s for Atto655) at 20 °C were used to fit the recorded FCS datapoint with a single diffusion component thus allowing the determination of the confocal volume parameters according to equations 2.26 and 2.27. The FCS characterization was performed using the 60x water immersion objective and the results are shown in Table 1. An ET520/40 bandpass emission filter was used for the blue channel, an ET595/50 emission filter for the yellow channel and a 635 long pass emission filter for the red channel (Figure A.2).

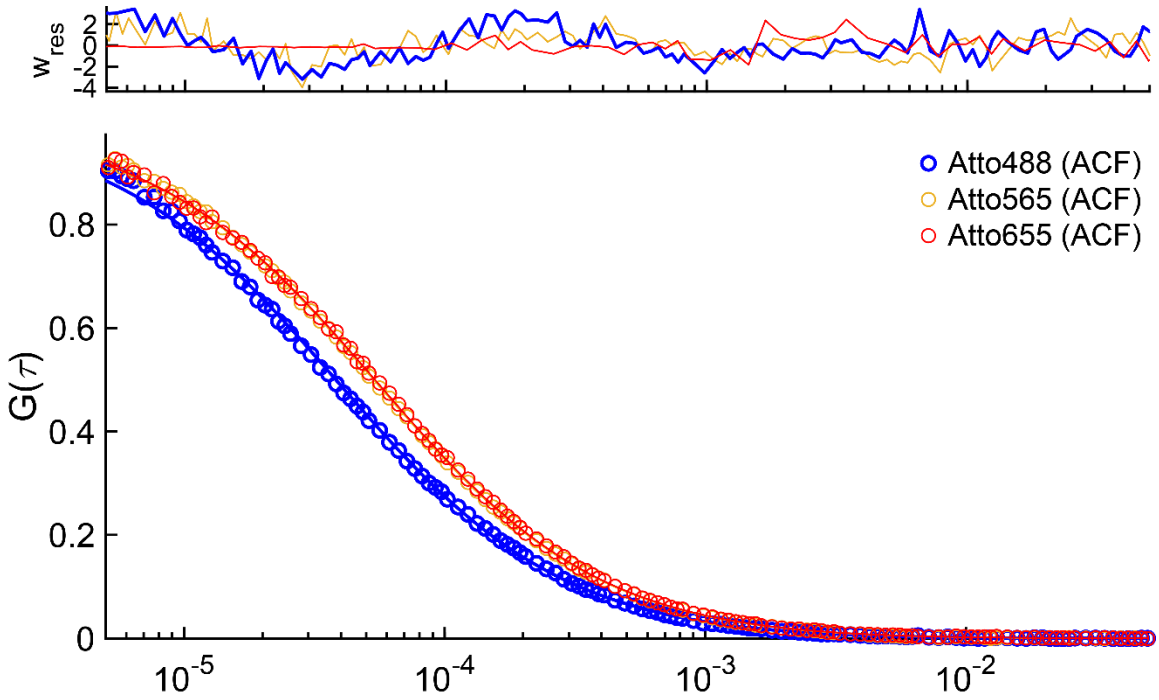

Figure 2.19: FCS results for the calibration sample (Atto488, Atto565 and Atto655) measured on the CLSM. The ACF is plotted for the three fluorophores. The symbols represent the measured data and the line is the fit based on equation (2.26). The results of the ACF are shown in Table 1 and the upper panel displays the weighted residuals (w_{res}) of the fit.

The ACF at zero lag time was used to determine the concentrations of the dyes in the calibration sample (Table 1) using the following equation:

$$C = \frac{n}{V} = \frac{\frac{\langle N \rangle}{N_A}}{\pi^{\frac{3}{2}} \omega_r^2 \omega_z} \quad (2.29)$$

Table 1: FCS values obtained from the calibration mixture of Atto488, Atto565 and Atto655.

Detector	***N***	**C** (nM)	$\boldsymbol{\varepsilon}$ (kHz/mol)	***D*** (µm²/s)	$\boldsymbol{\omega_r}$ (µm)	$\boldsymbol{\omega_z}$ (µm)
Blue	3.39	8.95	44.2	373	0.240	1.96
Yellow	0.541	0.950	81.5	373	0.285	2.08
Red	14.7	22.9	31.4	393	0.294	2.21

To determine the molecular brightness, not only in the center of the FOV, but across the whole ROI, two similar FCS measurements were conducted on two diagonally opposite corners. In this case, the ROI using the 60x water immersion objective has the size of 110 µm, meaning that the beam is positioned 55 µm away from the center of the ROI. The measured molecular brightness at the different positions in the ROI for the three different calibration dyes are shown in Table 2. The obtained results show that the brightness of the dyes decreases slightly on the corners, where the $\varepsilon_{\mathrm{Atto488}}$ decreases by ~1-10%, the $\varepsilon_{\mathrm{Atto565}}$ decreases by ~5-15% and the $\varepsilon_{\mathrm{Atto655}}$ decreases by ~1-15%. The brightness deviation at the corners typically rises from spherical aberrations of the optical components. However, for such a respectively large ROI (66 µm × 66 µm for the 100x oil immersion objective and 110 µm × 110 µm for the 60x water immersion objective), where the sample of interest is typically 10 µm to 30 µm in size, the deviations are minor. As optics are typically designed for beams going through the center, it is advisable to place the sample of interest at the center of the ROI.

Table 2: FCS values obtained from the calibration mixture measured at the center and corners of the ROI.

	$\boldsymbol{\varepsilon}$ (kHz/mol) at different positions in the ROI		
Detector	Center	Corner 1	Corner 2
Blue	44.2	39.6	43.1
Yellow	81.5	66.5	76.1
Red	31.4	27.6	31.2

As for FCS, ICS was also used to characterize the home-built CLSM. Here, images of multi-colored beads were recorded to characterize the scanning capabilities of the setup. Aberrations are often observed when scanning multi-colored images that are spectrally well separated. The aberrations problem arises from the properties of the setup's optical lenses that lead to chromatic and spherical aberrations. In case of chromatic aberrations, different wavelengths have different focal length. Such discrepancies occur since the index of refraction of materials such as lenes are wavelength dependent, which results in, for example, a blue laser being focused prior than a red one. Spherical aberrations appear when an incoming laser beam does not hit the lens at the center of its spherical surface, thus resulting in a sharper focusing of the beam hitting the periphery compared to the middle. Overall, these two aberration effects lower the quality of the image created by the optical system.

For this purpose, the CLSM was built with a telescope system consisting of highly aberration-corrected lenses, where a scan lens (SL50-CLS2, Thorlabs) and tube lens (TL200-CLS2, Thorlabs) (see section 2.4 for detailed CLSM components description) were paired together to minimize the aberrations. The system was tested by scanning images of 550 nm multi-colored beads using a blue and red laser to spectrally separate the images and compare them. For comparison, measurements with the previously built CLSM equipped with two achromatic doublet telescope lenses (AC254-050-A and AC254-200-A, Thorlabs) are shown (Figure 2.20 a). A significant decrease of the aberrations by using the high aberration-correction telescope system is clearly visible. Figure 2.20 b demonstrates the better overlap between the blue and red channels, moreover the particles off-center are well resolved with less blur in comparison to Figure 2.20 a. This indicates that the telescope system has a big influence on the clarity and quality of the obtained images. Additionally, ICCS was performed for both images (Figure 2.20 a and b) to determine the pixel shifts between the blue and red images thus examining the improvement achieved by using high aberration-correction telescope system (Figure 2.20 c and d, Table 3).

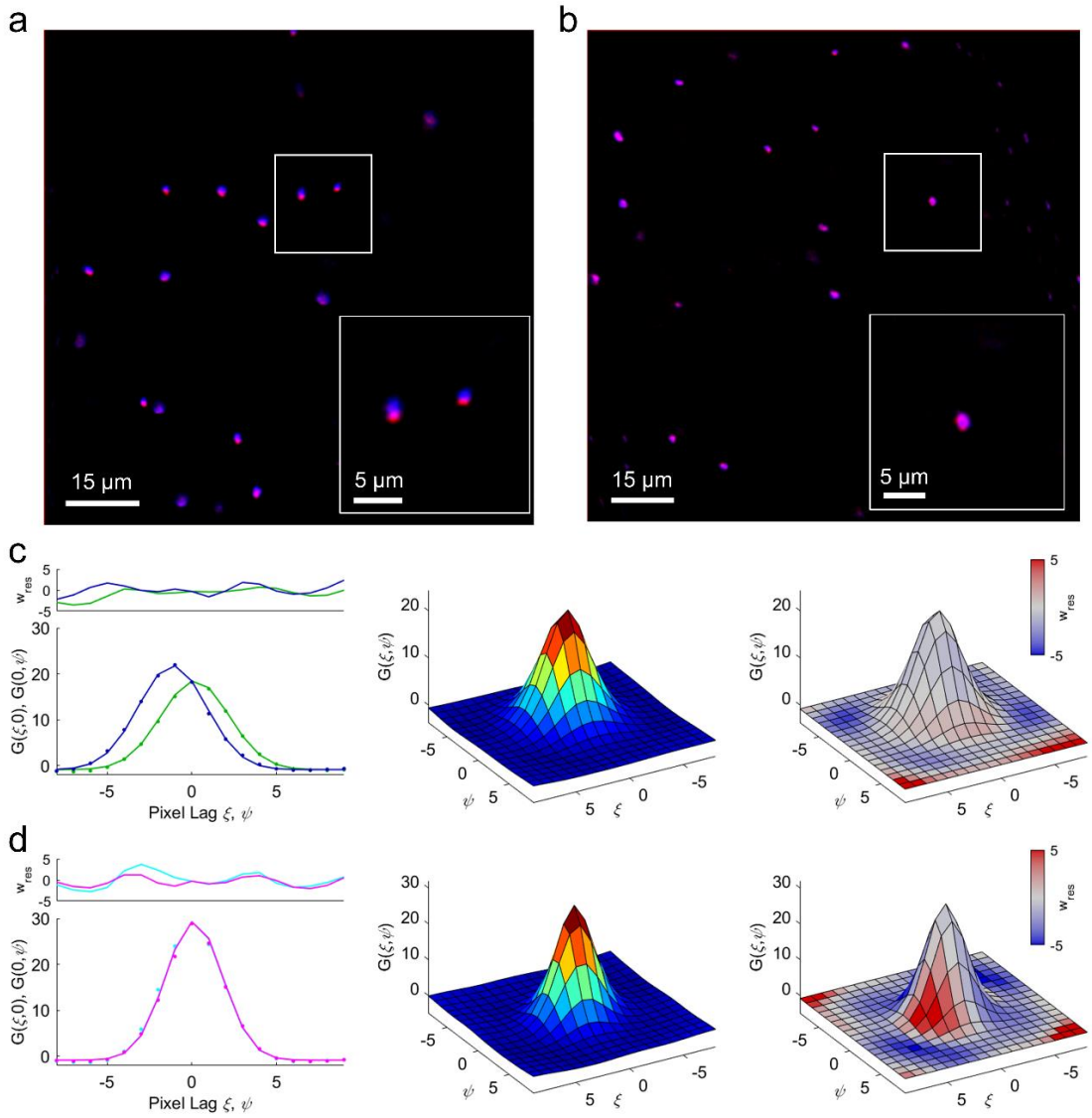

Figure 2.20: Scanned image and analysis of the 550 nm multi-color beads. a) and b) show the overlap of the blue and red images obtained with the achromatic doublet and the high aberration-correction telescope system, respectively. c) and d) show the ICCS analysis (with spatial pixel lag increments on the horizontal (ξ) and vertical (ψ) axes) of the blue and red images of the beads measured in panels (a) and (b), respectively. Panels (c) and (d) show: **left**, the on-axis correlation fits of the x-axis scanning (green in (c) and cyan in (d)) and the y-axis (dark blue in (c) and pink in (d)), **middle**, the mean spatial-CCF in 3D, color coded for the correlation values (red indicating high correlation values) and 3) **right**, fit of the data. Here, the fits are color coded according to the weighted residuals (w_{res}), where gray indicates a good fit while blue and red indicate fit regions with a standard deviation > 5.

Table 3: Shift between blue and red images along the horizontal (x-axis) and vertical (y-axis) directions.

	x-axis / nm	y-axis / nm
Figure 2.19 (a)	36.8	-230
Figure 2.19 (b)	23.9	27.2

To demonstrate the capabilities of RICS on the home-built CLSM, measurements of freely diffusing Atto488 fluorophores, and GFP in the cytoplasm and the membrane of transfected HeLa cells were performed. As shown in Figure 2.21 a, the fast diffusion of the small Atto488 fluorophores ($D \simeq 373$ µm^2/s at 20 °C) results in a correlation merely on the x-axis, which designates the fast correlations timescale. Diffusion of the GFP in the cytoplasm ($D \simeq 30$ µm^2/s at 20 °C) is slower than free Atto488. Although slower, the GFP diffusion correlates mainly on the fast x-axis timescale decaying on the range of ~20 pixels, still some diffusion is observed on the slower y-axis correlation (Figure 2.21 b, pixel lag from -10 to 10 pixels). The GFP diffusion in the membrane is significantly slower compared to the cytoplasm ($D \simeq 1$ µm^2/s at 20 °C), where on-axis correlations are observed in both the horizontal and vertical directions (Figure 2.21 c). These measurements demonstrate that RICS is a suitable method to study very fast to slow diffusion processes over a broad range of timescales. Likewise, RICS can be extended further to two or more colors (ccRICS)[95] as for FCS and ICS. In this case, a cross-correlation amplitude can be observed when concurrent diffusion and interactions of differently labeled particles occurs.

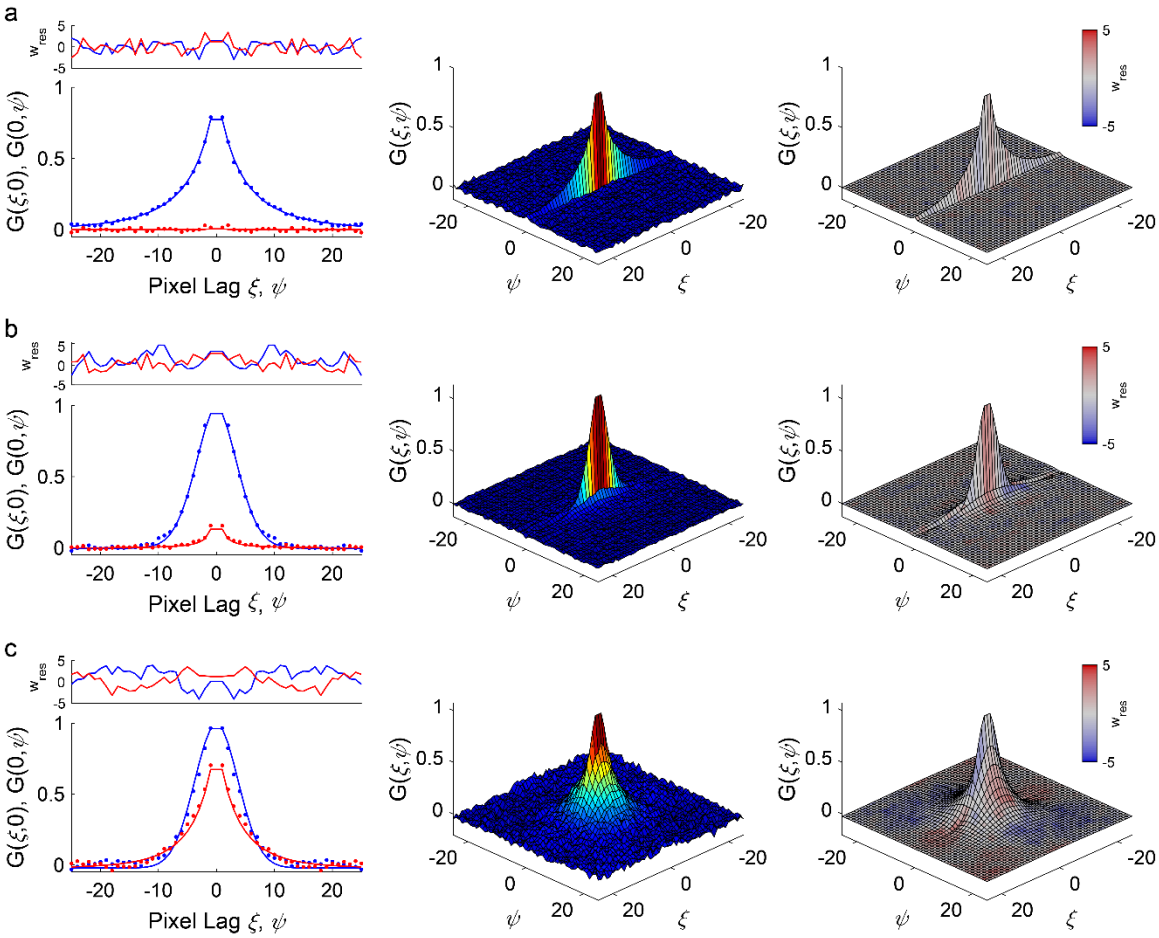

Figure 2.21: RICS characterization measurements performed on the CLSM and corresponding analysis. a) shows the diffusion analysis of Atto488 in water, while b) and c) show the diffusion analysis of GFP in the cytoplasm and membrane of HeLa cells, respectively. Shown in panels (a-c) are **left**, the on-axis correlation fits of the fast (horizontal) x-axis scan (with spatial pixel lag increments (ψ), blue) and the slow (vertical) y-axis scan (with spatial pixel lag increments (ξ), red), **middle**: mean spatial-ACF in 3D, color coded for the correlation values (red indicating high correlation values) and **right**: fit of the data. Here, the fits are color coded according to the value of the weighted residuals (w_{res}), where gray indicates a good fit while blue and red indicate fit regions with a standard deviation > 5.

2.6. Fluorescence Spectroscopy via Fluorimetry

The discussed fluorescence techniques so far dealt with experiments that study samples with relatively a small number of molecules. However, fluorescence spectroscopy is also very powerful in characterizing samples with ensemble measurements. The usage of a fluorimeter resolves the photoluminescence properties of a fluorophore via the steady state and time resolved fluorescence characterization. Steady state measurements characterize the fluorescence intensity vs. excitation or emission wavelengths. In this case, an emission spectrum is determined by fixing the excitation source to a certain wavelength while the emitted fluorescence intensity is acquired by scanning over the desired spectral range. An excitation spectrum is acquired in a similar manner, however, here the emission wavelength is fixed, and the excitation wavelength is scanned. For time resolved measurements, TCSPC, is used to characterize the fluorescence lifetime of the fluorophore and has been addressed in section 2.2.3. In this section, a brief description of the modular FLS1000 spectrofluorimeter (Edinburgh Instruments, EI) is presented, which is capable of recording fluorescence and phosphorescence spectra from the ultraviolet to the mid-infrared and measuring lifetimes from picoseconds to seconds.

Excitation source:

The fluorimeter is equipped with a 450 W ozone free xenon arc lamp, which enables a continuous wave excitation ranging from 230 nm up to ~1100 nm. Alternatively, different laser sources can be integrated into the system, which allow for pulsed excitation and thus time-resolved measurements. The repetition rate of the lasers is determined by the picosecond pulsed driver (PDL 828 Sepia II, PicoQuant) as shown in Figure 2.22.

Monochromator

The FLS1000 fluorimeter is equipped with a double monochromator in the excitation pathway. For detection a T-geometry configuration is used, where one of the two emission arms is equipped with double monochromators while the other arm has a single monochromator (Figure 2.22). Double monochromators mainly suppress stray light coming from the system or from scattering of the sample. All monochromators are equipped with automatically rotatable grating turrets (via the EI Fluoracle software) and allows the selection between two different diffraction gratings. The two Czerny-Turner gratings in the excitation pathway are a holographic grating blazed at 250 nm (1800 grooves/mm) and a ruled grating blazed at 500 nm (1200 grooves/mm). In the emission pathway, the two gratings are ruled and likewise blazed at 500 nm with grooves density at (300 grooves/mm) and (1200 grooves/mm), respectively. While the higher grooves density improves the spectral resolution, a lower grooves density lowers the temporal dispersion which improves the time resolution.

Sample holder

To obtain the fluorescence lifetime or measure a spectrum, the sample of interest is placed in a quartz cuvette (Hellma Analytics, Müllheim, Germany). A variety of cuvettes can be used depending on the sample volume, which is typically between 100 µL and 3 mL. Moreover, a water-coolant bath has been installed to monitor the fluorescence properties at different temperatures ranging from -10 °C to 100 °C. The temperature is controlled by the Fluoracle software.

Detectors

Two detector options are available for measuring the emitted photons from a sample: a high-speed PMT (HS-PMT 870, Hamamatsu) and a standard PMT (PMT-900, Hamamatsu) as shown in Figure 2.22. The PMT-900 has a longer spectral coverage, from 200 nm to 900 nm, while the quantum detection efficiency of the HS-PMT is drastically lower beyond 870 nm. The PMT-900 is cooled down to -20 °C, which reduces the otherwise high dark counts to ~100 cps and has a minimum response time width of 600 ps. This is the reason why the PMT-900 is explicitly used for acquiring steady-state spectra. On the other hand, the two HS-PMTs have slightly more dark counts (~130 cps). However, no cooling is required. The minimum response time for these two PMTs is significantly shorter (~180 ps) and hence, they are used for the fluorescence lifetime measurements. With the correct determination of the IRF (typically by measuring a ludox sample), a lifetime decay with lifetime values of ~50 ps can be resolved when analyzed using deconvolution fitting.

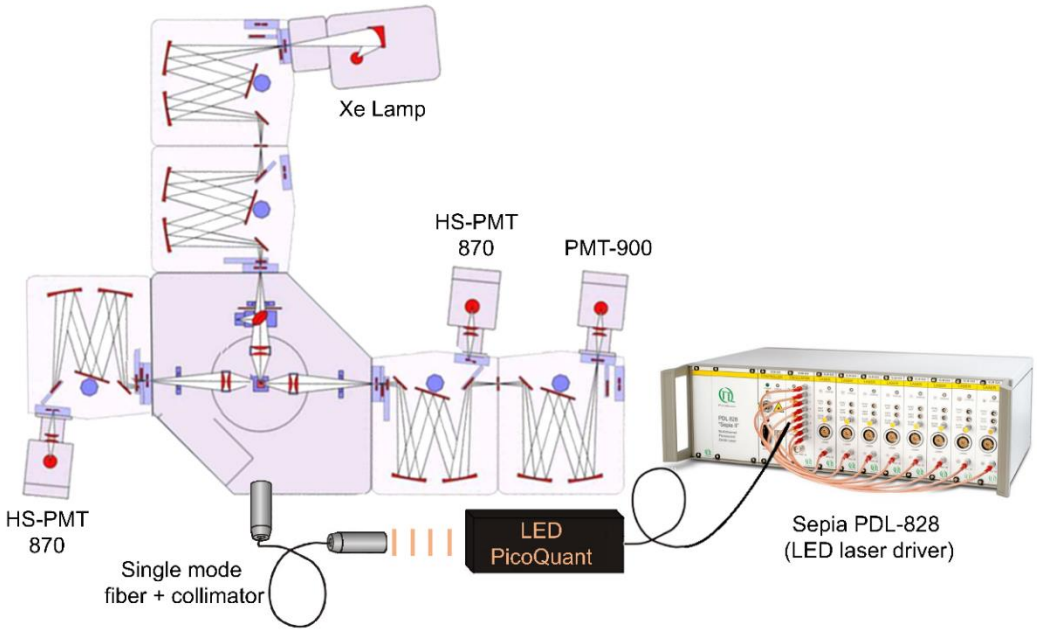

Figure 2.22: Schematic representation of the FLS1000 spectrofluorimeter. The sepia PDL 828 image is taken from PicoQuant's website: (https://www.picoquant.com/images/uploads/product_images/7920/pdl_828_large.jpg)

3. Overview of published work

This chapter provides a general overview of the conducted and published research in the scope of this thesis. The developed CLSM with the implemented advanced fluorescence methods, such as FCS-FCCS and FLIM, was utilized to investigate metal-organic frameworks (MOFs) and luminescent materials such as organic light-emitting diodes (OLEDs). Lastly, a study on a methanol dehydrogenase enzyme was performed by utilizing the luminescence properties of the co-factor and metal ion at the enzyme's active site using bulk fluorimetry experiments.

3.1. Paper 1: Coordinative Binding of Polymers to Metal-Organic Framework Nanoparticles for Control of Interactions at the Biointerface

Coordinative binding of polymers to metal–organic framework nanoparticles for control of interactions at the biointerface.

Zimpel A, **Al Danaf N**, Steinborn B, Kuhn J, Höhn M, Bauer T, Hirschle P, Schrimpf W, Engelke H, Wagner E, Barz M, Lamb DC, Lächelt U and Wuttke S, *ACS Nano* 2019, 13, 3884-3895.

DOI: 10.1021/acsnano.8b06287

In Zimpel et al., a straightforward approach for peripheral surface functionalization of Zr-based MOF nanoparticles is presented. The newly functionalized MOF nanoparticles were then tested for biological interactions, for example, interaction between their surfaces and the most abundant serum proteins albumin and immunoglobulin G (IgG).

3.1.1. Motivation and main results

The research field of designing and functionalizing MOFs has drastically advanced in the last 20 years and is now recognized as a driver for the development of key technologies and advanced functional materials.[96, 97] Developed MOFs have proven useful for various applications such as gas storage and separation, catalysis, sensing and other energy technologies.[98] These frameworks, consisting of inorganic centers that are coordinatively linked by bridging organic molecules, exhibit a stiff molecular structure and carry multiple Lewis base sites that can each bind to a metal ion. In this regard, the crystal structure of MOFs can be interpreted as an assembly of cages with defined pore openings and interior space. This key feature of MOFs has an immense impact on their usage for material-oriented applications. The desire to expand the applicability of MOFs and, in particular, nano MOFs for nanomaterial sciences is still ongoing. The conducted research in the scope of this paper encourages the manufacturing of MOF nanoparticles for new applications in the field of nanomedicine,[99] which might soon be used for therapeutics and

drug delivery applications. Here, we presented a simple approach to functionalize MOF nanoparticles for biological applications, in particular, to minimize their interactions with the most abundant serum proteins albumin and IgG. Developing an inert, *in-serum* nanomachine is critical for establishing relevant therapeutics and drug delivery agents.[100]

3.1.2. Brief description of the method

In this paper, we presented a simple method for the peripheral surface functionalization of Zr-fumarate MOF nanoparticles based on a self-assembly process. Here, different biomedically relevant polymers[101] were evaluated for their ability to self-assemble on the MOF surface (Figure 3.1 a). We studied the binding of different relevant polymers by a straightforward procedure of mixing them with the Zr-fumarate MOFs in a biological buffer at room temperature to identify genuine, scalable and consistent functionalization processes under mild and biocompatible conditions. The assembled Zr-fumarate nanoparticles featuring diverse polymer coatings were then characterized with respect to their physicochemical properties, zeta potential and colloidal stabilization. After performing the characterization experiments, we examined and screened these nanoparticles to assess their interactions at the biointerface (the interaction between the biomolecules and the proteins or the cells as shown in Figure 3.1 b), in particular their applicability for therapeutics and drug delivery. FCS and FCCS were utilized to address one aspect of the biointerface interactions that involve protein interactions. In this case, FITC-labeled albumin and IgG were tested, as the main abundant serum proteins, for their interaction with the differently coated MOF nanoparticles (Figure 3.1 c and d).

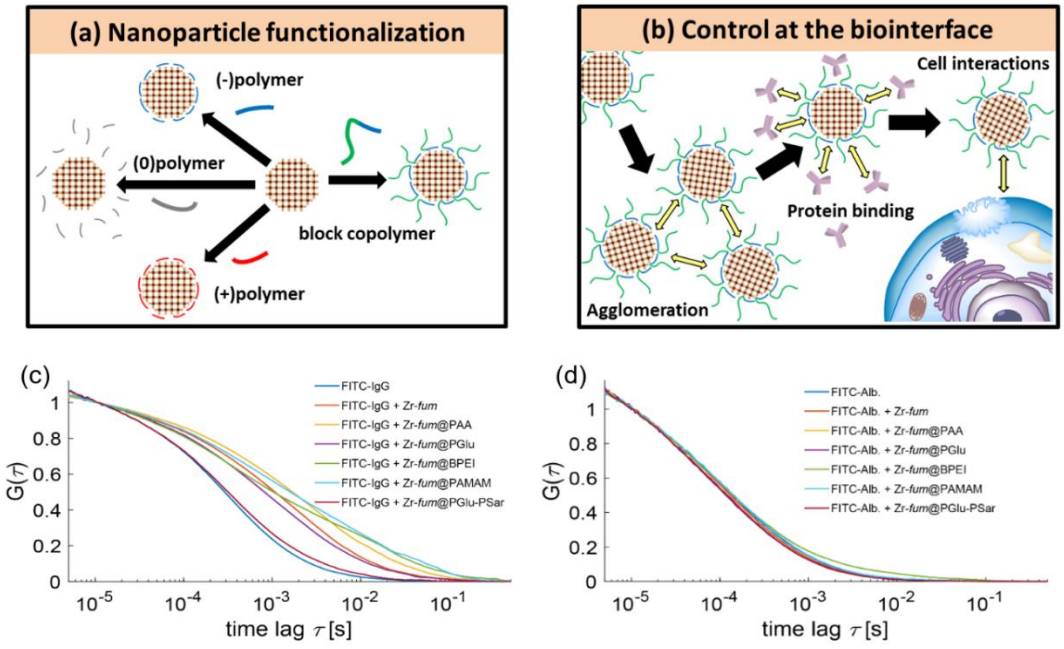

Figure 3.1: Schematic representation of the diverse functionalization of Zr-fumarate MOF nanoparticles and their biological interactions monitored by FCS. a) Schematic representation of the designing procedure of the

nanoparticles and their coating and b) the control of the nanoparticles by studying their agglomeration, protein binding, and cell interactions at the biointerface. c) and d) show the FCS measurements utilized to study the interactions between the FITC-IgG and FITC-Alb labeled proteins, respectively, and the different Zr-fumarate MOF nanoparticles. The figure is adapted from Zimpel et. al.[102]

3.1.3. Outlook

The unique physicochemical aspect of the cellular and protein interactions with the diversely surface-functionalized MOF nanoparticles opens the door for further applications utilizing the simple functionalization procedure reported within the scope of this study. For instance, we discovered that the inertness of the polyglutamate-b-polysarcosine (a hybrid block-co-polymer) coated nanoparticles prevented its binding to serum proteins, such as albumin and IgG. The fabrication of nanoparticles that are inert to *in serum* protein interactions showed a significant amount of cellular uptake with low extracellular aggregation, which is currently a highly desired property for the usage of nanoparticles as drug delivery vehicles or therapeutic agents. In this regard, it is important to highlight that this functionalization procedure, using similar biologically relevant polymers, can be tailored and expanded to a large number of MOFs as a tool for obtaining new surface-functionalization. Therefore, this study emphasizes the importance of tuning the surface properties of MOF nanoparticles for the efficient fabrication of their desired usage and applications.

3.2. Paper 2: Linker Exchange via Migration along Backbone in Metal-Organic Frameworks

Linker exchange via migration along the backbone in metal–organic frameworks.

Al Danaf N, Schrimpf W, Hirschle P, Lamb DC, Ji Z and Wuttke S, *J. Am. Chem. Soc.* 2021, 143, 10541-10546

DOI: 10.1021/jacs.1c04804

In Al Danaf et al., we utilized FLIM and fluorescence intensity imaging to address the post-synthetic modification (PSM) of MOF crystals. Using these two approaches, we observed an unexpected incorporation of a bulky linker into the crystal's interior, which opens the door for adding interesting new functionalities into the MOF pores.

3.2.1. Motivation and main results

The hybrid organic-inorganic nature of MOFs featuring porous solids with unique properties[98, 103-106] presents an exceptional scaffold for performing chemical transformations in single-crystals. MOFs introduce an extended periodic and crystalline structure, highly dependent on the topicity of the bridging organic linker molecules. This feature demonstrates the large degree of control one has during the synthesis of MOFs and separates them from regular coordination polymers. PSM of organic linkers, one of the most practiced chemical transformations, has played a central role in helping MOFs reach their full potential as a novel material class, mainly by allowing the incorporation of linkers bearing new functionalities of interest. The concept of PSM is to chemically modify the synthesized MOFs and thereby functionalize the framework post-assembly. In this case, PSM surpasses the limitations posed by the *de novo* synthesis to obtain functionalized MOFs that are deemed unattainable otherwise.

A special case of PSM, most commonly referred to as post-synthetic exchange (PSE), is observed in solution where MOFs are in a dynamic dissociation/formation equilibrium resulting in a mass transfer between the frameworks and their unbound components.[107] PSE is also commonly known as solvent-assisted linker exchange (SALE),[108] solvent-assisted ligand incorporation (SALI), among other names,[109-112] mainly to emphasize the importance of the solvent for the linker exchange. The solvent regulates the rate of exchange and its efficiency. Conventional linker exchange methods rely on molecules diffusing through the porous framework structure to selectively exchange one linker type in the original framework with secondary linkers, thereby achieving a post-synthetic functionalization.[113] This process, however, has been deemed unfeasible once the secondary ligand molecules exhibit sizes larger than the MOF pore windows that hinder the typical *through-window diffusion* routine.

In this study, we surprisingly observed that a bulky linker, larger than the windows of the MOF's pores, was able to penetrate the crystal. This observation led to our discovery of a new mechanism for achieving PSE in the crystal interior. We termed this mechanism *through-backbone diffusion* and investigated it by utilizing a fluorescently labeled linker (biphenyl-4,4′-dicarboxylic acid attached with rhodamine b, BPDC-RB) to study the observed PSE.

3.2.2. Brief description of the method

In this paper, we examined the through-backbone PSE mechanism, its spatial distribution and its progression with time in UiO-67 MOFs under different conditions. The *Universitetet i Oslo*-MOFs (UiO-MOFs) are versatile and multifunctional frameworks[114-116] that can be seen as a model compound for various studies related to the mechanisms of linker-exchange.[117-119] In our case, the observed PSE mechanism was characterized by advanced fluorescence microscopy methods, i.e., FLIM and phasor analysis. The FLIM approach analyzes the decays of the spatially-resolved fluorescence lifetime and has the advantages of high sensitivity and spatial resolution. The implementation of FLIM allows investigating the fluorescence lifetime changes that are highly influenced by the local nano-environment. For these reasons, FLIM has been used to investigate the nanoscopic environment of a material,[30, 120, 121] such as the morphology and chemical diversities within MOFs.[120, 122] However, the potential of FLIM for the characterization of material sciences, in general and the functionalization of MOFs in particular, is currently underutilized. In this study, we employed FLIM to examine the influence of the applied PSE conditions on the prevalence and distribution of linkers and their generated defects in the MOF crystals. Using FLIM we characterized the functionalization of MOFs with BPDC-RB, which allowed to elucidate the mechanism of PSE, its progression with time, and its correlation with the induced defects formation.

Exploiting the acquired fluorescence intensity images, we showed that PSE progresses with an outside-in mechanism, where a fast exchange starts at the surface (high intensity), and slowly disperses throughout the interior parts of the framework (decreasing intensity with penetration) as shown in the fluorescence intensity image of Figure 3.2 a. We demonstrated that the solvent plays a critical role in facilitating this process. In this case, an 80% methanol / 20 % DMF mixture (MeOH/DMF) considerably increased the degree of PSE in comparison to a DMF only mixture. Moreover, the temperature was identified as an important factor that influences the extent of PSE observed (Figure 3.2 b). We found that the progression of the PSE correlated with the degree of defects generated. For example, PSE in MeOH/DMF compared to DMF does not only result in a higher amount of linker incorporation (higher fluorescence intensity) but also correlates with a higher amount of defect formation. As shown previously,[120, 123] a decrease in fluorescence lifetime was observed via quenching upon the presence of defects, which correlates with the

incubation time and temperature used for PSE in MeOH/DMF (fluorescence lifetime image in Figure 3.2 a). With FLIM, the spatial distribution and mechanism of chemical diversity upon PSE in porous materials could be addressed. For this purpose, the sub-micrometer resolution of the microscope was utilized to uncover variations in the defects within an individual crystal, such as the fast exterior-surface linker exchange versus the slower-interior exchange (Figure 3.2 b). The fundamental outcome of this study highlighted the different conditions for achieving extended functionalization of MOFs using linkers larger than the pore windows.

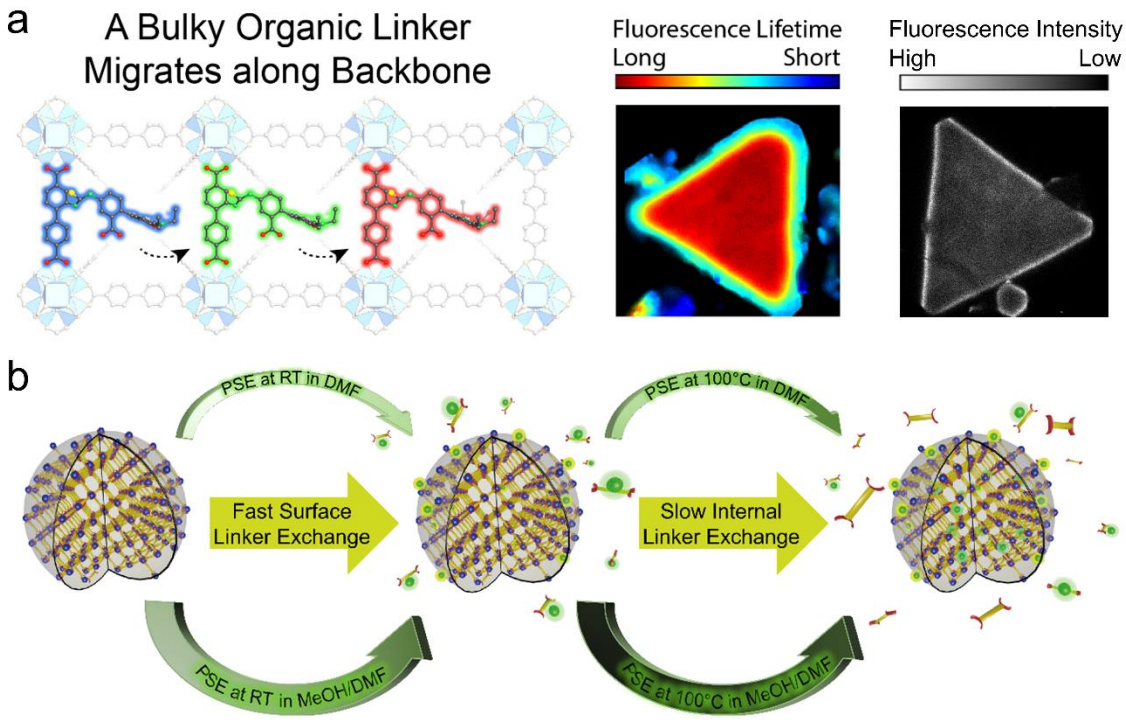

Figure 3.2: Schematic representation showing the PSE mechanism of a fluorescently labeled linker (in this case BPDC-RB) and its defects generation and spatial distribution within the UiO-67 MOF structure. a) The migration of the bulky BPDC-RB linker along the backbone (starting at the surface) shown schematically on the left was investigated via FLIM (middle) and fluorescence intensity images (right). The color-code of the linker and its corresponding fluorescence lifetime shown in the FLIM images, goes from blue (displaying the shortest fluorescence lifetime) to red (displaying the longest fluorescence lifetime). b) The observed PSE mechanism can be seen as a two-step process, initiating at the surface as a first step, followed by a gradual and slower in-depth linker exchange. MeOH/DMF as solvent facilitates the linker exchange to a higher degree than DMF - with the temperature being a critical factor for the slow internal exchange process. The figure is adapted from Al Danaf et. al.[124]

3.2.3. Outlook

We anticipate that our study of PSE via the through-backbone diffusion mechanism is a general approach that could be applied to other MOFs. Here, the only prerequisite is that the MOF of choice can undergo PSE, which needs to be tuned for finding the optimal linker exchange conditions by screening solvent, temperature, and other experimental parameters. Once these requirements are optimized, bulky linkers can penetrate a MOF by PSE of linkers gating the otherwise narrow windows. The discovery of this new mechanism unlocks the potential of incorporating bulky and sophisticated linkers into many types of MOFs, opening the way for new chemistry and applications of MOFs beyond what is currently possible. We believe this work will have a high impact in the field of MOFs, where the pore size and surface area of these porous materials can be tuned by the design of their linker molecules, thus featuring an excellent functionalization prospect. Moreover, the applicability of this approach on other solid materials is worth the investigation to provide a functionalization tool further than the current scope.

3.3. Paper 3: Methods for Elucidating the Structural-property Relationship in Luminescent Materials.

Methods for elucidating the structural-property relationship in luminescent materials.

Kirst C,† **Al Danaf N**, † Knechtel F, Arczynski T, Mayer P, Lamb DC and Karaghiosoff KL, *J. Mater. Chem. C* 2021

DOI:10.1039/D1TC02634H

In Kirst, Al Danaf et al., we developed and implemented FLIM in combination with the Hirshfeld surface (HS) analysis as a novel approach to gain insights into the characterization of luminescent materials. In particular, OLEDs, which are important for display and lighting technologies, were investigated and characterized with respect to their structural and luminescent properties.

3.3.1. Motivation and main results

In this study, we presented the advantages of combining FLIM with the HS analysis for the characterization of luminescent materials. By implementing this technique, we could gain further understanding into luminescent materials and, in particular, for OLEDs.[125] Nowadays, this technology is highly desirable for applications, such as mobile phones or smartwatch displays. Several OLED generations have been developed within the last decades.[126-128] Hitherto, several OLED synthesis approaches have been established, but the demand in optimizing OLEDs with respect to their properties and luminescent lifetimes to fully exploit their potential as new emitters (particularly in the blue region) is still not obtained.[129] Hence, current research is focusing on finding more straightforward OLED synthesis approaches, since the main syntheses procedures - so far - have been performed in a basic trial and error manner. The successful synthesis of light-emitting materials via trial and error is tedious, time-consuming, and most of the time not cost-effective. In addition, only limited knowledge regarding substituent effects and structural features has been considered in the design of light-emitting materials. Hence, additional tools are required to provide more insights into the structure-property relationship of these materials.

For this purpose, different prototype compounds of phosphine oxides were synthesized as a tool to study the structure-property relationship of luminescent materials. First, a detailed analytical characterization of the functionalized phosphine oxides by NMR, X-ray crystallography, MS, IR, UV-vis and fluorescence spectroscopy, were performed prior to our studies (Figure 3.3 a). The phosphine oxides comprised different heterocycles that differed not only in their nitrogen content but also in the methylation grade. They provided a good framework for substituents capable of efficiently modifying the luminescence properties of the compounds. Therefore, after their detailed characterization, we

investigated the differently functionalized phosphine oxides by analyzing and comparing the collected FLIM and HS analysis results (Figure 3.3 b and c). The obtained results revealed the presence of a correlation between the structures and their luminescent properties. The resulting data suggested that knowledge about morphology, crystal packing and the nature of intermolecular interactions is important for interpreting the uniformity and decay of the fluorescence lifetime, as well as the observed differences in the emitted light intensities. Such a correlation in luminescent materials has never been observed nor investigated before by the combination of such methods.

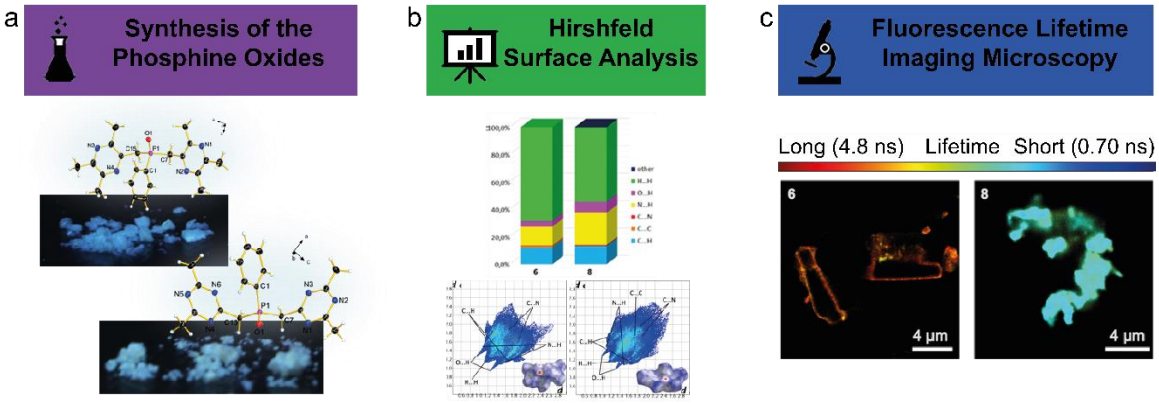

Figure 3.3: The combination of the HS analysis and FLIM to characterize newly synthesized phosphine oxides. a) Schematic of the molecular structures and a picture of the synthesized solid compounds upon UV excitation at 366 nm are shown. b) Fingerprint plots showing the bond content of the crystal packing from compounds 6 and 8. These bond contents were employed to determine interactions, which - in turn - were utilized for the HS analysis. c) FLIM images from the two compounds 6 and 8 are shown exhibiting spatial lifetime variations between the two structures. Figure adapted from Kirst, Al Danaf et. al.[130]

3.3.2. Outlook

Generally, we foresee the combination of FLIM with HS analysis becoming a valuable tool for the research and understanding of structure-property relationships in luminescent materials. The developed tool from this paper provides a new mean for investigating and designing luminescent materials in general, and OLEDs in particular. We anticipate that this approach can reduce the amount of trial and error necessary to design more efficient emitting materials, especially for OLEDs where there is a new demand for better blue emissive properties and lifetimes. For instance, modifying the intermolecular interactions, for example by introducing strong or weak H-bond acceptors, can be considered and investigated in combination with our developed tool to further characterize the emissive properties of OLEDs and similarly other luminescent materials.

3.4. Paper 4: Studies of Pyrroloquinoline Quinone Species in Solution and Lanthanide-dependent Methanol Dehydrogenases

Studies of Pyrroloquinoline Quinone Species in Solution and in Lanthanide-dependent Methanol Dehydrogenases.

Al Danaf N,† Kretzschmar J,† Jahn B, Singer H, Pol A, Op den Camp H, Steudtner R, Lamb DC, Drobot B and Daumann LJ, *in preperation*

In Al Danaf, Kretzschmar et al., we conducted a detailed characterization of the antioxidant and redox co-factor Pyrroloquinoline quinone (PQQ) in which we utilized the luminescent properties of both compounds, the PQQ and the Europium (Eu(III)) metal present to study the active center of the lanthanide-dependent methanol dehydrogenase (MDH) enzyme.

3.4.1. Motivation and key results

In the last 25 years, it has become clear that lanthanides (Ln) are relevant elements to study different biological samples. Their luminescent properties have been utilized as binding tags for proteins[131] or biomarkers in cells.[132, 133] Recently, even further significance of Ln has been reported for certain bacteria such as the thermoacidiphile *Methylacidiphilum fumariolicum* SolV that rely on Ln for their energy metabolism.[134] Specifically, in metalloenzymes such as methanol dehydrogenases (MDH), which is responsible for oxidizing methanol to formaldehyde, Ln were found to be essential metal ions in the active site.[135] The active site of a prototype Eu-MDH enzyme comprises the Eu metal ion complexed by the redox co-factor PQQ and four negatively-charged oxygen donor amino acids (Figure 3.4 a).[136] In this study, we exploited the excellent luminescent properties of the Eu(III) metal ion[137] to gain insight into Ln binding in MDH. The Eu(III) luminescence was investigated using the fluorescent PQQ co-factor as an antenna, which provided a direct approach to validate the presence of the Eu at the MDH enzyme active site and thereby study it. Prior to the MDH enzyme measurements, we characterized the PQQ co-factor under different conditions, which is relevant for understanding the various PQQ species that could be present in the studied enzymes. Subsequently, we compared the fluorescence emission of the Eu-MDH and La-MDH enzyme, where La replaces the luminescent Eu metal at its active site (where no Eu(III) emission at ~ 620 nm was observed in the luminescence spectrum, Figure 3.4 c). Furthermore, we monitored the fluorescence lifetime changes of the PQQ co-factor (on the ns timescale) and the Eu(III) luminescence (on the µs timescale) via the FLS 1000 spectrometer, as shown in Figure 3.4 b and d, respectively. In addition, time-resolved laser-induced fluorescence spectroscopy (TRLFS) was utilized for the direct excitation of Eu(III) at 395 nm. The measurements revealed three different Eu species present when titrating Eu to the MDH enzyme. These species were attributed to the Eu(III) aquo ion present in the solution, the Eu(III) bound to the MDH active site and the Eu(III) bound to PQQ. All in all, we validated

the presence of PQQ and its proximity to Eu at the active site by monitoring the spectral and lifetime changes of both, the PQQ and the Eu. As anticipated, we confirmed that the PQQ and Eu present at the MDH active site revealed different luminescence behaviors compared to their free solution forms.

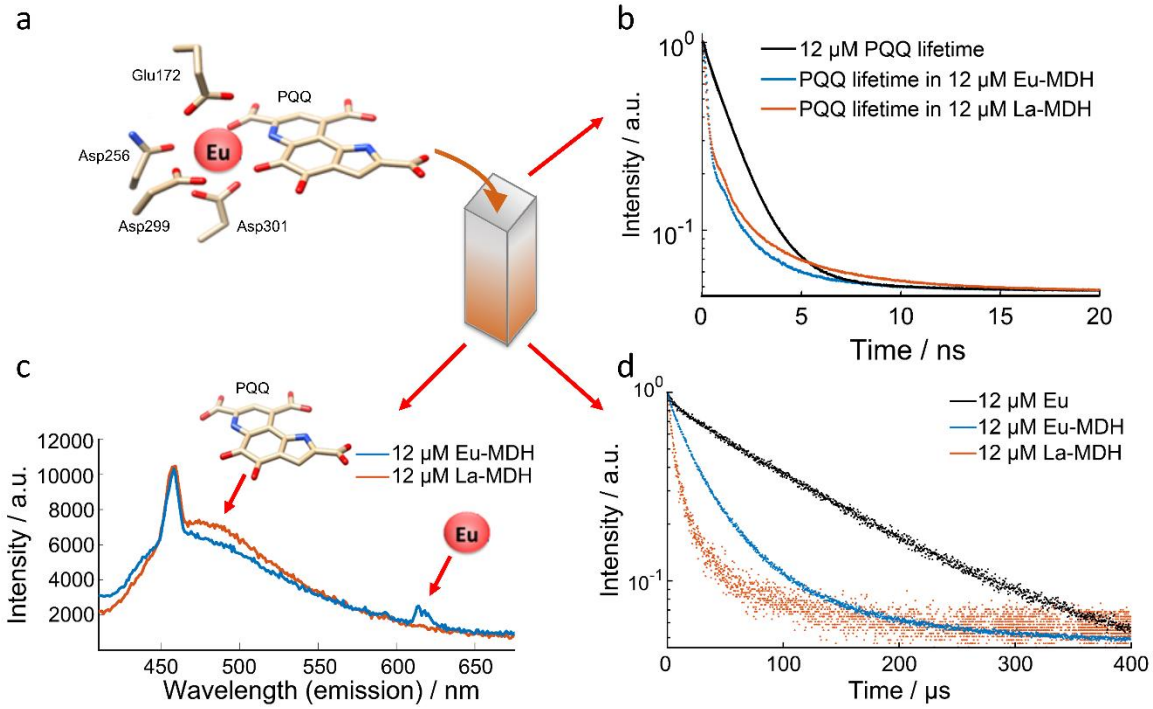

Figure 3.4: Steady-state and fluorescence lifetime characterization of the Eu-MDH enzyme. a) The structure of the MDH active site where the PQQ co-factor, which is close to the Eu is excited and an antenna effect is observed. b) The fluorescence lifetime of PQQ observed on the ns timescale: in solution (black), in Eu-MDH (blue) or La-MDH (orange). c) Emission spectra of 12 µM Eu-MDH showing the PQQ and Eu luminescence (blue). In the La-MDH (orange), no antenna effect is observed, which is seen by the absence of the Eu luminescence peak. d) The µs timescale lifetime decay of the Eu is shown: in solution (black), in Eu-MDH (blue) or La-MDH (orange). In all the performed experiments, a 375 nm diode laser (LDH-D-C-375, PicoQuant) was used for excitation.

3.4.2. Brief description of the method

To determine the equilibrium between the water adduct PQQ.H_2O and the PQQ species in solution under different conditions, the acid dissociation constants of the PQQ co-factor were characterized using NMR and UV-vis spectroscopy. After a detailed characterization of PQQ, Eu-MDH isolated from *Methylacidiphilum fumariolicum* (strain SolV) was investigated. For this purpose, we used two different methods that utilize the fluorescence of the PQQ and the luminescence of Eu(III). We employed TRLFS using a pulsed Nd:YAG OPO laser system (experiments performed at Helmholtz-Zentrum Dresden) for the direct excitation of the Eu(III). Alternatively, the antenna effect was studied by directly exciting the PQQ co-factor using a 375 nm laser (LDH-D-C-375, PicoQuant), which allowed simultaneous monitoring of the Eu(III) and PQQ lifetimes on a T-geometry fluorimeter (Figure 3.5). This fluorimeter, having the capabilities of TCSPC and equipped with an LED

laser, was used in the burst mode operation. Here, the laser pulses were synchronized in a burst mode of 500 µs per cycle, in which the laser pulsed for 5 µs of this timeframe. This allowed simultaneous µs and ns luminescence lifetime measurements to study the spectral and lifetime properties of Eu(III) and PQQ, both in solution and in the MDH active site under different conditions.

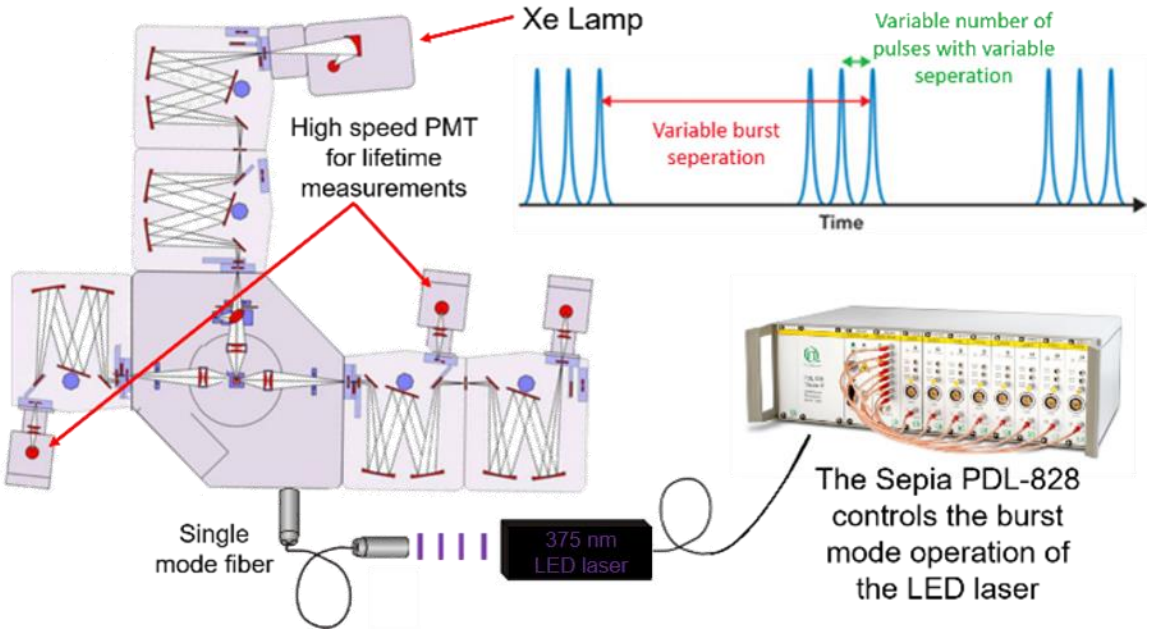

Figure 3.5: Schematic presentation of the FLS1000 fluorimeter used to obtain the steady-state emission spectra and perform the burst mode lifetime measurements. The latter allows simultaneous monitoring of the lifetimes of the Eu luminescence (µs lifetime timescale) and the PQQ co-factor fluorescence (ns lifetime timescale) studied in solution as well as in the MDH enzymes. The sepia PDL 828 image is taken from PicoQuant's website: (https://www.picoquant.com/images/uploads/product_images/7920/pdl_828_large.jpg)

3.4.3. Outlook

The current usage of rare earth elements (*i.e.* Ln) in a vast number of applications such as light sources especially for phone displays, MRI contrast agents and biological tags for different assays is an indication of their importance. In this regard, the presence of strictly rare earth elements dependent bacteria such as the methanotrophic bacterium *Methylacidiphilum fumariolicum* SolV is highly desired. We anticipate that the incorporation of Ln in the active center of the MDH enzyme, which the SolV and other similar bacteria possess, is a mean to recycle these Ln for different purposes. Therefore, utilizing the photophysical properties presented in the scope of this study can provide means to understand the MDH behavior and the occupancy of the Ln metal ion in its active site. Here, the luminescence of the Ln metal ion (if applicable) alongside the fluorescence of the PQQ and PQQ bound to Ln (at the active center of the MDH) present a promising tool that is applicable for different types of Ln-dependent bacteria.

3.5. Brief overview of other papers

Delivery of Cas9/sgRNA ribonucleoprotein complexes via hydroxystearyl oligoamino amides.

By Kuhn J, Lin Y, Krhac Levacic A, **Al Danaf N**, Peng L, Hoehn M, Lamb DC, Wagner E, Lachelt U.
Bioconjug. Chem. 2020, 31, 729-742

In this paper, the conducted research focuses on optimizing the delivery vehicles of the negatively charged ribonucleoprotein (RNP) complexes. These complexes, formed by the binding between different Cas9 proteins and single guide-RNA were then investigated. Subsequently, the formed RNP complexes were screened for binding to various oligo-ethylenamino amides, thus forming a stable nanoparticle delivery system capable of efficient cellular uptake and endosomal release. My contribution to this work lies in using FCS and FCCS to study the formation of the RNP complex, after which the RNP complex interaction with the most promising oligo-ethylenamino amide was characterized.

Supramolecular assembly of aminoethylene-lipopeptide PMO conjugates into RNA splice-switching nanomicelles.

By Kuhn J, Klein PM, **Al Danaf N**, Nordin JZ, Reinhard S, Loy DM, Höhn M, El Andaloussi S, Lamb DC, Wagner E, Aoki Y, Lehto T, Lächelt U
Adv. Funct. Mater. 2019, 29, 1906432

In this paper, the oligonucleotides of phosphorodiamidate Morpholino oligomers (PMO), typically used for pre-mRNA splicing modulation, were studied to optimize their intracellular transport. In this regard, finding an efficient system to deliver the PMO was tested with different oligo-ethylenamino amides. A linolenic acid-rich oligomer was identified as the highest splice-switching compound and was then used to form lipopeptide-PMO nanoparticles. My contribution to this work lies in using FCS to study the assembly of the different lipopeptide-PMO complexes and find the optimal PMO to lipopeptide ratio for the nanoparticle's formation.

Tuning porosity in macroscopic monolithic metal-organic frameworks for exceptional natural gas storage.

By Connolly BM, Aragones-Anglada M, Gandara-Loe J, **Danaf NA**, Lamb DC, Metha JP, Vulpe D, Wuttke S, Silvestre-Albero J, Moghadam PZ, Wheatley AEH, Fairen-Jimenez D
Nat. Comm. 2019, 10, 2345

In this paper, we demonstrated the production of highly porous UiO-66 MOFs by a simple variation of the synthetic and drying protocol, which enhanced their gas storage capabilities without the need to apply binders or pressure to pelletize the obtained solid compounds. My contribution to this work lies in utilizing the auto luminescence of the Ui-

O66 monoliths via FLIM to examine the relationship between the synthetic parameters and the morphology differences among the different UiO-66 monoliths.

Transcriptional effects of actin-binding compounds: the cytoplasm sets the tone.

Gegenfurtner FA, Zisis T, **Al Danaf N**, Schrimpf W, Kliesmete Z, Ziegenhain C, Enard W, Kazmaier U, Lamb DC, Vollmar AM, Zahler S
Cell. Mol. Life Sci. 2018, 75, 4539-4555

In this paper, we investigated the influence of two actin-binding compounds, the actin-polymerizing agent Miuranamide A and the actin-depolymerizing agent Latrunculin B, on the transcriptional regulation and nuclear actin dynamics of endothelial primary cells. My contribution to this work lies in implementing arbitrary region RICS as a tool to simultaneously test the effects of Miuranamide A and Latrunculin B on nuclear and cytoplasmic actin, respectively. This was realized by dually labeling the cellular actin with eGFP and mCherry fluorescent proteins and using the cross-correlation amplitude to quantify the temporal actin polymerization and depolymerization processes.

Tetrapyrrolic pigments are actin-targeting compounds.

By Karg C, Wang S, **Al Danaf N**, Pemberton R, Bernard D, Kretschmer M, Schneider S, Zisis T, Vollmar A, Lamb DC, Zahler S, Moser S
Angew. Chem. 2021

In this paper, we determined, for the first time, the potential of bilins (heme catabolite) and phyllobilins (chlorophyll catabolite) to directly bind cellular actin as a novel biological target and demonstrated an *in vitro* inhibition of the actin dynamics. My contribution to this work was using fluorescence spectroscopy to determine the binding affinity of the two compounds, phylloroseobilin (PrB, a phyllobilin) and bilirubin (BR, a bilin) to G-actin. Here, we monitored the fluorescence quenching upon the titration of different PrB and BR concentrations to labeled G-actin, after which their dissociation constants were determined. (The fluorescence measurements and analysis were performed with Dr. Cornelia Karg).

Aggregation induced emission in a flexible phosphine oxide and its Zn(II) complexes – a simple approach to blue luminescent materials.

Kirst C, Gensler M, Petersen J, Knechtel F, **Al Danaf N**, Fischermeier D, Wedel A, Lamb DC, Mitrć R, Karaghiosoff KL (in preperation)

In this paper, the conducted research focused on the simple synthetic procedure of multidentate phosphine oxides, which produced high compound yields and additionally demonstrated interesting luminescent properties, especially the emission in the blue region. My contribution to this work lies in utilizing FLIM to examine the photoluminescence of the synthesized compounds. Moreover, knowledge of the spatial lifetime variations observed via FLIM was utilized to investigate the relationship between the morphology of the structures and their luminescent properties. (in preperation)

4. Summary and Conclusions

This doctoral thesis focuses on the application of advanced fluorescence methods, such as auto- and cross-correlation analysis and fluorescence lifetime imaging microscopy, to investigate nano-properties and nano-interactions of different materials. The conducted research was accomplished using a modular home-built CLSM that was upgraded within the scope of the doctoral thesis. The upgraded CLSM included two integrated excitation pathways (confocal and wide-field / TIRF microscopy). All in all, the CLSM (described in section 2.5) is capable of wide-field and TIRF imaging (via the wide-field pathway) and FCS, FCCS, FLIM and different image (cross-)correlation spectroscopy methods (via the confocal pathway).

Two of the main studied projects utilized the CLSM to study metal-organic frameworks (MOFs). The crystalline structure of the MOF nanoparticles formed by cross-linking the inorganic metal ions via organic linkers makes them highly porous materials that are very well suited for different industrial applications. In the first study, we report a simple procedure for the peripheral surface functionalization of the well-known Zr-fumarate to produce MOF nanoparticles with unique properties. In particular, the hybrid polyglutamate-b-polysarcosine block-co-polymer functionalized nanoparticles exhibited advantageous properties such as their inertness to interactions with the most abundant serum proteins IgG and albumin. Moreover, these functionalized MOF nanoparticles demonstrated low extracellular aggregation and a significant cellular uptake. These properties are highly desirable for the medicinal application of MOF nanoparticles as therapeutic agents or drug delivery vehicles.

In the second paper, we investigated the post-synthetic exchange (PSE) mechanism of bulky linker molecules that are larger than the pore window, in a Zr-prototype UiO-67 MOF. The migration of the bulky linker into the interior of the MOF crystals occurred via an intriguing mechanism different from the ordinary PSE that takes place as a consequence of the linker's through-window diffusion. Combining the results of the fluorescence intensity images and the spatial lifetime variations obtained by phasor-FLIM, we discovered that the migration of the linker begins at the surface via a fast exchange and slowly moves into the crystal's interior, generating defects in its wake - a mechanism we termed through-backbone diffusion. The following study unravels the possibility of introducing new functionalities into the MOF pores by incorporating larger and more complex linkers, which have been deemed unfeasible up until now.

The capabilities of FLIM for applications in material sciences remain underutilized. An illustration of the insights FLIM can provide is demonstrated in the scope of the third paper. Here, we showed that the combination of FLIM with the Hirshfeld surface (HS) analysis is a valuable tool to study and characterize different luminescent materials. In particular, we

highlighted the importance of this approach for investigating a new class of picolyl-derived phosphine luminescent materials that have a great potential as organic light emitting diodes (OLEDs). In this regard, we established a relation between the different intermolecular interactions and the photophysical properties of the synthesized phosphines, particularly pertaining to their emission intensity and autofluorescence lifetimes. These findings open the door for the application of FLIM and HS analysis as a standard characterization approach to examine different luminescent materials.

The usage of advanced fluorescence methods is also possible by utilizing bulk fluorescence spectroscopy measurements. In the fourth paper, we conducted a thorough examination of the redox co-factor Pyrroloquinoline quinone (PQQ) under different pH and temperature conditions. The performed characterization of the PQQ was employed to determine its presence and possible configurations in the active site of the Eu-methanol dehydrogenase (Eu-MDH) enzyme, which was investigated subsequently in details. For this purpose, we exploited the luminescence of PQQ and Eu when being present in the active center. The simultaneous monitoring of the PQQ lifetime, on the ns timescale, and that of the Eu, on the µs timescale, was performed using a T-geometry fluorimeter (described in section 2.6). In this regard, the antenna effect via the direct excitation of PQQ using a 375 nm LED laser operated in burst mode was utilized. Implementing this new approach, we resolved the proximity of the PQQ to Eu at the active site and showed that the antenna effect, via the direct PQQ excitation, is a useful tool to investigate the Eu-MDH photophysical properties.

In conclusion, the power of advanced fluorescence methods has been demonstrated within the scope of this thesis. The central goal of the performed studies was to use these powerful methods, offered by the versatility of the developed CLSM, to gain new insights on materials in general, and functionalities of nanoparticles, in particular. The possession of such a microscope is optimal for addressing straightforward questions, such as identifying specific interactions at nanomolar concentrations, which is possible by a simple implementation of FCS. Nonetheless, a more complex approach is also applicable to delve into the details of different nano-systems, which was demonstrated via phasor-FLIM in combination with other methods. Employing the strength of these methods is a powerful tool to unravel a lot of structural-photophysical relationships on the nanoscale, both in the field of material- and life- sciences.

Bibliography

1. Orrit, M.; Bernard, J., Single pentacene molecules detected by fluorescence excitation in a p-terphenyl crystal. *Phys Rev Lett* **1990,** *65*, 2716-2719.

2. Moerner, W. E.; Kador, L., Optical detection and spectroscopy of single molecules in a solid. *Physical Review Letters* **1989,** *62*, 2535-2538.

3. Betzig, E.; Patterson, G. H.; Sougrat, R.; Lindwasser, O. W.; Olenych, S.; Bonifacino, J. S.; Davidson, M. W.; Lippincott-Schwartz, J.; Hess, H. F., Imaging Intracellular Fluorescent Proteins at Nanometer Resolution. *Science* **2006,** *313*, 1642-1645.

4. Hess, S. T.; Girirajan, T. P.; Mason, M. D., Ultra-high resolution imaging by fluorescence photoactivation localization microscopy. *Biophysical journal* **2006,** *91*, 4258-72.

5. Rust, M. J.; Bates, M.; Zhuang, X., Sub-diffraction-limit imaging by stochastic optical reconstruction microscopy (STORM). *Nature methods* **2006,** *3*, 793-5.

6. Stokes, G. G., XXX. On the change of refrangibility of light. *Philosophical Transactions of the Royal Society of London* **1852,** *142*, 463-562.

7. Monardes, N., *Dos libros: el vno trata de todas las cosas q[ue] trae[n] de n[uest]ras Indias Occide[n]tales, que siruen al vso de Medicina y como se ha de vsar de la rayz del Mechoaca[n], purga excele[n]tissima : el otro libro trata de dos medicinas marauillosas q[ue] son co[n]tra todo veneno, la piedra Bezaar y la yerua escuerçonera : con la cura de los venenados*. en casa de Sebastian Trugillo1565.

8. Acuña, A. U.; Amat-Guerri, F.; Morcillo, P.; Liras, M.; Rodríguez, B., Structure and Formation of the Fluorescent Compound of Lignum nephriticum. *Organic Letters* **2009,** *11*, 3020-3023.

9. Herschel, J. F. W., On a case of superficial colour presented by a homogeneous liquid internally colourless. *Philosophical Transactions of the Royal Society of London* **1845,** *135*, 143-145.

10. Einstein, A., Strahlungs-Emission und -Absorption nach der Quantentheorie. *Deutsche Physikalische Gesellschaft* **1916,** *18*, 318.

11. Hell, S. W.; Wichmann, J., Breaking the diffraction resolution limit by stimulated emission: stimulated-emission-depletion fluorescence microscopy. *Opt. Lett.* **1994,** *19*, 780-782.

12. Klar, T. A.; Hell, S. W., Subdiffraction resolution in far-field fluorescence microscopy. *Opt. Lett.* **1999,** *24*, 954-956.

13. Jabłoński, A., Über den Mechanismus der Photolumineszenz von Farbstoffphosphoren. *Zeitschrift für Physik* **1935,** *94*, 38-46.

14. Lakowicz, J. R., *Principles of fluorescence spectroscopy*. Springer US, Third edition, **2006**.

15. Kasha, M., Characterization of electronic transitions in complex molecules. *Discussions of the Faraday Society* **1950,** *9*, 14-19.

16. Franck, J.; Dymond, E. G., Elementary processes of photochemical reactions. *Transactions of the Faraday Society* **1926,** *21*, 536-542.

17. Abbe, E., Beiträge zur Theorie des Mikroskops und der mikroskopischen Wahrnehmung. *Archiv für Mikroskopische Anatomie* **1873,** *9*, 413-468.

18. Rayleigh, XXXI. Investigations in optics, with special reference to the spectroscope. *The London, Edinburgh, and Dublin Philosophical Magazine and Journal of Science* **1879,** *8*, 261-274.

19. Ambrose, E. J., A Surface Contact Microscope for the study of Cell Movements. *Nature* **1956,** *178*, 1194-1194.

20.Axelrod, D., Cell-substrate contacts illuminated by total internal reflection fluorescence. *Journal of Cell Biology* **1981,** *89*, 141-145.

21. Sako, Y.; Minoghchi, S.; Yanagida, T., Single-molecule imaging of EGFR signalling on the surface of living cells. *Nature Cell Biology* **2000,** *2*, 168-172.

22. Minsky, M. Microscopy apparatus. December 19 **1961.** US Patent 3,013,467.

23. Zachariasse, K. A., Einzelphotonenzählung: Time-Correlated Single Photon Counting. Von D. V. O'Connor und D. Phillips. Academic Press, London - New York 1984. VIII, 288 S., geb. $ 45,-. ISBN 0-12-524140-2. *Nachrichten aus Chemie, Technik und Laboratorium* **1985,** *33*, 896-896.

24. Becker, W., *Advanced Time-Correlated Single Photon Counting Techniques*. Springer Berlin Heidelberg2005.

25. Hendrix, J.; Schrimpf, W.; Höller, M.; Lamb, Don C., Pulsed Interleaved Excitation Fluctuation Imaging. *Biophysical journal* **2013,** *105*, 848-861.

26. Müller, B. K.; Zaychikov, E.; Bräuchle, C.; Lamb, D. C., Pulsed interleaved excitation. *Biophysical journal* **2005,** *89*, 3508-22.

27. van Munster, E. B.; Gadella, T. W. J., Fluorescence Lifetime Imaging Microscopy (FLIM). In *Microscopy Techniques: -/-*, Rietdorf, J., Ed. Springer Berlin Heidelberg: Berlin, Heidelberg, 2005; pp 143-175.

28. French, T.; So, P. T.; Dong, C. Y.; Berland, K. M.; Gratton, E., Fluorescence lifetime imaging techniques for microscopy. *Methods in cell biology* **1998,** *56*, 277-304.

29. Clegg, R. M.; Holub, O.; Gohlke, C., Fluorescence lifetime-resolved imaging: measuring lifetimes in an image. *Methods in enzymology* **2003,** *360*, 509-42.

30. Becker, W., Fluorescence lifetime imaging--techniques and applications. *J Microsc* **2012,** *247*, 119-36.

31. Heikal, A. A.; Hess, S. T.; Webb, W. W., Multiphoton molecular spectroscopy and excited-state dynamics of enhanced green fluorescent protein (EGFP): acid–base specificity. *Chemical Physics* **2001,** *274*, 37-55.

32. Liu, T.; Liu, X.; Spring, D. R.; Qian, X.; Cui, J.; Xu, Z., Quantitatively Mapping Cellular Viscosity with Detailed Organelle Information via a Designed PET Fluorescent Probe. *Scientific Reports* **2014,** *4*, 5418.

33. Ghale, G.; Nau, W. M., Dynamically Analyte-Responsive Macrocyclic Host–Fluorophore Systems. *Accounts of Chemical Research* **2014,** *47*, 2150-2159.

34. Okabe, K.; Inada, N.; Gota, C.; Harada, Y.; Funatsu, T.; Uchiyama, S., Intracellular temperature mapping with a fluorescent polymeric thermometer and fluorescence lifetime imaging microscopy. *Nature Communications* **2012,** *3*, 705.

35. Lakowicz, J. R.; Szmacinski, H.; Johnson, M. L., Calcium imaging using fluorescence lifetimes and long-wavelength probes. *Journal of Fluorescence* **1992,** *2*, 47-62.

36. de Silva, A. P.; de Silva, S. A., Fluorescent signalling crown ethers; 'switching on' of fluorescence by alkali metal ion recognition and binding in situ. *Journal of the Chemical Society, Chemical Communications* **1986**, 1709-1710.

37. Gadella, T. W. J.; Jovin, T. M.; Clegg, R. M., Fluorescence lifetime imaging microscopy (FLIM): Spatial resolution of microstructures on the nanosecond time scale. *Biophysical Chemistry* **1993,** *48*, 221-239.

38. Verkman, A. S.; Armijo, M.; Fushimi, K., Construction and evaluation of a frequency-domain epifluorescence microscope for lifetime and anisotropy decay measurements in subcellular domains. *Biophys Chem* **1991,** *40*, 117-25.

39. Fišerová, E.; Kubala, M., Mean fluorescence lifetime and its error. *Journal of Luminescence* **2012,** *132*, 2059-2064.

40. Sillen, A.; Engelborghs, Y., The Correct Use of "Average" Fluorescence Parameters. *Photochemistry and Photobiology* **1998,** *67*, 475-486.

41. Szabelski, M.; Ilijev, D.; Sarkar, P.; Luchowski, R.; Gryczynski, Z.; Kapusta, P.; Erdmann, R.; Gryczynski, I., Collisional quenching of erythrosine B as a potential reference dye for impulse response function evaluation. *Applied spectroscopy* **2009,** *63*, 363-8.

42. Van Den Zegel, M.; Boens, N.; Daems, D.; De Schryver, F. C., Possibilities and limitations of the time-correlated single photon counting technique: a comparative study of correction methods for the wavelength dependence of the instrument response function. *Chemical Physics* **1986,** *101*, 311-335.

43. O'Connor, D. V.; Ware, W. R.; Andre, J. C., Deconvolution of fluorescence decay curves. A critical comparison of techniques. *The Journal of Physical Chemistry* **1979,** *83*, 1333-1343.

44. Digman, M. A.; Caiolfa, V. R.; Zamai, M.; Gratton, E., The Phasor Approach to Fluorescence Lifetime Imaging Analysis. *Biophysical journal* **2008,** *94*, L14-L16.

45. Redford, G. I.; Clegg, R. M., Polar Plot Representation for Frequency-Domain Analysis of Fluorescence Lifetimes. *Journal of Fluorescence* **2005,** *15*, 805.

46. Rigler, R.; Elson, E. S., *Fluorescence Correlation Spectroscopy: Theory and Applications*. Springer Berlin Heidelberg2001.

47. Krichevsky, O.; Bonnet, G., Fluorescence correlation spectroscopy: the technique and its applications. *Reports on Progress in Physics* **2002,** *65*, 251-297.

48. Haustein, E.; Schwille, P., Fluorescence correlation spectroscopy: novel variations of an established technique. *Annual review of biophysics and biomolecular structure* **2007,** *36*, 151-69.

49. Tetin, S. Y., *Fluorescence Fluctuation Spectroscopy (FFS)*. Elsevier2013.

50. Bag, N.; Wohland, T., Imaging fluorescence fluctuation spectroscopy: new tools for quantitative bioimaging. *Annual review of physical chemistry* **2014,** *65*, 225-48.

51. Westgren, A., Eine neue Methode zur Prüfung der Gültigkeit des Boyle-Gay-Lussacschen Gesetzes für kolloide Lösungen. *Zeitschrift für Physikalische Chemie* **1913,** *83U*, 151-195.

52. Einstein, A. In *On the Motion of Small Particles Suspended in Liquids at Rest Required by the Molecular-Kinetic Theory of HeatB* 2004.

53. Magde, D.; Elson, E. L.; Webb, W. W., Fluorescence correlation spectroscopy. II. An experimental realization. *Biopolymers* **1974,** *13*, 29-61.

54. Rigler, R.; Mets, Ü.; Widengren, J.; Kask, P., Fluorescence correlation spectroscopy with high count rate and low background: analysis of translational diffusion. *European Biophysics Journal* **1993,** *22*, 169-175.

55. Kask, P.; Palo, K.; Ullmann, D.; Gall, K., Fluorescence-intensity distribution analysis and its application in biomolecular detection technology. *Proceedings of the National Academy of Sciences* **1999,** *96*, 13756-13761.

56. Chen, Y.; Müller, J. D.; So, P. T.; Gratton, E., The photon counting histogram in fluorescence fluctuation spectroscopy. *Biophysical journal* **1999,** *77*, 553-67.

57. Müller, J. D., Cumulant analysis in fluorescence fluctuation spectroscopy. *Biophysical journal* **2004,** *86*, 3981-3992.

58. Hink, M. A.; van Hoek, A.; Visser, A. J. W. G., Dynamics of Phospholipid Molecules in Micelles: Characterization with Fluorescence Correlation Spectroscopy and Time-Resolved Fluorescence Anisotropy. *Langmuir* **1999,** *15*, 992-997.

59. Magde, D.; Webb, W. W.; Elson, E. L., Fluorescence correlation spectroscopy. III. Uniform translation and laminar flow. *Biopolymers* **1978,** *17*, 361-376.

60. Elson, E. L., Fluorescence Correlation Spectroscopy Measures Molecular Transport in Cells. *Traffic* **2001,** *2*, 789-796.

61. Schwille, P.; Meyer-Almes, F. J.; Rigler, R., Dual-color fluorescence cross-correlation spectroscopy for multicomponent diffusional analysis in solution. *Biophysical journal* **1997,** *72*, 1878-1886.

62. Berland, K. M.; So, P. T.; Chen, Y.; Mantulin, W. W.; Gratton, E., Scanning two-photon fluctuation correlation spectroscopy: particle counting measurements for detection of molecular aggregation. *Biophysical journal* **1996,** *71*, 410-420.

63. Wiseman, P. W.; Squier, J. A.; Ellisman, M. H.; Wilson, K. R., Two-photon image correlation spectroscopy and image cross-correlation spectroscopy. *J Microsc* **2000,** *200*, 14-25.

64. Thompson, N. L., Fluorescence Correlation Spectroscopy. In *Topics in Fluorescence Spectroscopy: Techniques*, Lakowicz, J. R., Ed. Springer US: Boston, MA, 1999; pp 337-378.

65. Elson, E. L.; Magde, D., Fluorescence correlation spectroscopy. I. Conceptual basis and theory. *Biopolymers* **1974,** *13*, 1-27.

66. Magde, D.; Elson, E.; Webb, W. W., Thermodynamic Fluctuations in a Reacting System---Measurement by Fluorescence Correlation Spectroscopy. *Physical Review Letters* **1972,** *29*, 705-708.

67. Pieper, C. M.; Enderlein, J., Fluorescence correlation spectroscopy as a tool for measuring the rotational diffusion of macromolecules. *Chemical Physics Letters* **2011,** *516*, 1-11.

68. Kask, P.; Piksarv, P.; Pooga, M.; Mets, U.; Lippmaa, E., Separation of the rotational contribution in fluorescence correlation experiments. *Biophysical journal* **1989,** *55*, 213-20.

69. Kask, P.; Piksarv, P.; Mets, U.; Pooga, M.; Lippmaa, E., Fluorescence correlation spectroscopy in the nanosecond time range: rotational diffusion of bovine carbonic anhydrase B. *European biophysics journal : EBJ* **1987,** *14*, 257-61.

70. Ehrenberg, M.; Rigler, R., Rotational brownian motion and fluorescence intensify fluctuations. *Chemical Physics* **1974,** *4*, 390-401.

71. Kask, P.; Piksarv, P.; Mets, Ü., Fluorescence correlation spectroscopy in the nanosecond time range: Photon antibunching in dye fluorescence. *European Biophysics Journal* **1985,** *12*, 163-166.

72. Kimble, H. J.; Dagenais, M.; Mandel, L., Photon Antibunching in Resonance Fluorescence. *Physical Review Letters* **1977,** *39*, 691-695.

73. Sýkora, J.; Kaiser, K.; Gregor, I.; Bönigk, W.; Schmalzing, G.; Enderlein, J., Exploring Fluorescence Antibunching in Solution To Determine the Stoichiometry of Molecular Complexes. *Analytical Chemistry* **2007,** *79*, 4040-4049.

74. Patrick Ambrose, W.; Goodwin, P. M.; Enderlein, J.; Semin, D. J.; Martin, J. C.; Keller, R. A., Fluorescence photon antibunching from single molecules on a surface. *Chemical Physics Letters* **1997,** *269*, 365-370.

75. Schönle, A.; Von Middendorff, C.; Ringemann, C.; Hell, S. W.; Eggeling, C., Monitoring triplet state dynamics with fluorescence correlation spectroscopy: bias and correction. *Microscopy research and technique* **2014,** *77*, 528-36.

76. Widengren, J., Photophysical Aspects of FCS Measurements. In *Fluorescence Correlation Spectroscopy: Theory and Applications*, Rigler, R.; Elson, E. S., Eds. Springer Berlin Heidelberg: Berlin, Heidelberg, 2001; pp 276-301.

77. Widengren, J.; Mets, U.; Rigler, R., Fluorescence correlation spectroscopy of triplet states in solution: a theoretical and experimental study. *The Journal of Physical Chemistry* **1995,** *99*, 13368-13379.

78. Widengren, J.; Rigler, R.; Mets, Ü., Triplet-state monitoring by fluorescence correlation spectroscopy. *Journal of Fluorescence* **1994,** *4*, 255-258.

79. Widengren, J.; Schwille, P., Characterization of Photoinduced Isomerization and Back-Isomerization of the Cyanine Dye Cy5 by Fluorescence Correlation Spectroscopy. *The Journal of Physical Chemistry A* **2000,** *104*, 6416-6428.

80. Suren, F.; Stanislav, K.; Alessandro, V.; Claus, A. M. S. In *Filtered FCS and species cross correlation function*, Proc.SPIE2009.

81. Felekyan, S.; Kalinin, S.; Sanabria, H.; Valeri, A.; Seidel, C. A. M., Filtered FCS: species auto- and cross-correlation functions highlight binding and dynamics in biomolecules. *Chemphyschem* **2012,** *13*, 1036-1053.

82. Bacia, K.; Kim, S. A.; Schwille, P., Fluorescence cross-correlation spectroscopy in living cells. *Nature methods* **2006,** *3*, 83-9.

83. Rarbach, M.; Kettling, U.; Koltermann, A.; Eigen, M., Dual-color fluorescence cross-correlation spectroscopy for monitoring the kinetics of enzyme-catalyzed reactions. *Methods (San Diego, Calif.)* **2001,** *24*, 104-16.

84. Hess, S. T.; Huang, S.; Heikal, A. A.; Webb, W. W., Biological and Chemical Applications of Fluorescence Correlation Spectroscopy: A Review. *Biochemistry* **2002,** *41*, 697-705.

85. Bacia, K.; Schwille, P., Practical guidelines for dual-color fluorescence cross-correlation spectroscopy. *Nature Protocols* **2007,** *2*, 2842-2856.

86. Foo, Y. H.; Naredi-Rainer, N.; Lamb, D. C.; Ahmed, S.; Wohland, T., Factors affecting the quantification of biomolecular interactions by fluorescence cross-correlation spectroscopy. *Biophysical journal* **2012,** *102*, 1174-1183.

87. Srivastava, M.; Petersen, N. O., Image cross-correlation spectroscopy: A new experimental biophysical approach to measurement of slow diffusion of fluorescent molecules. *Methods in Cell Science* **1996,** *18*, 47-54.

88. Petersen, N. O.; Höddelius, P. L.; Wiseman, P. W.; Seger, O.; Magnusson, K. E., Quantitation of membrane receptor distributions by image correlation spectroscopy: concept and application. *Biophysical journal* **1993,** *65*, 1135-46.

89. Wiseman, P. W.; Petersen, N. O., Image correlation spectroscopy. II. Optimization for ultrasensitive detection of preexisting platelet-derived growth factor-beta receptor oligomers on intact cells. *Biophysical journal* **1999,** *76*, 963-77.

90. Hendrix, J.; Lamb, D. C., Implementation and application of pulsed interleaved excitation for dual-color FCS and RICS. *Methods in molecular biology (Clifton, N.J.)* **2014,** *1076*, 653-82.

91. Brown, C. M.; Dalal, R. B.; Hebert, B.; Digman, M. A.; Horwitz, A. R.; Gratton, E., Raster image correlation spectroscopy (RICS) for measuring fast protein dynamics and concentrations with a commercial laser scanning confocal microscope. *J Microsc* **2008,** *229*, 78-91.

92. Digman, M. A.; Sengupta, P.; Wiseman, P. W.; Brown, C. M.; Horwitz, A. R.; Gratton, E., Fluctuation Correlation Spectroscopy with a Laser-Scanning Microscope: Exploiting the Hidden Time Structure. *Biophysical journal* **2005,** *88*, L33-L36.

93. Gegenfurtner, F. A.; Zisis, T.; Al Danaf, N.; Schrimpf, W.; Kliesmete, Z.; Ziegenhain, C.; Enard, W.; Kazmaier, U.; Lamb, D. C.; Vollmar, A. M.; Zahler, S., Transcriptional effects of actin-binding compounds: the cytoplasm sets the tone. *Cellular and Molecular Life Sciences* **2018,** *75*, 4539-4555.

94. Hendrix, J.; Dekens, T.; Schrimpf, W.; Lamb, Don C., Arbitrary-Region Raster Image Correlation Spectroscopy. *Biophysical journal* **2016,** *111*, 1785-1796.

95. Digman, M. A.; Wiseman, P. W.; Horwitz, A. R.; Gratton, E., Detecting protein complexes in living cells from laser scanning confocal image sequences by the cross correlation raster image spectroscopy method. *Biophysical journal* **2009,** *96*, 707-16.

96. Long, J. R.; Yaghi, O. M., The pervasive chemistry of metal–organic frameworks. *Chemical Society Reviews* **2009,** *38*, 1213-1214.

97. Rowsell, J. L. C.; Yaghi, O. M., Metal–organic frameworks: a new class of porous materials. *Microporous and Mesoporous Materials* **2004,** *73*, 3-14.

98. Furukawa, H.; Cordova, K. E.; O'Keeffe, M.; Yaghi, O. M., The Chemistry and Applications of Metal-Organic Frameworks. *Science* **2013,** *341*, 1230444.

99. Chen, G.; Roy, I.; Yang, C.; Prasad, P. N., Nanochemistry and Nanomedicine for Nanoparticle-based Diagnostics and Therapy. *Chemical Reviews* **2016,** *116*, 2826-2885.

100. Wang, L.; Zheng, M.; Xie, Z., Nanoscale metal–organic frameworks for drug delivery: a conventional platform with new promise. *Journal of Materials Chemistry B* **2018,** *6*, 707-717.

101. Nel, A. E.; Mädler, L.; Velegol, D.; Xia, T.; Hoek, E. M. V.; Somasundaran, P.; Klaessig, F.; Castranova, V.; Thompson, M., Understanding biophysicochemical interactions at the nano–bio interface. *Nature Materials* **2009,** *8*, 543-557.

102. Zimpel, A.; Al Danaf, N.; Steinborn, B.; Kuhn, J.; Höhn, M.; Bauer, T.; Hirschle, P.; Schrimpf, W.; Engelke, H.; Wagner, E.; Barz, M.; Lamb, D. C.; Lächelt, U.; Wuttke, S., Coordinative Binding of Polymers to Metal–Organic Framework Nanoparticles for Control of Interactions at the Biointerface. *ACS Nano* **2019,** *13*, 3884-3895.

103. Kalaj, M.; Cohen, S. M., Postsynthetic Modification: An Enabling Technology for the Advancement of Metal-Organic Frameworks. *ACS Cent Sci* **2020,** *6*, 1046-1057.

104. Yin, Z.; Wan, S.; Yang, J.; Kurmoo, M.; Zeng, M.-H., Recent advances in post-synthetic modification of metal–organic frameworks: New types and tandem reactions. *Coordination Chemistry Reviews* **2019,** *378*, 500-512.

105. Mandal, S.; Natarajan, S.; Mani, P.; Pankajakshan, A., Post-Synthetic Modification of Metal–Organic Frameworks Toward Applications. *Advanced Functional Materials* **2021,** *31*, 2006291.

106. Ji, Z.; Wang, H.; Canossa, S.; Wuttke, S.; Yaghi, O. M., Pore Chemistry of Metal–Organic Frameworks. *Advanced Functional Materials* **2020,** *30*, 2000238.

107. Lian, X.; Feng, D.; Chen, Y. P.; Liu, T. F.; Wang, X.; Zhou, H. C., The preparation of an ultrastable mesoporous Cr(iii)-MOF via reductive labilization. *Chemical science* **2015,** *6*, 7044-7048.

108. Deria, P.; Mondloch, J. E.; Karagiaridi, O.; Bury, W.; Hupp, J. T.; Farha, O. K., Beyond post-synthesis modification: evolution of metal–organic frameworks via building block replacement. *Chemical Society Reviews* **2014,** *43*, 5896-5912.

109. Deria, P.; Bury, W.; Hod, I.; Kung, C.-W.; Karagiaridi, O.; Hupp, J. T.; Farha, O. K., MOF Functionalization via Solvent-Assisted Ligand Incorporation: Phosphonates vs Carboxylates. *Inorganic Chemistry* **2015,** *54*, 2185-2192.

110.Deria, P.; Bury, W.; Hupp, J. T.; Farha, O. K., Versatile functionalization of the NU-1000 platform by solvent-assisted ligand incorporation. *Chemical Communications* **2014,** *50*, 1965-1968.

111.Kim, M.; Cahill, J. F.; Su, Y.; Prather, K. A.; Cohen, S. M., Postsynthetic ligand exchange as a route to functionalization of 'inert' metal–organic frameworks. *Chemical science* **2012,** *3*, 126-130.

112.Kim, M.; Cahill, J. F.; Fei, H.; Prather, K. A.; Cohen, S. M., Postsynthetic Ligand and Cation Exchange in Robust Metal–Organic Frameworks. *Journal of the American Chemical Society* **2012,** *134*, 18082-18088.

113.Lalonde, M. B.; Mondloch, J. E.; Deria, P.; Sarjeant, A. A.; Al-Juaid, S. S.; Osman, O. I.; Farha, O. K.; Hupp, J. T., Selective Solvent-Assisted Linker Exchange (SALE) in a Series of Zeolitic Imidazolate Frameworks. *Inorg Chem* **2015,** *54*, 7142-4.

114.Yang, L.; Sun, L. X.; Xu, F.; Zou, Y. J.; Chu, H. L., Modulated Synthesis of UiO-67 for High Resistance to CH_2Cl_2. *Materials Science Forum* **2016,** *852*, 609-613.

115.Siu, P. W.; Brown, Z. J.; Farha, O. K.; Hupp, J. T.; Scheidt, K. A., A mixed dicarboxylate strut approach to enhancing catalytic activity of a de novo urea derivative of metal-organic framework UiO-67. *Chem Commun (Camb)* **2013,** *49*, 10920-2.

116.Katz, M. J.; Brown, Z. J.; Colon, Y. J.; Siu, P. W.; Scheidt, K. A.; Snurr, R. Q.; Hupp, J. T.; Farha, O. K., A facile synthesis of UiO-66, UiO-67 and their derivatives. *Chem Commun (Camb)* **2013,** *49*, 9449-51.

117.Marreiros, J.; Caratelli, C.; Hajek, J.; Krajnc, A.; Fleury, G.; Bueken, B.; De Vos, D. E.; Mali, G.; Roeffaers, M. B. J.; Van Speybroeck, V.; Ameloot, R., Active Role of Methanol in Post-Synthetic Linker Exchange in the Metal–Organic Framework UiO-66. *Chemistry of Materials* **2019,** *31*, 1359-1369.

118.Fluch, U.; Paneta, V.; Primetzhofer, D.; Ott, S., Uniform distribution of post-synthetic linker exchange in metal-organic frameworks revealed by Rutherford backscattering spectrometry. *Chem Commun (Camb)* **2017,** *53*, 6516-6519.

119.Taddei, M.; Wakeham, R. J.; Koutsianos, A.; Andreoli, E.; Barron, A. R., Post-Synthetic Ligand Exchange in Zirconium-Based Metal-Organic Frameworks: Beware of The Defects! *Angewandte Chemie* **2018,** *57*, 11706-11710.

120.Schrimpf, W.; Ossato, G.; Hirschle, P.; Wuttke, S.; Lamb, D. C., Investigation of the Co-Dependence of Morphology and Fluorescence Lifetime in a Metal-Organic Framework. *Small* **2016,** *12*, 3651-7.

121.Connolly, B. M.; Aragones-Anglada, M.; Gandara-Loe, J.; Danaf, N. A.; Lamb, D. C.; Mehta, J. P.; Vulpe, D.; Wuttke, S.; Silvestre-Albero, J.; Moghadam, P. Z.; Wheatley, A. E. H.; Fairen-Jimenez, D., Tuning porosity in macroscopic monolithic metal-organic frameworks for exceptional natural gas storage. *Nat Commun* **2019,** *10*, 2345.

122.Ameloot, R.; Vermoortele, F.; Hofkens, J.; De Schryver, F. C.; De Vos, D. E.; Roeffaers, M. B., Three-dimensional visualization of defects formed during the synthesis of metal-organic frameworks: a fluorescence microscopy study. *Angewandte Chemie* **2013,** *52*, 401-5.

123.Schrimpf, W.; Jiang, J.; Ji, Z.; Hirschle, P.; Lamb, D. C.; Yaghi, O. M.; Wuttke, S., Chemical diversity in a metal–organic framework revealed by fluorescence lifetime imaging. *Nature Communications* **2018,** *9*, 1647.

124.Al Danaf, N.; Schrimpf, W.; Hirschle, P.; Lamb, D. C.; Ji, Z.; Wuttke, S., Linker Exchange via Migration along the Backbone in Metal–Organic Frameworks. *Journal of the American Chemical Society* **2021,** *143*, 10541-10546.

125.Kamtekar, K. T.; Monkman, A. P.; Bryce, M. R., Recent Advances in White Organic Light-Emitting Materials and Devices (WOLEDs). *Advanced Materials* **2010,** *22*, 572-582.

126.Nakanotani, H.; Higuchi, T.; Furukawa, T.; Masui, K.; Morimoto, K.; Numata, M.; Tanaka, H.; Sagara, Y.; Yasuda, T.; Adachi, C., High-efficiency organic light-emitting diodes with fluorescent emitters. *Nature Communications* **2014,** *5*, 4016.

127.Baldo, M. A.; Lamansky, S.; Burrows, P. E.; Thompson, M. E.; Forrest, S. R., Very high-efficiency green organic light-emitting devices based on electrophosphorescence. *Applied Physics Letters* **1999,** *75*, 4-6.

128.Tang, C. W.; VanSlyke, S. A., Organic electroluminescent diodes. *Applied Physics Letters* **1987,** *51*, 913-915.

129.Lee, J.-H.; Chen, C.-H.; Lee, P.-H.; Lin, H.-Y.; Leung, M.-k.; Chiu, T.-L.; Lin, C.-F., Blue organic light-emitting diodes: current status, challenges, and future outlook. *Journal of Materials Chemistry C* **2019,** *7*, 5874-5888.

130.Kirst, C.; Danaf, N. A.; Knechtel, F.; Arczynski, T.; Mayer, P.; Lamb, D. C.; Karaghiosoff, K., Methods for elucidating the structural-property relationship in luminescent materials. *Journal of Materials Chemistry C* **2021**.

131.Allen, K. N.; Imperiali, B., Lanthanide-tagged proteins--an illuminating partnership. *Current opinion in chemical biology* **2010,** *14*, 247-54.

132.Butler, S. J.; Lamarque, L.; Pal, R.; Parker, D., EuroTracker dyes: highly emissive europium complexes as alternative organelle stains for live cell imaging. *Chemical science* **2014,** *5*, 1750-1756.

133.Walton, J. W.; Bourdolle, A.; Butler, S. J.; Soulie, M.; Delbianco, M.; McMahon, B. K.; Pal, R.; Puschmann, H.; Zwier, J. M.; Lamarque, L.; Maury, O.; Andraud, C.; Parker, D., Very bright europium complexes that stain cellular mitochondria. *Chemical Communications* **2013,** *49*, 1600-1602.

134.Op den Camp, H. J.; Islam, T.; Stott, M. B.; Harhangi, H. R.; Hynes, A.; Schouten, S.; Jetten, M. S.; Birkeland, N. K.; Pol, A.; Dunfield, P. F., Environmental, genomic and

taxonomic perspectives on methanotrophic Verrucomicrobia. *Environmental microbiology reports* **2009,** *1*, 293-306.

135.Keltjens, J. T.; Pol, A.; Reimann, J.; Op den Camp, H. J., PQQ-dependent methanol dehydrogenases: rare-earth elements make a difference. *Applied microbiology and biotechnology* **2014,** *98*, 6163-83.

136.Jahn, B.; Pol, A.; Lumpe, H.; Barends, T. R. M.; Dietl, A.; Hogendoorn, C.; Op den Camp, H. J. M.; Daumann, L. J., Similar but Not the Same: First Kinetic and Structural Analyses of a Methanol Dehydrogenase Containing a Europium Ion in the Active Site. *Chembiochem* **2018,** *19*, 1147-1153.

137.Binnemans, K., Interpretation of europium(III) spectra. *Coordination Chemistry Reviews* **2015,** *295*, 1-45.

List of Abbreviations

ACF	Auto-correlation function
ADC	Analogue-to-digital converter
AFM	Atomic force microscope
APD	Avalanche photodiode
ARICS	Arbitrary region raster image correlation spectroscopy
BFL	Back focal length
BPDC-RB	Biphenyl-4,4′-dicarboxylic acid attached with rhodamine b
BR	Bilirubin
CCF	Cross-correlation function
ccRICS	Raster image cross-correlation spectroscopy
CLSM	Confocal laser scanning microscopy/microscope
CW	Continuous wave
DMF	Dimethylformamide
DNA	Deoxyribonucleic acid
eGFP	Enhanced green fluorescence protein
EMCCD	Electron-multiplying charge-coupled device
Eu	Europium
FCS	Fluorescence correlation analysis
FCCS	Fluorescence cross-correlation spectroscopy
FFS	Fluorescence fluctuation spectroscopy
FPGA	Field Programmable Gate Array
FOV	Field of view
FITC	Fluorescein isothiocyanate
FLIM	Fluorescence lifetime image microscopy
FRET	Förster resonance energy transfer
HS	Hirshfeld surface
HS-PMT	High speed-photomultiplier tube
IC	Internal conversion
ICCS	Image cross-correlation spectroscopy
ICS	Image correlation spectroscopy
IgG	Immunoglobulin G
IR	Infrared
IRF	Instrument response function
ISC	Inter-system crossing
La	Lanthanum
LED	Light emitting diode
Ln	Lanthanides
MDH	Methanol dehydrogenase
MeOH	Methanol
MOF	Metal-organic framework
MS	Mass spectrometry
NA	Numerical aperture
NIM	Nuclear-instrumentation-module
NMR	Nuclear magnetic resonance
OLED	Organic light emitting diode
PALM	Photo-activated
PFS	Perfect focus system

PIE	Pulsed interleaved excitation
PMO	Phosphorodiamidate Morpholino oligomers
PMT	Photomultiplier tube
PQQ	Pyrroloquinoline quinone
PrB	Phylloroseobilin
PSD	Position-sensitive detector
PSE	Post-synthetic exchange
PSF	Point spread function
PSM	Post-synthetic modification
RICS	Raster image correlation spectroscopy
RNA	Ribonucleic acid
RNP	Ribonucleoprotein
ROI	Region of interest
RT	Room temperature
SALE	Solvent assisted linker exchange
SALI	Solvent assisted linker incorporation
SEM	Scanning electron microscopy
SPAD	Single-photon avalanche diode
STED	Stimulated emission depletion microscopy
STORM	Stochastic optical reconstruction microscopy
TAC	Time-to-amplitude converter
TCSPC	Time correlated single photon counting
TDC	Time-to-digital converter
TEM	Transmission electron microscopy
TRLFS	Time-resolved laser-induced fluorescence spectroscopy
TTL	Transistor-transistor logic
UiO	Universitetet i Oslo
UV-vis	Ultraviolet-visible
XRD	X-ray diffraction

Acknowledgments

Along the way of obtaining my PhD in Physical Chemistry, a lot of work was devoted for several years. The outcome would have not been possible without receiving a lot of support from many people who encouraged, helped and aided me with this work, both academically and non-academically. I would like to convey my deep gratitude to all of you.

Firstly, I would like to show my great appreciation towards my academic supervisor, Prof. Don C. Lamb, who always aided my work with his inspiring-hardcore scientific insights and ideas of what could be done, continuous guidance and support throughout my PhD study. He taught me that patience, good scientific practice and persistence are key factors for a scientific establishment, where hard work is always rewarded. For your constant supervision and advice alongside the freedom to let me try things out alone (being expensive sometimes), I am deeply grateful.

Secondly, I would like to thank my thesis second reviewer and instructor, Prof. Stefan Wuttke for being a great supporter throughout the years of my PhD, both personally and scientifically. You were always passionate about our work together and provided the necessary information and scientific knowledge. Pushing things to a better stage alongside the persistence and ambition to move things forward, is something I appreciate and learned a lot from. For this guidance and help I am very thankful.

I would like to gratefully acknowledge my thesis committee Prof. Christoph Bräuchle, Prof. Konstantin Karaghiosoff, Prof. Philip Tinnefeld and Prof. Achim Hartschuh for reviewing my dissertation and aiding with their feedback. I extend my thanks to the different funding agencies SFP 1032, NIM and CeNS that provided me, not only, with a financial support, but also with an opportunity to attend several workshops and to work on challenging projects with the possibility of different collaborations that boosted my interdisciplinary knowledge. In particular, I would like to thank Prof. Ernst Wagner, Dr. Ulrich Lachelt and Dr. Jasmin Kuhn for the successful collaborations that we had. Many thanks for the MOF collaborators Dr. Andreas Zimpel and Dr. Patrick Hirschle, for the MDH collaborators Prof. Lena Daumann and Dr. Berenice Jahn, for the Actin project collaborators Prof. Zahler, Dr. Simone Moser, Dr. Cornelia Karg and Dr. Florian Gegenfurtner, and last but not least for the OLED collaborators Prof. Konstantin Karaghiosoff and Christin Kirst.

I want to thank the former and present members of the Fablab for providing this scientific atmosphere and pleasurable environment that I enjoyed and profited from a lot. In particular, I would like to thank you Waldi for being the first supervisor during my PhD, which helped me a lot once we started working together on the MOF projects. We had a click, and it was very fruitful and yes complaining helps sometimes! I hope this heritage is

passed to Irene; it will bring you good luck with the RICS. Here, I would also like to thank Fabian for help in developing the RICS setup and the great drawings as well, I wish you good luck with your PhD and well done for the work during your master period, which was pleasant to supervise before 6:00 pm. Moving the setup from one building to the other was a lot of work, therefore the help of several people during this phase is appreciated. In particular, I would like to thank Frank, Adrian and Evelyn for the extra help to double check the electronics / software with me and help with integrating an FPGA into the setup.

Annoying and frustrating moments are definitely part of a PhD, thus having some time to enjoy without work is a must. Here, I would like to thank first all my Fablab colleagues for the science and beyond times. It was much fun showing GoT series and having movie nights with Waldi, Kira, Anders, Wehne and Ellen. Being a good Bavarian citizen, I really enjoyed the beer and schafkopf times with Frank, Adrian, Vanessa and Evelyn. The IT job was not that bad, I learned a lot from it and thanks for your help Wehne and Bässem.

Finally, the biggest thanks go to my parents and sister who always stood by my side and believed that I will contribute to the scientific community. Your help sculpted my personality (شكراً كتير على كل شي). Mein letzten Dank geht an dich ‘mein Bibi’ für die schöne Zeiten und Hilfe, wenn ich dich gebraucht habe.

Curriculum Vitae

Personal Profile

Highly motivated researcher holding a PhD in Physical chemistry, with solid hands-on experience in the assembly and usage of confocal laser scanning microscopes. Diligent, keen to learn and hardworking with a good team admiration and spirit. Research experience through various projects within both academic (mainly) and industry-oriented environments.

Education

Since 09/2015	**Ludwig Maximilian University, Munich** PhD in Physical Chemistry (Group of Prof. Don C. Lamb) Thesis Title: Advanced Fluorescence Methodologies for the Exploration of the Nanoworlds
09/2013 – 06/2015	**Jacobs University, Bremen** M.Sc. in Nanomolecular Science Major: Physical Sciences Thesis Title: A Supramolecular Fluorescence-Based Assay to Monitor the Activity of Vesicular Acetylcholine Transporter
02/2010 – 07/2013	**American University of Beirut, Beirut** B.Sc. in Chemistry Minors: Biology and Biomedical Engineering

Work Experience

Since 09/2015	**PhD researcher, Ludwig Maximilian University** • Usage of advanced fluorescence methods for investigating cellular systems and different material science • Setting up a confocal laser scanning microscope (CLSM) with the capabilities of widefield and total internal reflection microscopy • Utilization of the CLSM for fluorescence correlation spectroscopy (FCS), image correlation spectroscopy (ICS), fluorescence lifetime imaging microscopy (FLIM) and live-cellular imaging • IT job responsibilities for setting up data servers and measurements computers alongside maintaining them
Since 09/2015	**Student and Research assistant, Ludwig Maximilian University** Teaching assistant and advisor for undergraduate and master laboratory courses, which included the following responsibilities: • Tutor for undergraduate courses in Biophysical and Physical Chemistry

- Prepare and conduct experiments for Fluorescence Spectroscopy Labs

09/2013 – 07/2015 **Academic Researcher, Jacobs University, Bremen**
Research intern in the group of Prof. Werner Nau and Prof. Mathias Winterhalter conducting research to develop fluorescence based-assays
- Usage of UV-vis and fluorescence (with lifetime-resolved single photon counting capabilities) spectroscopy to develop an assay for analyte diffusion through parallel artificial membrane permeability assays (PAMPA)
- Permeation studies as a function of temperature, with emphasis on the diffusion kinetics using different liposome constructions

02/2014 – 07/2015 **Academic Researcher, Bayer CropScience, Monheim**
Research project in collaboration with Bayer CropScience for developing a supramolecular fluorescent based-assay to monitor the activity of vesicular acetylcholine transporter
- Study the diffusion kinetics of potential insecticides using different liposome constructions
- Usage of the developed assay to test the activity of different potential insecticides

02/2010 – 07/2013 **Bachelor Researcher, American University of Beirut**
Bachelor thesis on the photophysical properties of Rosmarinic acid and its interaction with native, unfolded and refolded state of human serum albumin. (Supervisor: Prof. Digambara Patra)

Prizes and Honours

Conferences:
- Methods and Applications in Fluorescence poster award (2017)
- Center for Nanoscience travel award (2019)

Awards:
- Center for Nanoscience publication award (2019)

Skills

Languages:
- German (C1 level / proficient)
- English (C2 level / native)
- Arabic (C2 level / native)

Others:
- MS Office (Word, Power-Point, Excel), advanced skills
- MATLAB, adobe illustrator, and 3D Max, intermediate skills
- Chemistry student society vice president (2012)
- Jacobs University chemistry club member (enrolled and participating in organising an English language course for Syrian refugees in Bremen-Germany).

A. Appendix

A.1. CLSM filters

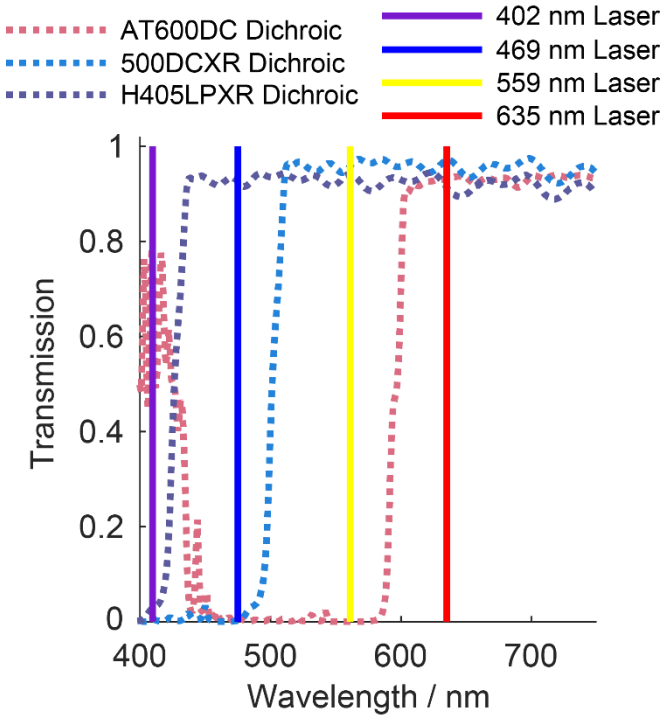

Figure A.1: The transmission spectra for the three different dichroic mirrors (dotted lines) used to combine the four different excitation lasers lines (solid lines).

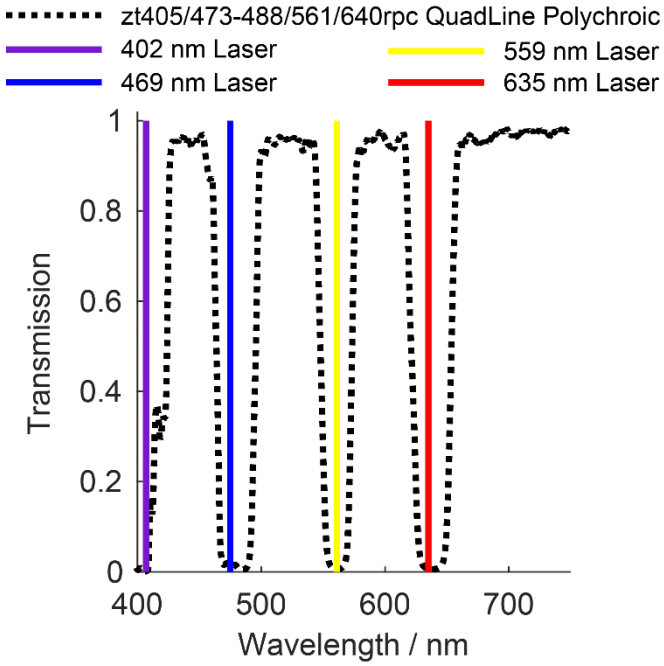

Figure A.2: The transmission spectra for the polychroic mirror zt405/473-488/561/640rcp (dotted lines) used to reflect the four different excitation lasers lines (solid lines) and let through the fluorescence emission.

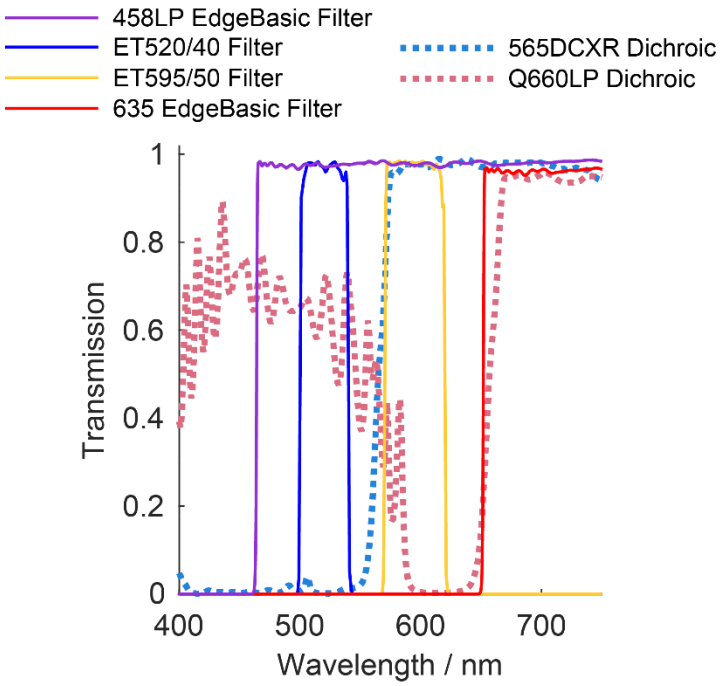

Figure A.3: The transmission spectra for the two dichroic mirrors (dashed lines) and the four emission filters (solid lines) that determine the fluorescence detection range. The three emission filters 635 Edge Basic, ET595/50 and ET520/40 are used in the red/IR, orange/red and blue/green detection channels, respectively, while the 458LP Edge Basic filter was used mainly in combination with the 402 nm laser for the autofluorescence experiments.

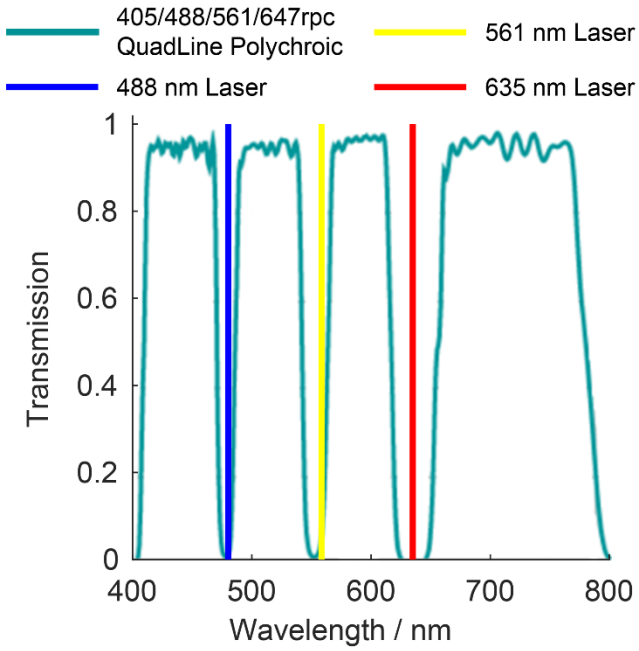

Figure A.4: The transmission spectra for the polychroic mirror (in the wide-field pathway) 405/488/561/647rcp (green line) used to reflect the three different excitation lasers lines (solid lines) and let through the fluorescence emission.

A.2. CLSM detailed parts list

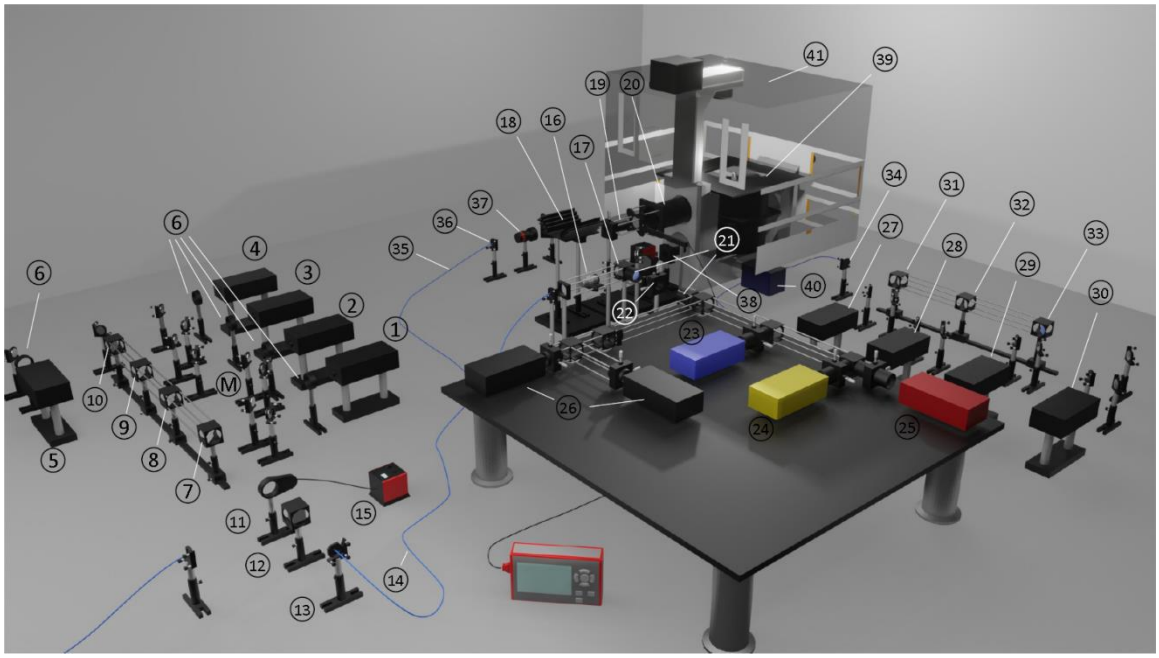

Figure A.4: Three-dimensional scheme of the CLSM with the detailed labeling of the different parts. Acknowledgement to Fabian Knechtel for preparing this 3D CLSM schematic.

Table 4: Detailed parts list of the home-built CLSM.

No.	Description	Part name	Manufacturer
1	402 nm Laser	PicoQuant LDH-P-C-400B	PicoQuant
2	437 nm Laser	PicoQuant LDH-P-C-440	PicoQuant
3	469 nm Laser	PicoQuant LDH-P-C-470	PicoQuant
4	559 nm Laser	PicoQuant LDH-P-FA-560	PicoQuant
5	635 nm Laser	PicoQuant LDH-P-C-635M	PicoQuant
6	Clean Up Filter	–	–
7	Dichroic	H405LPXR (reflects the 402 nm)	AHF
8	Dichroic	zt442 RDC flat (reflects the 437 nm)	AHF
9	Dichroic	500DCXR (reflects the 469 nm)	AHF
10	Dichroic	AT600DC (reflects the 559 nm)	AHF
11	Lambda Half Plate	AHWP05M-600	Thorlabs
12	Polarizing Beam Splitter	PBS	Thorlabs
13	Coupler	PAF2A	Thorlabs
14	Single Mode Fiber	QPMJ-A3A,3AF-488-3.5/125-3-5-1	OZ Optics
15	Servo Motor Controller	KDC101	Thorlabs
16	Collimator	Mitutoyo Plan Apochromat Objective20x	Mitutoyo / Thorlabs

No.	Description	Part name	Manufacturer
17	Polychroic Mirror	zt405/473-488/561/640rpc Quad Line	AHF / Chroma
18	Galvanometer Mirrors	Model 6210H Optical Scanner	Cambridge Technologies
19	Scan Lens	SL50-CLS2	Thorlabs
20	Tube Lens	TL200-CLS2	Thorlabs
21	Focus Lenses	Achromatic Lens AC254-060-A-ML	Thorlabs
22	Pinhole	80 µm	Newport
23	Blue APD	Count© blue	Laser Components
24	Yellow APD	SPCM-AQR-14	PerkinElmer
25	Red APD	Count©	Laser Components
26	Single-Photon Avalanche Diodes	PDM Series	PicoQuant / MPD
27	445nmLaser	MDL0445-06-01.0050-100	Cobolt
28	488nmLaser	55mW 488nm Diodelaser	Lasertack
29	561nmLaser	LC GCL-025-561-0.25%	CrystaLaser
30	635nmLaser	200 mW 635nm Diodelaser	Lasertack
31	Dichroic	Reflects 445nm	AHF
32	Dichroic	LP500	–
33	Dichroic	H568LPXRsuperflat	AHF
34	Coupler	–	OZ Optics
35	Single Mode Fiber	QPMJ-A3A,3A-488-3.5/125-3-4-1	OZ Optics
36	Collimator	HPUCO-23AF-400/700-P25AC	Coherent
37	Beam Expansion Telescope 10X	GBE10-A	Thorlabs
38	Focus Lens	Achromatic Lens AC254-300-A-ML	Thorlabs
39	Microscope Body	Eclipse Ti Series	Nikon
40	EMCCD Camera	IxonUltra897	Andor Technology
41	Incubator	Large Chamber Incubation	Pecon

B. Appended Papers

B.1. Paper 1: Coordinative Binding of Polymers to Metal-Organic Framework Nanoparticles for Control of Interactions at the Biointerface

ACSNANO
Cite This: ACS Nano 2019, 13, 3884−3895
www.acsnano.org

ARTICLE

Coordinative Binding of Polymers to Metal−Organic Framework Nanoparticles for Control of Interactions at the Biointerface

Andreas Zimpel,[†] Nader Al Danaf,[†] Benjamin Steinborn,[‡] Jasmin Kuhn,[‡] Miriam Höhn,[‡] Tobias Bauer,[§] Patrick Hirschle,[†] Waldemar Schrimpf,[†] Hanna Engelke,[†] Ernst Wagner,[‡] Matthias Barz,[§] Don C. Lamb,[†] Ulrich Lächelt,*[,‡] and Stefan Wuttke*[,†,∥]

[†]Department of Chemistry and Center for NanoScience (CeNS), LMU Munich, Butenandtstraße 11, 81377 Munich, Germany
[‡]Department of Pharmacy and Center for NanoScience (CeNS), LMU Munich, Butenandtstraße 5-13, 81377 Munich, Germany
[§]Institute of Organic Chemistry, Johannes Gutenberg-University Mainz, Duesbergweg 10-14, 55099 Mainz, Germany
[∥]School of Chemistry, College of Science, University of Lincoln, Brayford Way, Brayford Pool, Lincoln LN6 7TS, United Kingdom

Supporting Information

ABSTRACT: **Metal−organic framework nanoparticles (MOF NPs) are of growing interest in diagnostic and therapeutic applications, and due to their hybrid nature, they display enhanced properties compared to more established nanomaterials. The effective application of MOF NPs, however, is often hampered by limited control of their surface chemistry and understanding of their interactions at the biointerface. Using a surface coating approach, we found that coordinative polymer binding to Zr-*fum* NPs is a convenient way for peripheral surface functionalization. Different polymers with biomedical relevance were assessed for the ability to bind to the MOF surface. Carboxylic acid and amine containing polymers turned out to be potent surface coatings and a modulator replacement reaction was identified as the underlying mechanism. The strong binding of polycarboxylates was then used to shield the MOF surface with a double amphiphilic polyglutamate−polysarcosine block copolymer, which resulted in an exceptional high colloidal stability of the nanoparticles. The effect of polymer coating on interactions at the biointerface was tested with regard to cellular association and protein binding, which has, to the best of our knowledge, never been discussed in literature for functionalized MOF NPs. We conclude that the applied approach enables a high degree of chemical surface confinement, which could be used as a universal strategy for MOF NP functionalization. In this way, the physicochemical properties of MOF NPs could be tuned, which allows for control over their behavior in biological systems.**

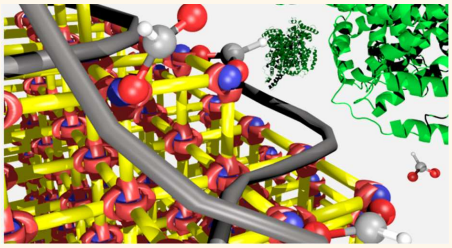

KEYWORDS: *metal−organic frameworks, nanoparticles, polymers, external surface functionalization, agglomeration, protein and cell interactions*

The chemistry of metal−organic frameworks (MOFs) provides great flexibility for the generation of crystalline inorganic−organic hybrid materials spanning an enormous chemical compound space for these materials.[1] By selection of appropriate inorganic building units (metal ions or metal oxide clusters) and organic linker molecules, a huge number of MOFs with tailor-made properties can be produced in simple, scalable, and cost-effective reactions driven by self-organizing processes.[1−5] Beside industrial applications, such as catalysis,[6−9] gas storage,[10] separation,[11,12] or sensing,[13−15] the material class of MOFs is also being explored for diagnostic and therapeutic purposes.[16−22] MOF nanoparticles (NPs) have already been used as carriers for drugs,[18,23−26] nucleic acids,[27] peptides, and proteins[28,29] as well as functional materials on their own, such as MRI contrast agents[30−33] or photosensitizers.[34] Considering the tunable properties of MOFs, it is expected that other biomedical applications will follow.[18−20] As with other classes of nanomaterials, the interaction of the MOF NP surface with their environment critically impacts the behavior in biological systems.[35−37] One rational approach to control interactions at the MOF biointerface and thereby increase the potential for

Received: August 17, 2018
Accepted: March 7, 2019
Published: March 7, 2019

DOI: 10.1021/acsnano.8b06287
ACS Nano 2019, 13, 3884−3895

Table 1. Summary of Selected Polymers Used in This Work[a]

Polymer	Charge at pH 7	Structure	Properties
BPEI	+		basic; high buffer capacity at endosomal pH; → intracellular drug delivery, non-viral nucleic acid transfections
PAMAM	+	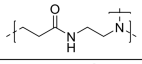	basic; high buffer capacity at endosomal pH; → intracellular drug delivery, non-viral nucleic acid transfections
PGlu	-	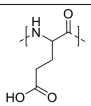	acidic, polypeptide, natural monomer sub-unit → polymer scaffold for drug delivery systems, drug packaging and delivery applications
PAA	-		acidic → polymer scaffold for drug delivery systems, binding agent for drug formulations
PEG	0		neutral, hydrophilic → shielding polymer, extends plasma half lives of drugs and drug carriers
Tween®	0	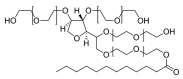	neutral, amphiphilic, nonionic surfactant → solubilizer, additive in drug formulations
PGlu-PSar	0/-	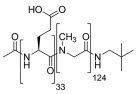	Block-co-polymer PGA: acidic, binding domain; PS: neutral, shielding domain → MOF surface functionalization polymer with separate assembly and shielding domains

[a]"Polymer" defines the abbreviations used in this work (BPEI, branched polyethylene imine; PAMAM, polyamidoamine dendrimer generation 4; PGlu, polyglutamic acid; PAA, polyacrylic acid; PEG, polyethylene glycole; Tween, polysorbate 20; PGlu-PSar, polyglutamate-*b*-polysarcosine block-co-polymer). "Charge" indicates positive (+), negative (−), or neutral (0) net charge at pH 7. "Structure" shows simplified molecular structure or repeating units of selected polymers. "Properties" exemplifies characteristics and biomedical applications.

biomedical applications is to functionalize the outer surface of the MOFs. Several postsynthetic modification procedures have been reported, such as surface adsorption,[38−40] lipid coating,[41−43] covalent conjugation,[32,44] and coordinative binding of functional units.[28] Here, we systematically investigated Zr-*fum* MOF NP surface coating with polymers by simply mixing them in an aqueous medium. Zr-*fum* MOF NPs were selected because of their favorable size distribution,[45] colloidal stability,[45] nanosafety profile,[46] and good cellular uptake.[28] Self-assembly of polymers on MOF NPs is assumed to be a powerful concept as it could potentially ensure a defined arrangement of these units at the outer surface without any guidance from external forces. This kind of process is ubiquitous in chemistry and biology and is increasingly used in industry as it simplifies manufacturing processes and lowers costs while offering molecular control and the generation of structures in three dimensions and on curved surfaces.[47] Because the feasibility of the polymer functionalization based on surface adsorption depends on the individual nature of the coating material, we selected representative polymers with relevance in the biomedical field but with different physicochemical properties (Table 1). The set contained two positively charged polymers (branched polyethylene imine, BPEI, and PAMAM dendrimer G4), two negatively charged polymers (polyglutamic acid, PGlu, and poly(acrylic acid), PAA), two uncharged polymers (polyethylene glycole, PEG and polysorbate 20, Tween), and one hybrid block-*co*-polymer (polyglutamate-*b*-polysarcosine, PGlu-PSar).

BPEI and PAMAM dendrimers are frequently used for nucleic acid transfections as well as for intracellular transport of other materials.[48,49] Because of their cationic nature, these polymers bind nucleic acids by electrostatic interaction and mediate cellular uptake of the resulting complexes.[50,51] BPEI can be considered to be an archetype of transfecting agents. Its beneficial buffer capacity in the acidic environment of endo- and lysosomes promotes cargo release into the cytosol due to the so-called "proton-sponge effect".[52,53] In contrast to the statistical polymerization product BPEI, PAMAM dendrimers represent perfectly defined monodisperse compounds. The anionic polymers PGlu, PAA and corresponding block copolymers have been widely used as polymer scaffolds for drug conjugation, NP functionalization, and hydrogel or micelle formation.[54−58] In contrast to anionic and cationic polymers, stealth-like polymers such as polyethylene glycol (PEG) or polysarcosine (PSar) are the most prominent agents used for shielding and colloidal stabilization of nanoparticles or biopharmaceuticals; "PEGylation" is even considered a generally accepted technical term in the pharmaceutical sciences.[59] PEG is a polyether with amphiphilic character, and it is able to accept multiple hydrogen bonds thus generating a hydrophilic layer in an aqueous environment. It also reduces adsorption or aggregation at surfaces due to sterical stabilization. Polysorbate 20 is a neutral surfactant which also contains PEG-like structural parts and is used in pharmaceutical products as solubilizer or emulsifier. In addition, a copolymer (PGlu-PSar), composed of a polyglutamate and a polysarcosine block, was used as an example for MOF surface functionalization with a polymer featuring a more sophisticated and advanced architecture.[60] Here, the PGlu block was expected to show binding properties similar to that of bare PGlu. The polysarcosine (or poly(*N*-methyl glycine))[61] is known to possess comparable solution properties

DOI: 10.1021/acsnano.8b06287
ACS Nano 2019, 13, 3884−3895

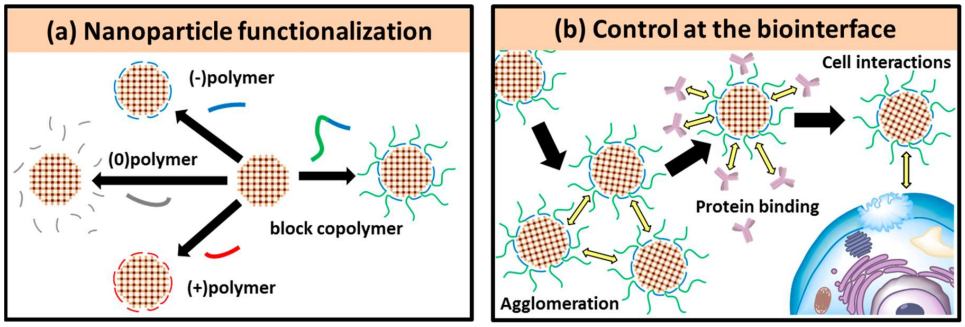

Figure 1. (a) Schematic illustration of the coating procedure with four different polymer groups (negatively charged, neutral, positively charged, and hybrid block copolymer) and (b) of the investigations performed with the functionalized MOF NPs (agglomeration, protein binding, and cell interactions).

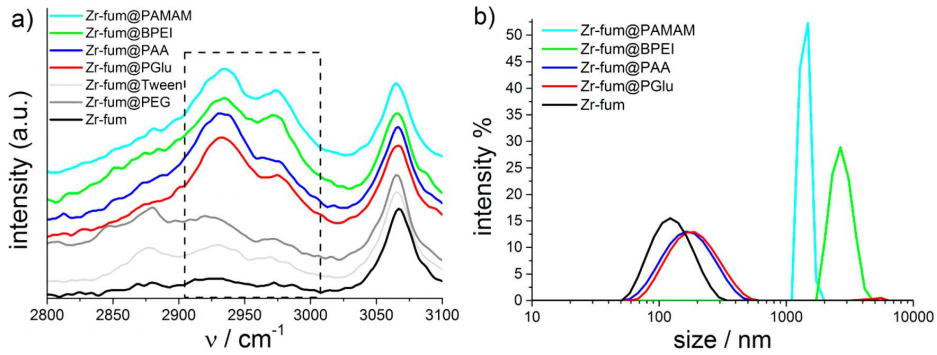

Figure 2. Characterization of the Zr-*fum*@polymer NPs. (a) Raman spectra (normalized to internal Zr-*fum* reference at 3065 cm^{-1}) of unfunctionalized Zr-*fum* NPs in comparison to Zr-*fum*@polymer NPs in the region of interest (2700−3100 cm^{-1}). For the full spectra, see SI, Figure S6. (b) DLS plots (by intensity) of Zr-*fum* NPs in comparison to Zr-*fum*@polymer NPs in HBG.

like PEG but is based on the endogenous amino acid sarcosine, which naturally occurs in our glycine metabolism.[62−64] Therefore, polysarcosine is considered a promising and less immunogenic alternative to the most frequently used shielding agent PEG for the enhancement of circulation lifetimes.[64−66]

In this work, we investigated the binding of different polymers by simple mixing in aqueous/ethanolic solution at room temperature in order to identify the most facile, reproducible, and scalable functionalization processes under mild and biocompatible conditions (Figure 1a).[19] We screened the selected polymers with regard to their ability to bind to Zr-*fum* NPs and investigated the physicochemical properties of these Zr-*fum*@polymer NPs and the interactions at the MOF biointerface. Evaluated key parameters were change of zeta-potential, colloidal stabilization, protein binding, and cellular interactions (Figure 1b). To the best of our knowledge, the physicochemical aspects of interaction between functional MOF NP surfaces and proteins have never been reported. It is worth stressing that both the functionalization concept and the used polymers can be applied to any other MOF NP. Thus, this study is considered to be fundamental as we established the efficient generation of MOF NPs with various surface properties. Moreover, our study identified the relationship between functionalized MOF NPs and the biointerface, which will help to guide the rational design of hybrid nanomaterials.

RESULTS AND DISCUSSION

Synthesis and Characterization of Zr-*fum* NPs. Zr-*fum* NPs were prepared according to Zahn et al.[67] under formic acid mediated hydrothermal conditions. The resulting NPs were dispersed in ethanol and characterized by dynamic light scattering (DLS), revealing a uniform size distribution of the Zr-*fum* NPs (72 ± 16 nm; Supporting Information (SI), Figure S1). A spherical shape of the particles and a homogeneous size distribution was confirmed by scanning electron microscopy (SEM; SI, Figure S2). Evaluation of the particle size by SEM showed slightly smaller diameters (46 ± 8 nm), which is in agreement with literature.[45] For zeta-potential measurements, HEPES buffered glucose (HBG) was chosen as a medium representing physiological pH and tonicity. Therein, bare Zr-*fum* NPs exhibited a negative potential of approximately −27 mV. Finally, the powder X-ray diffraction (PXRD) pattern of the Zr-*fum* MOF NPs featured well-defined reflections across the entire measurement range, indicating the formation of the expected framework (SI, Figure S3).

Polymer Binding. For assessment of polymer binding to bare Zr-*fum* NPs, a coating procedure was adopted from Bellido et al.[40] A Zr-*fum* NP suspension was added dropwise to an aqueous polymer solution under vigorous stirring. The resulting NP suspension was treated by sonication and stirred for three minutes. The obtained NPs were washed with bidistilled H_2O and stored as an aqueous suspension.

DOI: 10.1021/acsnano.8b06287
ACS Nano 2019, 13, 3884−3895

Table 2. Zeta-Potential Values of Different Coated Zr-*fum* NPs in HBG

MOF	Zr-*fum*@PAA	Zr-*fum*@PGlu	Zr-*fum*	Zr-*fum*@PAMAM	Zr-*fum*@BPEI
Zeta-pot, in mV	−30.2	−29.1	−25.0	−16.1	−11.6

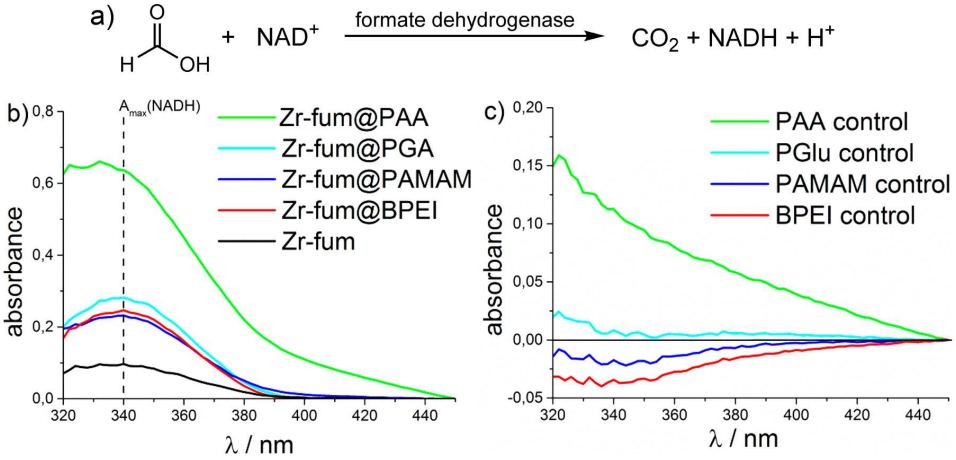

Figure 3. Spectroscopic investigation on the nature of binding by formic acid determination in the supernatant. (a) Reaction of the formic acid assay for its quantitative detection by UV−vis (NADH at λ = 340 nm). (b) UV−vis spectroscopic determination of NADH from the supernatant after coating reactions. Absorption at 340 nm was used for the determination of the formic acid release (SI, Table S1). (c) Control experiments of pure polymer solutions (c = 50 μg/mL), showing a steady increase for the PAA control which indicates assay interference (same assay with a 70:30 ethanol/water mixture was used for background subtraction).

All Zr-*fum* MOF NPs with various polymer coatings (Zr-*fum*@polymer NPs) were characterized by PXRD to prove their retained crystallinity after the coating procedure (SI, Figure S4). SEM images of the different Zr-*fum*@polymer NPs showed no change in morphology (SI, Figure S5). Raman spectroscopy of the different Zr-*fum*@polymer NPs was performed to confirm successful coating by detection of additional vibrational bonds introduced by the respective polymer (Figure 2a; SI, Figure S6, S7).

An increase of the CH_2 vibrational bands (asym stretch 2934 cm^{-1}, sym stretch 2975 cm^{-1}) of the aliphatic backbone, which is included in all polymers, indicated a successful attachment for cationic ((+)-polymer, BPEI and PAMAM) as well as anionic polymers ((−)-polymer, PGlu and PAA). Neutral polymers (PEG and Tween) showed a significantly lower intensity of the characteristic vibrations. The vibration triplet (approximately at 2875, 2925, and 2975 cm^{-1}), which is slightly visible for Zr-*fum* as well as for Zr-*fum*@PEG and Zr-*fum*@Tween NPs is attributed to ethanol and is covered by the more intense signals of polymer backbone modes in the case of successful coating (SI, Figure S7). Thus, both neutral polymers were considered unable to efficiently coat Zr-*fum* NPs and were excluded from further studies on the biophysical properties. Infrared (IR) spectroscopy was performed in addition to Raman spectroscopy but produced no further information as all significant organic vibrational bands from the polymer coating overlapped with the organic linker vibrational bands of fumaric acid (SI, Figure S8).

For DLS investigations, HEPES buffered glucose (HBG) solution was chosen as a medium to simulate physiological osmotic conditions and pH. The observed increase in NP size further confirmed successful attachment of cationic and anionic polymers (Figure 2b). For anionic polymer coated Zr-*fum* NPs, a significant shift of the peak maximum (≈ 125 nm for uncoated Zr-*fum* NPs to 170 nm for Zr-*fum*@(−)-polymer) could be detected. Cationic polymer coated Zr-*fum* NPs showed much higher values due to agglomeration of the NPs. Furthermore, zeta-potential measurements showed a significant shift of the Zr-*fum*@polymer NPs' surface charge depending on the nature of the polymer. While anionic polymers revealed a more negative zeta-potential compared to nonfunctionalized Zr-*fum* (Table 2), leading to an increased electrostatic repulsion and high colloidal stability, cationic polymers showed a shift toward neutrality, which could be an explanation for the observed enhanced agglomeration.

Nitrogen sorption measurements revealed a Brunauer−Emmett−Teller (BET) surface area for uncoated particles of 736 m^2/g and, as expected, a moderate decrease of BET surface for Zr-*fum*@polymer NPs ($\Delta \approx 200-350$ m^2/g; SI, Figure S9). This can be attributed to the attached amount of nonporous organic material on the external surface as well as to partial pore blocking by polymer chains during nitrogen sorption measurements.

Nature of Binding. Thermogravimetric analysis (TGA) provided hints on the nature of the polymer binding to Zr-*fum*. As expected, (−)-polymer coated Zr-*fum* NPs showed increased weight loss after combustion in comparison to nonfunctionalized particles, indicating the increased content of organic material (SI, Figure S10). In contrast, (+)-polymer coated NPs surprisingly showed lower weight loss. This is counterintuitive because addition of polymer should increase the organic content and thereby the weight loss during combustion as observed for the polymers. A possible explanation could be that the uncoated NPs already possess a "coating" by formic acid, which can coordinatively bind to the unsaturated Zr-ions via its carboxyl groups during the

DOI: 10.1021/acsnano.8b06287
ACS Nano 2019, 13, 3884−3895

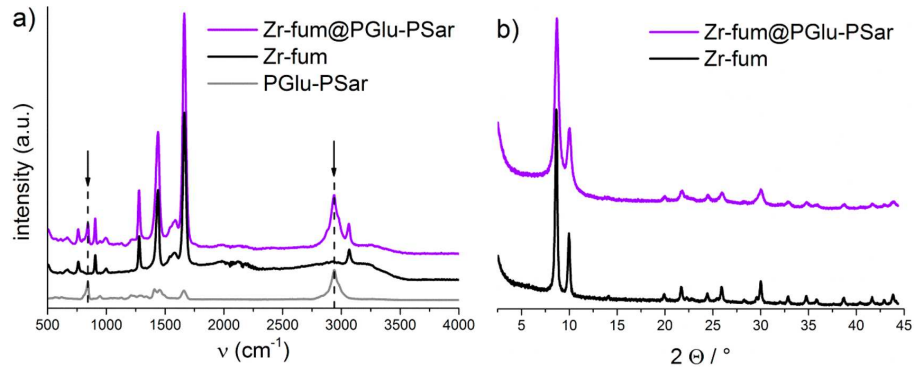

Figure 4. Raman (a) and XRD (b) spectra of Zr-*fum*@PGlu-PSar NPs compared to nonfunctionalized Zr-*fum*. Black arrows highlight the characteristic polymer vibrational bands.

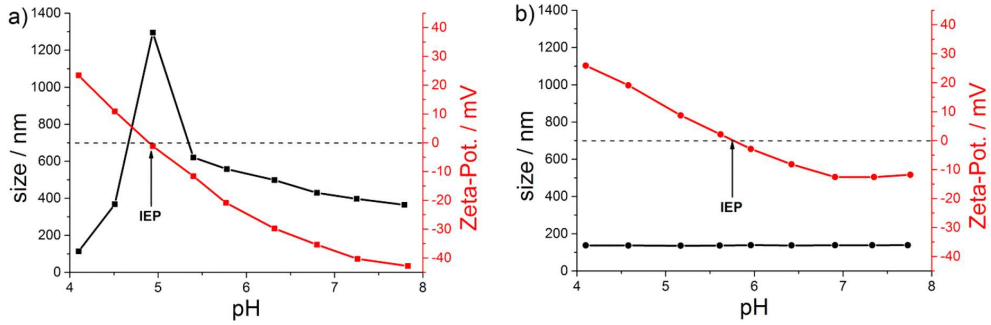

Figure 5. Nanoparticle size (Z-average, black) and zeta-potential measurements (red) of (a) Zr-*fum* NPs and (b) Zr-*fum*@PGlu-PSar NPs. Bare Zr-*fum* NPs show strong agglomeration at pH 5 (≈ IEP), while Zr-*fum*@PGlu-PSar NPs remain colloidal over the whole pH range.

modulation synthesis. During the polymer coating, this formic acid coating is replaced by polymer as the polymers contain coordinative groups as well (carboxylates + amines) and should therefore be able to replace formic acid by an entropically favored linker exchange reaction.[68] Depending on the molecular mass and the attached amount of polymer, the organic content of the MOF@polymer nanocomposites can increase or decrease. A detailed look at BET surface areas suggests a higher degree of attachment for PGlu and PAA as their surface areas decreased more significantly (736−413 m^2/g and 400 m^2/g, respectively) than observed for BPEI and PAMAM (736−472 m^2/g and 543 m^2/g, respectively). This is in agreement with the higher organic content for Zr-*fum*@(−)-polymer obtained from TGA measurements. The lower weight loss of Zr-*fum*@(+)-polymer NPs may be the result of formic acid depletion but comparably low degree of polymer attachment (SI, Figures S9−S11).

The postulated exchange mechanism was further confirmed by quantification of formic acid release by the polymer coating. An assay kit (K-FORM, Megazyme) was used to specifically quantify formic acid by conversion to carbon dioxide with formate dehydrogenase (Figure 3a). The molar amount of generated NADH (abs. 340 nm) is equal to the amount of formic acid present in the supernatant of the particle solution. As a control experiment, the reaction was performed without adding polymer to the solution and the supernatant was tested for free residual formic acid left in the MOF pores after synthesis and workup. Here, only a small amount of formic acid was detectable (Figure 3, left, "Zr-*fum*"). After coating with (−)- and (+)-polymers, a significantly higher amount of formic acid was present in the supernatant compared to the control experiment, which supports the assumption of an exchange between formic acid and polymer on the external MOF NP surface (Figure 3b). Additionally, pure polymer solutions (50 μg/mL ≡ 1 of $c_{max.}$) were tested to identify assay interference and false-positive effects. This control experiment showed a significant absorption only for the PAA control (Figure 3c), which explains the steady increase and higher absorption of the Zr-*fum*@PAA supernatant.

Therefore, Zr-*fum*@PAA was excluded from the calculations of the exchanged amount of formic acid from experimental data. The calculations resulted in approximately 10 μg formic acid per 1 mg provided Zr-*fum* NPs (≈ 1 wt %; SI, Table S1). This value is in excellent agreement with a theoretical estimate of a maximum amount of formic acid present on the external surface of Zr-*fum* NPs (≈ 0.8 wt %; SI, "*Theoretical Estimate*").

Considering all the above results, we propose the nature of interaction to be coordinative binding accompanied by an exchange of formic acid by the polymers' coordinative groups, similar to functionalization mechanisms published in the literature.[69,70]

Nanoparticle Functionalization. On the basis of the above results, the effective binding of PGlu was used as a molecular adapter for surface attachment and functionalization

DOI: 10.1021/acsnano.8b06287
ACS Nano 2019, 13, 3884−3895

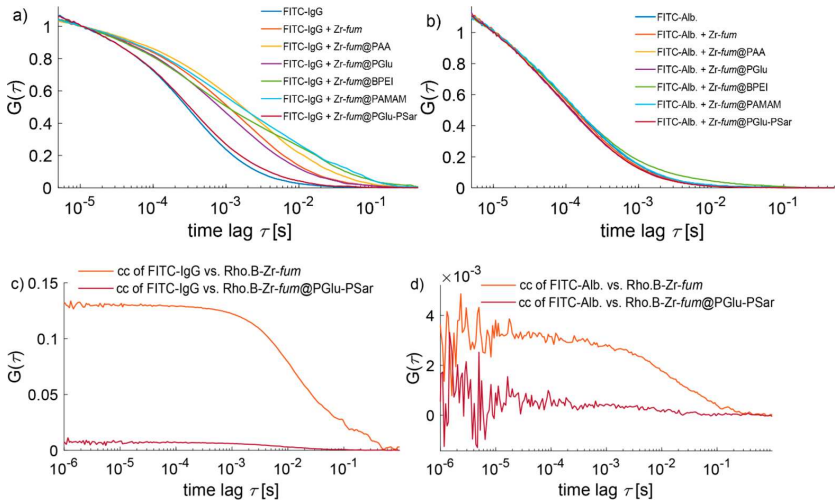

Figure 6. Interactions between protein and Zr-*fum*@polymer NPs monitored using FCS/FCCS. (a,b) The FCS measurements of FITC-IgG and FITC-Alb, respectively, in the absence (blue trace) and presence of various Zr-*fum*@polymer NPs. (c) The FCCS measurements shown by the cross-correlation of FITC-IgG with Rho.B−Zr-*fum* and Rho.B−Zr-*fum*@PGlu-PSar. (d) The FCCS measurements shown by the cross-correlation of FITC-Alb Rho.B−Zr-*fum* and Rho.B−Zr-*fum*@PGlu-PSar.

of MOF NPs with other moieties. To this end, the block copolymer PGlu-PSar[60] (Table 1) was attached to the Zr-*fum* NPs. The polymer consists of polysarcosine (PSar), a biopolymer based on the natural subunit sarcosine (*N*-methyl glycine), which is known to provide an effective shielding,[62,64,65] and polyglutamic acid (PGlu), which is working as a biocompatible binding domain. Preparation of Zr-*fum*@PGlu-PSar NPs was performed according to the procedure presented above.

Raman spectroscopy provided information about a significant attachment of the polymer onto the Zr-*fum* NPs (Figure 4a) and XRD measurements confirmed the retained crystallinity of the Zr-*fum* core (Figure 4b) as expected from previous polymer coatings. Furthermore, no change in morphology could be detected by SEM because the polymer coating contributes only a minor scattering contrast (SI, Figure S12).

Nanoparticle Agglomeration. Simultaneous measurements of the zeta-potential and size at different biologically relevant pH values (pH = 4 to pH = 8) revealed characteristic agglomeration behaviors of the various NP dispersions in aqueous solution. The pH range was chosen in view of prospective biomedical applications of the Zr-*fum*@polymer NPs (pH 7.4 within the bloodstream to approximately pH 4.5 in cell lysosomes).[71] As expected, the measurements revealed a shift of the isoelectric point (IEP, determined by interpolation of zeta-potential values) of the different formulations depending on the ionic nature (+ or −) of the polymer. The NP dispersions of bare Zr-*fum* as well as of (−)- and (+)-polymer coated Zr-*fum* tended to agglomerate at pH values close to the IEP (SI, Figure S13) where electrostatic repulsion is minimal.[72] For illustration, the titration curve of bare Zr-*fum* is shown in Figure 5a. In contrast, PGlu-PSar coated NPs showed a completely different behavior. Although the zeta-potential drops from approximately +25 mV at pH 4 to −12 mV at pH 8, resulting in an isoelectric point at pH 5.8, the NPs remain nanodispersed with a constant size of approximately 130 nm over the entire pH range (Figure 5b). This impressive colloidal stability demonstrates the high potential and utility of the polymer for MOF NP stabilization.

Protein Interactions. In view of the encouraging previous results, protein binding to Zr-*fum* NPs was investigated using fluorescence correlation spectroscopy (FCS).[73,74] FCS records the intensity fluctuations of the fluorescence signal caused, for example, by individual fluorescent particles diffusing through a small (≈fL) observation volume. From the temporal autocorrelation function (ACF) of this signal, the rate of diffusion and, consequently, the interaction between different particles can be deduced.

In the assay used here, fluorescently labeled proteins were incubated with the differently coated Zr-*fum* MOF NPs. Upon binding to the significantly larger NPs, the proteins' diffusion is greatly decreased, evidenced by a slower decay of the correlation function. Therefore, by observing the decay of the correlation function, interactions between proteins and the NPs with different coatings can be investigated. Additionally, we performed fluorescence cross-correlation spectroscopy (FCCS), a dual-color extension of standard FCS.[75] Here, both the proteins and the Zr-*fum* MOF particles were labeled with spectrally different fluorophores and the temporal cross-correlation functions (CCFs) between the detection channels for the two fluorescent labels were analyzed. In FCCS, a cross-correlation signal is only present in the case of concerted motion of the different labels, *i.e.*, if the proteins bind to the NPs. Thus, not only the temporal decay of the CCF is changed upon binding, but also the amplitude, making it much more sensitive as compared to standard FCS.[75,76]

The investigated proteins of interest were albumin (Alb) and immunoglobulin G (IgG). Albumin was chosen as it presents the protein most prominent in the human blood plasma (up to 60%), and IgG as the most abundant type of antibody, which mediates an immune response by activating the complement system of the human body thus leading to rapid particle clearance from the bloodstream.[77,78]

DOI: 10.1021/acsnano.8b06287
ACS Nano 2019, 13, 3884−3895

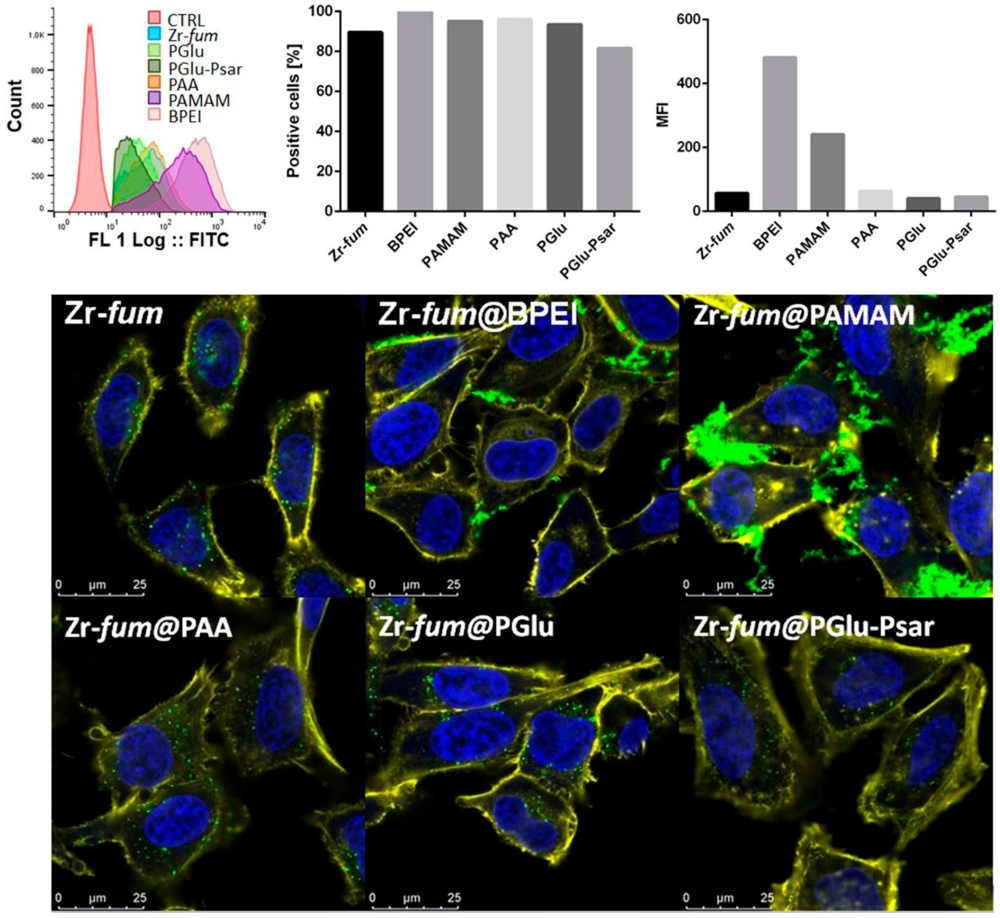

Figure 7. Cellular association, aggregation and uptake profile of Zr-*fum*@polymer NPs as determined by flow cytometry and confocal laser scanning microscopy (CLSM). Zr-*fum* NPs were labeled with calcein as described in the SI. All differently functionalized NPs were incubated on HeLa cells for 30 min at a final concentration of 50 μg/mL. (a) Single parameter histogram of cellular fluorescence, (b) percentage of calcein-positive cells, (c) median fluorescence intensities of calcein-positive cell subpopulation, and (d) live-cell images are shown. Nuclei were stained with DAPI (blue channel), F-actin was stained with phalloidin−rhodamine (yellow channel), and calcein-fluorescence is shown in green. PAMAM and BPEI-coated Zr-*fum* NPs exhibited the highest fluorescence intensity of cells indicating strongest cellular association. Coating with negatively charged polymers PGlu, PGlu-PSar, and PAA resulted in cellular association in a similar range as uncoated Zr-*fum*. BPEI-coated and PAMAM-coated Zr-*fum* NPs showed strong extracellular aggregation on the cell surface and low intracellular localization. Uncoated, PAA-coated, PGlu-coated, and PGlu-PSar-coated Zr-*fum* NPs all showed dispersed NPs in suitable size ranges and were internalized into cells. For easier differentiation, the fluorescence channels are shown in separate images in the SI (Figure S19).

Both FCS and FCCS indicate significant binding of fluorescein isothiocyanate (FITC)-labeled immunoglobulin G (FITC-IgG) to uncoated Zr-*fum* MOF NPs as well as to the negatively charged Zr-*fum*@PAA and Zr-*fum*@PGlu NPs and the positively charged Zr-*fum*@BPEI and Zr-*fum*@PAMAM NPs. As shown in Figure 6a, a component with a significantly slower ACF decay is observed. The diffusion of free FITC-IgG (~26 $\mu m^2/s$, obtained from fitting the ACF) decreases to ~3 $\mu m^2/s$ upon binding to the different Zr-*fum* MOF NPs, indicating that FITC-IgG binds to the different Zr-*fum* NPs (SI, Table S2). An apparent slower diffusion was observed in the presence of the Zr-*fum*@BPEI and Zr-*fum*@PAMAM NPs (~0.8 $\mu m^2/s$), which is attributed to the aggregation of these positively charged NPs (SI, Table S2). Such binding events of FITC-IgG to Zr-*fum* MOF particles are also observable in the fluorescence intensity traces as high intensity peaks (SI, Figure S14, left). In addition, the amplitude of the CCF further supports the binding of the FITC-IgG to the RhodamineB-labeled Zr-*fum* (Rh.B−Zr-*fum*), (Figure 6c) and the slow diffusion upon binding is visible in the ACFs of the labeled IgG and NPs (SI, Figure S15). FCS measurements with FITC-labeled albumin (FITC-Alb), on the other hand, indicate no binding of the proteins to the NPs regardless of coating. The temporal ACF is fully described by the ACF from the sample of FITC-Alb in the absence of NPs (Figure 6b). The fluorescence intensity traces of FITC-Alb with the different

DOI: 10.1021/acsnano.8b06287
ACS Nano 2019, 13, 3884−3895

Zr-*fum* MOF particles also did not show peaks (with the exception of one aggregate around ~700 s for Zr-*fum*@BPEI (SI, Figure S14, right)). Similarly, no slower diffusion is visible in the ACFs of the labeled Alb and NPs once compared to the labeled IgG and NPs (SI, Figures S15, S16). The ratio of the Zr-*fum* MOF bound protein to unbound and freely diffusing labeled protein was found to be much lower for Alb in comparison to IgG (SI, Tables S2, S3).

In contrast, we observed strongly decreased protein binding to polysarcosin coated Zr-*fum* NPs (Zr-*fum*@PGlu-PSar). For FITC-IgG, the ACF decay in the presence and absence of Zr-*fum*@PGlu-PSar showed no notable change (Figure 6a). The efficient shielding of the Rh.B−Zr-fum@PGlu-PSar NP is further supported from FCCS experiments where the CCF has a significantly lower amplitude compared to measurements with Rh.B−Zr-*fum* (Figure 6c). Consistent with the high shielding capacity of the PGlu-PSar coating, the amplitude of the CCF for FITC-Alb NPs measurements, although low in general, is even lower for the Zr-*fum*@PGlu-PSar (Figure 6d).

To test whether the binding of the FITC-IgG to a certain Zr-*fum* coated NP drastically changes its photophysical properties and thus influences FCS measurements, we measured the lifetime decay of FITC-IgG alone and in the presence of the variously coated NPs (SI, Figure S17). The lifetime of FITC-IgG in the absence and presence of NPs showed a similar decay, indicating no significant photophysical influence of the NPs on the labeled protein. In summary, FCS and FCCS experiments show that the coating is a determining factor for the interaction of Zr-*fum* NPs with different proteins and can be tuned based on the NP surface coating.

Because the interaction with proteins also affects the stability in biological environment, additional experiments were carried out using fluorescently labeled Zr-*fum*@Cy5.5-PGlu-PSar in fetal bovine serum as well as in mice *in vivo*. It could be observed that the majority of Cy5.5-PGlu-PSar stays associated with Zr-*fum* NP after incubation at 37 °C in 10% fetal bovine serum for up to 24 h (SI, Figure S20, S21). After intravenous injection into mice, free Cy5.5-PGlu-PSar seems to be rapidly excreted by renal clearance and no fluorescence signal is observable in any of the investigated organs (heart, kidneys, liver, lung, and spleen) after 24 h *ex vivo* (SI, Figure S22). In contrast, fluorescence intensity in the liver can still be detected after 24 h in mice injected with Zr-fum@Cy5.5-PGlu-PSar. This additionally confirms the stability of Zr-*fum* coating with PGlu-PSar even in the *in vivo* situation.

Cell Interactions. After evaluating the bio- and physicochemical characteristics of Zr-*fum*@polymer NPs in cell-free models, imaging measurements were carried out to investigate interactions between the NPs and cancer cells. First, MTT cell viability assays were performed to identify effects of the Zr-*fum* and Zr-*fum*@polymer NPs on cellular metabolism and toxic interactions. All formulations were well tolerated and showed no obvious toxicity up to concentrations of 400 μg/mL after 24 h of incubations (SI, Figure S18). Next, the cellular association, aggregation and cell uptake profile of the differently coated formulations was investigated by flow cytometry and confocal laser scanning microscopy (CLSM) after 30 min of incubation on HeLa cells (Figure 7). Flow cytometry data indicated a high degree of interaction between Zr-*fum*@PAMAM as well as Zr-*fum*@BPEI and HeLa cells, a finding most likely attributable to electrostatic adhesion to the cell membrane. In direct comparison, the percentage of fluorescence-positive cells was in the same range in the case of all formulations (Figure 7b), but median fluorescence intensity was strongly increased in the case of (+)-polymer coated Zr-*fum* NPs (Figure 7c). CLSM of HeLa cells fixed after 30 min exposure to Zr-*fum* and Zr-*fum*@polymer NPs provided information about the exact spatial localization of the NPs within the cells. The results from the images were in good agreement with the previously observed high cellular association of (+)-polymer coated Zr-*fum* NPs. However, only large aggregates on the cell surface and no intracellular particles were observed. In contrast, the other formulations did not show extracellular aggregation or detectable membrane binding, which indicates the NPs' colloidal stability also in a complex cell culture environment (Figure 7d). These findings confirm the expected strong interaction of (+)-polymer coated Zr-*fum* NPs with cellular membranes but also point to unfavorable aggregation under physiological conditions in contrast do (−)-polymer coated NPs.

CONCLUSIONS

In this paper, we report a straightforward functionalization approach for MOF NPs based on coordinative binding. Different polymers could be attached onto the external surface by an entropically preferred exchange of the modulator (formic acid) by the coordinating groups of the polymers. This process can be described as self-assembly modulator replacement. The released formic acid could be detected in the supernatant after the coating process, which supports the proposed mechanism. Exploiting this efficient modification approach, different MOF@polymer NP formulations were prepared, fully characterized, and tested for their behavior and interactions in a biologically relevant environment. The investigations revealed greatly improved colloidal stability of Zr-*fum* NPs mediated by coating them with the block copolymer PGlu-PSar. These Zr-*fum*@PGlu-PSar NPs retained their monodispersity independent of pH in a broad range of environments such as aqueous solutions, protein containing buffer solution, and cellular medium. Those findings make it a promising candidate for an intravenously injected nanocarrier system with stability in the human bloodstream which is mandatory for effective passive targeting on tumor tissue by the enhanced permeability and retention (EPR) effect. By applying different coatings, the Zr-*fum* NPs can be tuned toward the desired stability and activity, which has been shown for Zr-*fum*@PGlu-PSar NPs as they were inert to bloodstream proteins like albumin and IgG.

Our results suggest that MOF NPs can be easily functionalized with different kinds of polymers via coordinative binding. The coating with functional polymers is an efficient approach to "program" the MOF NP surface to (i) exhibit increased colloidal stability over physiological pH ranges, (ii) show increased colloidal stability in high ionic-strength buffers, (iii) control the protein binding in a biological environment, (iv) resist being scavenged by macrophages, (v) exhibit low nonspecific binding to healthy tissues, (vi) exhibit long circulation times, and (vii) influence biodistribution in a favorable way. Because of the easy integration of different functionalities (*e.g.*, shielding, targeting, bioresponsive domains, *etc.*) into the polymers and their straightforward attachment to MOF NP surfaces, we predict that this functionalization concept will develop into a general functionalization strategy for MOF NPs.

DOI: 10.1021/acsnano.8b06287
ACS Nano 2019, 13, 3884−3895

METHODS

Synthesis of Zr-*fum* NPs. $ZrCl_4$ (120.5 mg, 0.517 mmol) and fumaric acid (180.0 mg, 1.550 mmol) were dissolved in bidistilled H_2O (10 mL). Formic acid (0.975 mL, 1.190 g, 25.85 mmol) was added, and the reaction mixture was sealed in a 25 mL glass autoclave (Schott, Duran). The mixture was heated to 120 °C for 24 h and was allowed to cool down to room temperature afterward. Further, the resulting NPs were transferred in 15 mL Falcon tubes and centrifuged (7187 rcf/10 min). After redispersion in bidistilled H_2O (6 mL), the Zr-*fum* NPs were transferred to Eppendorf tubes and centrifuged (16900 rcf/10 min). The washing steps (dispersion + centrifugation) were repeated twice with EtOH, and Zr-*fum* NPs were stored in an ethanolic stock solution.

Dye Labeling of Zr-*fum* NPs. Zr-*fum* NPs were dispersed in an aqueous dye solution (0.25 mM calcein or rhodamine B, respectively) resulting in a 5 mg/mL dispersion. The NPs were shaken for 15 min (600 rpm) at room temperature, centrifuged, and washed with bidistilled H_2O, twice with HBG, and stored in an ethanolic stock solution.

Polymer Coating of Zr-*fum* NPs. Polymer solution (10 mg/mL; 20 or 400 μL, respectively) was provided in bidistilled H_2O (280 μL or 5.6 mL, respectively). Zr-*fum* NPs (1,43 mg/mL in EtOH; 0.7 or 14 mL, respectively) were added dropwise within 2 min, and the dispersion was allowed to stir for 3 min. Ultrasound was applied for 1 min, and the solution was again stirred for 3 min. The resulting particles were centrifuged (16900 rcf/10 min) and washed twice with bidistilled H_2O. Zr-*fum*@polymer NPs were stored in an aqueous stock solution.

Fluorescence (Cross-) Correlation Spectroscopy (FCS/FCCS). The fluorescence correlation spectroscopy (FCS) and dual-color fluorescence cross-correlation spectroscopy (FCCS) measurements were performed on a home-built microscope as described elsewhere.[79] A pulsed laser diode at 470 nm wavelength (LDH-P-C-470) was used for excitation of the FITC-dye labeled IgG/albumin, and a pulsed erbium-doped fiber laser (FFS.SYS-CONT-COMP-TSHG, Toptica Photonics, Gräfelfing, Germany) tuned to 562 nm was used for excitation of RhodamineB-labeled Zr-*fum* and Zr-*fum*@PGlu-PSar. A laser power of ~4.5 and 17.5 μW was used for the 470 and 562 nm lasers, respectively, measured at the sample using a slide power meter (S170C-Thorlabs). The measurements were performed using a 60× water immersion objective, NA 1.27 (Plan Apo 60 × WI, Nikon). The raw optical data and subsequent correlation analysis were performed with our PIE analysis with Matlab (PAM) software. PAM is a stand-alone program (MATLAB; The MathWorks GmbH) for integrated and robust analysis of fluorescence ensemble, single-molecule, and imaging data.[80] The software is available as a source code, requiring MATLAB to run, or as precompiled standalone distributions for Windows or MacOS at http://www.cup.uni-muenchen.de/pc/lamb/software/pam.html. The FCCS data were acquired by recording the detected photons of two single-photon avalanche photodiodes (SPADs) on two separate time correlated single-photon counting cards (TCSPC, SPC-150 Becker and Hickl) for a period of 15 min. Similarly, the FCS data were acquired by recording the photons with a single APD on a TCSPC card for a period of 15 min. Measurements were conducted in HEPES buffered glucose (HBG) for simulating physiological body conditions. For details, fitting, and calculations, see Supporting Information.

Confocal Laser Scanning Microscopy (CLSM). On the day prior to the measurements, HeLa cells were seeded in 8-well chamber slides (Thermo Fisher Scientific, 20000 cells in 300 μL medium per well). Cells were incubated at 37 °C and 5% CO_2. On the next day, the medium was aspirated and 300 μL of Zr-*fum*@polymer (50 μg/mL in medium) was added to each respective well. After 30 min of incubation (37 °C, 5% CO_2), each well was washed once with 400 μL of PBS and cells were subsequently fixated with 4% paraformaldehyde in PBS (30 min incubation at RT). After fixation, each well was once again washed with 400 μL of PBS, the cell nuclei were stained with DAPI (2 μg/mL) and F-actin was labeled with phalloidin−rhodamine (1 μg/mL). After 30 min of incubation (light protected at RT), the staining mixture was aspirated and replaced with 300 μL of PBS per well. Images were recorded utilizing a Leica-TCS-SP8 confocal laser scanning microscope equipped with an HC PL APO 63× 1.4 objective. DAPI emission was recorded at 460 nm, calcein at 530 nm, and rhodamine at 580 nm. Afterward, all images were processed by LAS X software from Leica.

Flow Cytometry. On the day prior to the measurements, HeLa cells were seeded in a 24-well plate (60000 cells in 1 mL medium per well). On the next day, the medium was aspirated and replaced with 475 μL of fresh medium. Then 25 μL of 1 mg/mL Zr-*fum*@polymer solution was added to the wells (2 wells per polymer). After 30 min of incubation, the medium was aspirated and cells were washed with 1 mL of PBS. Cells were then trypsinized with 200 μL of trypsin/EDTA (5 min, 37 °C), 400 μL of medium was added to each well, and the 2 wells per polymer were unified. Cells were centrifuged for 5 min at 1500 rpm and room temperature. The supernatant was removed, cells resuspended in 700 μL of FACS-buffer (10% FBS in PBS), and stored on ice. Shortly before the analysis, 2 μL of 1 mg/mL DAPI was added to each vial. Cells were appropriately gated by forward/sideward scatter and by pulse width for exclusion of cell aggregates. DAPI was used to discriminate between viable and dead cells. Only isolated viable cells were evaluated. Data were recorded by Cyan ADP flow cytometer (Dako, Hamburg, Germany) using Summit acquisition software (Summit, Jamesville, NY). Ten thousand gated cells per sample were collected. Analysis was done by FlowJo 7.6.5 flow cytometric analysis software. The threshold level for cellular association of calcein was set based on the fluorescence background of HBG treated negative control cells.

ASSOCIATED CONTENT

Supporting Information

The Supporting Information is available free of charge on the ACS Publications website at DOI: 10.1021/acsnano.8b06287.

Additional materials and methods, characterization of MOF nanoparticles, supplementary figures and tables (PDF)

AUTHOR INFORMATION

Corresponding Authors

*E-mail: stefan.wuttke@cup.uni-muenchen.de.
*E-mail: ulrich.laechelt@cup.uni-muenchen.de.

ORCID

Ernst Wagner: 0000-0001-8413-0934
Matthias Barz: 0000-0002-1749-9034
Don C. Lamb: 0000-0002-0232-1903
Ulrich Lächelt: 0000-0002-4996-7592
Stefan Wuttke: 0000-0002-6344-5782

Notes

The authors declare no competing financial interest.

ACKNOWLEDGMENTS

We are grateful for financial support from the Deutsche Forschungsgemeinschaft (DFG) through SFB 1032 (Projects B03 and B04), SFB 1066/1-2 and B5, and DFG-project WU 622/4-1, the Excellence Cluster Nanosystems Initiative Munich (NIM), and the Center for NanoScience Munich (CeNS). Furthermore, we thank Steffen Schmidt for assistance with the SEM measurements.

REFERENCES

(1) Furukawa, H.; Cordova, K. E.; O'Keeffe, M.; Yaghi, O. M. The Chemistry and Applications of Metal-Organic Frameworks. *Science* **2013**, *341*, 1230444.

DOI: 10.1021/acsnano.8b06287
ACS Nano 2019, 13, 3884−3895

(2) Moghadam, P. Z.; Li, A.; Wiggin, S. B.; Tao, A.; Maloney, A. G. P.; Wood, P. A.; Ward, S. C.; Fairen-Jimenez, D. Development of a Cambridge Structural Database Subset: A Collection of Metal−Organic Frameworks for Past, Present, and Future. *Chem. Mater.* **2017**, *29*, 2618−2625.
(3) Furukawa, H.; Müller, U.; Yaghi, O. M. Heterogeneity within Order" in Metal−Organic Frameworks. *Angew. Chem., Int. Ed.* **2015**, *54*, 3417−3430.
(4) Lu, W.; Wei, Z.; Gu, Z.-Y.; Liu, T.-F.; Park, J.; Park, J.; Tian, J.; Zhang, M.; Zhang, Q.; Gentle, T., Iii; Bosch, M.; Zhou, H.-C. Tuning the Structure and Function of Metal−Organic Frameworks *via* Linker Design. *Chem. Soc. Rev.* **2014**, *43*, 5561−5593.
(5) Rubio-Martinez, M.; Avci-Camur, C.; Thornton, A. W.; Imaz, I.; Maspoch, D.; Hill, M. R. New Synthetic Routes towards MOF Production at Scale. *Chem. Soc. Rev.* **2017**, *46*, 3453−3480.
(6) Rogge, S. M. J.; Bavykina, A.; Hajek, J.; Garcia, H.; Olivos-Suarez, A. I.; Sepulveda-Escribano, A.; Vimont, A.; Clet, G.; Bazin, P.; Kapteijn, F.; Daturi, M.; Ramos-Fernandez, E. V.; Llabres i Xamena, F. X.; Van Speybroeck, V.; Gascon, J. Metal−Organic and Covalent Organic Frameworks as Single-Site Catalysts. *Chem. Soc. Rev.* **2017**, *46*, 3134−3184.
(7) Zhu, L.; Liu, X.-Q.; Jiang, H.-L.; Sun, L.-B. Metal−Organic Frameworks for Heterogeneous Basic Catalysis. *Chem. Rev.* **2017**, *117*, 8129−8176.
(8) Lee, J.; Farha, O. K.; Roberts, J.; Scheidt, K. A.; Nguyen, S. T.; Hupp, J. T. Metal−Organic Framework Materials as Catalysts. *Chem. Soc. Rev.* **2009**, *38*, 1450−1459.
(9) Corma, A.; García, H.; Llabrés i Xamena, F. X. Engineering Metal Organic Frameworks for Heterogeneous Catalysis. *Chem. Rev.* **2010**, *110*, 4606−4655.
(10) He, Y.; Zhou, W.; Qian, G.; Chen, B. Methane Storage in Metal−Organic Frameworks. *Chem. Soc. Rev.* **2014**, *43*, 5657−5678.
(11) Van de Voorde, B.; Bueken, B.; Denayer, J.; De Vos, D. Adsorptive Separation on Metal−Organic Frameworks in the Liquid Phase. *Chem. Soc. Rev.* **2014**, *43*, 5766−5788.
(12) Adil, K.; Belmabkhout, Y.; Pillai, R. S.; Cadiau, A.; Bhatt, P. M.; Assen, A. H.; Maurin, G.; Eddaoudi, M. Gas/Vapour Separation Using Ultra-Microporous Metal−Organic Frameworks: Insights into the Structure/Separation Relationship. *Chem. Soc. Rev.* **2017**, *46*, 3402−3430.
(13) Falcaro, P.; Ricco, R.; Doherty, C. M.; Liang, K.; Hill, A. J.; Styles, M. J. MOF Positioning Technology and Device Fabrication. *Chem. Soc. Rev.* **2014**, *43*, 5513−5560.
(14) Stassen, I.; Burtch, N.; Talin, A.; Falcaro, P.; Allendorf, M.; Ameloot, R. An Updated Roadmap for the Integration of Metal-Organic Frameworks with Electronic Devices and Chemical Sensors. *Chem. Soc. Rev.* **2017**, *46*, 3185−3241.
(15) Kreno, L. E.; Leong, K.; Farha, O. K.; Allendorf, M.; Van Duyne, R. P.; Hupp, J. T. Metal−Organic Framework Materials as Chemical Sensors. *Chem. Rev.* **2012**, *112*, 1105−1125.
(16) Horcajada, P.; Gref, R.; Baati, T.; Allan, P. K.; Maurin, G.; Couvreur, P.; Férey, G.; Morris, R. E.; Serre, C. Metal−Organic Frameworks in Biomedicine. *Chem. Rev.* **2012**, *112*, 1232−1268.
(17) He, C.; Liu, D.; Lin, W. Nanomedicine Applications of Hybrid Nanomaterials Built from Metal−Ligand Coordination Bonds: Nanoscale Metal−Organic Frameworks and Nanoscale Coordination Polymers. *Chem. Rev.* **2015**, *115*, 11079−11108.
(18) Wuttke, S.; Lismont, M.; Escudero, A.; Rungtaweevoranit, B.; Parak, W. J. Positioning Metal-Organic Framework Nanoparticles within the Context of Drug Delivery − A Comparison with Mesoporous Silica Nanoparticles and Dendrimers. *Biomaterials* **2017**, *123*, 172−183.
(19) Freund, R.; Lächelt, U.; Gruber, T.; Rühle, B.; Wuttke, S. Multifunctional Efficiency: Extending the Concept of Atom Economy to Functional Nanomaterials. *ACS Nano* **2018**, *12*, 2094−2105.
(20) Doonan, C.; Riccò, R.; Liang, K.; Bradshaw, D.; Falcaro, P. Metal-Organic Frameworks at the Biointerface: Synthetic Strategies and Applications. *Acc. Chem. Res.* **2017**, *50*, 1423−1432.
(21) Wu, M.-X.; Yang, Y.-W. Metal−Organic Framework (MOF)-Based Drug/Cargo Delivery and Cancer Therapy. *Adv. Mater.* **2017**, *29*, 1606134.
(22) Chen, W.; Wu, C. Synthesis; Functionalization, and Applications of Metal−Organic Frameworks in Biomedicine. *Dalton Trans* **2018**, *47*, 2114−2133.
(23) Horcajada, P.; Chalati, T.; Serre, C.; Gillet, B.; Sebrie, C.; Baati, T.; Eubank, J. F.; Heurtaux, D.; Clayette, P.; Kreuz, C.; Chang, J. S.; Hwang, Y. K.; Marsaud, V.; Bories, P. N.; Cynober, L.; Gil, S.; Ferey, G.; Couvreur, P.; Gref, R. Porous Metal−Organic-Framework Nanoscale Carriers as a Potential Platform for Drug Delivery and Imaging. *Nat. Mater.* **2010**, *9*, 172−178.
(24) Simon-Yarza, T.; Gimenez-Marques, M.; Mrimi, R.; Mielcarek, A.; Gref, R.; Horcajada, P.; Serre, C.; Couvreur, P. A Smart Metal-Organic Framework Nanomaterial for Lung Targeting. *Angew. Chem., Int. Ed.* **2017**, *56*, 15565−15569.
(25) Zhuang, J.; Kuo, C.-H.; Chou, L.-Y.; Liu, D.-Y.; Weerapana, E.; Tsung, C.-K. Optimized Metal−Organic-Framework Nanospheres for Drug Delivery: Evaluation of Small-Molecule Encapsulation. *ACS Nano* **2014**, *8*, 2812−2819.
(26) Illes, B.; Wuttke, S.; Engelke, H. Liposome-Coated Iron Fumarate Metal-Organic Framework Nanoparticles for Combination Therapy. *Nanomaterials* **2017**, *7*, 351.
(27) He, C.; Lu, K.; Liu, D.; Lin, W. Nanoscale Metal−Organic Frameworks for the Co-Delivery of Cisplatin and Pooled siRNAs to Enhance Therapeutic Efficacy in Drug-Resistant Ovarian Cancer Cells. *J. Am. Chem. Soc.* **2014**, *136*, 5181−5184.
(28) Röder, R.; Preiss, T.; Hirschle, P.; Steinborn, B.; Zimpel, A.; Höhn, M.; Rädler, J. O.; Bein, T.; Wagner, E.; Wuttke, S.; Lächelt, U. Multifunctional Nanoparticles by Coordinative Self-Assembly of His-Tagged Units with Metal−Organic Frameworks. *J. Am. Chem. Soc.* **2017**, *139*, 2359−2368.
(29) Alsaiari, S. K.; Patil, S.; Alyami, M.; Alamoudi, K. O.; Aleisa, F. A.; Merzaban, J. S.; Li, M.; Khashab, N. M. Endosomal Escape and Delivery of CRISPR/Cas9 Genome Editing Machinery Enabled by Nanoscale Zeolitic Imidazolate Framework. *J. Am. Chem. Soc.* **2018**, *140*, 143−146.
(30) Della Rocca, J. D.; Lin, W. Nanoscale Metal−Organic Frameworks: Magnetic Resonance Imaging Contrast Agents and Beyond. *Eur. J. Inorg. Chem.* **2010**, *2010*, 3725−3734.
(31) Carne-Sanchez, A.; Bonnet, C. S.; Imaz, I.; Lorenzo, J.; Toth, E.; Maspoch, D. Relaxometry Studies of a Highly Stable Nanoscale Metal−Organic Framework Made of Cu(II), Gd(III), and the Macrocyclic DOTP. *J. Am. Chem. Soc.* **2013**, *135*, 17711−17714.
(32) Zimpel, A.; Preiß, T.; Röder, R.; Engelke, H.; Ingrisch, M.; Peller, M.; Rädler, J. O.; Wagner, E.; Bein, T.; Lächelt, U.; Wuttke, S. Imparting Functionality to MOF Nanoparticles by External Surface Selective Covalent Attachment of Polymers. *Chem. Mater.* **2016**, *28*, 3318−3326.
(33) Peller, M.; Boll, K.; Zimpel, A.; Wuttke, S. Metal−Organic Framework Nanoparticles for Magnetic Resonance Imaging. *Inorg. Chem. Front.* **2018**, *5*, 1760−1779.
(34) Lismont, M.; Dreesen, L.; Wuttke, S. Metal-Organic Framework Nanoparticles in Photodynamic Therapy: Current Status and Perspectives. *Adv. Funct. Mater.* **2017**, *27*, 1606314.
(35) Nel, A. E.; Madler, L.; Velegol, D.; Xia, T.; Hoek, E. M.; Somasundaran, P.; Klaessig, F.; Castranova, V.; Thompson, M. Understanding Biophysicochemical Interactions at the Nano-Bio Interface. *Nat. Mater.* **2009**, *8*, 543−557.
(36) Zyuzin, M. V.; Yan, Y.; Hartmann, R.; Gause, K. T.; Nazarenus, M.; Cui, J.; Caruso, F.; Parak, W. J. Role of the Protein Corona Derived from Human Plasma in Cellular Interactions between Nanoporous Human Serum Albumin Particles and Endothelial Cells. *Bioconjugate Chem.* **2017**, *28*, 2062−2068.
(37) Ke, P. C.; Lin, S.; Parak, W. J.; Davis, T. P.; Caruso, F. A Decade of the Protein Corona. *ACS Nano* **2017**, *11*, 11773−11776.
(38) Agostoni, V.; Horcajada, P.; Noiray, M.; Malanga, M.; Aykac, A.; Jicsinszky, L.; Vargas-Berenguel, A.; Semiramoth, N.; Daoud-Mahammed, S.; Nicolas, V.; Martineau, C.; Taulelle, F.; Vigneron, J.;

DOI: 10.1021/acsnano.8b06287
ACS Nano 2019, 13, 3884−3895

Etcheberry, A.; Serre, C.; Gref, R. A "Green" Strategy to Construct Non-Covalent, Stable and Bioactive Coatings on Porous MOF Nanoparticles. *Sci. Rep.* **2015**, *5*, 7925.
(39) Hidalgo, T.; Gimenez-Marques, M.; Bellido, E.; Avila, J.; Asensio, M. C.; Salles, F.; Lozano, M. V.; Guillevic, M.; Simon-Vazquez, R.; Gonzalez-Fernandez, A.; Serre, C.; Alonso, M. J.; Horcajada, P. Chitosan-Coated Mesoporous MIL-100(Fe) Nanoparticles as Improved Bio-Compatible Oral Nanocarriers. *Sci. Rep.* **2017**, *7*, 43099.
(40) Bellido, E.; Hidalgo, T.; Lozano, M. V.; Guillevic, M.; Simón-Vázquez, R.; Santander-Ortega, M. J.; González-Fernández, Á.; Serre, C.; Alonso, M. J.; Horcajada, P. Heparin-Engineered Mesoporous Iron Metal-Organic Framework Nanoparticles: Toward Stealth Drug Nanocarriers. *Adv. Healthcare Mater.* **2015**, *4*, 1246−1257.
(41) Wuttke, S.; Braig, S.; Preiss, T.; Zimpel, A.; Sicklinger, J.; Bellomo, C.; Rädler, J. O.; Vollmar, A. M.; Bein, T. MOF Nanoparticles Coated by Lipid Bilayers and Their Uptake by Cancer Cells. *Chem. Commun.* **2015**, *51*, 15752−15755.
(42) Liu, D.; Poon, C.; Lu, K.; He, C.; Lin, W. Self-Assembled Nanoscale Coordination Polymers with Trigger Release Properties for Effective Anticancer Therapy. *Nat. Commun.* **2014**, *5*, 4182.
(43) Illes, B.; Hirschle, P.; Barnert, S.; Cauda, V.; Wuttke, S.; Engelke, H. Exosome-Coated Metal−Organic Framework Nanoparticles: An Efficient Drug Delivery Platform. *Chem. Mater.* **2017**, *29*, 8042−8046.
(44) Hintz, H.; Wuttke, S. Postsynthetic Modification of an Amino-Tagged MOF Using Peptide Coupling Reagents: A Comparative Study. *Chem. Commun.* **2014**, *50*, 11472−11475.
(45) Hirschle, P.; Preiß; Auras, F.; Pick, A.; Volkner, J.; Valdeperez, D.; Witte, G.; Parak, W. J.; Rädler, J. O.; Wuttke, S. Exploration of MOF Nanoparticle Sizes Using Various Physical Characterization Methods − Is What You Measure What You Get? *CrystEngComm* **2016**, *18*, 4359−4368.
(46) Wuttke, S.; Zimpel, A.; Bein, T.; Braig, S.; Stoiber, K.; Vollmar, A.; Müller, D.; Haastert-Talini, K.; Schaeske, J.; Stiesch, M.; Zahn, G.; Mohmeyer, A.; Behrens, P.; Eickelberg, O.; Bölükbas, D. A.; Meiners, S. Validating Metal-Organic Framework Nanoparticles for Their Nanosafety in Diverse Biomedical Applications. *Adv. Healthcare Mater.* **2017**, *6*, 1600818.
(47) Boncheva, M.; Whitesides, G. M. Making Things by Self-Assembly. *MRS Bull.* **2005**, *30*, 736−742.
(48) Xia, T.; Kovochich, M.; Liong, M.; Meng, H.; Kabehie, S.; George, S.; Zink, J. I.; Nel, A. E. Polyethyleneimine Coating Enhances the Cellular Uptake of Mesoporous Silica Nanoparticles and Allows Safe Delivery of siRNA and DNA Constructs. *ACS Nano* **2009**, *3*, 3273−3286.
(49) Shan, Y.; Luo, T.; Peng, C.; Sheng, R.; Cao, A.; Cao, X.; Shen, M.; Guo, R.; Tomas, H.; Shi, X. Gene Delivery Using Dendrimer-Entrapped Gold Nanoparticles as Nonviral Vectors. *Biomaterials* **2012**, *33*, 3025−3035.
(50) Zhang, Y.; Satterlee, A.; Huang, L. *In Vivo* Gene Delivery by Nonviral Vectors: Overcoming Hurdles? *Mol. Ther.* **2012**, *20*, 1298−1304.
(51) Lächelt, U.; Wagner, E. Nucleic Acid Therapeutics Using Polyplexes: A Journey of 50 Years (and Beyond). *Chem. Rev.* **2015**, *115*, 11043−11078.
(52) Behr, J.-P. The Proton Sponge: a Trick to Enter Cells the Viruses Did Not Exploit. *CHIMIA Int. J. Chem.* **1997**, *51*, 34−36.
(53) Akinc, A.; Thomas, M.; Klibanov, A. M.; Langer, R. Exploring Polyethylenimine-Mediated DNA Transfection and the Proton Sponge Hypothesis. *J. Gene Med.* **2005**, *7*, 657−663.
(54) Conejos-Sanchez, I.; Cardoso, I.; Oteo-Vives, M.; Romero-Sanz, E.; Paul, A.; Sauri, A. R.; Morcillo, M. A.; Saraiva, M. J.; Vicent, M. J. Polymer-Doxycycline Conjugates as Fibril Disrupters: An Tpproach Towards the Treatment of a Rare Amyloidotic Disease. *J. Controlled Release* **2015**, *198*, 80−90.
(55) Duro-Castano, A.; England, R. M.; Razola, D.; Romero, E.; Oteo-Vives, M.; Morcillo, M. A.; Vicent, M. J. Well-Defined Star-Shaped Polyglutamates with Improved Pharmacokinetic Profiles As Excellent Candidates for Biomedical Applications. *Mol. Pharmaceutics* **2015**, *12*, 3639−3649.
(56) Nino-Pariente, A.; Arminan, A.; Reinhard, S.; Scholz, C.; Kos, P.; Wagner, E.; Vicent, M. J.; Design of Poly-l-Glutamate-Based Complexes for pDNA Delivery; *Macromol. Biosci.*, **2017**, *17*, DOI: 10.1002/mabi.201700245.
(57) Consiglio, G.; Di Pietro, P.; D'Urso, L.; Forte, G.; Grasso, G.; Sgarlata, C.; Cossement, D.; Snyders, R.; Satriano, C. Surface Tailoring of Polyacrylate-Grafted Graphene Oxide for Controlled Interactions at the Biointerface. *J. Colloid Interface Sci.* **2017**, *506*, 532−542.
(58) Simoes, M. G.; Hugo, A.; Alves, P.; Perez, P. F.; Gomez-Zavaglia, A.; Simoes, P. N. Long Term Stability and Interaction with Epithelial Cells of Freeze-Dried pH-Responsive Liposomes Functionalized with Cholesterol-Poly(acrylic Acid). *Colloids Surf., B* **2018**, *164*, 50−57.
(59) Harris, J. M.; Chess, R. B. Effect of Pegylation on Pharmaceuticals. *Nat. Rev. Drug Discovery* **2003**, *2*, 214.
(60) Yoo, J.; Birke, A.; Kim, J.; Jang, Y.; Song, S. Y.; Ryu, S.; Kim, B.-S.; Kim, B.-G.; Barz, M.; Char, K. Cooperative Catechol-Functionalized Polypept(o)ide Brushes and Ag Nanoparticles for Combination of Protein Resistance and Antimicrobial Activity on Metal Oxide Surfaces. *Biomacromolecules* **2018**, *19*, 1602−1613.
(61) Sigmund, F.; Wessely, F. Untersuchungen über α-Amino-N-Carbonsäure-anhydride. *Hoppe-Seyler's Z. Physiol. Chem.* **1926**, *157*, 91.
(62) Birke, A.; Ling, J.; Barz, M. Polysarcosine-Containing Copolymers: Synthesis, Characterization, Self-Assembly, and Applications. *Prog. Polym. Sci.* **2018**, *81*, 163.
(63) Weber, B.; Birke, A.; Fischer, K.; Schmidt, M.; Barz, M. Solution Properties of Polysarcosine: From Absolute and Relative Molar Mass Determinations to Complement Activation. *Macromolecules* **2018**, *51*, 2653−2661.
(64) Huesmann, D.; Sevenich, A.; Weber, B.; Barz, M. A Head-to-head Comparison of Poly(Sarcosine) and Poly(Ethylene Glycol) in Peptidic, Amphiphilic Block Copolymers. *Polymer* **2015**, *67*, 240−248.
(65) Barz, M.; Luxenhofer, R.; Zentel, R.; Vicent, M. J. Overcoming the PEG-Addiction: Well-Defined Alternatives to PEG, From Structure−Property Relationships to Better Defined Therapeutics. *Polym. Chem.* **2011**, *2*, 1900−1918.
(66) Klein, P.; Klinker, K.; Zhang, W.; Kern, S.; Kessel, E.; Wagner, E.; Barz, M. Efficient Shielding of Polyplexes Using Heterotelechelic Polysarcosines. *Polymers* **2018**, *10*, 689.
(67) Zahn, G.; Schulze, H. A.; Lippke, J.; König, S.; Sazama, U.; Fröba, M.; Behrens, P. A water-born Zr-based porous coordination polymer: Modulated synthesis of Zr-fumarate MOF. *Microporous Mesoporous Mater.* **2015**, *203*, 186−194.
(68) Kondo, M.; Furukawa, S.; Hirai, K.; Kitagawa, S. Coordinatively Immobilized Monolayers on Porous Coordination Polymer Crystals. *Angew. Chem., Int. Ed.* **2010**, *49*, 5327−5330.
(69) Abánades Lázaro, I.; Haddad, S.; Rodrigo-Muñoz, J. M.; Orellana-Tavra, C.; del Pozo, V.; Fairen-Jimenez, D.; Forgan, R. S. Mechanistic Investigation into the Selective Anticancer Cytotoxicity and Immune System Response of Surface-Functionalized, Dichloroacetate-Loaded, UiO-66 Nanoparticles. *ACS Appl. Mater. Interfaces* **2018**, *10*, 5255−5268.
(70) Deria, P.; Mondloch, J. E.; Karagiaridi, O.; Bury, W.; Hupp, J. T.; Farha, O. K. Beyond Post-Synthesis Modification: Evolution of Metal−Organic Frameworks *via* Building Block Replacement. *Chem. Soc. Rev.* **2014**, *43*, 5896−5912.
(71) Chou, L. Y. T.; Ming, K.; Chan, W. C. W. Strategies for the Intracellular Delivery of Nanoparticles. *Chem. Soc. Rev.* **2011**, *40*, 233−245.
(72) Tay, C. Y.; Setyawati, M. I.; Xie, J.; Parak, W. J.; Leong, D. T. Back to Basics: Exploiting the Innate Physico-chemical Characteristics of Nanomaterials for Biomedical Applications. *Adv. Funct. Mater.* **2014**, *24*, 5936−5955.

DOI: 10.1021/acsnano.8b06287
ACS Nano 2019, 13, 3884−3895

(73) Magde, D.; Elson, E.; Webb, W. W. Thermodynamic Fluctuations in a Reacting System—Measurement by Fluorescence Correlation Spectroscopy. *Phys. Rev. Lett.* **1972**, *29*, 705−708.
(74) Elson, E. L.; Magde, D. Fluorescence Correlation Spectroscopy. I. Conceptual Basis and Theory. *Biopolymers* **1974**, *13*, 1−27.
(75) Schwille, P.; Meyer-Almes, F. J.; Rigler, R. Dual-Color Fluorescence Cross-Correlation Spectroscopy for Multicomponent Diffusional Analysis in Solution. *Biophys. J.* **1997**, *72*, 1878−1886.
(76) Müller, B. K.; Zaychikov, E.; Bräuchle, C.; Lamb, D. C. Pulsed Interleaved Excitation. *Biophys. J.* **2005**, *89*, 3508−3522.
(77) Diebolder, C. A.; Beurskens, F. J.; de Jong, R. N.; Koning, R. I.; Strumane, K.; Lindorfer, M. A.; Voorhorst, M.; Ugurlar, D.; Rosati, S.; Heck, A. J.; van de Winkel, J. G.; Wilson, I. A.; Koster, A. J.; Taylor, R. P.; Olmann Saphire, E.; Burton, D. R.; Schuurman, J.; Gros, P.; Parren, P. W. Complement is Activated by IgG Hexamers Assembled at the Cell Surface. *Science* **2014**, *343*, 1260−1263.
(78) Monopoli, M. P.; Aberg, C.; Salvati, A.; Dawson, K. A. Biomolecular Coronas Provide the Biological Identity of Nanosized Materials. *Nat. Nanotechnol.* **2012**, *7*, 779−786.
(79) Hendrix, J.; Baumgärtel, V.; Schrimpf, W.; Ivanchenko, S.; Digman, M. A.; Gratton, E.; Kräusslich, H.-G.; Müller, B.; Lamb, D. C. Live-Cell Observation of Cytosolic HIV-1 Assembly Onset Reveals RNA-Interacting Gag Oligomers. *J. Cell Biol.* **2015**, *210*, 629−646.
(80) Schrimpf, W.; Barth, A.; Hendrix, J.; Lamb, D. C. PAM: A Framework for Integrated Analysis of Imaging, Single-Molecule, and Ensemble Fluorescence Data. *Biophys. J.* **2018**, *114*, 1518−1528.

DOI: 10.1021/acsnano.8b06287
ACS Nano 2019, 13, 3884−3895

Supporting Information

Coordinative Binding of Polymers to Metal-Organic Framework Nanoparticles for Control of Interactions at the Biointerface

Andreas Zimpel,[a] Nader Al Danaf,[a] Benjamin Steinborn,[b] Jasmin Kuhn,[b] Miriam Höhn,[b] Tobias Bauer,[c] Patrick Hirschle,[a] Waldemar Schrimpf,[a] Hanna Engelke,[a] Ernst Wagner,[b] Matthias Barz,[c] Don C. Lamb,[a] Ulrich Lächelt,[b]* and Stefan Wuttke[a,d]*

[a] *Department of Chemistry and Center for NanoScience (CeNS), LMU Munich, Butenandtstraße 11, 81377 Munich, Germany*

[b] *Department of Pharmacy and Center for NanoScience (CeNS), LMU Munich, Butenandtstraße 11, 81377 Munich, Germany*

[c] *Institute of Organic Chemistry, Johannes Gutenberg-University Mainz Duesbergweg 10-14, 55099 Mainz*

[d] *School of Chemistry, College of Science, University of Lincoln, Brayford Way, Brayford Pool, Lincoln LN6 7TS, United Kingdom*

E-Mail corresponding authors: stefan.wuttke@cup.uni-muenchen.de and ulrich.laechelt@cup.uni-muenchen.de

Table of Contents

1. Methods and Characterization

1.1. Powder X-ray diffraction (PXRD)

X-ray diffraction was measured with the STOE transmission diffractometer system Stadi MP with Cu $K\alpha_1$ radiation ($\lambda = 1.54060$ Å) and a Ge(111) single crystal monochromator. Diffraction patterns were recorded with a DECTRIS solid-state strip detector MYTHEN 1K in an omega-2-theta scan mode using a step size of 4.71° and a counting time of 80 s per step.

1.2. Dynamic light scattering (DLS) and zeta-potential measurements

DLS and zeta-potential measurements were carried out using a Malvern Zetasizer (Nano Series, Nano-ZS). For pH dependent zeta-potential measurements, the Zetasizer was equipped with a Malvern Multi Purpose Titrator (MPT-2). 10 mL of an aqueous solution of nanoparticles (0.1 mg/mL) was lowered to pH 4 with HCl (0.1 M) and titrated stepwise (steps of 0.5) to pH 8 with NaOH (0.01 or 0.1 M, respectively).

1.3. Thermogravimetric analysis (TGA)

Thermogravimetric analysis was performed using a thermo-microbalance (Netzsch, STA 449 C Jupiter) with a heating rate of 10 °C/min up to 900°C. Approximately 10 mg of the material were heated under synthetic air conditions at flow rate of 25 mL/min.

1.4. Sorption measurements

Nitrogen sorption isotherms were measured at 77 K with a Quantachrome Autosorb-1 instrument. Approximately 10 - 20 mg of MOF NPs was degassed at 120 °C in high vacuum for at least 12 h prior to the measurement. Evaluation of the sorption data was carried out using the ASiQwin^{TM} software (Version 2.0, Quantachrome Instruments). BET surface areas were calculated employing the linearized form of the BET equation. For all samples the correlation coefficient was higher than 0.999. Adsorption isotherms were used to calculate the pore size distribution by employing quenched solid density functional theory (QSDFT, nitrogen at 77 K on carbon, slit/cylindrical pores equilibrium model).

1.5. Infrared (IR) spectroscopy

IR spectroscopy was performed on an FT-IR spectrometer (Thermo Scientific, NICOLET 6700) in transmission mode. Transparent potassium bromide pellets (150 mg) served as a matrix for 1 mg of MOF NPs.

1.6. UV-Vis spectroscopy

UV-Vis spectra were recorded using a Perkin-Elmer Lambda 1050 spectrometer equipped with a 150 mm integrating sphere.

1.7. Raman spectroscopy

Raman spectroscopy was performed on a Bruker Equinox 55 FRA 106/S Spectrometer operating at 100 mW laser power. A few milligrams of the MOF NPs were placed onto the sample holder and measured for 5000 scans. The collected spectra were analyzed using the OPUS spectroscopy software.

1.8. Scanning electron microscopy

SEM measurements were carried out using a FEI HELIOS NANOLAB G3 UC microscope equipped with a field emission gun and operated at acceleration voltages between 2 and 20 kV. The nanoparticle suspension (30 µL, 1 mg/mL) was dropped on a carbon grid placed on the SEM sample holder and was dried overnight.

1.9. Fluorescence (cross-) correlation spectroscopy (FCS/FCCS)

The fluorescence correlation measurements (FCS) and dual-color fluorescence cross-correlation measurements (FCCS) were performed on a home-built microscope as described elsewhere.[1] A pulsed laser diode at 470-nm wavelength (LDH-P-C-470) was used for excitation of the FITC-dye labeled IgG / Albumin and a pulsed Erbium-doped fiber laser (FFS.SYS-CONT-COMP-TSHG, Toptica Photonics, Gräfelfing, Germany) tuned to 562 nm was used for excitation of RhodamineB-labeled Zr-*fum* and Zr-*fum*@PGlu-PSar. The laser power ~ 4.5 and 17.5 µW for the 470 and 562-nm lasers, respectively measured at the sample using a slide power meter (S170C-Thorlabs). The measurements were performed using a 60x water immersion objective, NA 1.27 (Plan Apo 60 x WI, Nikon). The raw optical data and subsequent correlation analysis were performed with our PIE analysis with Matlab (PAM) software.[2] PAM is a stand-alone program (MATLAB; The MathWorks GmbH) for integrated and robust analysis of fluorescence ensemble, single-molecule, and imaging data.

The FCCS data were acquired by recording the detected photons of two single photon avalanche photodiodes (SPADs) on two separate time correlated single photon counting cards (TCSPC, SPC-150 Becker and Hickl) for a period of 15 minutes. Similarly, the FCS data were acquired by recording the photons with a single APD on a TCSPC card for a period of 15 minutes. Measurements were conducted in HEPES buffered glucose (HBG) for simulating

physiological body conditions.

The autocorrelation functions (ACFs) were fit using a three-component model assuming a 3D Gaussian focus shape was used for fitting the autocorrelation functions (ACFs)of the point-spread function (eq. 1).

$$G(\tau) = \frac{\gamma}{(N_1 + N_2 + N_3)^2} \cdot \left[\left(N_1\left(1 + \frac{4D_1 \cdot \tau}{{\omega_r}^2}\right)^{-1} \cdot \left(1 + \frac{4D_1 \cdot \tau}{{\omega_z}^2}\right)^{-\frac{1}{2}}\right) + \left(N_2\left(1 + \frac{4D_2 \cdot \tau}{{\omega_r}^2}\right)^{-1} \cdot \left(1 + \frac{4D_2 \cdot \tau}{{\omega_z}^2}\right)^{-\frac{1}{2}}\right) + \left(N_3\left(1 + \frac{4D_3 \cdot \tau}{{\omega_r}^2}\right)^{-1} \cdot \left(1 + \frac{4D_3 \cdot \tau}{{\omega_z}^2}\right)^{-\frac{1}{2}}\right)\right] \quad (1)$$

where N is the apparent average number of particles in the observation volume. The N_1 fraction accounts for residual unbound FITC present in the protein solution. The N_2 fraction refers to the unbound, freely diffusing labeled protein, while N_3 corresponds to the NP bound protein. D_1, D_2, and D_3 refer to the respective diffusion coefficients of N_1, N_2, and N_3 fractions, respectively. The time delay of the autocorrelation is represented by τ. ω_r and ω_z are the lateral and axial focus sizes, respectively, defined as the distance from the focus center to the point where the signal intensity has decreased to $1/e^2$ of the maximum. The shape factor γ is $2^{-3/2}$ for a 3D Gaussian. The fitting was used to extract the fraction of freely diffusing FITC-dye labeled IgG / Albumin (Alb) and FITC-dye labeled IgG / Alb bound to the Zr-*fum*. The residual unbound FITC diffusion coefficient D_1 was fixed in the fitting to the value of 373 $\mu m^2/s$, which was previously determined by measuring FITC alone. Similarly, the unbound freely diffusing FITC-IgG and FITC-Alb diffusion coefficients D_2 were fixed in the fitting to the value of 26 and 36 $\mu m^2/s$, which was previously determined by measuring FITC-IgG and FITC-Alb alone, respectively.

1.10. Confocal laser scanning microscopy (CLSM)

On the day prior to the measurements, HeLa cells were seeded in 8 well-chamber slides (Thermo Fisher Scientific, 20.000 cells in 300 µL medium per well). Cells were incubated at 37 °C and 5% CO_2. On the next day, the medium was aspirated and 300 µL Zr-*fum*@polymer (50 µg/mL in medium) was added to each respective well. After 30 min of incubation (37 °C, 5% CO_2), each well was washed once with 400 µL PBS and cells were subsequently fixated with 4% paraformaldehyde in PBS (30 min incubation at RT). After fixation, each well was once again washed with 400 µL PBS, the cell nuclei were stained with DAPI (2 µg/mL) and F-Actin was labeled with phalloidin-rhodamine (1µg/mL). After 30 min of incubation (light protected at RT), the staining mixture was aspirated and replaced with 300 µL PBS per well.

Images were recorded utilizing a Leica-TCS-SP8 confocal laser scanning microscope equipped with an HC PL APO 63x 1.4 objective. DAPI emission was recorded at 460 nm, calcein at 530 nm and rhodamine at 580 nm. Afterwards, all images were processed by LAS X software from Leica.

1.11. Flow Cytometry

On the day prior to the measurements, HeLa cells were seeded in a 24 well plate (60,000 cells in 1 mL medium per well). On the next day, the medium was aspirated and replaced with 475 µL fresh medium. 25 µL of 1 mg/mL Zr-*fum*@polymer solution was added to the wells (2 wells per polymer). After 30 minutes of incubation, the medium was aspirated and cells were washed with 1 mL PBS. Cells were then trypsinized with 200 µL Trypsin/EDTA (5 min, 37 °C). 400 µL medium was added to each well and the 2 wells per polymer were unified. Cells were centrifuged for 5 min at 1500 rpm and room temperature. The supernatant was removed, cells resuspended in 700 µL FACS-buffer (10 % FBS in PBS) and stored on ice. Shortly before the analysis, 2 µL of 1 mg/mL DAPI was added to each vial. Cells were appropriately gated by forward/sideward scatter and by pulse width for exclusion of cell aggregates. DAPI was used to discriminate between viable and dead cells. Only isolated viable cells were evaluated. Data were recorded by Cyan ADP flow cytometer (Dako, Hamburg, Germany) using Summit acquisition software (Summit, Jamesville, NY). Ten thousand gated cells per sample were collected. Analysis was done by FlowJo 7.6.5 flow cytometric analysis software. The threshold level for cellular association of calcein was set based on the fluorescence background of HBG treated negative control cells.

2. Experimental Section

2.1. Chemicals

Zirconium (IV) chloride ($ZrCl_4$, Aldrich, ≥ 99.0%), fumaric acid (Sigma-Aldrich, ≥ 99.9% trace metals basis), 2-[4-(2-hydroxyethyl)piperazine-1-yl]ethanesulfonic acid (HEPES, Biomol GmbH), glucose (Applichem), poly-L-glutamic acid sodium salt (PGlu, Sigma-Aldrich, MW 15.000-50.000), polyacrylic acid (PAA, Sigma-Aldrich, average MW ~15.000), branched polyethylene imine (BPEI, Sigma-Aldrich, average MW ~25.000), polyamidoamine dendrimer (PAMAM, Sigma-Aldrich, ethylenediamine core, generation 4.0), poly(ethylene glycol) methyl ether (PEG, Sigma-Aldrich, average M_n ~ 5.000), TWEEN® 20 (Tween, Sigma-Aldrich, MW ~1228) and the formic acid assay kit (K-Form, Megazyme) were used as received. Cell culture media, antibiotics and fetal bovine serum (FBS) were purchased from Life Technologies or Sigma-Aldrich, respectively.

2.2. Synthesis of Zr-fum NPs

Zr-*fum* NPs were synthesized according to a procedure reported by *Zahn et al.*[3]. $ZrCl_4$ (120.5 mg, 0.517 mmol) and fumaric acid (180.0 mg, 1.550 mmol) were dissolved in bi-distilled H_2O (10 mL). Formic acid (0.975 mL, 1.190 g, 25.85 mmol) was added and the reaction mixture was sealed in a 25 mL glass autoclave (Schott, Duran®). The mixture was heated to 120 °C for 24 h and was allowed to cool down to room temperature afterwards. Further, the resulting NPs were transferred in 15 mL Falcon® tubes and centrifuged (7187 rcf / 10 min). After re-dispersion in bi-distilled H_2O (6 mL), the Zr-*fum* NPs were transferred to Eppendorf® tubes and centrifuged (16900 rcf / 10 min). The washing steps (dispersion + centrifugation) were repeated twice with EtOH, and Zr-*fum* NPs were stored in an ethanolic stock solution.

2.3. Dye labeling of Zr-fum NPs

Zr-*fum* NPs were dispersed in an aqueous dye solution (0.25 mM calcein or rhodamine B, respectively) resulting in a 5 mg/mL dispersion. The NPs were shaken for 15 min (600 rpm) at room temperature, centrifuged and washed with bi-distilled H_2O, twice with HBG and stored in an ethanolic stock solution.

2.4. Preparation of Polymer stock solutions

Polymers were dissolved in bi-distilled H_2O, resulting in an aqueous solution of 10 mg/mL and stored at 7 °C.

2.5. Polymer coating of Zr-fum NPs

Polymer solution (10 mg/mL; 20 µL or 400 µL, respectively) was provided in bi-distilled H_2O (280 µL or 5.6 mL, respectively). Zr-*fum* NPs (1,43 mg/mL in EtOH; 0.7 mL or 14 mL, respectively) were added dropwise within two minutes and the dispersion was allowed to stir for three minutes. Ultrasound was applied for one minute and the solution was again stirred for three minutes. The resulting particles were centrifuged (16900 rcf / 10 min) and washed twice with bi-distilled H_2O (see section 2.2.). Zr-*fum*@polymer NPs were stored in an aqueous stock solution.

2.6. Detection of formic acid after coating of Zr-fum NPs in supernatant using a formic acid assay kit (K-Form, Megazyme)

Approx. 900 µL supernatant of the coating reactions (1 mg coating procedure) were aspirated after centrifugation of the NPs (16900 rcf / 10 min), transferred into an Eppendorf® tube and centrifuged again (16900 rcf / 10 min) to remove NPs that might have stayed in dispersion after the first centrifugation step. 300 µL of this supernatant were dissolved in 1.8 mL bi-distilled H_2O in a quartz cuvette (QS, SUPRASIL®; Hellma Anlaytics). 200 µL buffer solution ("Bottle 1" from K-Form, Megazyme) and 200 µL NAD+-solution ("Bottle 2" from K-Form, Megazyme) were added and the mixture was allowed to homogenize for approx. 5 minutes. UV-Vis absorption was measured (A1) and 50 µL formate dehydrogenase ("Bottle 3" from K-Form, Megazyme) was added afterwards. The solution was mixed by gentle inversion of the cuvette and the reaction was allowed to run for approx. 12 minutes. The UV-Vis absorption was measured and the absorbance different was calculated (see Figure 2 and Table S1). Control experiments were performed according to the same procedure, using 50 µg/mL polymer solutions in an ethanol/water mixture (70:30).

2.7. Synthesis of PGlu-PSar (Synthesis of $PSar_{124}$-b-$PGlu_{33}$)

PGlu-PSar was synthesized according to the procedure published in the literature.[4] For simplification, $PSar_{124}$-*b*-$PGlu_{33}$ was abbreviated by PGlu-PSar.

2.8. Cell Culture

HeLa cells were cultured at 37 °C and 5% CO_2 in Dulbecco's modified Eagle's medium (DMEM), supplemented with 10% FBS, 100 U/mL penicillin and 100 µg/mL streptomycin.

2.9. Preparation of HEPES-buffered glucose (HBG)

HEPES (2.38 g, 10 mmol) and glucose monohydrate (28.95 g, resulting in 5 w% glucose) were dissolved in bi-distilled H_2O (490 mL) and the pH was adjusted to 7.4 by the addition of NaOH (approx. 10 mL, 0.5 M).

2.10. Metabolic activity assay of Zr-*fum* NPs and Zr-*fum*@polymer NPs (MTT assay)

HeLa cells were seeded in 96-well plates at a density of 5.000 cells/ well 24 h prior to incubation with the different particle concentrations. Before incubation with the Zr-*fum* NPs, medium was replaced with 100 µL fresh medium. Particles diluted in 20 µL HBG were added to each well and incubated with cells for 24 h at 37 °C in 5% CO_2. 100 µL of MTT solution (3-(4,5-dimethylthia-zol-2-yl)-2,5-diphenyltetrazolium bromide in medium; 0.5 mg/mL) were added after removing the medium. After an incubation time of 2 h, unreacted dye and medium were removed and the 96-well plates were frozen at −80 °C for at least 30 min. The purple formazan product was then dissolved in 100 µL DMSO (dimethyl sulfoxide) per well and quantified by measuring the absorbance using a microplate reader (TecanSpectrafluor Plus, Tecan, Switzerland) at 590 nm with background correction at 630 nm. All studies were performed in triplicate. The relative cell viability (%) related to control wells treated only with 20 µL HBG was calculated as ([A] test/[A] control) × 100%.

2.11. Cy5.5 labeling of PGlu-PSar

PGlu-PSar was labeled statistically with 1 eq of Sulfo-Cy5.5 per polymer on average by the following procedure. 5 mg of $PSar_{124}$-b-$PGlu_{33}$ (385 nmol, 12.7 µmol -COOH) were dissolved in 950 µL TES buffer (0.1 M, pH 6). 200 µL of 200 mM N-hydroxysuccinimide in TES-buffer (40 µmol) were added to the polymer solution which was subsequently vortexed and cooled to 4 °C. 20 µL 200 mM EDC in H_2O (4 µmol) were added to the polymer solution and mixed rapidly. The solution was allowed to warm up to room temperature and incubated for 30 minutes under agitation. After adjusting the pH to 7.2 by addition of 1M NaOH, 208 µL of 2 mg/mL Sulfo-Cy5.5-amine (0.416 mg, 385 nmol) were added to the polymer solution which was then vortexed and incubated for 2 h at room temperature under agitation. The obtained product was purified by dialysis (Spectrapor MWCO 2 kDa, Repligen GmbH, Ravensburg, Germany) against Millipore-water (overnight, 4 °C, water was changed once). The purified polymer was frozen in liquid nitrogen and freeze-dried (Christ Alpha 2-4 LD plus, Martin Christ, Gefriertrocknungsanlagen GmbH, Osterode, Germany) over 2 days. 2.6 mg of light-blue product corresponding to a yield of 48% were obtained.

2.12. Cy5.5-PGlu-PSar coating of Zr-fum NPs

For loading determination, serum stability experiments and animal experiments Zr-*fum* NPs were coated with Cy5.5-PGlu-PSar analog to the description in 2.5. with the exception of a final HBG wash to result in a suspension in physiological medium. 875 µL Zr-*fum* dispersed in an ethanolic solution (1.43 mg/mL) was given to 375 µL Cy5.5-PGlu-PSar solution (0.66 mg/mL) over the course of 2 min. After incubating for 3 min at room temperature, the coating mixture was sonicated for 1 min and afterwards incubated for additional 3 min. The coated particles were then washed via centrifugation (16900 rcf, 10 min) and redispersion in 1.25 mL HBG. This was repeated for one additional time resulting in a final mixture of Zr-*fum*@Cy5.5-PGlu-PSar (1 mg/mL).

2.13. Loading determination

Loading of Zr-*fum* NP was determined photometrically at 684 nm with Zr-*fum*@Cy5.5-PGlu-PSar. 100 µL of unlabeled Zr-*fum*@PGlu-PSar (1 mg/mL) was used as blank. 100 µL of labeled Zr-*fum*@Cy5.5-PGlu-PSar (1 mg/mL) was measured at 684 nm and absorption was determined to be 0.185. With the extinction coefficient of Cy5.5 this results in a loading of 0.885 nmol PGlu-Psar per 1 mg of Zr-*fum* NP. Based on the particle parameters and theoretical estimates of section 5 “Theoretical Estimate (w% formic acid per NP)”, average mass of Zr-*fum* was determined according to the following formula:

$$\boldsymbol{M_{total} = 11.96 \cdot 10^{6}\, Da \cong 11.96 \cdot 10^{6} \cdot 1.66 \cdot 10^{-21}\, mg = 1.985 \cdot 10^{-14}\, mg}$$

With this, 1 mg Zr-*fum* NP corresponds to the following number of particles:

$$\boldsymbol{n_{1mg} = (1.985 \cdot 10^{-14})^{-1} = 5.0 \cdot 10^{13}}$$

This results in a number of attached polymer per single particle of

$$\boldsymbol{PGlu - PSar/NP = 0.885 \cdot 6.022 \cdot 10^{14} \cdot (5.0 \cdot 10^{13})^{-1} = 10.7}$$

2.14. Serum stability of Zr-fum@Cy5.5-PGlu-PSar

The serum stability of Zr-*fum*@Cy5.5-PGlu-PSar was determined by photometrical quantification of released Cy5.5-PGlu-PSar after incubation for different times (30 min, 1 h, 2 h, 4 h, 24 h) in 10 % fetal bovine serum (FBS) at 37 °C under shaking (400 rpm shaking, Eppendorf tabletop shaker). For each timepoint, 250 µg loaded MOF (250 µL, 1 mg/mL) were centrifuged (10 min, 14680rpm, Eppendorf tabletop centrifuge). The supernatant was carefully removed without damaging the pellet and each pellet was redispersed in 100 µL, 10 % FBS. After incubation at 37 °C, each sample was centrifuged (10 min, 14680rpm, Eppendorf tabletop centrifuge) and 80 µL of supernatant was transferred to a microcuvette. The amount of released Cy5.5-PGlu-PSar was determined photometrically (Thermo Scientific Genesys 10S UV-Vis) at 684 nm (blank was performed against 10 % FBS). Using the obtained absorption together with the extinction coefficient for Cy5.5 (209000 $M^{-1} \cdot cm^{-1}$) and initial loading (0.885 nmol/mg) the percentage of released polymer was calculated according to the following formula: [Released Cy5.5-PGlu-PSar / initially bound Cy5.5-PGlu-PSar] x 100 %.

2.15. NIR imaging of Cy5.5-PGlu-PSar after intravenous injection into mice

To investigate the *in vivo* stability and biodistribution of Zr-*fum*@PGlu-PSar, 50 µg of Zr-*fum*@Cy5.5-PGlu-PSar were injected into mice and compared to free Cy5.5-PGlu-PSar. Female six- to eight-week-old nude mice, Rj: NMRI-nu (nu/nu) (Janvier, Le Genest-Saint-Isle, France), were housed under specific pathogen-free conditions in isolated ventilated cages at a 12 h light/dark interval. Prior to experiments, they were acclimated in the facility for at least 7 days. Food and water were provided *ad libitum*. The body weight was recorded daily. The experiments were performed according to guidelines of the German Animal Welfare Act and approved by the local animal ethics committee.

For the biodistribution study, two mice were intravenously injected with 50 µL of Zr-*fum*@Cy5.5-PGlu-PSar (1 mg/mL) or 50 µL Cy5.5-PGlu-PSar (1.52 µM). Mice were anesthetized with 3 % isoflurane in oxygen and NIR fluorescence bioimaging was performed at different time points over 24 h using a CCD camera. After 24 h animals were sacrificed and organs were harvested for *ex vivo* imaging. For the evaluation fluorescence intensity scales of the images were equalized using the Living Image software (Caliper Life Sciences, Hopkinton, MA, USA).

3. Supplementary Figures

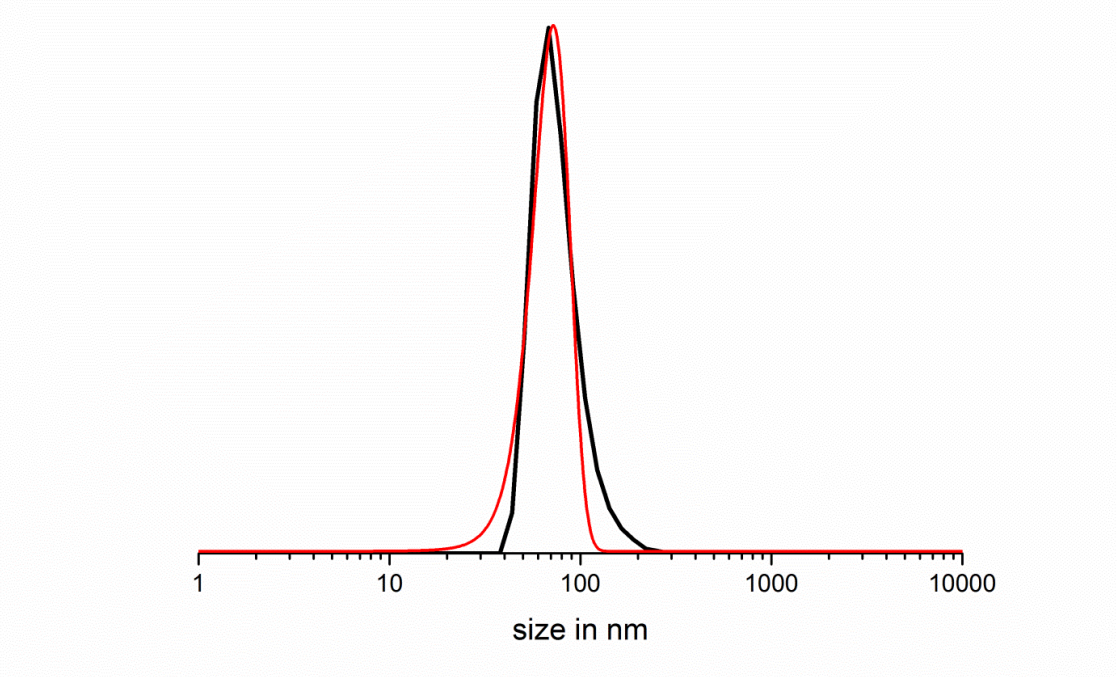

Figure S1. The DLS size distribution **(black)** and Gauss-fit **(red)** of Zr-fum NPs in ethanolic dispersion

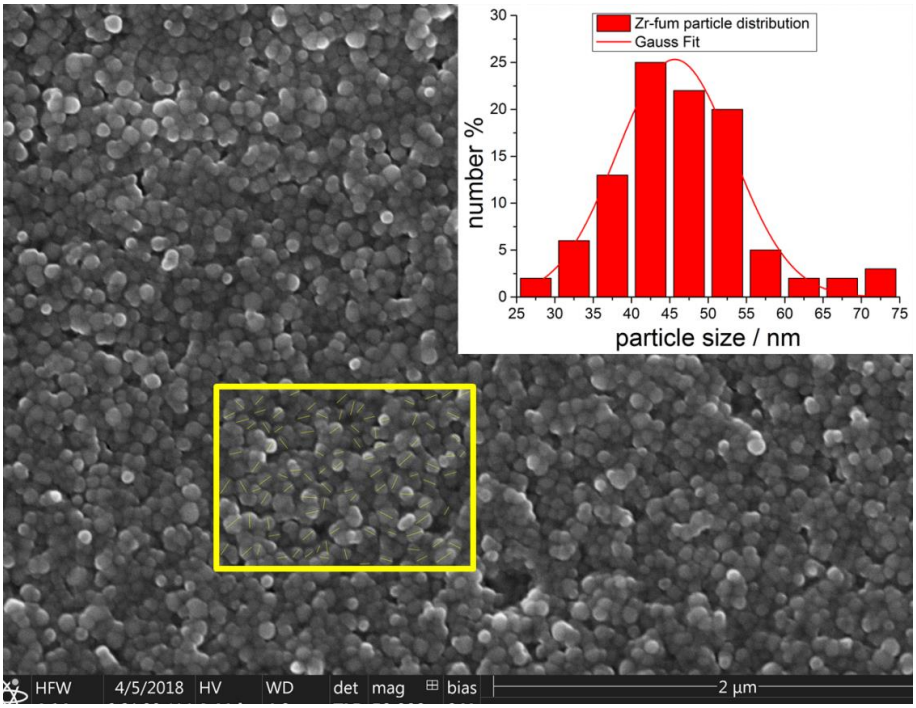

Figure S2. SEM overview of Zr-*fum* NPs with the size distribution **(inset)** determined from the region of interest **(yellow box).**

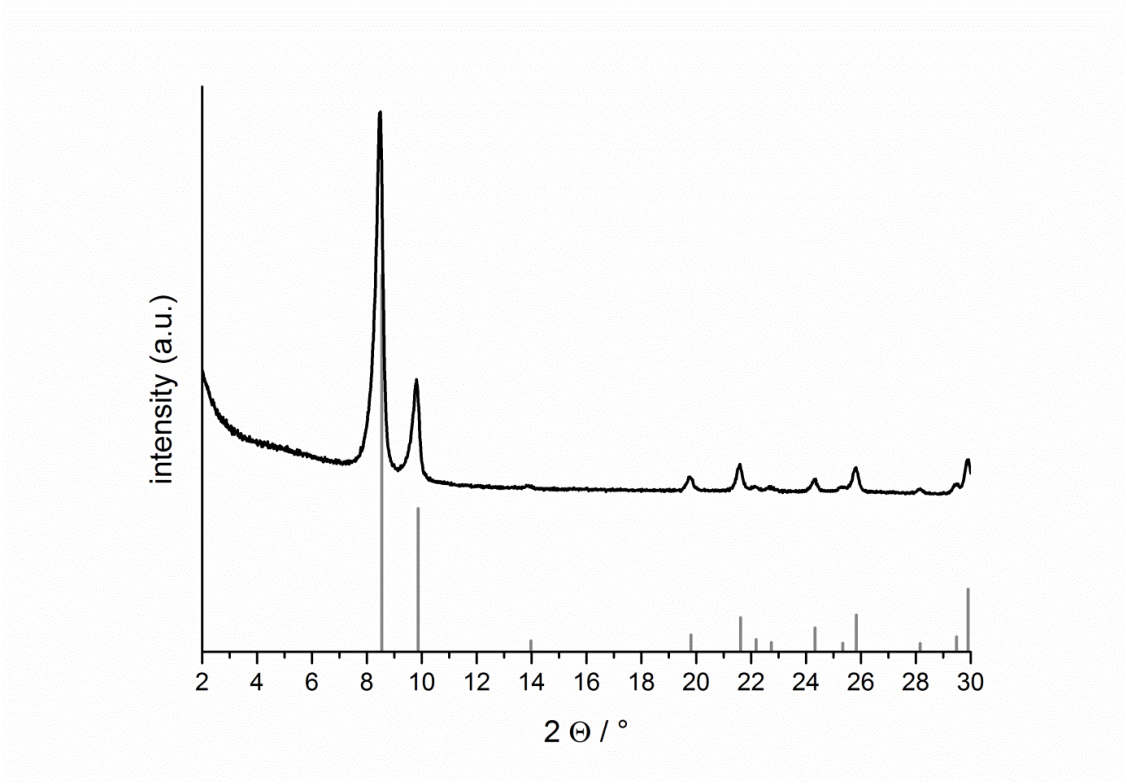

Figure S3. An XRD spectrum of Zr-fum NP. For comparison, the calculated peaks for the expected Zr-fum structure are shown

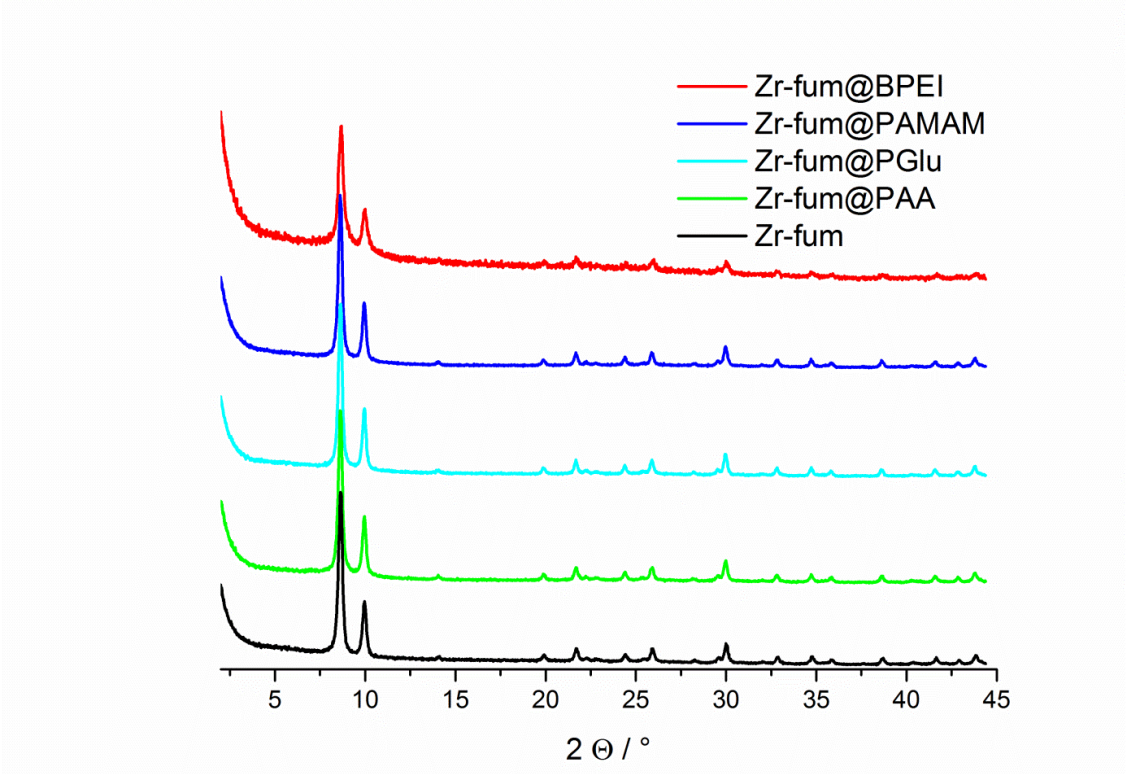

Figure S4. PXRD spectra of non-functionalized Zr-*fum* and Zr-*fum*@polymer

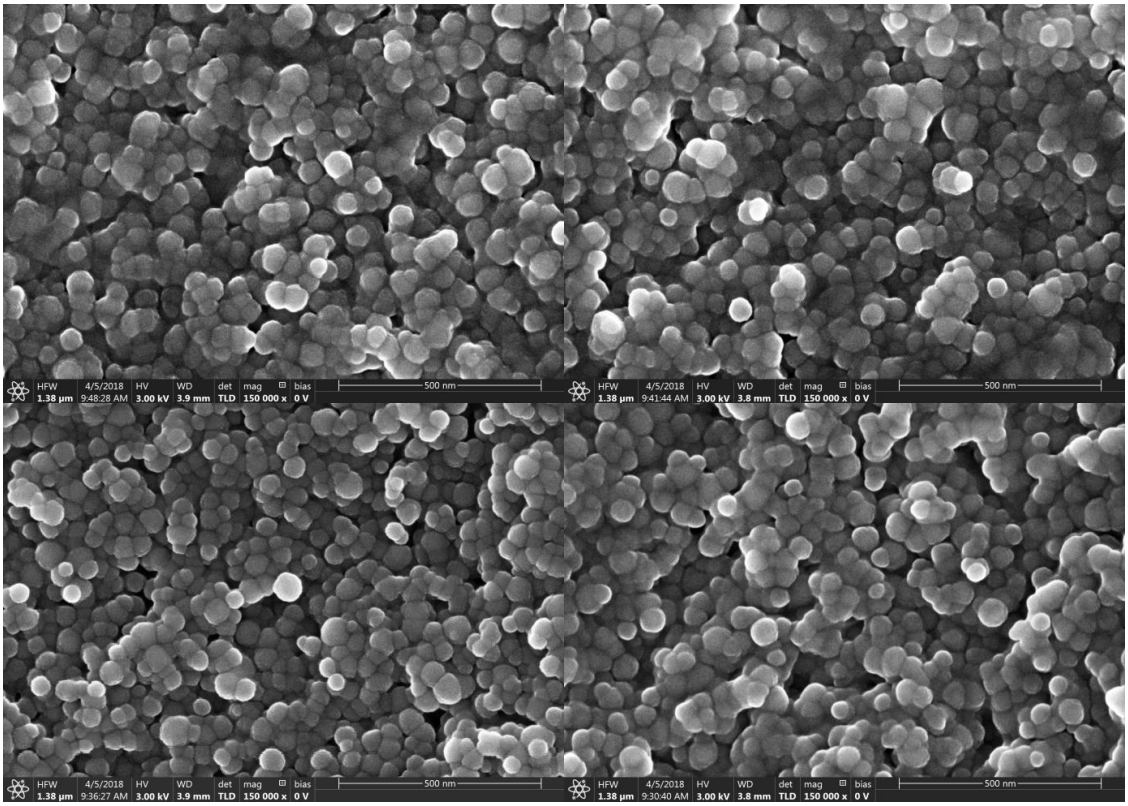

Figure S5. A comparison of SEM images between Zr-*fum*@polymer NPs: Zr-*fum*@BPEI **(top left)**; Zr-*fum*@PAMAM **(top right)**; Zr-*fum*@PAA **(bottom left)**; Zr-*fum*@PGlu **(bottom right)**

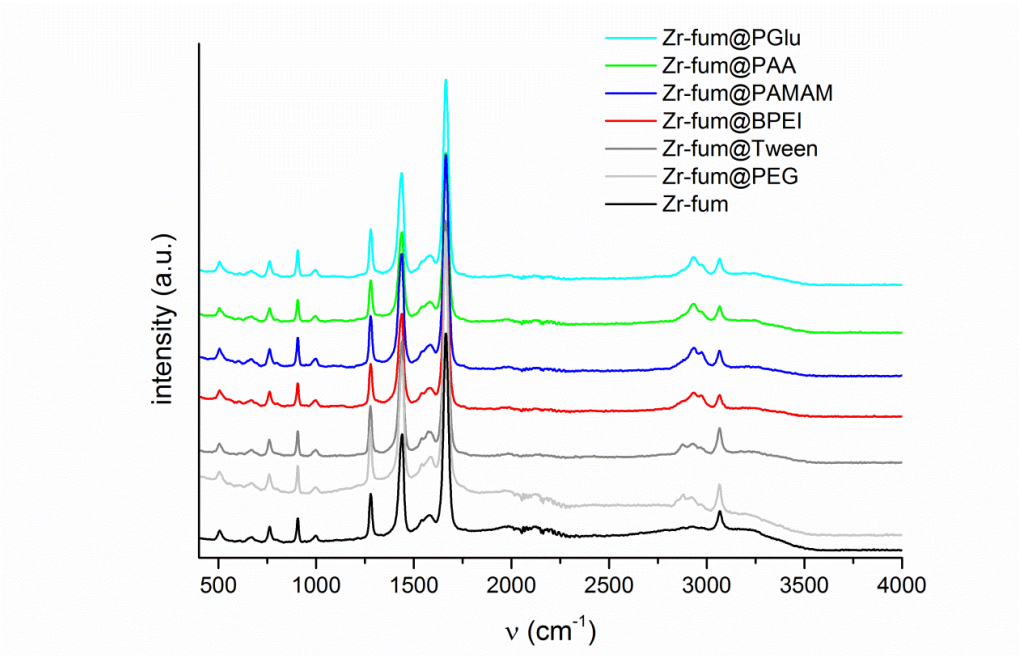

Figure S6. Full Raman spectra (as measured) of non-functionalized Zr-*fum* and Zr-*fum*@polymer

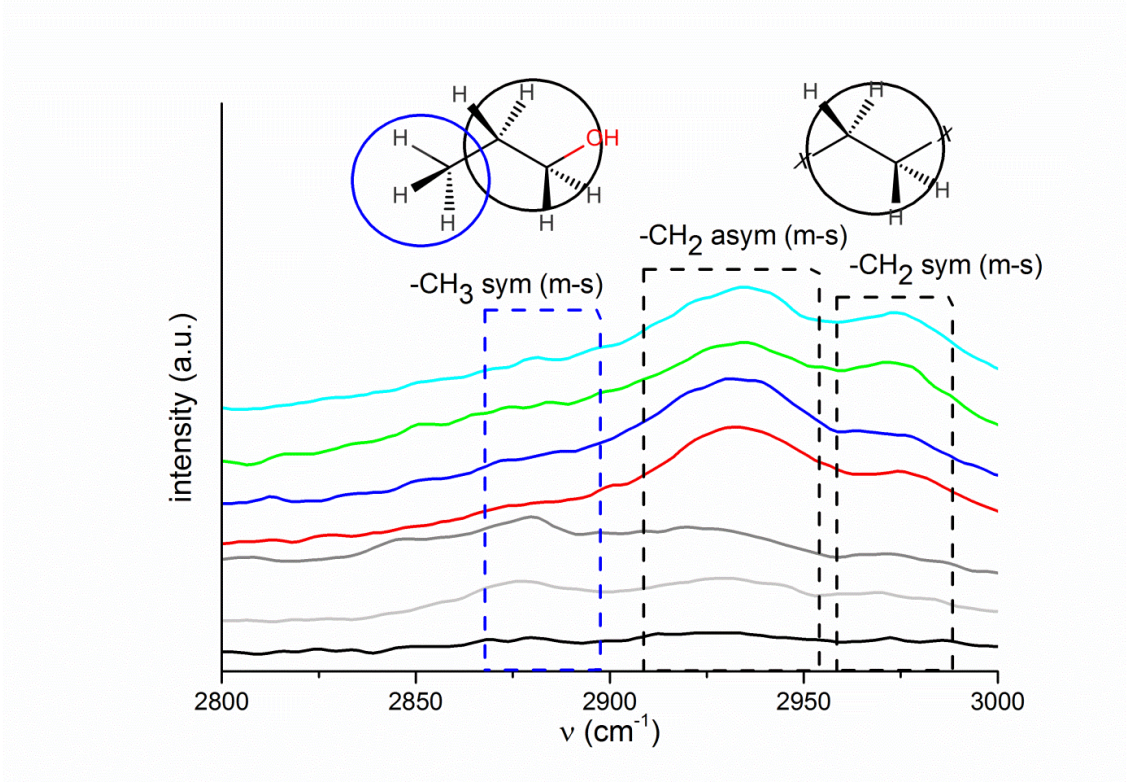

Figure S7. A zoom in of the Raman spectra shown in Figure S6 (normalized to an internal standard: fumaric acid C-H vibration at 3064 cm^{-1}) with indications for strong appearing $–CH_3$ and $–CH_2$ stretching vibrations.[5] The blue box shows more pronounced $-CH_3$ bonds for PEG and Tween, which results from EtOH residues after drying. For legend, see Figure S6.

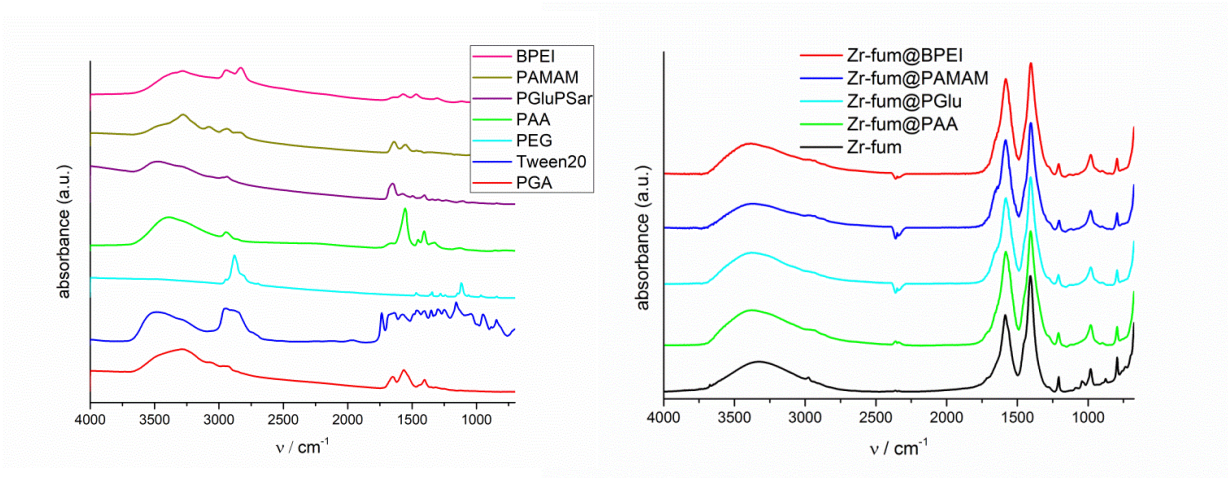

Figure S8. FTIR spectra of the used polymers (left). FTIR spectra of the non-functionalized Zr-*fum* and Zr-*fum*@polymer (right).

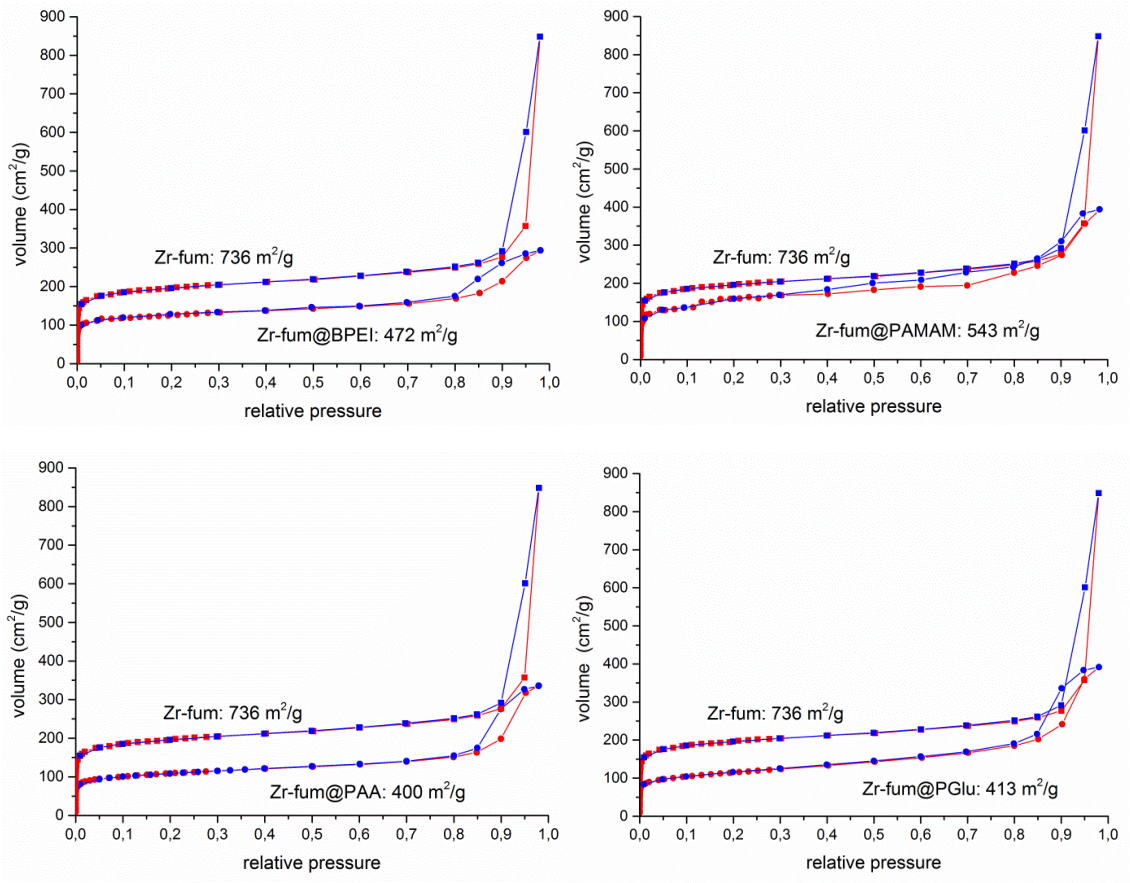

Figure S9. Nitrogen sorption isotherms of Zr-*fum*@polymer NPs in comparison to Zr-*fum* NPs.

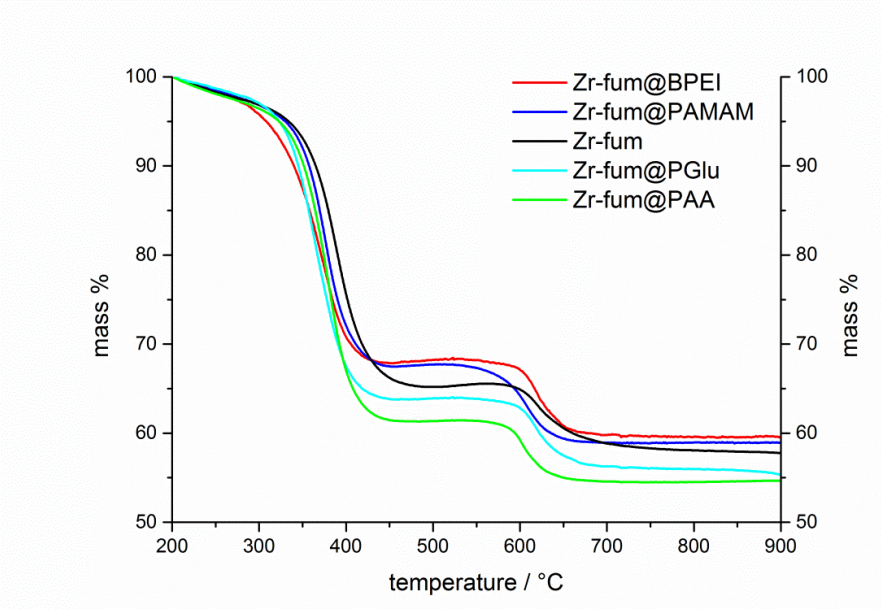

Figure S10. TGA comparison of different Zr-*fum*@polymer fomulations

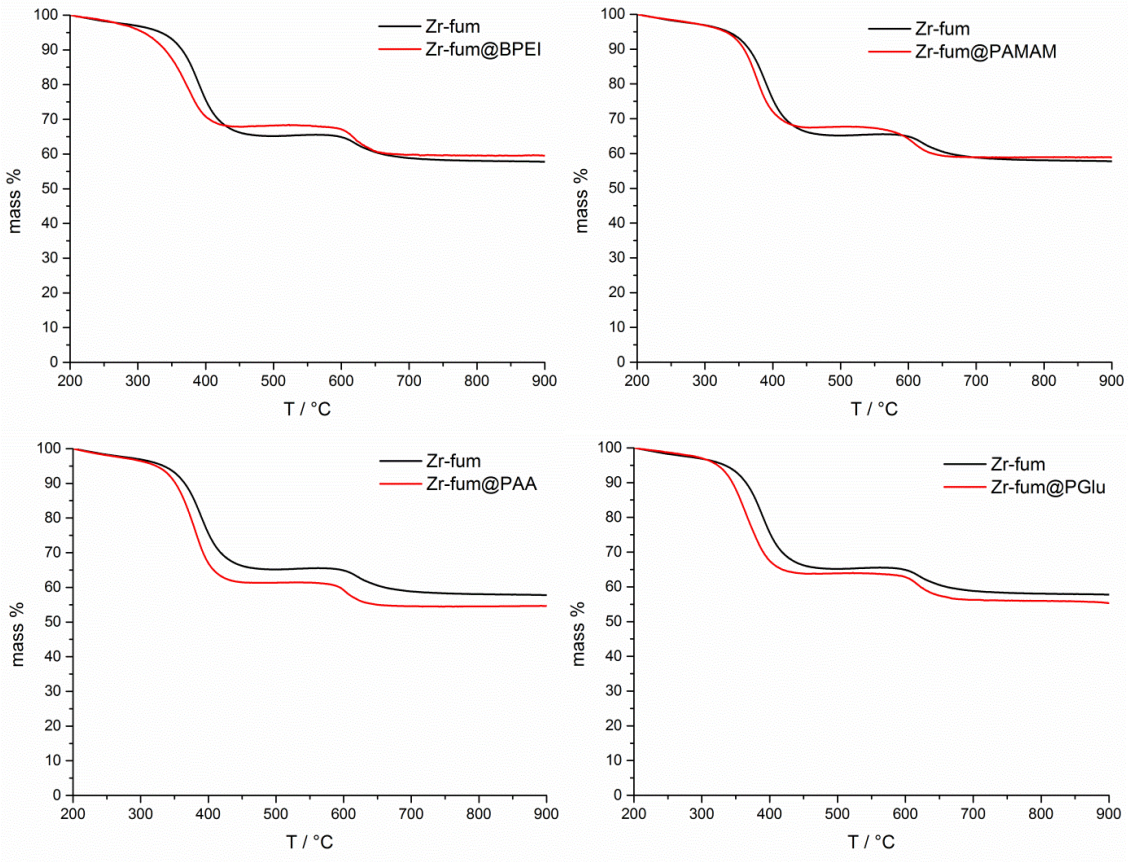

Figure S11. TGA of Zr-*fum*@polymer NPs in comparison to Zr-*fum* NPs.

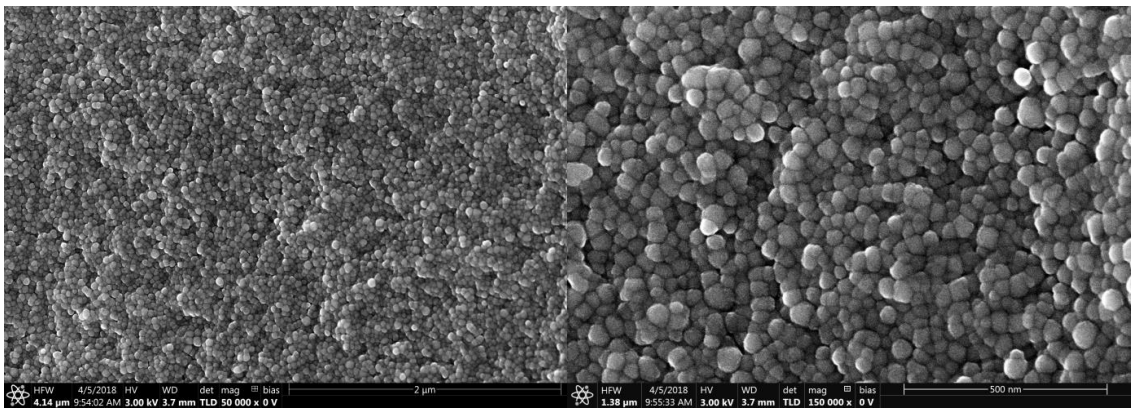

Figure S12. SEM imgaes of Zr-*fum*@PGlu-PSar NPs at two different magnifications (left: × 50000; right: × 150000).

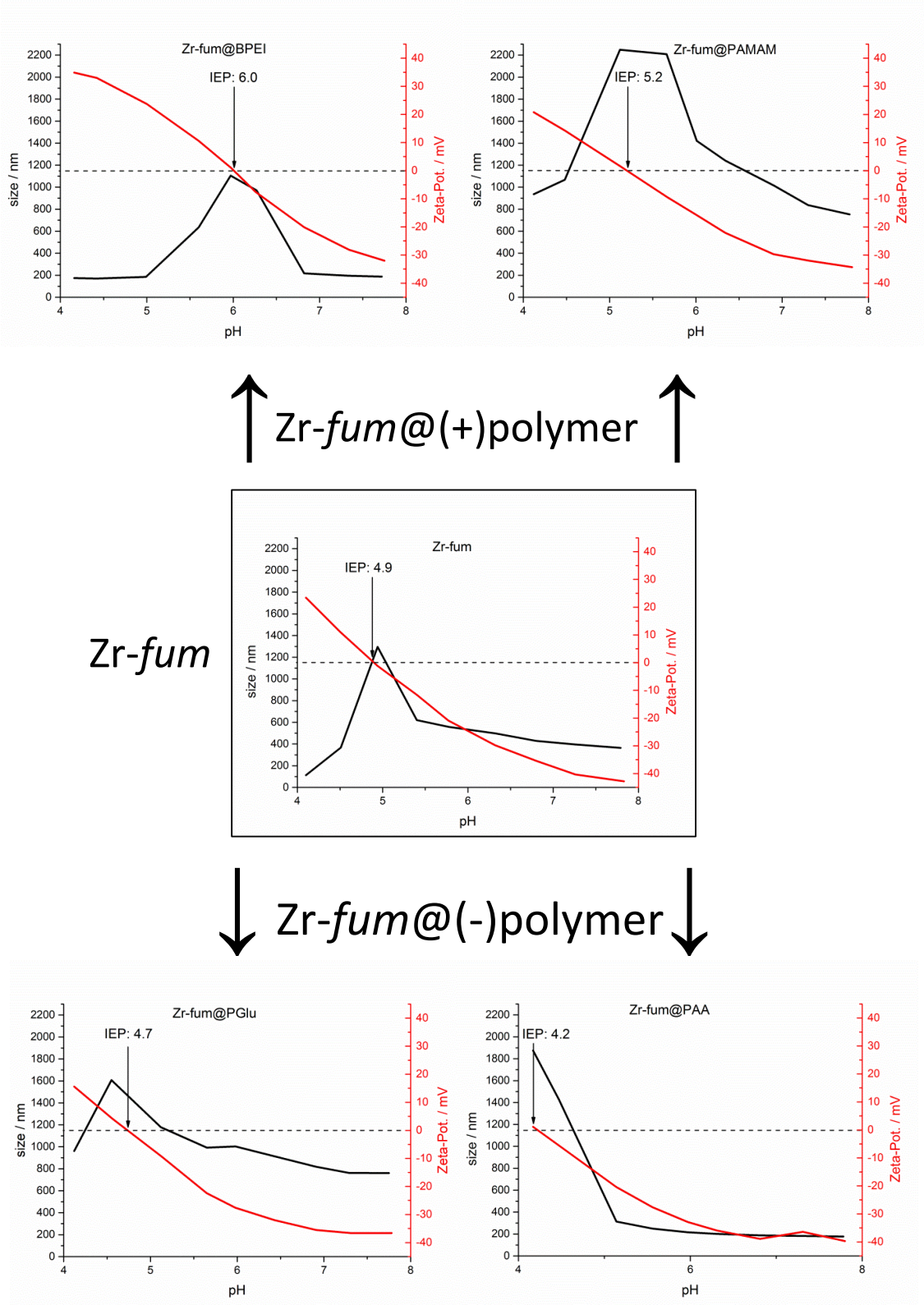

Figure S13. Titration curves of non-functionalized Zr-*fum* and Zr-*fum*@polymer. Size (Z-average) and Zeta-potential is plotted as a function of the pH of the dispersion. Zr-*fum*@(+)polymer NPs are plotted on the top, non-functionalized Zr-*fum* in the middle and Zr-*fum*@(-)polymer NPs at the bottom of the figure.

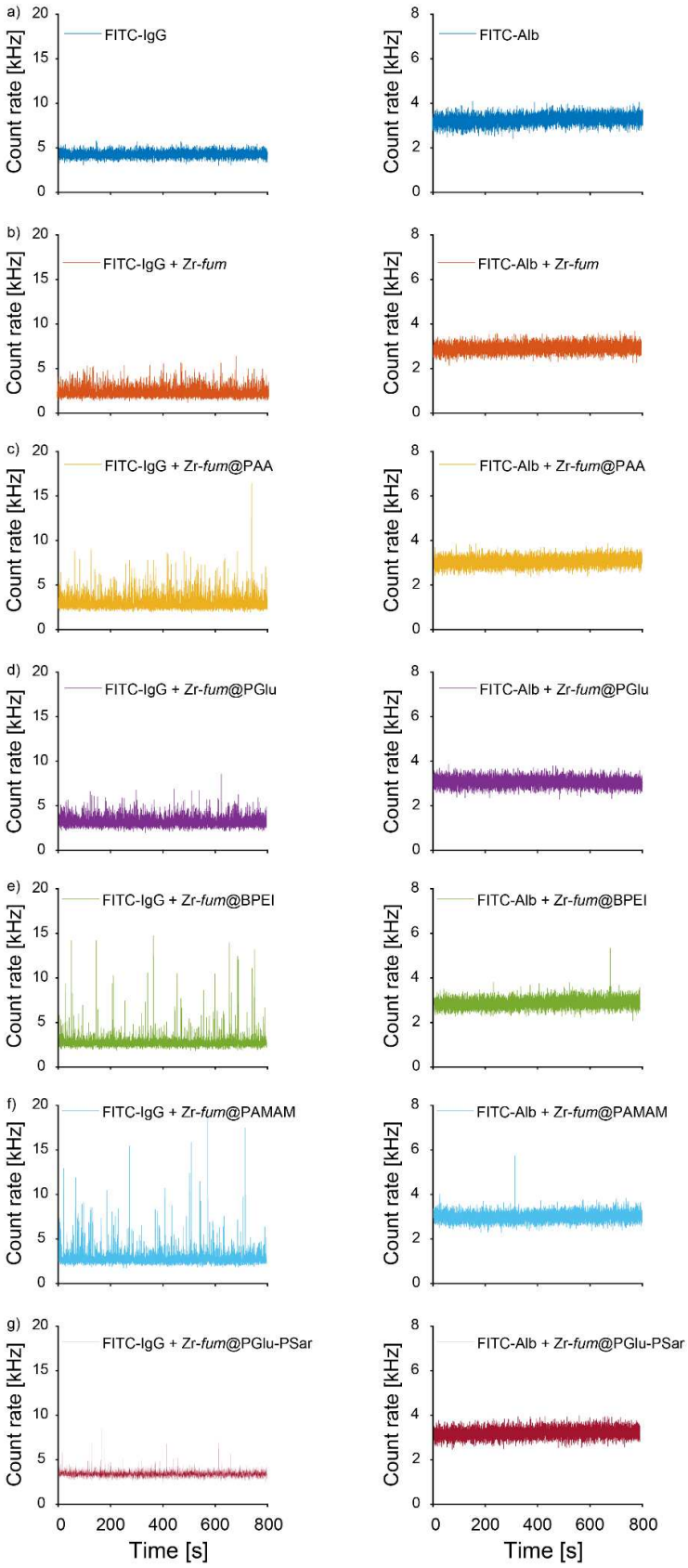

Figure S14. Fluorescence intensity trace of FITC-IgG (**left**) and FITC-albumin (**right**) in the absence (**a**) and presence of Zr-*fum* (**b**) and Zr-*fum*@polymer NPs (**c-g**). The binning time was 100 ms.

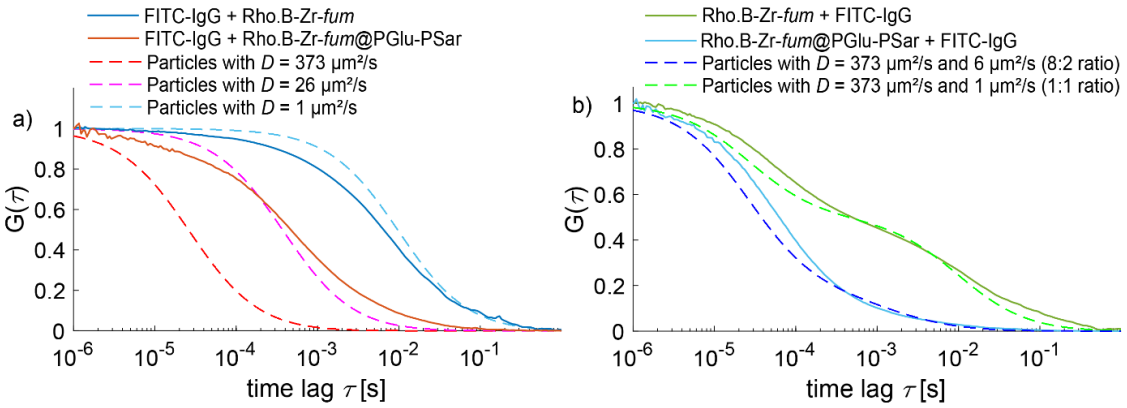

Figure S15. The corresponding ACFs for FITC-IgG interaction with MOF NPs from the obtained FCCS data. (**a**) The ACF of FITC-IgG in the presence of Rho.B-Zr-*fum* and Rho.B-Zr-fum@PGlu-PSar, respectively. The dashed lines display a comparison of the ACF of FITC-IgG with a set of three particles diffusing at 373 µm^2/s, 26 µm^2/s, and 1 µm^2/s, featuring the diffusion of free FITC, FITC-IgG, and NP bound FITC-IgG, respectively. (**b**) The ACF of Rho.B-Zr-*fum* and Rho.B-Zr-*fum*@PGlu-PSar in the presence of FITC-IgG. The dashed lines display a comparison of the ACF of Rho.B-Zr-*fum* NPs with a set of particles diffusing at 373 and 1 µm^2/s, featuring the diffusion of free Rho.B and Rho.B-Zr-*fum* bound FITC-IgG, respectively, and another set of particles diffusing at 373 and 6 µm^2/s, featuring the diffusion of free Rho.B and Rho.B-Zr-*fum*@PGlu-PSar bound FITC-IgG, respectively. The ratio of 8:2 (free RhoB. and Rho.B-Zr-*fum*@PGlu-PSar bound FITC-IgG, respectively) was chosen mimicking the low fraction of FITC-IgG binding to the PGlu-PSar coated NPs observed.

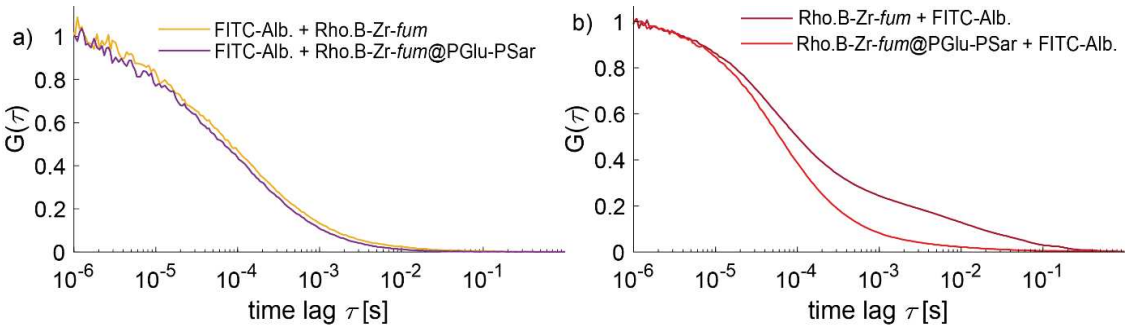

Figure S16. The corresponding ACFs for FITC-Alb interaction with MOF NPs from the obtained FCCS data. (**a**) The ACF of FITC-Alb in the presence of Rho.B-Zr-*fum* and Rho.B-Zr-fum@PGlu-PSar, respectively. (**b**) The ACF of Rho.B-Zr-*fum* and Rho.B-Zr-*fum*@PGlu-PSar in the presence of FITC-Alb.

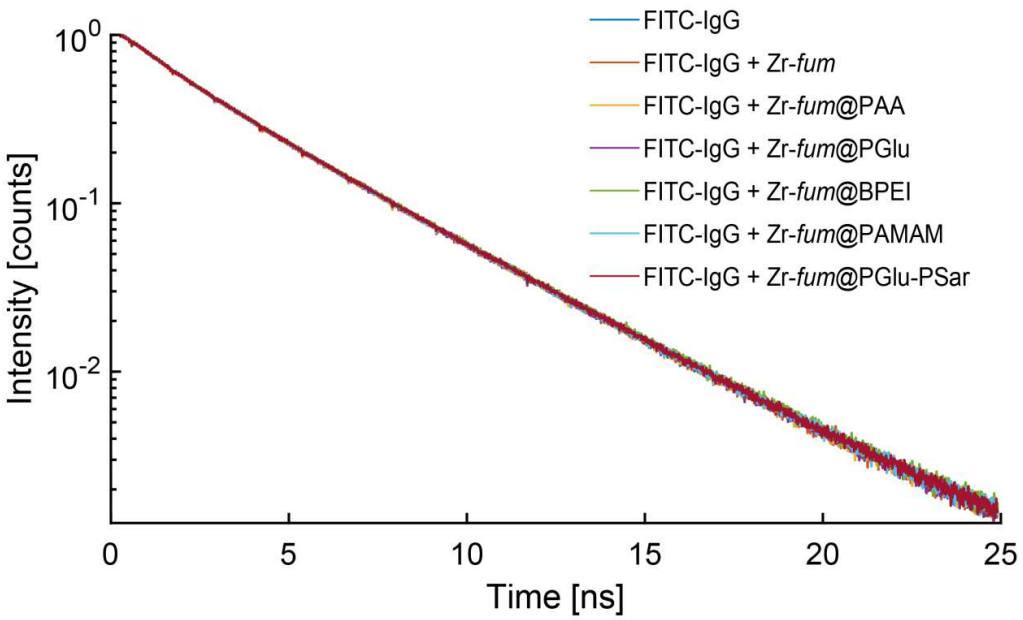

Figure S17. Lifetime decay traces of FITC-IgG in the absence and presence Zr-*fum* and Zr-*fum*@polymer NPs. The lifetime showed a consistent biexponential decay in all cases, with lifetimes τ_1 ~ 3.8 ns and τ_2 ~ 1.77 ns, corresponding to the free FITC dye and FITC-IgG lifetimes, respectively.

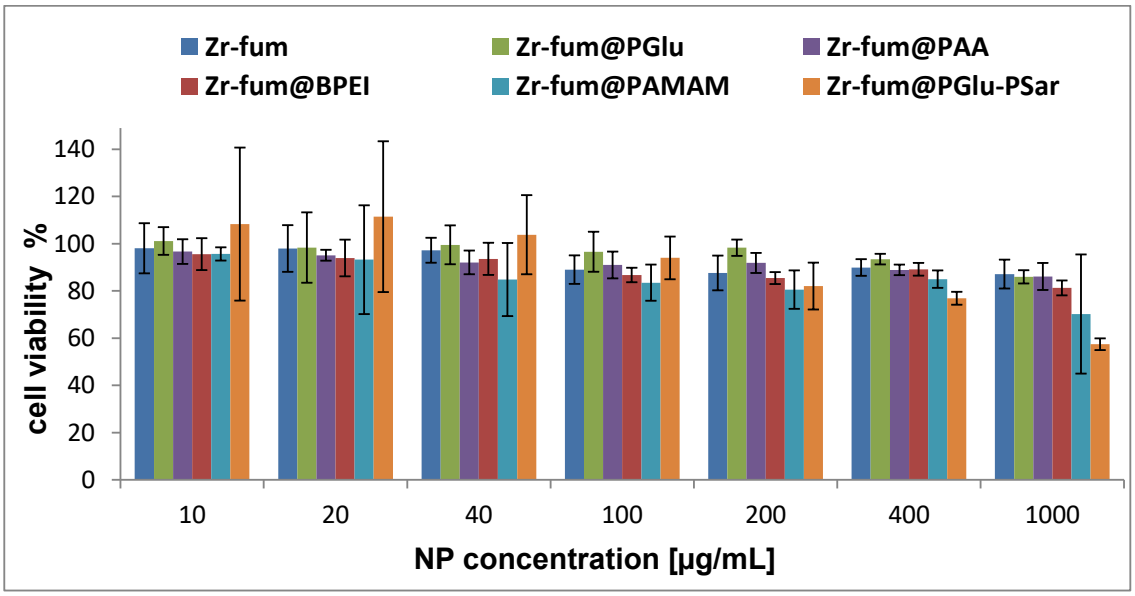

Figure S18. MTT cell viability assays of all Zr-*fum*@polymer formulations as well as non-functionalized Zr-*fum*. No significant toxicity was observed up to concentrations of 0.4 mg/mL. At highest concentration of 1 mg/mL effects on metabolic activity become apparent.

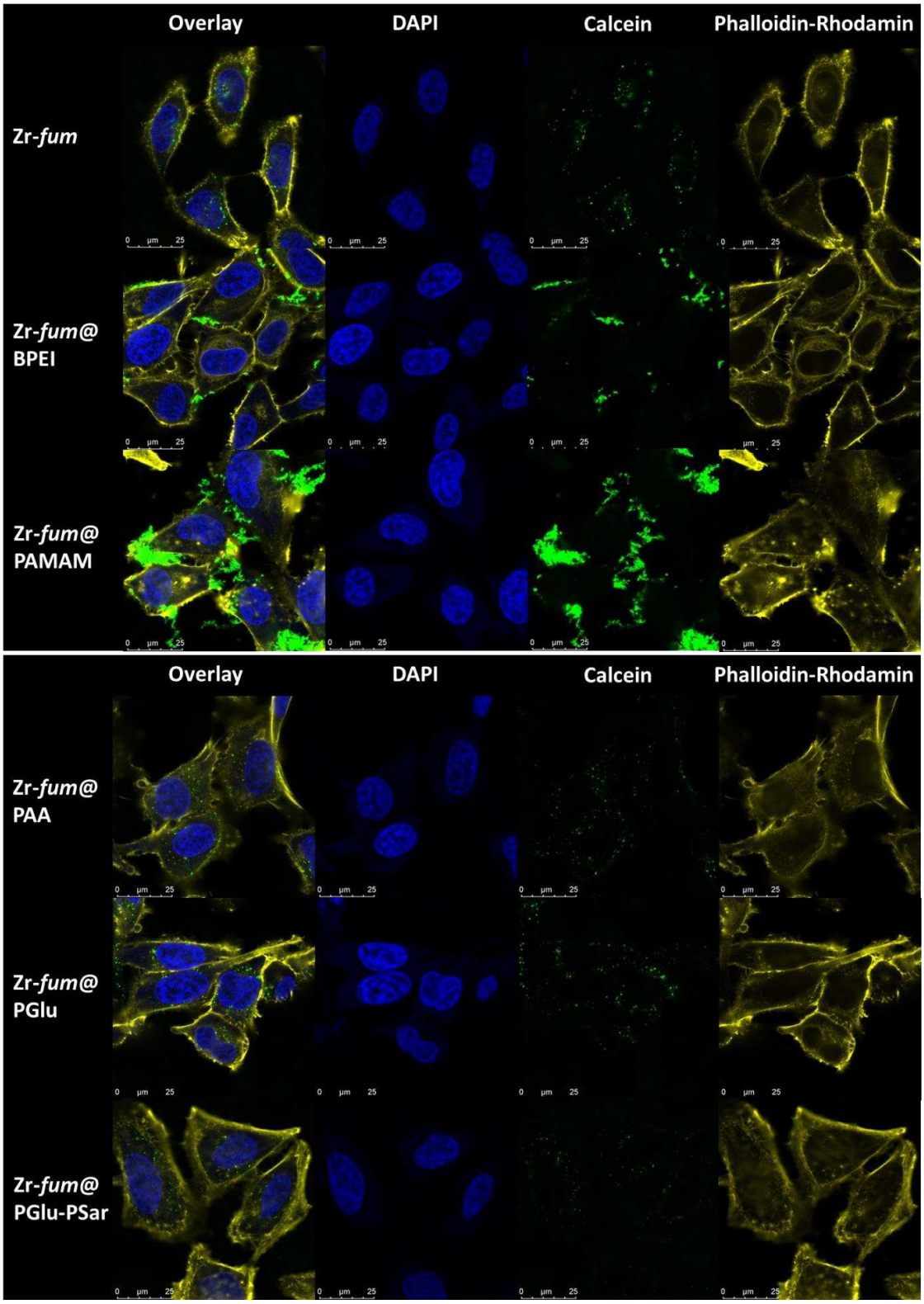

Figure S19. CLSM images of Figure 7 (Overlay) and separate channels

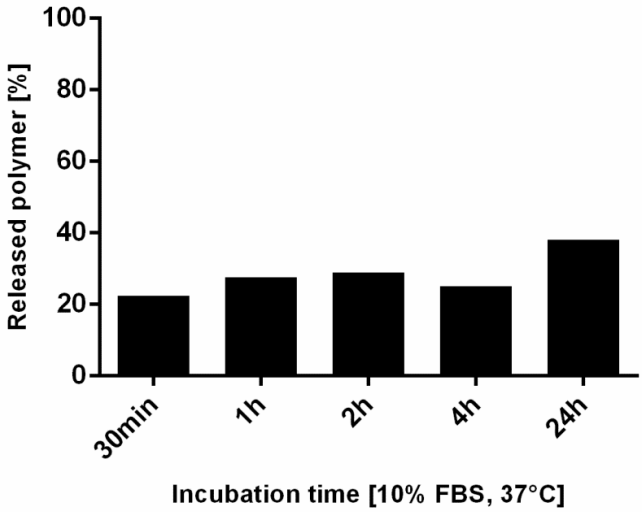

Figure S20. Serum stability assay. Zr-*fum*@Cy5.5-PGlu-PSar NPs were incubated in 10 % FBS at 37 °C for different times and the fraction of released Cy5.5-PGlu-PSar in the supernatant was quantified photometrically at 684 nm.

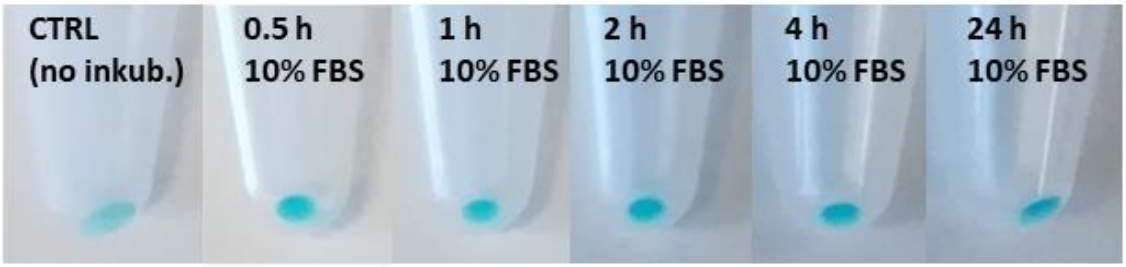

Figure S21. Zr-*fum*@Cy5.5-PGlu-PSar NP pellets after incubation in 10 % FBS for different times and centrifugation. Persisting color indicates stability of the polymer coating under serum containing conditions.

A)

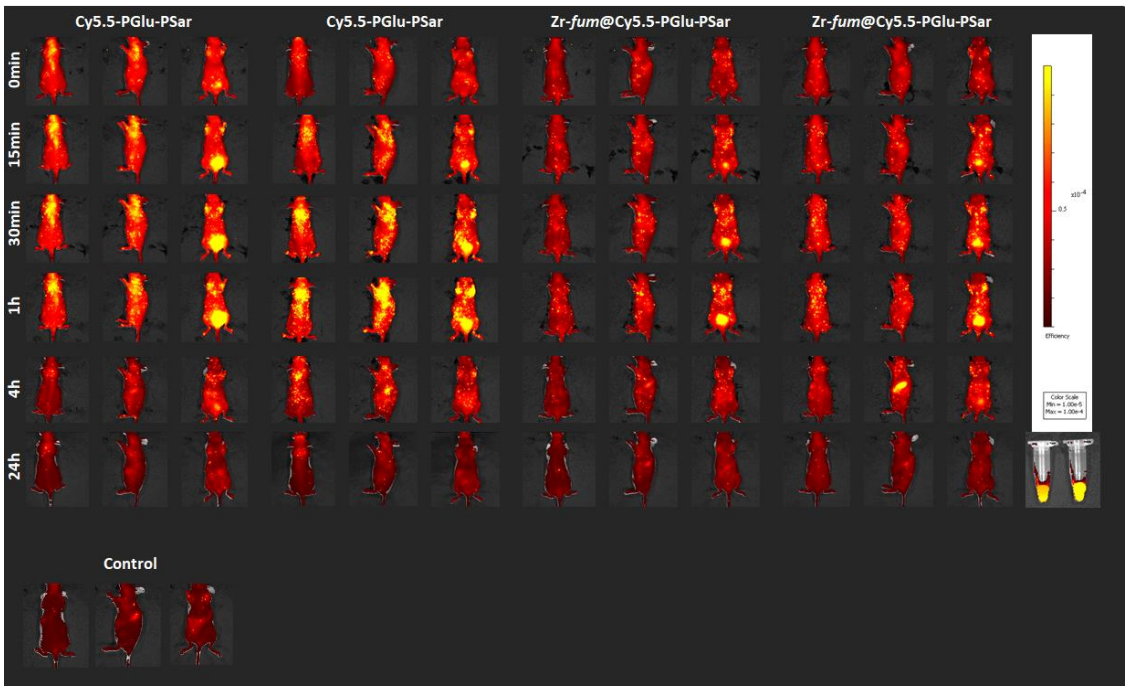

B)

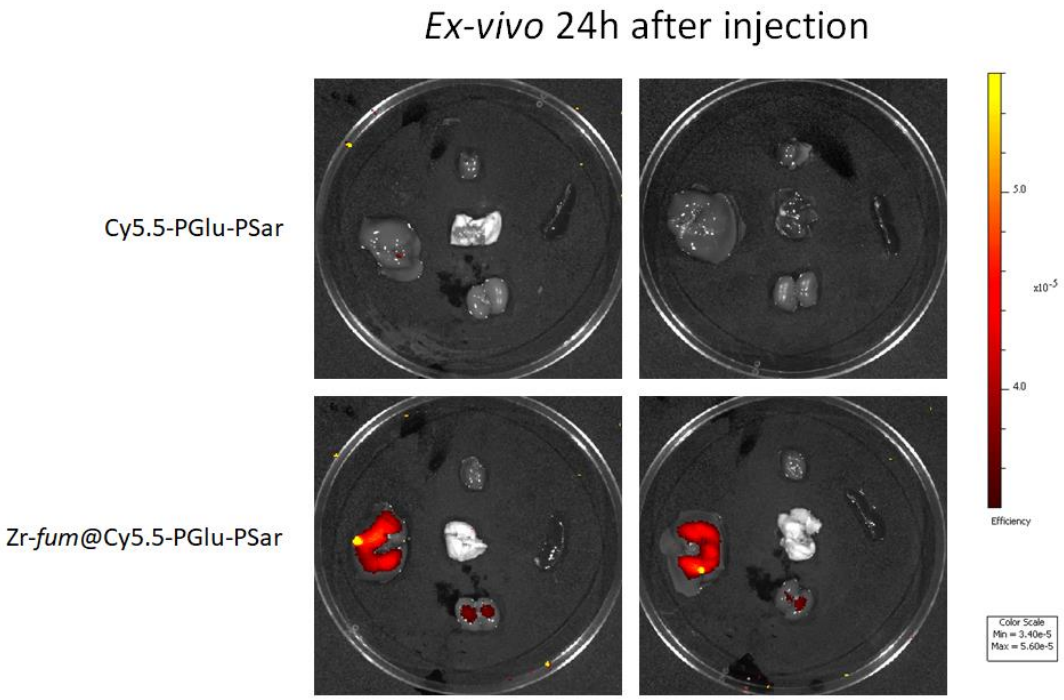

Figure S22. NIR imaging of Cy5.5-PGlu-PSar after intravenous injection into mice. A) Biodistribution at different time points after injection. The two reaction tubes show the fluorescence intensity of the two injected solutions Cy5.5-PGlu-PSar and Zr-*fum*@Cy5.5-PGlu-PSar. Control images show background fluorescence of untreated mice. After 24 h no fluorescence above background (Control) is observable *in vivo*. B) *Ex vivo* imaging of harvested organs (heart, liver, lung, spleen, kidneys) 24 h after injection. Cy5.5 fluorescence was only detectable in livers of mice injected with Zr-*fum*@Cy5.5-PGlu-PSar in contrast to free Cy5.5-PGlu-PSar.

4. Supplementary Tables

Table S1. Determination of formic acid concentration in supernatant of different polymer coating reactions.

The calculations were done using Mega-Calc™ (freeware supplied by Megazyme). A1 represents the absorption value before addition of formate dehydrogenase, A2 represents the absorption value after the completed reaction (approx. 12 min).

Blank absorbance values (EtOH/H2O 70:30)

A1	A2
0,4669	0,7127

Absorbance values (at 340 nm; Reference at 450 nm)

Sample	A1	A2
Zr-*fum*@PGlu	0,4873	1,0151
Zr-*fum*@PAMAM	0,5322	1,0099
Zr-*fum*@BPEI	0,5618	1,0539
Zr-*fum*@PAA	0,5259	1,4079
Zr-*fum*	0,5326	0,8752

Results

Abs (Formic Acid)	Formic Acid (g/L)
0,2820	0,018
0,2319	0,014
0,2463	0,015
0,6362	0,040
0,0969	0,006

Average amount of formic acid after polymer coating of 1 mg MOF (in 1mL coating supernatant, taking PGlu, PAMAM and BPEI into consideration):
(18 µg + 14 µg + 15 µg)/3 = 16 µg
Total amount of coordinatively bound formic acid per mg (after substraction of free formic acid):
16 µg – 6 µg = 10 µg
→ 10 µg formic acid / 1 mg MOF **≈ 1 w%**

Table S2. The values obtained from the FCS measurements of IgG, applying a 3-Component diffusion fit, where A_1 is the (size-weighted) relative amplitude of free dye ($A_1 = N_1 / N_{total}$), A_2 is the FITC-Alb relative amplitude ($A_2 = N_2 / N_{total}$), A_3 is the relative amplitude of the FITC-Alb fraction interacting with the Zr-*fum* and Zr-*fum*@polymer NPs ($A_3 = N_3 / N_{total}$), and D_3 is the respective diffusion coefficient of N_3.

	A_1	A_2	A_3	D_3 (µm²/s)	Ratio = A_3 / (A_2 + A_3)
IgG	0.26	0.74	-	-	-
IgG + Zr-*fum*	0.20	0.25	0.55	3.8	**0.69**
IgG + Zr-*fum*@PAA	0.16	0.28	0.56	2.0	**0.67**
IgG + Zr-*fum*@PGlu	0.21	0.34	0.45	3.7	**0.57**
IgG + Zr-*fum*@BPEI	0.22	0.41	0.37	0.72	**0.48**
IgG + Zr-*fum*@PAMAM	0.16	0.38	0.45	0.84	**0.54**
IgG + Zr-*fum*@PGlu-PSar	0.29	0.60	0.11	6.0	**0.15**

Table S3. The values obtained from the FCS measurements of Alb, applying a 3-Component diffusion fit, where A_1 is the (size-weighted) relative amplitude of free dye ($A_1 = N_1 / N_{total}$), A_2 is the FITC-Alb relative amplitude ($A_2 = N_2 / N_{total}$), A_3 is the relative amplitude of the FITC-Alb fraction interacting with the Zr-*fum* and Zr-*fum*@polymer NPs ($A_3 = N_3 / N_{total}$), and D_3 is the respective diffusion coefficient of N_3.

	A_1	A_2	A_3	D_3 (μm²/s)	Ratio = A_3 / (A_2 + A_3)
Alb	0.538	0.457	-	-	-
Alb + Zr-*fum*	0.573	0.427	0.001	0.011	0.001
Alb + Zr-*fum*@PAA	0.604	0.395	0.001	0.010	0.003
Alb + Zr-*fum*@PGlu	0.609	0.390	0.001	0.014	0.003
Alb + Zr-*fum*@BPEI	0.549	0.408	0.043	0.570	0.095
Alb + Zr-*fum*@PAMAM	0.517	0.479	0.004	0.140	0.009
Alb + Zr-*fum*@PGlu-PSar	0.604	0.396	-	-	-

5. Theoretical Estimate (w% formic acid per NP)

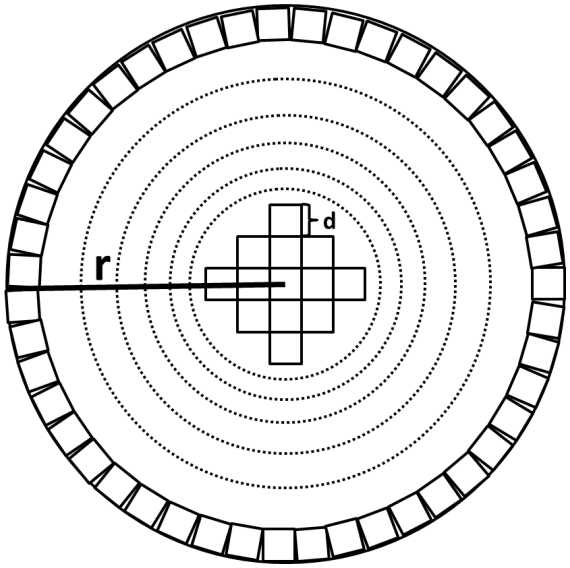

Figure „Theoretical Estimate“: Schematical drawing of a spherical Zr-*fum* NPs with radius r = 23 nm, consisting of unit cells with an edge length of d = 1,79 nm.

Assuming Zr-*fum* NPs to be spherical with an average diameter of 46 nm (from SEM; Figure S9), one derives a particle surface and volume of:

$$\boldsymbol{V_{NP} = \frac{4}{3}\pi r^3 = \frac{4}{3}\pi(23\ nm)^3 = 5.1 \cdot\ 10^4\ nm^3}$$

$$\boldsymbol{S_{NP} = 4\pi r^2 = 4\pi(23\ nm)^2 = 6.65\ \cdot\ 10^3\ nm^2}$$

The dimensions of a Zr-*fum* cubic unit cell were taken from Wißmann *et al.*[6] resulting in a volume of:

$$\boldsymbol{V_{UC} = d^3 =\ (1.79\ nm)^3 = 5.74 \cdot nm^3}$$

This results in a total number of unit cells per particle:

$$\boldsymbol{N_{total} = \frac{V_{NP}}{V_{UC}} = \frac{5.1 \cdot\ 10^4\ nm^3}{5.74 \cdot nm^3} = 8885}$$

The total number of unit cells on the external surface (which can carry formic acid) can be calculated, assuming the surface of a unit cell on the external surface to be

$$S_{UC} = d^2 = (1.79\ nm)^2 = 3.2\ nm^2$$

resulting in

$$N_{surface} = \frac{S_{NP}}{S_{UC}} = \frac{6.65\ \cdot\ 10^3\ nm^2}{3.2\ nm^2} = 2078$$

Considering 6 cubic faces of the unit cell as well as 6 fumaric acids, one fumaric acid (the one the external NP surface) will be theoretically replaced by formic acid. This means 2078 unit cells per NP consist of $[Zr_6O_4(OH)_4(O_2C–(CH)_2–CO_2)_5(HCOO)]$ = ①, while 8885 – 2078 = 6807 unit cells contain the usual chemical formula $[Zr_6O_4(OH)_4(O_2C–(CH)_2–CO_2)_6]$ ^{6} = ②. Taking into account the different atomic masses of internal ($M_{②}$) and external ($M_{①}$)unit cells, the total atomic mass per NP is:

$$M_{total} = M_{①} + M_{②} = 2078 \times 1293\ Da + 6807 \times 1362\ Da = 11.96 \cdot 10^6\ Da$$

The atomic mass of formic acid per particle can be calculated by:

$$M_{formic\ acid} = 2078 \times 45\ Da = 9.4 \cdot 10^4\ Da$$

The weight percent (w%) of formic acid in the material is therefore given by:

$$\frac{M_{formic\ acid}}{M_{total}} = \frac{9.4 \cdot 10^4\ Da}{11.96 \cdot 10^6\ Da} = 0.8\ w\%$$

This estimation is in very good agreement with experimental data, revealing approx. 1 w% of formic acid released by the coating procedure.

6. References

1. J. Hendrix, V. Baumgärtel, W. Schrimpf, S. Ivanchenko, M. A. Digman, E. Gratton, H.-G. Kräusslich, B. Müller, D. C. Lamb; Live-Cell Observation of Cytosolic HIV-1 Assembly Onset Reveals RNA-Interacting Gag Oligomers; *J. Cell Biol.,* 2015, **210**, 629-646.

2. W. Schrimpf, A. Barth, J. Hendrix, D. C. Lamb; PAM: A Framework for Integrated Analysis of Imaging, Single-Molecule, and Ensemble Fluorescence Data. *Biophys. J.*, 2018, **114**, 1518-1528.

3. G. Zahn, H. A. Schulze, J. Lippke, S. König, U. Sazama, M. Fröba and P. Behrens; A water-born Zr-based porous coordination polymer: Modulated synthesis of Zr-fumarate MOF; *Microporous Mesoporous Mater.*, 2015, **203**, 186-194.

4. J. Yoo, A. Birke, J. Kim, Y. Jang, S. Y. Song, S. Ryu, B. S. Kim, B. G. Kim, M. Barz, K. Char; Cooperative Catechol-Functionalized Polypept(o)ide Brushes and Ag Nanoparticles for Combination of Protein Resistance and Antimicrobial Activity on Metal Oxide Surfaces. *Biomacromolecules*, 2018, **19**, 1602-1613.

5. G. Socrates, *Infrared and Raman Characteristic Group Frequencies: Tables and Charts*, 3rd Edition edn. John Wiley and Sons, Ltd. (2001).

6. G. Wißmann, A. Schaate, S. Lilienthal, I.Bremer, A. M. Schneider, P. Behrens; Modulated Synthesis of Zr-fumarate MOF; *Microporous Mesoporous Mater.*, 2012, **152**, 64-70.

B.2. Paper 2: Linker Exchange via Migration along Backbone in Metal-Organic Frameworks

JACS
JOURNAL OF THE AMERICAN CHEMICAL SOCIETY
pubs.acs.org/JACS
Communication

Linker Exchange via Migration along the Backbone in Metal–Organic Frameworks

Nader Al Danaf, Waldemar Schrimpf, Patrick Hirschle, Don C. Lamb, Zhe Ji,* and Stefan Wuttke*

Cite This: *J. Am. Chem. Soc.* 2021, 143, 10541–10546
Read Online
ACCESS | Metrics & More | Article Recommendations | Supporting Information

ABSTRACT: In metal–organic frameworks (MOFs), organic linkers are subject to postsynthetic exchange (PSE) when new linkers reach sites of PSE by diffusion. Here, we show that during PSE, a bulky organic linker is able to penetrate narrow-window MOF crystals. The bulky linker migrates by continuously replacing the linkers gating the otherwise impassable windows and serially occupying an array of backbone sites, a mechanism we term *through-backbone diffusion*. A necessary consequence of this process is the accumulation of missing-linker defects along the diffusion trajectories. Using fluorescence intensity and lifetime imaging microscopy, we found a gradient of missing-linker defects from the crystal surface to the interior, consistent with the spatial progression of PSE. Our success in incorporating bulky functional groups via PSE extends the scope of MOFs that can be used to host sizable, sophisticated guest species, including large catalysts or biomolecules, which were previously deemed only incorporable into MOFs of very large windows.

Metal–organic frameworks (MOFs) are extended, porous structures built by connecting metal-containing clusters with organic linkers.[1] These rigid, sizable molecular building units create interconnected pore space amenable to guest incorporation and chemical functionalization, by, for instance, using organic linkers bearing chemical moieties of interest.[2,3] To incorporate a functionalized linker, a strategy termed postsynthetic exchange (PSE) has been developed, presynthesized MOFs are soaked in the solution of a new linker, which replaces the original linker without altering the overall MOF structures.[4−13] Applying PSE enables the synthesis of otherwise unattainable MOFs when *de novo* synthesis results in linker decomposition or amorphous products.[14]

When performing PSE, it is a common practice to choose a linker smaller than the window (*i.e.*, pore aperture) of the MOF, for fear that a larger linker will be blocked from accessing the interior of MOF crystals. This is based on the assumption that the new linker has to first diffuse through windows before reaching the site of PSE at a distant pore.[15] We sought to explore the possibility of performing PSE in a prototypical MOF, UiO-67,[16] using a bulky linker, biphenyl-4,4′-dicarboxylic acid attached with rhodamine b (BPDC-RB, Figure 1a), a fluorophore serving to report PSE progression. RB is small enough to fit in the octahedral pore in UiO-67, yet larger than the window (Figure 1b, Figure S5, and section S2 in the Supporting Information), through which diffusion cannot occur (Figure S6). Surprisingly, we observed a substantial amount of BPDC-RB incorporated into the interior of UiO-67 crystals. This is not due to the windows enlarged by missing-linkers (Figure S7); a low fraction of missing-linkers (<0.2%) was found in the UiO-67 crystals that we synthesized (Figure S7). Additionally, UiO-67 is a rather rigid MOF that cannot undergo excessive pore swelling or breathing necessary for accommodating incoming bulky linkers.[17] Hence, there must be a mechanism different from through-window diffusion (Figure 1c) for PSE.

We postulated that a bulky linker could migrate across a narrow-window MOF by continuously replacing the linkers gating the windows. When an original linker dissociates from the MOF backbone under PSE conditions,[18] it opens the otherwise narrow window,[19] allowing the new linker to move its bulky group from one pore to the other and then reinsert into the backbone (Figure 1d). The net result is that the new linker migrates along the MOF backbone by one pore; multiple rounds of these actions enable diffusion for a long distance within the crystal. We term this process *through-backbone diffusion* to distinguish it from the conventional *through-window diffusion*.

For migration from the crystal surface all the way to the center, through-backbone diffusion requires PSE to occur in every pore that the new linker passes through. Every time the linker transits toward the next pore, it has to first dissociate from the current site of the backbone, leaving behind a vacancy (i.e., missing-linker defect). This eventually results in an array of missing-linker defects along the diffusion trajectory (Figure 1d), provided that the defects are not healed by other free linkers. In contrast, through-window diffusion creates only one defect when the migrating linker departs from the backbone; no more defects are created because it passes through windows without PSE (Figure 1c).

Received: May 9, 2021
Published: July 6, 2021

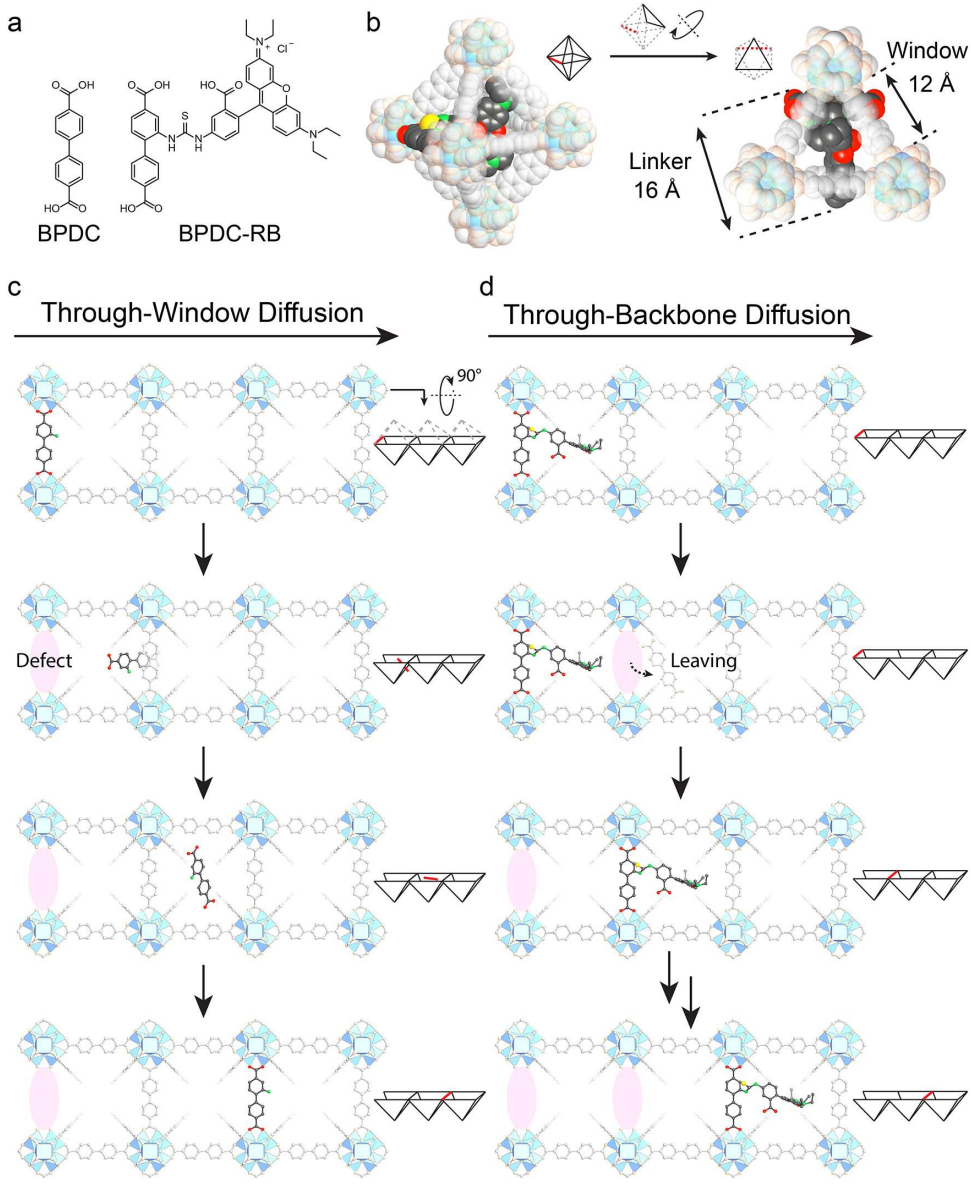

Figure 1. (a) Molecular structures of BPDC and BPDC-RB. (b) Space-filling model of an octahedron unit in UiO-67, which comprises a BPDC-RB linker, and a projection of BPDC-RB beneath a triangular window. (c) Structure illustration of through-window diffusion of a small linker and (d) through-backbone diffusion of the bulky linker BPDC-RB in UiO-67. The horizontal arrows indicate the average direction of many diffusion events, which follows the concentration gradient established from the crystal surface to its center. Color code for BPDC-RB: C, gray; O, red; S, yellow; N, green. Color code for other UiO-67 components: Zr cluster, blue; C and O, off-white.

Here, we use fluorescence imaging to monitor the migration of the bulky BPDC-RB linker across UiO-67 crystals and observed that the PSE propagated from the surface to the center of the crystals, establishing a concentration gradient of the new linker. To investigate how the bulky linker can migrate across the narrow-window MOF, we performed fluorescence lifetime imaging microscopy (FLIM)[20] to examine the change in the chemical environment[21−23] along the PSE gradient. The lifetime was observed to decline toward the edge of the crystal, indicating the accumulation of missing-linker defects during PSE, a distinctive feature supporting the through-backbone diffusion mechanism.

UiO-67 was synthesized as single crystals (~50 μm), far larger than the spatial resolution of conventional fluorescence microscopy, therefore serving as a suitable object for our studies. The obtained crystals were subjected to PSE through incubation with BPDC-RB in a mixture of methanol (MeOH) and *N*-*N*′-dimethylformamide (DMF) at a ratio of 80:20 (v/v). We chose this solvent mixture (MeOH/DMF) because it has been reported that MeOH facilitates linker substitution in

https://doi.org/10.1021/jacs.1c04804
J. Am. Chem. Soc. 2021, 143, 10541−10546

UiO-67[18] and DMF allows for high temperature incubation. To investigate the effect of time and temperature on PSE, incubation was performed at room temperature or 100 °C for 1 day or for 7 days (1d-RT, 1d-100 °C, 7d-RT, and 7d-100 °C). After PSE, we did not observe any change in crystal morphology and crystallinity (Figure S9) or any photophysical damage to the RB moiety (Figures S10–S12 and Table S1).

Fluorescence intensity imaging microscopy was employed to measure the spatial distribution of BPDC-RB incorporated inside UiO-67 crystals. These crystals, octahedral in shape (Figure 2a), were oriented along the [111] direction, with

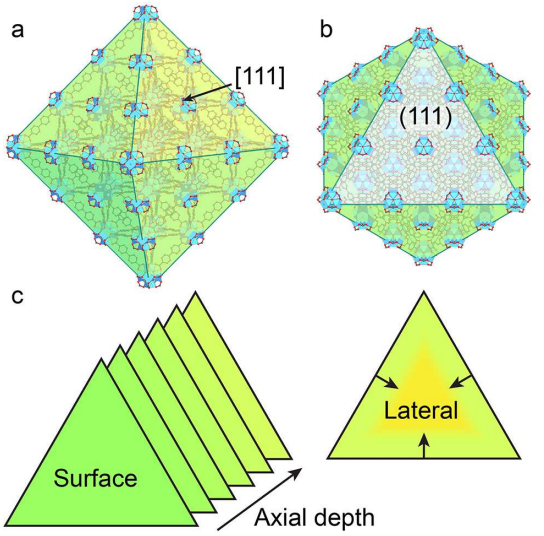

Figure 2. (a) Schematic diagram of an octahedral crystal of UiO-67, (b) crystal is oriented along the [111] direction, and (c) fluorescence and lifetime images were collected both laterally and axially.

triangle and hexagonal cross sections displayed on the focal plane (Figure 2b). The fluorescence intensity of RB was mapped in the focal plane (lateral) and along the optical axis (axial) (Figure 2c), both displaying a profile that peaks at the surface and slowly decreases toward the center (Figure 3).

We noticed that progression of PSE is highly dependent on the incubation temperature. A significant increase in fluorescence was observed when performing PSE at 100 °C as compared to RT (Figure 3a–d). At RT, a longer reaction time led to more PSE on the surface but was not effective in promoting PSE in the crystal interior. In contrast, longer reaction times at 100 °C resulted in more BPDC-RB penetrating into the crystals. The solvent dependence of PSE was tested by using DMF as an alternative solvent. For DMF, PSE was found sluggish and required high temperature to achieve any noticeable progress (Figure S14). The heterogeneous distribution of BPDC-RB, which concentrates on the surface and declines toward the crystal interior, reveals that linker diffusion becomes the rate-limiting step of PSE. This step, unlike the free diffusion of linkers in solution and in large-window MOFs, likely involves a high energy barrier, indicated by the dependence of PSE progression on temperature, time (weekly scale), and solvent. In fact, the diffusion of RB alone is prohibited inside UiO-67. After soaking UiO-67 crystals with RB in DMF for 7 days, only fluorescence emission from the

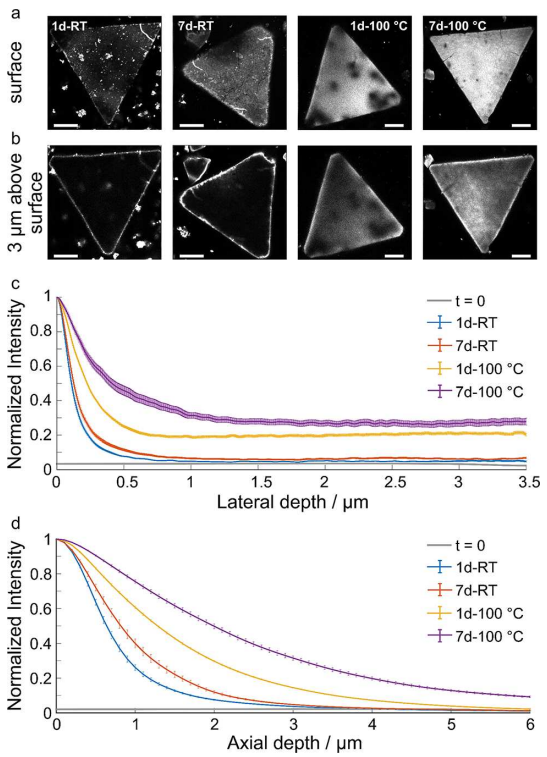

Figure 3. Fluorescence imaging of UiO-67 crystals after PSE in MeOH/DMF: (a) fluorescence images taken at the surface and (b) 3 μm above the surface. The scale bar is 15 μm. (c) Fluorescence intensity profile along lateral and (d) axial directions (error bars from measurements on 8–10 crystals of UiO-67 per condition). The curves recorded at t = 0 (before any PSE takes place) display the autofluorescence of the pristine crystals (Figure S8).

crystal surface was observed (Figure S6), indicating that RB itself cannot diffuse through the window, let alone the bulkier BPDC-RB. Alternatively, through-backbone diffusion becomes a plausible mechanism to account for the slow penetration of BPDC-RB.

To elucidate the mechanism of linker migration, we employed FLIM, a technique used to acquire spatially resolved fluorescence lifetime information. In the phasor approach, the obtained fluorescence lifetime decay (Figure 4a) is transformed into Fourier space followed by a graphical translation into a phasor plot,[24,25] with long lifetimes near (0.5, 0.5) and short ones near (1, 0) (Figure 4b, section S1.6 in the Supporting Information). In a previous study, we established a correlation between the fluorescence lifetime and local defects in UiO-67: more defects result in shorter lifetime.[26] Thus, by using BPDC-RB as both a PSE participant and a fluorescence lifetime reporter, we investigated the formation and spatial distribution of defects accompanying the progression of PSE. The measured lifetime values vary from 0.65 ns (high defect level) to 2.91 ns (low defect level) (Figures S16–S20). A lifetime of 2.91 ns is even larger than the lifetime of BPDC-RB in solvents (2.1–2.3 ns) (Table S1), suggesting suppression of nonradiative pathways and stabilization of fluorescence in the MOF.

https://doi.org/10.1021/jacs.1c04804
J. Am. Chem. Soc. 2021, 143, 10541–10546

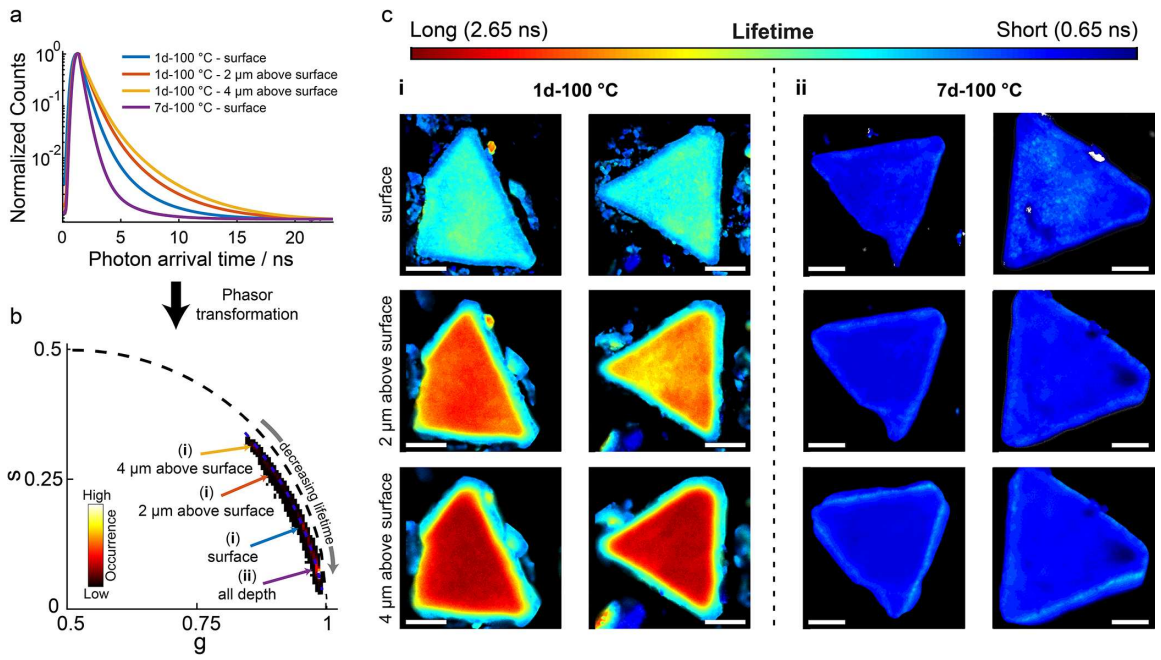

Figure 4. Fluorescence lifetime analysis of UiO-67 crystals after PSE in MeOH/DMF: (a) fluorescence lifetime decay, (b) phasor plot of lifetime, and (c) FLIM images of UiO-67 crystals. The scale bar is 15 μm.

For PSE conducted for 1 day at 100 °C, the FLIM results displayed significant differences in lifetime between the crystal surface and interior (Figure 4c(i)). The lifetimes measured at the surface (1.36 ± 0.22 ns) are shorter than those inside the crystals. The FLIM images taken at 2 μm above surface showed a lifetime of 2.14 ± 0.20 ns at the core while the edge exhibited the same short lifetime observed for the surface plane. By shifting the focal plane deeper (4 μm above surface), even longer lifetimes (2.55 ± 0.15 ns) were observed in the crystal core, establishing a gradient of lifetime increasing from the edge to the center. Interestingly, such a gradient in lifetime is analogous to the previously measured fluorescence profile, which exhibits a decay in fluorescence intensity from the outside toward inside of the crystal. This correlation suggests that the progression of PSE is accompanied by the generation of missing-linker defects, i.e., PSE leaves defects in its wake.

There are two possible origins for the missing-linker defects. The first possibility is that MeOH, a PSE solvent, can replace the original BPDC linker in UiO-67 by coordinating to the zirconium clusters. However, this process alone cannot establish and maintain a defect gradient more than 1 day, because the diffusion of methanol is largely unimpeded due to its small size. This claim is supported by previous observations that the incorporation of linker-substituting MeOH into UiO-67 plateaued within 1 day, even at 40 °C.[18] An alternative explanation for the observed gradient of missing-linker defects would be that these defects are the product of PSE according to the through-backbone diffusion mechanism. This mechanism agrees well with our observation that there are more defects on the surface where many through-backbone trajectories start from and fewer defects in the core where only a few PSE events reach this depth.

Prolonged PSE for 7 days at 100 °C resulted in a higher level of fluorescence quenching; a shorter lifetime of 0.90 ± 0.21 ns was found. Interestingly, a homogeneous distribution of short lifetime was observed both at the surface and deeply in the interior of the crystals (Figure 4c(ii)). This is in contrast to the lifetime gradient observed for 1d-100 °C and matches the trend of PSE progression: the BPDC-RB concentration increases throughout the whole crystal when PSE is prolonged to 7 days (Figure 3c,d). Nevertheless, compared with the interior, the surface still has a higher level of PSE, but its defect level does not increase correspondingly. This might result from an equilibrium between defect generation and healing at high levels of PSE; replaced BPDC linkers can be reincorporated and thus heal missing-linker defects during their migration toward the outside, the opposite direction of BPDC-RB migration. This hypothesis is supported by a careful investigation of the FLIM data, which exhibits slightly higher lifetime at the surfaces compared to the interior (Figure S20).

We further investigated PSE at RT and found long lifetimes (Figures S16–S18) and hence low concentrations of defects, consistent with the low level of BPDC-RB incorporation. Extension of PSE from 1 day to 7 days led to a moderate decrease in lifetime. Likewise, PSE conducted in pure DMF resulted in a similar yet less pronounced temperature dependence: higher fluorescence lifetimes were observed at RT as compared to 100 °C, the latter showing a lifetime gradient from outside toward inside (Figures S21–S25). We argue that PSE at RT is in general unproductive because it failed to initiate the dissociation of BPDC, an energetically expensive step yet a prerequisite for the subsequent through-backbone diffusion of BPDC-RB. Once this energy barrier is overcome and the migration of BPDC-RB is initiated, more and more missing-linker defects will be created. These defects

https://doi.org/10.1021/jacs.1c04804
J. Am. Chem. Soc. 2021, 143, 10541−10546

can act to accelerate the following PSE events by opening the narrow windows, making the whole process autocatalytic. This highlights the importance of finding the optimal conditions for preforming PSE with bulky linkers.

Our studies of PSE using BPDC-RB present a unique scenario where only through-backbone diffusion is possible. For linkers smaller than the MOF window, we envision that both through-backbone diffusion and through-window diffusion can occur. PSE will proceed via the mechanism that is most efficient. We expect that PSE via through-backbone diffusion is applicable to many other MOFs, allowing for the incorporation of sizable, sophisticated functional groups.

■ ASSOCIATED CONTENT

Supporting Information

The Supporting Information is available free of charge at https://pubs.acs.org/doi/10.1021/jacs.1c04804.

Experimental, crystallographic, photophysical, and microscopy data including PXRD, SEM, fluorescence spectroscopy, and FLIM results (PDF)

■ AUTHOR INFORMATION

Corresponding Authors

Zhe Ji − *Department of Chemistry, University of California-Berkeley, Berkeley, California 94720, United States;* Present Address: Department of Chemistry, Stanford University, Stanford, CA 94305; orcid.org/0000-0002-8532-333X; Email: zhej@stanford.edu

Stefan Wuttke − *Department of Chemistry and Center for NanoScience, University of Munich, 81377 Munich, Germany; BCMaterials (Basque Center for Materials, Applications & Nanostructures), 48940 Leioa, Spain; IKERBASQUE, Basque Foundation for Science, 48009 Bilbao, Spain;* orcid.org/0000-0002-6344-5782; Email: stefan.wuttke@bcmaterials.net

Authors

Nader Al Danaf − *Department of Chemistry and Center for NanoScience, University of Munich, 81377 Munich, Germany*

Waldemar Schrimpf − *Department of Chemistry and Center for NanoScience, University of Munich, 81377 Munich, Germany*

Patrick Hirschle − *Department of Chemistry and Center for NanoScience, University of Munich, 81377 Munich, Germany*

Don C. Lamb − *Department of Chemistry and Center for NanoScience, University of Munich, 81377 Munich, Germany;* orcid.org/0000-0002-0232-1903

Complete contact information is available at: https://pubs.acs.org/10.1021/jacs.1c04804

Notes

The authors declare no competing financial interest.

■ ACKNOWLEDGMENTS

We thank O. M. Yaghi (University of California, Berkeley) for providing resources, mentorship, support, and helpful discussions. We thank H. Wang (University of California, Berkeley) for help with the NMR data analysis. We are grateful for financial support from the Deutsche Forschungsgemeinschaft (DFG) and the SFB1032 (Project-B3, D.C.L.). We also thankfully acknowledge the support of the Excellence Cluster Nanosystems Initiative Munich (NIM), the Center for NanoScience Munich (CeNS), and the LMU innovative BioImaging Network.

■ REFERENCES

(1) Furukawa, H.; Cordova, K. E.; O'Keeffe, M.; Yaghi, O. M. The Chemistry and Applications of Metal-Organic Frameworks. *Science* **2013**, *341* (6149), 1230444.

(2) Eddaoudi, M.; Kim, J.; Rosi, N.; Vodak, D.; Wachter, J.; O'Keeffe, M.; Yaghi, O. M. Systematic Design of Pore Size and Functionality in Isoreticular MOFs and Their Application in Methane Storage. *Science* **2002**, *295* (5554), 469−472.

(3) Ji, Z.; Wang, H.; Canossa, S.; Wuttke, S.; Yaghi, O. M. Pore Chemistry of Metal−Organic Frameworks. *Adv. Funct. Mater.* **2020**, *30* (41), 2000238.

(4) Cohen, S. M. The Postsynthetic Renaissance in Porous Solids. *J. Am. Chem. Soc.* **2017**, *139* (8), 2855−2863.

(5) Cohen, S. M. Postsynthetic Methods for the Functionalization of Metal−Organic Frameworks. *Chem. Rev.* **2012**, *112* (2), 970−1000.

(6) Haneda, T.; Kawano, M.; Kawamichi, T.; Fujita, M. Direct Observation of the Labile Imine Formation through Single-Crystal-to-Single-Crystal Reactions in the Pores of a Porous Coordination Network. *J. Am. Chem. Soc.* **2008**, *130* (5), 1578−1579.

(7) Wang, Z.; Cohen, S. M. Postsynthetic Covalent Modification of a Neutral Metal−Organic Framework. *J. Am. Chem. Soc.* **2007**, *129* (41), 12368−12369.

(8) Wu, C.-D.; Hu, A.; Zhang, L.; Lin, W. A Homochiral Porous Metal−Organic Framework for Highly Enantioselective Heterogeneous Asymmetric Catalysis. *J. Am. Chem. Soc.* **2005**, *127* (25), 8940−8941.

(9) Seo, J. S.; Whang, D.; Lee, H.; Jun, S. I.; Oh, J.; Jeon, Y. J.; Kim, K. A homochiral metal−organic porous material for enantioselective separation and catalysis. *Nature* **2000**, *404* (6781), 982−986.

(10) Kiang, Y. H.; Gardner, G. B.; Lee, S.; Xu, Z.; Lobkovsky, E. B. Variable Pore Size, Variable Chemical Functionality, and an Example of Reactivity within Porous Phenylacetylene Silver Salts. *J. Am. Chem. Soc.* **1999**, *121* (36), 8204−8215.

(11) Kim, M.; Cahill, J. F.; Fei, H.; Prather, K. A.; Cohen, S. M. Postsynthetic Ligand and Cation Exchange in Robust Metal−Organic Frameworks. *J. Am. Chem. Soc.* **2012**, *134* (43), 18082−18088.

(12) Deria, P.; Mondloch, J. E.; Karagiaridi, O.; Bury, W.; Hupp, J. T.; Farha, O. K. Beyond post-synthesis modification: evolution of metal−organic frameworks via building block replacement. *Chem. Soc. Rev.* **2014**, *43* (16), 5896−5912.

(13) Karagiaridi, O.; Lalonde, M. B.; Bury, W.; Sarjeant, A. A.; Farha, O. K.; Hupp, J. T. Opening ZIF-8: a catalytically active zeolitic imidazolate framework of sodalite topology with unsubstituted linkers. *J. Am. Chem. Soc.* **2012**, *134* (45), 18790−6.

(14) Karagiaridi, O.; Bury, W.; Sarjeant, A. A.; Stern, C. L.; Farha, O. K.; Hupp, J. T. Synthesis and characterization of isostructural cadmium zeolitic imidazolate frameworks via solvent-assisted linker exchange. *Chemical Science* **2012**, *3* (11), 3256−3260.

(15) Boissonnault, J. A.; Wong-Foy, A. G.; Matzger, A. J. Core−Shell Structures Arise Naturally During Ligand Exchange in Metal−Organic Frameworks. *J. Am. Chem. Soc.* **2017**, *139* (42), 14841−14844.

(16) Cavka, J. H.; Jakobsen, S.; Olsbye, U.; Guillou, N.; Lamberti, C.; Bordiga, S.; Lillerud, K. P. A New Zirconium Inorganic Building Brick Forming Metal Organic Frameworks with Exceptional Stability. *J. Am. Chem. Soc.* **2008**, *130* (42), 13850−13851.

(17) Liu, Y.; Ma, Y.; Yang, J.; Diercks, C. S.; Tamura, N.; Jin, F.; Yaghi, O. M. Molecular Weaving of Covalent Organic Frameworks for Adaptive Guest Inclusion. *J. Am. Chem. Soc.* **2018**, *140* (47), 16015−16019.

(18) Marreiros, J.; Caratelli, C.; Hajek, J.; Krajnc, A.; Fleury, G.; Bueken, B.; De Vos, D. E.; Mali, G.; Roeffaers, M. B. J.; Van Speybroeck, V.; Ameloot, R. Active Role of Methanol in Post-Synthetic Linker Exchange in the Metal−Organic Framework UiO-66. *Chem. Mater.* **2019**, *31* (4), 1359−1369.

(19) Morabito, J. V.; Chou, L.-Y.; Li, Z.; Manna, C. M.; Petroff, C. A.; Kyada, R. J.; Palomba, J. M.; Byers, J. A.; Tsung, C.-K. Molecular

Encapsulation beyond the Aperture Size Limit through Dissociative Linker Exchange in Metal−Organic Framework Crystals. *J. Am. Chem. Soc.* **2014**, *136* (36), 12540−12543.
(20) Becker, W. Fluorescence lifetime imaging–techniques and applications. *J. Microsc.* **2012**, *247* (2), 119−36.
(21) Ameloot, R.; Vermoortele, F.; Hofkens, J.; De Schryver, F. C.; De Vos, D. E.; Roeffaers, M. B. Three-dimensional visualization of defects formed during the synthesis of metal-organic frameworks: a fluorescence microscopy study. *Angew. Chem., Int. Ed.* **2013**, *52* (1), 401−5.
(22) Schrimpf, W.; Ossato, G.; Hirschle, P.; Wuttke, S.; Lamb, D. C. Investigation of the Co-Dependence of Morphology and Fluorescence Lifetime in a Metal-Organic Framework. *Small* **2016**, *12* (27), 3651−7.
(23) Connolly, B. M.; Aragones-Anglada, M.; Gandara-Loe, J.; Danaf, N. A.; Lamb, D. C.; Mehta, J. P.; Vulpe, D.; Wuttke, S.; Silvestre-Albero, J.; Moghadam, P. Z.; Wheatley, A. E. H.; Fairen-Jimenez, D. Tuning porosity in macroscopic monolithic metal-organic frameworks for exceptional natural gas storage. *Nat. Commun.* **2019**, *10*, 2345.
(24) Digman, M. A.; Caiolfa, V. R.; Zamai, M.; Gratton, E. The Phasor Approach to Fluorescence Lifetime Imaging Analysis. *Biophys. J.* **2008**, *94* (2), L14−L16.
(25) Redford, G. I.; Clegg, R. M. Polar Plot Representation for Frequency-Domain Analysis of Fluorescence Lifetimes. *J. Fluoresc.* **2005**, *15* (5), 805.
(26) Schrimpf, W.; Jiang, J.; Ji, Z.; Hirschle, P.; Lamb, D. C.; Yaghi, O. M.; Wuttke, S. Chemical diversity in a metal-organic framework revealed by fluorescence lifetime imaging. *Nat. Commun.* **2018**, *9*, 1647.

https://doi.org/10.1021/jacs.1c04804
J. Am. Chem. Soc. 2021, 143, 10541−10546

Supporting Information

Linker Exchange via Migration along Backbone in Metal-Organic Frameworks

Nader Al Danaf,[†] Waldemar Schrimpf,[†] Patrick Hirschle,[†] Don C. Lamb,[†] Zhe Ji,[*,‡,§] and Stefan Wuttke,[*,†,∥,⊥]

[†] Department of Chemistry and Center for NanoScience, University of Munich, Butenandtstraße 5-13, 81377 Munich, Germany.

[‡] Department of Chemistry, University of California-Berkeley, Berkeley, California 94720.

[§] Present address: Department of Chemistry, Stanford University, Stanford, California 94305.

[∥] BCMaterials (Basque Center for Materials, Applications & Nanostructures), Bldg. Martina Casiano, 3rd. Floor, Barrio Sarriena s/n, 48940, Leioa, Spain.

[⊥] IKERBASQUE, Basque Foundation for Science, 48009 Bilbao, Spain.

* zhej@stanford.edu, stefan.wuttke@bcmaterials.net

able of Contents

1. Experimental Section

1.1. Chemicals and supplies.

Anhydrous N,N-dimethylformamide (DMF), anhydrous methanol, and glacial acetic acid were obtained from EMD Millipore Chemicals. Ethyl acetate (99.9%, HPLC Plus), ethanol (≥ 99.5%, ACS Reagent), isopropyl alcohol (≥ 99.5%, BioReagent), tetrahydrofuran (THF, ≥ 99.9%, for high performance liquid chromatography (HPLC)), nitric acid (70%, ACS Reagent), sulfuric acid (95.0–98.0%, ACS Reagent), hydrochloric acid (37%, ACS Reagent), sulfuric acid (95.0–98.0%, ACS Reagent), hydrochloric acid (37%, ACS Reagent), sodium bicarbonate (BioReagent), sodium sulfate (≥ 99.0, ACS Reagent), palladium on carbon (Pd/C, 10 wt.% loading), potassium hydroxide (90%), zirconium chloride ((≥ 99.5%, trace metal basis), BPDC (97%), dimethyl biphenyl-4,4'- dicarboxylate (99%), and rhodamine B-isothiocyanate (RB, mixed isomers) were obtained from Sigma-Aldrich. Ultra-high-purity grade H_2 gas (Praxair, 99.999% purity) was used for the hydrogenation reaction. All starting materials, reagents, and solvents were used without further purification.

1.2. Synthesis of dye-functionalized linkers.

The dye-modified linkers were synthesized in a multi-step procedure (Fig. S1). The synthesis procedure is illustrated in Figure S1. Dimethyl 2-nitrobiphenyl-4,4'-dicarboxylate (II): A solution of 10 g (37 mmol) of dimethyl biphenyl-4,4'-dicarboxylate (I) in 100 mL of concentrated sulfuric acid was cooled to 0 °C and a mixture of 5 mL of 58% nitric acid and 7.5 mL of concentrated sulfuric acid was added dropwise over a period of 30 min under stirring, maintaining the temperature at 0–5 °C. The mixture was then stirred for 1 h at 0–5 °C, diluted with 100 mL of water, and extracted with ethyl acetate. The extract was washed with water and a solution of sodium bicarbonate (7.5%), dried over anhydrous sodium sulfate and evaporated. The residue was recrystallized from isopropyl alcohol. Yield: 9.9 g (31 mmol, 85%). 1H NMR (600 MHz, $CDCl_3$), parts per million [p.p.m.]: 3.98 (s, 3H), 4.02 (s, 3H), 7.43 (d, *J* = 8.4 Hz, 2H), 7.57 (d, *J* = 8.0 Hz, 1H), 8.14 (d, *J* = 8.4 Hz, z2H), 8.32 (dd, *J* = 8.0, 1.7 Hz, 1H), 8.58 (d, *J* = 1.7 Hz, 1H) (Fig. S2).

Dimethyl 2-aminobiphenyl-4,4'-dicarboxylalte (III): A mixture of 9.9 g (31 mmol) of compound II, 100 mL of acetic acid, and 5 g of 10% Pd/C in a high-pressure reactor was hydrogenated at room temperature using a hydrogen pressure of 10–50 atm until hydrogen was no longer consumed. The mixture was filtered and acetic acid in the filtrate was removed under vacuum. The crude product was recrystallized from ethanol. Yield: 8.8 g (29 mmol, 94%). 1H NMR (600 MHz, $CDCl_3$), [p.p.m.]: 3.93 (broad s, 2H), 3.94 (s, 3H), 3.98 (s, 3H), 7.21 (d, *J* = 8.0 Hz, 1H), 7.47 (d, *J* = 1.6 Hz, 1H), 7.51 (dd, *J* = 8.0, 1.6 Hz, 1H), 7.58 (d, *J* = 8.5 Hz, 2H), 8.15 (d, *J* = 8.5 Hz, 2H) (Fig. S3).

2-Aminobiphenyl-4,4'-dicarboxylic acid (NH_2-BPDC, IV): A solution of 4.95 g (20 mmol), compound III, in THF (180 mL) and MeOH (130 mL) was mixed with a solution of potassium hydroxide (10 g, 178 mmol) in water (200 mL). The reaction mixture was heated and allowed to reflux overnight. After all the volatiles were removed under vacuum, it was diluted with 200 mL of water, and acidified with 6 M hydrochloric acid until a pH value of 2 was obtained. The precipitates were collected, washed with water and dried in air. The yield was 4.3 g (17 mmol, 85%). 1H NMR (400 MHz, dimethyl sulfoxide-d6 (DMSO-d6)), [p.p.m.]: 5.18 (s, 2H), 7.11 (d, *J* = 7.9 Hz, 1H), 7.21 (dd, *J* = 7.9 Hz, 2H), 7.41 (s, 1H), 7.57 (d, *J* = 8.3 Hz, 2H), 8.01 (d, *J* = 8.3 Hz, 2H), 12.84 (s, 2H) (Fig. S4).

2-RhodamineB-isothiocyanate-biphenyl-4,4'-dicarboxylic acid (BPDC-RB, VI): A solution of 0.25 g (0.95 mmol) of compound IV in DMF (5 mL) was added to 0.51 g (0.95 mmol) of Rhodamine B isothiocyanate (RB, mixed isomers, V). The reaction solution was stirred for 24 h at room temperature. The mixture was then diluted with 100 mL of 1 M hydrochloric acid. The precipitates were collected by filtration, washed with water and dried in air. The crude product was subjected to purification by HPLC preparation (stationary phase: C18; mobile phase: MeOH/water/0.1% TFA). The eluent was freeze-dried and the orange solid was collected. The yield was 0.30 g (0.36 mmol, 38%). MS (ESI+, m/z): [M] calculated for $C_{43}H_{41}O_7N_4S^+$, 757.27; found, 757.30.

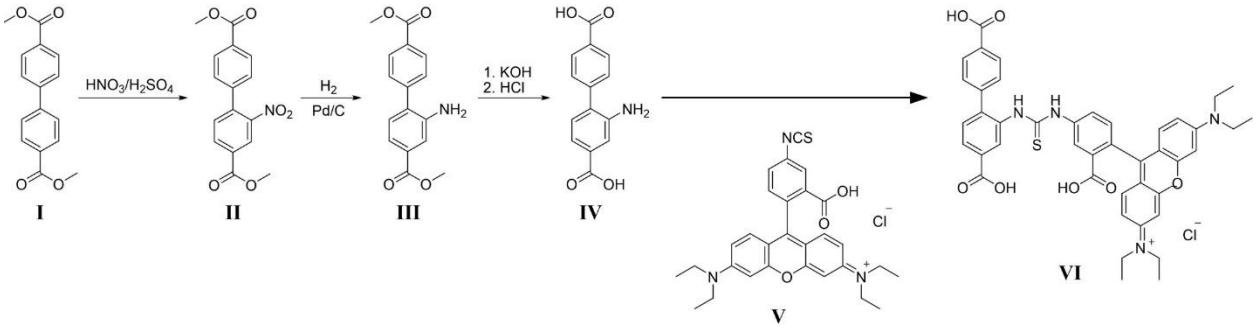

Figure S1: Synthetic pathway to the BPDC-RB linker.

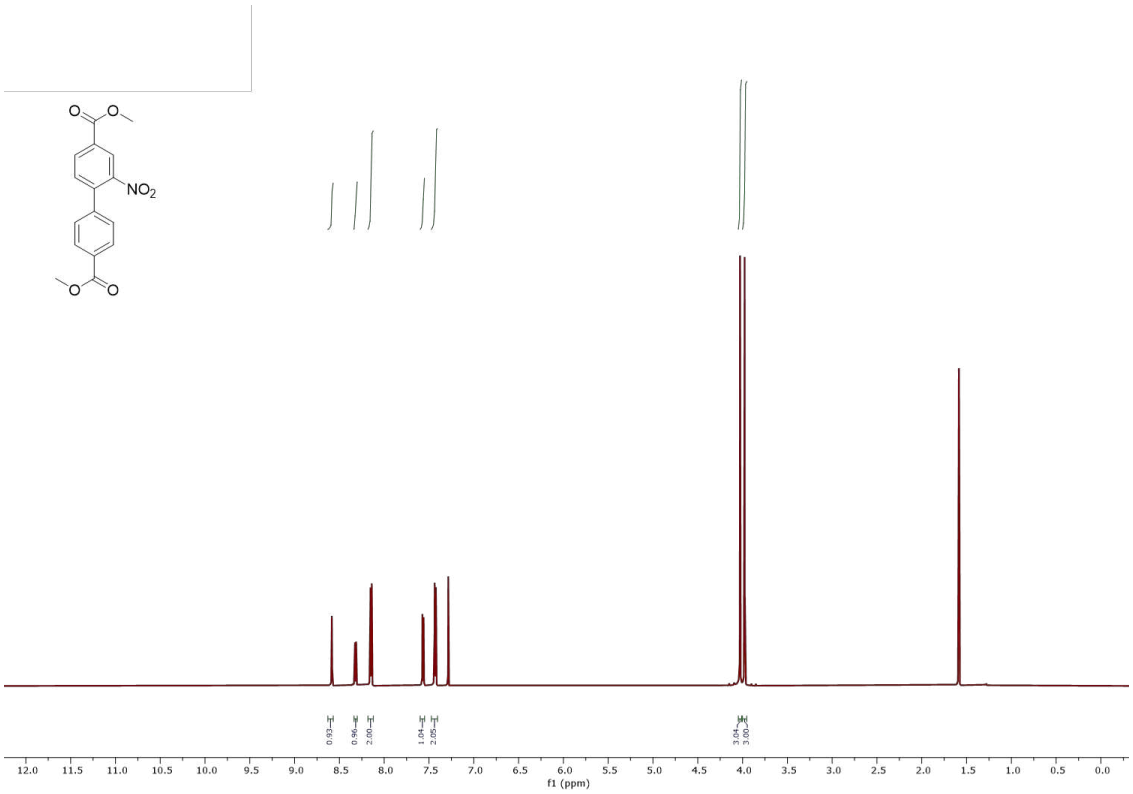

Figure S2: Liquid ^{1}H NMR spectrum of dimethyl 2-nitrobiphenyl-4,4'-dicarboxylate in $CDCl_3$.

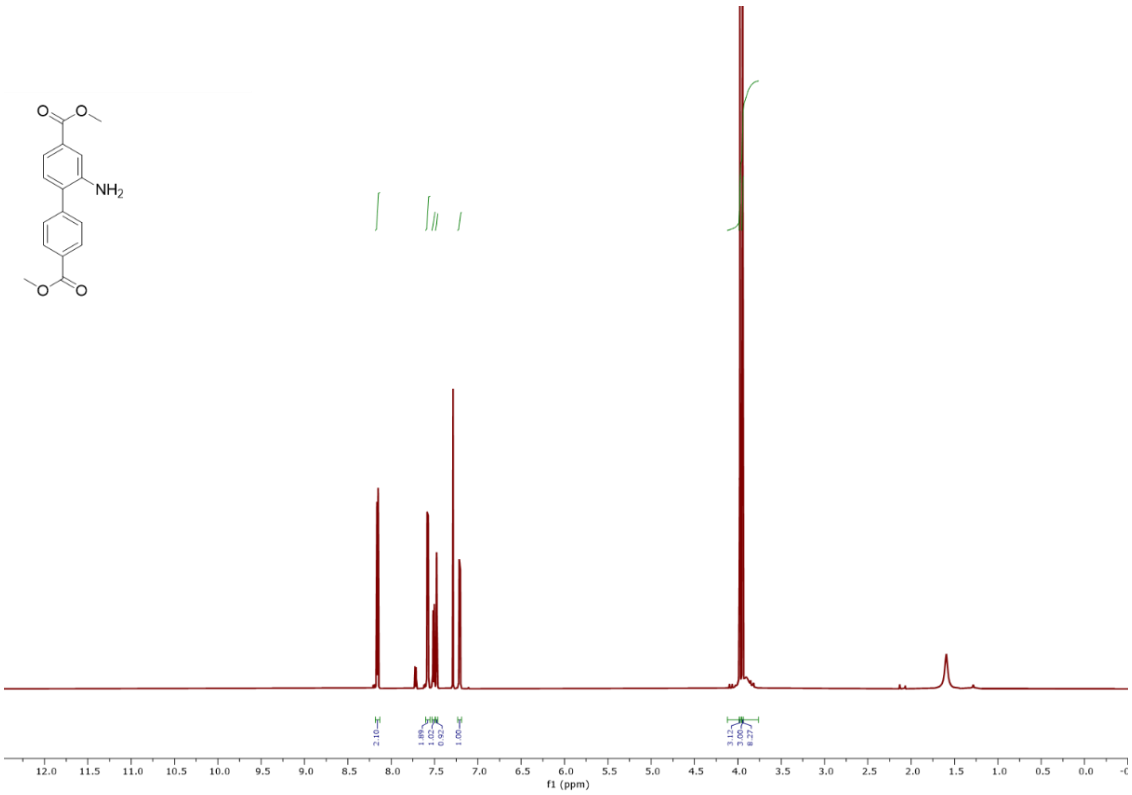

Figure S3: Liquid ^{1}H NMR spectrum of dimethyl 2-aminobiphenyl-4,4'-dicarboxylalte in $CDCl_3$.

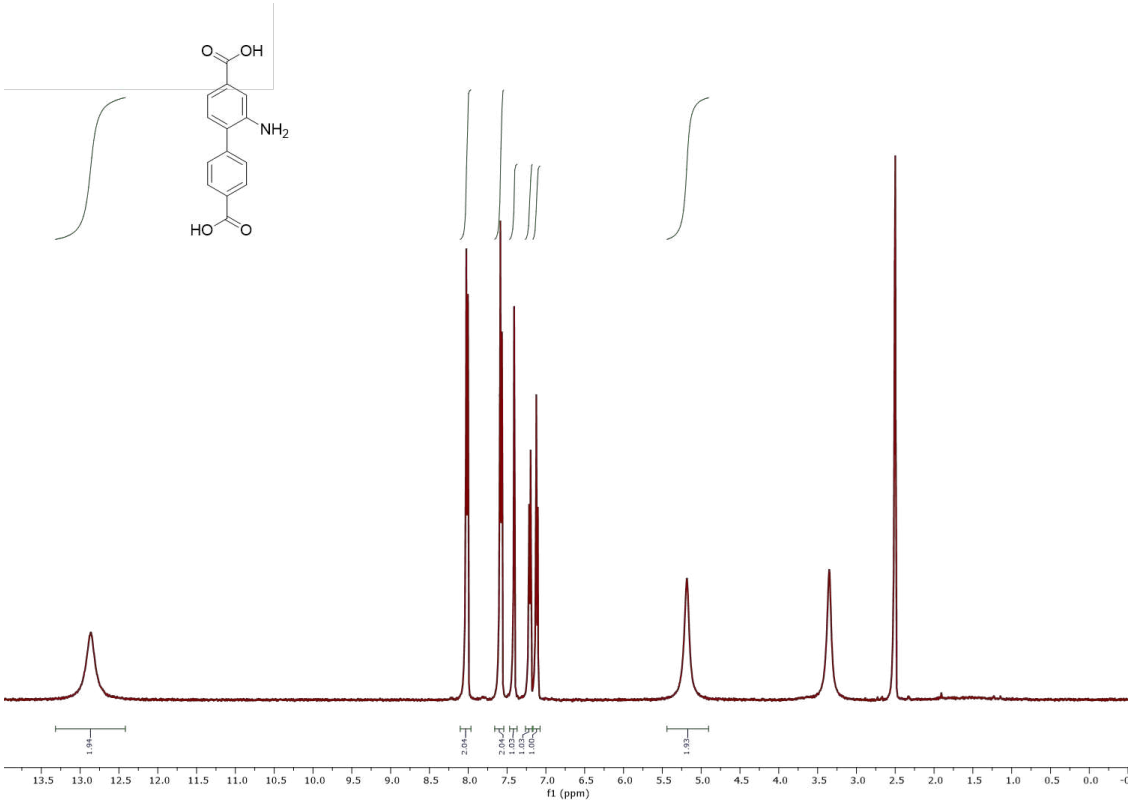

Figure S4: Liquid ^{1}H NMR spectrum of 2-aminobiphenyl-4,4'-dicarboxylic acid in DMSO-d6.

1.3. Synthesis of large crystal UiO-67.

Large, single UiO-67 crystals were synthesized following the procedure of Ko et al.[1] A mixture of BPDC (85 mg, 0.35 mmol), zirconium(IV) chloride (82 mg, 0.35 mmol) and benzoic acid (1.28 g, 10.5 mmol) was dissolved in DMF (20 mL) in a 20 mL vial. The vial was capped and heated in an isothermal oven at 120 °C for 2 days to yield octahedral-shaped crystals of ~ 50 µm diameter. The reaction mixture was allowed to cool down to room temperature and then washed with DMF (three times per day for 3 days) and acetone (three times per day for 3 days). The solvent exchanged samples were then evacuated at 120 °C to 30 mTorr.

1.4. Post-synthetic linker exchange (PSE).

The fluorophore-labelled linker (2-amino-biphenyl-4,4'-dicarboxylic acid labelled with rhodamine B isothiocyanate, BPDC-RB) was incorporated into UiO-67 via a solvothermal approach: Each sample was prepared by immersing UiO-67 (~3 mg) with BPDC-RB (0.1 mg/mL) in DMF or a 20% DMF / 80% MeOH mixture using a tightly capped 25 ml glass bottle (classic version Duran bottle, Schott) for the reaction. This reaction mixture was incubated for four different time periods: 1 day and 7 days at RT and 1 day and 7 days at 100 °C in a glass reactor (Scheme S1). Subsequently, the resulting product was washed via centrifuging (2000 rpm, 3 min) first with DMF (3 x 5 mL) and then with MeOH (3 x 5 mL). Afterwards, the samples were dried at 70 °C for 8 hours.

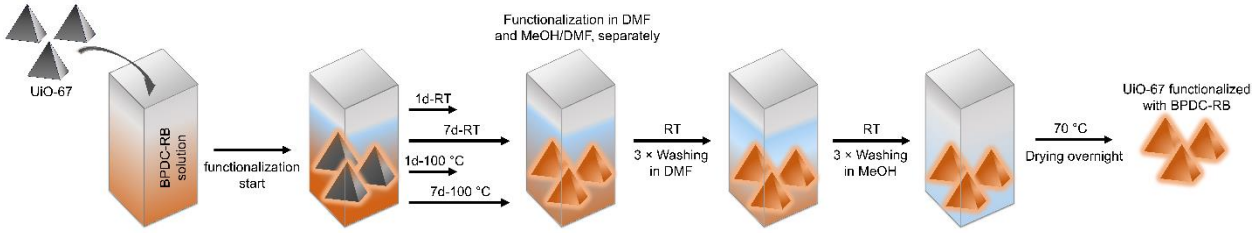

Scheme S1: Schematic representation showing the procedure followed to functionalize the UiO-67 samples with BPDC-RB.

1.5. Fluorescence measurements on digested UiO-67 crystals.

The fraction of dyes in the UiO-67 samples was determined via fluorimetry. The incorporated BPDC-RB within the UiO-67 framework was set free via incubation of the host-particles in a digestion solution. For the different functionalization experiments, 0.25 mg per condition was used, where the respective samples were given to a mixture of CsF (0.23 mol/L) in DMSO/H_2O (3 mL), in a ratio of 9:5 DMSO/H_2O (v/v). The samples were then sonicated for 30 minutes leading to the destruction of the UiO-67. The digested samples were allowed to sit for two hours after which bulk fluorescence experiments were performed to determine the amount of incorporated BPDC-RB linker and the exchange ratio observed for the different PSE conditions.

Measurements were done on an FLS 1000 Fluorimeter (Edinburgh Instruments). A pulsed laser diode at 561 nm (LDH-FA-560, PicoQuant) was used for measuring the different emission spectra and the bulk lifetime measurements. The fluorescence emission was recorded using a photon multiplier tube (PMT 900 detector, Hamamatsu) and the lifetime decays were measured on a high speed PMT (H10720-01 High speed PMT, Hamamatsu) using a laser repetition rate of 32 MHz. The digested UiO-67 samples were measured in a 3.5 mL quartz cuvette (119F-10-40, Hellma Analytics). For the emission spectra, a 1 nm emission slit width and an excitation power of 1 mW were used. The spectra were recorded in 0.5 nm steps with 0.5 seconds acquisition time per step across the spectral range of interest. The fluorescence lifetime measurements were performed using time-correlated single-photon counting (TCSPC), where the raw

lifetime data and subsequent lifetime fits resulted in a single exponential decay. The lifetime fits were obtained according to the following equation:

$$I(t) = I_0 e^{-\frac{t}{\tau}} + c$$

where τ is the decay lifetime with I_0 being the decay intensity at t = 0 and c being the offset value relative to I_0. The lifetime fits were performed with our home written software PIE analysis with Matlab (PAM). PAM is a stand-alone program (MATLAB; The MathWorks GmbH) for integrated and robust analysis of fluorescence ensemble, single-molecule, and imaging data.[2]

1.6. Fluorescence intensity and fluorescence lifetime imaging microscopy (FLIM).

Fluorescence intensity and lifetime measurements were performed using a house-built laser scanning confocal microscope equipped with pulsed interleaved excitation and TCSPC detection, as described elsewhere with a few modifications.[3] Briefly, a pulsed laser diode at 561 nm wavelength (LDH-FA-560, PicoQuant) driven by a laser driver (PDL 828 Sepia II, PicoQuant) at 40 MHz was used for excitation of the BPDC-RB functionalized UiO-67. For the measurements, the UiO-67 powder was suspended in water and vortexed for ~3 min. From the suspension, ~ 30 µL was added to an 8-well LabTek I slide (VWR) and the UiO-67 fragments allowed to sediment. The surface was imaged using a 60x, 1.27 numerical aperture water-immersion objective (Plan Apo IR × 60 WI, Nikon). The fluorescence emission was collected with the same objective, separated from the excitation using a polychroic mirror (Semrock Di01-R405/488/561/635, AHF Analysentechnik, Tübingen, Germany) and a 595/50 nm long pass filter (ET 595/50, Chroma), and recorded using a single photon avalanche photodiode (SPCM-AQR-14, Perkin-Elmer). Typical scan regions were between 60 µm × 60 µm and 90 µm × 90 µm, depending on the size of the measured UiO-67 crystal. Scans were performed with a pixel size of 200 nm, resulting in images between 300 × 300 pixels and 450 × 450 pixels. The fluorescence intensity images were collected at different depths within the crystal with 500 nm separation between the different planes providing the three-dimensional intensity distribution of the crystals. For FLIM, scans were performed at the surface, and at 2 µm and 4 µm above surface with image acquisition times of 200-400 s to ensure the detection of 200-1000 photons per pixel. To ensure a good signal-to-noise ratio while minimizing the influence of photon pile-up and other high-signal artifacts, the count rate was kept below 1000 kHz. The desired count rate was achieved by adjusting the power of the 561 nm wavelength laser using a neutral density filter-wheel (NDC-100C-2M, Thorlabs). Laser power ranged from 5 to 500 nW measured before the objective (S130VC Slim Photodiode Power Sensor, Thorlabs). A phasor analysis[4-5] was applied to the data using our software framework PAM.[2] To improve the FLIM analysis, the data were spatially smoothed with a 3 pixel × 3 pixel sliding window.

The FLIM phasor approach, as described by Digman and co-workers,[5] allows a graphical interpretation of the measured fluorescence lifetime, thus avoiding a more complicated fit-based analysis that can result in a biased interpretation of the data when a wrong fit model is used. From the FLIM measurements, the sine and cosine Fourier components of the lifetime decay are calculated for every pixel in an image, yielding the two phasor coordinates g and s:

$$g_{i,j}(\omega) = \frac{\int_0^{2\pi} I_{i,j}(t) \cdot cos(\omega t - \varphi_{Inst})\, dt}{\left(M_{Inst} \cdot \int_0^{2\pi} I_{i,j}(t) dt\right)}$$

$$s_{i,j}(\omega) = \frac{\int_0^{2\pi} I_{i,j}(t) \cdot sin(\omega t - \varphi_{Inst})\, dt}{\left(M_{Inst} \cdot \int_0^{2\pi} I_{i,j}(t) dt\right)}$$

where the indices i and j define the pixel of the image and $I_{i,j}(t)$ gives the photon counts of the time bin, t, of the lifetime decay histogram of the corresponding pixel. The frequency, ω, corresponds to $2\pi/T$ where T is the full timescale of the lifetime decay histogram (here 40 ns). φ_{Inst} and M_{Inst} are correction terms for the phase shift and demodulation caused by the instrument response function. The correction terms were calculated using a reference sample with known lifetime (Atto 565, 4.0 ns, Atto-Tec).

From the two phasor coordinates, two lifetime values can be determined, one based on the phase (τ_φ) and the second on the modulation (τ_M):

$$\tau_\varphi(\omega) = \frac{1}{\omega} \cdot \frac{s}{g} \quad \text{and} \quad \tau_M(\omega) = \frac{1}{\omega}\sqrt{\frac{1}{g^2+s^2} - 1}$$

For a purely mono-exponential decay, these two lifetimes are identical and correspond to the correct lifetime. In the case of multi-exponential components, the phase and modulation lifetimes are different and do not correspond directly and unambiguously to the pure species. In the phasor approach, multiple species will be added vectorially. For example, a mixture of two species with different mono-exponential lifetimes will lie on a line connecting the individual components of the two species on the unit circle. Where the mixture falls on this line depends on the relative population of the two species. To get a single apparent lifetime for each sample, the mean τ_φ and τ_M were calculated from all pixels above a threshold of ~ 200 photons. The arithmetic average of the mean phase and modulation lifetimes was then used to calculate an apparent lifetime. The uncertainty corresponds to the standard deviation of the pixel distribution.

1.7. Powder X-ray diffraction (PXRD).

PXRD measurements were conducted on a Bruker D8-Venture diffractometer with a Mo-target (0.71073 Å) and Cu-target (1.54184 Å) microfocus X-ray generators. The theta-theta geometry device was equipped with a PHOTON-100 CMOS detector, measuring the samples between 2° and 50° 2θ, with a step-size of 0.02° 2θ.

1.8. Scanning electron microscopy (SEM).

A Zeiss NVision40 microscope was used to record SEM images. Secondary electron images were acquired using the InLens detector at a low acceleration voltage of 5 kV. To avoid charging effects, a thin carbon film coating was applied on the samples before the measurements. The carbon deposition was performed using a BAL-TEC coating system.

1.9. Thermogravimetric analysis (TGA).

A Netzsch Jupiter ST 449 C instrument equipped with a controller (Netzsch TASC 414/4) was used to determine the missing linker defects within the pristine UiO-67. A sample of ~ 8 mg pristine UiO-67 was loaded into an aluminum oxide crucible and heated from the range of 25 °C to 900 °C at a heating rate of 10 °C/min under synthetic air flow conditions (containing ~ 21% O_2 from the air liquid supplier).

2. Precluding the possibility of through-window diffusion

2.1. Estimation of the size of guest molecules.

To estimate the size of the guest molecules, their geometries were optimized using density functional theory (DFT) at the b3lyp/6-311++g(2d,2p) level. Multiple orientations of these molecules were sampled to identify the one with the smallest projection areas. For this particular orientation, the longest distance spanning the molecule represents its size. If this size is smaller than a pore window, the guest molecule can pass through the window. The structures, orientations, and sizes of the guest molecules are depicted in Fig.S5. The sizes of fluorescein, rhodamine b isothiocyanate (RB), and BPDC-RB is 11.6 Å, 15.2 Å, and 15.8 Å, respectively. The edge length of the triangular window of UiO-67 is ~12 Å. Based on these results, we predicted that only fluorescein is able to pass through the window, while RB and BPDC-RB are unable to penetrate UiO-67 crystals via through-window diffusion.

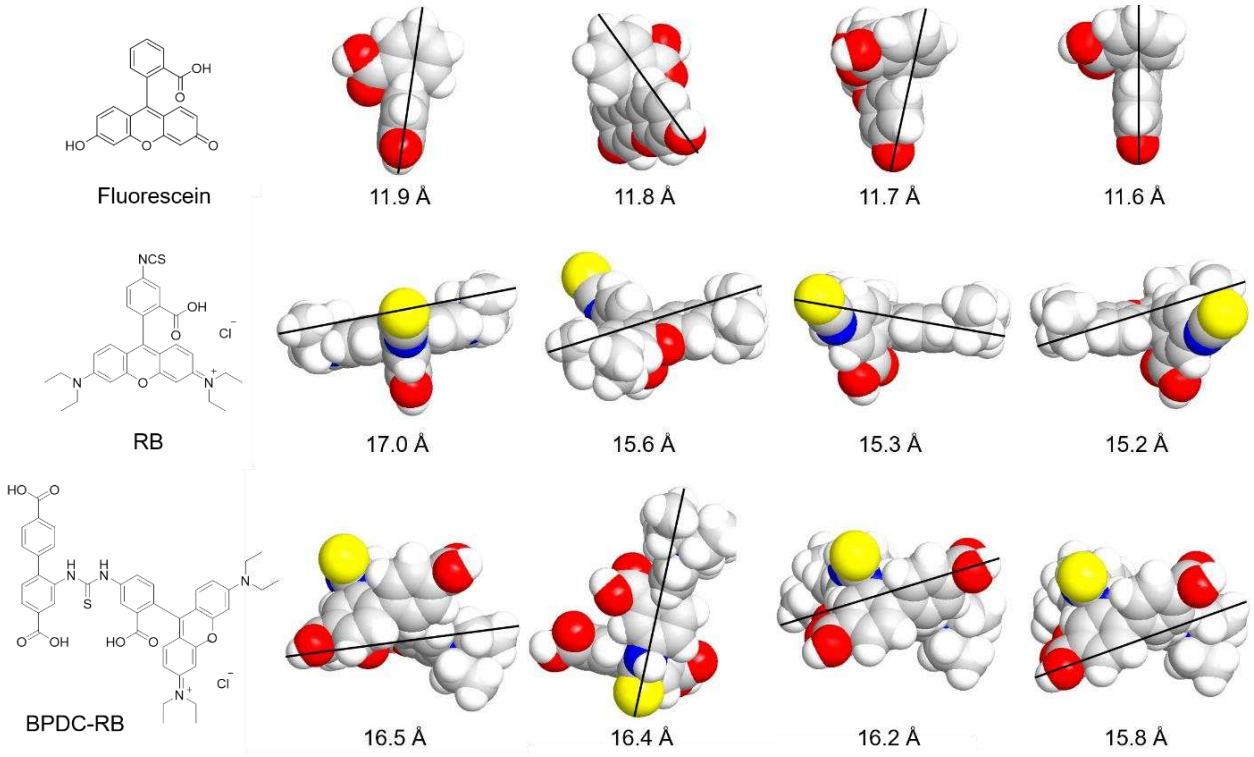

Figure S5: The structure and Van der Waal models for the guest molecules. From left to right, the structure followed by four projections of fluorescein (upper row), RB (middle row) and BPDC-RB (bottom row) are shown. The projection radius decreases and the orientation on the right end presents the minimum size of the molecule.

2.2. Penetration test using fluorescence imaging.

Our prediction on the penetrability of fluorescein and RB was confirmed by soaking UiO-67 in solutions of the two fluorophores for 7 days at RT in DMF. As we expected, after soaking with RB, no fluorescence signal was observed in the interior of the crystal, while the surface of the crystal shows high fluorescence intensity (Fig.S6). In contrast, soaking with fluorescein led to deep penetration of the dye into the MOF. This observation confirms that RB is too large to pass through the window of UiO-67, while fluorescein, a smaller dye, can pass through the window and exhibits through-window diffusion behavior. Considering that BPDC-RB is even larger than RB, it cannot pass through the window as well. This matches with the result of a penetration test of BPDC-RB under the same condition (see Fig. S14), which displayed no

penetration. Therefore, we postulate that the unusual penetration of BPDC-RB, when MeOH/DMF is used as the incubation solvent, must indicate a penetration mechanism other than through-window diffusion.

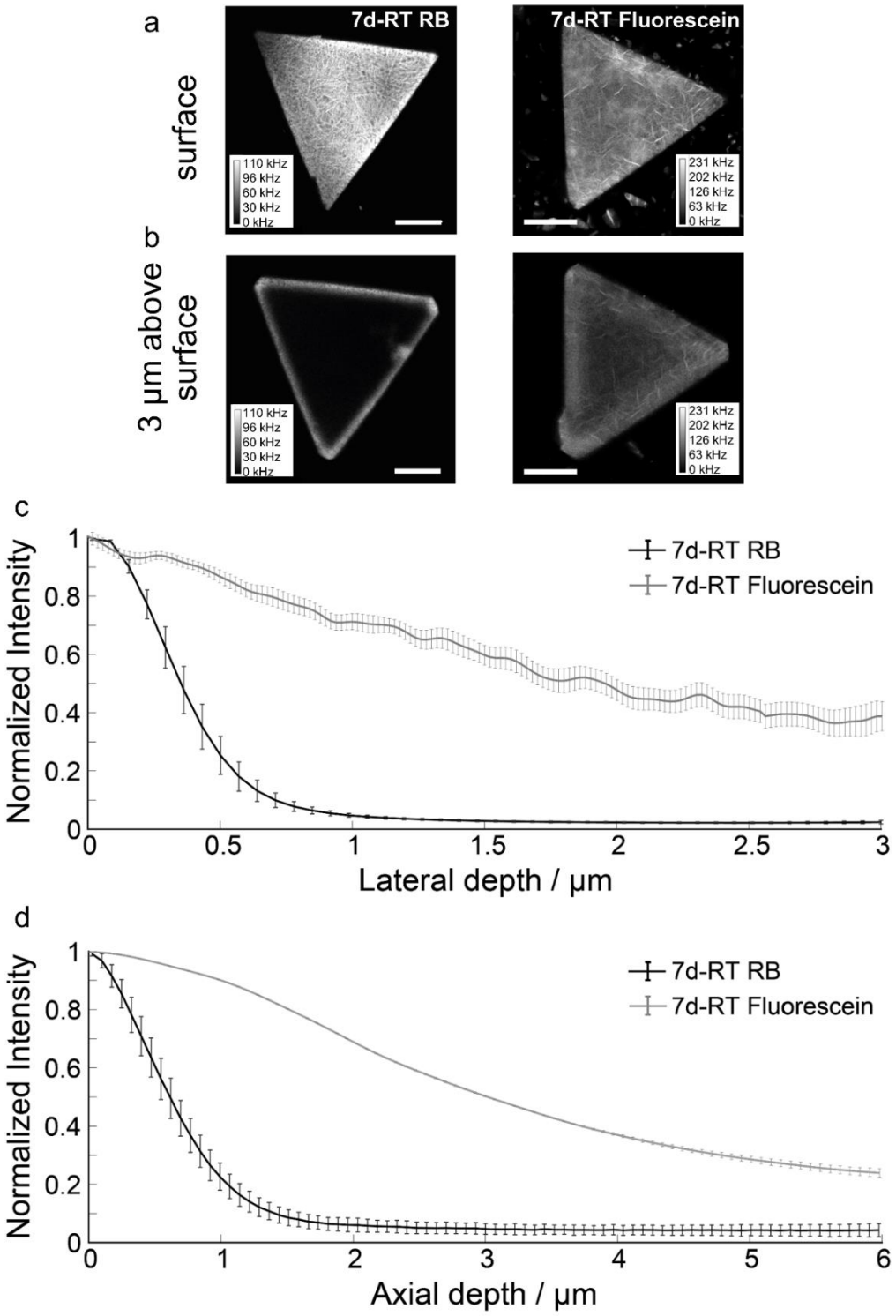

Figure S6: Fluorescence imaging of UiO-67 crystals after incubation with RB and fluorescein for 7 days at RT in DMF. **a**) Fluorescence images of a UiO-67 crystal taken at the surface and (**b**) 3 µm above the surface. The scale bars are 15 µm. **c**) The fluorescence intensity profile along lateral direction 3 µm above the surface and (**d**) in the axial direction. Error bars are determined from measurements on 3 crystals of UiO-67 per condition.

2.3. Analysis of missing-linker defects in pristine UiO-67.

Although the size of UiO-67 window is ~12 Å, the presence of missing-linker defects can create windows of larger sizes. These larger-sized windows could allow for the otherwise forbidden through-window diffusion across the defect sites. To preclude the possibility that missing-linker defects present in pristine UiO-67 alter the diffusion behavior of BPDC-RB, we analyzed the number of missing-linker defects present in our UiO-67 crystals and evaluated their impact.

We employed TGA to calculate the defect level. As shown in Fig. S7, a loss of 4.3% of the mass before 275 °C can be ascribed to the leaving of adsorbed moisture, benzoate, and formate ligands, and to the dehydration of the Zr cluster, according to

$$Zr_6O_4(OH)_4(BPDC)_x(benzoate)_y(formate)_z \rightarrow Zr_6O_6(BPDC)_x, \qquad x + 0.5y + 0.5z = 6.$$

The remaining loss of 61.7% of the mass is due to the decomposition of BPDC from 400 °C to 660 °C, which leaves the remaining 34.0% of the mass to be ZrO_2, according to:

$$Zr_6O_6(BPDC)_x \rightarrow 6\ ZrO_2.$$

Based on the loss of mass and the molecular weight of the leaving components, we calculated x = 5.99, indicating a very low level of missing-linker defects (0.01 out of 6).

In the above calculation, we assume that the amount of missing-cluster defects is negligible, as we do not observe any forbidden low-angle reflections in PXRD (see Fig. S9).

Compared with literature,[6] our TGA matches very well with those obtained for defect-free UiO-67 samples.

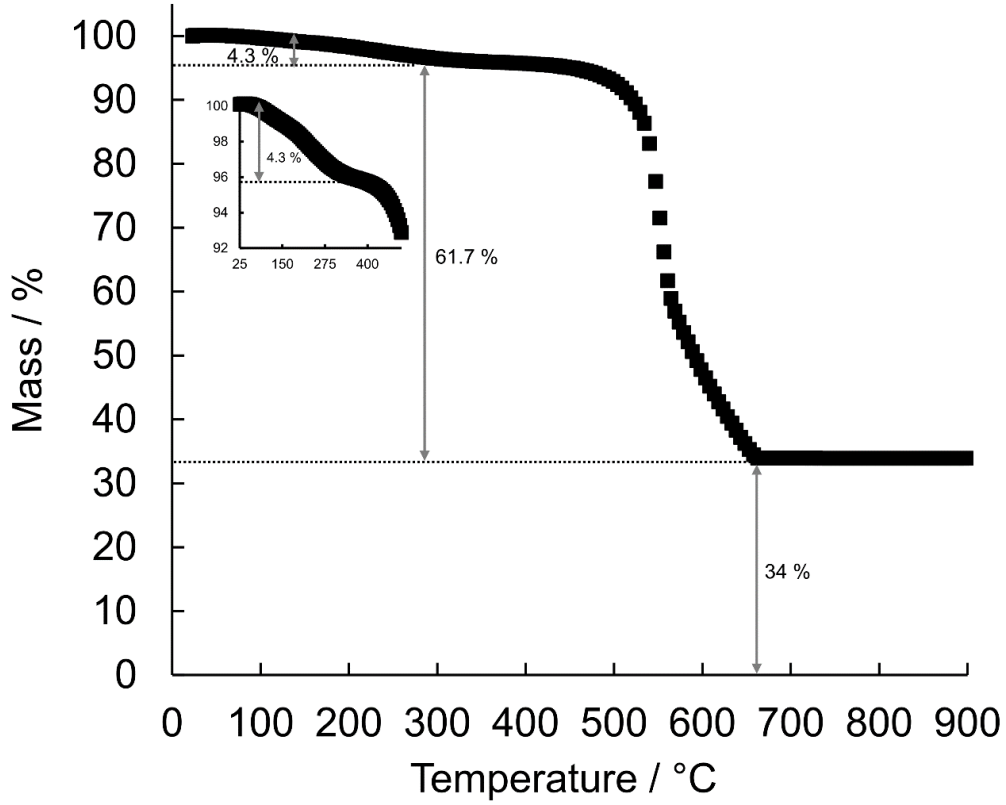

Figure S7: TGA of pristine UiO-67 crystals.

3. Single-crystal characterization

In this study, the spatial and mechanistic aspects of PSE were investigated in a prototypical zirconium-based MOF. For this, large UiO-67 crystals, ~50 µm in diameter, were synthesized and subsequently functionalized with fluorescently labeled linkers using linker exchange. The fluorophore served hereby as a probe for investigating the spatial and mechanistic progression of PSE. It has been demonstrated that this MOF prototype is as a robust platform for PSE due to its unique thermal and chemical stability.[7] Consequently, the large UiO-67 crystals were chosen to provide a three dimensional scaffold that includes tetrahedral and octahedral pores, where the later are large enough for the fluorescently labeled linker to get incorporated in the UiO-67 lattice without altering its topology.

Prior to the PSE studies, additional experiments were performed to characterize the autoluminescence properties of the pristine UiO-67 crystals. In this regard, the fluorescence properties of the UiO-67 crystals (*i.e.* the autofluorescence intensity and autofluorescence lifetime) were determined. We observed a weak autofluorescence signal, which would correspond to ~ 5 kHz during our measurements with BPDC-RB (which is a factor of 20x to 100x less than the intensity obtained for the different PSE conditions investigated) via direct excitation at 561 nm (Fig. S8 a and b). Similarly, the direct excitation of the pristine UiO-67 exhibited an autofluorescence lifetime of ~ 3.3 ns (Fig S8 c and d).

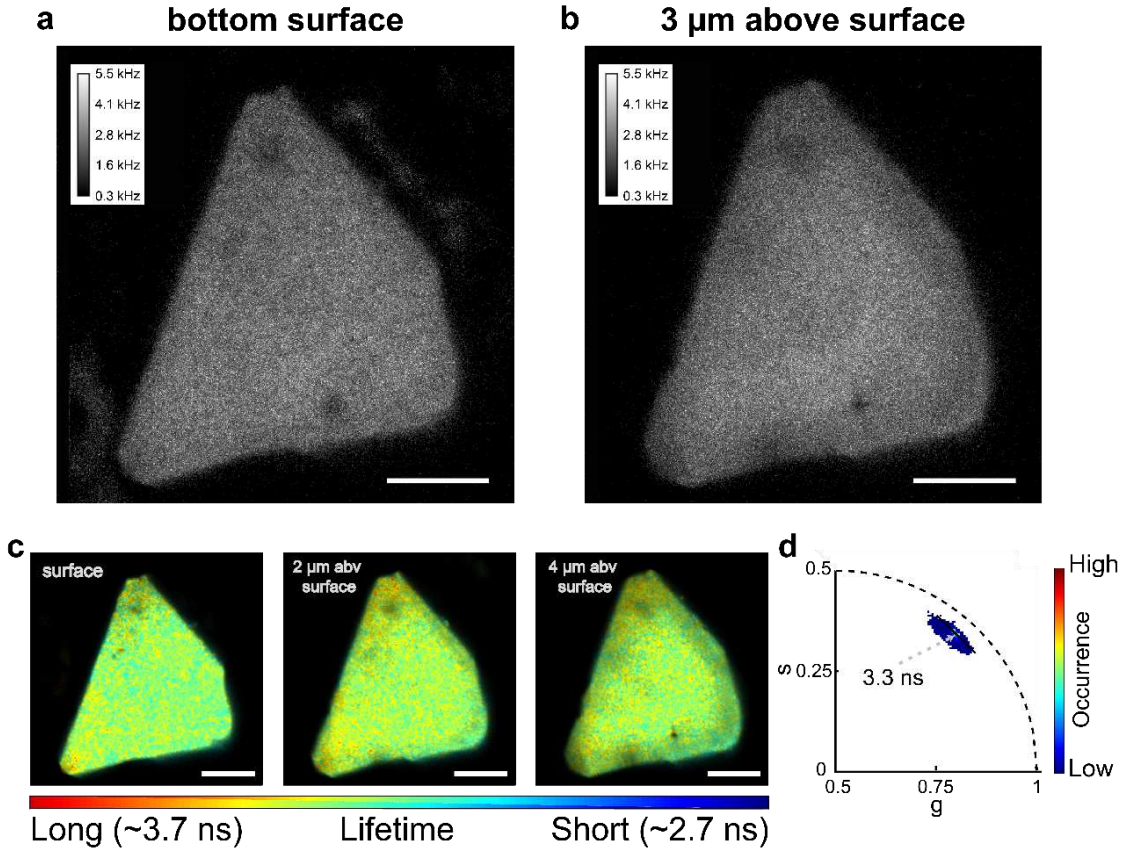

Figure S8: Autofluorescence intensity and lifetime of pristine UiO-67 via direct excitation at 561 nm. **a**) Fluorescence images taken at the surface and (**b**) 3 µm above the surface. **c**) FLIM images and **d**) the corresponding phasor plot of the three FLIM images in panel **c**. The color in the phasor plots corresponds to the number of pixels exhibiting the phasor value (blue indicating the lowest occurrence and red indicating the highest occurrence); see color bar. The scale bar is 15 µm.

The BPDC-RB was incubated with UiO-67 in either a solution of 80% methanol / 20% DMF v/v (for brevity, this mixture is further on referred to as MeOH/DMF) or alternatively in DMF alone. We performed the UiO-67 functionalization with BPDC-RB under four different conditions for each medium (as shown in Scheme 1): 1 day and 7 days at RT (referred to as 1d-RT and 7d-RT), and similarly 1 day and 7 days at

100 °C (referred to as 1d-100 °C and 7d-100 °C). PXRD and SEM showed that the treatment did not alter the morphology and crystallinity of the functionalized UiO-67 crystals (Fig.S9).

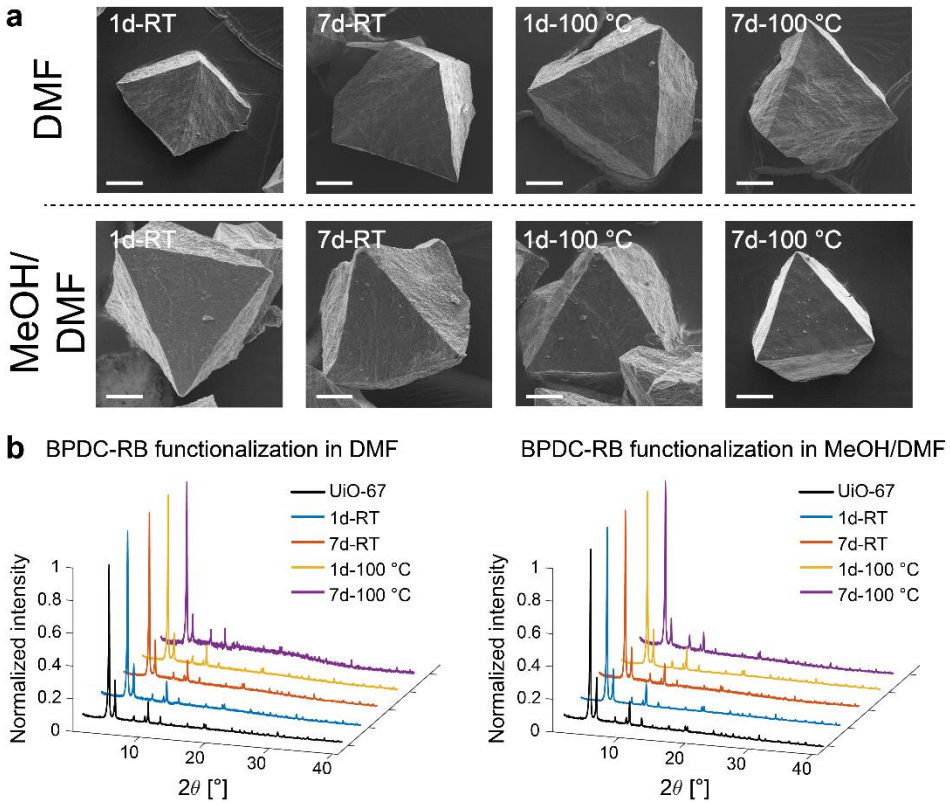

Figure S9: SEM images and XRD patterns of the different UiO-67 samples after PSE. **a**) SEM images of UiO-67 crystals in DMF (upper row) and MeOH/DMF (lower row). **b**) PXRD spectra of UiO-67 crystals in DMF (left) and MeOH/DMF (right).

4. Bulk fluorescence measurements.

4.1. Examination of photophysical damage to BPDC-RB under PSE conditions.

After UiO-67 functionalization with BPDC-RB, we observed a color change on the UiO-67 solid samples. All reactions performed in DMF resulted in a pale pinkish color while, in MeOH, a clear, gradual, color shift from light pink (1d-RT) to dense red (7d-100 °C) was observed (Fig.S10 a), which is the first indication that linker exchange in MeOH/DMF is significantly faster than in DMF.

Before performing the single crystal fluorescence studies, we characterized the fluorescence properties in bulk. These control experiments were conducted to investigate the photophysical properties of free BPDC-RB and those released from the digested UiO-67. Also, we investigated whether the change in color from the different incubation conditions correlates the overall fluorescence emission of the BPDC-RB and the degree of PSE observed. For this purpose, 0.25 mg/mL of UiO-67 crystals (solid) were digested in a DMSO/H_2O solution containing CsF and characterized in bulk solution using a fluorimeter (Fig.S10 b and Section S1.5). After the digestion of the UiO-67 crystals, the fluorescence emission and lifetime were characterized.

The fluorescence intensity observed for the digested UiO-67 functionalized in MeOH/DMF showed a noticeably higher amount of BPDC-RB compared to DMF (Fig.S10 c, e, and g). However, in both incubation media, the extent of linker exchange showed a similar trend (*i.e.* more BPDC-RB with increasing the incubation time and temperature). For comparison, we measured the spectrum of UiO-67 in the absence of a fluorescence linker, which showed a minor Raman peak at 582 nm which is also observable for UiO-67 functionalized in DMF (Fig.S10 c). The emission maxima of BPDC-RB in DMF was observed to be around 578 to 580 nm (Fig.S10 c). A similar fluorescence emission behaviour was observed for UiO-67 functionalized in MeOH/DMF with a slight bathochromic shift of the emission maxima ranging between 580 and 582 nm (Fig.S10 e).

Furthermore, we measured the lifetimes of BPDC-RB after digesting the functionalized UiO-67 to check whether the different PSE conditions resulted in alterations in the fluorescence properties of the fluorophores themselves. For both media and all four conditions, the resulting lifetimes were very similar (2.14-2.15 ns) indicating that the handling of the MOFs did not affect the fluorescence properties. (Fig.S10 d, f, and Table S1).

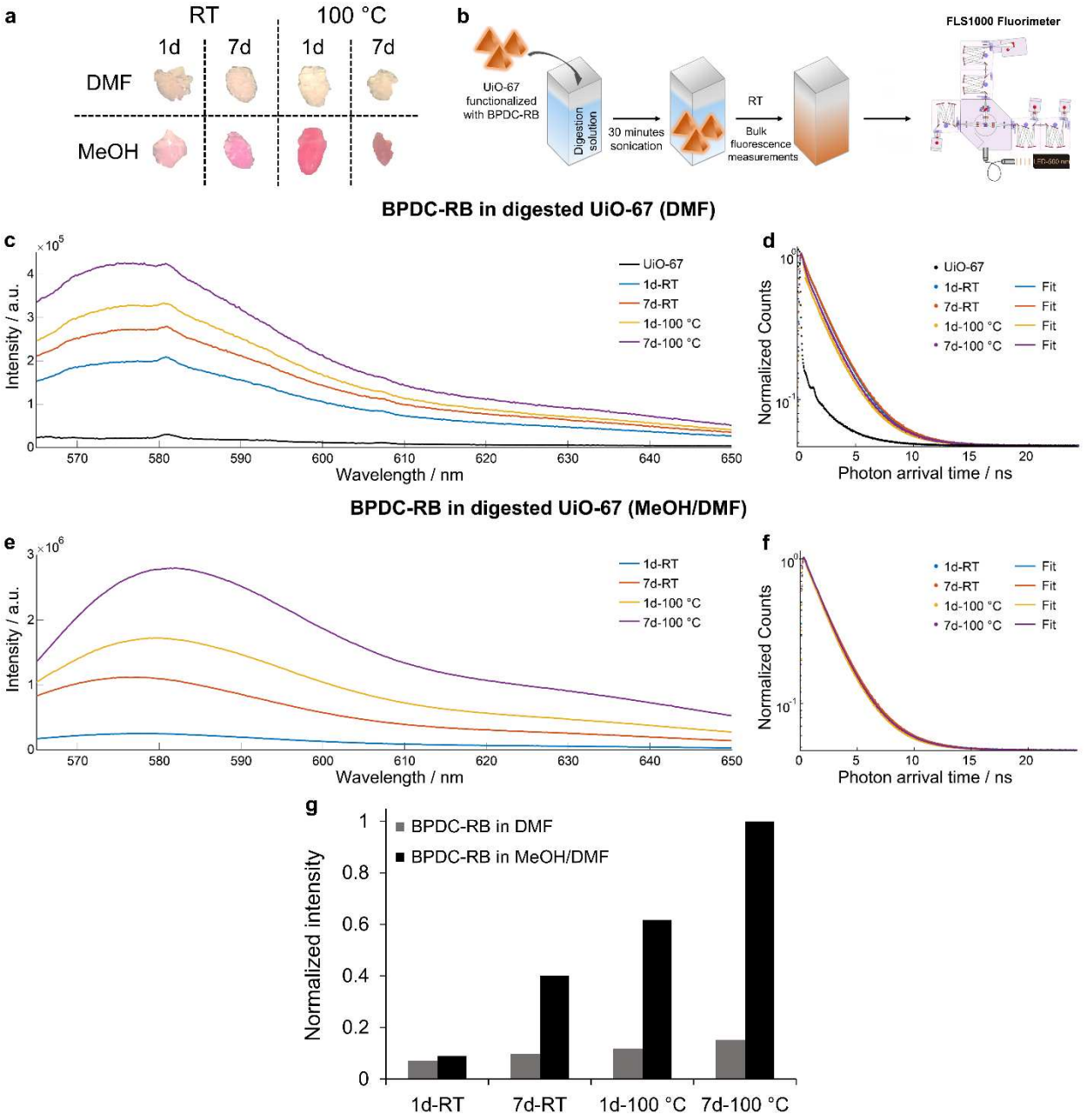

Figure S10: Bulk observations and fluorescence characterization of the different UiO-67 samples after PSE in DMF and MeOH/DMF. **a**) Optical images of the solid UiO-67 samples showing the change in color upon PSE. **b**) Schematic presentation of the steps for digesting the UiO-67 and performing the fluorescence measurements. **c)** The fluorescence emission and **d**) lifetime decays for the digested UiO-67 in DMF. **e**) The fluorescence emission and **f**) lifetime decays for the digested UiO-67 after PSE in MeOH/DMF. **g**) Normalized intensity values for the BPDC-RB in the digested UiO-67 relative to the fluorescence intensity (at $\lambda_{emission}$ maximum) of the digested UiO-67 after PSE for 7d-100 °C in MeOH/DMF.

Similarly, the BPDC-RB lifetime behaviour was investigated, to make sure that the lifetime differences within the UiO-67 crystals are due to the local nano-environment changes owing to the PSE and not the degradation of the fluorophore itself. Here, the BPDC-RB lifetime (alone, in the absence of any MOF) was investigated under the four different incubation conditions (1d-RT, 7d-RT, 1d-100 °C and 7d-100 °C) in DMF and MeOH/DMF, respectively. The obtained BPDC-RB lifetimes are 2.30 ± 0.06 ns in DMF (Fig.S11 and Table S1) and 2.23 ± 0.10 ns in MeOH/DMF (Fig.S12 and Table S1). The measured lifetimes of the

BPDC-RB alone showed a monoexponential lifetime decay under the four different conditions tested, which confirmed the absence of an unexpected dye photophysical behaviour that might influence lifetime measurements in the single UiO-67 crystals.

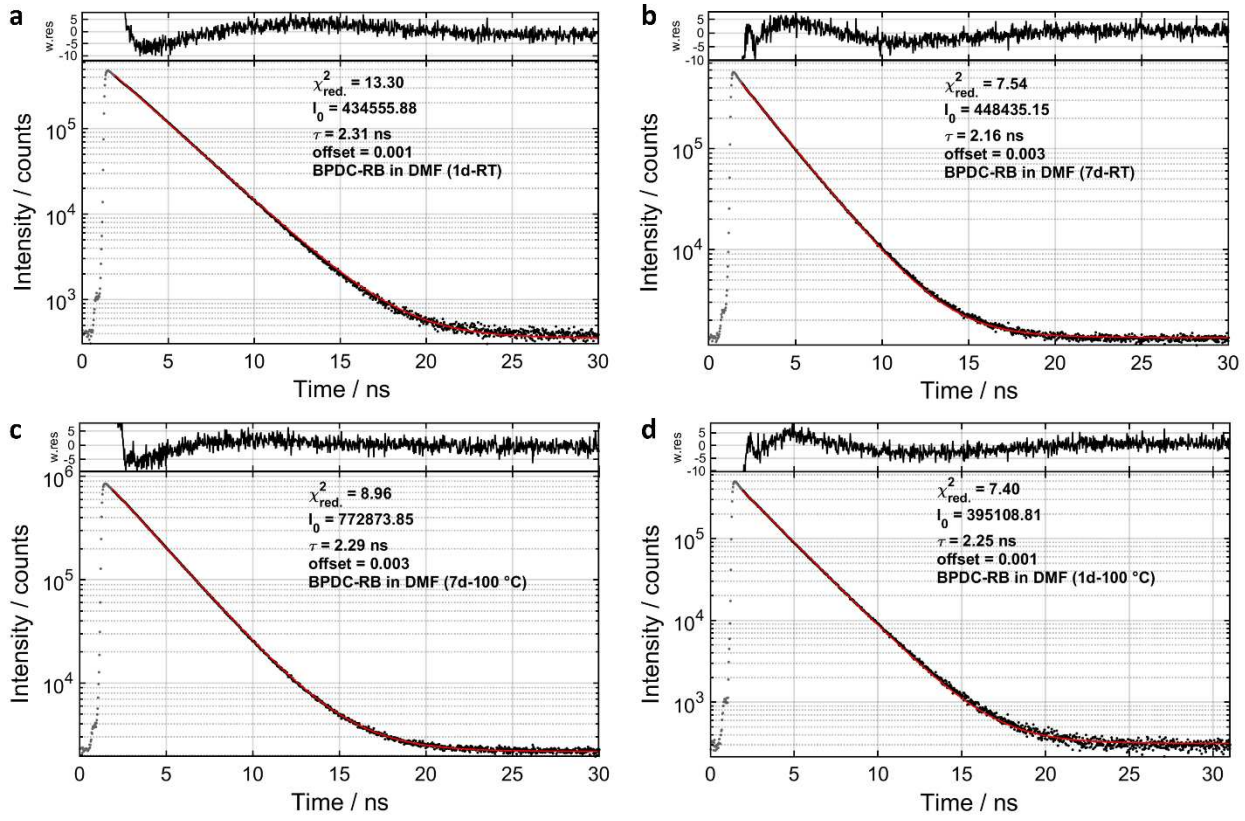

Figure S11: Fluorescence lifetime decay data and fits obtained for the BPDC-RB (alone) investigated under similar conditions used for PSE in DMF **a**) for 1d-RT, **b**) for 7d-RT, **c**) for 1d-100 °C and **d**) for 7d-100 °C.

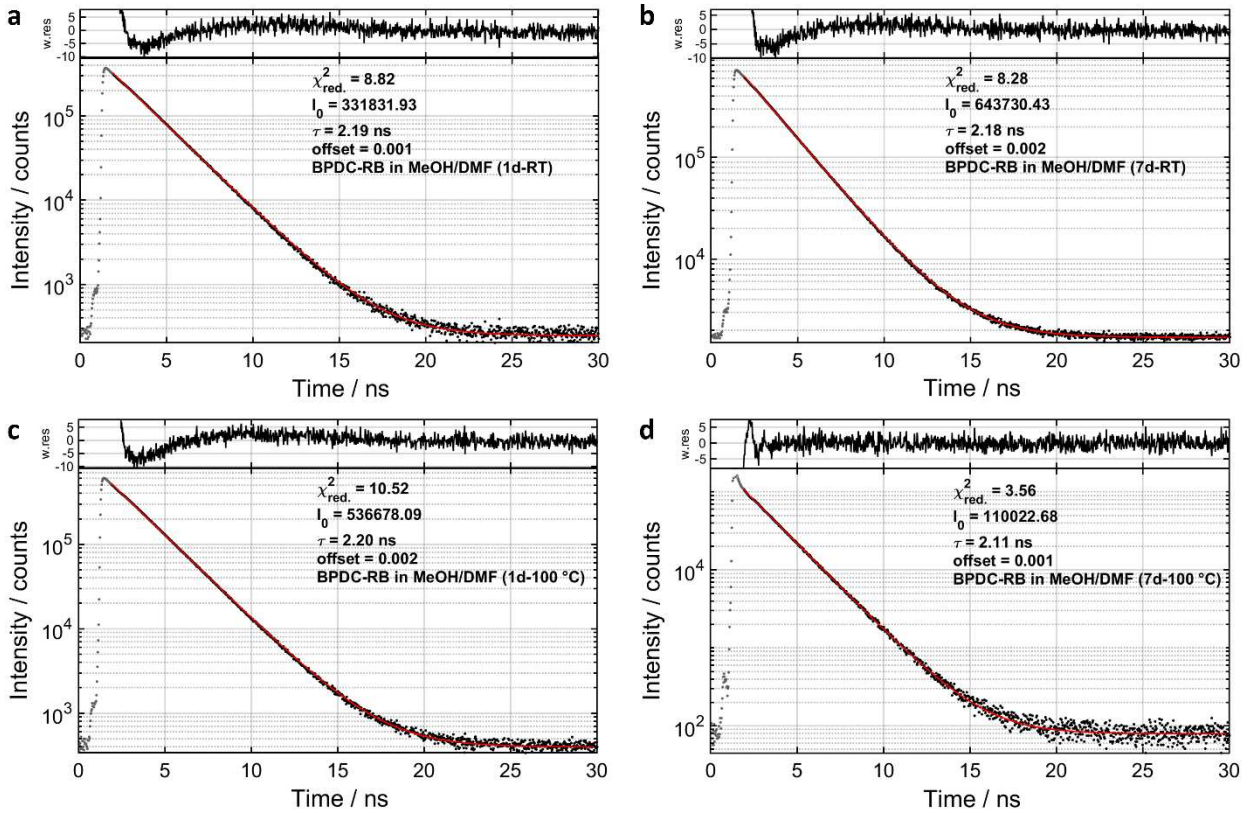

Figure S12: Fluorescence lifetime decay data and fits obtained for the BPDC-RB (alone) investigated under similar conditions used for PSE in MeOH/DMF **a**) for 1d-RT, **b**) for 7d-RT, **c**) for 1d-100 °C and **d**) for 7d-100 °C.

Table S1: Fluorescence lifetime decay values obtained for the BPDC-RB alone and BPDC-RB in digested UiO-67 solutions under the same conditions used for PSE.

	BPDC-RB in DMF; τ (ns)		**BPDC-RB in MeOH/DMF; τ (ns)**	
	in absence of UiO-67	in UiO-67*	in absence of UiO-67	in UiO-67*
1d-RT	2.31	2.14	2.19	2.19
7d-RT	2.16	2.18	2.18	2.20
1d-100 °C	2.29	2.11	2.20	2.10
7d-100 °C	2.25	2.12	2.11	2.13
RB alone	2.21		2.17	

*BPDC-RB lifetimes in digested UiO-67 according to the indicated procedure in Fig.S10 b.

4.2. Determination of the BPDC-RB linker exchange ratio.

To determine the amount of incorporated BPDC-RB linker and its exchange ratio after PSE, the fluorescence intensities obtained from the digested UiO-67 crystals were quantified (Fig.S10 c and e). Here, we compared the raw BPDC-RB intensities (measured alone under identical conditions and fit with a linear function, Fig.S13) to the signal obtained from the digested UiO-67 where four different PSE conditions were applied. This comparison of the signals was used to calculate concentrations (based on the linear function

calibration curve) and hence an estimate of the amount of BPDC-RB in the digested UiO-67 was obtained. The PSE efficiency was calculated as the molar ratio between the BPDC-RB and the total linkers (Table S2).

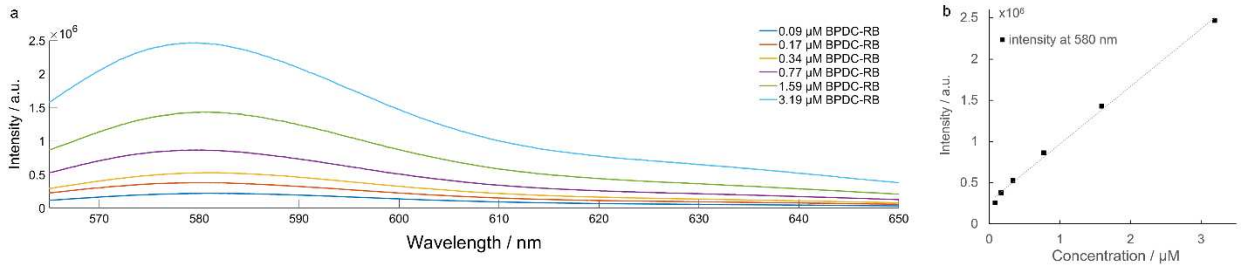

Figure S13: Fluorescence emission of different BPDC-RB concentrations used to estimate the amount of exchanged linker in the digested UiO-67. **a**) Steady state spectra ($\lambda_{excitation}$ = 561 nm) and **b**) fluorescence intensity vs. [BPDC-RB] monitored at 580 nm.

Table S2: Estimated amount of BPDC-RB linker and its exchange ratio in the digested (0.25 mg) UiO-67 crystals studied under four different PSE conditions.

	BPDC-RB in DMF		**BPDC-RB in MeOH/DMF**	
	amount (µg) per 0.25 mg UiO-67	PSE efficiency*	amount (µg) per 0.25 mg UiO-67	PSE efficiency*
1d-RT	0.09	0.09 %	0.76	0.68 %
7d-RT	0.27	0.22 %	2.9	2.6 %
1d-100 °C	0.41	0.35 %	4.9	4.4 %
7d-100 °C	0.65	0.57 %	8.4	7.4 %

* The PSE efficiency was calculated as the molar ratio between the BPDC-RB and the total linkers.

5. Spatial characterization of PSE with 3D fluorescence imaging.

The 3D spatial characterization of PSE was obtained by recording a z-stack of 2D-slices of fluorescence intensity images at height intervals of 500 nm. We analyzed the 3D-fluorescence intensity distribution within the crystal, perpendicular to the surface. This analysis was done in the lateral direction by taking a single z-slice collected at 3 µm above the surface and in the axial direction by taking the same region of interest (ROI) throughout the z-stack (Fig.2). This allowed us to obtain and analyze the 3D penetration depth of the labeled linker. It is worth noting that, for conditions where the label is only bound on or near the surface, the measured spatial distribution will be limited by the diffraction limit of the microscopy (~0.3 µm and ~2 µm for the lateral and axial dimensions, respectively) rather than the actual spatial distribution of the fluorophores (e.g. RB penetration in Fig.S6).

To quantify the PSE, we looked at the fluorescence intensity ratio between a point inside of the crystal (3 µm above the surface) and its surface. We choose 3 µm inside the crystals as the intensity is still high enough to make meaningful comparisons between different conditions. The functionalization of the UiO-67 with BPDC-RB was investigated with different incubation media (DMF and MeOH/DMF solvents) and temperatures (RT and 100 °C). Generally, we observed a very low PSE progression in DMF under all conditions and the only significant amount of linker exchange was observed for 7d-100 °C (Fig.S14). After 7d-100 °C functionalization, a penetration ratio of ~ 7% was observed 3 µm above the surface (Fig.S14 c). In MeOH/DMF, on the other hand, the extent of PSE is significantly higher, especially for longer incubation times at 100 °C, where the penetration ratio 3 µm above surface increased from ~ 14% (after 1d) to ~ 32% (after 7d) (Fig.S14 c).

For incubation in MeOH/DMF, we measured the fluorescence after 1d, 4d, and 7d (Fig. S15). The 1d and 7d images are reproduced from Fig. 3. The additional 4d image and its fluorescence intensity profile show a PSE level between that of 1d and 7d, indicating a gradual progression of PSE on the time frame of 7d.

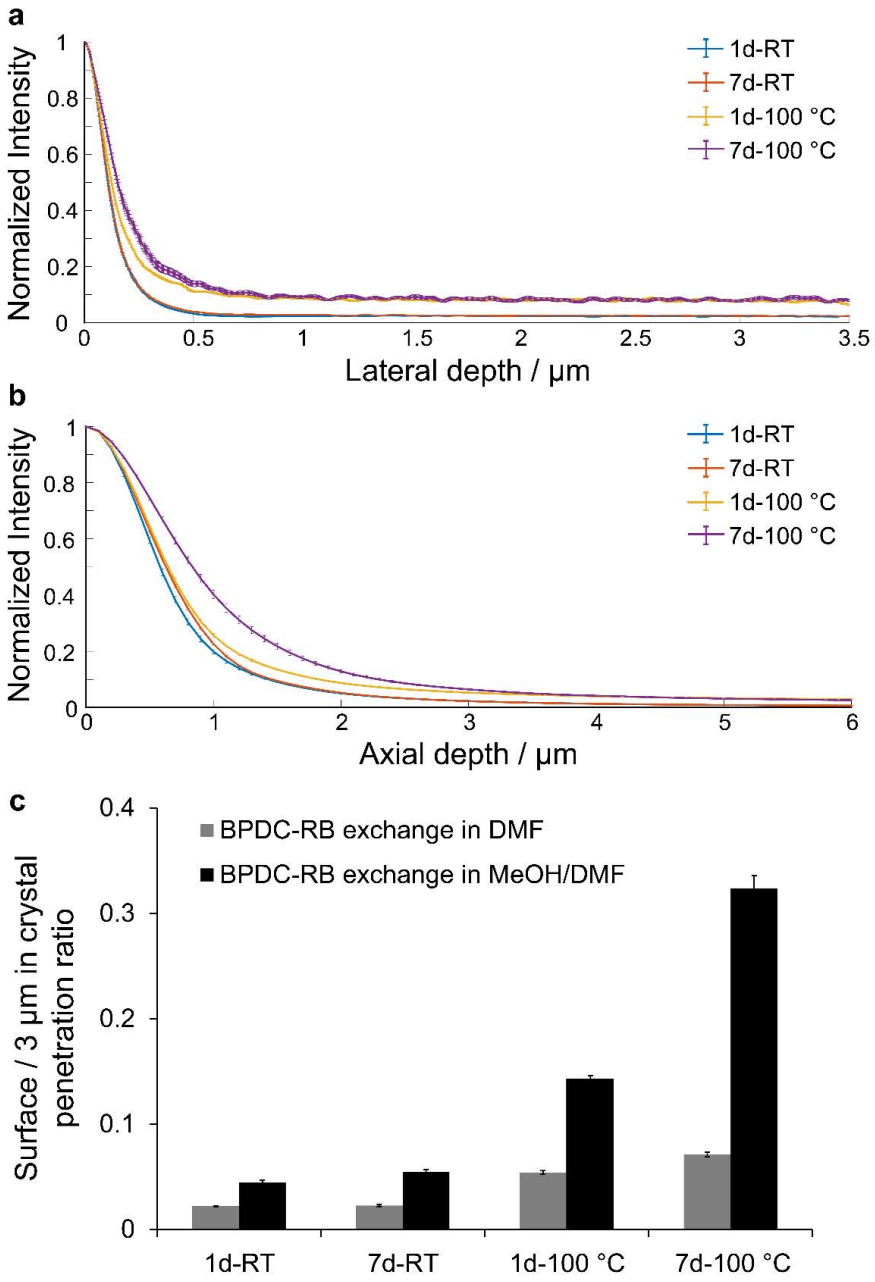

Figure S14: The fluorescence intensity distribution in UiO-67 crystals after PSE in DMF. **a**) Fluorescence intensity profile along lateral direction and (**b**) axial direction (error bars from measurements on 8-10 UiO-67 crystals per condition). **c**) The ratio of fluorescence intensity at 3 µm above surface to the that at the surface (penetration ratio) obtained for UiO-67 crystals after PSE in DMF and MeOH/DMF. The panels of 1d and 7d are reproduced from Fig. 3.

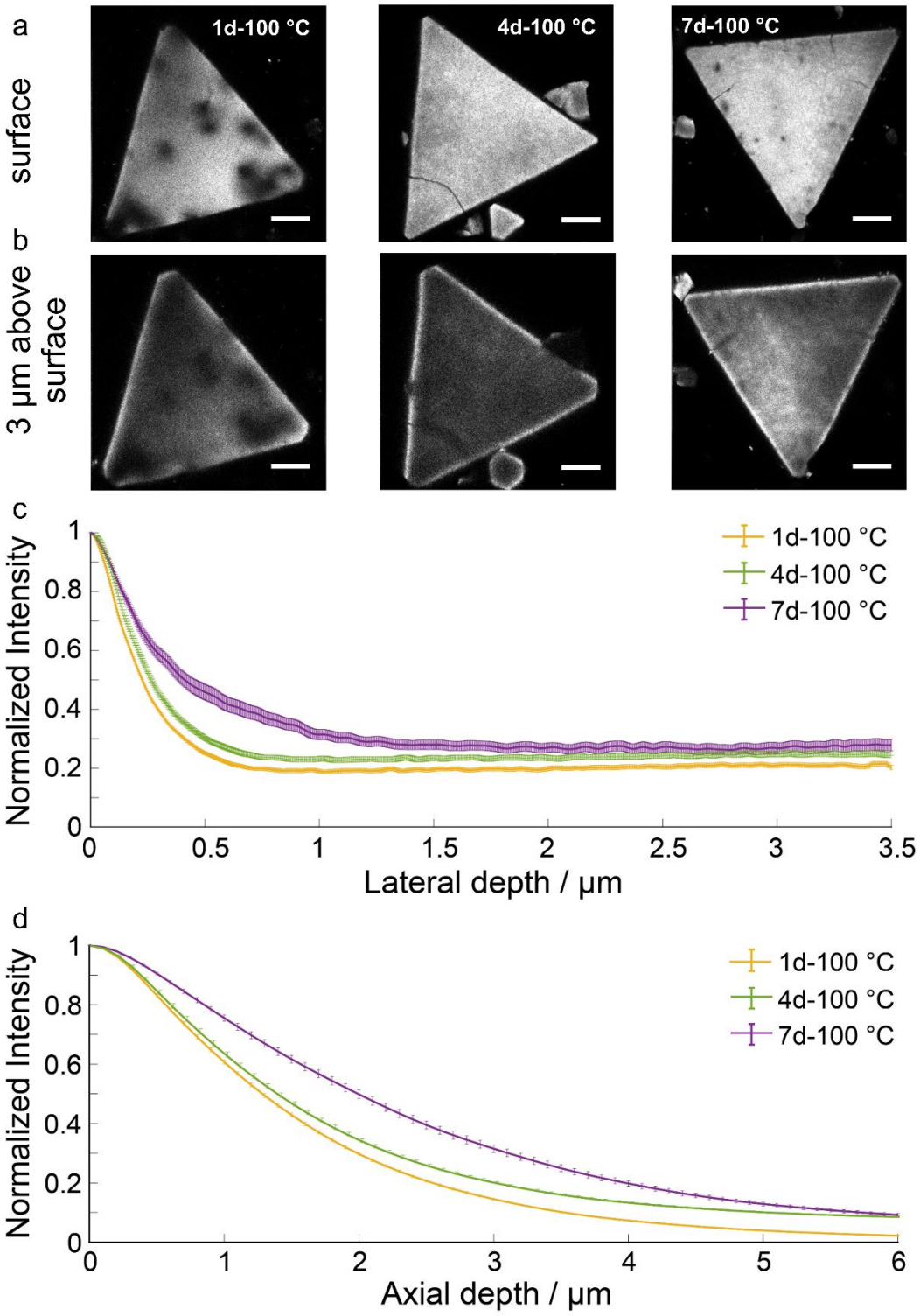

Figure S15: Fluorescence imaging of UiO-67 crystals after PSE in MeOH/DMF for 1d, 4d, and 7d at 100 °C. **a**) Fluorescence images taken at the surface and (**b**) 3 µm above the surface. The scale bar is 15 µm. **c**) Fluorescence intensity profile along lateral and (**d**) axial directions (error bars from measurements on 8-10 UiO-67 crystals per condition).

6. Investigation of defect formation during PSE in MeOH/DMF

To address the PSE induced structural changes, fluorescence lifetime imaging microscopy (FLIM) was performed where the fluorescence lifetime of BPDC-RB was utilized to examine local defect formation after PSE in UiO-67 under different conditions in MeOH/DMF.

UiO-67 after PSE at RT in MeOH/DMF showed significant lifetime differences between 1d and 7d functionalization, where the lifetime decreased from 2.31 ± 0.34 ns after 1d (Fig.S16 c, red) to 1.46 ± 0.45 ns after 7d (Fig.S16 d, yellow-cyan). This would indicate the presence of more detects in the crystal after PSE for 7d. It is worth mentioning that there are minimal differences in the fluorescence lifetime between the crystal surfaces and their interior under RT conditions (Fig.S16-S19), although the low signal in the interior of the crystal makes it more difficult to visualize the lifetime in the image. On the other hand, PSE after 1d-100 °C displayed significant spatial lifetime differences between the crystal surfaces and their interior indicating enhanced defects formation at this elevated temperature (Fig. S16 and S19). Here, a significantly longer lifetime (2.54 ± 0.13 ns, Fig.S16 e, surface, red color) was observed in the crystal interior compared to the lifetime at the surface (1.35 ± 0.20 ns, Fig.S16 e, 4 µm above surface, cyan). This observation correlates well with the fluorescence intensity distribution. This suggests that, as linker exchange advances via the *through-backbone diffusion*, PSE leaves behind a wake of missing linkers. Hence, regions of higher fluorescence intensity where more linker exchange has occurred also have a shorter lifetime due to more defect-induced quenching.

The UiO-67 after PSE for 7d-100 °C resulted in further lifetime quenching compared to the 1d-100 °C functionalization, where a shorter lifetime of 0.89 ± 0.20 ns was measured (Fig.S16 d, blue color). The spatial distribution was much more uniform (Fig.S20). The lack of spatial differentiation, in this case, points towards an equilibrium in defect formation, where defect formation and healing are occurring at similar rates. However, due to the high amount of quenching after 7d, it is very difficult to judge the concentration of defects under such conditions. The high quenching (very short fluorescence lifetimes ~ 1 ns) reduces both the fluorescence lifetime and the photon emission rate. Therefore, a single fluorophore that is - by chance - in a region with low defect concentration, might overwhelm the signal of several dyes that are much closer to a defect and thus quenched even more strongly. Hence, it is possible that we are reaching the limit of sensitivity of our probe.

It is also interesting to note that, for all UiO-67 crystals after PSE for 7d-100 °C, a slight increase in lifetime at the surfaces is observed. This may indicate that defects are being refilled near the surface with the linkers released during linker exchange. The surface would have the highest concentration of released linkers and reannealing of the defects would decrease quenching and result in an increase in lifetime.

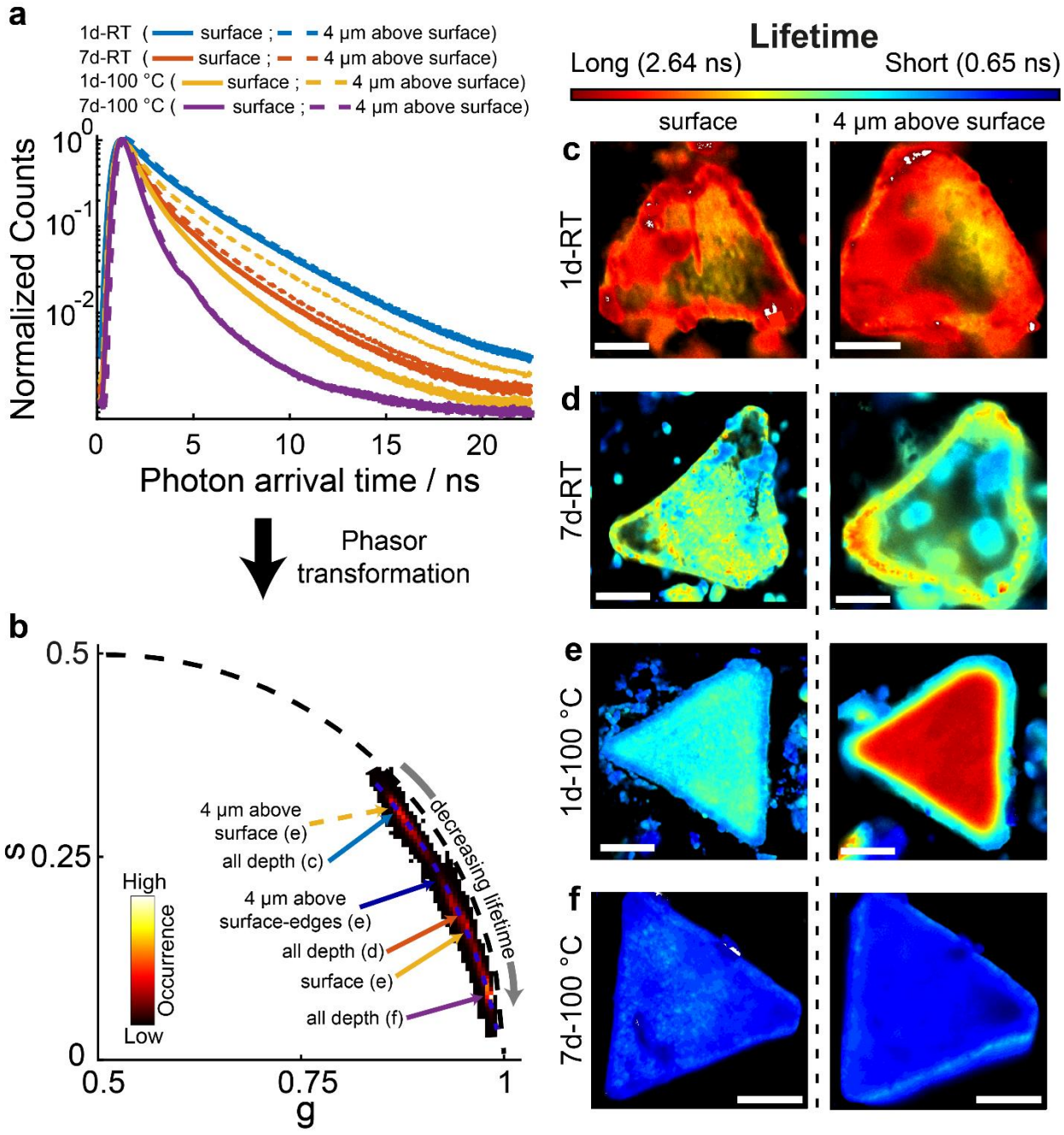

Figure S16: Crystals after PSE under different conditions in MeOH/DMF were characterized using FLIM. **a**) Fluorescence lifetime decays and **b**) the corresponding phasor plot (obtained via the Fourier transformation from the lifetimes in **a**) for the eight FLIM images shown in (**c**-**f**). The color in the phasor plot corresponds to the number of pixels exhibiting the particular phasor value (black indicating the lowest occurrence and yellow indicating the highest occurrence). The dotted-blue line in the phasor plots is used for generating the color table for the fluorescence lifetimes in the FLIM images. **c**-**f**) FLIM images after PSE for 1d-RT (**c**), 7d-RT (**d**), 1d-100 °C (**e**), and 7d-100 °C (**f**). The scale bar is 15 µm.

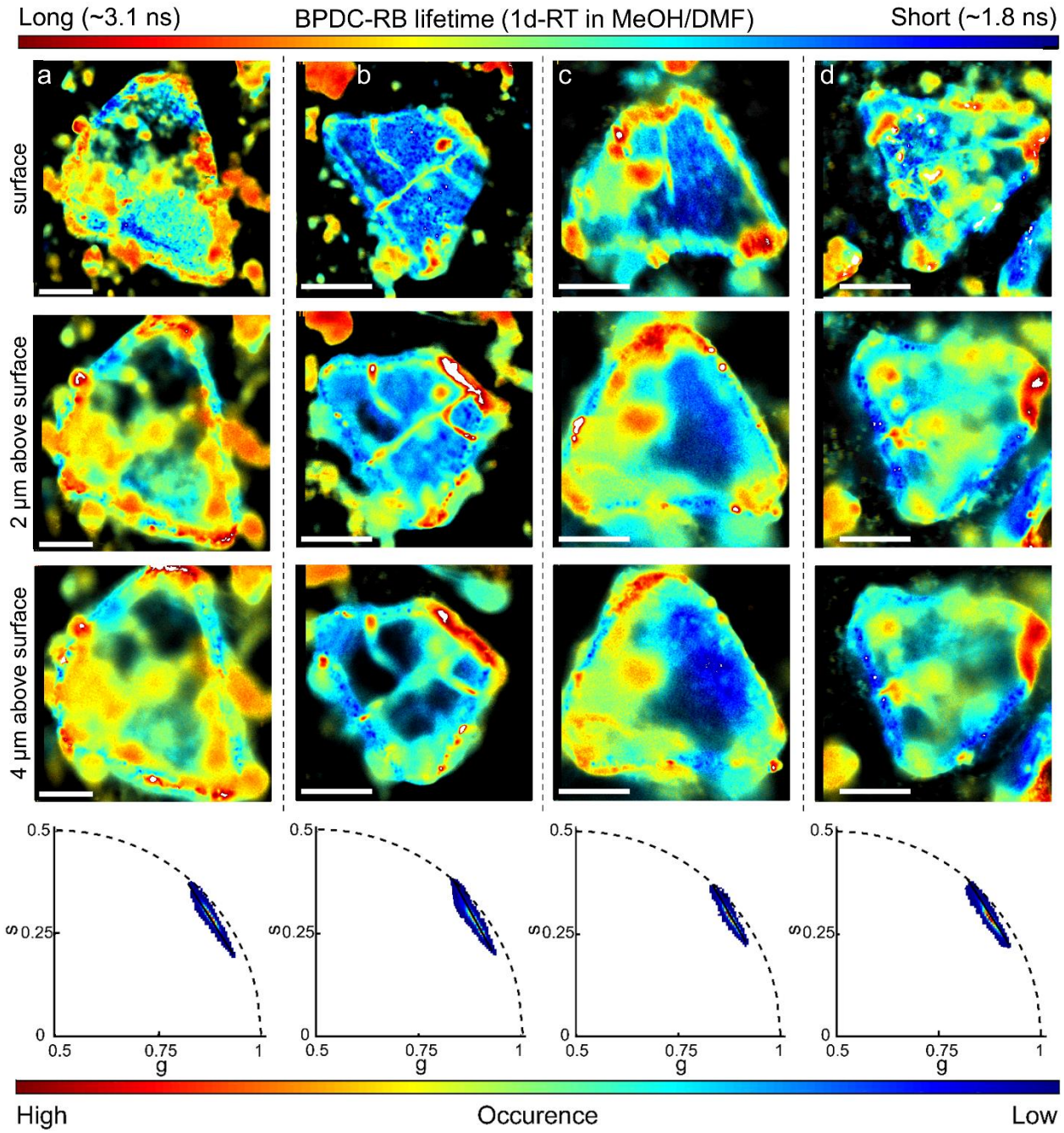

Figure S17: Four crystals after PSE in MeOH/DMF for 1d-RT were characterized using FLIM (panels **a-d**). The scale bar in all images is 15 µm. The last row of each panel shows the corresponding phasor plot of the three FLIM images in panels **a**, **b**, **c** and **d**, respectively. The color in the phasor plots corresponds to the number of pixels exhibiting the particular phasor value (blue indicating the lowest occurrence and red indicating the highest occurrence); see the lower color bar.

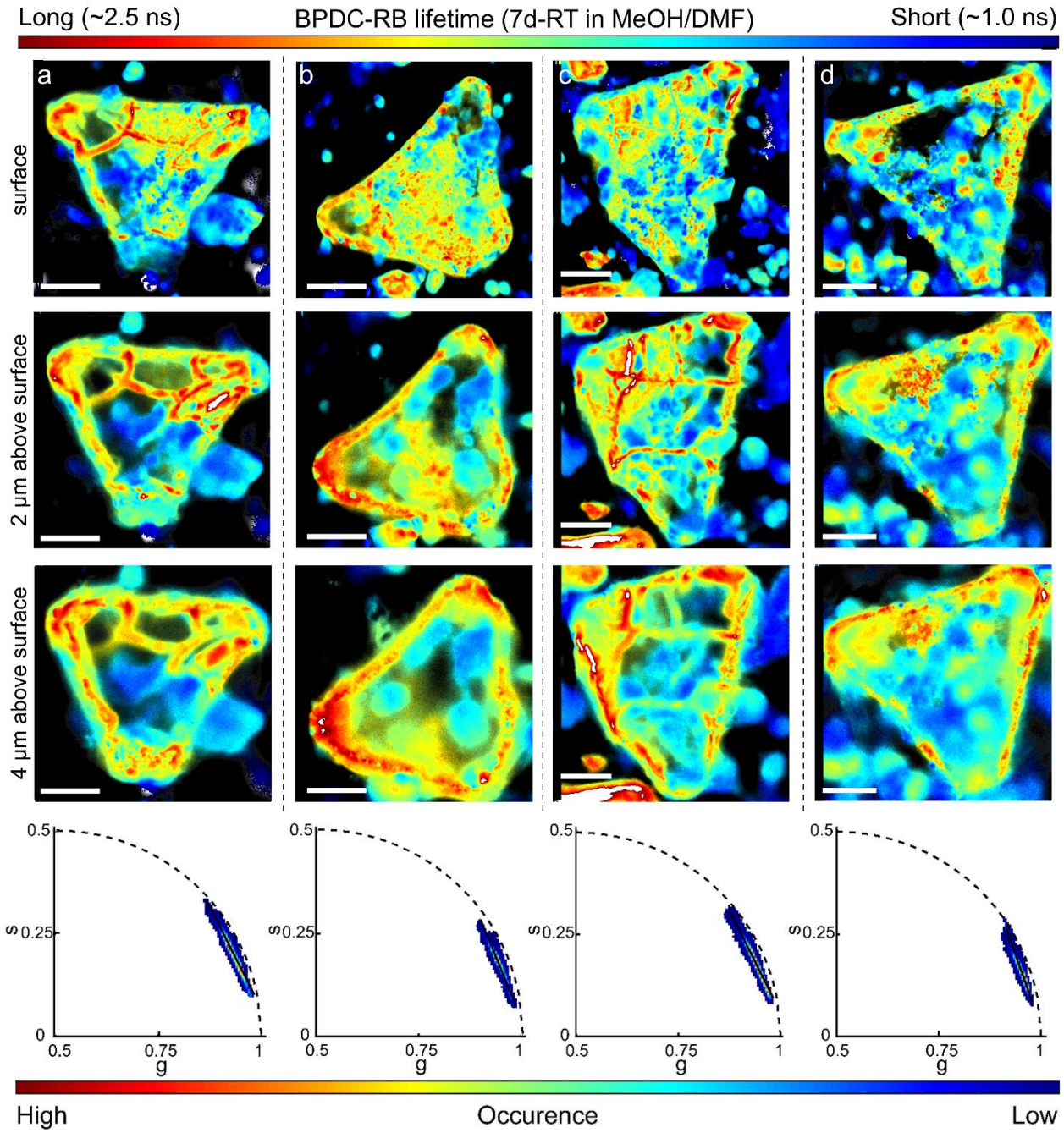

Figure S18: Four crystals after PSE in MeOH/DMF for 7d-RT were characterized using FLIM (panels **a-d**). The scale bar in all images is 15 µm. The last row of each panel shows the corresponding phasor plot of the three FLIM images in panels **a**, **b**, **c** and **d**, respectively. The color in the phasor plots corresponds to the number of pixels exhibiting the particular phasor value (blue indicating the lowest occurrence and red indicating the highest occurrence); see the lower color bar.

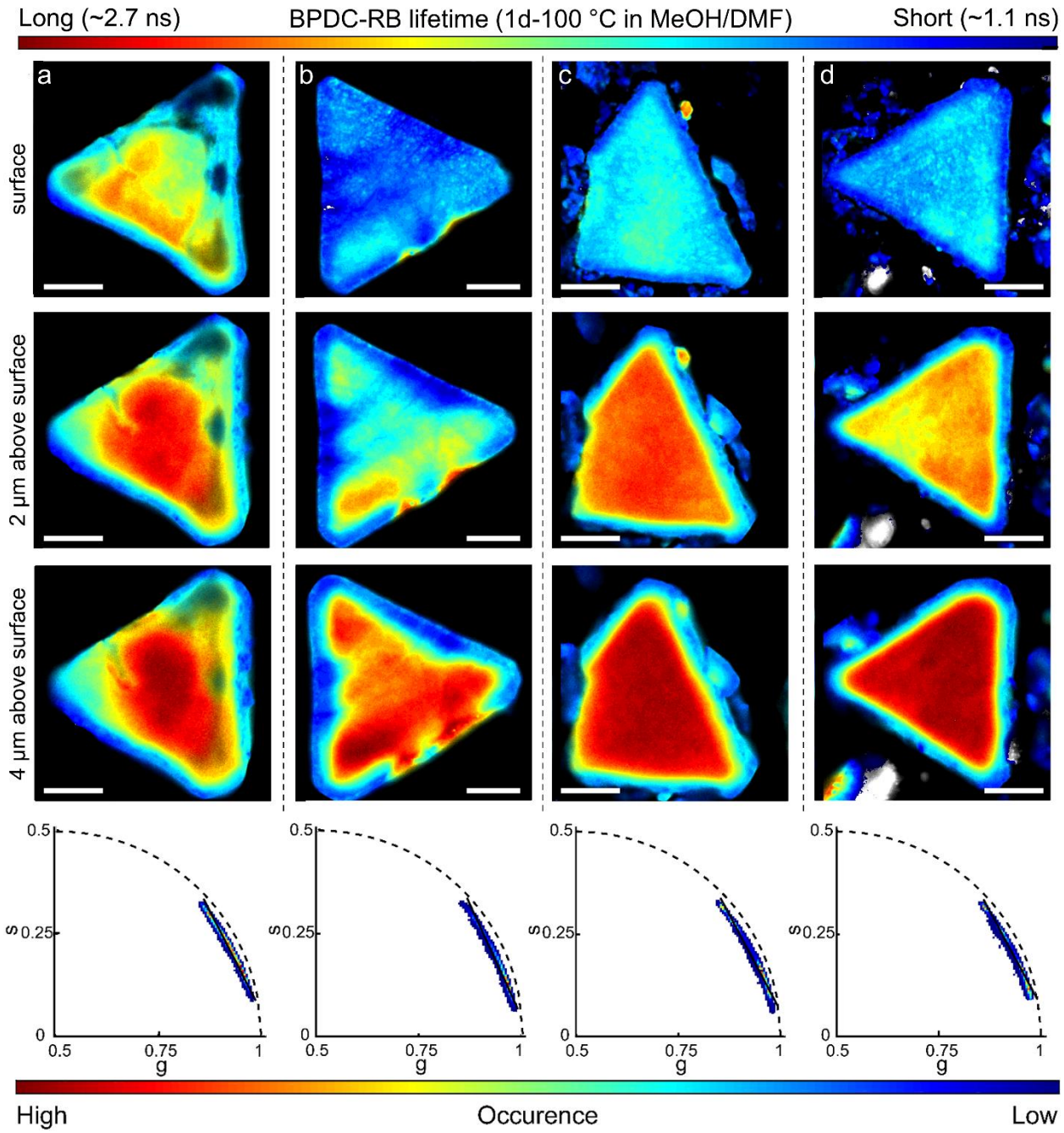

Figure S19: Four crystals after PSE in MeOH/DMF for 1d-100 °C were characterized using FLIM (panels **a-d**). The scale bar in all images is 15 µm. The last row of each panel shows the corresponding phasor plot of the three FLIM images in panels **a**, **b**, **c** and **d**, respectively. The color in the phasor plots corresponds to the number of pixels exhibiting the particular phasor value (blue indicating the lowest occurrence and red indicating the highest occurrence); see the lower color bar.

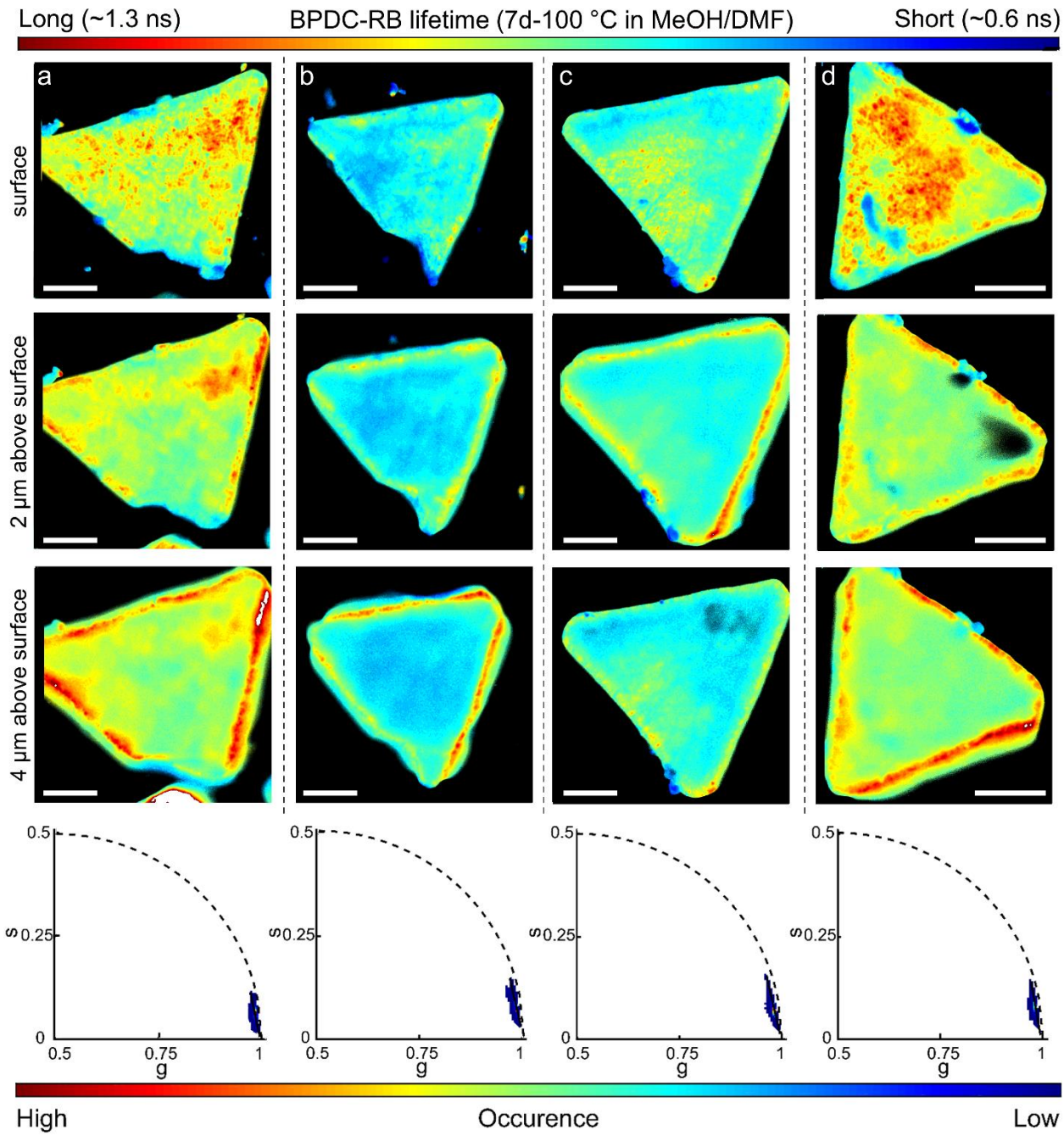

Figure S20: Four crystals after PSE in MeOH/DMF for 7d-100 °C were characterized using FLIM (panels **a-d**). The scale bar in all images is 15 µm. The last row of each panel shows the corresponding phasor plot of the three FLIM images in panels **a**, **b**, **c** and **d**, respectively. The color in the phasor plots corresponds to the number of pixels exhibiting the particular phasor value (blue indicating the lowest occurrence and red indicating the highest occurrence); see the lower color bar.

7. Investigation of defect formation during PSE in DMF

We observed very little differences in lifetime between UiO-67 crystals functionalized with BPDC-RB in DMF for 1d-RT and 7d-RT. A uniform lifetime distribution of 2.91 ± 0.18 ns was observed throughout the whole crystal (Fig.S21 c and d, orange-red). This lifetime is significantly higher than that of BPDC-RB in solvent, indicating that the local environment of the MOF has a stabilizing effect on the fluorophore and thereby reduces the rate of non-radiative transitions, which may also decrease in efficiency when local defects are present. This lifetime is the highest that we have measured, indicating the absence or minimum number of PSE generated defects in these crystals (Fig.S21-S23). Although the autoluminesce of UiO-67 has a longer lifetime of ~ 3.3 ns (as shown in Fig.S8 c and d), its contribution to the measured lifetime is minimal as the fluorescence signal in the crystals is a factor 20-100 higher than the autoluminesce intensity (Fig.S8 a and b). Contrary to the RT experiments, UiO-67 functionalized with BPDC-RB at 100 °C showed interesting spatial lifetime changes. The PSE induced defects in DMF medium at 100 °C displayed an overall shorter lifetime compared to RT. The lifetime value at the surface after 1d-100 °C and 7d-100 °C linker exchange was 2.18 ± 0.23 ns (Fig.S21 e and f, surface, cyan-blue), which suggests that there are more defects generated near the crystal's surface. Interestingly, the PSE induced defects after 1d and 7d (100 °C) are located at the outer surface and differences in lifetime between the surface and the interior were observed (Fig.S21 and S24-S25). A longer lifetime (2.52 ± 0.30 ns, yellowish color) was obtained 4 µm inside the crystal compared to the surface and edges (2.25 ± 0.40 ns, blueish color) (Fig.S21 e and f, 4 µm above surface, yellow-green). The fluorescence intensity distribution observed in DMF after PSE at 100 °C suggests that migration of BPDC-RB from the outside of the crystal to the interior is less efficient than in MeOH/DMF and requires elevated temperatures to initiate. Interestingly, even after PSE in DMF for 7d-100 °C, a spatial distribution in fluorescence lifetime is still present indicating that an equilibration of defects has not yet occurred, in contrast to what was observed for PSE in MeOH/DMF. This is consistent with the even slower linker *through-backbone diffusion* measured in DMF.

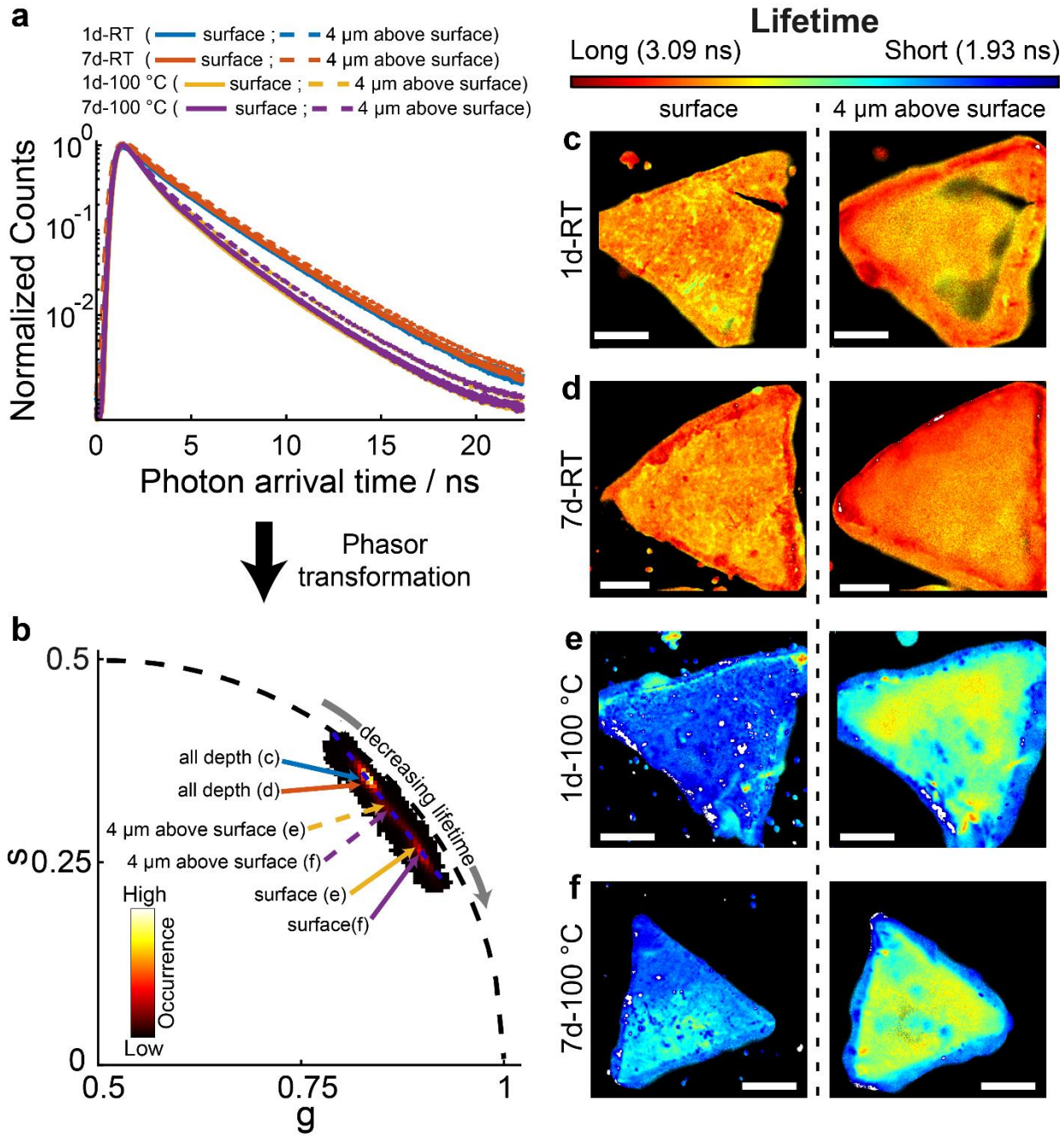

Figure S21: Crystals after PSE under different conditions in DMF were characterized using FLIM. **a**) Fluorescence lifetime decay and **b**) the corresponding phasor plot (obtained via the Fourier transformation from the lifetimes in **a**) for the eight FLIM images shown in (**c**-**f**). The color in the phasor plot corresponds to the number of pixel exhibiting the particular phasor value (black indicating the lowest occurrence and yellow indicating the highest occurrence). The dotted-blue line in the phasor plots is used for generating the color table for the fluorescence lifetimes in the FLIM images. **c**-**f**) FLIM images after PSE for 1d-RT (**c**), 7d-RT (**d**), 1d-100 °C (**e**), and 7d-100 °C (**f**). The scale bar is 15 µm.

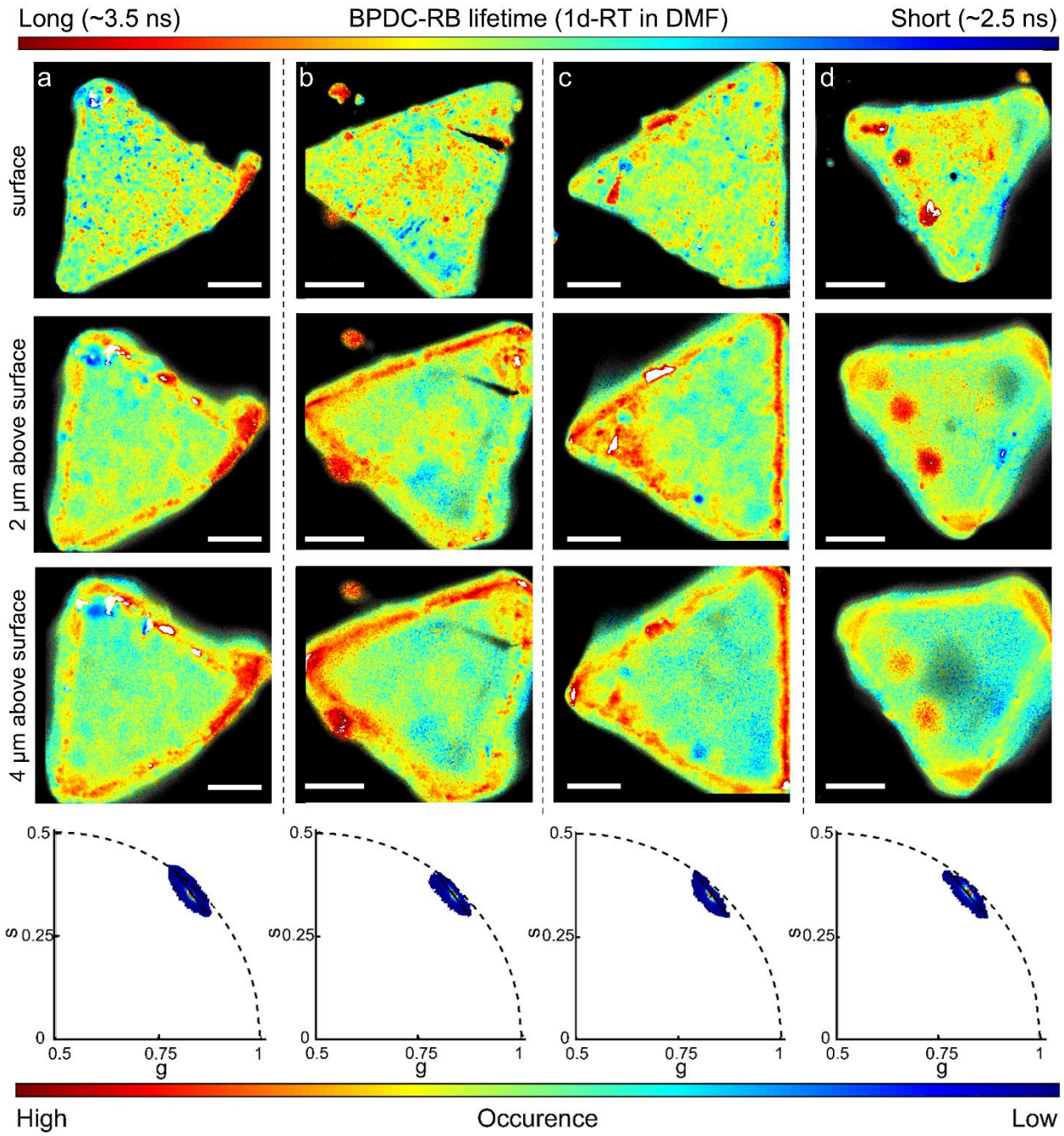

Figure S22: Four crystals after PSE in DMF for 1d-RT were characterized using FLIM (panels **a-d**). The scale bar in all images is 15 µm. The last row of each panel shows the corresponding phasor plot of the three FLIM images in panels **a**, **b**, **c** and **d**, respectively. The color in the phasor plots corresponds to the number of pixels exhibiting the particular phasor value (blue indicating the lowest occurrence and red indicating the highest occurrence); see the lower color bar.

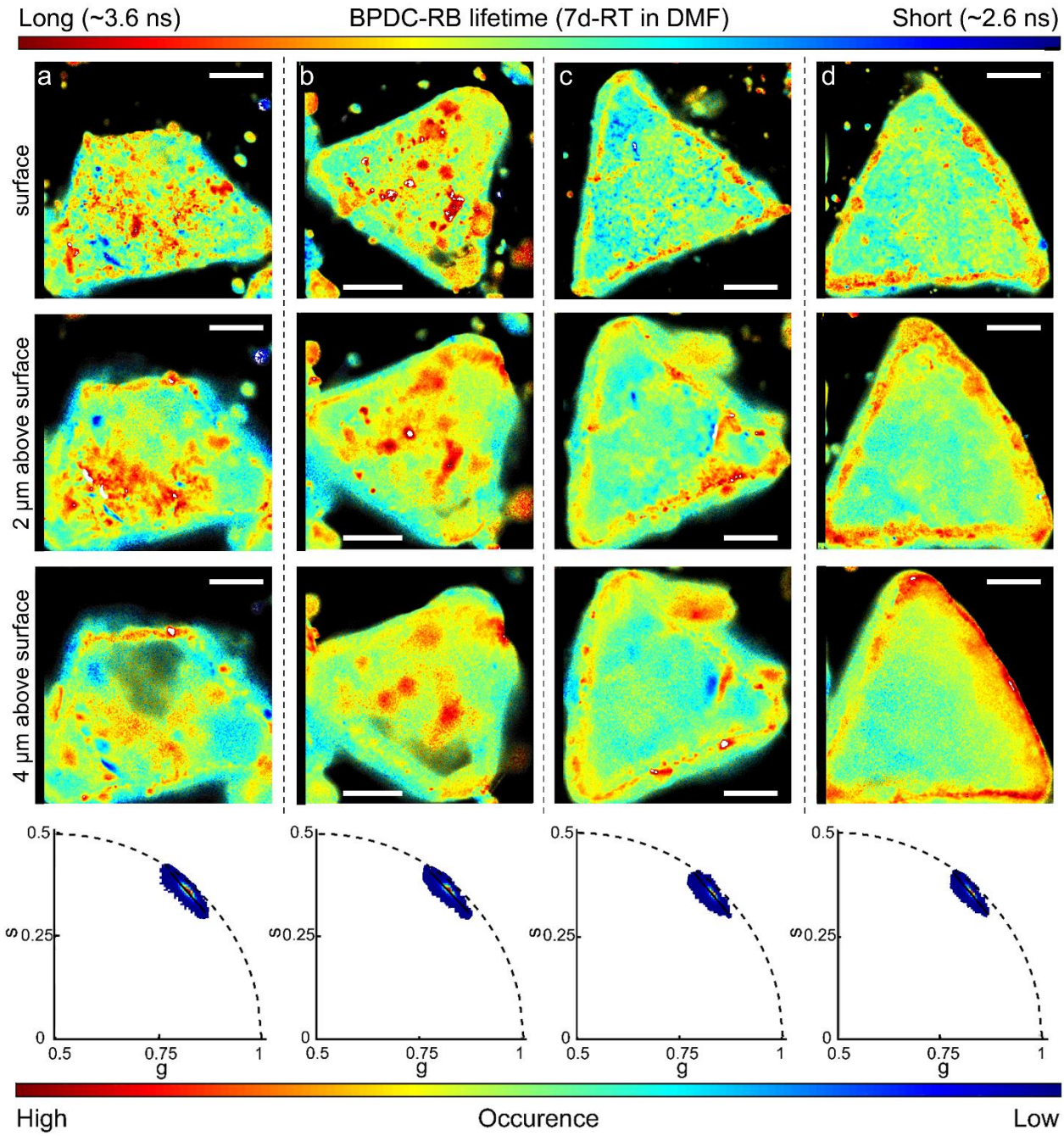

Figure S23: Four crystals after PSE in DMF for 7d-RT were characterized using FLIM (panels **a-d**). The scale bar in all images is 15 µm. The last row of each panel shows the corresponding phasor plot of the three FLIM images in panels **a**, **b**, **c** and **d**, respectively. The color in the phasor plots corresponds to the number of pixels exhibiting the particular phasor value (blue indicating the lowest occurrence and red indicating the highest occurrence); see the lower color bar.

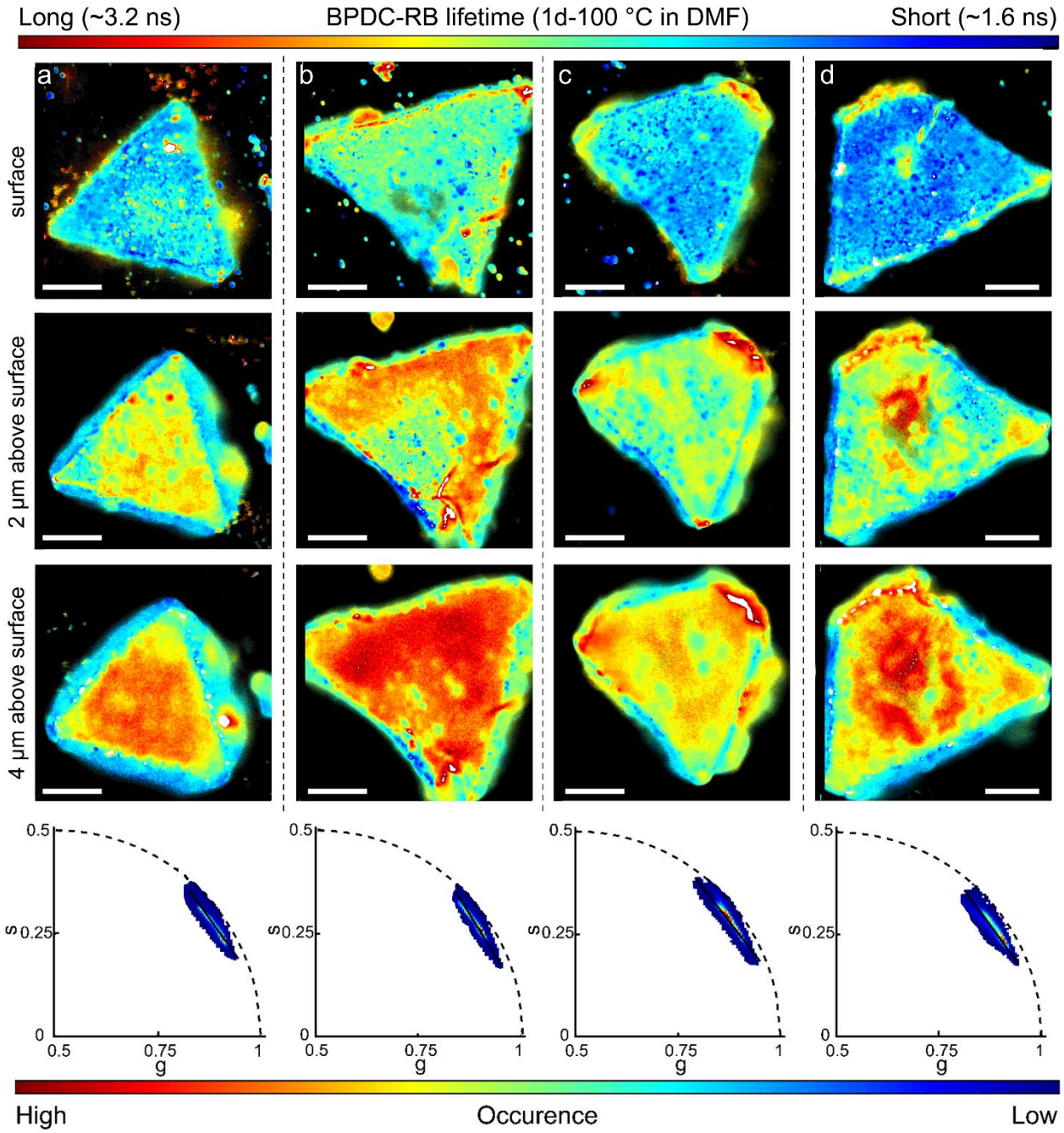

Figure S24: Four crystals after PSE in DMF for 1d-100 °C were characterized using FLIM (panels **a-d**). The scale bar in all images is 15 µm. The last row of each panel shows the corresponding phasor plot of the three FLIM images in panels **a**, **b**, **c** and **d**, respectively. The color in the phasor plots corresponds to the number of pixels exhibiting the particular phasor value (blue indicating the lowest occurrence and red indicating the highest occurrence); see the lower color bar.

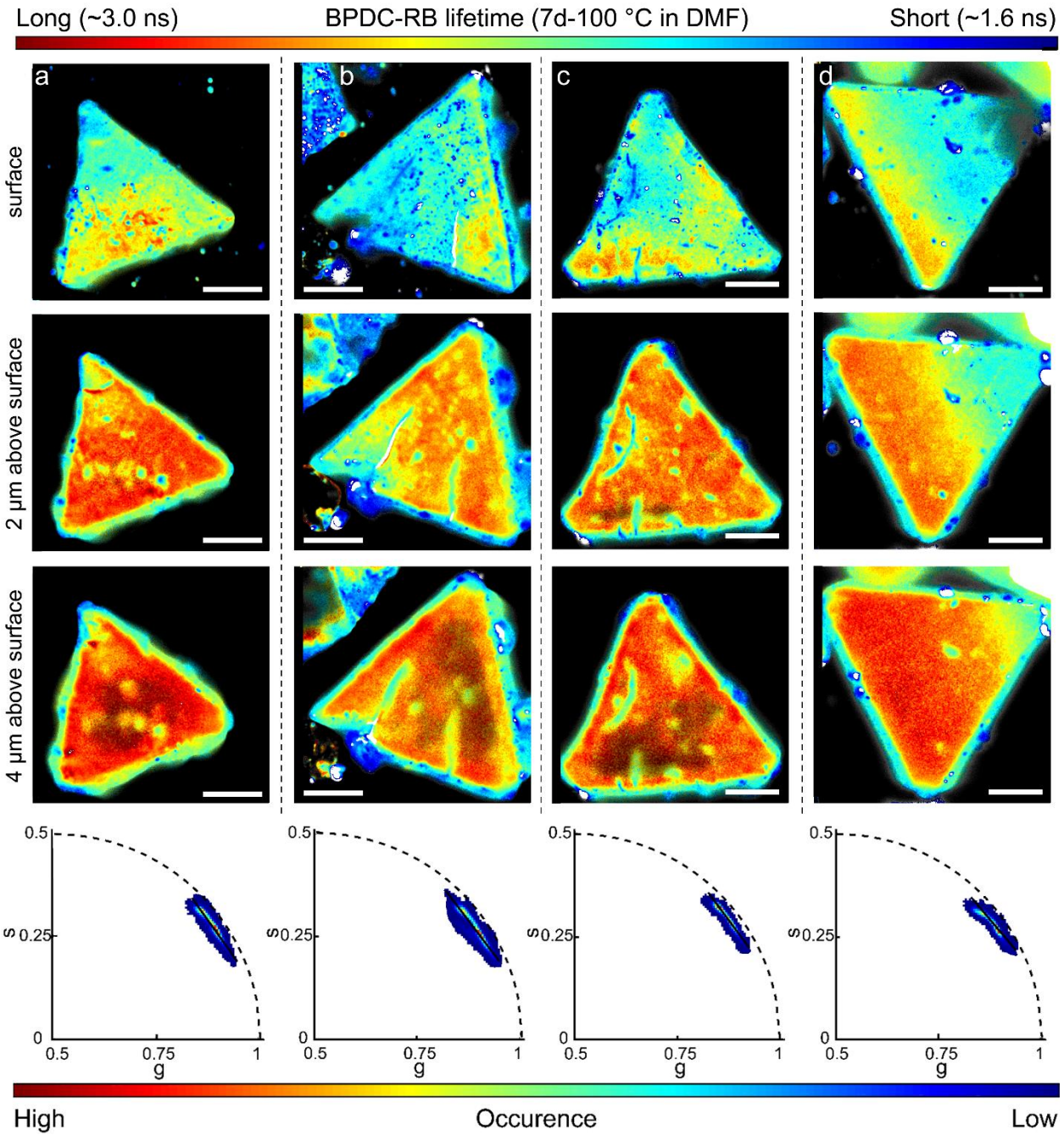

Figure S25: Four crystals after PSE in DMF for 7d-100 °C were characterized using FLIM (panels **a-d**). The scale bar in all images is 15 µm. The last row of each panel shows the corresponding phasor plot of the three FLIM images in panels **a**, **b**, **c** and **d**, respectively. The color in the phasor plots corresponds to the number of pixels exhibiting the particular phasor value (blue indicating the lowest occurrence and red indicating the highest occurrence); see the lower color bar.

References

1. Ko, N.; Hong, J.; Sung, S.; Cordova, K. E.; Park, H. J.; Yang, J. K.; Kim, J., A significant enhancement of water vapour uptake at low pressure by amine-functionalization of UiO-67. *Dalton Trans* **2015,** *44* (5), 2047-51.
2. Schrimpf, W.; Barth, A.; Hendrix, J.; Lamb, D. C., PAM: A Framework for Integrated Analysis of Imaging, Single-Molecule, and Ensemble Fluorescence Data. *Biophys J* **2018,** *114* (7), 1518-1528.
3. Hendrix, J.; Schrimpf, W.; Holler, M.; Lamb, D. C., Pulsed interleaved excitation fluctuation imaging. *Biophys J* **2013,** *105* (4), 848-61.
4. Redford, G. I.; Clegg, R. M., Polar Plot Representation for Frequency-Domain Analysis of Fluorescence Lifetimes. *Journal of Fluorescence* **2005,** *15* (5), 805.
5. Digman, M. A.; Caiolfa, V. R.; Zamai, M.; Gratton, E., The Phasor Approach to Fluorescence Lifetime Imaging Analysis. *Biophysical journal* **2008,** *94* (2), L14-L16.
6. Kaur, G.; Øien-Ødegaard, S.; Lazzarini, A.; Chavan, S. M.; Bordiga, S.; Lillerud, K. P.; Olsbye, U., Controlling the Synthesis of Metal–Organic Framework UiO-67 by Tuning Its Kinetic Driving Force. *Crystal Growth & Design* **2019,** *19* (8), 4246-4251.
7. Cavka, J. H.; Jakobsen, S.; Olsbye, U.; Guillou, N.; Lamberti, C.; Bordiga, S.; Lillerud, K. P., A new zirconium inorganic building brick forming metal organic frameworks with exceptional stability. *J Am Chem Soc* **2008,** *130* (42), 13850-1.

B.3. Paper 3: Methods for Elucidating the Structural-property Relationship in Luminescent Materials.

ARTICLE

Methods for elucidating the structural-property relationship in luminescent materials.

Received 8th June 2021,
Accepted 17th August 2021

DOI: 10.1039/D1TC02634H

Christin Kirst,†[a] Nader A. Danaf,†[a,b] Fabian Knechtel,[a,b] Tim Arczynski,[a] Peter Mayer,[a] Don C. Lamb*[a,b] and Konstantin L. Karaghiosoff *[a]

The search for efficient and stable new blue luminescent compounds is still ongoing. In this respect, knowledge of the structure-property relationship is essential for the design and evaluation of blue emitting materials. However, several uncertainties still exist, such as crystal packing and intermolecular interactions, that can significantly complicate the design process. The application of fluorescence lifetime imaging microscopy in combination with Hirshfeld surface analysis for the characterization of luminescent materials are powerful tools that can be used to investigate the structure-property relationship in an emitting substance. However, they have been vastly underutilized in this field. Our results, based on exemplary, new, functionalized phosphine oxides, show that indeed general trends concerning the relationship between photoluminescence lifetimes, emitted light intensities, attractive intermolecular interactions and overall morphology of a compound can be derived through the combination of both analytical methods.

Introduction

Although knowledge regarding substituent effects and structural features, such as steric restrictions and hindrances, are considered in the design of light emitting materials, the basic design is still largely based on trial and error.[1,2] Hence, additional tools are needed to provide more insights into the structure-property relationship. Here, we demonstrate the advantages of combining fluorescence lifetime imaging microscopy (FLIM) with the Hirshfeld surface (HS) analysis to provide additional insights and thereby reduce the amount of trial and error necessary.

We demonstrate the power of this approach on a new, promising class of luminescent materials: functionalized phosphines. In particular, we investigated picolyl derived phosphine compounds that are successively utilized as catalysts.[3–9] Moreover, the group of A. Artem'ev and others have demonstrated luminescent properties of very similar pyridylphosphine derivatives and complexes thereof, as well as investigated their potential use as OLED materials.[10–16] The compounds show promising results in regards to their photo- and electroluminescent properties. Additionally, their synthesis is quick and high yielding, use inexpensive starting materials and avoid rare metal catalysts. Another advantage of using such functionalized phosphines is that their optical properties can be easily adjusted *via* variations in the aromatic systems.[10,17,18] By introduction of a methylene bridge between the nitrogen containing moiety and the phosphorus atom, an even more flexible ligand is obtained.[19] This unique property allows the ligand to adapt to metals with different coordination geometries and sizes more easily (e.g. formation of polynuclear, mixed-metal complexes or coordination polymers), which has the possibility to improve catalytic properties, and generate interesting material properties such as high luminescence or porosity like in MOFs.[17,20–27] Additionally, the normally rather labile P–C bond can be stabilized *via* complexation, which reduces its flexibility.[28–30] The resulting, more rigid structure minimizes quenching and provides, in general, a more thermally-stable compound. A subsequent oxidation of the phosphine to the phosphine oxide results in air and moisture stable compounds. This stability is beneficial for applications utilizing luminescent materials such as long-lasting OLED devices, because it facilitates processing and enhances longevity.[31–33]

The characterization of luminescent compounds is usually done in the solid state, in thin films or in solution by measuring the UV/Vis absorption and emission spectra. This is, in general, a convenient way to characterize the bulk material. However, these methods provide little information regarding the intermolecular interactions between the single molecules in the crystal or powder and the influence such structural features can have on the photophysical properties.

FLIM uses spatially resolved fluorescence lifetime decays to gain insight into the nanoscopic environment of a material, such as its defects and morphologies.[34–37] FLIM is a fluorescence imaging technique where the contrast is based on the lifetime of individual fluorophores rather than their emission spectra. FLIM has been widely utilized during the last few years in

[a] Department of Chemistry, Ludwig Maximilian University of Munich, Butenandtstr. 5-13 (D), 81377 Munich, Germany. E-mail: klk@cup.uni-muenchen.de.
[b] Center for NanoScience (CeNS), NanoSystems Initiative Munich (NIM) and Center for Integrated Protein Science Munich (CIPSM), Ludwig Maximilian University of Munich, Butenandtstr. 5-13, 81377 Munich, Germany. E-mail: d.lamb@cup.uni-muenchen.de
† These authors contributed equally to this work.
Electronic Supplementary Information (ESI) available. See DOI: 10.1039/D1TC02634H

different research fields such as medicine and biology, and has recently been applied to material sciences.[38–40] Common implementations of FLIM allow nanoscopic investigations of a wealth of parameters in the vicinity of the sample of interest. This includes local environment sensing (pH, temperature, ion concentration, etc.), detection of molecular interactions and conformational changes in cellular biology.[41–43] However, in the field of material science, the potential of FLIM has been underutilized.[44,45] Although the characterization of luminescent materials utilizes time-correlated single photon counting (TCSPC) for lifetime measurements, the imaging technology of FLIM has not been exploited. Having both spatial imaging and lifetime information with FLIM is very useful for understanding important structure-property relationships of an emitting substance and to explain photophysical properties of the material, such as quantum yield, based on the observed structural motives or morphologies.

HS analysis can further aid in the interpretation of structural features and gives additional information based on the crystal structure data such as intermolecular interactions and, in particular, attractive hydrogen bonding.[46] It is known that, after photoexcitation, a delocalization of the excitation through hydrogen bond channels can occur and excimers can form.[1,47–50] Normally, upon formation of the excimer, structural rearranges are necessary and the dimer becomes unstable upon deexcitation. This procedure consumes a lot of excited state energy and quenches the fluorescence. However, in the case of an excimer connected by hydrogen bonds, the structural changes with respect to the monomers are small, resulting in minimal energy loss when returning to the ground state. Consequently. the luminescence is enhanced.[47,51,52] This knowledge can be beneficial when developing and evaluating the suitability of new luminescent materials for different applications such as OLEDs and should, therefore, become a standard characterization tool.

Herein, we present new functionalized phosphine oxides, which contain pyrazine and triazine derivatives in the heteroaromatic part, and their photophysical properties. The synthesized compounds were characterized *via* single crystal X-ray diffraction, multinuclear NMR, IR, MS and EA. Furthermore, their photophysical properties were measured either in solution or in the solid state. FLIM measurements were done to gain insight into the lifetime of the photoluminescence decay in the compounds. The combination of FLIM measurements together with quantitative HS analysis provided further insights into structural-property information, which can be broadly applied in the design and development of new luminescent materials.

Results and discussion

Synthesis

The synthesis of the trimethylsilyl (TMS) compounds used as precursors for the respective phosphines are shown in **Scheme 1**. Compound **1** has been mentioned and used before in the literature, but a synthesis procedure has not yet been described.[53,54] Whereas compounds **2** and **3** could be synthesized with *n*-butyllithium (*n*BuLi), the milder lithiation reagent lithium diisopropylamine (LDA) has to be used for a successful reaction of compound **1**. The beginning substance for compound **3**, 2,4,6-trimethyl-1,3,5-triazine, was synthesized according to literature.[55,56] The corresponding TMS compound **3** has a very characteristic smell, which is reminiscent of sweet popcorn. All TMS compounds synthesized are viscous colorless liquids and should be stored in sealed containers under protective gas.

Preparation of the phosphine oxides starting from their corresponding trimethylsilyl compounds is shown in **Scheme 2**. The synthesis is well established in our lab and was first described by Braunstein for bis(picolyl)phenylphosphine.[57] This synthetic route is very advantageous when compared to the classic route, where the dichlorophosphine is allowed to react directly with the lithiated picolyl derivative. The so called "Braunstein-route" allows for synthesis of 5 g of ligands or more with quantitative yields and an easy workup. Any excess TMS compound can be easily removed under vacuum. All phosphine oxides are colorless powders when isolated. The compounds were further characterized by multinuclear NMR spectroscopy, high-resolution mass spectrometry, elemental analysis, infrared spectroscopy and thermogravimetry (for details, see ESI†).

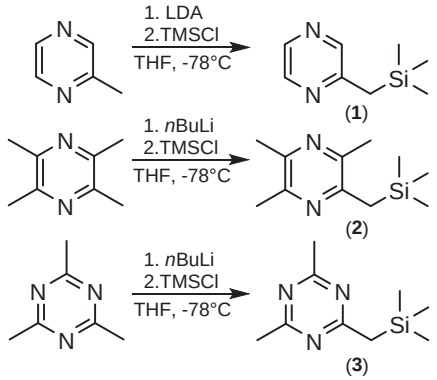

Scheme 1. Synthesis of the TMS compounds **1–3**.

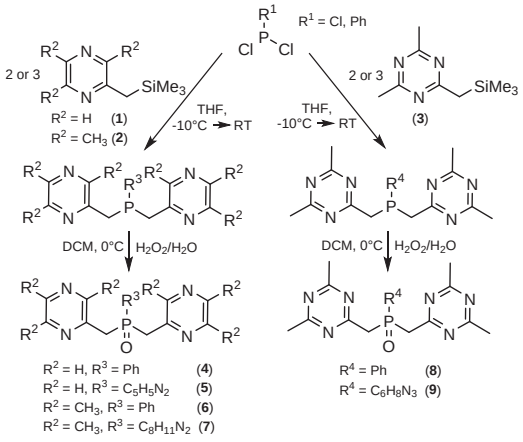

Scheme 2. Synthesis of phosphine oxide ligands **4–9**.

Structural Characterization

Next, we investigated the structure of the different compounds and their packing within the crystal using X-ray crystallography. Crystals of phosphine oxides **4**–**6** and **8** were obtained by slow diffusion of hexane into a solution of dichloromethane. Crystals of **7** and **9** were generated *via* slow evaporation of a solution of the compound in tetrahydrofuran. Crystallographic details and refinement data can be found in the Supporting Information (**Table S2** and **Table S3**).

All compounds crystallize in monoclinic space groups (**4** and **8** in $P2_1/n$; **5** and **6** in $P2_1/c$, **9** in $C2/c$) with four or eight units in the unit cell (**Figure 1**), except for **7**, which crystallizes in the tetragonal space group $I4_1/a$ with 16 units in the unit cell. In all structures, the O–P–C angles are larger and the C–P–C angles are smaller than the ideal tetrahedron angle of 109.5°. Similar values have been reported for comparable phosphine oxides.[8,19,58,59] Additionally, in all structures, weak, non-classical hydrogen bonds between the oxygen and methylene hydrogen atoms are observed.[60] These interactions play an important role in the formation of the structures in the crystal, which may influence their luminescence properties.

The molecules of **4** form antiparallel chains in the crystal, which are stacked along the *b* axis (**Figure S8**). Compound **5** forms zig-zag chains along the *c* axis in the crystal (**Figure S9**). Additional weak, face-to-face π-π interactions are present between two neighboring pyrazine rings with an average distance of 3.50 Å.[61,62] Compound **6**, like **5**, forms zig-zag chains along the *c* axis (**Figure S10**). Weak, offset π-π interactions are present between neighboring trimethylpyrazine rings with an average distance of 3.50 Å.[61,62]

Compound **7** arranges in a helix along the c axis (**Figure S11**). Steric hinderance of the methyl groups prohibit possible close π-π interactions. The aromatic rings in the spiral are offset from each other with the closest distance being 3.73 Å. Solvent molecules tend to intercalate between the different helices causing structural disorders. However, an appropriate model to resolve the disorder could not be determined.

Compound **8**, on the other hand, forms pairs of molecules in the crystal, which are arranged as H-bonded chains along the *b* axis (**Figure S12**). Compound **9** forms anti-parallel layers along the *b* axis in the crystal (**Figure S13**, left). The single molecules in these layers are arranged in chains along the *b* axis (**Figure S13**, right).

Photophysical Characterization

When the solid compounds **4**–**9** were irradiated with UV light (366 nm), a blue photoluminescence was observed (**Figure 1**). Further photophysical measurements were conducted to gain more insight into the luminescent properties of these compounds.

The UV-Vis absorption spectra recorded for the solid compounds **4**–**9** displayed maxima at 384 nm for **5**, **7** and **8**, 375 nm for **6** and 356 nm for **4** and **9** (**Figure S14**). The absorption spectra have a width of around 100 nm and the tails even reach the region of the visible light. For compounds **4**–**6** and **8**, excitation and emission spectra were recorded in acetonitrile (**Figure S15** and **Figure S16**). The photoluminescence maximum of the excitation scan was selected as λ_{exc} for the emission scan. Compounds **4** and **5** show the highest fluorescence emission when excited at 347 nm with a larger tail for **4**.

Figure 1. Molecular structure of the asymmetric unit of the phosphine oxides **4**–**9** in the crystal and a picture of the solid

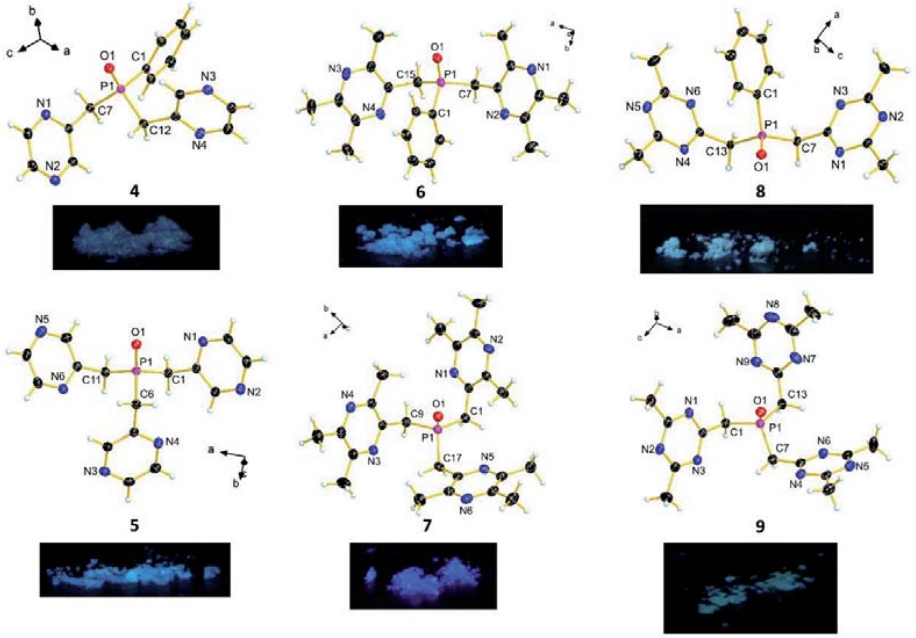

compounds under UV illumination (366 nm). Diamond 3 representation, thermal ellipsoids are drawn at 50 % probability level.

Similarly, **6** shows the highest fluorescence emission when excited at 341 nm and **8** shows the highest hypsochromic shift with the highest emission for 336 nm excitation (**Figure S15**). Compounds **5** and **8** show an emission maximum at 430 nm and 425 nm, respectively. In agreement with the excitation spectra, **4** and **6** show the highest bathochromic shift with the highest emission at ~450 nm when exited at ~365 nm (**Figure S16**). The small spikes in the spectra result from Raman peaks of the solvent and can be seen in the solvent excitation and emission spectrum (**Figure S15** and **Figure S16**, black spectra). These results show, that the functionalized phosphine oxides are promising candidates and may be used in the future as ligands for the possible development of luminescent metal complexes. When looking at the absorption and excitation/emission spectra, no clear trend with respect to structural properties of the compounds is discernable. The nitrogen content and/or the number of methyl groups on the heteroaromatic substituent has no apparent effect on the emission properties.

Lifetime Characterization

For further investigations, we focused on the photoluminescence and structural properties of the phosphine oxides **4**–**6** and **8**. Solvent molecules were observed within the crystal structures of compounds **7** and **9** and were therefore not further analyzed to avoid potential ambiguities in the FLIM data due to the presence of the solvent molecules. Compounds **4**, **5**, **6** and **8** were diluted in acetonitrile solution and investigated using FLIM. FLIM measurements showed the samples to consist of smaller microstructures with either distinct crystalline or amorphous morphology and different photoluminescence lifetimes (**Figure 2a**). Lifetimes between 1.8 and 4.05 ns were measured, indicative of single-single electronic transitions (i.e. fluorescence). Compound **4** shows a high homogeneity of rod-like crystals with a uniform fluorescence lifetime of ~1.80 ns (**Figure 2a**(**i**), blue), the shortest of the four compounds. Compound **5** displays an interesting morphology mainly comprised of quasi-spherically elongated and oval-like particles with a uniform fluorescence lifetime of ~2.35 ns (**Figure 2a**(**ii**), cyan, light green). Compound **6** shows distinct morphologies, mainly comprised of thick plate-like crystals. The fluorescence lifetime distribution is the most uniform between crystals and has the longest fluorescence lifetime decay of ~4.05 ns (**Figure 2a**(**iii**), orange). However, it displays a heterogeneous fluorescence intensity distribution with the majority of photons being emitted from the edges. In addition, the overall number of detected photons was very low even at maximum laser power (50 μW, see ESI for more details) indicating that the emissive property of this compound is less efficient than compounds **4**, **5** and **8** (**Figures S17–S20**, fluorescence intensity images). Compound **8**, in contrast to **4** or **6**, shows a more amorphous like morphology with a quite homogeneous fluorescence lifetime of ~2.75 ns (**Figure 2a**(**iv**), cyan). **Figure 2b** and **Figure 2c** show the FLIM data analysis by either analyzing the TCSPC data directly (**Figure 2b**) or via the phasor approach, which graphically translates the fluorescence lifetime from **Figure 2b** into Fourier space (**Figure 2c**).[63,64] In the phasor plot, mono-exponential decays fall along an arc of radius 0.5 with long lifetime components located near the origin (0, 0) and short lifetime components near (1, 0). Multi-exponential decays comprise a weighted vector of the constituent phasors, meaning that all decay pathways in phasor space lie within the arc.[63,65] For the different compounds investigated (**4**–**6** and **8**), the phasor space occupied by all crystals lies within the arc, indicating a multiexponential decay (biexponential in this case). A biexponential function was also sufficient to describe the fluorescence lifetime for the four different crystals of each compound (**Figures S21–S24**, **Table S10**). The short lifetime component (~1 ns) is similar for all constructs whereas the longer lifetime component varies slightly between them(~3–5 ns). Interestingly, the average fluorescence lifetime decreases with increasing brightness (**Figure S25a**). A detailed analysis of the FLIM data shows that the fluorescence brightness increases with the fraction of light coming from the short lifetime component (**Figure S25b**). This indicates that the inherent fluorescence properties of the compounds are different and not dominated by various quenching pathways. Here, the observed high brightness and short lifetime indicate an improved quantum yield in the shorter lifetime species, which also protects the substance against photodegradation typically occurring from the excited state.

The shortest average fluorescence lifetime populations obtained were for the crystalline rod-like compound **4**, followed by the oval-like particles of compound **5** and compound **8** with an amorphous like morphology. However, compound **4** displays spatial lifetime differences, where a longer lifetime is observed on the edges in comparison with the crystals' interior **Figure S17**). The shorter lifetime component inside the crystals correlates with the higher brightness observed in the interior, which is in line with the improved quantum yield in the shorter lifetime species (**Figure S17**). On the other hand, **8** showed a more uniform lifetime distribution with minor differences between the internal and external parts of the amorphous structure (**Figure S20**). Compound **5**, similar to compound **8,** exhibits no significant lifetime differences between the internal and external parts of the structures (**Figure S18**).

Combining Hirshfeld surface analysis with the FLIM results

The FLIM results alone are insufficient for providing a direct correlation between structure-property relationship and normal crystal density packing (**Table S2 of ESI**). That is, the lifetime does not only depend on the density of the structures and the materials' morphology. Other factors that can also influence the fluorescence lifetime include strong intermolecular interactions such as π-π interactions and H-bonds, intra/intermolecular charge transfer processes, or excimer formation can be considered as contributing factors for lifetime changes.

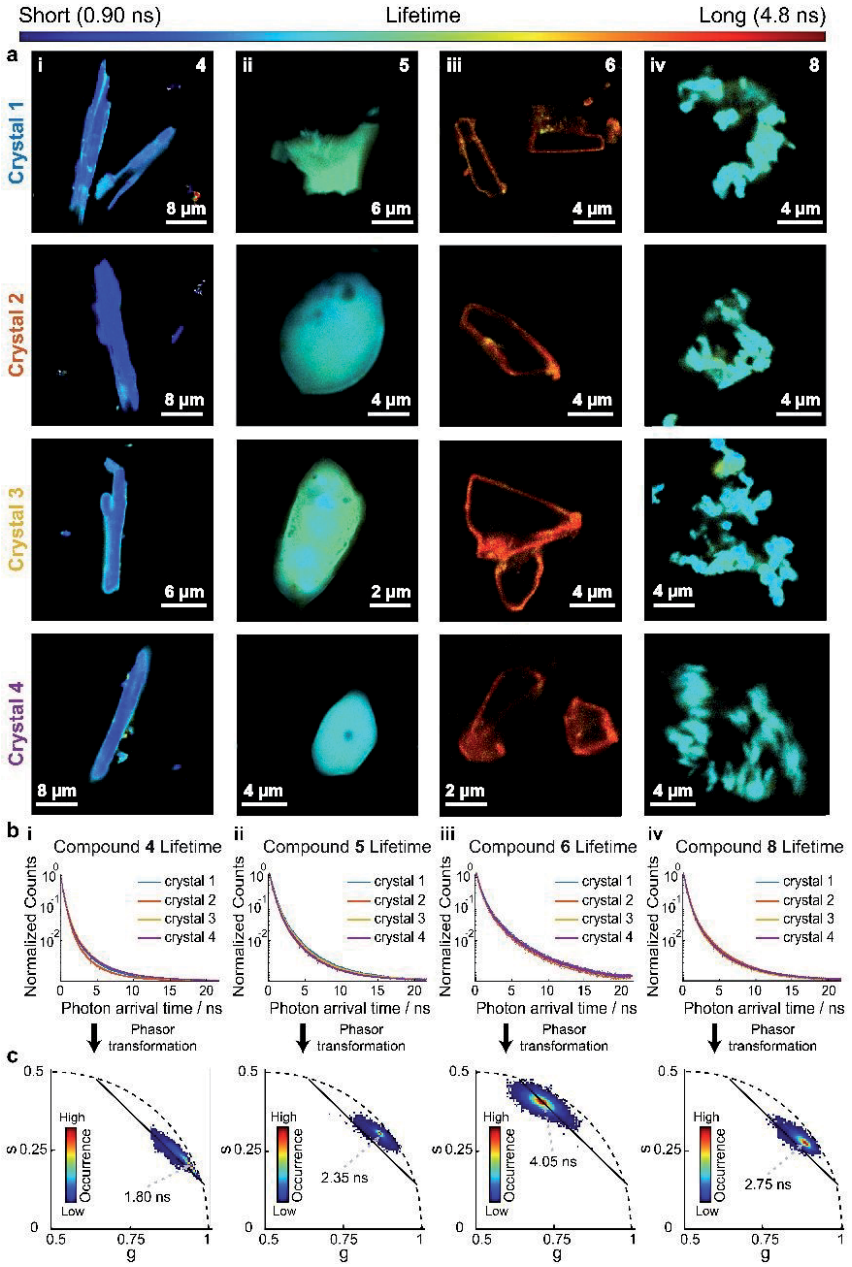

Figure 2. Fluorescence lifetime decays and FLIM images of the different compounds showing the diverse structural morphologies they possess. a) Representative FLIM images are shown for the four compounds i) **4**, ii) **5**, iii) **6** and iv) **8**. The color-code corresponding to the fluorescence lifetime displayed on the FLIM images, goes from blue (indicating the shortest fluorescence lifetime) over green and yellow to orange and red (indicating the longest fluorescence lifetime), see the color bar for fluorescence lifetime. b) From the FLIM images, the fluorescence lifetime decay is plotted for the different compounds i) **4**, ii) **5**, iii) **6** and iv) **8**. c) The corresponding phasor plot of the four FLIM images for each compound i) **4**, ii) **5**, iii) **6** and iv) **8** is shown, which is the Fourier transformation of the lifetimes plotted in panel b. The dotted-grey arrows indicate the average phasor positions of the four FLIM images, with the indicated lifetime values. The color in the phasor plots corresponds to the number of pixels exhibiting the particular phasor value (blue indicating the lowest occurrence and red indicating the highest occurrence), see the occurrence color bar within the phasor plot. The black line in the phasor plots is used for generating the color table for the fluorescence lifetimes in the FLIM images in panel a. The pixel brightness corresponds to total counts, while the hue indicates the pixels' proximity to the black line.

Here, we applied the Hirshfeld surface analysis for a quantitative comparison of intermolecular interactions between molecules in the crystal based on the crystallographic output file (.cif) obtained from single crystal X-ray diffraction.[46,66] Short contacts are visualized by red dots in the d_{norm} maps and by sharp spikes in the fingerprint plots (**Figure 3a-d**). These data can aid in the interpretation of the FLIM results and overall luminescent properties, and enable the possibility of investigating correlating effects.

The HS analysis of compound **4** reveals a high percentage of attractive C–H···N (26.2 %) and C–H···O (7.7 %) interactions (see **Figure 4**).[1,48,49] For compound **5**, a slightly higher percentage of attractive C–H···N (29.4 %) and C–H···O (9.5 %) interactions are observed. Compound **6** has the highest number of C–H···H (68.5 %) interactions and the lowest number of attractive C–H···N (13.9 %) and C–H···O (4.1 %) interactions of the investigated compounds limiting excimer formation between the single molecules in the structure.[1,48,49] Compound **8** has a similar amount of attractive interactions to compounds **4** and **5** with C–H···N content of 23.6 % and C–H···O content of 7.8 %. Weak π-π-interactions, present in all compounds, are visible as C···H , C···N and C···C contacts in the fingerprint plots (27.3 % for **4**, 18.8 % for **5**, 13.9 % for **8** and 13.6 % for **6**; **Figure 3**), with the C···H interactions being the major contributor. All π-π-interactions are below the values for face-to-face (<3.8 Å), offset (<3.4 Å) and/or T-shaped (<4.9 Å) π-π-interactions of pyridine, which indicates that these π-π contacts count as attractive interactions and influence the structural geometry.[61,62]

By combining the HS analysis and the FLIM information, we can investigate whether there is a correlation between the intermolecular bonding interactions and the fluorescence properties. With increasing attractive C–H···N and C–H···O interactions within the crystals, we observe an increase in the fluorescence brightness (**Figure 3f**) and an overall trend of decreasing average lifetimes (**Figure S25a**). We attribute this to an increase in the fraction of light emitted from the short lifetime component (**Figure S25b**). This suggests that the short lifetime component is coming from the excimer state, indicating that there is a relationship between the material properties, morphology and crystal packing. Alongside the structural parameters, these interactions are crucial in understanding the differences in the emissive properties of the different compounds and the way these particles interact with each other under different structural conditions in the crystals. Hence, the FLIM measurements combined with the Hirschfield surface analysis reinforce our understanding of the morphology and its role for the observed photophysical differences among the diverse compounds. For example, the FLIM images of compound **6,** which has the longest fluorescence lifetime decay of the four investigated compounds, reveal quenching in the middle of the crystal and weak luminescent properties of the compound. In addition, the HS analysis discloses that this compound has the lowest amounts of π-π-interactions and attractive C–H···N and C–H···O interactions in the crystal, in addition to the loose packing of its structure (**Table S2**). On the other hand, compound **5** seems to possess the best overall properties of the four compounds that were more closely investigated.

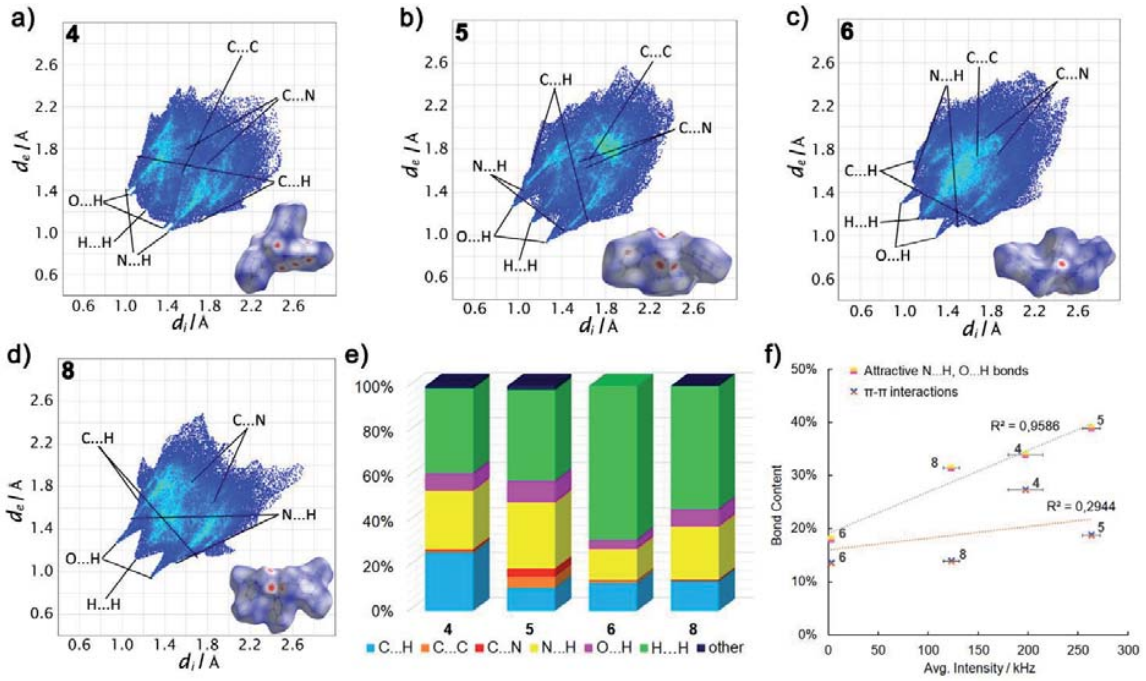

Figure 3. d_{norm} maps and fingerprint plots of compounds **4**–**6** and **8** (a–d). e) Diagram showing the percentages of the close contacts in the crystal packing of the selected compounds. f) correlation of intermolecular interactions in the crystal versus average intensity.

Its fairly high emissive properties with a maximum at 425 nm is in the ideal wavelength region for a blue emitter. The fluorescence lifetime decay is short (2.35 ns), but uniformly spread over the spherical structure, which suggests a homogenous emission throughout the structure. Additionally, **5** exhibits the highest intensity of emitted light, which is supported by the HS analysis showing the highest percentage of attractive C–H···N and C–H···O interactions.

Conclusions

The synthesis of six multidentate phosphine oxides was reported. The compounds were characterized using NMR, MS, IR spectroscopy, EA and X-ray crystallography. The solid compounds show fluorescence when irradiated with UV light (366 nm). A closer characterization of the photophysical properties of these compounds was done by absorption and fluorescence excitation/emission spectroscopy. The preliminary results show that the developed phosphine oxides are promising candidates for blue emitters.

The combination of FLIM measurements and the quantitative Hirshfeld surface analysis made it possible to elucidate structural-property-relationships of the synthesized luminescent phosphine oxide ligands. The data suggests that knowledge about morphology, crystal packing and nature of intermolecular interactions is important for interpreting the uniformity and decay of the fluorescence lifetime, as well as the observed differences in the emitted light intensities. With increasing attractive C–H···N and C-H···O interactions within the crystals, an increase in the fluorescence brightness and a decrease in the average lifetime are observed. Although these types of hydrogen bond acceptors (C–H···N and C-H···O) are of a relatively weak nature, they still seem to have an impact on the luminescent properties of the compounds.

Our results also provide a basis for more in depth investigations using quantum-chemical simulations. These could provide additional insights into how phenomena such as quenching, charge-transfer or morphology can influence the photoluminescent properties of the materials.

In general, novel insights can be obtained by combining FLIM information with a quantitative Hirshfeld surface analysis and should be taken into account when designing and investigating future luminescent materials for e.g. OLED applications. In this particular case, the FLIM and HS analysis combination provides an important preselection tool for choosing potential compounds based on their photoluminescence properties. Additionally, the introduction of weak and/or strong hydrogen bond acceptors is an option that can be employed as means to improve the luminescence lifetime and intensity of the compounds.

Author Contributions

Author 1 and Author 2 contributed equally to this work.

Conflicts of interest

There are no conflicts to declare.

Acknowledgements

The German Federal Ministry for Economic Affairs and Energy on the basis of a decision by the German Bundestag (ZIM, Grant ZF4477702SL7) supported this work financially as well as by the Deutsche Forschungsgemeinschaft (DFG, German Research Foundation) – Project-ID 201269156 – SFB 1032 Project B03. The financial support of Ludwig-Maximilian University of Munich via the Department of Chemistry, the Center for NanoScience (CeNS) and the LMUinnovativ initiative BioImaging Network (BIN) is also gratefully acknowledged. Additionally, we are particularly grateful to Prof. Dr. T. M. Klapötke for his continuous support over the years.

References

(1) Gierschner, J.; Park, S. Y. Luminescent Distyrylbenzenes: Tailoring Molecular Structure and Crystalline Morphology. *J. Mater. Chem. C* **2013**, *1* (37), 5818–5832. https://doi.org/10.1039/c3tc31062k.

(2) Poriel, C.; Rault-Berthelot, J. Designing Host Materials for the Emissive Layer of Single-Layer Phosphorescent Organic Light-Emitting Diodes: Toward Simplified Organic Devices. *Adv. Funct. Mater.* **2021**, *2010547*, 1–43. https://doi.org/10.1002/adfm.202010547.

(3) Adrio, L. A.; Hii, K. K. *Organometallic Chemistry*; Fairlamb, I. J. S., Lynam, J. M., Eds.; Organometallic Chemistry; Royal Society of Chemistry: Cambridge, 2009; Vol. 35. https://doi.org/10.1039/9781847551030.

(4) Carroll, M. P.; Guiry, P. J. P,N Ligands in Asymmetric Catalysis. *Chem. Soc. Rev.* **2014**, *43* (3), 819–833. https://doi.org/10.1039/C3CS60302D.

(5) Tang, W.; Zhang, X. New Chiral Phosphorus Ligands for Enantioselective Hydrogenation. *Chem. Rev.* **2003**, *103* (8), 3029–3070. https://doi.org/10.1021/cr020049i.

(6) Musina, E. I.; Balueva, A. S.; Karasik, A. A. Phosphines: Preparation, Reactivity and Applications. In *Organophosphorus Chemistry*; 2019; Vol. 48, pp 1–63. https://doi.org/10.1039/9781788016988-00001.

(7) Hettstedt, C.; Unglert, M.; Mayer, R. J.; Frank, A.; Karaghiosoff, K. Methoxyphenyl Substituted Bis(Picolyl)Phosphines and Phosphine Oxides. *Eur. J. Inorg. Chem.* **2016**, *2016* (9), 1405–1414. https://doi.org/10.1002/ejic.201600032.

(8) Hettstedt, C.; Köstler, P.; Ceylan, E.; Karaghiosoff, K. Synthesis of the First Representatives of Amino Bis(Picolyl) and Amino Bis(Quinaldinyl) Phosphines. *Tetrahedron* **2016**, *72* (23), 3162–3170. https://doi.org/10.1016/j.tet.2016.04.021.

(9) Gavrilov, K. N.; Polosukhin, A. I. Chiral P,N-Bidentate Ligands in Coordination Chemistry and Organic Catalysis Involving Rhodium and Palladium. *Russ. Chem. Rev.* **2000**, *69* (8), 661–682.

https://doi.org/10.1070/RC2000v069n08ABEH000559.

(10) Artem'ev, A. V.; Ryzhikov, M. R.; Taidakov, I. V.; Rakhmanova, M. I.; Varaksina, E. A.; Bagryanskaya, I. Y.; Malysheva, S. F.; Belogorlova, N. A. Bright Green-to-Yellow Emitting Cu(i) Complexes Based on Bis(2-Pyridyl)Phosphine Oxides: Synthesis, Structure and Effective Thermally Activated-Delayed Fluorescence. *Dalton Trans.* **2018**, *47* (8), 2701–2710. https://doi.org/10.1039/c7dt04758d.

(11) Baranov, A. Y.; Berezin, A. S.; Samsonenko, D. G.; Mazur, A. S.; Tolstoy, P. M.; Plyusnin, V. F.; Kolesnikov, I. E.; Artem'Ev, A. V. New Cu(i) Halide Complexes Showing TADF Combined with Room Temperature Phosphorescence: The Balance Tuned by Halogens. *Dalton Trans.* **2020**, *49* (10), 3155–3163. https://doi.org/10.1039/d0dt00192a.

(12) Artem'ev, A. V.; Doronina, E. P.; Rakhmanova, M. I.; Sutyrina, A. O.; Bagryanskaya, I. Y.; Tolstoy, P. M.; Gushchin, A. L.; Mazur, A. S.; Gusarova, N. K.; Trofimov, B. A. Luminescent Cu I Thiocyanate Complexes Based on Tris(2-Pyridyl)Phosphine and Its Oxide: From Mono-, Di- and Trinuclear Species to Coordination Polymers. *New J. Chem.* **2016**, *40* (12), 10028–10040. https://doi.org/10.1039/C6NJ02087A.

(13) Berezin, A. S.; Artem'ev, A. V.; Komarov, V. Y.; Baranov, A. Y. A Copper(<scp>i</Scp>) Bromide Organic–Inorganic Zwitterionic Coordination Compound with a New Type of Core: Structure, Luminescence Properties, and DFT Calculations. *New J. Chem.* **2020**, *44* (23), 9858–9862. https://doi.org/10.1039/D0NJ01835J.

(14) Artem'ev, A. V.; Baranov, A. Y.; Rakhmanova, M. I.; Malysheva, S. F.; Samsonenko, D. G. Copper(<scp>i</Scp>) Halide Polymers Derived from Tris[2-(Pyridin-2-Yl)Ethyl]Phosphine: Halogen-Tunable Colorful Luminescence Spanning from Deep Blue to Green. *New J. Chem.* **2020**, *44* (17), 6916–6922. https://doi.org/10.1039/D0NJ00894J.

(15) Shameem, M. A.; Orthaber, A. Organophosphorus Compounds in Organic Electronics. *Chem. - A Eur. J.* **2016**, *22* (31), 10718–10735. https://doi.org/10.1002/chem.201600005.

(16) Bestgen, S.; Schoo, C.; Neumeier, B. L.; Feuerstein, T. J.; Zovko, C.; Köppe, R.; Feldmann, C.; Roesky, P. W. Intensely Photoluminescent Diamidophosphines of the Alkaline-Earth Metals, Aluminum, and Zinc. *Angew. Chem. Int. Ed.* **2018**, *57* (43), 14265–14269. https://doi.org/10.1002/anie.201806943.

(17) Rogovoy, M. I.; Davydova, M. P.; Bagryanskaya, I. Y.; Artem'ev, A. V. Efficient One-Pot Synthesis of Diphenyl(Pyrazin-2-Yl)Phosphine and Its AgI, AuI and PtII Complexes. *Mendeleev Commun.* **2020**, *30* (3), 305–307. https://doi.org/10.1016/j.mencom.2020.05.014.

(18) Joly, D.; Bouit, P.-A.; Hissler, M. Organophosphorus Derivatives for Electronic Devices. *J. Mater. Chem. C* **2016**, *4* (17), 3686–3698. https://doi.org/10.1039/C6TC00590J.

(19) Kirst, C.; Zoller, F.; Bräuniger, T.; Mayer, P.; Fattakhova-Rohlfing, D.; Karaghiosoff, K. Investigation of Structural Changes of Cu(I) and Ag(I) Complexes Utilizing a Flexible, Yet Sterically Demanding Multidentate Phosphine Oxide Ligand. *Inorg. Chem.* **2021**, *60* (4), 2437–2445. https://doi.org/10.1021/acs.inorgchem.0c03334.

(20) Nojiri, A.; Kumagai, N.; Shibasaki, M. Linking Structural Dynamics and Functional Diversity in Asymmetric Catalysis. *J. Am. Chem. Soc.* **2009**, *131* (10), 3779–3784. https://doi.org/10.1021/ja900084k.

(21) Crawford, J.; Sigman, M. Conformational Dynamics in Asymmetric Catalysis: Is Catalyst Flexibility a Design Element? *Synth.* **2019**, *51* (05), 1021–1036. https://doi.org/10.1055/s-0037-1611636.

(22) Schäfer, S.; Gamer, M. T.; Lebedkin, S.; Weigend, F.; Kappes, M. M.; Roesky, P. W. Bis(6-Methylene-2,2'-Bipyridine)Phenylphosphine-A Flexible Ligand for the Construction of Trinuclear Coinage-Metal Complexes. *Chem. - A Eur. J.* **2017**, *23* (50), 12198–12209. https://doi.org/10.1002/chem.201701091.

(23) Tazelaar, C. G. J.; Slootweg, J. C.; Lammertsma, K. Coordination Chemistry of Tris(Azolyl)Phosphines. *Coord. Chem. Rev.* **2018**, *356*, 115–126. https://doi.org/10.1016/j.ccr.2017.10.024.

(24) Robson, R. Design and Its Limitations in the Construction of Bi- and Poly-Nuclear Coordination Complexes and Coordination Polymers (Aka MOFs): A Personal View. *Dalton Trans.* **2008**, No. 38, 5113. https://doi.org/10.1039/b805617j.

(25) Bai, S.-Q.; Young, D. J.; Hor, T. S. A. Nitrogen-Rich Azoles as Ligand Spacers in Coordination Polymers. *Chem. - An Asian J.* **2011**, *6* (2), 292–304. https://doi.org/10.1002/asia.201000698.

(26) Blackman, A. G. Tripodal Tetraamine Ligands Containing Three Pyridine Units: The Other Polypyridyl Ligands. *Eur. J. Inorg. Chem.* **2008**, *2008* (17), 2633–2647. https://doi.org/10.1002/ejic.200800115.

(27) Rogovoy, M. I.; Berezin, A. S.; Samsonenko, D. G.; Artem'ev, A. V. Silver(I)–Organic Frameworks Showing Remarkable Thermo-, Solvato- And Vapochromic Phosphorescence As Well As Reversible Solvent-Driven 3D-to-0D Transformations. *Inorg. Chem.* **2021**, *60* (9), 6680–6687. https://doi.org/10.1021/acs.inorgchem.1c00480.

(28) Lin, N.; Qiao, J.; Duan, L.; Li, H.; Wang, L.; Qiu, Y. Achilles Heels of Phosphine Oxide Materials for OLEDs: Chemical Stability and Degradation Mechanism of a Bipolar Phosphine Oxide/Carbazole Hybrid Host Material. *J. Phys. Chem. C* **2012**, *116* (36), 19451–19457. https://doi.org/10.1021/jp305415x.

(29) Katagiri, K.; Yamamoto, Y.; Takahata, Y.; Kishibe, R.; Fujimoto, N. Photoreaction of Anthracenyl Phosphine Oxides: Usual Reversible Photo- and Heat-Induced Emission Switching, and Unusual Oxidative P C Bond Cleavage. *Tetrahedron Lett.* **2019**, *60* (30), 2026–2029. https://doi.org/10.1016/j.tetlet.2019.06.063.

(30) Li, H.; Hong, M.; Scarpaci, A.; He, X.; Risko, C.; Sears, J. S.; Barlow, S.; Winget, P.; Marder, S. R.; Kim, D.; Brédas, J.-L. Chemical Stabilities of the Lowest Triplet State in Aryl Sulfones and Aryl Phosphine Oxides Relevant to OLED Applications. *Chem. Mater.* **2019**, *31* (5), 1507–1519. https://doi.org/10.1021/acs.chemmater.8b04235.

(31) Azrain, M. M.; Mansor, M. R.; Fadzullah, S. H. S. M.; Omar, G.; Sivakumar, D.; Lim, L. M.; Nordin, M. N. A. Analysis of Mechanisms Responsible for the Formation of Dark Spots in Organic Light Emitting Diodes (OLEDs): A Review. *Synth. Met.* **2018**, *235* (December 2017), 160–175. https://doi.org/10.1016/j.synthmet.2017.12.011.

(32) Schmidbauer, S.; Hohenleutner, A.; König, B. Chemical Degradation in Organic Light-Emitting Devices: Mechanisms and Implications for the Design of New Materials. *Adv. Mater.* **2013**, *25* (15), 2114–2129. https://doi.org/10.1002/adma.201205022.

(33) Chen, L.-L.; Tan, W.-Y.; Zhu, X.-H. Phosphine Oxide Derivatives as a Robust Component for Optoelectronics. *Sci. Bull.* **2020**, *65* (24), 2033–2035. https://doi.org/10.1016/j.scib.2020.08.034.

(34) Becker, W. Fluorescence Lifetime Imaging - Techniques and Applications. *J. Microsc.* **2012**, *247* (2), 119–136. https://doi.org/10.1111/j.1365-2818.2012.03618.x.

(35) Schrimpf, W.; Ossato, G.; Hirschle, P.; Wuttke, S.; Lamb, D. C. Investigation of the Co-Dependence of Morphology and Fluorescence Lifetime in a Metal-Organic Framework. *Small* **2016**, *12* (27), 3651–3657. https://doi.org/10.1002/smll.201600619.

(36) Connolly, B. M.; Aragones-Anglada, M.; Gandara-Loe, J.; Danaf, N. A.; Lamb, D. C.; Mehta, J. P.; Vulpe, D.; Wuttke, S.; Silvestre-Albero, J.; Moghadam, P. Z.; Wheatley, A. E. H.; Fairen-Jimenez, D. Tuning Porosity in Macroscopic Monolithic Metal-Organic Frameworks for Exceptional Natural Gas Storage. *Nat. Commun.* **2019**, *10* (1), 2345. https://doi.org/10.1038/s41467-019-10185-1.

(37) Al Danaf, N.; Schrimpf, W.; Hirschle, P.; Lamb, D. C.; Ji, Z.; Wuttke, S. Linker Exchange via Migration along the Backbone in Metal–Organic Frameworks. *J. Am. Chem. Soc.* **2021**, *143* (28), 10541–10546. https://doi.org/10.1021/jacs.1c04804.

(38) Periasamy, A.; Clegg, R. M. *FLIM Microscopy in Biology and Medicine*, 1st ed.; Periasamy, A., Clegg, R. M., Eds.; Chapman and Hall/CRC, 2009. https://doi.org/10.1201/9781420078916.

(39) Giansante, C.; Raffy, G.; Schäfer, C.; Rahma, H.; Kao, M.-T.; Olive, A. G. L.; Del Guerzo, A. White-Light-Emitting Self-Assembled NanoFibers and Their Evidence by Microspectroscopy of Individual Objects. *J. Am. Chem. Soc.* **2011**, *133* (2), 316–325. https://doi.org/10.1021/ja106807u.

(40) Huang, J.-H.; Chien, F.-C.; Chen, P.; Ho, K.-C.; Chu, C.-W. Monitoring the 3D Nanostructures of Bulk Heterojunction Polymer Solar Cells Using Confocal Lifetime Imaging. *Anal. Chem.* **2010**, *82* (5), 1669–1673. https://doi.org/10.1021/ac901992c.

(41) Lin, H.-J.; Herman, P.; Lakowicz, J. R. Fluorescence Lifetime-Resolved PH Imaging of Living Cells. *Cytometry* **2003**, *52A* (2), 77–89. https://doi.org/10.1002/cyto.a.10028.

(42) Bennet, M. A.; Richardson, P. R.; Arlt, J.; McCarthy, A.; Buller, G. S.; Jones, A. C. Optically Trapped Microsensors for Microfluidic Temperature Measurement by Fluorescence Lifetime Imaging Microscopy. *Lab Chip* **2011**, *11* (22), 3821. https://doi.org/10.1039/c1lc20391f.

(43) Lahn, M.; Dosche, C.; Hille, C. Two-Photon Microscopy and Fluorescence Lifetime Imaging Reveal Stimulus-Induced Intracellular Na + and Cl − Changes in Cockroach Salivary Acinar Cells. *Am. J. Physiol. Physiol.* **2011**, *300* (6), C1323–C1336. https://doi.org/10.1152/ajpcell.00320.2010.

(44) Liao, Y. Y.; Melissen, S. T. A. G.; Audibert, J. F.; Vu, T. T.; Clavier, G.; Méallet-Renault, R.; Retailleau, P.; Lemaistre, J. P.; Génot, V.; Pansu, R. Fluorescence Spectroscopy of AdamBODIPY Single Crystals. *ChemPhotoChem* **2018**, *2* (2), 72–80. https://doi.org/10.1002/cptc.201700173.

(45) Korshunov, V. M.; Chmovzh, T. N.; Golovanov, I. S.; Knyazeva, E. A.; Mikhalchenko, L. V.; Saifutyarov, R. S.; Avetisov, I. C.; Woollins, J. D.; Taydakov, I. V.; Rakitin, O. A. Candle Light-Style OLEDs with Benzochalcogenadiazoles Cores. *Dye. Pigment.* **2021**, *185*, 108917. https://doi.org/10.1016/j.dyepig.2020.108917.

(46) Spackman, M. A.; Jayatilaka, D. Hirshfeld Surface Analysis. *CrystEngComm* **2009**, *11* (1), 19–32. https://doi.org/10.1039/b818330a.

(47) Liu, Y.; Tao, X.; Wang, F.; Shi, J.; Sun, J.; Yu, W.; Ren, Y.; Zou, D.; Jiang, M. Intermolecular Hydrogen Bonds Induce Highly Emissive Excimers: Enhancement of Solid-State Luminescence. *J. Phys. Chem. C* **2007**, *111* (17), 6544–6549. https://doi.org/10.1021/jp070288f.

(48) Zhao, G.-J.; Han, K.-L. Hydrogen Bonding in the Electronic Excited State. *Acc. Chem. Res.* **2012**, *45* (3), 404–413. https://doi.org/10.1021/ar200135h.

(49) Yoon, S.-J.; Chung, J. W.; Gierschner, J.; Kim, K. S.; Choi, M.-G.; Kim, D.; Park, S. Y. Multistimuli Two-Color Luminescence Switching via Different Slip-Stacking of Highly Fluorescent Molecular Sheets. *J. Am. Chem. Soc.* **2010**, *132* (39), 13675–13683. https://doi.org/10.1021/ja1044665.

(50) Zhang, K.; Liu, J.; Zhang, Y.; Fan, J.; Wang, C.-K.; Lin, L. Theoretical Study of the Mechanism of Aggregation-Caused Quenching in Near-Infrared Thermally Activated Delayed Fluorescence Molecules: Hydrogen-Bond Effect. *J. Phys. Chem. C* **2019**, *123* (40), 24705–24713. https://doi.org/10.1021/acs.jpcc.9b06388.

(51) Sims, M.; Bradley, D. D. C.; Ariu, M.; Koeberg, M.; Asimakis, A.; Grell, M.; Lidzey, D. G. Understanding the Origin of the 535 Nm Emission Band in Oxidized Poly(9,9-Dioctylfluorene): The Essential Role of Inter-Chain/Inter-Segment Interactions. *Adv. Funct. Mater.* **2004**, *14* (8), 765–781. https://doi.org/10.1002/adfm.200305149.

(52) Birks, J. B. *Photophysics of Aromatic Molecules*; Whiley: London, 1970. https://doi.org/10.1002/bbpc.19700741223.

(53) Konakahara, T.; Murayama, T.; Sano, K.; Kubota, S. ChemInform Abstract: Novel One-Pot Synthesis of 2-Pentafluoroethyl-3-Trifluoromethyl-4H- Quinolizin-4-Ones and Related Compounds. *ChemInform* **2010**, *27* (32). https://doi.org/10.1002/chin.199632188.

(54) Olesen, P. H.; Hansen, J. B.; Hansen, H. C. Novel Substituted Azacyclic or Azabicyclic Compounds. WO 97/11072, 1996.

(55) Schaefer, F. C.; Peters, G. A. Synthesis of the S-Triazine

System. III. Trimerization of Imidates. *J. Org. Chem.* **1961**, *26* (8), 2778–2784. https://doi.org/10.1021/jo01066a036.
(56) Schaefer, F. C.; Peters, G. A. Synthesis of the S-Triazine System. IV. Preparation of Monosubstituted s-Triazines by Reaction of s-Triazine with Imidates. *J. Org. Chem.* **1961**, *26* (8), 2784–2786. https://doi.org/10.1021/jo01066a037.
(57) Kermagoret, A.; Tomicki, F.; Braunstein, P. Nickel and Iron Complexes with N,P,N-Type Ligands: Synthesis, Structure and Catalytic Oligomerization of Ethylene. *Dalton Trans.* **2008**, *22*, 2945–2955. https://doi.org/10.1039/b802009d.
(58) Malysheva, S.; Gusarova, N.; Belogorlova, N.; Sutyrina, A.; Litvintsev, Y.; Albanov, A.; Sterkhova, I.; Artem'ev, A. Efficient One-Pot Synthesis of Mono- and Bis[Di(2-Pyridyl)Phosphine Oxides] from Tris(2-Pyridyl)Phosphine. *Synlett* **2016**, *27* (17), 2451–2454. https://doi.org/10.1055/s-0035-1562485.
(59) Malysheva, S. F.; Belogorlova, N. A.; Kuimov, V. A.; Litvintsev, Y. I.; Sterkhova, I. V.; Albanov, A. I.; Gusarova, N. K.; Trofimov, B. A. PCl3- and Organometallic-Free Synthesis of Tris(2-Picolyl)Phosphine Oxide from Elemental Phosphorus and 2-(Chloromethyl)Pyridine Hydrochloride. *Tetrahedron Lett.* **2018**, *59* (8), 723–726. https://doi.org/10.1016/j.tetlet.2018.01.021.
(60) Steiner, T. The Hydrogen Bond in the Solid State. *Angew. Chem. Int. Ed.* **2002**, *41*, 48–76. https://doi.org/10.1002/1521-3773(20020104)41:1<48::AID-ANIE48>3.0.CO;2-U.
(61) Janiak, C. A Critical Account on π–π Stacking in Metal Complexes with Aromatic Nitrogen-Containing Ligands †. *Dalton Trans.* **2000**, No. 21, 3885–3896. https://doi.org/10.1039/b003010o.
(62) Jennings, W. B.; Farrell, B. M.; Malone, J. F. Attractive Intramolecular Edge-to-Face Aromatic Interactions in Flexible Organic Molecules. *Acc. Chem. Res.* **2001**, *34* (11), 885–894. https://doi.org/10.1021/ar0100475.
(63) Digman, M. A.; Caiolfa, V. R.; Zamai, M.; Gratton, E. The Phasor Approach to Fluorescence Lifetime Imaging Analysis. *Biophys. J.* **2008**, *94* (2), L14–L16. https://doi.org/10.1529/biophysj.107.120154.
(64) Redford, G. I.; Clegg, R. M. Polar Plot Representation for Frequency-Domain Analysis of Fluorescence Lifetimes. *J. Fluoresc.* **2005**, *15* (5), 805–815. https://doi.org/10.1007/s10895-005-2990-8.
(65) Schrimpf, W.; Jiang, J.; Ji, Z.; Hirschle, P.; Lamb, D. C.; Yaghi, O. M.; Wuttke, S. Chemical Diversity in a Metal–Organic Framework Revealed by Fluorescence Lifetime Imaging. *Nat. Commun.* **2018**, *9* (1), 1647. https://doi.org/10.1038/s41467-018-04050-w.
(66) Turner, M. J.; McKinnon, J. J.; Wolff, S. K.; Grimwood, D. J.; Spackman, P. R.; Jayatilaka, D.; Spackman, M. A. *CrystalExplorer17*; University of Western Australia, Australia, 2017.

Supporting Information for:

Methods for elucidating the structural-property relationship in luminescent materials

Christin Kirst,†[a] Nader A. Danaf,†[a,b] Fabian Knechtel,[a,b] Tim Arczynski,[a] Peter Mayer,[a] Don C. Lamb*[a,b] and Konstantin L. Karaghiosoff*[a]

a Department of Chemistry
Ludwig-Maximilians University of Munich
Butenandtstr. 5-13, 81377 Munich (Germany)
E-mail: klk@cup.uni-muenchen.de

b Center for NanoScience (CeNS), NanoSystems Initiative Munich (NIM) and Center for Integrated Protein Science Munich (CIPSM)
Ludwig-Maximilians University of Munich
Butenandtstr. 5-13, 81377 Munich (Germany)
E-mail: d.lamb@cup.uni-muenchen.de

Table of Content

Experimental Details

General Methods: All compounds were handled using Schlenk techniques under dry Ar. Unless otherwise specified, all reagents and solvents were purchased from commercial sources and used as received. The tetrahydrofuran used for the synthesis of the phosphines was dried, freshly distilled and degassed prior to use. As the drying agent, elemental sodium was used. The deuterated $CDCl_3$ was distilled and stored under protective atmosphere over molecular sieves. **NMR spectra** were recorded on a Bruker Avance III spectrometer working at 400.1 MHz (^{1}H), 161.9 MHz (^{31}P), 100.6 MHz (^{13}C), 79.5 MHz (^{29}Si) and 40.5 MHz (^{15}N) at ambient temperature. Chemical shifts are in reference to tetramethylsilane (^{1}H, ^{13}C, ^{29}Si), 85 % H_3PO_4 (^{31}P) and $MeNO_2$ (^{15}N) as external standards. The assignment of the signals was conducted based on 2D (^{1}H,^{1}H–COSY, ^{1}H,^{13}C–HMQC and ^{1}H,^{13}C–HMBC) experiments. Coupling constant (*J*) values are given in Hertz (Hz). The multiplicity of each resonance observed in the NMR spectra is reported as s = singlet; d = doublet; t = triplet; q = quartet; or m = multiplet. The samples for **infrared spectroscopy** were placed under ambient conditions without further preparation onto a Smith DuraSampLIR II ATR device using a Perkin Elmer BX II FT-IR System spectrometer. Additionally, an FT-IR Perkin Elmer Spectrum BXII/1000 equipped with a Smiths ATR polarimeter Krüss P8000 was used for the infrared spectroscopy measurements. **Melting points** were detected using an OZM DTA 552-Ex instrument. The scanning temperature range was set from 293 to 673 K with a scanning rate of 5 K min^{-1}. **ESI** measurements were done using a Thermo Finnigan LTQ FT Ultra Fourier Transform Ion Cyclotron Resonance Mass Spectrometer. **Elemental analysis** was performed using an Elementar vario micro cube instrument and an Elementar vario EL instrument. **Solid-state UV Vis spectra** were recorded on a Cary 500 equipped with a Praying-Mantis-AddOn and an integrating sphere. The solid samples were placed between two quartz plates for the measurement. The **single crystals** of all phosphine oxide ligands were introduced into perfluorinated oil and a suitable single crystal was cautiously mounted on top of a thin glass wire. Data collection for compound **5**–**8** was performed with a Rigaku Oxford Xcalibur 3 diffractometer equipped with a Spellman generator (50 kV, 40 mA) and a Kappa CCD detector, operating with Mo-Kα radiation. The data collection for compounds **4** and **9** was performed with a Bruker D8 Venture TXS system equipped with a multilayer mirror optics monochromator and a Mo Kα rotating-anode. Data collection and data reduction for compounds **5**–**8** were performed with the CrysAlisPro software. For compounds **4** and **9**, the Bruker SAINT software package utilizing a narrow-frame algorithm was used. Absorption correction using the multi-scan method was applied. All structures were solved with SIR2014,[1] refined with SHELXL-2018/1[2,3] and finally checked using PLATON[4] integrated in WinGX.[5] Non-hydrogen atoms were refined anisotropically. The finalized CIF files were checked with checkCIF. Crystallographic data and structure refinements are listed in Table S1. Molecular plots were performed with DIAMOND 3.2k.[6] CCDC data can be found, free of charge, at The Cambridge Crystallographic Data Center: ccdc.cam.ac.uk/structures.

Photophysical Characterization: Measurements were performed on an FLS 1000 Fluorimeter (Edinburgh Instruments). A 450 W continuous wave Xenon lamp was used for obtaining the different excitation and emission spectra. The fluorescence emission and excitation spectra were measured on the same photon multiplier tube (PMT 900 detector, Hamamatsu). The compounds investigated were dissolved in acetonitrile and measured using a 3.5 mL quartz cuvette (119F-10-40, Hellma Analytics). For the excitation and emission spectra, the same settings were applied using an excitation/emission slit width of 2 nm centred at the excitation or emission wavelengths provided in the figures, respectively. The spectra were measured in 0.5 nm steps with two seconds dwell time across the spectral range of interest. The same measurements conditions were used for characterizing the acetonitrile only solution.

Fluorescence lifetime imaging microscopy: FLIM measurements were performed using a house-built laser scanning confocal microscope equipped with pulsed interleaved excitation and time-correlated single photon counting detection, as described elsewhere with a few modifications.[7] Briefly, a pulsed laser diode at 405 nm wavelength (LDH-P-C-405) driven by a picosecond pulsed driver (PDL 828 Sepia II, PicoQuant) at 40 MHz was used for excitation of the different samples. For the measurements, the solid compounds were gently grounded with a glass rod and the resulting powder was suspended in acetonitrile. For improving the solubility, some compounds were vortexed for ~3 min. From the acetonitrile suspension, ~100 µL was added to an 8-well LabTek I slide (VWR) and suspensions allowed to sediment. The surface was imaged using a 100x, 1.49 numerical aperture oil-immersion objective (CFI Apochromat TIRF, 100× Oil, Nikon). The fluorescence emission was collected with the same objective, separated from the excitation using a polychroic mirror (Chroma zt405/473-488/561/640rpc, AHF Analysentechnik, Tübingen, Germany) and a 460 nm long pass filter (460 LP, Chroma), and recorded using a photon counting detector (PDM series, Micro Photon Devices). To test the effect of the emission wavelength on the obtained lifetime values, we investigated the same structure of compounds **4**, **5** and **8** under three different emission wavelength ranges 420 ± 10 nm (FB420-10, Thorlabs), 450 ± 10 nm (FB450-10, Thorlabs) and 460 ± 10 nm (FL460-10, Thorlabs).

Typical scan regions were between 10 µm × 10 µm and 40 µm × 40 µm, depending on size of the measured structure. Scans were performed at a resolution of 500 pixels × 500 pixels, resulting in pixel sizes ranging between 20 nm and 80 nm. To ensure a good signal-to-noise ratio while minimizing the influence of photon pile-up and other high-signal artefacts, the count rate was kept below 800 kHz. The desired count rate was achieved by adjusting the power of the 405 nm wavelength laser using a neutral density filter-wheel (NDC-100C-2M, Thorlabs). The power used ranged from 10 to 50 µW measured before the objective (S130VC Slim Photodiode Power Sensor, Thorlabs). Image acquisition times of 200-400 s ensured the detection of 100-1000 photons per pixel, after which the phasor analysis was applied.[8] To improve the FLIM analysis, the data were spatially smoothed with a 3 pixel × 3 pixel sliding window. All analysis was performed using the software framework PAM.[9]

The FLIM phasor approach, as described by Digman and co-workers[8], was used for analyzing the FLIM measurements. This approach allows a graphical interpretation of the measured fluorescence lifetime and thus avoids a more complicated fit-based analysis. From the FLIM measurements, the sine and cosine Fourier components of the lifetime decay are calculated for every pixel of an image, yielding the two phasor coordinates *g* and *s*, calculated using equations 1 and 2:

$$g_{i,j}(\omega) = \int_0^T I_{i,j}(t) \cdot cos(\omega t - \varphi_{Inst})\, dt / \left(M_{Inst} \cdot \int_0^T I_{i,j}(t) dt\right) \quad [1]$$

$$s_{i,j}(\omega) = \int_0^T I_{i,j}(t) \cdot sin(\omega t - \varphi_{Inst})\, dt / \left(M_{Inst} \cdot \int_0^T I_{i,j}(t) dt\right) \quad [2]$$

where the indices *i* and *j* define the pixel of the image and *I*(*t*) represents the photon counts of the time bin, *t,* in the lifetime decay histogram. The frequency, ω, corresponds to $2\pi/T$, where *T* is the full timescale of the lifetime decay histogram (here 40 ns). φ_{Inst} and M_{Inst} are correction terms for the phase shift and demodulation caused by the instrument response function (IRF) that induces a rotation and scaling of the phasor plot. They were calculated using a reference sample with known lifetime (Atto 425, 3.6 ns, Atto-Tec).

From the two phasor coordinates, two lifetime values can be determined, one based on the phase (τ_φ) and the other on the modulation (τ_M):

$$\tau_\varphi(\omega) = \frac{1}{\omega} \cdot \frac{s}{g} \quad [3]$$

$$\tau_M(\omega) = \frac{1}{\omega}\sqrt{\frac{1}{g^2+s^2} - 1} \quad [4]$$

For a mono-exponential decay, these two lifetimes are identical and correspond to the correct mono-exponential lifetime and the data point will line on an arc of radius 0.5 starting at the origin and end at position (0,1). In the phasor approach, multiple species added vectorially and a mixture of two species with different mono-exponential lifetimes will lie on a line connecting the individual components of the two species on the unit circle. Where the mixture falls on this line depends on the relative population of the two species. Also, the phase and modulation lifetimes are different for a multiexponential decay and do not correspond directly and unambiguously to a pure species. To obtain a single apparent lifetime for each sample, the mean τ_φ and τ_M were calculated from all pixels above a threshold of ~300 photons. The arithmetic average of the mean phase and modulation lifetimes was then used to calculate an apparent lifetime. The uncertainty corresponds to the standard deviation of the pixel distribution.

Additional to the phasor approach, the raw fluorescence lifetime data and the subsequent lifetime fits obtained via the deconvolution accounting for the IRF were performed and resulted in a bi-exponential decay. The lifetime fits were obtained according to the following equation:

$$I(t) = IRF \times (I_0 e^{-\frac{t}{\tau}} + c)$$

Where $I(t)$ represents the measured intensity decay, τ is the decay lifetime with I_0 being the decay intensity at $t = 0$, *c* being the offset and × denotes the mathematical operation of the deconvolution that accounts to the IRF. The obtained full width at half maximum (FWHM) value for the measured IRF was ~ 250 ps.

To estimate the brightness of the compounds, we calculated the brightness from a pixel averaged over the entire crystal. As all FLIM images were collected using the same objective, the point-spread-function for all images should be the same. Due to the difference in the absorption coefficient at 405 nm, the wavelength used for excitation (Figure S15, inset, grey dotted line), we adjusted the measured brightness for compounds **5** and **8** accordingly (scaling them by factors of 3.6 and 2.9, respectively). In addition, only a fraction of the emission is detected. Due to the differences in the emission spectra (Figure S16), a higher fraction of the emission from compounds **4** passes through the 460 nm long pass filter and is detected in comparison to compounds **5**, **6** and **8**. Hence, an additional factor of 1.5 was applied for compounds **5** and **8**, where a

correction factor of 1.2 was applied for compound **6** to compensate for the differences in fluorescence detection.
The lifetime changes relative to the emission wavelength changes was investigated by measuring the same structure of compounds **4**, **5** and **8** under three different emission wavelength ranges 420 ± 10 nm, 450 ± 10 nm and 460 ± 10 nm (Figure S17). This aimed to explore the extent to which a bathochromic or hypochromic shift changes the obtained lifetime. As seen in the performed experiments, minor lifetime changes resulted once the same structures of compounds **4**, **5** and **8** were investigated at different wavelengths. Noteworthy, the emission intensity at 420 nm was significantly lower than the intensities at 450 and 460 nm. This is the reason why compound 5 was investigated at 450 and 460 nm. As for compound 6 that showed the lowest emission intensity, the photon counts were too low to monitor them at three different wavelengths.

Synthesis

2-((trimethylsilyl)methyl)pyrazine (**1**): 2-Methylpyrazine (20 mL, 219 mmol) was dissolved in 40 mL tetrahydrofuran and cooled down to −78 °C. Freshly prepared lithium diisopropylamine (1 eq., 153 mL, 219 mmol) was added dropwise while stirring. The yellow solution turned orange and, after stirring for another hour, trimethylsilyl chloride (2 eq., 56 mL, 438 mmol) was added dropwise to the mixture at −78 °C. The color of the mixture turned clear red and was allowed to warm up to RT overnight. The solvent was removed under vacuum. After distillation (10^{-3} bar, 28 °C, 60 °C oil bath), **1** was received as a yellow oil. Yield: 10 g (27.5 %). ^{1}H ($CDCl_3$, 400 MHz): δ [ppm] = 8.31 (s, 1 H, CH_{Ar}), 8.22 (s, $^{2}J_{H,Si}$ = 8.6 Hz, 1 H, CH_{Ar}), 8.18 (d, $^{1}J_{H,H}$ = 2.5 Hz, 1 H, CH_{Ar}), 2.27 (s, 2 H, CH_2), −0.04 (s, $^{2}J_{H,Si}$ = 58.7 Hz, 9 H, Si–CH_3). ^{13}C{^{1}H} ($CDCl_3$, 100 MHz): δ [ppm] = 157.6 (s, *C*q), 143.9 (s, *C*H_{Ar}), 143.7 (s, *C*H_{Ar}), 140.2 (s, *C*H_{Ar}), 27.4 (s, $^{1}J_{C,Si}$ = 21.2 Hz, *C*H_2), −1.7 (s, $^{1}J_{C,Si}$ = 25.8 Hz, Si–*C*H_3). ^{29}Si INEPT ($CDCl_3$, 80 MHz): δ [ppm] = 3.2 (s). Elemental analysis calculated (%) for [$C_8H_{14}N_2Si$]: C 57.78, H 8.49, N 16.85; found C 57.86, H 8.19, N 17.07. GC/EI MS (positive mode) m/z calculated for [$C_8H_{14}N_2Si$] $[M]^+$: 166.0926, found 166.0918. IR: $\tilde{\nu}$ [cm^{-1}] = 3054 (vw), 2956 (w), 2901 (vw), 1575 (vw), 1521 (w), 1472 (m), 1409 (m), 1393 (m), 1304 (w), 1248 (s), 1169 (w), 1145 (m), 1070 (w), 1014 (m), 848 (vs), 749 (m), 695 (m), 636 (w), 405 (s).

2,3,5-trimethyl-6-((trimethylsilyl)methyl)pyrazine (**2**): 2,3,5,6-tetra-methylpyrazine (15.0 g, 110 mmol) was dissolved in 50 mL tetrahydrofuran and cooled down to −78 °C. *n*-Butyllithium (0.95 eq., 43.6 mL, 105 mmol, 2.40 M in hexane) was added dropwise while stirring. The solution turns deep red and, after stirring for another hour, trimethylsilyl chloride (1.5 eq, 21.0 mL, 165 mmol) was added dropwise to the mixture at −78 °C. The color of the mixture turned colorless and was allowed to warm up to RT overnight. The solvent was removed under vacuum. After distillation (10^{-3} bar, 50 °C, 80 °C oil bath), **2** was received as a colorless, viscos oil. Yield: 19.9 g (86.7 %).
^{1}H ($CDCl_3$, 400 MHz): δ [ppm] = 2.40 (s, 9 H, CH_3), 2.26 (s, 2 H, CH_2), 0.01 (s, $^{2}J_{H,Si}$ = 3.0 Hz, $^{1}J_{H,C}$ = 58.7 Hz, 9 H, Si–CH_3). ^{13}C{^{1}H} ($CDCl_3$, 100 MHz): δ [ppm] = 151.7 (s), 148.1 (s), 146.7 (s), 146.2 (s), 25.7 (s), 22.0 (s), 21.5 (s), 21.4 (s), −1.0 (s, $^{1}J_{C,Si}$ = 25.8 Hz, Si–*C*H_3). ^{29}Si INEPT ($CDCl_3$, 80 MHz): δ [ppm] = 3.3 (s, $^{2}J_{Si,C}$ = 25.3 Hz). Elemental analysis calculated (%) for [$C_{11}H_{20}N_2Si$]: C 63.40, H 9.67, N 13.44; found C 62.92, H 9.32, N 13.26. GC/EI MS (positive mode) m/z calculated for [$C_9H_{17}N_3Si$] $[M]^+$: 208.1396, found 208.1389. IR: $\tilde{\nu}$ [cm^{-1}] = 2952 (w), 2918 (vw), 1546 (vw), 1444 (w), 1412 (m), 1393 (m), 1372 (w), 1357 (vw), 1284 (vw), 1247 (m), 1222 (m), 1188 (w), 1151 (w), 1126 (vw), 1077 (w), 1021 (vw), 987 (m), 841 (vs), 819 (s), 779 (w), 749 (w), 722 (w), 693 (m), 666 (w).

2,4-dimethyl-6-((trimethylsilyl)methyl)-1,3,5-triazine (**3**): 2,4,6-Trimethyl-1,3,5-triazine was synthesized according to adapted literature procedures.[10] A 300 mL *Erlenmeyer*-flask was charged with potassium carbonate (34.6 g, 250 mmol, 1.04 eq.) in 120 mL H_2O and 60 mL dichloromethane. Ethyl acetimidate hydrochloride (29.7 g, 240 mmol, 1.00 eq.) was added at RT and the resulting solution was stirred for 15 min. After separation of the organic phase, the aqueous layer was extracted with dichloromethane (2 x 60 mL). The combined organic layers were dried over K_2CO_3 and stored overnight in the fridge. The reaction mixture was filtered and the residue was extracted with dichloromethane (2 x 20 mL). Dichloromethane was removed carefully from the resulting filtrate *via* distillation at 37 °C. Glacial acetic acid (1.00 mL, 17.5 mmol, 0.07 eq.) was added to the remaining solution over 20 min at RT. After 1.5 h of stirring, the resulting cloudy solution was allowed to stand overnight. The remaining acid was neutralized with a K_2CO_3/H_2O-mixture. The organic layer was separated and dried over K_2CO_3. and the resulting precipitate was filtered off. The organic solvent is carefully removed *in vacuo* and the remaining solid was dissolved in Et_2O (30 mL). After separating any resulting precipitate, the crude product was concentrated *in vacuo* to obtain 2,4,6-trimethyl-1,3,5-triazine (4.90 g, 39.8 mmol, 50 % yield) as colorless crystals. For the synthesis of the trimethylsilyl-compound, 2,4,6-trimethyl-1,3,5-triazine (4.90 g, 39.8 mmol) was dissolved in 40 mL tetrahydrofuran and cooled down to −78 °C. *n*-Butyllithium (0.97 eq., 16.0 mL, 38.4 mmol, 2.40 M in hexane) was added dropwise while stirring.

The solution turned yellow and, after stirring for another hour, trimethylsilyl chloride (1.2 eq, 6.10 mL, 47.9 mmol) was added dropwise to the mixture at −78 °C. The color of the mixture turned colorless and was allowed to warm up to RT overnight. The solvent was removed under vacuum. After distillation (10^{-3} bar, 33 °C, 50 °C oil bath), **3** was received as a colorless liquid. Yield: 2.68 g (34.0 %).
^{1}H ($CDCl_3$, 400 MHz): δ [ppm] = 2.40 (s, 6 H, CH_3), 2.29 (s, 2 H, CH_2), −0.07 (s, $^{1}J_{H,Si}$ = 8.3 Hz, 9 H, Si–CH_3); ^{13}C{^{1}H} ($CDCl_3$, 100 MHz): δ [ppm] = 178.9 (s, *C*q), 175.2 (s, *C*q), 31.9 (s, $^{1}J_{C,Si}$ = 38.2 Hz, *C*H_2), 25.5 (s, *C*H_3), −1.6 (s, $^{1}J_{C,Si}$ = 52.5 Hz, Si–*C*H_3). ^{29}Si INEPT ($CDCl_3$, 80 MHz): δ [ppm] = 4.5 (s). ^{15}N *via* ^{1}H,^{15}N-HMBC ($CDCl_3$, 41 MHz): δ [ppm] = −136.3 (s). Elemental analysis calculated (%) for [$C_9H_{17}N_3Si$]: C 55.34, H 8.77, N 21.51, found: C 55.15, H 8.53, N 21.55. GC/EI MS (positive mode) m/z calculated for [$C_9H_{17}N_3Si$] $[M]^+$: 195.1192, found 195.1184. IR: $\tilde{\nu}$ [cm^{-1}] = 2957 (w), 2897 (vw), 1530 (vs), 1434 (m), 1391 (m), 1349 (m), 1250 (m), 1136 (m), 1036 (w), 960 (w), 938 (w), 845 (vs), 697 (m), 566 (m).

bis(pyrazin-2-ylmethyl)phenylphosphine oxide (**4**): Compound **1** (3 eq., 7.48 g, 45.0 mmol) was dissolved in 30 mL of dry, degassed tetrahydrofuran and cooled to −10 °C. Dichlorophenylphosphine (2.04 mL, 15.0 mmol) was added dropwise while stirring. The solution turned from bright yellow to pale yellow, to orange and a colorless precipitate was formed. The reaction mixture was warmed up to RT overnight. The volatiles were removed in vacuo and bis(pyrazin-2-ylmethyl)phenylphosphine was obtained as an orange viscos oil (^{31}P NMR δ = −12.8 ppm). The freshly synthesized phosphine (15.0 mmol, 4.41 g) was dissolved in 30 mL dichloromethane. A water/H_2O_2 mixture (2 mL 30 % H_2O_2 in 5 mL water) was added dropwise to the mixture at −10 °C and stirred for 5 h. The solvent was removed under reduced pressure. The left-over mixture was dissolved in dichloromethane and extracted with water three times. The dichloromethane fractions were combined and all volatiles were removed. **4** was received as a colorless solid. Crystalline yield: 3.11 g (66.8 %), mp 170 °C.
^{1}H ($CDCl_3$, 400 MHz): δ [ppm] = 8.49 (d, $^{2}J_{H,H}$ = 1.7 Hz, 2 H, CH_{pyr}), 8.42 (dt, $J_{H,P}$ = 11.9 Hz, $J_{H,H}$ = 2.0 Hz, 2 H, CH_{pyr}), 7.56 (m, 2 H, CH_{phenyl}), 7.49 (tq, $^{3}J_{H,H}$ = 6.5, $J_{H,H}$ = 1.4 Hz, 1 H, CH_{phenyl}), 7.39 (m, 2 H, CH_{phenyl}), ABX spin system (A = B = H, X = P) 3.76 (dd, $^{2}J_{A,B}$ = 14.5, $^{2}J_{X,B}$ = 15.0 Hz, 2 H, CH_2), 3.73 (dd, $^{2}J_{A,B}$ = 14.5, $^{2}J_{A,X}$ = 14.4 Hz, 2 H, CH_2). ^{13}C{^{1}H} ($CDCl_3$, 100 MHz): δ [ppm] = 149.0 (d, $^{2}J_{C,P}$ = 7.9 Hz, *C*q), 146.1 (d, $^{3}J_{C,P}$ = 4.6 Hz, *C*$_{Ar}$), 144.2 (d, $^{3}J_{C,P}$ = 2.3 Hz, *C*$_{Ar}$), 143.1 (d, $^{4}J_{C,P}$ = 3.0 Hz, *C*$_{Ar}$), 132.5 (d, $^{3}J_{C,P}$ = 2.8 Hz, *C*$_{Ar}$), 130.4 (d, $^{1}J_{C,P}$ = 98.1 Hz, *C*q), 130.7 (d, $^{2}J_{C,P}$ = 9.2 Hz, *C*$_{Ar}$), 128.8 (d, $^{1}J_{C,P}$ = 11.9 Hz, *C*$_{Ar}$), 38.1 (d, $^{1}J_{C,P}$ = 61.4 Hz, *C*H_2). ^{31}P ($CDCl_3$, 162 MHz): δ [ppm] = 35.1 (hept, $^{2}J_{P,H}$ = 14.3 Hz). ^{15}N *via* ^{1}H,^{15}N-HMBC ($CDCl_3$, 41 MHz): δ [ppm] = −68.0 (s). Elemental analysis calcaulted (%) for [$C_{16}H_{15}N_4PO$]: C 61.93, H 4.87, N 18.06; found: C 61.98, H 5.03 N 17.85. ESI MS (positive mode) m/z calculated for [$C_{16}H_{15}N_4PO$] $[M+H]^+$: 311.1017, found 311.1059. IR: $\tilde{\nu}$ [cm^{-1}] = 3077 (vw), 2965 (w), 2933 (w), 2880 (w), 1606 (vs), 1577 (w), 1524 (w), 1471 (m), 1402 (m), 1318 (w), 1258 (m), 1199 (s), 1157 (m), 1115 (s), 1057 (m), 1018 (s), 867 (s), 756 (m), 731 (vs), 694 (s), 609 (w), 498 (vs), 434 (s), 408 (vs).

tris(pyrazin-2-ylmethyl)phosphine oxide (**5**): Compound **1** (3.5 eq, 9.98 g, 60.0 mmol) was dissolved in 30 mL of dry, degassed tetrahydrofuran and cooled to −10 °C. PCl_3 (1.31 mL, 15.0 mmol) was added dropwise while stirring. The reaction mixture was warmed up to RT overnight. The volatiles were removed in vacuo and tris(pyrazin-2-ylmethyl)phosphine was obtained as an orange viscos oil (^{31}P NMR δ = −12.6 ppm). The freshly synthesized phosphine (15.0 mmol, 4.66 g) was dissolved in 30 mL dichloromethane. A water/H_2O_2 mixture (2 mL 30 % H_2O_2 in 5 mL water) was added dropwise to the mixture at −10 °C and stirred for 5 h. The solvent was removed under reduced pressure. The left-over mixture was dissolved in dichloromethane and extracted with water three times. The dichloromethane fractions were combined and all volatiles were removed. **5** was received as a colorless solid. Crystalline yield: 2.98 g (60.9 %), m.p. 130 °C.
^{1}H ($CDCl_3$, 400 MHz): δ [ppm] = 8.62 (t, ^{4}J = 1.5 Hz, 3 H, CH_{pyr}), 8.50 (dd, ^{3}J = 1.5 Hz, 3 H, CH_{pyr}), 8.47 (dd, $^{3}J_{H,H}$ = 1.9 Hz, 3 H, CH_{pyr}), 3.59 (d, $^{2}J_{H,P}$ = 14.9 Hz, 6 H, CH_2). ^{13}C{^{1}H} ($CDCl_3$, 100 MHz): δ [ppm] = 149.1 (d, $^{2}J_{C,P}$ = 7.9 Hz, *C*q), 146.3 (d, $^{3}J_{C,P}$ = 5.4 Hz, *C*H$_{pyr}$), 144.2 (d, $^{5}J_{C,P}$ = 2.3 Hz), 143.3 (d, $^{4}J_{C,P}$ = 2.7 Hz, *C*H$_{pyr}$), 36.1 (d, $^{1}J_{C,P}$ = 60.1 Hz, *C*H_2). ^{31}P{^{1}H} ($CDCl_3$, 162 MHz): δ [ppm] = 42.2 (s). ^{31}P ($CDCl_3$, 162 MHz): δ [ppm] = 42.2 (sept, $^{2}J_{P,H}$ = 15.2 Hz). ^{15}N *via* ^{1}H,^{15}N-HMBC ($CDCl_3$, 41 MHz): δ [ppm] = −69.1 (s). Elemental analysis calculated (%) for [$C_{15}H_{15}N_6PO$]: C 55.21, H 4.63, N 25.76 found: C 55.11, H 4.62, N 25.75. ESI MS (positive mode) m/z calculated for [$C_{15}H_{15}N_6PO$] $[M+H]^+$: 327.1097, found 327.1119. IR: $\tilde{\nu}$ [cm^{-1}] = 3136 (w), 3060 (w), 2951 (w), 2908 (w), 2841 (w), 1582 (w), 1524 (w), 1504 (m), 1475 (m), 1401 (m), 1315 (w), 1257 (m), 1198 (m), 1160 (m), 1090 (m), 1058 (m), 1018 (s), 932 (w), 865 (s), 844 (m), 762 (w), 732 (m), 671 (w), 610 (w), 490 (m), 405 (vs).

bis((3,5,6-trimethylpyrazin-2-yl)methyl)phenylphosphine oxide (**6**): Compound **2** (2.1 eq, 6.56 g, 31.5 mmol) was dissolved in 30 mL of dry, degassed tetrahydrofuran and cooled to −10 °C. Dichlorophenylphosphine (2.04 mL, 15.0 mmol) was added dropwise while stirring. The solution stays colorless. The reaction mixture was warmed up to RT overnight. The volatiles were removed in vacuo and

phenylbis((3,5,6-trimethylpyrazin-2-yl)methyl)phosphine was obtained as a yellow viscos oil (^{31}P NMR δ = −23.7 ppm). The freshly synthesized phosphine (15.0 mmol, 5.68 g) was dissolved in 30 mL dichloromethane. A water/H_2O_2 mixture (2 mL 30 % H_2O_2 in 5 mL water) was added dropwise to the mixture at −10 °C and stirred for 5 h. The solvent was removed under reduced pressure. The left-over mixture was dissolved in dichloromethane and extracted with water three times. The dichloromethane fractions were combined and all volatiles were removed. **6** was received as a colorless solid. Crystalline yield: 5.10 g (86.2 %), mp 140 °C.
^{1}H ($CDCl_3$, 400 MHz): δ [ppm] = 7.60 (dd, $^3J_{H,H}$ = 7.0 Hz, $^4J_{H,H}$ = 1.3 Hz, 2 H, C*H*$_{Phenyl}$), 7.74 (t, $^3J_{H,H}$ = 7.4 Hz, $^4J_{H,H}$ = 1.1 Hz, 1 H, C*H*$_{Phenyl}$), 7.36 (t, $^3J_{H,H}$ = 7.5 Hz, $^3J_{H–H}$ = 1.3 Hz, 2 H, C*H*$_{Phenyl}$), ABX spin system (A = B = H, X = P) 3.77 (dd, $^2J_{A,B}$ = 14.8, $^2J_{X,B}$ = 15.1 Hz, 2 H, C*H*$_2$), 3.73 (dd, $^2J_{A,B}$ = 14.6, $^2J_{X,B}$ = 14.1 Hz, 2 H, C*H*$_2$), 2.42 (d, $^2J_{H,P}$ = 2.2 Hz, 6 H, C*H*$_3$), 2.36 (s, 12 H, C*H*$_3$). ^{13}C{^{1}H} ($CDCl_3$, 100 MHz): δ [ppm] = 149.9 (d, $^3J_{C,P}$ = 5.1 Hz, *C*q–CH_3), 148.7 (d, $^4J_{C,P}$ = 2.4 Hz, *C*q–CH_3), 148.3 (s, *C*q–CH_3), 143.4 (d, $^2J_{C,P}$ = 8.8 Hz, *C*q), 132.1 (d, $^4J_{C,P}$ = 2.6 Hz, *C*H$_{Phenyl}$), 132.0 (s, second peak missing, *C*$_{q,Phenyl}$), 131.0 (d, $^3J_{C,P}$ = 9.6 Hz, *C*H$_{Phenyl}$), 128.3 (d, $^2J_{C,P}$ = 11.7 Hz, *C*H$_{Phenyl}$), 37.2 (d, $^1J_{C,P}$ = 62.4 Hz, *C*H$_2$), 21.5 (t, $^4J_{C,P}$ = 1.0 Hz, *C*H$_3$), 21.2 (s, CH_3). ^{31}P{^{1}H} ($CDCl_3$, 162 MHz): δ [ppm] = 37.9 (s). ^{31}P ($CDCl_3$, 162 MHz): δ [ppm] = 37.9 (quintet, $^2J_{P,H}$ = 14.6 Hz). ^{15}N *via* ^{1}H,^{15}N-HMBC ($CDCl_3$, 41 MHz): δ [ppm] = −69.7 (s), −71.6 (s). Elemental analysis calculated (%) for [$C_{22}H_{27}N_4PO$]: C 66.99, H 6.90, N 14.20, found: C 66.73, H 6.77, N 14.20. ESI MS (positive mode) m/z calculated for [$C_{22}H_{27}N_4PO$] [M+H]$^+$: 395.1956 found 395.1994. IR: $\tilde{\nu}$ [cm^{-1}] = 2988 (vw), 2962 (w), 2919 (w), 1592 (vw), 1432 (m), 1406 (vs), 1221 (m), 1195 (vs), 1114 (m), 1069 (w), 989 (m), 863 (w), 803 (m), 726 (s), 697 (m), 631 (s), 515 (m), 437 (vs), 415 (s).

tris((3,5,6-trimethylpyrazin-2-yl)methyl)phosphine oxide (**7**): Compound **2** (3.5 eq, 9.98 g, 47.9 mmol) was dissolved in 30 mL of dry, degassed tetrahydrofuran and cooled to −10 °C. PCl_3 (1.31 mL, 13.7 mmol) was added dropwise while stirring. The reaction mixture was warmed up to RT overnight. The volatiles were removed *in vacuo* and tris((3,5,6-trimethylpyrazin-2-yl)methyl)phosphine was obtained as an orange viscos oil, which hardens after a while (^{31}P NMR δ = −25.9 ppm). The freshly synthesized phosphine (15.0 mmol, 4.66 g) was dissolved in 30 mL dichloromethane. A water/H_2O_2 mixture (2 mL 30 % H_2O_2 in 5 mL water) was added dropwise to the mixture at −10°C and stirred for 1 h. Leftover tetramethylpyrazin crystallizes at −10 °C and can be filtered off. The solvent was removed under reduced pressure and **7** was received as a colorless solid. Yield: 5.12 g (82.7 %), mp 190 °C.
^{1}H ($CDCl_3$, 400 MHz): δ [ppm] = 3.66 (d, $^3J_{H,P}$ = 14.6 Hz, 6 H, C*H*$_2$), 2.44 (s, 18 H, C*H*$_3$). ^{13}C{^{1}H} ($CDCl_3$, 101 MHz): δ [ppm] = 149.7 (d, $^3J_{C,P}$ = 5.8 Hz, *C*q–CH_3), 149.3 (d, $^4J_{C,P}$ = 3.2 Hz, *C*q–CH_3), 148.5 (d, $^5J_{C,P}$ = 1.9 Hz, *C*q–CH_3), 144.3 (d, $^2J_{C,P}$ = 8.5 Hz, *C*q), 36.7 (d, $^1J_{C,P}$ = 60.4 Hz, *C*H$_2$), 21.7 (d, $^4J_{C,P}$ = 0.9 Hz, *C*H$_3$), 21.6 (d, $^5J_{C,P}$ = 0.9 Hz, *C*H$_3$), 21.6 (s, *C*H$_3$). ^{31}P{^{1}H} ($CDCl_3$, 162 MHz): δ [ppm] = 44.4 (s). ^{31}P ($CDCl_3$, 162 MHz): δ [ppm] = 44.4 (septet, $^2J_{P,H}$ = 14.8 Hz). ^{15}N *via* ^{1}H,^{15}N-HMBC ($CDCl_3$, 41 MHz): δ [ppm] = −68.8 (s). ESI MS (negative mode) m/z calculated for [$C_{24}H_{33}N_6PO$] [M−H]$^-$: 451.23752, found 451.2380. IR: $\tilde{\nu}_{max}$ (cm^{-1}) = 2988 (vw), 2920 (w), 1442 (m), 1412 (vs), 1397 (s), 1286 (vw), 1244 (w), 1234 (w), 1190 (m), 1168 (vs), 1127 (w), 1089 (w), 1029 (w), 1010 (w), 988 (s), 875 (m), 803 (m), 782 (w), 743 (w), 711 (w), 690 (w).

bis((4,6-dimethyl-1,3,5-triazin-2-yl)methyl)phenylphosphine oxide (**8**): Compound **3** (2.10 eq., 2.38 g, 12.2 mmol) was dissolved in 40 mL of dry, degassed tetrahydrofuran and cooled to −10 °C. Dichlorophenylphosphine (1.00 eq, 0.79 mL, 5.83 mmol) was added dropwise while stirring. The solution stays colorless. The reaction mixture was warmed up to RT overnight. The volatiles were removed *in vacuo* and bis((4,6-dimethyl-1,3,5-triazin-2-yl)methyl)phenyl-phosphine was obtained as a yellow viscos oil (^{31}P NMR δ = −13.8 ppm). The freshly synthesized phosphine (5.83 mmol) was dissolved in 50 mL dichloromethane. A water/H_2O_2 mixture (1 mL 30 % H_2O_2 in 5 mL water) was added dropwise to the mixture at −10 °C and stirred for 5 h. The solvent was removed under reduced pressure. The left-over mixture was dissolved in dichloromethane and extracted with water three times. The dichloromethane fractions were combined and all volatiles were removed. **8** was received as a colorless solid. Crystalline yield: 0.50 g (23.0 %) mp 148 °C.
^{1}H ($CDCl_3$, 400 MHz): δ [ppm] = 7.70 (ddt, $^3J_{H,P}$ = 12.1 Hz, $^3J_{H,H}$ = 7.0 Hz, $^4J_{H,H}$ = 1.1 Hz, 2 H, C*H*$_{Phenyl}$), 7.50 (tq, $^3J_{H,H}$ = 7.4 Hz, $^4J_{H,H}$ = 1.4 Hz, $^5J_{H,P}$ = 1.3 Hz, 1H, C*H*$_{Phenyl}$), 7.42 (tdd, $^3J_{H,H}$ = 7.3 Hz, $^4J_{H,P}$ = 3.3 Hz, $^4J_{H,H}$ = 1.2 Hz, 2 H, C*H*$_{Phenyl}$), ABX spin system (A = B = H, X = P) 3.94 (dd, $^2J_{A,B}$ = 13.9, $^2J_{X,B}$ = 15.6 Hz, 2 H, C*H*$_2$), 3.92 (dd, $^2J_{A,B}$ = 13.9, $^2J_{X,B}$ = 15.5 Hz, 2 H, C*H*$_2$), 2.52 (s, $^1J_{H,C}$ = 128.7 Hz, 12 H, C*H*$_3$). ^{13}C{^{1}H} ($CDCl_3$, 101 MHz): δ [ppm] = 176.5 (d, $^4J_{C,P}$ = 1.2 Hz, *C*q–CH_3), 171.6 (d, $^2J_{C,P}$ = 7.1 Hz, *C*q), 132.3 (d, $^4J_{C,P}$ = 3.0 Hz, C*H*$_{Phenyl}$), 131.5 (d, $^1J_{C,P}$ = 101.0 Hz, *C*q$_{,Phenyl}$), 130.9 (d, $^3J_{C,P}$ = 9.5 Hz, *C*H$_{Phenyl}$), 128.4 (d, $^2J_{C,P}$ = 12.2 Hz, *C*H$_{Phenyl}$), 42.0 (d, $^1J_{C,P}$ = 60.7 Hz, *C*H$_2$), 25.6 (s, *C*H$_3$). ^{31}P ($CDCl_3$, 162 MHz): δ [ppm] = 34.2 (quintet, $^2J_{P,H}$ = 15.3 Hz). ^{15}N *via* ^{1}H,^{15}N-HMBC ($CDCl_3$, 41 MHz): δ [ppm] = −129.2 (s), −131.3 (s). EI MS (positive mode) m/z calculated for [$C_{18}H_{21}N_6PO$] [M+H]$^+$: 369.1592, found 369.1591. IR: $\tilde{\nu}$ [cm^{-1}] = 3058 (vw), 3012 (vw), 2975 (w), 2926 (w), 2513 (vw), 1527 (vs), 1434 (s), 1390 (m), 1352 (s), 1284 (w), 1231 (w), 1206 (s), 1192 (s), 1161 (m), 1114 (m), 1074 (w), 1033 (m), 992 (w), 968 (w), 935 (m), 865 (m), 841 (m), 750 (w), 728 (s), 695 (s), 676 (m), 593 (w), 581 (vw), 564 (m), 550 (s), 501 (s), 432 (s), 401 (m).

tris((4,6-dimethyl-1,3,5-triazin-2-yl)methyl)phosphine oxide (**9**): Compound **3** (3.5 eq., 9.98 g, 51.1 mmol) was dissolved in 30 mL of dry, degassed tetrahydrofuran and cooled to −10 °C. PCl_3 (1.31 mL, 14.6 mmol) was added dropwise while stirring. The reaction mixture was warmed up to RT overnight. The volatiles were removed *in vacuo* and tris((4,6-dimethyl-1,3,5-triazin-2-yl)methyl)-phosphine was obtained as a yellow viscos oil, which hardens after a while (^{31}P NMR δ = −16.8 ppm). The freshly synthesized phosphine (15.0 mmol, 4.66 g) was dissolved in 30 mL dichloromethane. A water/H_2O_2 mixture (2 mL 30 % H_2O_2 in 5 mL water) was added dropwise to the mixture at −10 °C and stirred for 1 h. The solvent was removed under reduced pressure and **9** was received as a colorless solid. Crystalline yield: 4.88 g (80.9 %), mp 143 °C.
^{1}H ($CDCl_3$, 400 MHz): δ [ppm] = 3.91 (d, $^2J_{H,P}$ = 16.1 Hz, 6 H, CH_2), 2.57 (s, 18 H, CH_3); ^{13}C{^{1}H} ($CDCl_3$, 101 MHz): δ [ppm] = 176.6 (d, $^4J_{C,P}$ = 0.7 Hz, *C*q–CH_3), 171.7 (d, $^2J_{C,P}$ = 6.4 Hz, *C*q), 40.8 (d, $^1J_{C,P}$ = 61.5 Hz, *C*H_2), 25.7 (s, *C*H_3). ^{31}P{^{1}H} ($CDCl_3$, 162 MHz): δ [ppm] = 40.3 (s). ^{31}P ($CDCl_3$, 162 MHz): δ [ppm] = 40.3 (septet, $^2J_{P,H}$ =16.0 Hz). ^{15}N *via* ^{1}H,^{15}N HMBC ($CDCl_3$, 41 MHz): δ [ppm] = −130.3 (s). EI MS (positive mode) m/z calculated for $C_{18}H_{24}N_9PO$ $[M-H]^-$: 412.1763, found 412.1768. IR: $\tilde{\nu}_{max}$ (cm^{-1}) = 2976 (vw), 2926 (w), 1623 (vw), 1527 (vs), 1427 (s), 1390 (s), 1353 (s), 1216 (m), 1192 (s), 1171 (m), 1103 (w), 1033 (m), 967 (m), 940 (m), 854 (m), 824 (w), 801 (w), 740 (m), 690 (vw), 666 (w), 591 (vw), 567 (s), 487 (vw), 459 (vw).

The IR spectra of all TMS compounds show the typical band for the ν(Si(CH_3)$_3$) at 1258 cm^{-1} in **1**, 1250 cm^{-1} in **2** and 1247 cm^{-1} in **3**.[11]
The IR spectra of all phosphine oxides show the typical band for ν(PO) at 1199 cm^{-1} in **4**, 1198 cm^{-1} in **5**, 1195 cm^{-1} in **6**, 1190 cm^{-1} in **7**, 1192 cm^{-1} in **8** and 1192 cm^{-1} in **9** (1192 cm^{-1} in $OPPh_3$).[12]

NMR Characterization

To characterize the new compounds in solution, NMR spectroscopy was performed. The chemical shifts for the TMS compounds in the ^{29}Si NMR are within the expected ranges for such compounds (**1** at 3.2 ppm, **2** at 3.3 ppm and **3** at 4.2 ppm).[13,14]
The methylene protons of the bis-substituted phosphine oxides (**4**, **6**, **8**) are diastereotopic and show in the ^{1}H NMR spectra the typical AB part of an ABX coupling pattern (A = B = ^{1}H, X = ^{31}P) (**Figure S1**, **Table S1**). The two diastereotopic protons of one methylene group show only slightly different $^{2}J_{P,H}$ couplings to the phosphorus atom. The $^{2}J_{H,H}$ coupling constants (13.9–14.9 Hz) are all within the expected ranges and comparable to previously published values.[15,16] In the ^{1}H NMR spectrum of the tris-substituted phosphine oxides (**5**, **7**, **9**), a doublet is observed for the methylene protons. The observed coupling is to the ^{31}P atom with $^{2}J_{P,H}$ = 14.5–16.0 Hz. In the ^{31}P NMR spectrum, the tris-substituted phosphine oxides display a shift to higher frequencies when compared to their corresponding bis-substituted phosphine oxide (see **Table S1**).

Table S1. Selected NMR data of the phosphine oxide ligands **4**–**9.** Chemical shifts δ in ppm and in reference to $CDCl_3$.

	4	**5**	**6**	**7**	**8**	**9**
^{31}P	35.1 ($^{2}J_{P,H}$ = 14.3 Hz)	42.2 ($^{2}J_{P,H}$ = 14.8 Hz)	37.9 ($^{2}J_{P,H}$ = 14.6 Hz)	45.0 ($^{2}J_{P,H}$ = 14.5 Hz)	34.2 ($^{2}J_{P,H}$ = 15.3 Hz)	40.3 ($^{2}J_{P,H}$ = 16.0 Hz)
^{1}H (CH_2-group)	3.74 (dd, 2H, $^{2}J_{H,H}$ = 14.6 Hz, $^{2}J_{P,H}$ = 3.8 Hz), 3.73 (dd, 2H, $^{2}J_{H,H}$ = 14.5 Hz, $^{2}J_{P,H}$ = 3.1 Hz)	3.59 ($^{2}J_{P,H}$ = 14.9 Hz)	3.77 (dd, 2H, $^{2}J_{H,H}$ = 14.9 Hz, $^{2}J_{P,H}$ = 2.3 Hz), 3.73 (dd, 2H, $^{2}J_{H,H}$ = 14.5 Hz, $^{2}J_{P,H}$ = 2.3 Hz)	3.69 ($^{2}J_{P,H}$ = 14.7 Hz)	3.94 (dd, 2H, $^{2}J_{H,H}$ = 13.9 Hz, $^{2}J_{P,H}$ = 4.6 Hz), 3.93 (dd, 2H, $^{2}J_{H,H}$ = 13.9 Hz, $^{2}J_{P,H}$ = 4.5 Hz)	3.91 ($^{2}J_{P,H}$ = 16.1 Hz)

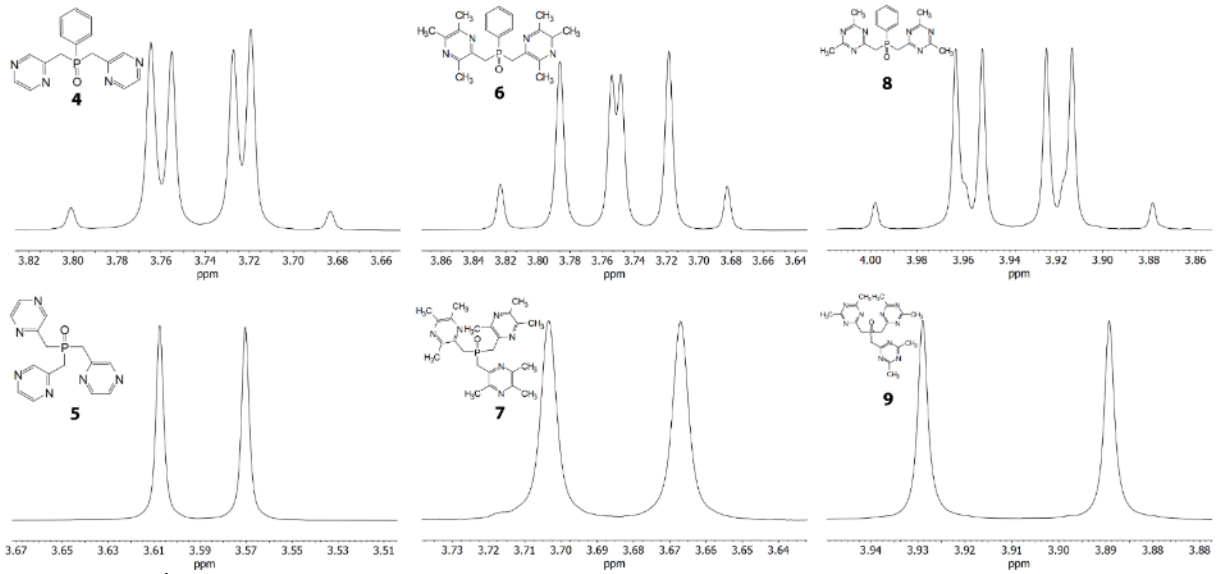

Figure S1. ^{1}H NMR signal of the methylene groups of the phosphine oxides in $CDCl_3$. The bis-substituted phosphine oxides (**2**, **5**, **8**) show the typical AB part of an ABX spectrum. The tris-substituted phosphine oxides (**3**, **6**, **9**) show a normal doublet.

Crystallographic data and figures

Table S2. Crystallographic and refinement data for compounds **4-6**.

	4	**5**	**6**
Formula	$C_{16}H_{15}N_4PO$	$C_{15}H_{15}N_6PO$	$C_{22}H_{27}N_4PO$
Formula weight [g·mol^{-1}]	310.29	326.30	394.44
Color	colorless	yellow	colorless
Habit	block	prism	Block
T [K]	110	130	123
λ [Å]	0.71073	0.71073	0.71073
Crystal system	monoclinic	monoclinic	monoclinic
Space group	$P2_1/n$	$P2_1/c$	$P2_1/c$
a [Å]	12.2538(6)	18.8494(8)	14.1437(4)
b [Å]	5.6173(3)	10.2782(4)	17.3752(7)
c [Å]	20.9600(11)	7.9072(3)	8.7363(3)
α [°]	90	90	90
β [°]	96.397(2)	91.332(4)	97.662(3)
γ [°]	90	90	90
V [Å^3]	1,433.76(13)	1,531.51(11)	2,127.77(13)
Z	4	4	4
ρ_{calc} [g·cm^{-3}]	1.437	1.415	1.231
μ [mm^{-1}]	0.199	0.194	0.149
F(0 0 0)	648	680	840
Crystal size [mm]	0.07×0.03×0.02	0.45×0.20×0.10	0.40×0.35×0.08
Θ range [°]	3.211–26.373	3.407–29.570	3.322–28.277
Index ranges	$-15 \le h \le 15$	$-26 \le h \le 23$	$-18 \le h \le 18$
	$-7 \le k \le 7$	$-14 \le k \le 14$	$-23 \le k \le 22$
	$-25 \le l \le 26$	$-10 \le l \le 10$	$-11 \le l \le 11$
reflns collected	21,161	15,018	21,576
Independent reflns	2,910 [R_{int} = 0.0588]	4,273 [R_{int} = 0.0502]	5,250 [R_{int} = 0.0493]
Completeness to theta	99.7 %	99.7 %	99.6 %
Refinement method	Full-matrix least-squares on F^2	Full-matrix least-squares on F^2	Full-matrix least-squares on F^2
Data/ restraints/ Parameters	2,910 / 0 / 199	4,273 / 0 / 208	5,250 / 0 / 259
Hydrogen atom treatment	constrained	constrained	constrained
R_1/wR_2 (I > 2 σ (I))	0.0327/0.0758	0.0463/0.0959	0.0447/0.1035
R_1/wR_2 (all data)	0.0433/0.0828	0.0737/0.1104	0.0685/0.1175
Goodness-of-fit on F^2	1.021	1.029	1.019
larg. diff peak/hole [e·Å^{-3}]	0.328/−0.347	0.387/−0.352	0.326/−0.290
CCDC No.	2072432	2072408	2072409

Table S3. Crystallographic and refinement data for compounds **7**-**9**.

	7	**8**	**9**
Formula	$C_{24}H_{33}N_6OP$	$C_{18}H_{21}N_6OP$	$C_{18}H_{25.13}N_9O_{1.56}P$
Formula weight [g·mol^{-1}]	452.53	368.38	423.59
Color	colorless	colorless	colorless
Habit	Rod	Rod	block
T [K]	123	123	102
λ [Å]	0.71073	0.71073	0.71073
Crystal system	tetragonal	monoclinic	monoclinic
Space group	$I4_1/a$	$P2_1/n$	C2/c
a [Å]	23.6498(4)	13.1900(7)	33.2658(19)
b [Å]	23.6498(4)	5.2949(3)	4.8664(3)
c [Å]	19.4811(7)	25.7235(13)	27.5320(15)
α [°]	90	90	90
β [°]	90	97.212(5)	105.702(2)
γ [°]	90	90	90
V [Å^3]	10,896.0(5)	1,782.31(17)	4,290.7(4)
Z	16	4	8
ρ_{calc} [g·cm^{-3}]	1.103	1.373	1.311
μ [mm^{-1}]	0.126	0.175	0.160
F(0 0 0)	3872	776	1789
Crystal size [mm]	0.40×0.10×0.10	0.456×0.133×0.064	0.06×0.05×0.04
Θ range [°]	2.191–26.021	2.687–28.280	2.992–26.733
Index ranges	$-29 \le h \le 29$	$-14 \le h \le 17$	$-42 \le h \le 39$
	$-29 \le k \le 29$	$-7 \le k \le 6$	$0 \le k \le 6$
	$-24 \le l \le 24$	$-28 \le l \le 34$	$0 \le l \le 34$
reflns collected	72,022	8,533	4,419
Independent reflns	5,359 [R_{int} = 0.0964]	4,406 [R_{int} = 0.0425]	4,419 [R_{int} = 0.0683]
Completeness to theta	99.9 %	99.8 %	98.4 %
Refinement method	Full-matrix least-squares on F^2	Full-matrix least-squares on F^2	Full-matrix least-squares on F^2
Data/ restraints/ Parameters	5,359 / 0 / 298	4,406 / 0 / 239	4,419 / 0 / 279
Hydrogen atom treatment	constrained	constrained	constrained
R_1/wR_2 (I > 2 σ (I))	0.0501/0.1166	0.0505/0.0975	0.0556/0.1143
R_1/wR_2 (all data)	0.0775/0.1303	0.0847/0.1110	0.0752/0.1235
Goodness-of-fit on F^2	1.027	1.018	1.118
larg. diff peak/hole [e·Å^{-3}]	0.414/-0.273	0.427/−0.402	0.322/-0.297
CCDC No.	2072410	2072407	2069784

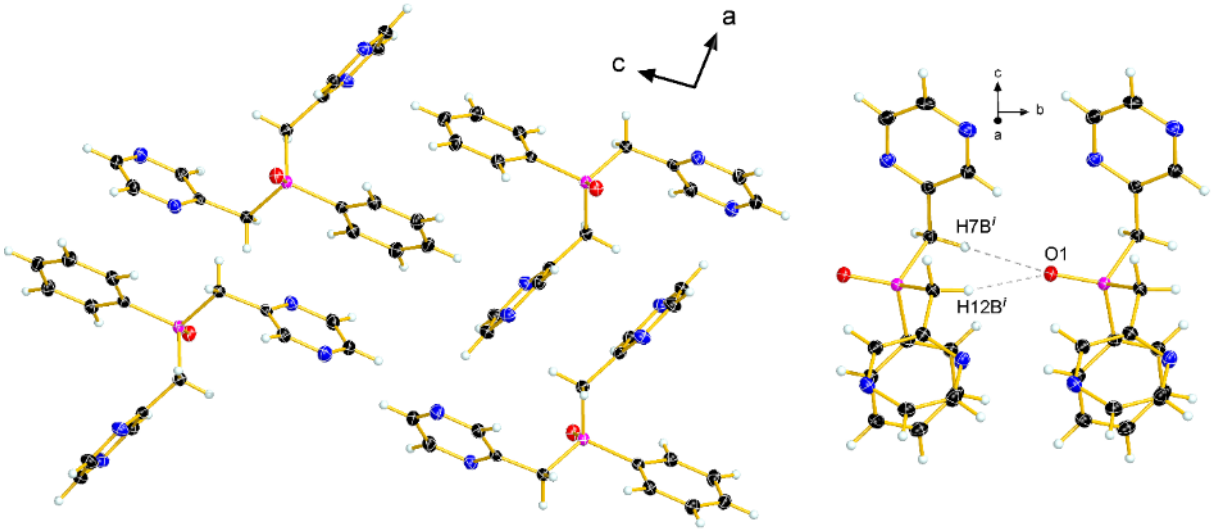

Figure S8. Arrangement of the molecules of **4** in the crystal (left) and visualization of the non-classical hydrogen bonds (right). Diamond representation, thermal ellipsoids are drawn at 50 % probability level. Bond lengths of hydrogen bonds [Å]: O1···H7B^{i} 2.732, O1···H12B^{i} 2.512. Symmetry code: *i* = *x*, 1+*y*, *z*.

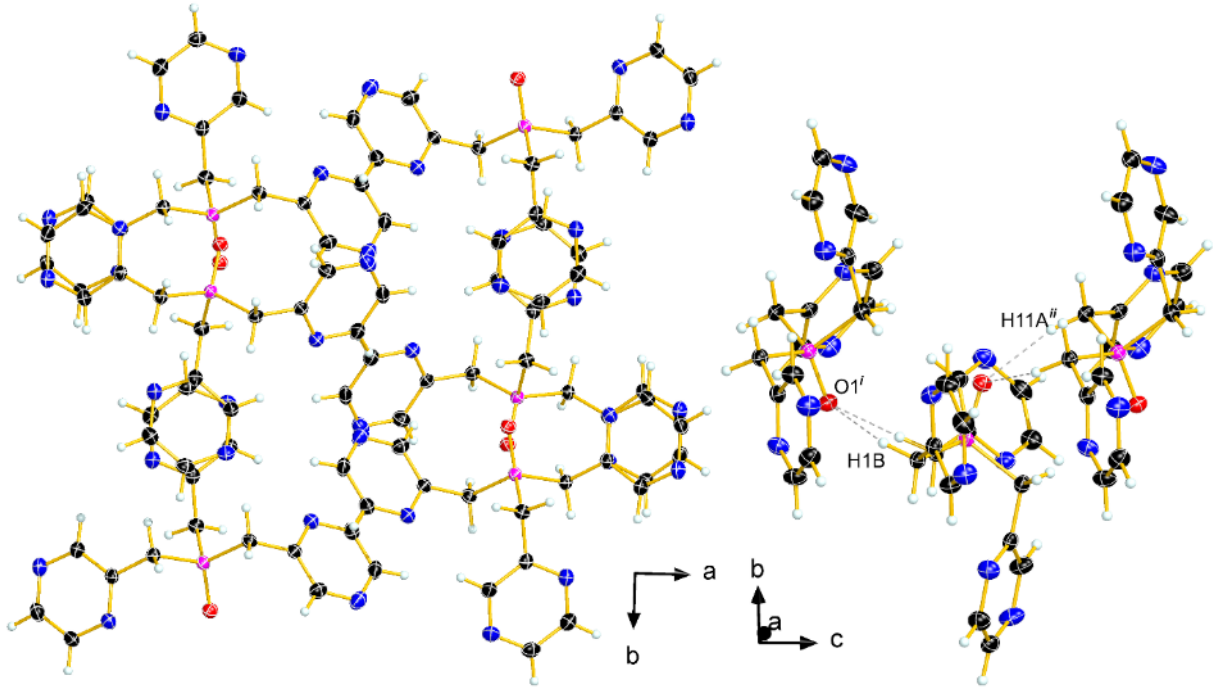

Figure S9. Arrangement of the molecules of **5** in the crystal (left) and visualization of the non-classical hydrogen bonds (right). Diamond representation, thermal ellipsoids are drawn at 50 % probability level. Bond lengths of hydrogen bonds [Å]: O1···H1B^{i} 2.336, O1···H11A^{i} 2.279. Symmetry code: *i* = *x*, 0.5−*y*, 0.5+*z*.

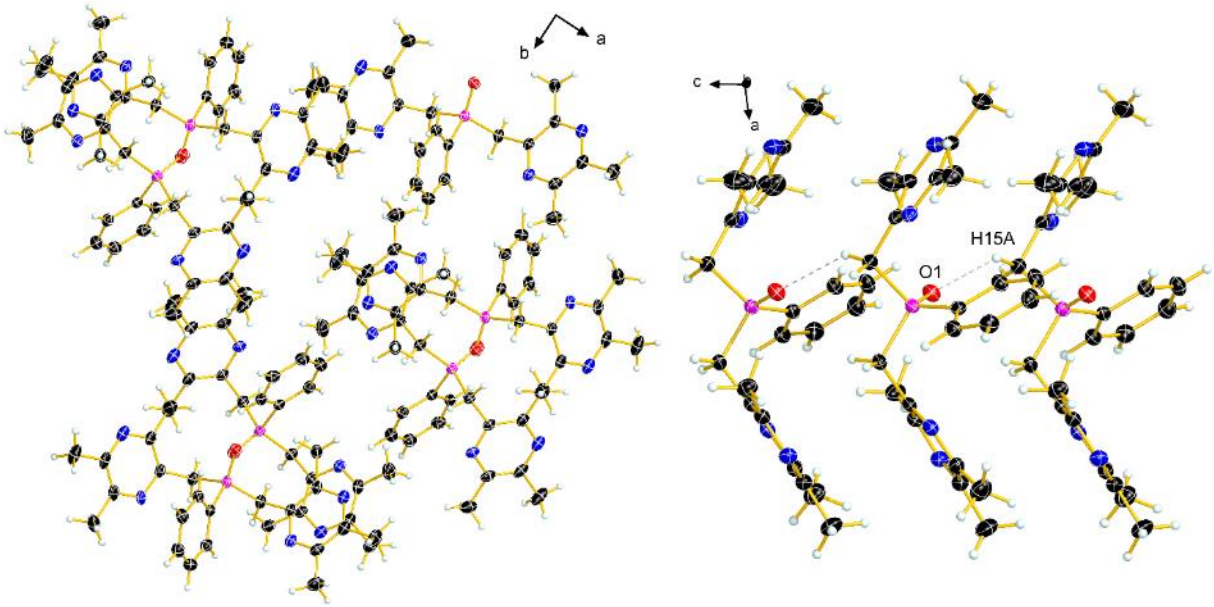

Figure S10. Arrangement of the molecules of **6** in the crystal (left) and visualization of the non-classical hydrogen bonds (right). Diamond representation, thermal ellipsoids are drawn at 50 % probability level. Bond lengths of hydrogen bonds [Å]: O1···H15A^{i} 2.859, O1···H7B^{i} 2.375. Symmetry code: *i* = *x*, 0.5−*y*, 0.5+*z*.

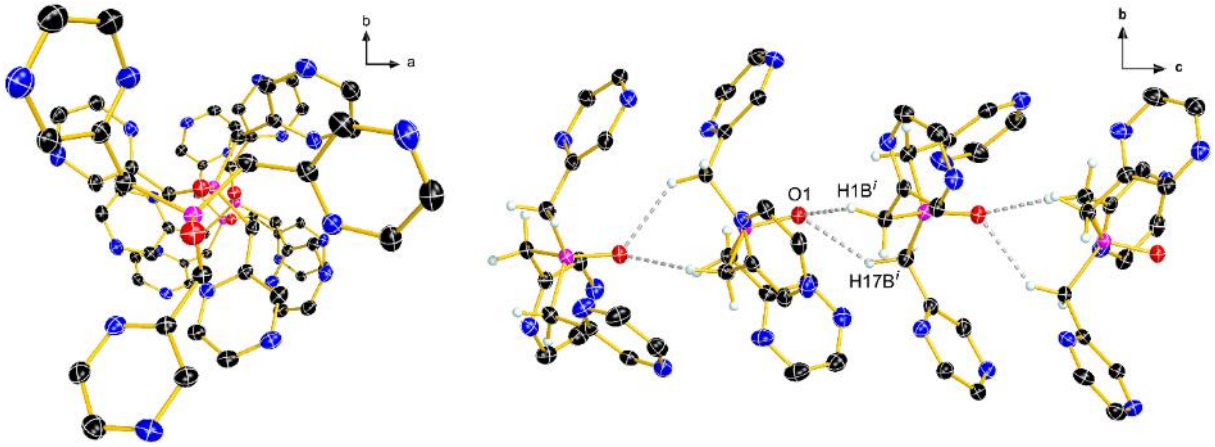

Figure S11. Spiral arrangement of the molecules of **7** in the crystal along the *c* axis (left) and visualization of the non-classical hydrogen bonds (right). Diamond representation, thermal ellipsoids are drawn at 50 % probability level. Methyl groups and some hydrogen atoms are omitted for clarity. Bond lengths of hydrogen bonds [Å]: O1···H1B^{i} 2.358, O1···H17B^{i} 2.411. Symmetry code: *i* = −0.25+*x*, 1.25−*y*, −0.25+*z*.

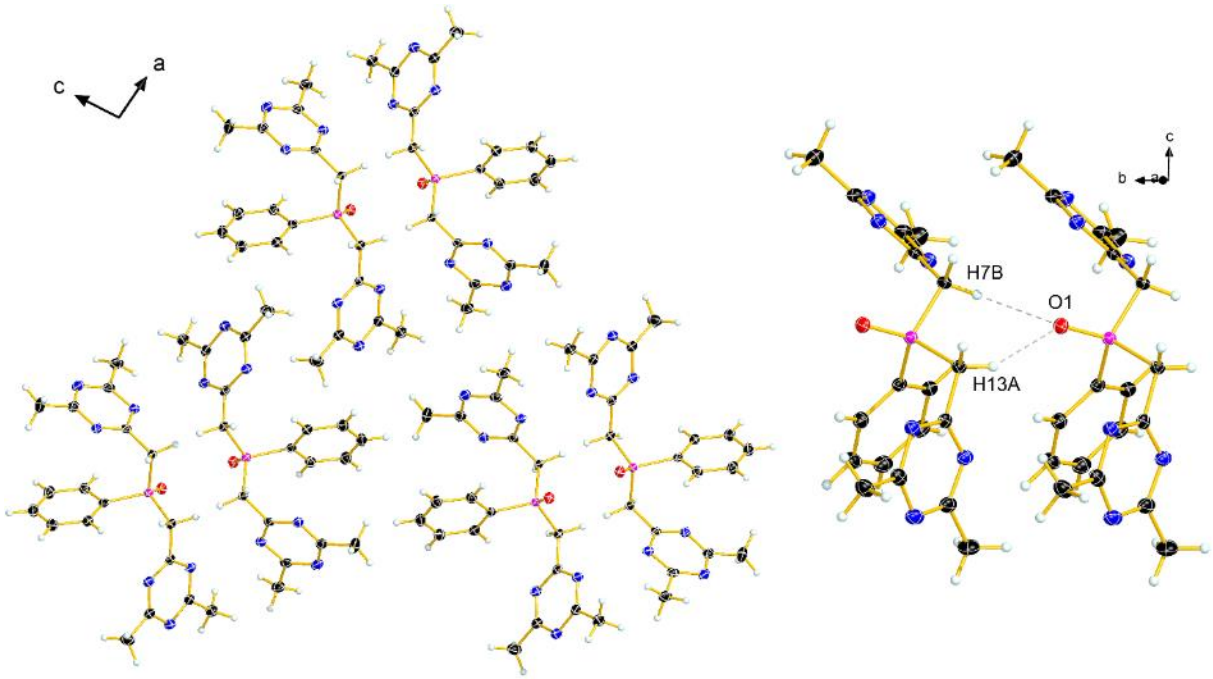

Figure S12. Arrangement of the molecules of **8** in the crystal (left) and visualization of the non-classical hydrogen bonds (right). Diamond representation, thermal ellipsoids are drawn at 50 % probability level. Bond lengths of hydrogen bonds [Å]: O1···H7A^{i} 2.619, O1···H13B^{i} 2.400. Symmetry code: *i* = 1.5−*x*, 0.5+*y*, 1.5−*z*.

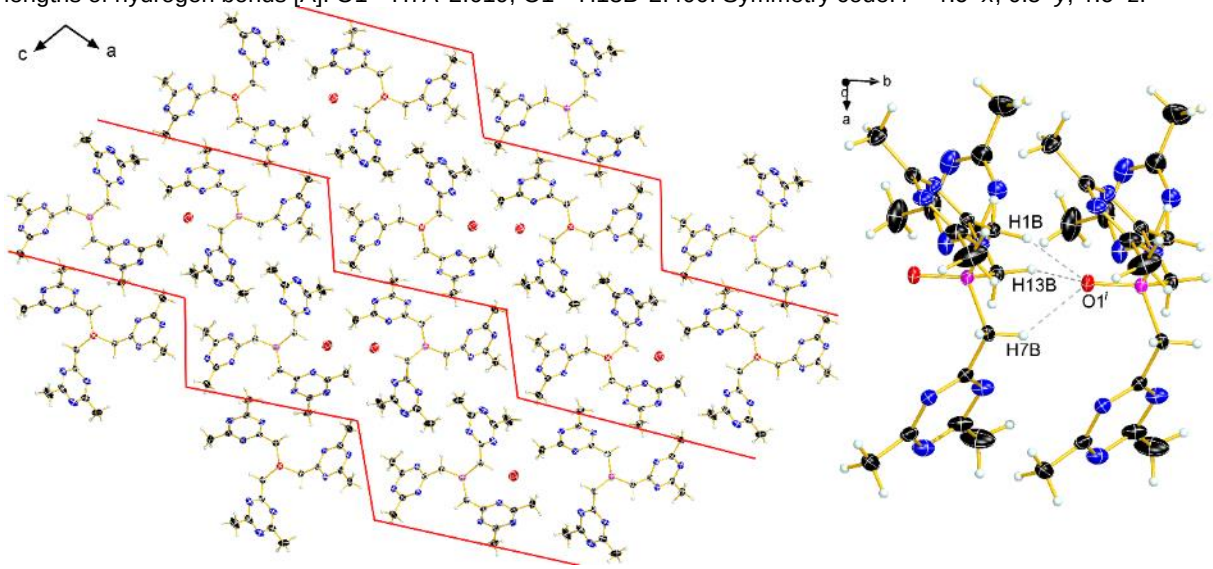

Figure S13. Arrangement of the molecules of **9** in the crystal (left) and visualization of the non-classical hydrogen bonds (right). Diamond representation, thermal ellipsoids are drawn at 50 % probability level. Bond lengths of hydrogen bonds [Å]: O1···H1B^{i} 2.328, O1···H7B^{i} 2.368, O1···H13B^{i} 2.343. Symmetry code: *i* = *x*, −1+*y*, *z*.

Table S9. Selected bond lengths [Å] and angles [°].

4			
P1–O1	1.488(2)	O1–P1–C7	115.2(7)
P1–C1	1.804(2)	O1–P1–C12	114.6(7)
P1–C7	1.817(2)	C1–P1–C7	105.8(7)
P1–C12	1.815(2)	C1–P1–C12	106.0(7)
O1–P1–C1	112.4(7)	C7–P1–C12	102.0(7)
5			
P1–O1	1.484(2)	O1–P1–C6	111.5(8)
P1–C1	1.816(2)	O1–P1–C11	112.6(8)
P1–C6	1.822(2)	C1–P1–C6	106.3(8)
P1–C11	1.806(2)	C1–P1–C11	105.2(8)
O1–P1–C1	113.1(7)	C6–P1–C11	107.6(8)
6			
P1–O1	1.489(2)	O1–P1–C7	113.3(7)
P1–C1	1.797(2)	O1–P1–C15	113.4(7)
P1–C7	1.819(2)	C1–P1–C7	109.5(8)
P1–C15	1.825(2)	C1–P1–C15	104.1(8)
O1–P1–C1	111.3(7)	C7–P1–C15	104.7(7)
7			
P1–O1	1.489(2)	O1–P1–C9	112.0(9)
P1–C1	1.813(2)	O1–P1–C17	113.7(9)
P1–C9	1.822(2)	C1–P1–C9	106.1(1)
P1–C17	1.825(2)	C1–P1–C17	107.0(1)
O1–P1–C1	113.0(9)	C9–P1–C17	104.4(1)
8			
P1–O1	1.481(2)	O1–P1–C9	114.6(9)
P1–C1	1.804(2)	O1–P1–C17	113.6(9)
P1–C9	1.811(2)	C1–P1–C9	109.8(9)
P1–C17	1.821(2)	C1–P1–C17	104.4(9)
O1–P1–C1	111.0(9)	C9–P1–C17	102.7(9)
9			
P1–O1	1.486(2)	O1–P1–C9	112.7(7)
P1–C1	1.809(2)	O1–P1–C17	113.1(7)
P1–C9	1.814(2)	C1–P1–C9	106.6(7)
P1–C17	1.814(2)	C1–P1–C17	104.9(7)
O1–P1–C1	113.3(7)	C9–P1–C17	105.6(7)

Photophysical spectra

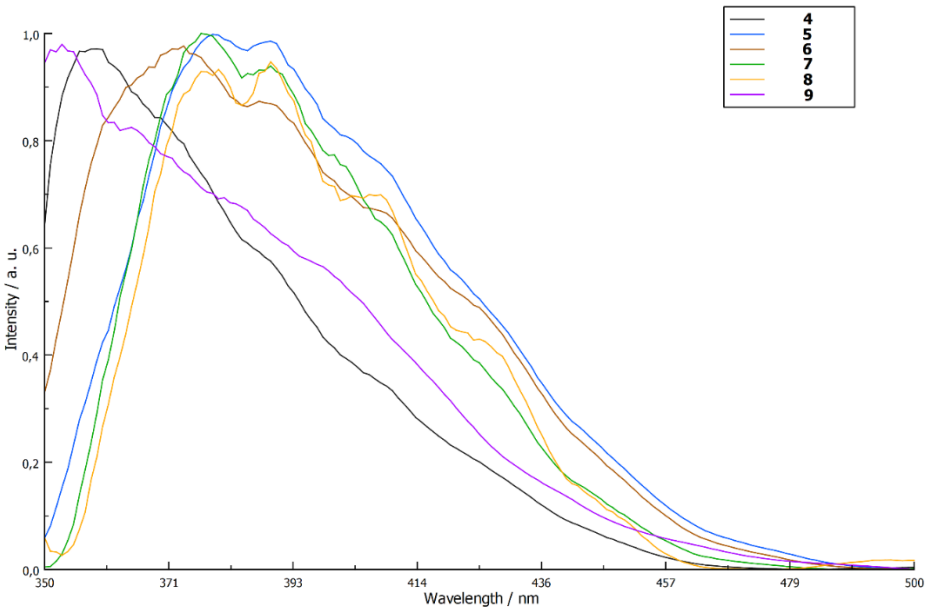

Figure S14. UV Vis spectra of the solid compounds **4**–**9**. Normalized to 1 in the region from 500–350 nm. Data were smoothed using a linear moving average (interval = five data points).

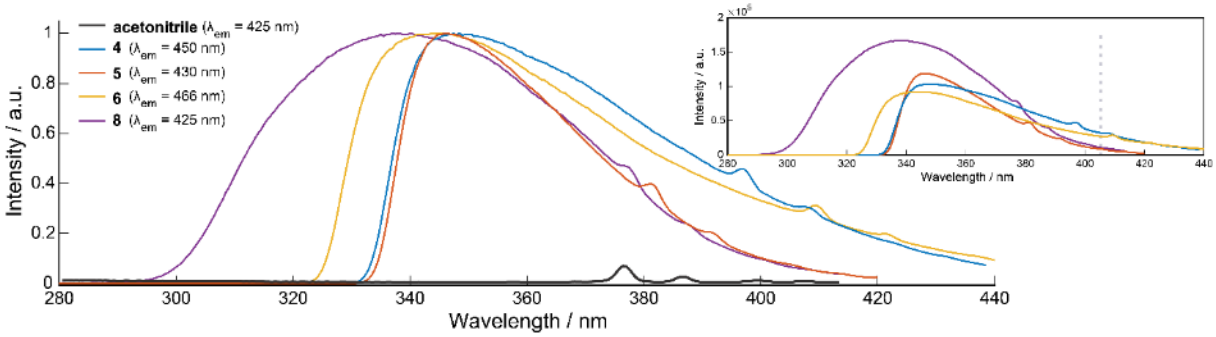

Figure S15. Excitation spectra of compounds **4**–**6** and **8** (a concentration of ~10 mM was used) normalized to the maximum, with a spectrum of the acetonitrile solvent (black) plotted to show the position of the Raman peaks at 425 nm emission. The inset shows the unnormalized excitation spectra, where the dotted line shows the wavelength of excitation used for the FLIM measurements and the differences in absorption ratio were calculated for the compounds **5** and **8** and were scaled relative to compounds **4** and **6** (factors of 3.6 and 2.9, respectively).

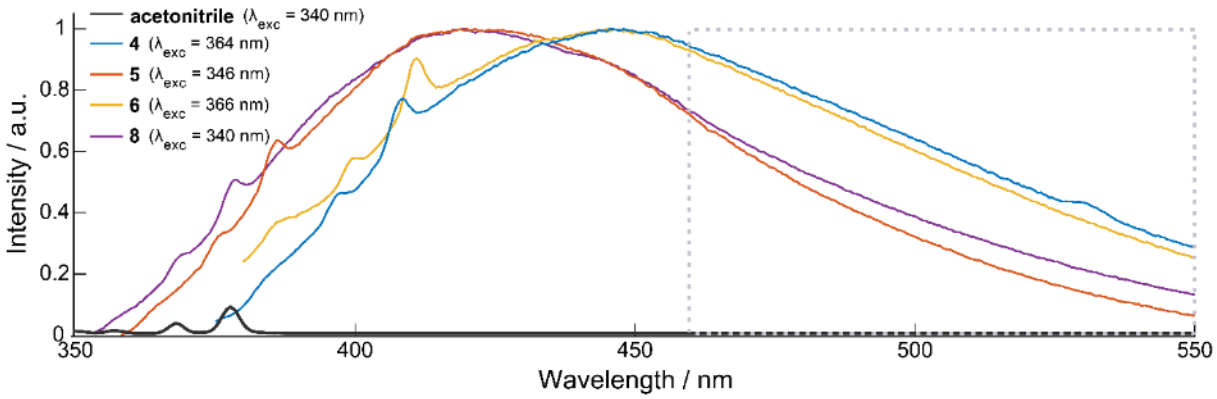

Figure S16. Emission spectra of compounds **4**–**6** and **8** (a concentration of ~10 mM was used) normalized to the maximum, with a spectrum of the acetonitrile solvent (black) plotted to show the position of the Raman peaks at 340 nm excitation. For the FLIM measurements, the detected photons must pass of a long pass filter that transmits above 460 nm. The rectangular box indicates the region of the spectrum that is detected by the instrument. To compensate for the relative differences between compounds **5**, **6** and **8**, relative to compound **4**, an additional factor of ~1.5 was applied for compounds **5** and **8**, where a correction factor of 1.2 was applied for compound **6**.

Fluorescence lifetime and FLIM images

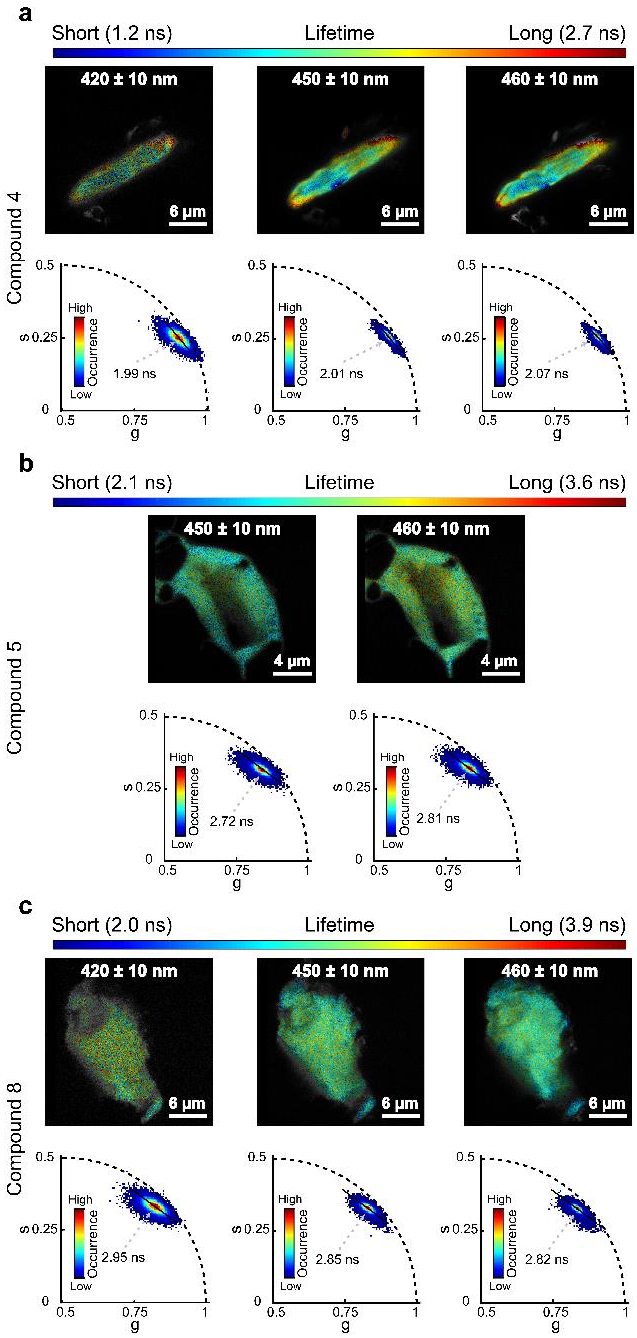

Figure S17. FLIM images of three different structures of compounds **4**, **5** and **8** monitored at three different ranges of emission wavelength. a) Three FLIM images (upper panel) of compound **4** monitored at 420 ± 10 nm, 450 ± 10 nm and 460 ± 10 nm, respectively. b) Two FLIM images (upper panel) of compound **5** monitored at 450 ± 10 nm and 460 ± 10 nm, respectively. c) Three FLIM images (upper panel) of compound **8** monitored at 420 ± 10 nm, 450 ± 10 nm and 460 ± 10 nm, respectively. The lower row of panels a), b) and c) shows the corresponding phasor plot of the FLIM images. The color in the phasor plot corresponds to the number of pixels exhibiting the particular phasor value (blue indicating the lowest occurrence and red indicating the highest occurrence, see occurrence on the color bar. The black line in the phasor plots is used for the color coding of the fluorescence lifetimes in the FLIM images, where the pixel brightness corresponds to counts, while the hue indicates the pixels' proximity to the black line. The color-code corresponding to the fluorescence

lifetime displayed on the FLIM images, goes from blue (indicating the shortest fluorescence lifetime) over green and yellow to orange and red (indicating the longest fluorescence lifetime), see color bar.

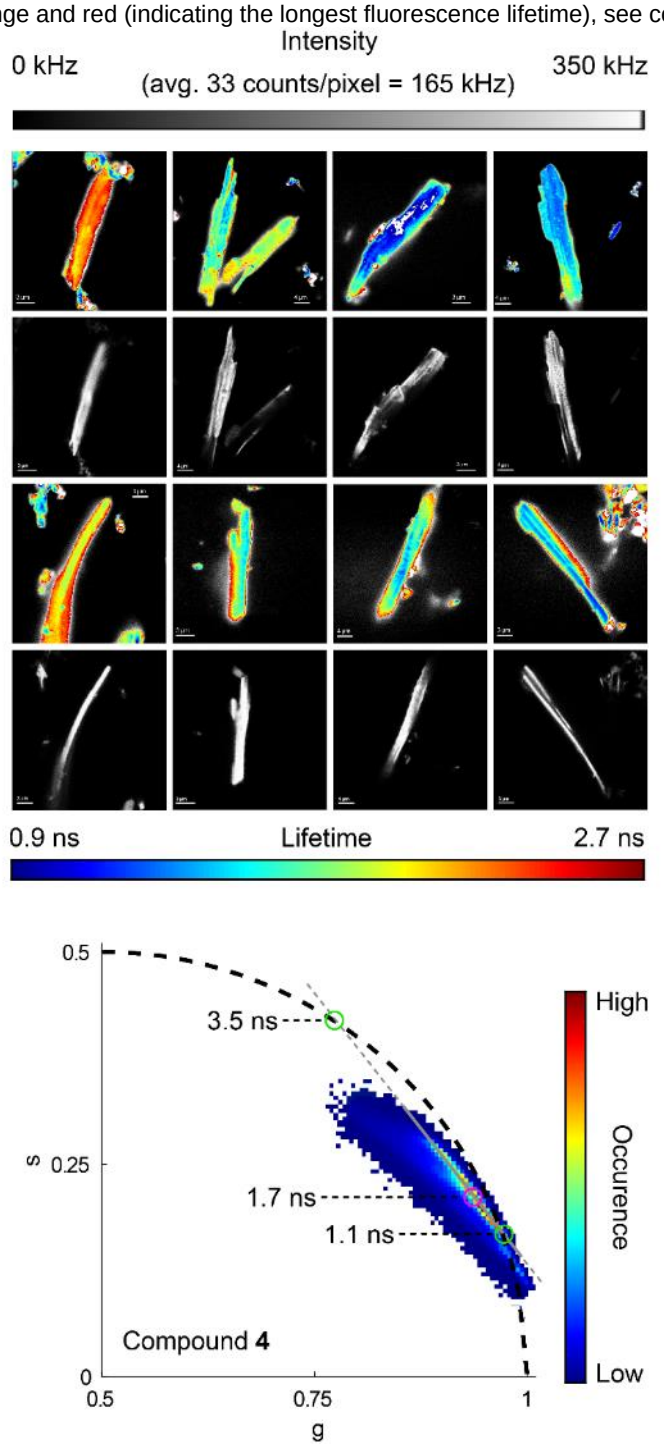

Figure S18. Fluorescence intensity and FLIM images of compound **4** showing its rod-like crystal structure. The intensity images show the photon counts per pixel for the different crystals, see upper intensity color bar. The last panel shows the corresponding phasor plot of the different FLIM images. The color in the phasor plot corresponds to the number of pixels exhibiting the particular phasor value (blue indicating the lowest occurrence and red indicating the highest occurrence, see occurrence on the color bar. The black line in the phasor plots is used for the color coding of the fluorescence lifetimes in the FLIM images, where the pixel brightness corresponds to counts, while the hue indicates the pixels' proximity to the black line. The color-

code corresponding to the fluorescence lifetime displayed on the FLIM images, goes from blue (indicating the shortest fluorescence lifetime) over green and yellow to orange and red (indicating the longest fluorescence lifetime), see lifetime color bar.

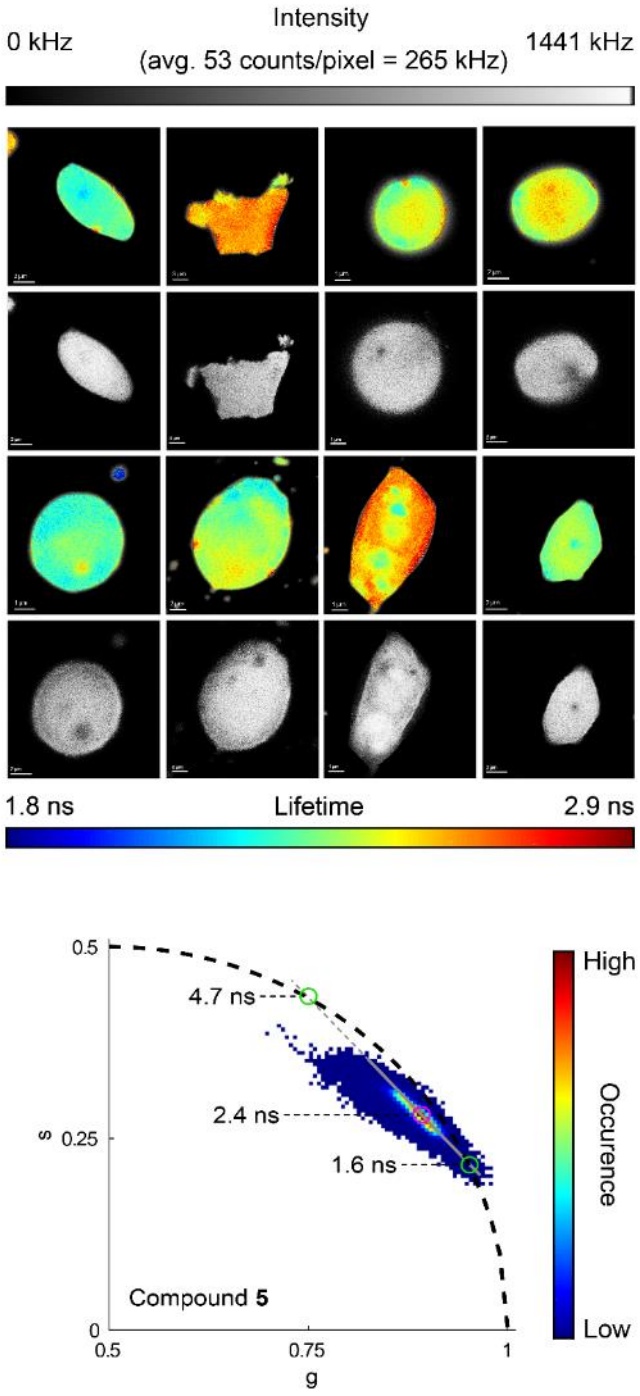

Figure S19. Fluorescence intensity and FLIM images of **5** showing its quasi-spherically elongated and oval-like structure. The intensity images show the photon counts per pixel for the different crystals, see upper intensity color bar. The intensity values were adjusted based on the excitation and emission correction factors (check the FLIM section, SI for the correction factor details). The last panel shows the corresponding phasor plot of the different FLIM images. The color in the phasor plot corresponds to the number of pixels exhibiting the particular phasor value (blue indicating the lowest occurrence and red indicating the highest occurrence,

see occurrence on the color bar. The black line in the phasor plots is used for the color coding of the fluorescence lifetimes in the FLIM images, where the pixel brightness corresponds to counts, while the hue indicates the pixels' proximity to the black line. The color-code corresponding to the fluorescence lifetime displayed on the FLIM images, goes from blue (indicating the shortest fluorescence lifetime) over green and yellow to orange and red (indicating the longest fluorescence lifetime), see color bar.

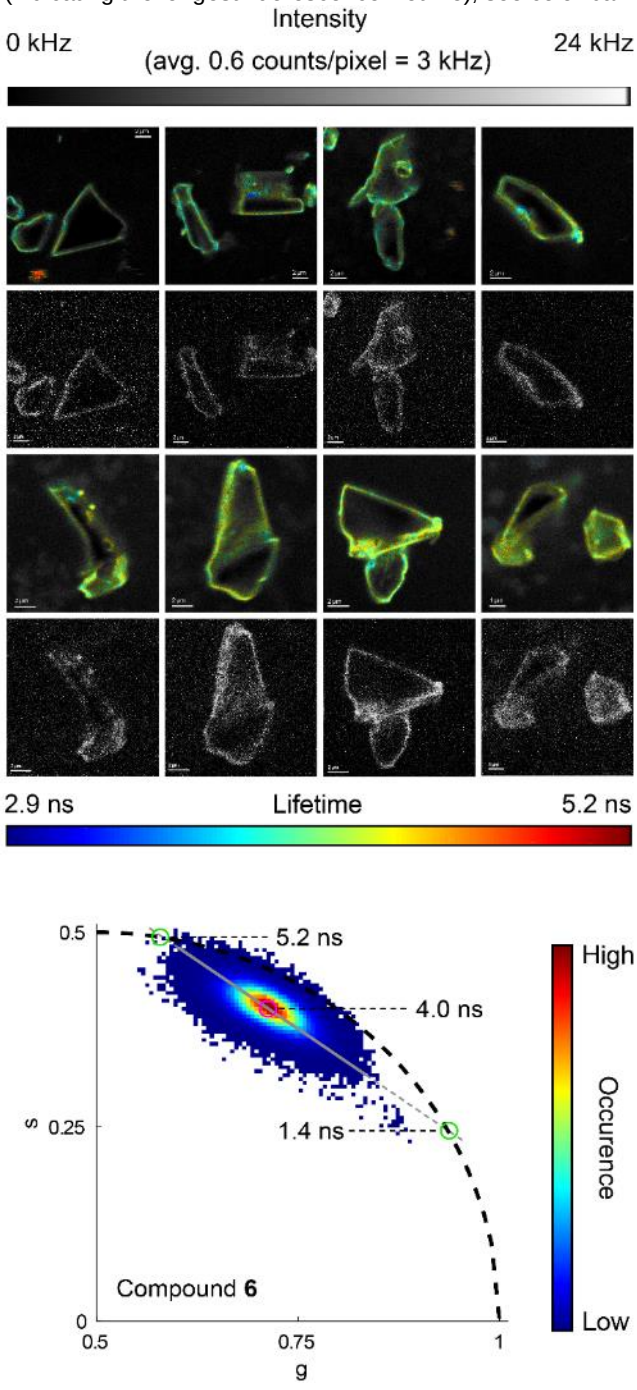

Figure S20. Fluorescence intensity and FLIM images of **6** showing its diversely shaped structures. The intensity images show the photon counts per pixel for the different crystals, see upper intensity color bar. The intensity values were adjusted based on the emission correction factors (check the FLIM section, SI for the correction factor details). The last panel shows the corresponding phasor plot of the different FLIM images. The color in the phasor plot corresponds to the number of pixels exhibiting the particular phasor value (blue

indicating the lowest occurrence and red indicating the highest occurrence, see occurrence on the color bar. The black line in the phasor plots is used for the color coding of the fluorescence lifetimes in the FLIM images, where the pixel brightness corresponds to counts, while the hue indicates the pixels' proximity to the black line. The color-code corresponding to the fluorescence lifetime displayed on the FLIM images, goes from blue (indicating the shortest fluorescence lifetime) over green and yellow to orange and red (indicating the longest fluorescence lifetime), see color bar.

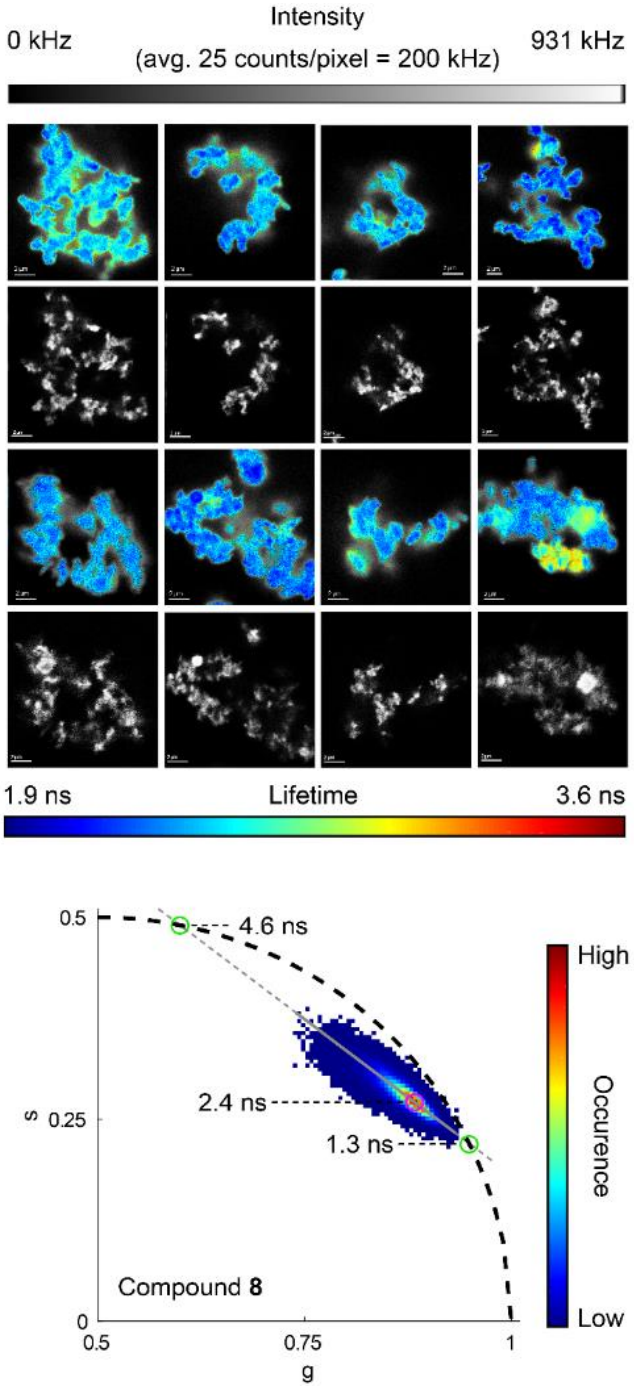

Figure S21. Fluorescence intensity and FLIM images of **8** showing its amorphous-like structure. The intensity images show the photon counts per pixel for the different crystals, see upper intensity color bar. The intensity values were adjusted based on the excitation and emission correction factors (check the FLIM section, SI for the correction factor details). The last panel shows the corresponding phasor plot of the different FLIM images.

The color in the phasor plot corresponds to the number of pixels exhibiting the particular phasor value (blue indicating the lowest occurrence and red indicating the highest occurrence, see occurrence on the color bar. The black line in the phasor plots is used for the color coding of the fluorescence lifetimes in the FLIM images, where the pixel brightness corresponds to counts, while the hue indicates the pixels' proximity to the black line. The color-code corresponding to the fluorescence lifetime displayed on the FLIM images, goes from blue (indicating the shortest fluorescence lifetime) over green and yellow to orange and red (indicating the longest fluorescence lifetime), see color bar.

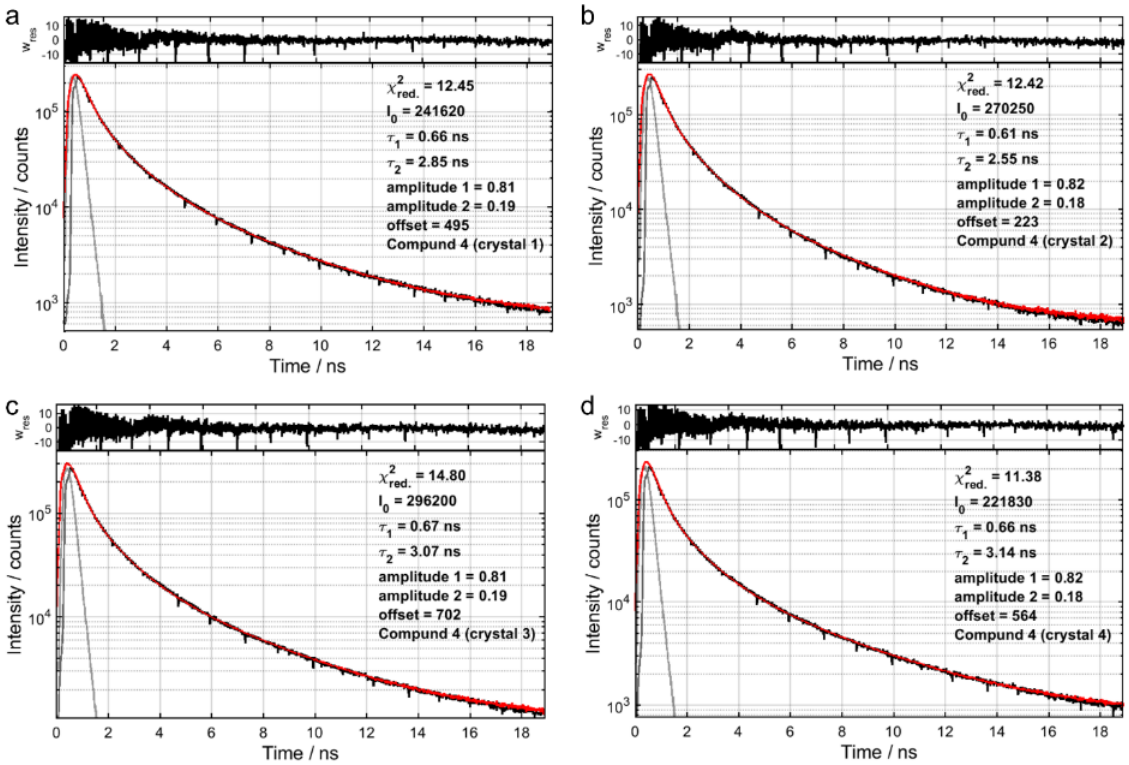

Figure S22. Fluorescence lifetime decay data and fits obtained for the four crystals (**i**) of compound **4** imaged in Figure 2, which shows a bi-exponential fluorescence lifetime decay.

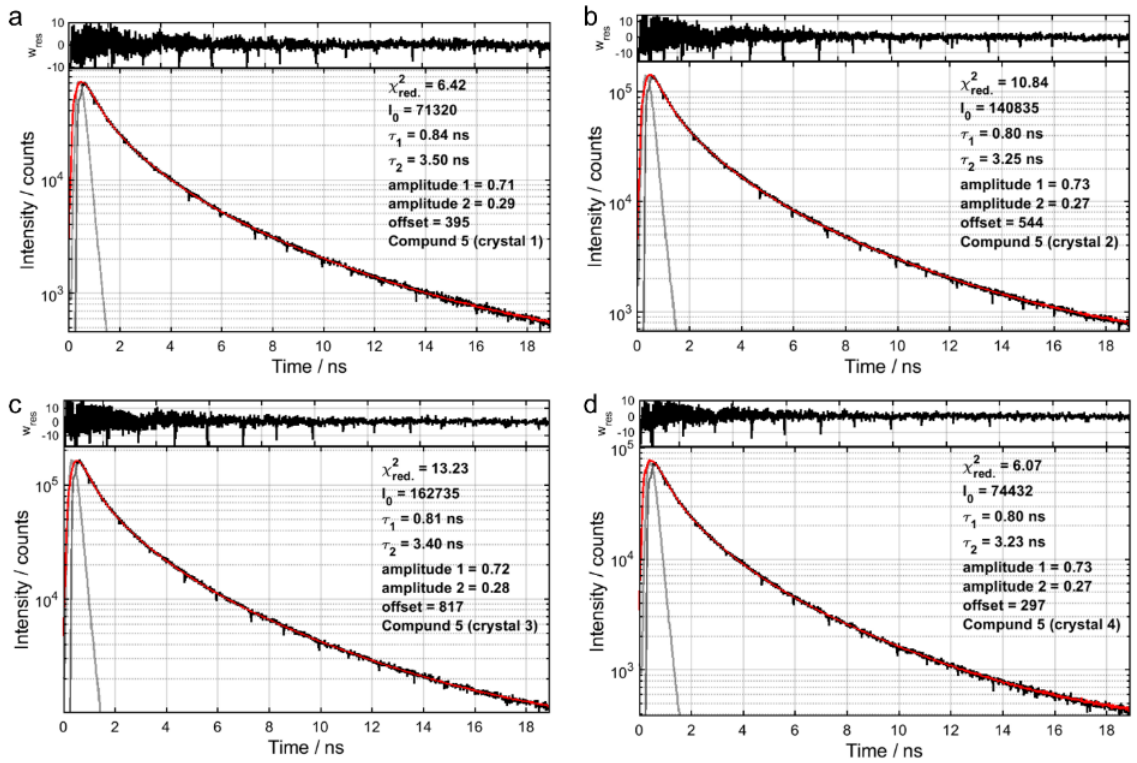

Figure S23. Fluorescence lifetime decay data and fits obtained for the four crystals (**ii**) of compound **5** imaged in Figure 2, which shows a bi-exponential fluorescence lifetime decay.

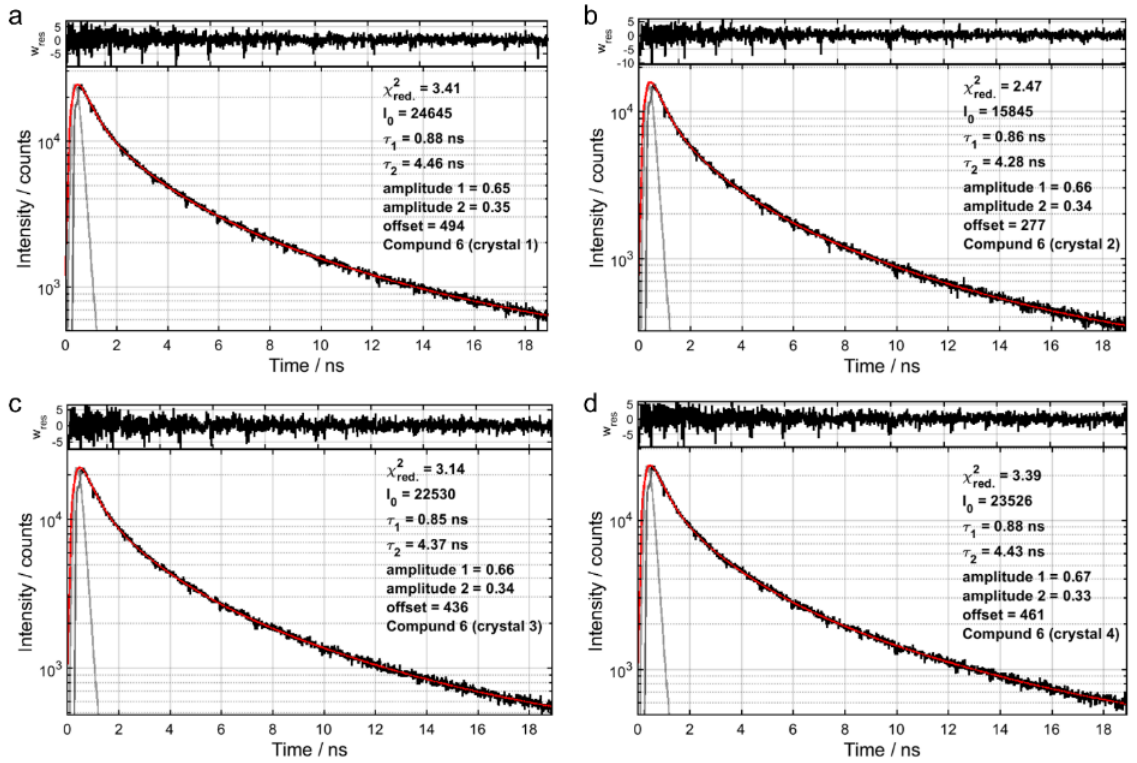

Figure S24. Fluorescence lifetime decay data and fits obtained for the four crystals (**iii**) of compound **6** imaged in Figure 2, which shows a bi-exponential fluorescence lifetime decay.

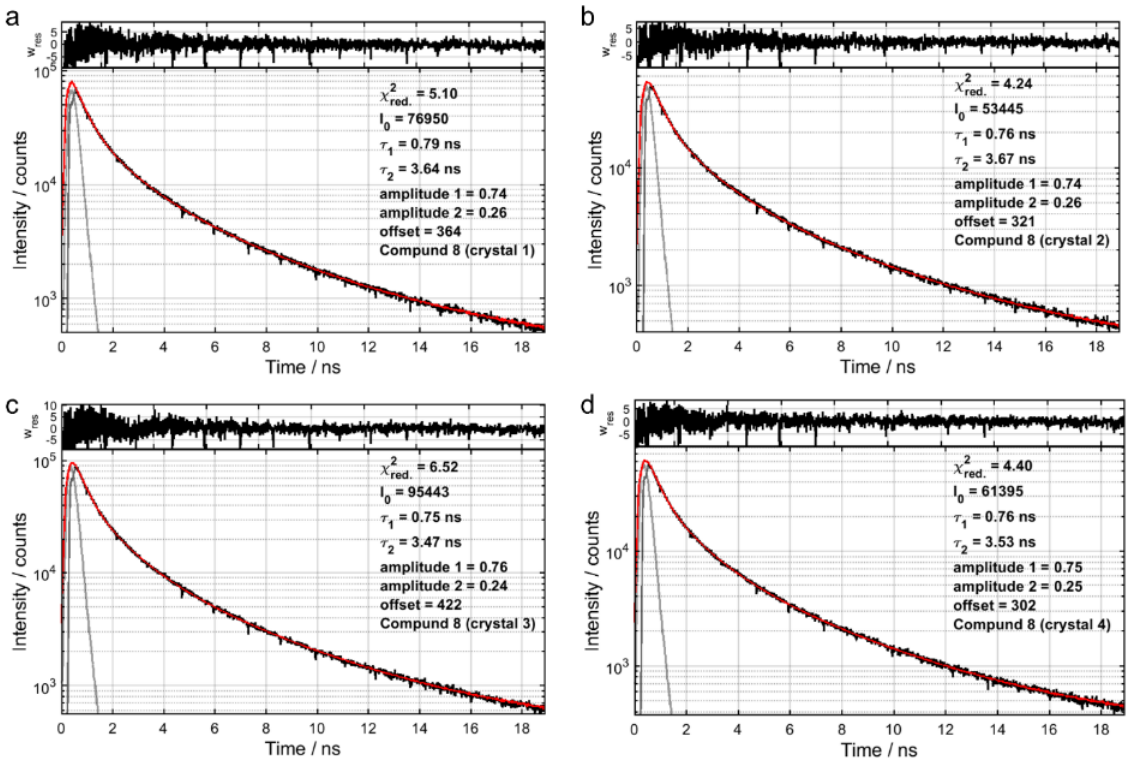

Figure S25. Fluorescence lifetime decay data and fits obtained for the four crystals (**iv**) of compound **8** imaged in Figure 2, which shows a bi-exponential fluorescence lifetime decay.

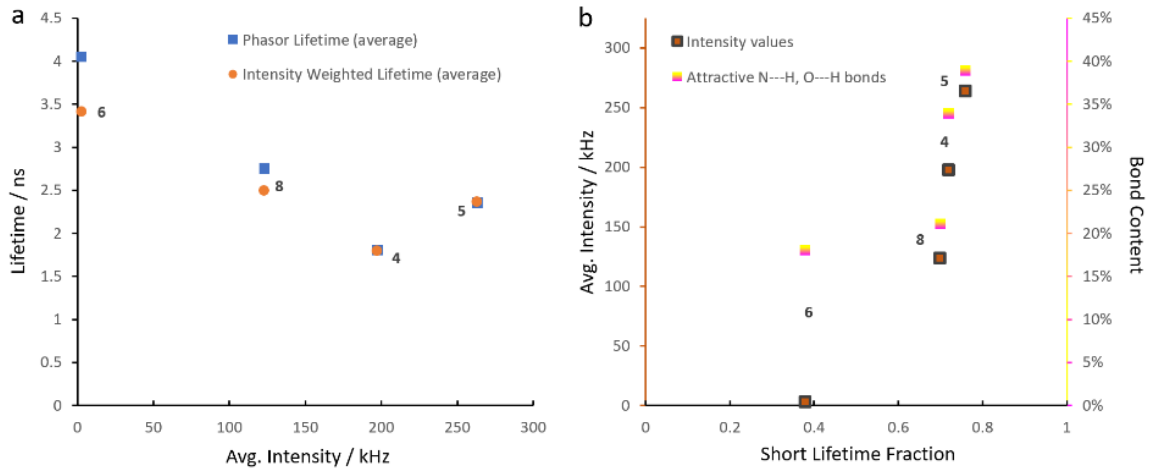

Figure S26. The relation between the fluorescence lifetime and intensity relative to the attractive bond contents for the four crystals of the different compounds imaged in Figure 2. a) Average fluorescence lifetimes obtained from the phasor and tail fits to the TCSPC data showing an increase of fluorescence intensity with decrease in the lifetime average. b) The increase in the short lifetime fraction correlates with the increase in fluorescence intensity and attractive bond contents within the investigated crystals.

Table S10. Fluorescence lifetime decay values obtained for the different four crystals measured in Figure 3 for each of the compounds.

Compound 4	Compound 5	Compound 6	Compound 8

	τ_1 /ns (A_1)[a]	τ_2 /ns (A_2)[b]	τ_1 /ns (A_1)[a]	τ_2 /ns (A_2)[b]	τ_1 /ns (A_1)[a]	τ_2 /ns (A_2)[b]	τ_1 /ns (A_1)[a]	τ_2 /ns (A_2)[b]
Crystal 1	0.66 (81%)	2.85 (19%)	0.84 (71%)	3.50 (29%)	0.88 (65%)	4.46 (35%)	0.79 (74%)	3.64 (26%)
Crystal 2	0.61 (82%)	2.55 (18%)	0.80 (73%)	3.25 (27%)	0.86 (66%)	4.28 (34%)	0.76 (74%)	3.67 (26%)
Crystal 3	0.67 (81%)	3.07 (19%)	0.81 (72%)	3.40 (28%)	0.85 (66%)	4.37 (34%)	0.75 (76%)	3.47 (24%)
Crystal 4	0.66 (82%)	3.14 (18%)	0.80 (73%)	3.23 (27%)	0.88 (67%)	4.43 (33%)	0.76 (75%)	3.53 (25%)
Crystals[c] average	**0.65±0.02 (0.82)**	**2.90±0.19 (0.18)**	**0.81±0.02 (0.72)**	**3.35±0.11 (0.28)**	**0.87±0.01 (0.66)**	**4.39±0.07 (0.34)**	**0.77±0.02 (0.75)**	**3.58±0.08 (0.25)**
Intensity weighted lifetime[d]	**1.79 ± 0.16**		**2.36 ± 0.11**		**3.41 ± 0.06**		**2.49 ± 0.09**	
Phasor lifetimes	**0.90[e] (0.72)**	**2.75[f] (0.28)**	**1.56[e] (0.76)**	**3.95[f] (0.24)**	**1.70[e] (0.38)**	**5.50[f] (0.62)**	**1.42[e] (0.70)**	**4.25[f] (0.30)**
Average intensity / kHz[g]	**198 ± 17.4**		**263 ± 8.83**		**2.93 ± 0.07**		**123 ± 8.05**	

[a]Short lifetime component and its relative population (A_1) from a biexponential fit to the cumulative TCSPC data coming from the crystals. [b]Long lifetime component and its relative population (A_2) from a biexponential fit to the cumulative TCSPC data coming from the crystals. [c]Average lifetime values (mean) and standard deviation of the individual components for the four different crystals. [d]The average fluorescence lifetime (τ_{avg}) values were obtained by using the following equation: $\tau_{avg} = (\sum_{i=1}^{n} A_i\tau_i^2)/(\sum_{i=1}^{n} A_i\tau_i)$; where τ_i is the individual lifetime with corresponding amplitude A_i

[e]Short lifetime component taken from its position on the phasor semicircle. [f]Long lifetime component taken from its position on the phasor semicircle. [g]The intensity values are obtained by performing a mask to select for the pixels with the crystals, where the average counts for each compound (averaging over the four crystals) is shown.

References

[1] M. C. Burla, R. Caliandro, B. Carrozzini, G. L. Cascarano, C. Cuocci, C. Giacovazzo, M. Mallamo, A. Mazzone, G. Polidori, *J. Appl. Crystallogr.* **2015**, *48*, 306–309.
[2] C. B. Hübschle, G. M. Sheldrick, B. Dittrich, *J. Appl. Crystallogr.* **2011**, *44*, 1281–1284.
[3] G. M. Sheldrick, *Acta Crystallogr. Sect. C Struct. Chem.* **2015**, *71*, 3–8.
[4] A. L. Spek, *Acta Crystallogr. Sect. E Crystallogr. Commun.* **2020**, *76*, 1–11.
[5] L. J. Farrugia, *J. Appl. Crystallogr.* **2012**, *45*, 849–854.
[6] H. Putz, K. Brandenburg, Crystal Impact GbR, **2014**.
[7] J. Hendrix, W. Schrimpf, M. Höller, D. C. Lamb, *Biophys. J.* **2013**, *105*, 848–861.
[8] M. A. Digman, V. R. Caiolfa, M. Zamai, E. Gratton, *Biophys. J.* **2008**, *94*, L14–L16.
[9] W. Schrimpf, A. Barth, J. Hendrix, D. C. Lamb, *Biophys. J.* **2018**, *114*, 1518–1528.
[10] F. C. Schaefer, G. A. Peters, *J. Org. Chem.* **1961**, *26*, 2784–2786.
[11] P. Launer, B. Arkles, *Infrared Analysis of Organsilicon Compounds: Spectra-Structure Correlations*, Gelest Inc., **2008**.
[12] O. V. Kotova, S. V. Eliseeva, A. A. Volosnikov, V. A. Oleinikov, L. S. Lepnev, A. G. Vitukhnovskii, N. P. Kuz'mina, *Russ. J. Coord. Chem.* **2006**, *32*, 901–909.
[13] C. Hettstedt, P. Köstler, E. Ceylan, K. Karaghiosoff, *Tetrahedron* **2016**, *72*, 3162–3170.
[14] K. Junge, B. Wendt, F. A. Westerhaus, A. Spannenberg, H. Jiao, M. Beller, *Chem. A Eur. J.* **2012**, *18*, 9011–9018.
[15] C. Hettstedt, M. Unglert, R. J. Mayer, A. Frank, K. Karaghiosoff, *Eur. J. Inorg. Chem.* **2016**, *2016*, 1405–1414.
[16] S. Schäfer, M. T. Gamer, S. Lebedkin, F. Weigend, M. M. Kappes, P. W. Roesky, *Chem. - A Eur. J.* **2017**, *23*, 12198–12209.

B.4. Paper 4: Studies of Pyrroloquinoline Quinone Species in Solution and Lanthanide-dependent Methanol Dehydrogenases

Studies of Pyrroloquinoline Quinone Species in Solution and in Lanthanide-dependent Methanol Dehydrogenases

Nader AL Danaf[a]†, Jerome Kretzschmar[b]†, Berenice Jahn[a], Helena Singer[a], Arian Pol[c], Huub J.M. Op den Camp[c], Robin Steudtner[b], Don Lamb[a], Björn Drobot*[b] and Lena J. Daumann*[a]

[a] Department of Chemistry
Ludwig-Maximilians-University Munich
Butenandtstraße 5 – 13, 81377 München (Germany)
[b] Institute of Resource Ecology
Helmholtz-Zentrum Dresden-Rossendorf e.V.
Bautzner Landstraße 400, 01328 Dresden (Germany)
[c] Department of Microbiology
Radboud University
Heyendaalseweg 135, 6525 AJ, Nijmegen (The Netherlands)
† Shared first author.
* Corresponding authors: b.drobot@hzdr.de, lena.daumann@lmu.de

Abstract

Pyrroloquinoline quinone (PQQ) is a redox cofactor in calcium- and lanthanide-dependent alcohol dehydrogenases that has been known and studied for over 40 years. Despite its long history, many questions regarding fluorescence properties, speciation in solution and in the active site of alcohol dehydrogenase remain open. Here we investigate the effects of pH and temperature on the distribution of different PQQ species (H_3PQQ to PQQ^{3-} as well as water adducts and in complex with lanthanides (Lns)) using NMR and UV-Vis spectroscopy as well as time-resolved laser-induced fluorescence spectroscopy (TRLFS). Using a europium derivative of recently discovered new class of lanthanide-dependent methanol dehydrogenase (MDH) enzymes, we report two techniques to monitor Ln binding to the active sites of these enzymes. Using TRLFS, we were able to follow Eu^{3+} binding directly to the active site of MDH using its luminescence. Additionally, we used the antenna effect to study PQQ and simultaneously Eu in the active site.

Introduction

In the past 20 years the use of luminescent lanthanides (Lns) for the study of various aspects of biological samples such as cells, proteins, DNA, biomarkers, along with the use of luminescent lanthanide binding tags (LBT) to investigate protein interactions has increased dramatically.[132, 133, 137-140] The use of luminescent Lns such as Tb^{3+} and Eu^{3+} in proteins has so far been as substitutes for the native metal ions such as Ca^{2+}, Mg^{2+} or Co^{2+}.[141] However, with the advent of the new biological role of lanthanides for numerous bacteria (mostly methanotrophs and methylotrophs but other examples such as *P. putida* are known to encode Ln-dependent enzymes[142]) it has now become possible to use the attractive photophysical properties of Ln in their natural biological environments.[143-147] The active sites of known lanthanide dependent enzymes (methanol dehydrogenases, MDH/XoxF, or ethanol dehydrogenase/ExaF, or alcohol dehydrogenase/PedH in *P.putida*) include the redox cofactor pyrroloquinoline quinone (PQQ) and an early Ln ion that is complexed by four amino acids bearing hard, negatively charged oxygen donors: Glu172, Asn256, Asp299 and Asp301 (Figure 1).[146, 148, 149]

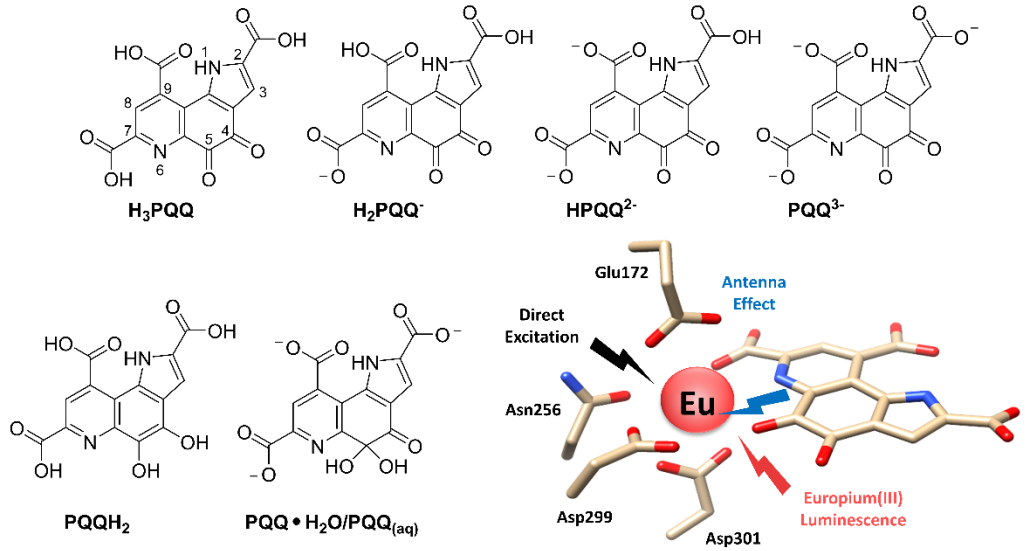

Figure 1 PQQ species discussed here. Numbering scheme of PQQ is shown, water adduct PQQ•H_2O forms readily in water, the reduced diol form $PQQH_2$ is the product after MeOH oxidation by MDH. If protonation state or general form, reduced, oxidized, semiquinone is unknown, just "PQQ" for the cofactor will be used herein. Eu-MDH active site. Eu-luminescence can be observed by either directly exciting Eu or using the antenna effect with PQQ.

The PQQ cofactor was first isolated and characterized by Anthony and Zatman in 1967.[150] Under aerobic conditions, free PQQ prevails in one of its oxidized ortho-quinone forms. Isolated PQQ readily adds nucleophiles at the C5 position, forming the water adduct PQQ•H_2O or PQQ hemiketal species with alcohols (Figure 1).[151, 152] Formation of PQQ adducts with ammonia, cyanide and other components present in enzyme preparations have also been reported for PQQ within the MDH active site, each one of them with a possibly different UV-vis signature.[153-155] The correct position

of the nucleophilic attack of water and methanol (MeOH) in free PQQ were studied by both experiment and theory.[156-158] Duine et al. reported a PQQ : PQQ•H_2O molar ratio of 2 : 1 in D_2O pD 6 solution. Unfortunately, the authors did not state the concentration, the temperature, or acquisition parameters for their NMR measurements. A temperature-dependent equilibrium between PQQ and PQQ•H_2O, and its shift towards the latter at low temperatures was noticed by Dekker et al., evaluating NMR, UV/Vis absorption and fluorescence spectra.[159] Although they determined the fractions of both components for at least two different temperatures, they do not state straightforwardly computable figures such as the equilibrium constant, reaction enthalpy or entropy. Anthony further described that for Ca-MDH a UV-Vis spectrum of Ca-MDH bearing an oxidized PQQ cofactor is inherently difficult to obtain and looks markedly different than the one with reduced cofactor $PQQH_2$.[160] Although the cofactor is non-covalently bound in the enzyme active site it has been described difficult to reconstitute a PQQ-free active site of MDH with this cofactor. Multiple literature reports indicate that no 100% PQQ occupancy in the active site is observed, even though the absence of this cofactor was seen in some of the crystal structures.[142, 160-162] Here, the cofactor is usually refined as the oxidized PQQ form.[142, 161, 163, 164] However, this might not reflect the actual state of PQQ, other forms are possible: Stepwise electrochemical reduction of free PQQ via a semiquinone radical,[165] or in the course of MeOH oxidation in MDH-bound PQQ, yields the corresponding catechol, $PQQH_2$.[165] In MDH during two of the one-electron oxidation steps a semiquinone radical PQQH• also occurs as an intermediate.[166] However, it has been proposed that, in the case of Ca-MDH, the PQQ (directly after purification) is most likely in its semiquinone or reduced $PQQH_2$ state.[154, 160, 167] DFT-Calculations by Schelter and coworkers suggest that the semiquinone state is stable for Ce-MDH.[168] Taking all reports in the literature together, even after more than 50 years it remains mostly undefined in which state the cofactor is in the active site of MDH (H_3PQQ, H_2PQQ^-, $HPQQ^{2-}$, PQQ^{3-}, $PQQH_2$, semiquinone or any of the C5 adducts) under certain conditions. Further, most crystal structures, calculations and generic structure representations show PQQ with fully protonated carboxyl groups, corresponding to H_3PQQ, in the active site of MDH, although the pK_a values suggest that at physiological pH at least the three carboxylic acids are deprotonated, thus PQQ^{3-}. Kano et al. determined PQQ's pK_a values in 0.5 M KCl solution by means of spectrophotometry as follows: 0.30 (N6), 1.60 (C7-COOH), 2.20 (C9-COOH), 3.30 (C2-COOH), 10.30 (N1),[169] however, the authors did not state uncertainties with these values. Considering the uncertainties over the protonation state, form of the cofactor, a non-innocent ligand (oxidized, reduced, partially oxidized, adducts) and occupancy of PQQ in the active site, we set out to investigate these matters by exploiting not only the spectroscopic properties of PQQ but also these of europium(III), which as a direct binding partner in the active site, is an additional excellent luminescent probe. Analyzing PQQ fluorescence and Eu luminescence properties makes it possible to gain further knowledge about active site of MDH. Luminescence

spectroscopy is a powerful tool to study the biochemistry of Eu(III) in trace concentration. From the emission spectra we observe direct information about the changes in the local environment of Eu(III) and together with state of the art data analysis we gain deeper information on the Eu(III)-PQQ system. Parallel factor analysis (PARAFAC) is a tool for direct determination of unique explanatory factors (See fluorescence spectroscopy, SI). In the present case, the latter correspond to chemical species. Simultaneous analysis of multi-way data with at least three independent variables measured in a crossed fashion, allows for a unique solution of such a model. Time-resolved laser-induced luminescence spectroscopy (TRLFS) is an excellent method providing three independent variables, i.e., pH-dependent distribution of a species as well as its associated emission spectrum and characteristic luminescence decay lifetime. Furthermore, fluorescence spectroscopy was employed for a simultaneous lifetime characterization of the PQQ and the Eu in MDH active site, which was monitored by spectrally separating the emission wavelengths using a T-geometry fluorimeter (see fluorescence spectroscopy, SI).

Results and Discussion

PQQ Species in Solution

Acid Dissociation Constants of PQQ and Equilibrium between PQQ and PQQ•H_2O species

PQQ (and its derivatives) exhibit a low solubility in water, especially in acidic media, with the solubility limit reported as 1.2×10^{-5} M for $H_3PQQ_{(aq)}$.[156, 158, 169] Thus, NMR spectroscopy of aqueous solutions is limited to ^{1}H nuclei. The ^{1}H NMR signal assignment to PQQ and PQQ•H_2O is explained in detail in the supporting information. Figure 2 shows the pH-titration spectra in the pH range 0.5 – 4 with increments of about 0.25 units, as well as the corresponding plot of the pH-dependent chemical shifts. For pK_a determination, sigmoidal dose-response fits were applied to the data. Unfortunately, only two (i.e., the lowest and highest) of the three carboxyl group associated pK_a values could be determined with sufficient certainty. These values amount to 1.47 ± 0.04 and 3.02 ± 0.01 for PQQ, and 1.58 ± 0.04 and 3.10 ± 0.02 for PQQ•H_2O, respectively corresponding to C7-COOH and C2-COOH.

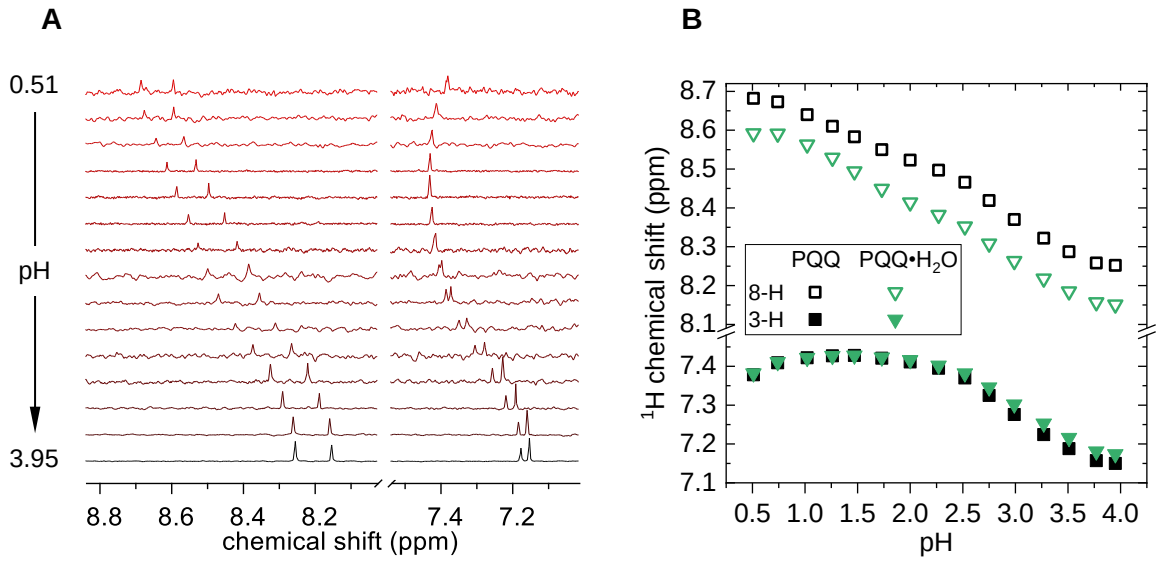

Figure 2 ^{1}H NMR pH-titration spectra (25 °C) of PQQ dissolved in 100 mM NaCl H_2O solution containing 10% D_2O (A), and the corresponding chemical shift vs. pH plot (B).

In addition to the NMR spectra, a UV/Vis series of 50 µM PQQ in 100 mM NaCl as a function of pH were recorded. The measured UV/Vis and deconvoluted single component spectra of the PQQ water system are shown in Figure 3. We observe a strong shift of the broad and significant absorption band from 363 to 333 nm in the acidic pH range. Furthermore, the absorption maximum at 248 nm shifts to 254 nm and a formation of shoulder at 275 nm becomes visible with increasing pH. Above pH 5 no further spectral changes are identifiable. Regarding the pH range and NMR results, PQQ can release three protons from the carboxylic groups at C2, C9 and C7. The calculated single component spectra of the three different aqueous species are shown in Figure 3. The herein presented (lower) values obtained from 100 mM NaCl solutions are in fair agreement with those reported for 0.5 M KCl.[169] The differences are ascribed to different concentrations and types of background electrolytes. Nonetheless, the obtained data is fundamental for subsequent pH-dependent metal-ion complexation investigations in aqueous solution. Protonation constants were also determined using the obtained fluorescence excitation–emission scans (Figure S1). Here, applying the PARAFAC analysis revealed the following pKa values: pK_{a1} = 1.2, pK_{a2} = 1.35 and pK_{a3} = 3.4 that are in good agreement with the absorption data.

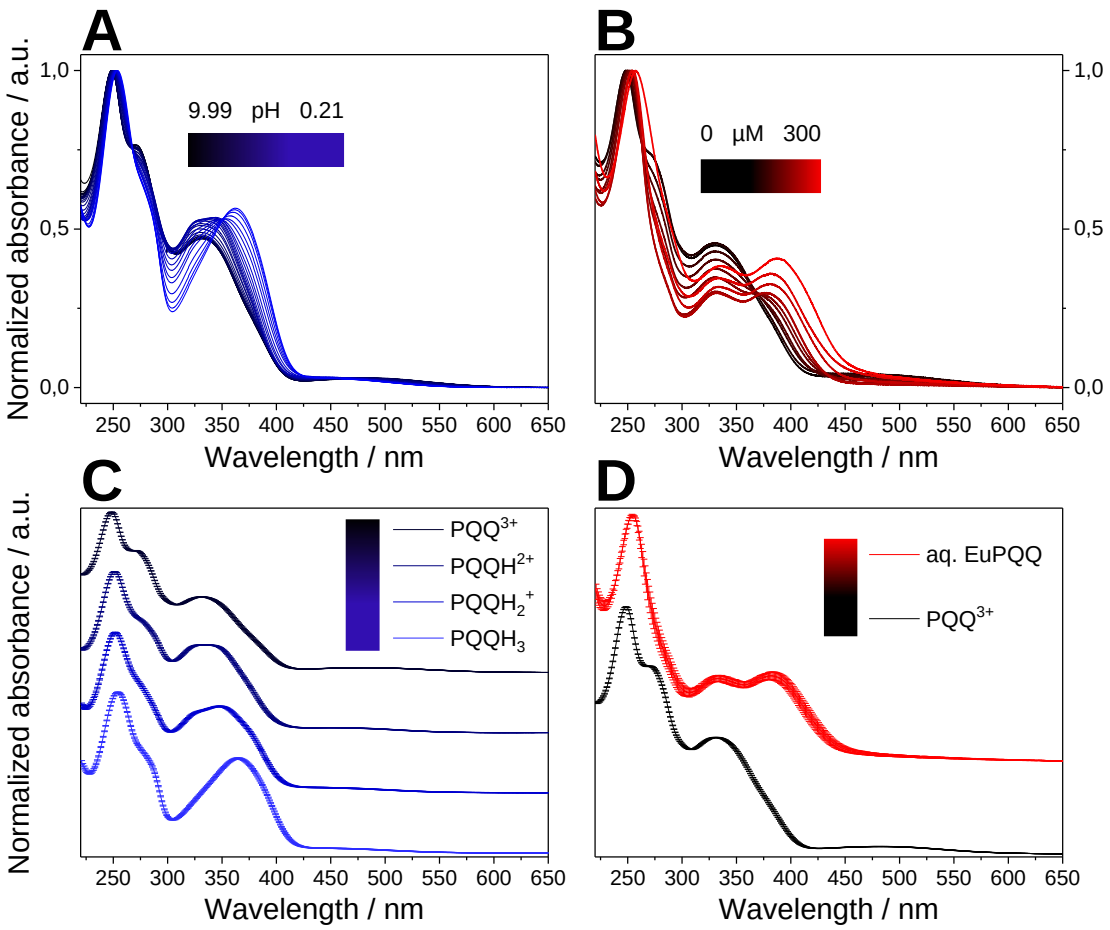

Figure 3 Measured UV/Vis and deconvoluted single-component spectra of the PQQ – Eu(III) – H2O system. Series 1 – PQQ pH-titration and absorption spectra of the PQQ protonation species (A and C). Series 2 – Eu(III)-titration to PQQ3− and absorption spectra of the aq. EuPQQ complex at pH 6.5 (B and D).

Speciation of PQQ depending on the temperature

PARAFAC analysis was also used to follow the interconversion between PQQ^{3-} and its water adduct upon changing temperature. As previously reported, the fraction of PQQ increases with increasing temperature (Figure 4C).[159] At room temperature (and at pH 6.5) both species occur roughly at a ratio of 1:1. The emission intensity of the PQQ^{3-} species is lower than that of the $PQQ•H_2O^{3-}$ species (Figure 4 E and F).

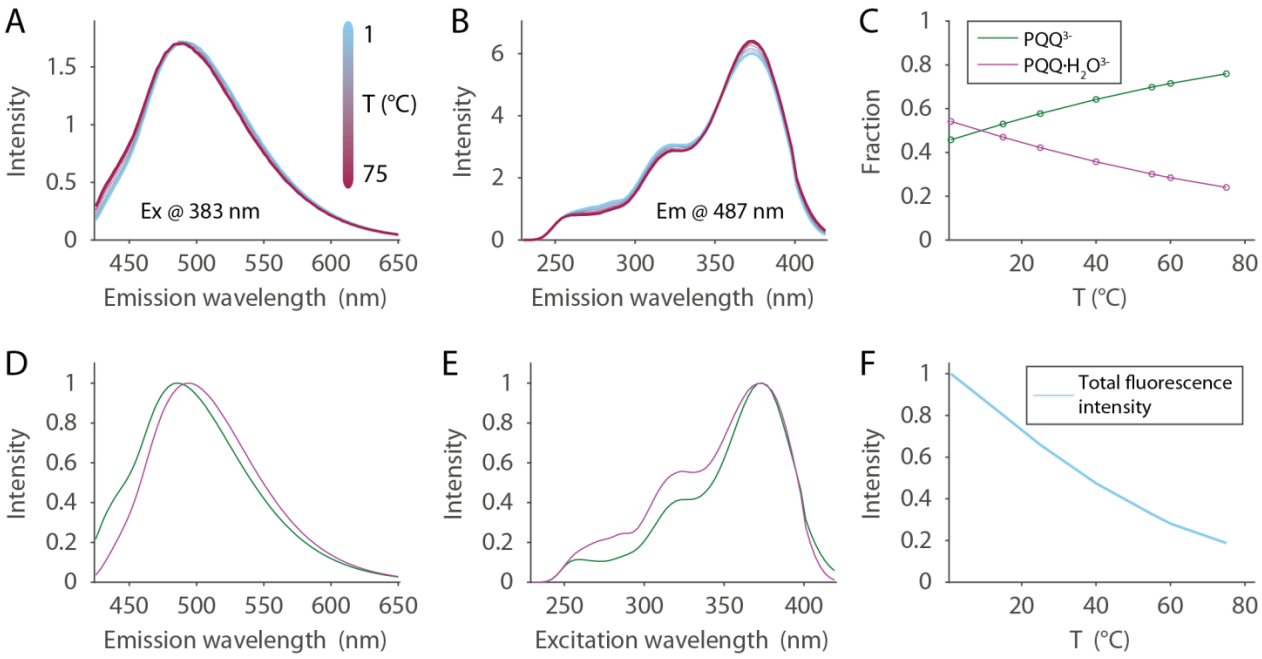

Figure 4 Fluorescence excitation–emission scans of a temperature series (1 to 75 °C) of PQQ aqueous 0.1 M NaCl solution at pH 6.5. Minor changes in the normalized emission (A) and excitation (B) spectra at specific wavelength are visible within the studied temperature range. The PARAFAC deconvolution provides two species. The distribution of PQQ^{3-} (green) and $PQQ{\bullet}H_2O^{3-}$ (magenta) is shown in (C), their individual emission spectra in (D) and excitation spectra in (E). The overall emission intensity decreases with temperature (F).

The temperature dependence of the chemical equilibrium between PQQ^{3-} and $PQQ{\bullet}H_2O^{3-}$ at pH 4.0 was investigated by variable temperature (VT-NMR) depicted in Figure S2A together with the corresponding van 't Hoff plot in Figure S2B. For the 1 mM pH 4.0 sample the obtained enthalpy and entropy of hydration values are $\Delta_h H = (-13 \pm 1)$ kJ mol^{-1} and $\Delta_h S = (-47 \pm 2)$ J mol^{-1} K^{-1}, respectively. On the other hand, the obtained $\Delta_h H$ and $\Delta_h S$ values for the 0.5 mM pD 6.8 sample (VT-NMR spectra in Figure S2C) are -14 ± 1 kJ mol^{-1} and -51 ± 3 J mol^{-1} K^{-1}, respectively. Using the relative concentrations of both PQQ and $PQQ{\bullet}H_2O$ quoted by Dekker et al. determined for a pD 7 D_2O solution at 24 °C and 42 °C,[159] the respective values can be calculated as −15.2 kJ mol^{-1} and −55 J mol^{-1} K^{-1}, which fully agrees with our reported results. Since there were only these previous data for two different temperatures at one given pD, we have expanded our analysis allowing for a better data basis on the hydration reaction equilibrium. In addition, the obtained values are in line with literature thermodynamic parameters for the hydration reactions of other ketones.[170, 171] Consequently, the formation of $PQQ{\bullet}H_2O$ is mildly exothermic, hence favoring PQQ at elevated temperatures. In this regard, a decrease in the intensity of the NMR signals (3' and 8'), associated with a lower $PQQ{\bullet}H_2O$ concentration, was observed with increasing the temperature. Likewise, an increase in the intensity of NMR signals (3 and 8) indicated the increase of the PQQ concentration. The quite negative entropy value is plausible as the number of free molecules reduces during the reaction. According to Buschmann et al.,[172] who studied hydration reactions of

various aldehydes and ketones, the entropy contribution is about 25 J mol^{-1} K^{-1} per mole water involved in the reaction. It is thus concluded that in addition to the one water being the nucleophile reacting with the carbonyl carbon, one more water molecule is required to stabilize the water adduct upon hydrogen bonding.

Investigations pertaining to the pH-dependence of the PQQ – PQQ•H_2O equilibrium allows for an advanced understanding of the principal reaction behavior of PQQ towards nucleophiles in general, and water in particular. As seen in Figure 5, at 25 °C, for pH < 2 PQQ•H_2O predominates, whereas for pH ≥ 2 PQQ predominates. Upon increasing pH, the PQQ•H_2O : PQQ ratio (equivalent to K_h) reveals a continuous decrease up to pH ~ 5, and then the curve flattens, approaching a K_h of about 0.55 for strongly alkaline medium. Although the hydration reaction (see statements for Water Adduct Equilibrium, SI) does not involve explicit H^+, the pH apparently impacts the yield of the water adduct owing to species-dependent electrophilicity of PQQ.

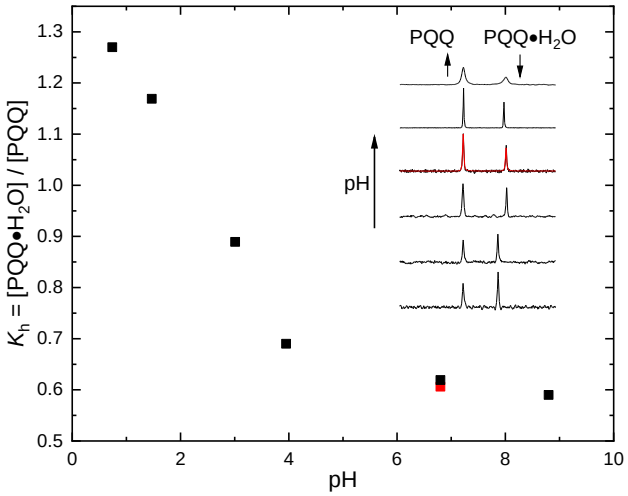

Figure 5. Plot showing the pH-dependence of the PQQ – PQQ•H_2O equilibrium at 25 °C as determined from pH-dependent ^1H NMR signal integrals of corresponding signals associated with 8-H (inset; arbitrary scaling). Note the two data sets for pH 6.8 solution: total PQQ concentrations were 0.5 mM (black) and 5 mM (red).

Chemical Exchange Reaction Kinetics in the PQQ – PQQ•H_2O Equilibrium

NMR line shapes are sensitive to processes on the millisecond to microsecond time-scale, such as chemical exchange, since the inverse (in frequency units) covers the NMR spectral width. The observability of the very close signals 3 and 3' ($\Delta\nu$ = 15 Hz in acid solution, Figure S2A) is already a strong indication that the exchange is slow on the NMR time-scale, even at 60 °C. Thus, a first approximation for the exchange rate can be given as $k_{ex} \ll 15\ s^{-1}$. To qualitatively assess the dynamic equilibrium between PQQ and PQQ•H_2O in general, and to determine the exchange rate, 1D- and 2D-EXSY (exchange spectroscopy) spectra were acquired. The correlation signals caused

by chemical exchange, unlike those due to the NOE (nuclear Overhauser effect), show the same phase (sign) as the diagonal signals. This can be seen at the dynamic equilibrium (pH 4.3 and 25 °C) in the 2D- and 1D-EXSY spectra (SI Figures S3 and S4, respectively), where the forward reaction yielding PQQ•H_2O proceeds with a rate of 0.9×10^{-1} s^{-1} and the reverse reaction yielding PQQ proceeds with a rate of 1.1×10^{-1} s^{-1}. Two further 2D-EXSY spectra were acquired at 60 °C. Assuming the exchange reaction to accelerate, mixing times of 125 and 400 ms were opted and an exchange rate k_{ex}(60 °C) = $(18.0 \pm 1.9) \times 10^{-1}$ s^{-1} was obtained indicating a 9-fold increase of the exchange rate for a temperature difference of 35 K.

Table 1 summarizes the complete set of temperature-dependent exchange rate constants $k_{ex}(T)$. Since both T_1 (see Table S1 and NMR Spectroscopy, SI) and k_{ex} notably increase upon increasing pH (see Table 1 and inset in Figure 6) where applicable, the exchange rate can be determined from the signals' line width, as applied to pD 6.8 spectra at different temperatures (Figure S2C and Table 1) as well as pH-dependent (25 °C) spectra (inset in Figure 6).

Table 1. Temperature-dependent exchange rate constants.

	$k_{ex}(T)$ / 10^{-1} s^{-1}	
T / °C	10 mM PQQ, pH 4.3	5 mM PQQ, pD 6.8
1		[c] 16 ± 2
15		[c] 19 ± 3
25	[a] 2.0 ± 0.1	[c] 21 ± 4 [b] 22 ± 1
35	[b] 2.7 ± 0.1	[c] 63 ± 9 [b] 70 ± 5
45	[b] 5.6 ± 0.1	[c] 135 ± 24 [b] 127 ± 7
55		[c] 273 ± 33
60	[a] 18.0 ± 1.9 [b] 18.0 ± 0.4	

[a] 2D-^{1}H,^{1}H-EXSY; [b] selective excitation 1D-EXSY; [c] Line width analyses

Plotting ln($k_{ex}(T)/T$) vs. $1/T$ results in the graph shown in Figure S5, from which following values were calculated: $\Delta H^{\ddagger}$ = (50 ± 6) kJ mol^{-1} and $\Delta S^{\ddagger}$ = (−91 ± 18) J mol^{-1} K^{-1} for 10 mM pH 4.3 solution, and $\Delta H^{\ddagger}$ = (66 ± 4) kJ mol^{-1} and $\Delta S^{\ddagger}$ = (−17 ± 13) J mol^{-1} K^{-1} for 5 mM pD 6.8 solution, respectively corresponding to $\Delta G^{\ddagger}$ (25 °C) values of 78 and 71 kJ mol^{-1}. The significantly lower $\Delta S^{\ddagger}$

determined for the pH 4.3 solution indicates a higher requirement for water solvation in the transition state than in the diol. The absolute value itself corresponds to four water molecules involved for pH 4.3, while for pD 6.8 only one water molecule is critical (according to 25 J mol^{-1} K^{-1} per mole water[172]). This can be interpreted as a highly ordered cyclic hydrogen-bonded transition state at pH 4.3, involving three water molecules, one of which is the nucleophile (Figure S6A) plus one additional water for solvation. In contrast, at pD 6.8 the hydroxide ion, being the better nucleophile, can directly attack the C5 carbonyl carbon even when only present in small concentrations.

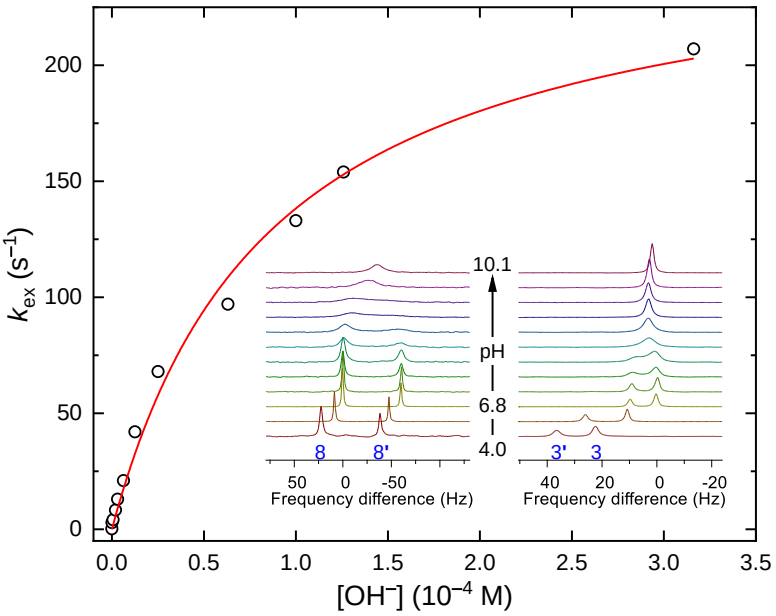

Figure 6. Plot showing the pH-dependent rate of PQQ – PQQ•H_2O interconversion as determined from line shape analyses at 25 °C. The pH 6.8 spectrum serves as reference since both forms occur exclusively as their tri-anionic species, so no additional protonation–deprotonation dynamics have to be considered. Note the frequency difference between the signals of corresponding sites at low pH, hence the different pH-dependent line broadenings and coalescences (merging) of the respective signal pairs.

To sum up, PQQ undergoes hydration *via* two different, pH-dependent mechanisms. From a thermodynamic point of view, the increased enthalpy of activation (corresponding to activation energy, E_a, in collision theory) impedes PQQ•H_2O formation, mirroring the shift of the equilibrium towards PQQ upon increasing pH. From a kinetic point of view, however, the cyclic transition state requires all involved molecules to arrange with high demands on geometry, slowing down the reaction rates for both hydration and dehydration. With increasing pH, *i.e.* increasing the concentration of OH^-, the nucleophile can directly attack the carbonyl group *via* formation of a tetrahedral transition state (Figure S6B) with much less geometric demands (much less negative $\Delta S^{\ddagger}$). Apparently, the reaction rates accelerate notably (Figure 6), however, not only for the forward

reaction yielding PQQ•H_2O, but also for the reverse reaction, *i.e*. dehydration, yielding PQQ. Just by comparing pH 4.3 and pD 10.1, the interconversion rates increase by three orders of magnitude, but their ratio r_{hyd}/r_{deh} corresponding to PQQ•H_2O : PQQ ratio = K_h (see Eqns.4 and 8 in the SI), changes only from ~ 0.7 to ~ 0.55 (asymptotic approach). After gathering a thorough understanding of PQQ, its protonation states and equilibrium with its corresponding C5 water adduct PQQ•H_2O, we analyzed the properties and behavior of PQQ within Eu-MDH.

PQQ and Europium in Methanol Dehydrogenase

We have observed that the Eu-MDH enzyme readily loses PQQ during storage and washing procedures, which explains the Eu(III) occupancy being around 70% as shown per ICP-OES.[142, 173] Others have reported complete loss of PQQ in Ln-MDH crystal structures.[161] It is often not clear in which oxidation state or form the cofactor PQQ is present in the active sites of MDH enzymes, although this has been extensively explored in the past for the calcium containing MDH. As described by Goodwin and Anthony, spectra of MDH with and without Ca^{2+} differ, however both spectra reveal the concurrent presence of different states of PQQ indicated by varying intensity of peaks at 345 and 400 nm.[174, 175] In the inactive apo form (without Ca^{2+}), it was suggested that PQQ is mainly present in its oxidized form since strong absorbance at 400 nm can be detected. [174, 176] Subsequent metal addition reveals an increased reduced state of PQQ which can be followed by an increase of absorbance at 345 nm.[174, 176] This observation was explained with the presence of the – up to date – still not understood endogenous substrate, which is immediately oxidized by the enzyme. Accordingly, the mainly observed reduced state is substantiated by the presence of substrates and the following reduction of the prosthetic group. Goodwin and Anthony stated, that they were able to isolate only the oxidized MDH by replacing Ca^{2+} with Ba^{2+} in the active site.[174-176] This results in a spectrum with a prominent peak at 405 nm which decreases over time, while a peak at 345 nm emerges.[174, 175] Since an isosbestic point is observed, it is assumed that only the two species, oxidized and reduced, are present.[175]

Nowadays, it is presumed that PQQ is present in its semiquinone form and needs to be oxidized first prior to substrate conversion.[177] This is supported by DFT calculations based on the crystal structure of Ce-MDH.[168] Also, it might be conceivable that additional factors such as the presence of reducing or oxidizing reagents, activators (e.g. cyanide) and electron acceptors such as O_2 or even H_2O that might affect the prosthetic group.[178] Further, an effect of pH on the shape of the PQQ fingerprint in the UV-vis spectrum of Ca-MDH has been observed.[154, 179, 180] However, it is more likely that the MDH contains a mixture of multiple species given the non-innocent nature of PQQ and its reactivity towards nucleophiles.

To gain further insight into possible PQQ species and their interconversion in the active site of MDH, the impact of temperature (5°C to 55°C) and the presence of the substrate MeOH on the absorption spectra of Eu-MDH was studied. Note, the ratio of ‘free’ PQQ in solution to its water species at 5°C

amounts to a 1:1 ratio, and 3:1 ratio at 55 °C, respectively. The typical PQQ fingerprint of MDH isolated from the methanotrophic bacterium *Methylacidiphilum fumariolicum* SolV (SolV) is present in all collected spectra (Figure 7). As previously described for Eu-MDH isolated from SolV, this species displays an absorption maximum at 355 nm and a shoulder at 400 nm.[181] Interestingly, depending on the presence or absence of MeOH, we see two opposite trends of the PQQ fingerprint absorbance values at 355 nm and 400 nm upon heating. Absence of MeOH first leads to a small increase of the signal at 355 nm followed by the reduction of the signal with increasing temperature. The shoulder at 400 nm also increases slowly at first, but when 40 °C is reached, this band intensifies (Figure 7A). Spectra of Eu-MDH supplemented with MeOH reveal a small increase of the peak at 355 nm while absorbance at 400 nm remains unchanged (Figure 7B). For both treated Eu-MDH samples, the described changes of spectra appear mainly around 35 °C to 40 °C and intensify with elevating temperature. Changes are more visible when MeOH was omitted during heating. The two observed peaks at 355 nm and 400 nm indicate different states of the prosthetic group. At the beginning, PQQ might be mainly present in its semiquinone or quinol form, independent of MeOH addition, since the absorbance at 355 nm is clearly visible. At the same time, some of the oxidized form might also be present due to the observed shoulder at 400 nm. As of temperatures above 35 °C in presence of the substrate MeOH, the amount of reduced $PQQH_2$ or half reduced PQQH• radical species might increase. This is supported by the fact that these changes start to occur around 35 °C, which is the minimum temperature for substrate conversion. At lower temperatures, no or little enzymatic activity is observed for Eu-MDH. At 45 °C and 50 °C, the signal at 355 nm decreases while the signal at 400 nm increases. Compared to literature, this points to a decrease of the $PQQH_2$ or PQQH• state while more oxidized PQQ is present. Since the experiments were conducted under an ambient atmosphere, O_2 might serve as a terminal oxidant at elevated temperatures. To sum up, a clear identification of the state of the redox cofactor is not possible. However, the results point to an important influence for the temperature and the presence of MeOH.

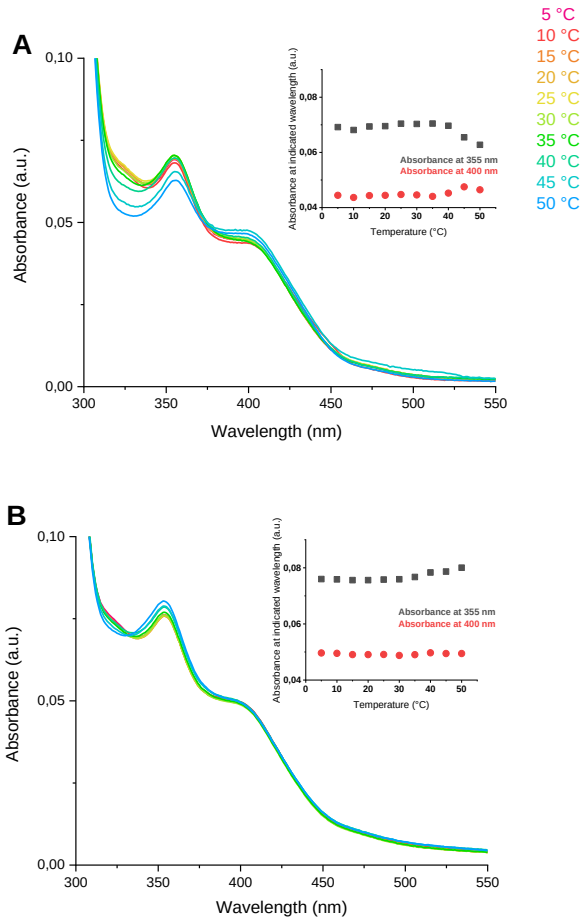

Figure 7. Normalized temperature-dependent UV-vis spectra of Eu-MDH in 100 mM NaCl pH 6.5 solution recorded in absence **A** and in presence **B** of 1 mM MeOH, and corresponding absorbance values at 355 nm and 400 nm.

Determination of the different Eu(III) and Eu(III) bound to PQQ species by TRLFS

The titration of Eu(III) to Ln-apo MDH purified from SolV can reconstitute a catalytically competent active site.[142, 182] Addition of Lns results in a gradual increase of enzymatic activity and upon 100 % occupation of the active site a saturation behavior can be observed.[182] Titrations of Eu(III) to Eu-MDH (with only partially occupied Eu-sites) using TRLFS with a direct excitation of Eu(III) at 394 nm were thus used to probe different Eu(III) species directly. Prior to the TRLFS experiments we checked the effect of the laser irradiation on the Eu-MDH to choose the desired laser power that does not destroy the probed sample (Figure S7). To avoid additional Eu-buffer complex species, this experiment was carried out in NaCl solution. For the titration experiments, two solutions were prepared for the metal titration: 10 µM Eu-MDH and 3 mM $EuCl_3$ both in 100 mM NaCl at pH 6.5, both with only partially occupied Eu-sites, to which 1 mM MeOH was added (see Experimental section in the Supporting Information for details). During the titration both the symmetry-forbidden F_0 transition peak and the F_2 transition decreased. This is already indicative for increasing Eu(III)

aquo ion concentration during the titration (Fig 4A). PARAFAC revealed a three species model, where an overall explained variation of 98.3 % is achieved, as shown for the emission spectrum of 40 µM $EuCl_3$ (Figure S8). The distribution of the three Eu(III) species is shown in Figure 8: the Eu(III) aquo ion in green, the active site-bound Eu(III) in magenta and a third Eu(III) species which could not be assigned to a specific binding site at the enzyme. The assignment of the Eu(III) aquo ion is straightforward. The green emission spectrum provides the typical F_1/F_2 ratio, the lifetime is 111 µs and its concentration increases with higher Eu(III) concentration. The assignment of the magenta complex is supported by ICP-OES measurements, which reveal a fraction of approximately 70% MDH being occupied by Eu(III). This is in good agreement with the magenta species present at the beginning of the titration, where no Eu(III) was added. The maximal increase of about 25% in the magenta distribution indicates a similar initial occupation as determined previously by ICP-OES.[142] The prolonged luminescence decay time of 290 µs for this species indicates a highly complexed environment. By means of the Horrocks equation the remaining number of coordination water molecules is determined to be 3. The pronounced F_0 transition (increased emission at ~580 nm) results from an asymmetric Eu(III) coordination environment, which further supports the assignment of the magenta species to the Eu-MDH complex. To identify the third, yellow species, we decided to compare it with Eu(III) complexed to PQQ, where both emission spectra had a similar shape and no difference was observed. Additionally, both show unusually short lifetimes (75 µs yellow, 84 µs Eu-PQQ complex), which had to be caused by quenchers other than water. The third, yellow, species is therefore assigned to Eu(III) bound to PQQ, which dissociated from the MDH. This shows that PQQ dissociates from MDH after washing, which explains the decreasing specific activities during sample handling and storage on ice over a day (or even during crystallization). From the titration graph a dissociation constant of 3.2×10^{-6} for the active site-bound Eu (magenta) was calculated (Figure 8C). This is in good agreement with Eu(III) interaction with other proteins, e.g. calmodulin.[183]

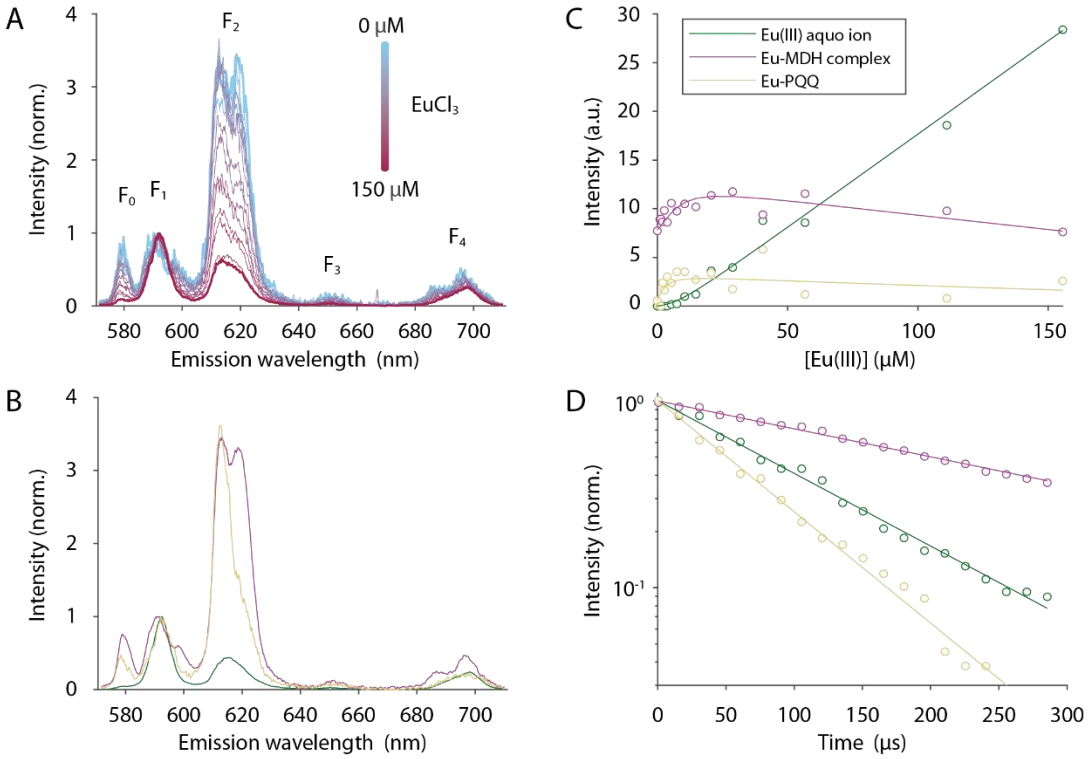

Figure 8. TRLFS of Eu(III) titration to the MDH. **A** Normalized (F_1) emission spectra of the Eu(III) titration series for t = 0 µs. B to D are the results from PARAFAC deconvolution with **B** F_1 normalized emission spectra of the three chemical species that are formed during the Eu(III) titration. The spectra were assigned to the Eu(III) aquo ion (green), Eu(III) in the active site of the MDH (magenta) and Eu-PQQ (yellow). **C** Corresponding distribution of the three different Eu(III) species and **D** their luminescence decays. The decrease in intensity of the magenta and yellow species is caused by sample dilution during Eu(III) titration.

After thoroughly investigating the photophysical properties of both PQQ and Eu(III), we ought to utilize the antenna effect by directly exciting PQQ and thus only observe the Eu(III) bound in the active site. Using this approach, we gain simultaneous insights on the PQQ and Eu interactions in the active site of the MDH enzyme by observing both the steady-state fluorescence emission and fluorescence lifetime of the different species (Figure 9 B and D).

PQQ proximity to Eu in the Eu-MDH active site

The presence of different metal occupations in the MDH active site influences the emissive and fluorescence lifetime properties of the PQQ present in the proximity of the metal ion. Furthermore, depending on the Ln ion present at the MDH active site, a distinct PQQ-Ln behavior is observed and can be utilized to gain further knowledge about the MDH active site. For this purpose, we directly excited the PQQ at 375 nm focusing on its emission and lifetime properties in the Eu-MDH (Figure 9A). As an alternative enzyme, La-MDH was tested to establish the particularity of PQQ-metal ion behavior based on their proximity and the metal ion occupancy. The luminescence of Eu in the presence of PQQ was characterized (Figure S9). The antenna effect or energy transfer from PQQ (excited state) to the Eu in its proximity is demonstrated by both steady state and lifetime

measurements. An increase in the induced electric dipole transition $^5D_0 \rightarrow {}^7F_2$ of 1 mM Eu in the absence vs. presence of PQQ is shown in the steady state measurements (Figure S9 A). Interestingly, under the conducted experimental conditions (20 mM PIPES pH 7.2 at 22 °C) the mixture of PQQ•H_2O : PQQ (ratio ~ 0.6 as shown in Figure 5) shows a mono-exponential lifetime of ~ 1.3 ns, which indicates that both species share almost identical fluorescence lifetimes. We similarly observed the fluorescence lifetime of the PQQ•H_2O : PQQ species in the presence of higher Eu concentrations, which resulted in further lifetime quenching indicating the energy transfer from PQQ to Eu (Figure S9 D). Utilizing this photophysical feature we examined the proximity of PQQ to Eu in the Eu-MDH active site. Primarily, a proof-of-concept measurement is conducted comparing Eu-MDH with La-MDH. Here, we observed that the induced electric dipole transition $^5D_0 \rightarrow {}^7F_2$ peak in Eu-MDH is, as expected, absent in the case of La-MDH (Figure 9 C).

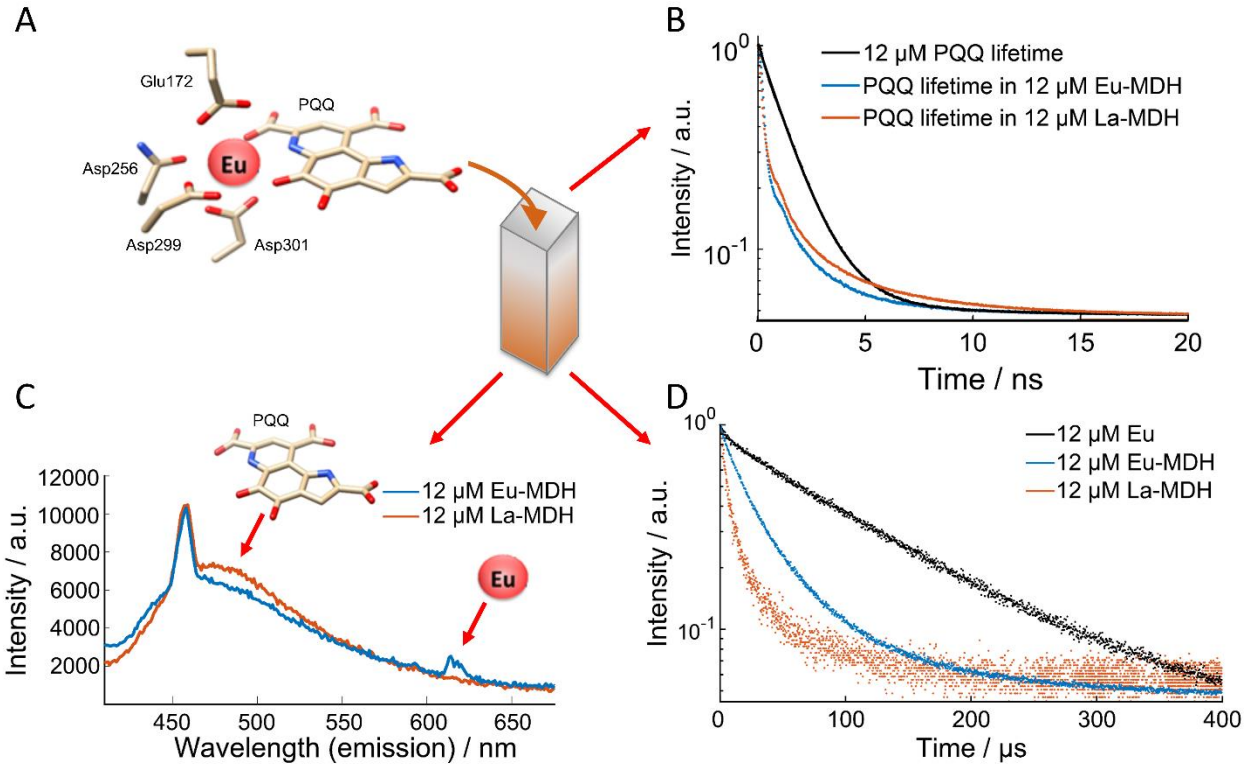

Figure 9 Different set of measurements performed for characterizing the luminescence features of the Eu-MDH.

Additionally, we monitored the spectral and lifetime changes of both, the PQQ fluorescence and the Eu luminescence in the Eu-MDH before and after its denaturation with Hellmanex III (Figure S10 A). Likewise, we tested the La-MDH denaturation for a comparison and validation of the assay, which shows that the PQQ proximity to La in the active site influences the PQQ luminescence lifetime. Here we observed that the PQQ proximity to Eu in the Eu-MDH and to La in the La-MDH,

respectively, had a similar effect on quenching PQQ fluorescence. The quenching of La to PQQ, however, is not as significant once compared to Eu, which clearly provides a better energy transfer from the PQQ excited state (Figure S10 B). This could be the reason why the PQQ fluorescence was more prominent in La-MDH than the Eu-MDH. The fluorescence of PQQ in Eu-MDH, however, varies with the Eu occupancy of the Eu-MDH active site, which has been observed among the several measurements performed. Furthermore, we performed additional experiments to characterize the PQQ fluorescence in the presence of La (Figure S11) to validate our reasoning of the PQQ behavior in the MDH. Monitoring MDH fluorescence at 500 nm in the presence of 1 mM La vs. 1 mM Eu shows that the quenching due to Eu is ~ 10 times stronger (Intensity at 500 nm in the presence of 1 mM La = $(1.50 \pm 0.19) \times 10^4$ vs. intensity at 500 nm in the presence of 1 mM Eu = $(1.41 \pm 0.18) \times 10^3$). Denaturation of Eu-MDH shows that the PQQ emission spectrum is retained due to the absence of Eu in its proximity after denaturation, similarly the 1.3 ns PQQ lifetime is retained upon the denaturation. To ensure that the observed changes upon the Eu-MDH denaturation are not artifacts due to the Hellmanex III detergent, control measurements were performed. The effect of 2% Hellmanex III on the spectral and lifetime behavior of PQQ in the absence of Eu-MDH (Figure S12) showed that this denaturing agent has no direct effect on the PQQ fluorescence.

Conclusion

The thorough characterization of PQQ and the effect of pH and temperature on the different PQQ species formation confirms the importance of a detailed PQQ understanding prior to investigating its presence in the Eu-MDH enzyme. We studied the different PQQ species in solution by using NMR and UV-vis spectroscopy and showed that PQQ and its species, H_3PQQ to PQQ^3, complex with Lns and form water adducts as well. Subsequently, we investigated the PQQ in the Eu-MDH active site by combining two fluorescence spectroscopy techniques, TRLFS and burst mode lifetime measurements. Using TRLFS a direct excitation of the Eu(III) at 395 nm was possible, which enabled a direct investigation of the Eu species. Through this approach we revealed that three different Eu(III) species exist in the Eu-MDH environment. Next to the aquo Eu present in solution we determined the amount of Eu(III) bound to PQQ and the Eu(III) present in the MDH active site. The latter is essential to understand the photophysical properties of the Eu-MDH and is, as well, a great attribute that one can exploit. In this regard, we utilized the fluorescence of the PQQ and the luminescence of the Eu(III) as a tool to simultaneously monitor the photophysical features of the Eu-MDH and thereby gain extra knowledge on its active site. The proximity of the PQQ to the Eu(III) in the active site and its effect on the Eu luminescent properties was validated via the antenna effect by the direct excitation of PQQ using 375 nm laser (operated in burst mode).

Acknowledgements

We thank Heidrun Neubert and Dominik Goldbach (HZDR) for their support in the lab. LJD would like to acknowledge a grant from the Deutsche Forschungsgemeinschaft (DFG)-392552271.

References

[1] aE. G. Moore, A. P. S. Samuel, K. N. Raymond, *Accounts of Chemical Research* **2009**, *42*, 542-552; bK. N. Allen, B. Imperiali, *Current Opinion in Chemical Biology* **2010**, *14*, 247-254; cJ. W. Walton, A. Bourdolle, S. J. Butler, M. Soulie, M. Delbianco, B. K. McMahon, R. Pal, H. Puschmann, J. M. Zwier, L. Lamarque, O. Maury, C. Andraud, D. Parker, *Chemical Communications* **2013**, *49*, 1600-1602; dS. J. Butler, L. Lamarque, R. Pal, D. Parker, *Chemical Science* **2014**, *5*, 1750-1756; eK. Binnemans, *Coordination Chemistry Reviews* **2015**, *295*, 1-45; fT. J. Sorensen, A. M. Kenwright, S. Faulkner, *Chemical Science* **2015**, *6*, 2054-2059.

[2] C. H. Evans, *Biochemistry of the Lanthanides*, Springer Science & Business Media, New York, **1990**.

[3] B. Jahn, A. Pol, H. Lumpe, T. R. M. Barends, A. Dietl, C. Hogendoorn, H. J. M. Op den Camp, L. J. Daumann, *Chembiochem* **2018**, *19*, 1147-1153.

[4] aE. Skovran, N. C. Martinez-Gomez, *Science* **2015**, *348*, 862-863; bL. Chistoserdova, *World Journal of Microbiology & Biotechnology* **2016**, *32*, 138-+; cJ. A. Cotruvo, *Acs Central Science* **2019**, *5*, 1496-1506; dL. J. Daumann, *Angewandte Chemie-International Edition* **2019**, *58*, 12795-12802; eN. Picone, H. J. M. Op den Camp, *Current Opinion in Chemical Biology* **2019**, *49*, 39-44.

[5] aN. M. Good, H. N. Vu, C. J. Suriano, G. A. Subuyuj, E. Skovran, N. C. Martinez-Gomez, *Journal of Bacteriology* **2016**, *198*, 3109-3118; bM. Wehrmann, P. Billard, A. Martin-Meriadec, A. Zegeye, J. Klebensberger, *Mbio* **2017**, *8*.

[6] C. Z. L. J. Anthony, *Biochem. J.* **1967**, *104*, 953-959.

[7] aH. Lumpe, L. J. Daumann, *Inorg. Chem.* **2019**, *58*, 8432-8441; bS. Itoh, M. Ogino, Y. Fukui, H. Murao, M. Komatsu, Y. Ohshiro, T. Inoue, Y. Kai, N. Kasai, *J. Am. Chem. Soc.* **1993**, *115*, 9960-9967.

[8] aJ. A. Duine, J. Frank, Jr, *Biochem. J.* **1980**, *187*, 213-219; bJ. Frank, M. Dijkstra, J. A. Duine, C. Balny, *Eur. J. Biochem.* **1988**, *174*, 331-338; cT. K. Harris, V. L. Davidson, *Biochemistry* **1993**, *32*, 4362-4368.

[9] aJ. A. Duine, J. Frank, P. E. J. Verwiel, *Eur. J. Biochem.* **1981**, *118*, 395-399; bY.-J. Zheng, T. C. Bruice, *Proc. Natl. Acad. Sci.* **1997**, *94*, 11881; cH. Lumpe, L. J. Daumann, *Inorg. Chem.* **2019**, *58*, 8432-8441.

[10] R. H. Dekker, J. A. Duine, J. Frank, J. P. E. J. Verwiel, J. Westerling, *Eur. J. Biochem.* **1982**, *125*, 69-73.

[11] C. Anthony, *Subcellular Biochemistry* **2000**, *35*, 73-117.

[12] aN. M. Good, M. Fellner, K. Demirer, J. Hu, R. P. Hausinger, N. C. Martinez-Gomez, *J. Biol. Chem.* **2020**, *295*, 8272-8284; bB. Jahn, N. S. W. Jonasson, H. Hu, H. Singer, A. Pol, N. M. Good, H. J. M. O. den Camp, N. C. Martinez-Gomez, L. J. Daumann, *JBIC Journal of Biological Inorganic Chemistry* **2020**, *25*, 199-212.

[13] aY. W. Deng, S. Y. Ro, A. C. Rosenzweig, *J. Biol. Inorg. Chem.* **2018**, *23*, 1037-1047; bA. Pol, T. R. M. Barends, A. Dietl, A. F. Khadem, J. Eygensteyn, M. S. M. Jetten, H. J. M. O. d. Camp, *Environ. Microbiol.* **2014**, *16*, 255-264.

[14] S. Itoh, H. Kawakami, S. Fukuzumi, *J. Am. Chem. Soc.* **1998**, *120*, 7271-7277.

[15] C. W. M. Kay, B. Mennenga, H. Görisch, R. Bittl, *J. Biol. Chem.* **2006**, *281*, 1470-1476.

[16] M. Dijkstra, J. Frank, Jr, J. A. Duine, *Biochem. J.* **1989**, *257*, 87-94.

[17] J. A. Bogart, A. J. Lewis, E. J. Schelter, *Chem. – Eur. J.* **2014**, *21*, 1743–1748.

[18] K. Kano, K. Mori, B. Uno, T. Kubota, T. Ikeda, M. Senda, *Bioelectrochem. Bioenerg.* **1990**, *24*, 193-201.

[19] aH.-J. Buschmann, H.-H. Füldner, W. Knoche, *Ber. Bunsenges. Phys. Chem.* **1980**, *84*, 41-44; bP. Greenzaid, Z. Rappoport, D. Samuel, *Trans. Faraday Soc.* **1967**, *63*, 2131-2139.

[20] H.-J. Buschmann, E. Dutkiewicz, W. Knoche, *Ber. Bunsenges. Phys. Chem.* **1982**, *86*, 129-134.
[21] B. Jahn, N. S. W. Jonasson, H. Hu, H. Singer, A. Pol, N. M. Good, H. J. M. O. den Camp, N. C. Martinez-Gomez, L. J. Daumann, *JBIC Journal of Biological Inorganic Chemistry* **2020**.
[22] aC. Anthony, in *Enzyme-Catalyzed Electron and Radical Transfer: Subcellular Biochemistry* (Eds.: A. Holzenburg, N. S. Scrutton), Springer US, Boston, MA, **2000**, pp. 73-117; bM. G. Goodwin, C. Anthony, *Biochem. J.* **1996**, *318*, 673-679.
[23] M. G. Goodwin, A. Avezoux, S. L. Dales, C. Anthony, *Biochemical Journal* **1996**, *319*, 839-842.
[24] P. D. Sarmiento-Pavía, M. E. Sosa-Torres, *Journal of biological inorganic chemistry : JBIC : a publication of the Society of Biological Inorganic Chemistry* **2021**.
[25] R. de Beer, J. A. Duine, J. Frank, J. Westerling, *Eur J Biochem* **1983**, *130*, 105-109.
[26] aH. T. C. Chan, C. Anthony, *FEMS Microbiology Letters* **1992**, *97*, 293-297; bJ. Frank Jzn, M. Dijkstra, J. A. Duine, C. Balny, *European Journal of Biochemistry* **1988**, *174*, 331-338.
[27] B. Jahn, A. Pol, H. Lumpe, T. R. M. Barends, A. Dietl, C. Hogendoorn, H. J. M. Op den Camp, L. J. Daumann, *ChemBioChem* **2018**, *19*, 1147-1153.
[28] H. Lumpe, A. Pol, H. J. M. Op den Camp, L. J. Daumann, *Dalton Trans.* **2018**, *47*, 10463-10472.
[29] B. Drobot, M. Schmidt, Y. Mochizuki, T. Abe, K. Okuwaki, F. Brulfert, S. Falke, S. A. Samsonov, Y. Komeiji, C. Betzel, T. Stumpf, J. Raff, S. Tsushima, *Phys. Chem. Chem. Phys.* **2019**.

Supporting Information for
Studies of Pyrroloquinoline Quinone Species in Solution and in Lanthanide-dependent Methanol Dehydrogenases

Nader AL Danaf[a]†, Jerome Kretzschmar[b]†, Berenice Jahn[a], Helena Singer[a], Arian Pol[c], Huub J.M. Op den Camp[c], Robin Steudtner[b], Don Lamb[a], Björn Drobot*[b] and Lena J. Daumann*[a]

[a] Department of Chemistry
Ludwig-Maximilians-University Munich
Butenandtstraße 5 – 13, 81377 München (Germany)
[b] Institute of Resource Ecology
Helmholtz-Zentrum Dresden-Rossendorf e.V.
Bautzner Landstraße 400, 01328 Dresden (Germany)
[c] Department of Microbiology
Radboud University
Heyendaalseweg 135, 6525 AJ, Nijmegen (The Netherlands)
† Shared first author.
* Corresponding authors: b.drobot@hzdr.de, lena.daumann@lmu.de

Experimental

Enzyme and PQQ preparations: Eu-MDH was purified according to a previously published protocol.[136] La-MDH was purified in the same way but using phosphate buffer instead of Pipes. During cultivation of strain SolV 5 µM $LaCl_3$ instead of $EuCl_3$ was added to the growth medium. PQQ was used as disodium salt that had previously been isolated from vitamin capsules.[151]

MDH sample preparation for TRLFS: Eu-MDH samples were re-buffered twice in 100 mM NaCl, with additional 1 mM MeOH, pH 6.5 using a spin filter (Amicon Ultra, 30 kDa MWCO) at 4,500 rpm and 4 °C. The protein concentration was determined with a NanoDrop uv/vis spectrophotometer. For the measurement a concentration of 10 µM MDH was adjusted.

MDH sample preparation for the fluorimeter measurement: MDH was washed twice in 20 mM PIPES pH 7.2 using a spin filter (Amicon Ultra, 30 kDa MWCO) at 4,500 rpm and 4 °C. The protein concentration was determined with the fiber-optic ultra-micro measuring cell Traycell. For the measurement a concentration of 12 µM MDH was adjusted.

Protonation Constants: The calculation of the protonation constants based on the variation in the absorption spectra were done using the HypSpec program.[184, 185]

Nuclear Magnetic Resonance (NMR) Spectroscopy: PQQ disodium salt was dissolved in Milli-Q water (18.2 MΩ cm), containing 0.1 M NaCl, to yield a 10 mM stock solution (pH = 4.3). Aliquots of the latter were further diluted to 1 mM and pH-adjusted with NaOH and HCl to yield 17 samples in the range of $0 \leq pH \leq 4$ with increments of 0.25 pH units, containing 10% D_2O by volume. Due to the lowered solubility upon decreasing pH, PQQ precipitated. Thus, after adjustment to the desired pH value (± 0.05 units) the samples were centrifuged. The clear supernatants – considered as saturated solutions at given pH – were then used for NMR measurement.

Samples dedicated for studies at near-neutral and alkaline conditions and at concentrations in the micromolar range were prepared by dissolution of appropriate amounts of PQQ disodium salt in 0.1 M NaCl D_2O solution and pD-adjusted using NaOD and DCl.

NMR spectra were recorded on an Agilent DD2-600 system, operating at 14.1 T with a corresponding ^1H resonance frequency of 599.82 MHz using a 5 mm oneNMR™ probe.

NMR spectra were measured with 3 s acquisition time after application of a 2 s pre-saturation pulse with offset on the water resonance for water signal suppression and a π/6 observation pulse, accumulating 128 – 2k transitions. For chemical shift determination only (as for pK_a determination), the relaxation delay (d1) was set to 3 s. In case of quantitative spectra ($d1 \geq 5 \times T_1$), for samples with solution pH up to 4.3 d1 = 20 s was applied, while for samples with pD as of 6.8 and above, d1 was set to 60 s. Since the longitudinal relaxation times are quite long, especially for the pyrrol ^1H nuclei (cf. Table S1), and because of the appropriate signal separation (cf. Figure S2) signals 8 and 8' were used for quantification.

Table S1. Selected relaxation times of aqueous PQQ solutions 10 mM at pH 4.26 and 5 mM at pD 6.80 as determined by the inversion recovery (T_1) and by the Carr–Purcell–Meiboom–Gill (CPMG) pulse sequence (T_2).

		H-8	H-8'	H-3'	H-3
pH 4.3	T_2 / s (25 °C)	0.30 ± 0.01	0.71 ± 0.02	1.32 ± 0.05	1.49 ± 0.02
	T_1 / s (25 °C)	2.8 ± 0.1	3.3 ± 0.1	4.8 ± 0.1	4.8 ± 0.1
	T_1 / s (60 °C)	4.4 ± 0.7	4.8 ± 1.2	6.3 ± 1.2	4.8 ± 0.4
pD 6.8	T_1 / s (25 °C)	10.2 ± 0.5	8.9 ± 0.8	13.4 ± 1.5	14.4 ± 1.2

Fluorescence spectroscopy: Excitation–emission scans were performed on a FluoTime 300 fluorescence spectrometer equipped with a 300 W Xenon arc lamp (PicoQuant). Fluorescence was recorded using a slit width of 2 mm and an integration time of 0.5 s. Emission spectra (425 to 650 nm, 2 nm resolution) were recorded for each excitation wavelength (230 to 420 nm, 3 nm resolution) and combined for each sample to a 2D data matrix. Matrices were stacked to a 3D data cube and analyzed using parallel factor analysis (PARAFAC) implemented as N-way toolbox for Matlab[186] using non-negative constrains for the excitation and emission spectra and the speciation constrain for the distribution described elsewhere.[187]

The time-resolved laser-induced fluorescence spectroscopy (TRLFS) measurements were performed at 4 °C (Eu-MDH) with a pulsed Nd:YAG OPO laser system (Powerlite Precision II 9020 laser with a Green Panther EX OPO, Continuum Electro-Optics, San Jose, USA) equipped with a multi-channel optical analysis system consisting of Kymera 328i spectrograph and an Andor iStar ICCD camera (both Quantum Design GmbH, Darmstadt, Germany). For the conducted measurements, experiments were performed at an excitation wavelength of 394 nm. The luminescence spectra were recorded in the wavelength range from 500 to 760 nm (grating: 300 lines/mm with a resolution of 0.25 nm). To record the time-dependent luminescence spectra, the delay time between laser pulse and camera control was sampled in dynamic time intervals (usually between 1 and 301 µs). The recorded 2D sample data were stacked to a 3D data cube. This data cube was analyzed using PARAFAC implemented as N-way toolbox for Matlab[186], including exponential decay constrain[187]. In Eu(III) systems – in the absence of other quenchers – the number

of water molecules in the first coordination sphere can be calculated from the luminescence lifetime using the Horrocks equation[188-191]

$n_{H2O} \pm 0.5 = 1.07 \times k_{exp} - 0.62$ (Eqn. 1)

Here n is the number of remaining water molecules and k_{exp} is the decay rate in ms^{-1} ($1/\tau$).

Additional measurements were performed on an FLS 1000 Fluorimeter (Edinburgh Instruments). A pulsed laser diode at 375 nm wavelength (LDH-D-C-375, PicoQuant) was used for excitation of the Eu-MDH. The dual mode laser head was operated in continuous wave mode for obtaining the steady state emission and the pulsed mode was used for the lifetime measurements. The laser pulses were synchronized in a burst mode of 500 µs per cycle, in which the laser pulsed for 5 µs of this timeframe. The emission from the Eu-MDH was monitored using the T-geometry of the fluorimeter. Thus, we obtained on one (H10720-01 High speed PMT, Hamamatsu) PMT the fluorescence of the PQQ (emission band width of 5 nm centered at 495 nm) and the second PMT obtained the luminescence of the Eu^{3+} (emission band width of 40 nm centered at 620 nm). The fluorescence lifetime measurements were performed by time-correlated single-photon counting with the same FLS 1000 fluorimeter. The raw lifetime data and subsequent lifetime fits were performed with our home written software PIE analysis with Matlab (PAM). PAM is a stand-alone program (MATLAB; The MathWorks GmbH) for integrated and robust analysis of fluorescence ensemble, single-molecule, and imaging data. The average fluorescence lifetime (τ_{avg}) values were obtained by using the equation below:

$\tau_{avg} = (\sum_{i=1}^{n} \alpha_i \tau_i^2)/(\sum_{i=1}^{n} \alpha_i \tau_i)$ (Eqn. 2)

where τ_i is the individual lifetime with corresponding amplitude α_i.

UV-vis measurements: Eu-MDH was stored at -80 °C in PIPES buffer (10 mM, pH 7.2) supplemented with 1 mM MeOH and was re-buffered either in NaCl (100 mM, pH 6.5) or in NaCl with 1 mM MeOH for the experiments. Washing procedure of the protein was required due to re-buffering but also to remove degraded protein, pre-used storage buffer, residual methanol, formaldehyde and formic acid from the enzyme. Eu-MDH was transferred to an equilibrated spin filter (Amicon Ultra, 30 kDa MWCO, rinsed twice with MilliQ water and then with the required NaCl solution) with tenfold surplus of the requested buffer and centrifuged (4 °C, 4500 rpm, 15 min). Once the initial volume of the enzyme sample was reached, the procedure was repeated by adding a tenfold surplus of buffer. Measurements were performed on Agilent Cary 60 UV/Vis spectrophotometer connected to a Peltier element with a commercially available aquarium pump. Spectra were recorded in a micro quartz glass cuvette (Hellma) with path length of 10 mm after 2 min of equilibrium time and manual mixing by pipetting at the set temperature. For all spectra, blank buffer sample was subtracted prior to all measurements as well as a baseline correction to 675 nm was performed. To ensure a comparability of the different treated samples, all spectra were normalized to total protein peak at 280 nm.

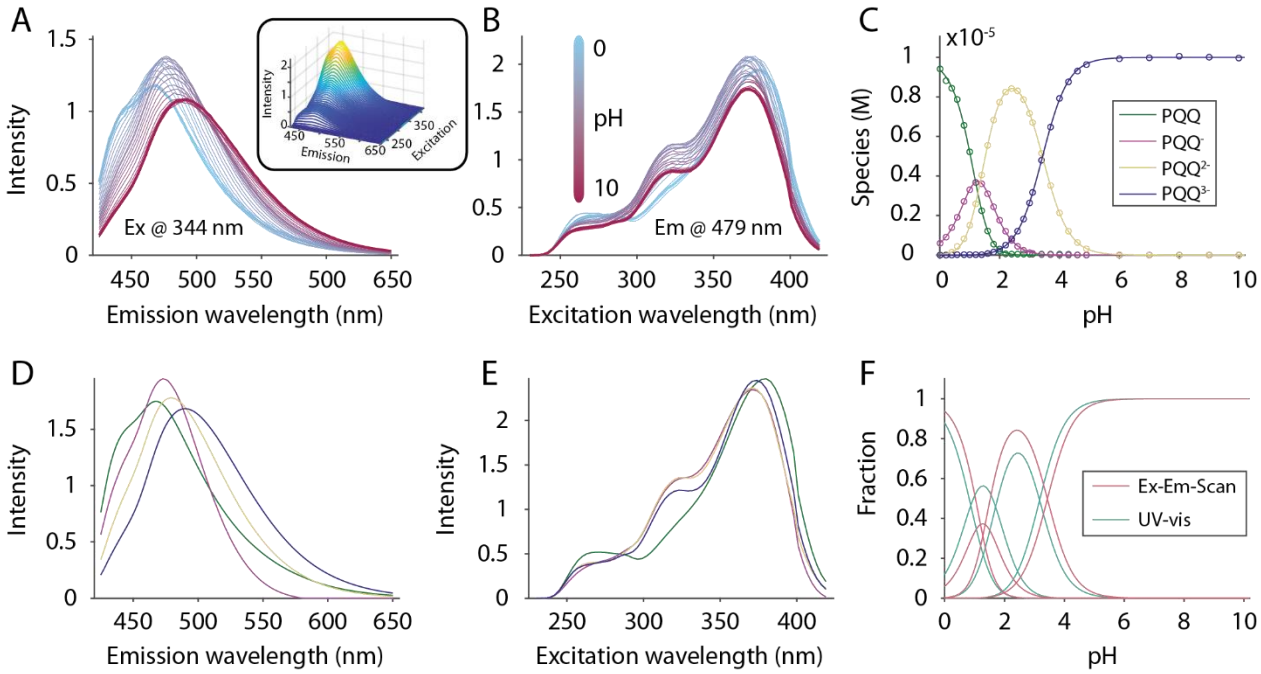

Figure S1 Fluorescence excitation–emission scans of a pH series of PQQ. A complete excitation–emission spectrum of PQQ was recorded from each pH value (inset). Changes in emission (A) and excitation (B) spectra at specific wavelengths demonstrate the sensitivity of the fluorescence on protonation state. Deconvolution using PARAFAC revealed the distribution (C), emission spectra (D) and excitation spectra (E) of four different protonation states. The corresponding pK_a values are pK_{a1} = 1.2, pK_{a2} = 1.35, pK_{a3} = 3.4. This is in good agreement with the extracted values from UV-vis, which is proven by similar calculated speciation based on the pK_a values (F)

Water Adduct Equilibrium: Formation of the water adduct can be expressed by the following reaction equation:

$$\mathrm{PQQ} + \mathrm{H_2O} \rightleftharpoons \mathrm{PQQ{\cdot}H_2O} \quad \text{(Eqn. 3)}$$

Since water acts as both solvent and reactant and is thus in large excess, its activity can be assumed to remain constant during the reaction and to be equal to unity, and since the overall concentration of PQQ is sufficiently low, the law of mass action can be written as:

$$K_\mathrm{h} = \frac{[\mathrm{PQQ{\cdot}H_2O}]}{[\mathrm{PQQ}]} \quad \text{(Eqn. 4)}$$

where K_h denotes the equilibrium constant for the hydration reaction, and the square brackets denote (relative) concentrations determined from spectral deconvolution.

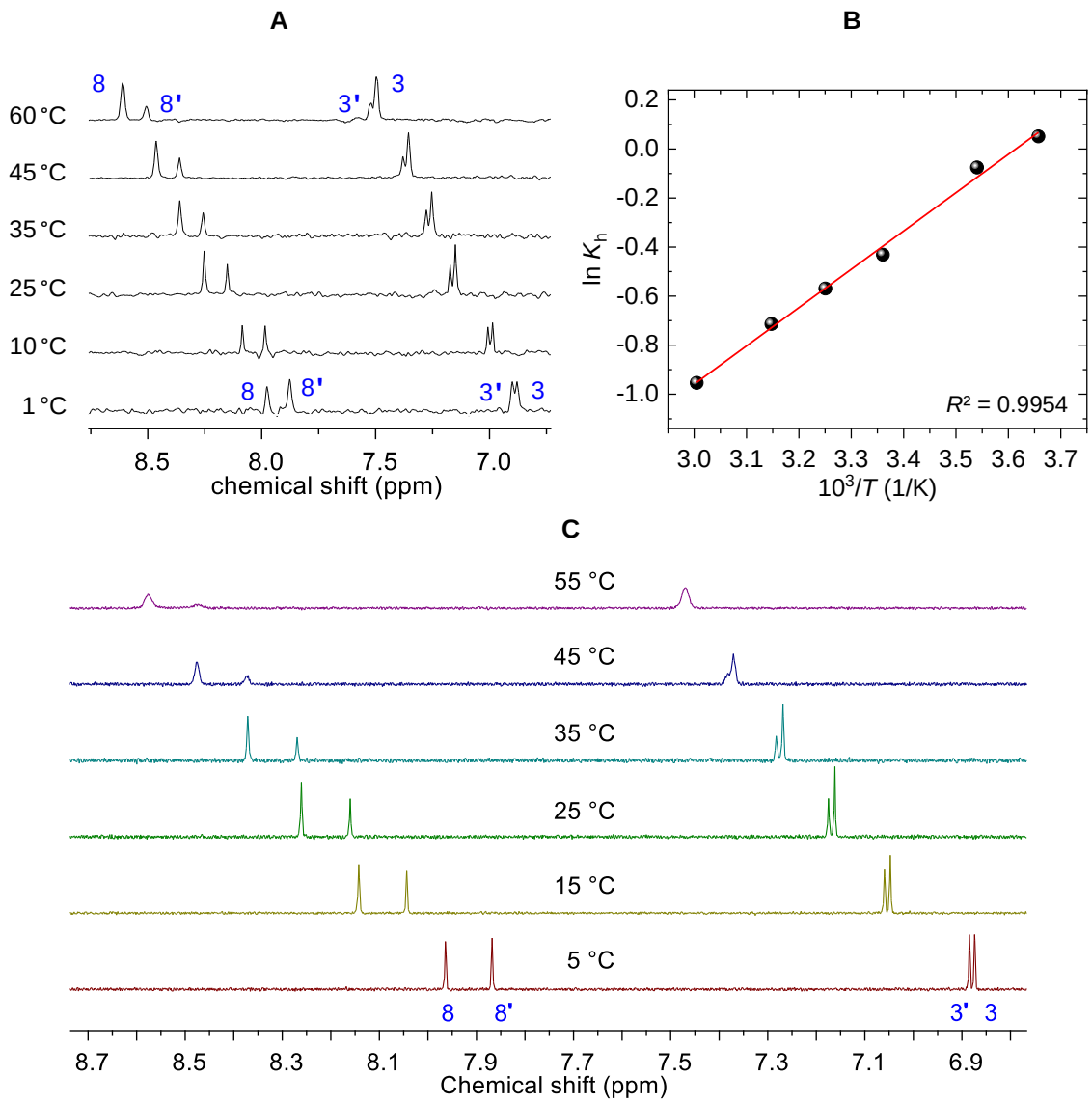

Figure S2. Quantitative ^{1}H NMR spectra of 1 mM PQQ in 100 mM NaCl pH 4.0 90/10 (v/v) H_2O/D_2O solution acquired at different temperatures (A) and the corresponding van 't Hoff plot (B), where ln K_h was determined as shown in Eqn. 5. Note the unchanged relative position of the components' signals as indicated for the limiting spectra. (C) Temperature-dependent ^{1}H NMR spectra of 0.5 mM PQQ in 100 mM NaCl pD 6.8 D_2O solution together with signal assignment, with prime notation for PQQ•H_2O. Note that for the given pD conditions both forms occur solely as their tri-anionic species.

By means of the relationship

$$\ln K_\mathrm{h} = \frac{-\Delta_\mathrm{h}H}{R}\frac{1}{T} + \frac{\Delta_\mathrm{h}S}{R} \quad \text{(Eqn. 5)}$$

enthalpy and entropy of hydration, Δ_hH and Δ_hS respectively, can be calculated. R denotes the molar gas constant (~ 8.3145 J mol^{-1} K^{-1}) and T represents the absolute temperature.

The absolute concentration appears to have only a minor influence as concluded from K_h determination for PQQ total concentrations of 0.5 mM (black data point) and 5 mM (red data point; corresponding red spectrum as inset in Figure 5) at pH 6.8. PQQ's speciation is directly associated with decreasing electrophilicity of C(5). Starting at high [H^+], equivalent to low pH, PQQ dominates as the neutral $H_3PQQ_{(aq)}$ species. Upon increasing pH, successive deprotonation yields H_2PQQ^-, $HPQQ^{2-}$, and finally PQQ^{3-} (for the considered pH range up to pH 10; Figure 5). This stepwise deprotonation is accompanied by an increase of negative charges, which is well mirrored by the increasing shielding of all ^1H nuclei, corresponding to decreasing chemical shift values (Figure 2 and inset in Figure 6). Increasing the number of negative charges in the PQQ molecule reduces the electrophilicity of C(5), *i.e.* increases its local electron density, thereby reducing the affinity to be attacked by a nucleophile. Consequently, increasing pH shifts the equilibrium towards PQQ.

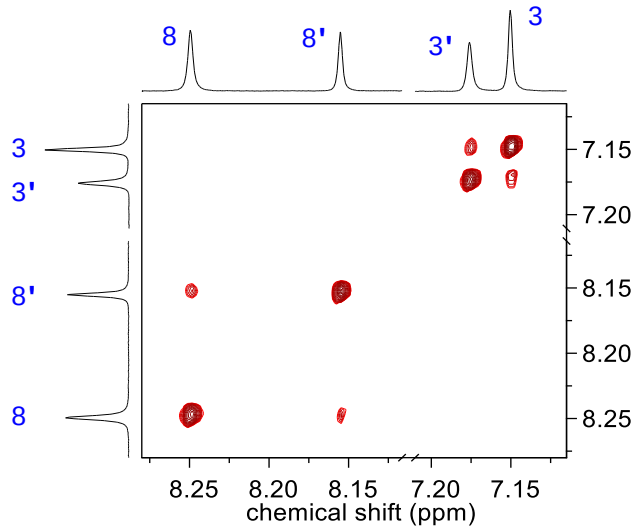

Figure S3 Exemplary quantitative H,H-EXSY spectrum of a 10 mM PQQ aqueous solution containing 10% D_2O at pH 4.3, acquired with 1500 ms mixing time at 25 °C. Signal labeling is according to the atomic numbering in Figure 1, with prime notation for PQQ•H_2O.

The correlation (off-diagonal) signals in Figure S3 unambiguously demonstrate the chemical exchange between the two PQQ forms of interest. According to Perrin and Dwyer,[192] evaluation of the volume integrals of the EXSY spectrum allows for the extraction of the rate constant.

$$k_{\mathrm{ex}} = \frac{1}{t_{\mathrm{mix}}} \ln \frac{q+1}{q-1} \quad \text{(Eqn. 6)}$$

$$\text{where } q = 4x_{\mathrm{A}}x_{\mathrm{B}}(I_{\mathrm{AA}} + I_{\mathrm{BB}})/(I_{\mathrm{AB}} + I_{\mathrm{BA}}) - (x_{\mathrm{A}}x_{\mathrm{B}})^2 \quad \text{(Eqn. 7)}$$

and where t_{mix} is the mixing time, x_i is the mole fraction of form i, and I_{ii} and I_{ij} are the volume integrals of the diagonal and the off-diagonal signals, respectively. Taking the EXSY volume integrals obtained for t_{mix} = 1500 ms (Figure S3) and t_{mix} = 500 ms (not shown), and the mole

fractions obtained from quantitative 1D-^{1}H measurements, the rate constant for the chemical exchange k_{ex}(25 °C) = (2.0 ± 0.1) × 10^{-1} s^{-1}.

From

$$K_h = r_{hyd}/r_{deh} \quad \text{(Eqn. 8)},$$

$$x_{PQQ}\, r_{hyd} = x_{PQQ\cdot H2O}\, r_{deh} \text{ (Eqn. 9), and}$$

$$k_{ex} = r_{hyd} + r_{deh} \text{ (Eqn. 10)}$$

follows that

$$r_{hyd} = x_{PQQ\cdot H2O}\, k_{ex} \text{ (Eqn. 11) and}$$

$$r_{deh} = x_{PQQ}\, k_{ex} \text{ (Eqn. 12)}$$

where r_{hyd} and r_{deh} are the apparent rates of the hydration (forward) and dehydration (backward) reaction, respectively.

The 2D-EXSY is a quite time-consuming experiment – in this case about three days owing to quantitative acquisition conditions, the rather long spin-lattice relaxation times (T_1) (*cf.* Table S1), the slow exchange rate and the thus required long mixing times. Therefore, another approach was used for exchange rate determination, *viz*. the one-dimensional 1D-EXSY, applying a double pulsed field gradient spin echo sequence for narrow band excitation. After selective excitation of 8-H (↯), the peak evolving from dynamic exchange, 8', corresponding to the correlation signal in the 2D experiment, will rise in intensity for increasing mixing times, see Figure S4.

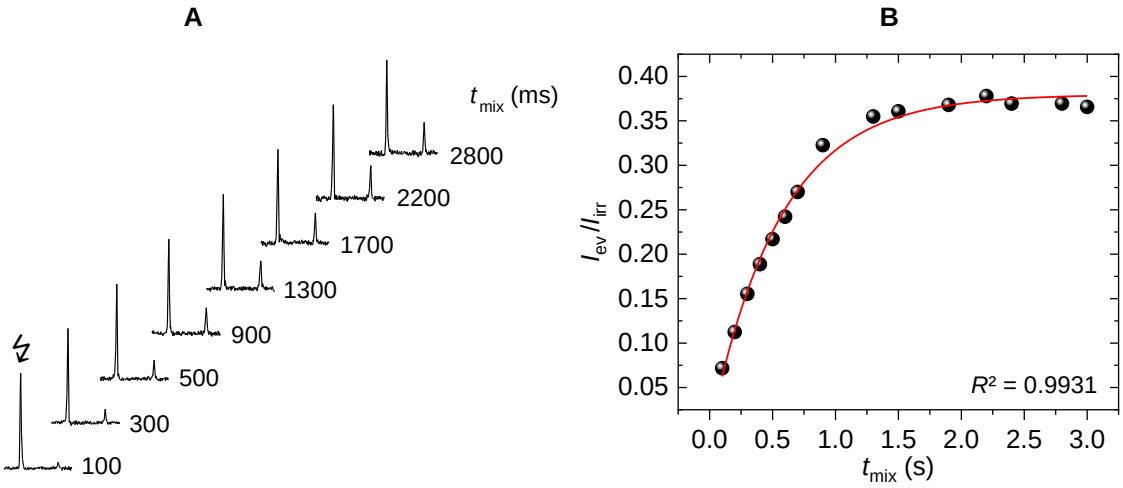

Figure S4. (A) Exemplary selective 1D-EXSY spectra of the 10 mM pH 4.3 PQQ sample acquired at 60 °C for different mixing times, t_{mix}, normalized to the signal being irradiated (↯). (B) Ratio of the intensities of the evolved and irradiated signal in dependence of applied mixing time.

The obtained spectra were integrated by spectral deconvolution and the ratio of the integrals of the evolving and irradiated signals (I_{ev}/I_{irr}) plotted against the respectively applied mixing times. For exchange rate constant determination, the data were fitted according to:

$$\frac{I_{\mathrm{ev}}}{I_{\mathrm{irr}}} = \left(\frac{I_{\mathrm{ev}}}{I_{\mathrm{irr}}}\right)_0 (1 - e^{-k_{\mathrm{ex}} t_{\mathrm{mix}}})$$ (Eqn. 13)

where $(I_{ev}/I_{irr})_0$ is the respective ratio without irradiation, corresponding to K_h for the given temperature. The thus calculated exchange rate constant, k_{ex}(60 °C), amounts to (18.0 ± 0.4) × 10^{-1} s^{-1}. This value is considered reliable since the method for determination is very robust, and is in excellent agreement with the related value determined from 2D-EXSY. Corresponding figures for 35 °C and 45 °C were obtained analogously.

As per *transition state theory*, rate constants determined at different temperatures allow for the calculation of Gibbs energy of activation $\Delta G^{\ddagger}$, as well as the so-called activation parameters enthalpy and entropy of activation, $\Delta H^{\ddagger}$ and $\Delta S^{\ddagger}$, respectively, which are related corresponding to

$$k_{\mathrm{ex}}(T) = \frac{k_{\mathrm{B}} T}{h} \exp\left\{\frac{-\Delta H^{\ddagger}}{RT}\right\} \exp\left\{\frac{-\Delta S^{\ddagger}}{R}\right\}$$ (Eqn. 14)

where h is Planck's constant (~ 6.626 × 10^{-34} J s), and k_B is the Boltzmann constant (~ 1.381 × 10^{-23} J K^{-1}).

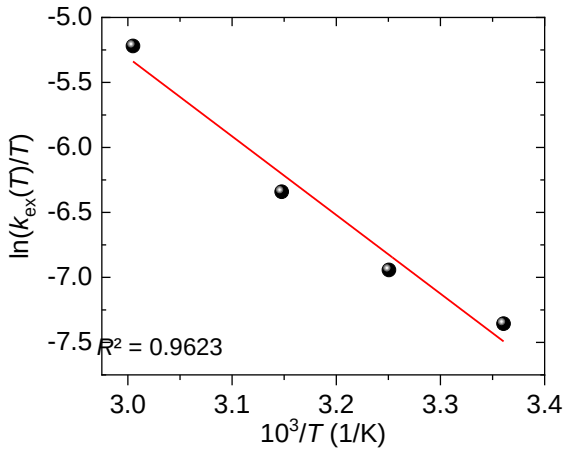

Figure S5. Eyring plot obtained from temperature-dependent exchange rates as determined by exchange spectroscopies for the 10 mM PQQ (100 mM NaCl) pH 4.3 solution.

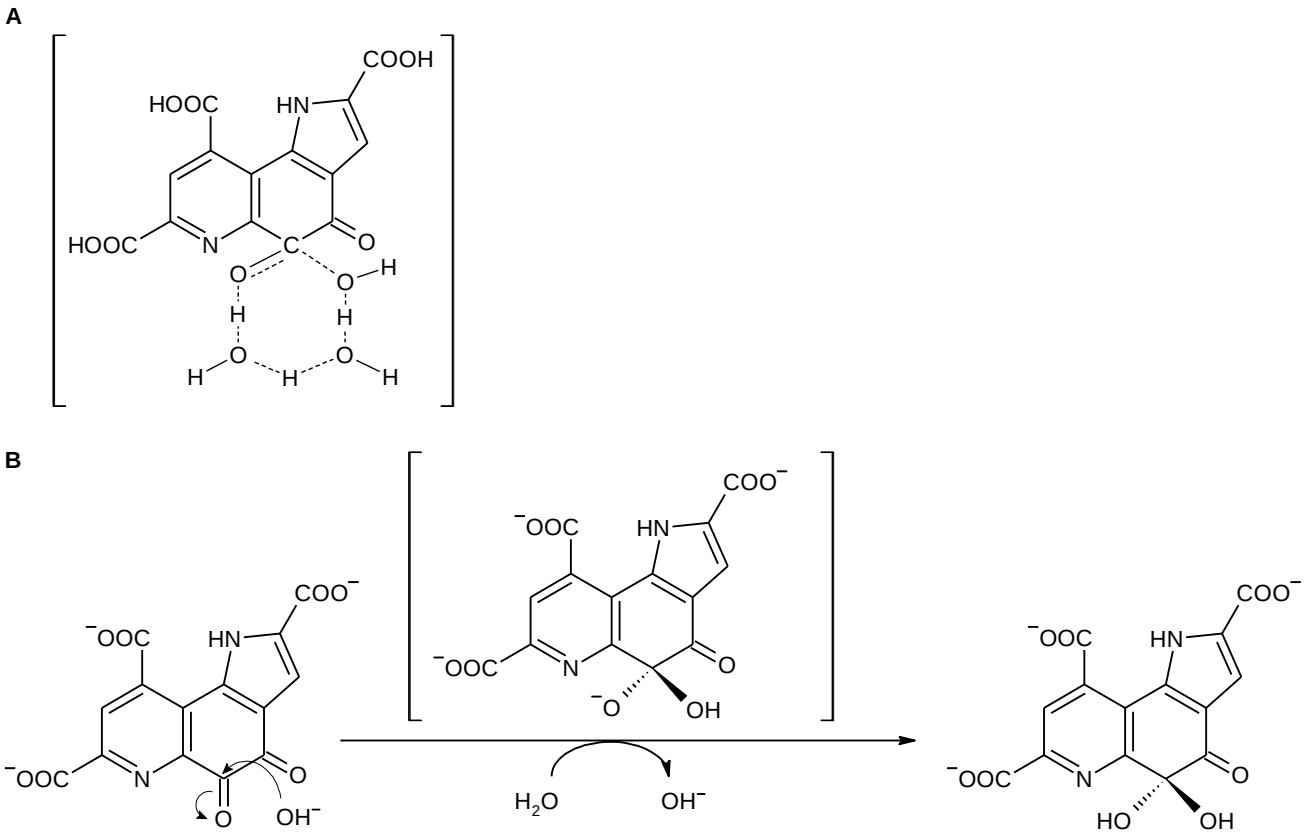

Figure S6. Suggested structure of the highly ordered cyclic hydrogen-bonded transition state for water adduct formation to carbon C(5) for sufficiently low pH where water is the nucleophile (A), and sketched reaction for water adduct formation to carbon C(5) via tetrahedral transition state where the hydroxide ion acts as the nucleophile (B).

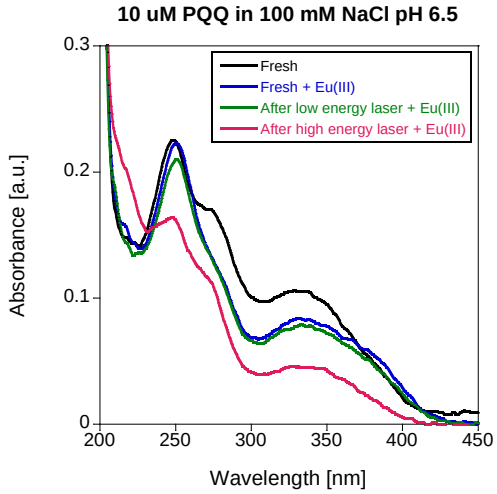

Figure S7. Uv/vis spectra of PQQ with added $EuCl_3$ before and after irradiation with a high or low energy laser. Spectra were collected at room temperature in 100 mM NaCl pH 6.5.

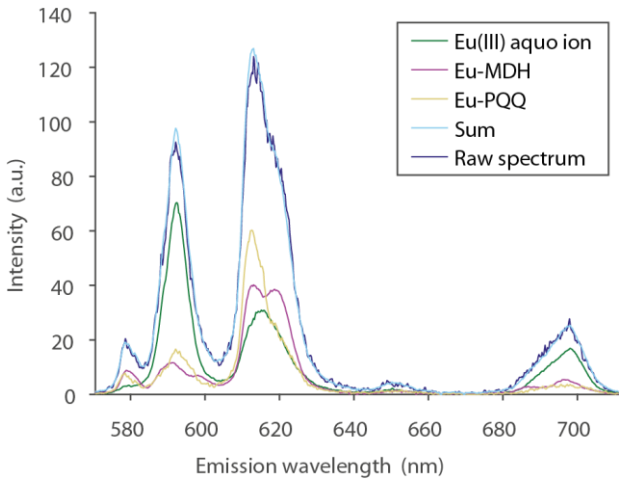

FigureS8. Example of the deconvolution of the emission spectrum of 40 µM $EuCl_3$. The raw spectrum (dark blue) is well reproduced by the sum (light blue) of the individual species (green, magenta, yellow).

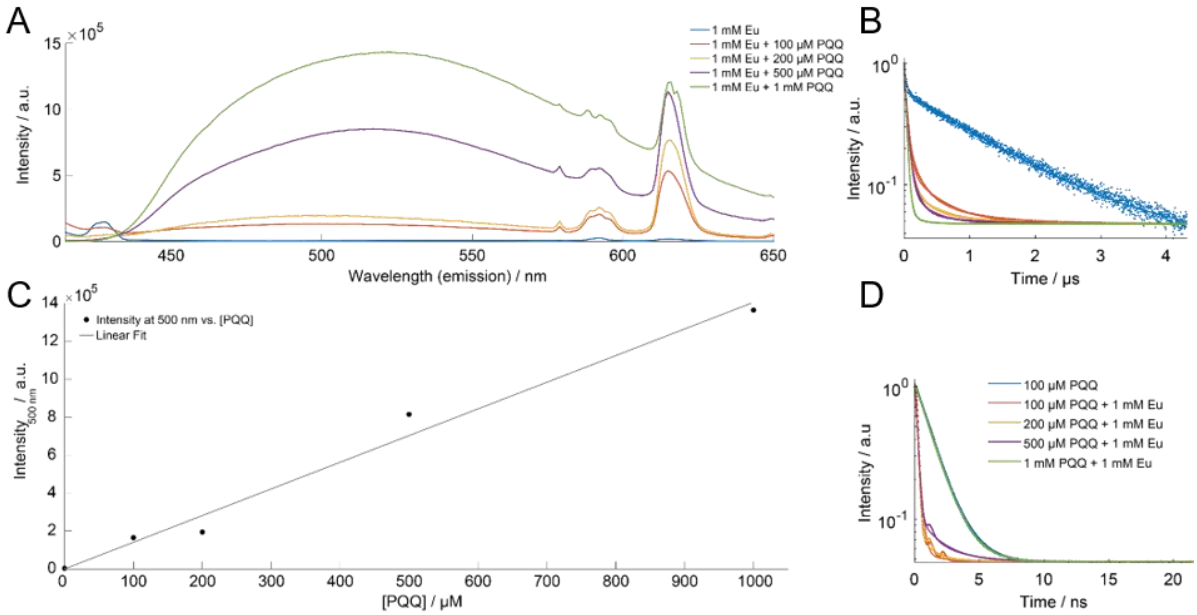

Figure S9. Titration of PQQ to 1 mM Eu in 20 mM PIPES. A) shows the obtained steady state measurement. B) shows the lifetime decay on the µs timescale. C) PQQ intensity (monitored at 500 nm) vs. [PQQ] and D) shows the ns timescale lifetime of PQQ in this titration series.

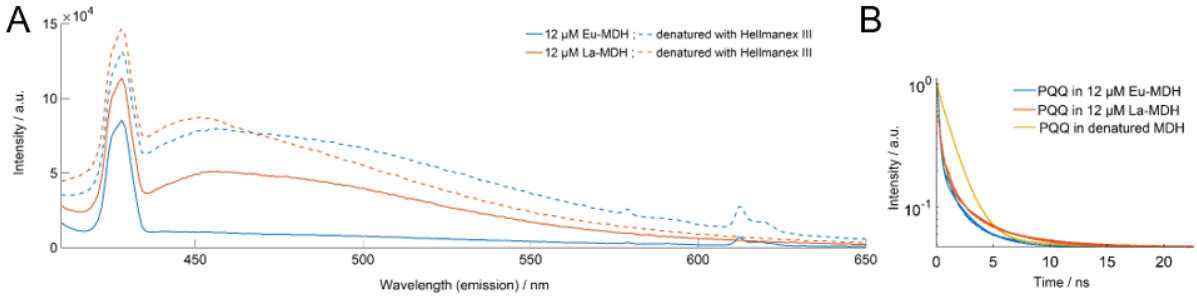

Figure S10. Fluorescence of the Eu-MDH and La-MDH enzyme in 20 mM PIPES before and after denaturation. A) shows the steady state measurement and B) shows the ns timescale lifetime of PQQ in the Eu-MDH and La-MDH before and after denaturation.

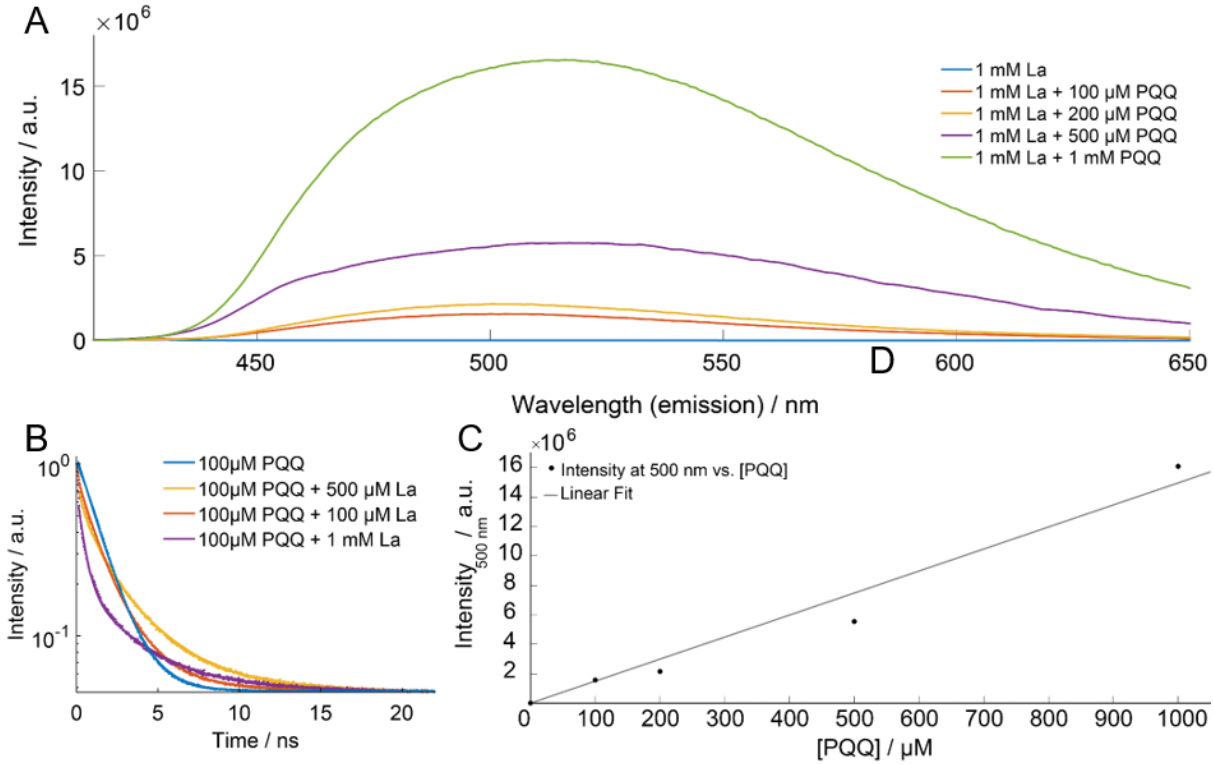

Figure S11. Titration of PQQ to 1 mM La in 20 mM PIPES. A) shows the obtained steady state measurement. B) shows the ns timescale lifetime of PQQ in this titration series and C) PQQ intensity (monitored at 500 nm) vs. [PQQ].

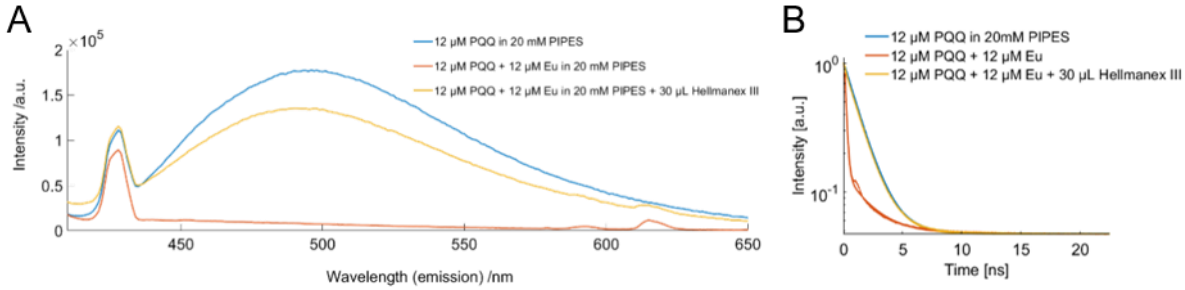

Figure S12. PQQ in 20 mM PIPES upon the addition of Eu and afterwards Hellmanex, as a control tested under similar concentrations to the Eu-MDH. A) shows the steady state measurement and B) shows the ns timescale lifetime of PQQ under the different conditions of this measurements.

References

[1] B. Jahn, A. Pol, H. Lumpe, T. R. M. Barends, A. Dietl, C. Hogendoorn, H. J. M. Op den Camp, L. J. Daumann, *Chembiochem* **2018**, *19*, 1147-1153.

[2] H. Lumpe, L. J. Daumann, *Inorg. Chem.* **2019**, *58*, 8432-8441.

[3] a) P. Gans, A. Sabatini, A. Vacca, *Talanta* **1996**, *43*, 1739-1753; b) P. Gans, A. Sabatini, A. Vacca, *Ann. chim* **1999**, *89*, 45-49.

[4] C. Andersson, R. Bro, *Chemom. Intell. Lab. Syst.* **2000**, *52*, 1-4.

[5] B. Drobot, A. Bauer, R. Steudtner, S. Tsushima, F. Bok, M. Patzschke, J. Raff, V. Brendler, *Anal. Chem.* **2016**, *88*, 3548-3555.

[6] a) W. D. Horrocks, D. R. Sudnick, *J. Am. Chem. Soc.* **1979**, *101*, 334-340; b) T. Kimura, Y. Kato, *J. Alloys Compd.* **1998**, *275–277*, 806-810; c) P. P. Barthelemy, G. R. Choppin, *Inorg. Chem.* **1989**, *28*, 3354-3357; d) T. Kimura, G. R. Choppin, *J. Alloys Compd.* **1994**, *213-214*, 313-317.
[7] W. Schrimpf, A. Barth, J. Hendrix, D. C. Lamb, *Biophys. J.* **2018**, *114*, 1518-1528.
[8] C. L. Perrin, T. J. Dwyer, *Chem. Rev.* **1990**, *90*, 935-967.